Pacific National University

NUCLEAR THEORY IN THE SUPERCOMPUTING ERA – 2014 (NTSE-2014)

International Conference

Khabarovsk, Russia, June 23–28, 2014

PROCEEDINGS

Editors A. M. Shirokov and A. I. Mazur

Khabarovsk, Russia
Pacific National University
2016

УДК 539.14
ББК В38я431
N 91

N 91 **Nuclear** Theory in the Supercomputing Era – 2014 (NTSE-2014): International Conference. Khabarovsk, Russia, June 23–27, 2014. Proceedings. Eds. A. M. Shirokov and A. I. Mazur. — Khabarovsk, Russia: Pacific National University, 2016. — 259 p.
ISBN 978-5-7389-2023-3

The primary motivation for the series of International Conference "Nuclear Theory in the Supercomputing Era (NTSE)" (http://ntse.khb.ru) was the rapid growth of supercomputers and the impact they, along with theoretical and algorithmic developments, are having on nuclear theory. The first conferences in this series, "Horizons of Innovative Theories, Experiments, and Supercomputing in Nuclear Physics" (HITES-2012) and NTSE-2012, were hosted respectively by the Louisiana State University in New Orleans, Louisiana, USA in June 4–7, 2012 (http://www.phys.lsu.edu/hites2012) and by the Pacific National University, Khabarovsk, Russia in June 18–22, 2012 (http://www.ntse-2012.khb.ru). These conferences were proceeded later under the common title NTSE. The NTSE-2013 (http://ntse.khb.ru/2013) was hosted by the Iowa State University, Ames, Iowa, USA in May 13–17, 2013 and celebrated the 70th birthday of Professor James Vary.

These proceedings includes talks presented at the NTSE-2014 Conference hosted by the Pacific National University, Khabarovsk, Russia in June 23–27, 2014. The Conference was sponsored by the Pacific National University, Khabarovsk, Russia and by the Russian Foundation for Basic Research.

The contributions to the NTSE-2014 Proceedings published here, are also available online at http://www.ntse-2014.khb.ru/proceedings/.

УДК 539.14
ББК В38я431

ISBN 978-5-7389-2023-3

Preface

The International Conference on Nuclear Theory in the Supercomputing Era — 2014 (NTSE-2014) brought together experts in nuclear theory and high-performance computing in Khabarovsk, Russia, from June 23 to June 27, 2014. This conference series was started in 2012 by the NTSE-2012 and HITES-2012 conferences which were proceeded later under the common title NTSE. The NTSE conferences focus on forefront challenges in physics, namely the fundamentals of nuclear structure and reactions, the origin of the strong inter-nucleon interactions from QCD, and computational nuclear physics with leadership class supercomputer facilities to provide forefront simulations leading to new discoveries.

The conference welcomed many young scientists, including graduate students in nuclear physics, computational science and applied mathematics. All participants together made the conference a great success.

The conference topics,

(1) *Ab initio* nuclear structure;
(2) Microscopic approaches to nuclear reactions;
(3) Origin and properties of the strong interactions; and
(4) Computational science and applied mathematics,

reflect current world-wide research interests and encompass a broad area of fundamental physics and high-performance computing.

We would like to express our appreciation to all participants of the NTSE-2014 conference, to all contributors to these proceedings, to all members of the Scientific Advisory Committee and to the NTSE-2014 sponsors including Pacific National University and the Russian Foundation for Basic Research.

The organizing committee:

Sergey Ivanchenko (Chair), Pacific National University, Russia
Dana Basharymova, Pacific National University, Russia
Leonid Blokhintsev (Vice Chair), Moscow State University, Russia
Sergey Burkov, Pacific National University, Russia
Alexander Mazur (Scientific secretary), Pacific National University, Russia
Evgeny Mazur, Pacific National University, Russia
Pieter Maris, Iowa State University, USA
Andrey Shirokov (Vice Chair), Moscow State University, Russia
James Vary (Vice Chair), Iowa State University, USA
Xingbo Zhao, Iowa State University

NTSE-2014 Scientific Advisory Committee:

- **James Vary (Chair)**, Iowa State University, USA
- **Bruce Barrett**, University of Arizona, USA
- **Leonid Blokhintsev**, Moscow State University, Russia
- **Stanley J. Brodsky**, SLAC-Stanford, USA
- **Ümit Çatalyürek**, The Ohio State University, USA
- **Mark Caprio**, University of Notre Dame, USA
- **David Dean**, Oak Ridge National Laboratory, USA
- **Jerry Draayer**, Louisiana State University, USA
- **Victor Efros**, Russian Research Centre Kurchatov Institute, Russia
- **Evgeny Epelbaum**, University of Bochum, Germany
- **Morten Hjorth-Jensen**, University of Oslo, Norway and Michigan State University, USA
- **Youngman Kim**, Institute for Basic Science, South Korea
- **Ruprecht Machleidt**, University of Idaho, USA
- **Pieter Maris**, Iowa State University, USA
- **Alexander Mazur**, Pacific National University, Russia
- **Alexander Motovilov**, Joint Institute for Nuclear Research, Russia
- **Petr Navrátil**, TRIUMF, Canada
- **Esmond Ng**, Lawrence Berkeley National Laboratory, USA
- **W. Erich Ormand**, Lawrence Livermore National Laboratory, USA
- **Takaharu Otsuka**, University of Tokyo, Japan
- **Wayne Polyzou**, University of Iowa, USA
- **Jianwei Qiu**, Brookhaven National Laboratory, USA
- **Sophia Quaglioni**, Lawrence Livermore National Laboratory, USA
- **Andrey Shirokov**, Moscow State University, Russia
- **Masha Sosonkina**, Old Dominion University, USA

NTSE-2014 Organizing Committee:

- **Sergey Ivanchenko (Chair)**, Pacific National University, Russia
- **Dana Basharymova**, Pacific National University, Russia
- **Leonid Blokhintsev (Vice Chair)**, Moscow State University, Russia
- **Sergey Burkov**, Pacific National University, Russia
- **Alexander Mazur (Scientific secretary)**, Pacific National University, Russia
- **Evgeny Mazur**, Pacific National University, Russia
- **Pieter Maris**, Iowa State University, USA
- **Andrey Shirokov (Vice Chair)**, Moscow State University, Russia
- **James Vary (Vice Chair)**, Iowa State University, USA
- **Xingbo Zhao**, Iowa State University, USA

Program of International Conference on Nuclear Theory in the Supercomputing Era — 2014 (NTSE-2014)

Sunday, June 22

Arrival

3:00 pm	*Picnic*

Monday, June 23

Conference Hall

9:30–2:50pm	*Registration*
10:00–10:50am	*Conference opening*

10:50–11:20am	*Coffee break*

Chair: Yutaka Utsuno

11:20–12:10pm	**Takashi Nakatsukasa** Time-dependent density-functional calculation of nuclear response functions
12:10–1:00pm	**Jun Terasaki** Effects of QRPA correlations on nuclear matrix elements of neutrinoless double-beta decay through overlap matrix

1:00–2:00pm	*Lunch break*

Chair: Kazuhiro Yabana

2:00–2:50pm	**Junchen Pei** Exotic halos and collective excitations in weakly-bound deformed nuclei

2:50–3:10pm	*Coffee break*

Room 201

Chair: Andrey Shirokov

3:10–5:00pm	Discussions, additional questions to speakers

6:00 pm	*Welcome party*

Tuesday, June 24

Conference Hall

Chair: Alexander Motovilov

9:00–9:50am	**Yutaka Utsuno** Large-scale shell-model studies for exotic nuclei: probing shell evolution
9:50–10:40am	**Alexander Volya** Computational approaches to many-body dynamics of unstable nuclear systems

10:40–11:10am	*Coffee break*

Chair: Takashi Abe

11:10–12:00pm	**Kazuhiro Yabana** Cluster structures of light nuclei superposing multiple Slater determinants
12:00–12:50pm	**Yurii Tchuvil'sky** Study of cluster reactions in advanced shell model approaches

1:00–2:00pm	*Lunch break*

Chair: Takashi Nakatsukasa

2:00–2:50pm	**Furong Xu** From Gogny force to shell-model calculations
2:50-3:40pm	**Tomáš Dytrych** Emergence of simple patterns in complex atomic nuclei from first principles
3:40-4:10pm	**Andrey Chibisov** *Ab initio* investigation of oxygen absorption by titanium nanoparticles

4:10–4:30pm	*Coffee break*

Room 201

Chair: Jun Terasaki

4:30–6:10pm	Discussions, additional questions to speakers

Wednesday, June 25

Conference Hall

Chair: Evgeny Epelbaum

9:00–9:50am	**Leonid Blokhintsev** Vertex Functions and Asymptotics of Nuclear Bound-State Wave Functions
9:50–10:40am	**Alexander Motovilov** Bounds on variation of the spectrum and spectral subspaces of a few-body Hamiltonian

10:40–11:10am	*Coffee break*

Chair: Furong Xu

11:10–12:00pm	**Charlotte Elster** The Coulomb Problem in Momentum Space without Screening
12:00–12:50pm	**Sergey Yurev** Three-nucleon calculations within Bethe-Salpeter approach with separable kernel

1:00–2:00pm	*Lunch break*

Chair: Kimiko Sekiguchi

2:00–2:50pm	**Konstantin Kouzakov** Problems of theoretical interpretation of COLTRIMS results on ionization of helium by fast bare-ion impact
2:50-3:10pm	**Maxim Aleshin** Quasi-Sturmian functions in the continuum spectrum problems
3:10-4:00pm	**Sergey Zaytsev** Convoluted quasi-Sturmians basis in Coulomb three-body problems

4:00–4:20pm	*Coffee break*

Room 201

Chair: Tomáš Dytrych

4:20–6:00pm	Discussions, additional questions to speakers

Thursday, June 26

Conference Hall

Chair: Leonid Blokhintsev

9:00–9:50am	**James Vary** *Ab Initio* no core shell model — recent results and future prospects
9:50–10:40am	**Takashi Abe** No-core Monte Carlo shell model in light nucle

10:40–11:00am	*Coffee break*

Chair: Ruprecht Machleidt

11:00–11:50am	**Andrey Shirokov** Recent results obtained with JISP16
11:50–12:40pm	**Alexander Mazur** J-matrix analysis of resonant states in the shell model
12:40–1:00pm	**Igor Mazur** J-matrix analysis of resonant states in the shell model: charged particles

1:00–2:00pm	*Lunch break*

Chair: Alexander Volya

2:00–2:50pm	**Ik Jae Shin** *Ab initio* study of natural and unnatural parity states of ^{6}Li
2:50-3:40pm	**Nikolay Khokhlov** Electromagnetic deuteron form factors in point form of relativistic quantum mechanics

3:40–4:00pm	*Coffee break*

Room 201

Chair: Junchen Pei

4:00–5:50pm	Discussions, additional questions to speakers

6:00 pm	*Conference dinner*

Friday, June 27

Conference Hall

Chair: Charlotte Elster

9:00–9:50am	**Kimiko Sekiguchi** Approach to three nucleon forces from experiment
9:50–10:40am	**Evgeny Epelbaum** Chiral nuclear forces: State of the art and future perspectives

10:40–11:00am	*Coffee break*

Chair: James Vary

11:00–11:50am	**Ruprecht Machleidt** Chiral EFT and nuclear forces: Are we in trouble?
11:50–1:30pm	Discussions, additional questions to speakers *(Room 201)*
1:30–2:00pm	**Conference closing** *(Conference Hall)*

1:00–2:00pm	*Lunch break*

3:00–5:00 pm	*Excursion*

5:00 pm	*Picnic*

Contents

International Conference

NUCLEAR THEORY IN THE SUPERCOMPUTING ERA – 2014 (NTSE-2014)

INVITED TALKS

Time-Dependent Density-Functional Calculation of Nuclear Response Functions

Takashi Nakatsukasa

Center for Computational Sciences, University of Tsukuba, Tsukuba 305-8577, Japan
RIKEN Nishina Center, Wako 351-0198, Japan

Abstract

Basic issues of the time-dependent density-functional theory are discussed, especially a real-time calculation of linear response functions. Some remarks on the derivation of the time-dependent Kohn–Sham equations and on the numerical methods are given.

Keywords: *Time-dependent density-functional theory; time-dependent variational principle; strength function*

1 Introduction

The time-dependent density-functional theory (TDDFT) provides us with a practical tool to study quantum dynamics of many-body systems. It is conceptually very similar to the one known as the time-dependent Hartree–Fock (TDHF) theory with a density-dependent effective interaction in nuclear physics [1]. Although it is much more feasible than directly treating many-body wave functions of many-particle systems, the studies of full dynamics taking into account both the mean-field and the pairing correlations are still computationally highly challenging, even at present. In this paper, for simplicity, I will concentrate the discussion on the time-dependent Kohn–Sham (TDKS) equations, without the Bogoliubov-type extension including pair densities.

There is a number of recent developments in the studies of nuclei with the density functional approaches. For these, there are recent review papers [2–5]. Thus I do not intend here to review all these developments. Instead I would like to present some issues which are not well addressed in published articles. The first issue presented in Sec. 2, is a derivation of the time-dependent Kohn–Sham equations based on the time-dependent variational principle. Exactly the same argument is applicable to the variational derivation of the time-dependent Hartree–Fock equations. Especially, I would like to clarify that the gauge degrees of freedom naturally emerge in the proper derivation. This may be trivial to some readers, however, I think it is not so for non-practitioners. It may be also useful for students. Then, in Sec. 3, I will present some practical issues on numerical calculations such as the choice of the gauge functions, some speed-up techniques, etc.

Proceedings of the International Conference 'Nuclear Theory in the Supercomputing Era — 2014' (NTSE-2014), Khabarovsk, Russia, June 23–27, 2014. Eds. A. M. Shirokov and A. I. Mazur. Pacific National University, Khabarovsk, Russia, 2016, p. 15.

http://www.ntse-2014.khb.ru/Proc/Nakatsukasa.pdf.

2 Remarks on the time-dependent Kohn–Sham equations

2.1 Time-dependent variational principle

It is well-known that the time-dependent Kohn–Sham equations can be obtained using the time-dependent variational principle [6]. In literature, we often find the following arguments: Starting from the action integral

$$S \equiv \int_{t_i}^{t_f} \left\{ \langle \Psi_D(t)| i\frac{\partial}{\partial t} |\Psi_D(t)\rangle - E[\rho(t)] \right\} dt \tag{1}$$

$$= \int_{t_i}^{t_f} \left\{ \sum_{i=1}^{N} \langle \psi_i(t)| i\frac{\partial}{\partial t} |\psi_i(t)\rangle - E[\rho(t)] \right\} dt, \tag{2}$$

the stationary action principle, $\delta S = 0$, leads to the time-dependent Kohn–Sham (TDKS) equations

$$i\frac{\partial}{\partial t}|\psi_i(t)\rangle = h[\rho(t)]|\psi_i(t)\rangle, \quad i = 1, \cdots, N. \tag{3}$$

Here, $E[\rho]$ is the energy density functional and $|\Psi_D(t)\rangle$ is the time-dependent Slater determinant,

$$|\Psi_D(t)\rangle = \frac{1}{\sqrt{N!}} \det\{|\psi_i(t)\rangle_j\}_{i,j=1,\cdots,N}. \tag{4}$$

The Kohn–Sham (single-particle) Hamiltonian is formally defined by

$$h[\rho]|\psi_i\rangle = \frac{\delta E}{\delta \langle \psi_i|}. \tag{5}$$

In the case of TDHF with an effective Hamiltonian, the energy density functional is given by the expectation value of the Hamiltonian as $E[\rho(t)] = \langle \Psi_D(t)|H|\Psi_D(t)\rangle$. In general, $E[\rho]$ can be a more general functional of one-body density ρ in the TDDFT.

Since the TDKS equations (3) are so common in literature, I think, many people take them for granted. However, it is somewhat strange that we have reached the equations which can uniquely determine the Kohn–Sham orbitals, because the Slater determinant $|\Psi_D(t)\rangle$ is invariant under a unitary transformation among the occupied orbitals. Namely, the same Slater determinant $|\Psi_D(t)\rangle$ can be expressed by different orbitals, $|\psi_i'(t)\rangle = \sum_{j=1}^{N} U_{ij}(t)|\psi_j(t)\rangle$, as Eq. (4), where $\{U_{ij}(t)\}$ is an arbitrary time-dependent unitary matrix. Thus, the Kohn–Sham orbitals have gauge degrees of freedom associated with the $U(N)$ transformation.

Apparently, the TDKS equation (3) uniquely determines the time evolution of each single-particle orbital $|\psi_i(t)\rangle$. Since we have not imposed any gauge fixing condition when we derived Eq. (3) from the stationary action principle, $\delta S = 0$, for Eq. (2), the Kohn–Sham (single-particle) orbitals should not be unique.

In fact, to my opinion, the derivation above is not satisfactory because we have used the orthonormal condition among the orbitals, $\langle \psi_i(t)|\psi_j(t)\rangle = \delta_{ij}$, to obtain Eq. (2) from Eq. (1). Therefore, the full variation with respect to each $\langle \psi_i(t)|$ should not be taken. I think that the proper derivation is either (i) the orthonormal relations are not assumed in the first place, or (ii) the variational space is restricted by the constraints $\langle \psi_i(t)|\psi_j(t)\rangle = \delta_{ij}$. In the following, I would like to present these proper derivations of the TDKS equations and to show that the gauge degrees of freedom appear naturally.

2.2 Derivation of TDKS equations (1)

To allow us to take full variation with respect to $\psi_i(t)$, we should not assume the orthonormal relation among $\{|\psi_i\rangle\}$. Let us derive the equations, starting from the action

$$S \equiv \int_{t_i}^{t_f} \left\{ \frac{\langle \Psi_D(t)|i\frac{\partial}{\partial t}|\Psi_D(t)\rangle}{\langle \Psi_D(t)|\Psi_D(t)\rangle} - E[\rho(t)] \right\} dt. \tag{6}$$

In order to perform calculation of the functional derivatives, some formulae, which are well-known in the generator coordinate method (GCM) [7], are very helpful. First, it is useful to define the overlap matrix,

$$B_{ij}(t) \equiv \langle \psi_i(t)|\psi_j(t)\rangle, \quad i,j = 1,\cdots,N, \tag{7}$$

which leads to the following expressions for the norm and the time derivative.

$$\langle \Psi_D(t)|\Psi_D(t)\rangle = \det B, \tag{8}$$

$$\langle \Psi_D(t)|i\frac{\partial}{\partial t}|\Psi_D(t)\rangle = \det B \sum_{ij} \langle \psi_i(t)|i\frac{\partial}{\partial t}|\psi_j(t)\rangle \left(B^{-1}\right)_{ji}. \tag{9}$$

Hereafter, $\sum_i$ means the summation with respect to the occupied (hole) orbitals, $i = 1,\cdots,N$, and the time-dependent overlap matrix $B(t)$ is simply denoted as B for simplicity. Using the cofactor expansion of the inverse matrix B^{-1}, we can prove that

$$\frac{\delta \left(B^{-1}\right)_{ij}(t')}{\delta\langle\psi_k(t)|} = -\left(B^{-1}\right)_{ik} \sum_l |\psi_l\rangle \left(B^{-1}\right)_{lj} \delta(t-t'). \tag{10}$$

In the same manner, the one-body density matrix can be written as

$$\rho(t) = \sum_{ij} |\psi_i(t)\rangle \left(B^{-1}\right)_{ij} \langle\psi_j(t)|. \tag{11}$$

Then, the derivative of $E[\rho]$ with respect to the bra state $\langle\psi_k(t)|$ becomes

$$\frac{\delta E[\rho]}{\delta\langle\psi_k(t)|} = h[\rho(t)] \sum_j |\psi_j(t)\rangle \left(B^{-1}\right)_{jk}. \tag{12}$$

Now it is easy to derive the TDKS equations

$$\left(1 - \sum_l |\psi_l(t)\rangle \left(B^{-1}\right)_{lj} \langle\psi_j(t)|\right) \left(i\frac{\partial}{\partial t} - h[\rho(t)]\right) \sum_k |\psi_k(t)\rangle \left(B^{-1}\right)_{ki} = 0. \tag{13}$$

This looks different from the well-known form of Eq. (3).

We may simplify Eq. (13) by assuming that the orbitals are orthonormal at a certain time t, $\langle\psi_i(t)|\psi_j(t)\rangle = \delta_{ij}$. In this case, we have $B_{ij}(t) = (B^{-1})_{ij} = \delta_{ij}$. Then, Eq. (13) can be written as

$$\left(1 - \sum_j |\psi_j(t)\rangle\langle\psi_j(t)|\right) \left(i\frac{\partial}{\partial t} - h[\rho(t)]\right) |\psi_i(t)\rangle = 0 \tag{14}$$

at time t. This means that the states

$$\left(i\frac{\partial}{\partial t} - h[\rho(t)]\right) |\psi_i(t)\rangle \tag{15}$$

do not contain the particle (unoccupied) orbitals at time t. In other words, they can be expanded in terms of the hole (occupied) orbitals only,

$$i\frac{\partial}{\partial t}|\psi_i(t)\rangle = h[\rho(t)]|\psi_i(t)\rangle + \sum_k \lambda_{ij}(t)|\psi_j(t)\rangle. \tag{16}$$

Although $\lambda_{ij}(t)$ are in principle arbitrary, choosing the Hermitian matrix $\lambda_{ik}(t)$ will conserve the orthonormal relation among the orbitals $\langle\psi_i(t+\Delta t)|\psi_j(t+\Delta t)\rangle = \delta_{ij}$. Therefore, provided that $\lambda_{ij}(t)$ are Hermitian, Eq. (16) can be true for any time t. They can be regarded as a general form of the TDKS equations. Here, the time-dependent Hermitian matrix $\lambda_{ij}(t)$ is a kind of gauge function for fixing the Kohn–Sham orbitals.

Equation (16) is also consistent with the well-known form of the equation for the one-body density matrix. Since the orthonormal relation is kept all the time, the density matrix of Eq. (11) can be simplified by assuming $B_{ij}^{-1} = \delta_{ij}$. Then, the time derivative of $\rho(t)$ can be calculated as

$$i\frac{\partial\rho}{\partial t} = \sum_i \left(h|\psi_i\rangle + \sum_j \lambda_{ij}|\psi_j\rangle\right)\langle\psi_i| - \sum_i |\psi_i\rangle\left(\langle\psi_i|h + \sum_j \langle\psi_j|\lambda_{ij}^*\right) \tag{17}$$

$$= \sum_i \left(h|\psi_i\rangle\langle\psi_i| - |\psi_i\rangle\langle\psi_i|h\right) \tag{18}$$

$$= [h[\rho(t)], \rho(t)]. \tag{19}$$

2.3 Derivation of TDKS equations (2)

We saw in the previous section that the calculation of the functional derivative of the action S in Eq. (6) is rather tedious. The use of Lagrange multipliers may greatly facilitate this calculation. One of the great advantages of the Lagrange multipliers is that, when we impose the constraints in terms of the Lagrange multipliers, we may simplify the functionals (functions) by using the constraints *before variations*. Now, we can use the action S in the simple form of Eq. (2) but with the Lagrange multipliers to impose the constraints of the orthonormal relation $\langle\psi_i(t)|\psi_j(t)\rangle = \delta_{ij}$,

$$\delta\left\{S - \sum_{ij}\lambda_{ij}(t)\left(\langle\psi_i(t)|\psi_j(t)\rangle - \delta_{ij}\right)\right\} = 0. \tag{20}$$

The variation immediately leads to Eq. (16). The form of Eq. (16) with the Hermitian matrix $\lambda(t)$ can be regarded as a general form of the TDKS equations.

Before ending this section, let us show that we can use the constraint conditions to simplify the functions before variation when the Lagrange multipliers are utilized. We consider here a problem of finding extrema of a function $F(\vec{x})$ with a constraint $g(\vec{x}) = 0$. Using the Lagrange multiplier λ, it can be given by the following variational form:

$$\delta\left\{F(\vec{x}) - \lambda g(\vec{x})\right\} = 0 \quad \rightarrow \quad \nabla F(\vec{x}) - \lambda\nabla g(\vec{x}) = 0 \quad \text{with } g(\vec{x}) = 0. \tag{21}$$

Namely, $\nabla F(\vec{x})$ is parallel to $\nabla g(\vec{x})$ which is the condition of the extrema under the constraint of $g(\vec{x}) = 0$. Now let us assume that the functional form of $F(\vec{x})$ can be modified (simplified) into $\tilde{F}(\vec{x})$ if we use the constraint $g(\vec{x}) = 0$,

$$\tilde{F}(\vec{x}) = f(\vec{x}; g = 0), \tag{22}$$

where $f(\vec{x}; g(\vec{x}))$ is a function of $\vec{x}$ and $g(\vec{x})$ satisfying $f(\vec{x}; g(\vec{x})) = F(\vec{x})$. From these, we can rewrite Eq. (21) as

$$\nabla\tilde{F}(\vec{x}) - \left(\lambda - \frac{\partial f}{\partial g}\right)\nabla g(\vec{x}) = 0 \quad \text{with } g(\vec{x}) = 0. \tag{23}$$

This means that $\nabla\tilde{F}(\vec{x})$ is also parallel to $\nabla g(\vec{x})$ at the extrema with $g(\vec{x}) = 0$. Therefore it is identical to the following variation for finding the extrema:

$$\delta\left\{\tilde{F}(\vec{x}) - \lambda g(\vec{x})\right\} = 0 \quad \rightarrow \quad \nabla\tilde{F}(\vec{x}) - \lambda\nabla g(\vec{x}) = 0 \quad \text{with } g(\vec{x}) = 0. \tag{24}$$

Thus we can replace $F(\vec{x})$ by $\tilde{F}(\vec{x})$ for the variational calculation with the Lagrange multiplier λ: $\tilde{F}(\vec{x}) = F(\vec{x})$ where $g(\vec{x}) = 0$ is satisfied. An extension of the present argument to the case of multiple constraints is straightforward.

3 Remarks on the numerical calculations

The Kohn–Sham orbitals are evolved in time according to Eq. (16). As is shown in the previous section, there are gauge degrees of freedom ($\lambda_{ij}(t)$) which we can choose arbitrarily. Although the choice of the gauge should not affect the physical quantities, the feasibility of numerical simulations sometimes depends on it.

3.1 Preparation of the initial state

In most applications, the initial state of the time evolution is prepared by solving the static Kohn–Sham equations:

$$h[\rho]|\psi_i\rangle = \epsilon_i|\psi_i\rangle, \quad \text{and} \quad \rho = \sum_i |\psi_i\rangle\langle\psi_i|. \tag{25}$$

Of course, this is not the only way of constructing the ground-state Kohn–Sham orbitals. Again, the $U(N)$ gauge degrees of freedom exist for the ground state. Nevertheless, they are somewhat special in the sense that both the Hamiltonian $h[\rho]$ and the density ρ are diagonal in these orbitals. They are often called "canonical orbitals".

To reach the ground state, the imaginary-time method is one of the most prevalent methods in nuclear physics [8]. We start from given initial wave functions for $|\psi_i^{(0)}\rangle$ which are orthonormalized to each other. Then, at the (n+1)-th iteration, the imaginary-time evolution of a small time step Δt is calculated as

$$|\psi_i^{(n+1)}\rangle = \exp(-\Delta t\ h[\rho^{(n)}])|\psi_i^{(n)}\rangle \approx \left(1 - \Delta t\ h[\rho^{(n)}]\right)|\psi_i^{(n)}\rangle, \tag{26}$$

where the Kohn–Sham Hamiltonian is constructed at the density of $\rho^{(n)}$ which is defined by

$$\rho^{(n)} = \sum_i |\psi_i^{(n)}\rangle\langle\psi_i^{(n)}|. \tag{27}$$

At each iteration, the Gram-Schmidt orthonormalization must be performed. This procedure converges to the solutions of Eq. (25) from the eigenstate of the lowest energy ϵ_1 to that of the N-th eigenvalue ϵ_N. You may also calculate the particle (unoccupied) states ($i > N$) if you want.

An advantage of the imaginary-time method is that it is a very stable iteration procedure to reach the convergence, though it may require a large number of iterations. Diagonalizing $h[\rho^{(n)}]$ in the space spanned by the set of states $\{|\psi_i^{(n)}\rangle\}_{i=1,\cdots,N}$ may speed up the convergence. Sometimes an additional damping factor associated with the kinetic energy terms, $1/p^2$, could help to lower the energy quickly, especially at the beginning stage of the iterations.

3.2 Strength functions in the linear response

The linear response in real time can be numerically realized if we slightly distort the ground-state density and start the time evolution. The distortion is made by a weak

external field, $V_{\rm ext}(t)$. The time profile of the external field determines the frequency range contained in $V_{\rm ext}(t)$,

$$V_{\rm ext}(t) = \frac{1}{2\pi}\int \tilde{V}_{\rm ext}(\omega)e^{-i\omega t}d\omega. \tag{28}$$

One of the popular choices is the instantaneous field, $V_{\rm ext}(t) \propto \delta(t)$, which correspond to the constant field in the frequency domain, $\tilde{V}_{\rm ext}(\omega) \sim V_0$. An advantage of this instantaneous external field is that the calculation of a single time evolution provides information on the whole frequency (energy) range.

The strength functions can be calculated within the real-time method as follows. Suppose we would like to calculate the strength function associated with the one-body Hermitian operator F for a system whose energy eigenstates are denoted by $|\Phi_n\rangle$. The initial state is constructed by applying the instantaneous external field $V_{\rm ext}(t) = -\eta F\delta(t)$ at $t = 0$, which leads to $|\Psi(t = 0+)\rangle = e^{i\eta F}|\Psi_0\rangle$. Here we adopt a small parameter η to perform numerically the linear approximation. The time-dependent state $|\Psi(t)\rangle$ can be decomposed in terms of $|\Phi_n\rangle$ as

$$|\Psi(t)\rangle = e^{-iHt}e^{i\eta F}|\Psi_0\rangle = e^{-iE_0t}|\Phi_0\rangle + i\eta\sum_n e^{-iE_nt}|\Phi_n\rangle\langle\Phi_n|F|\Phi_0\rangle + \mathcal{O}(\eta^2). \tag{29}$$

Therefore, the calculation of the expectation value of F leads to

$$\langle\Psi(t)|F|\Psi(t)\rangle = \langle\Phi_0|F|\Phi_0\rangle + 2\eta\sum_n |\langle\Phi_n|F|\Phi_0\rangle|^2 \sin\{(E_n - E_0)t\}. \tag{30}$$

Then the strength function is obtained by the Fourier transform:

$$\begin{aligned} S(E;F) &\equiv \sum_n |\langle\Phi_n|F|\Phi_0\rangle|^2\delta(E - (E_n - E_0)) \\ &= \frac{1}{\pi\eta}\int_0^\infty \sin(Et)\{\langle\Psi(t)|F|\Psi(t)\rangle - \langle\Phi_0|F|\Phi_0\rangle\}. \end{aligned} \tag{31}$$

In practice it is impossible to perform the time evolution up to $t = \infty$. Usually we introduce an artificial damping (smearing) factor γ to multiply the integrand of Eq. (31) by $e^{-\gamma t/2}$, and stop integration at $t = T$. The magnitude of the damping factor γ is related to the time duration T. To obtain a smooth curve as a function of energy E, we need to have $\gamma \gtrsim 2\pi/T$.

3.3 Choice of the gauge functions

Canonical orbitals of the ground state defined by Eq. (25) should correspond to stationary solutions of the TDKS equations (16). However, apparently, off-diagonal parts of the gauge functions $\lambda_{ij}(t)$ make the solution non-stationary since a mixing among the hole orbitals takes place in time. When we choose the gauge $\lambda_{ij}(t) = -\epsilon_i\delta_{ij}$, the static canonical orbitals of Eq. (25) become stationary, $\partial\psi_i/\partial t = 0$.

In the real-time calculation of the linear response, the state stays very close to the ground state, only a small part of the Kohn–Sham wave functions is fluctuating. Therefore it is convenient to adopt the same gauge as above, $\lambda_{ij}(t) = -\epsilon_i\delta_{ij}$. Of course, the choice of the gauge is completely arbitrary and should not affect the final results. However this choice has some numerical advantage because the time-dependent phase change of each Kohn–Sham orbital is minimized.

For calculation of nuclear dynamics beyond the linear regime such as a simulation of heavy-ion collisions, the choice of $\lambda_{ij}(t) = -\epsilon_i\delta_{ij}$ is no longer advantageous. Instead, we may adopt $\lambda_{ij}(t) = -\delta_{ij}\langle\psi_i(t)|h[\rho(t)]|\psi_i(t)\rangle$, for instance.

3.4 Numerical applications

In this article we do not show results of numerical calculations. I would like readers to refer to our previous papers [3, 9–25].

4 Acknowledgements

This work is supported by Grant-in-Aid for Scientific Research (Nos. 25287065 and 13327989). Computational resources were partially provided by the HPCI Systems Research Projects (hp120192).

References

[1] J. W. Negele, Rev. Mod. Phys. **54**, 913 (1982).

[2] M. Bender, P. H. Heenen and P.-G. Reinhard, Rev. Mod. Phys. **75**, 121 (2003).

[3] T. Nakatsukasa, Prog. Theor. Exp. Phys. **2012**, 01A207 (2012).

[4] C. Simenel, Eur. Phys. J. A **48**, 152 (2012).

[5] J. A. Maruhn, P.-G. Reinhard, P. D. Stevenson and A. S. Umar, Comp. Phys. Comm. **185**, 2195 (2014).

[6] A. K Kerman and S. E Koonin, Ann. Phys. (NY) **100**, 332 (1976).

[7] P. Ring and P. Schuck, *The nuclear many-body problem*. Springer, New York, 1980.

[8] K. T. R. Davies, H. Flocard, S. Krieger and M. S. Weiss, Nucl. Phys. A **342**, 111 (1980).

[9] T. Nakatsukasa and K. Yabana, J. Chem. Phys. **114**, 2550 (2001).

[10] T. Nakatsukasa and K. Yabana, Progr. Theor. Phys. Suppl. **146**, 447 (2002).

[11] T. Nakatsukasa, M. Ueda and K. Yabana, in *Proc. Int. Symp. Frorntiers of Collective Motions (CM2002)*, eds. H. Sagawa and H. Iwasaki. World Scientific, Singapore, 2003, p. 267.

[12] T. Nakatsukasa and K. Yabana, Eur. Phys. J. A **20**, 163 (2004).

[13] T. Nakatsukasa and K. Yabana, in *Proc. Int. Conf. New Era of Nucl. Structure*, eds. Y. Suzuki, S. Ohya, M. Matsuo and T. Ohtsubo. World Scientific, Singapore, 2004, p. 251.

[14] T. Nakatsukasa and K. Yabana, Phys. Rev. C **71**, 024301 (2005).

[15] T. Nakatsukasa and K. Yabana, Eur. Phys. J. A Suppl. **25**, 527 (2005).

[16] T. Nakatsukasa and K. Yabana, Nucl. Phys. A **788**, 349c (2007).

[17] T. Nakatsukasa, K. Yabana and M. Ito, Eur. Phys. J. Special Topics **156**, 249 (2008).

[18] T. Nakatsukasa and K. Yabana, in *Condensed Matter Theories* **21**, eds. H. Akai, A. Hosaka, H. Toki and F. B. Malik. Nova Science Publishers, New York, 2008, p. 61.

[19] Y. Kawashita, K. Yabana, M. Noda, K. Nobusada and T. Nakatsukasa, J. Mol. Struc. THEOCHEM **914**, 130 (2009).

[20] S. Ebata, T. Nakatsukasa, T. Inakura, K. Yoshida, Y. Hashimoto and K. Yabana, Phys. Rev. C **82(3)**, 034306 (2010).

[21] S. Ebata, T. Nakatsukasa and T. Inakura, J. Phys. Conf. Ser. **381**, 012104 (2012).

[22] S. Ebata, T. Nakatsukasa and T. Inakura, Progr. Theor. Phys. Suppl. **196**, 316 (2012).

[23] L. Guo and T. Nakatsukasa, EPJ Web of Conf. **38**, 09003 (2012).

[24] T. Nakatsukasa. J. Phys. Conf. Ser. **402(1)**, 012032 (2012).

[25] S. Ebata, T. Nakatsukasa and T. Inakura, Phys. Rev. C **90**, 024303 (2014).

Effects of QRPA Correlations on Nuclear Matrix Elements of Neutrinoless Double-Beta Decay through Overlap Matrix

J. Terasaki

Division of Physics and Center for Computational Sciences, University of Tsukuba, Tsukuba, 305-8577, Japan

Abstract

We show an improvement of the quasiparticle random-phase approximation (QRPA) approach for calculating the nuclear matrix elements (NMEs) of the neutrinoless double-beta decay. One of the techniques of obtaining the NME is to calculate the overlaps of the QRPA excited states obtained from the initial and final states, and these overlaps should be calculated using the QRPA ground states defined as the vacuum of the QRPA quasibosons. The significant difference from the usual method is that a normalization factor arises from this definition, and this factor is much larger than one.

Keywords: *QRPA; nuclear matrix elements; neutrinoless double-beta decay*

1 Introduction

The determination of the effective neutrino mass is one of the most important subjects in physics now due to multiple reasons. The neutrino has been assumed to be massless in the standard theory, however, the neutrino oscillations showed that the neutrino is actually massive [1–4]. Mass of elementary particle is a basic physical constant that we cannot leave unknown. The effective neutrino mass affects the fluctuation of the mass distribution in the universe [5]. The neutrino also plays an important role in the energy and momentum transport in the supernova explosion [6].

The neutrino oscillations also provided us with most of the matrix elements of the transformation matrix between the mass eigen and flavor states. This information is, however, not sufficient for determining the absolute neutrino masses. One of few methods which can provide the expectation value of neutrino mass (effective neutrino mass) is the neutrinoless double-beta ($0\nu\beta\beta$) decay which occurs if the neutrino is a Majorana particle. This decay can occur in nuclei if the mass of the nucleus with (proton number, neutron number) = $(Z+2,N-2)$ (daughter nucleus) is smaller than that with (Z,N) (parent nucleus). For experiments, other conditions are necessary to be satisfied: e. g., a suppression of the single-beta decay, a separation of the spectrum of the two-neutrino double-beta decay from that of the neutrinoless one, and a productibility of the parent nucleus. Many experiments are now in preparation for observing the $0\nu\beta\beta$ decay, see, e. g., Ref. [7].

A challenging problem for nuclear theory is to calculate the respective nuclear matrix elements (NMEs) accurately; these are the transition matrix elements between the initial and final nuclear states in the $0\nu\beta\beta$ decay, and the decay probability is

Proceedings of the International Conference 'Nuclear Theory in the Supercomputing Era — 2014' (NTSE-2014), Khabarovsk, Russia, June 23–27, 2014. Eds. A. M. Shirokov and A. I. Mazur. Pacific National University, Khabarovsk, Russia, 2016, p. 23.

http://www.ntse-2014.khb.ru/Proc/Terasaki.pdf.

proportional to the absolute value of the NME squared and the effective neutrino mass squared. Currently, we are facing a problem that the calculated values significantly depend on the methods and differ by a factor of 2 approximately [8]. The decay probability is also proportional to the so-called phase-space factor which is the electron component of the transition matrix element, and the calculation of this factor is well-established. Several methods have been used for calculating the NME. An approach using the quasiparticle random-phase approximation (QRPA) is one of the oldest methods (see, e. g., Ref. [9]), and many improvements have been made, e. g., an introduction of the deformation (see, e. g., Ref. [10]), the extension to the renormalized QRPA (see, e. g., Ref. [11]), an extension of the wave-function space (see, e. g., Ref. [12]), and an introduction of the effective-operator method in calculating the matrix elements of the transition operator (see, e. g., Ref. [13]). The above discrepancy problem is not yet solved in spite of these improvements. In particular, the QPRA values are larger than the shell-model values by a factor of 2 in more than several decay instances systematically.

In this paper, we introduce another improvement of the QRPA approach, which has not been exploited. The NME is obtained as the trace of the product of four matrices: the matrix of the transition operator (neutrino potential), two transition matrices from the initial and final states to the intermediate states, and the overlap matrix of two intermediate states which are obtained by two QRPA calculations based on the initial and final states. In our new method, the overlap matrix is calculated using the QRPA ground state defined as the vacuum of the QRPA quasibosons. The equation of the QRPA ground state has been known since some decades ago (see, e. g., Ref. [14]), however, our study is the first application of that formulation to the NME.

2 Two QRPA approaches

The decay probability of the $0\nu\beta\beta$ decay is given by

$$1/T_{0\nu}(0^+ \to 0^+) = \left| M^{(0\nu)} \right|^2 G_{01} \left(\langle m_\nu \rangle / m_e \right)^2 , \tag{1}$$

where $T_{0\nu}(0^+ \to 0^+)$ denotes the half-life of the decay, and 0^+ indicates the initial and final states having $J^\pi = 0^+$. $M^{(0\nu)}$ and G_{01} are the NME and the phase-space factor, respectively. $\langle m_\nu \rangle$ is the effective neutrino mass, and m_e is the electron mass. Under the closure approximation replacing the intermediate-state energy with an average value $\bar{E}$, the equation of the NME can be written

$$M^{(0\nu)} \simeq \sum_{pp'nn'} \sum_{b_f b_i} \langle pp'|V(\bar{E})|nn'\rangle \langle 0^+_{pn,f}|c^\dagger_{p'} c_{n'}|b_f\rangle \langle b_f|b_i\rangle \langle b_i|c^\dagger_p c_n|0^+_{pn,i}\rangle, \tag{2}$$

where b_i and b_f denote the proton-neutron QRPA excited states based on the initial and final states, respectively. $V(\bar{E})$ is the transition operator of the $0\nu\beta\beta$ decay. The symbols pp' and nn' denote the proton and neutron single-particle states, respectively, and c_p and $c^\dagger_p$ denote the annihilation and creation operators, respectively. $|0^+_{pn,i}\rangle$ ($|0^+_{pn,f}\rangle$) is the initial (final) state obtained by the proton-neutron QRPA. Using the closure relation with respect to the intermediate states, we also have

$$M^{(0\nu)} \simeq \sum_{pp'nn'} \sum_{b_f b_i} \langle pp'|V(\bar{E})|nn'\rangle \langle 0^+_{\mathrm{like},f}|c^\dagger_{p'} c^\dagger_p|b_f\rangle \langle b_f|b_i\rangle \langle b_i|c_n c_{n'}|0^+_{\mathrm{like},i}\rangle, \tag{3}$$

where b_i and b_f denote those obtained by the like-particle QRPA. In our first attempt, we use this like-particle QRPA version because it is known that this QRPA is a good approximation in the well-deformed heavy mass ($A \sim 150$) region.

3 Formulation of QRPA ground state and overlap of QRPA states

Hereafter, we omit the subscript "like" in the symbols that we use. The QRPA ground state as the vacuum of the QRPA quasibosons is written as

$$|0_i^+\rangle = \prod_{K\pi} \frac{1}{\mathcal{N}_i^{K\pi}} \exp\left[v_i^{(K\pi)}\right] |0^+_{\mathrm{HFB},i}\rangle, \tag{4}$$

where $K\pi$ denotes the combination of the K quantum number and parity of the nuclear state, and $|0^+_{\mathrm{HFB},i}\rangle$ is the Hartree–Fock–Bogoliubov (HFB) (initial) ground state. $\mathcal{N}_i^{K\pi}$ is the normalization factor. In the quasiboson approximation ignoring exchange terms, we get

$$v_i^{(K\pi)} = \sum_{\mu\nu\mu'\nu'} \frac{1}{1+\delta_{K0}} \left(Y^{i,K\pi} \frac{1}{X^{i,K\pi}} \right)^\dagger_{\mu\nu,\mu'\nu'} a^{i\dagger}_\mu a^{i\dagger}_\nu a^{i\dagger}_{\mu'} a^{i\dagger}_{\nu'}, \tag{5}$$

$X^{i,K\pi}$ and $Y^{i,K\pi}$ are matrices consisting of forward and backward amplitudes of the QRPA state,

$$\begin{aligned} |b_i\rangle &= O_b^{i\dagger}|0_i^+\rangle \\ &= \sum_{\mu\nu\mu'\nu'} \left(X^{i,K\pi}_{\mu\nu,b} a^{i\dagger}_\mu a^{i\dagger}_\nu - Y^{i,K\pi}_{-\mu-\nu,b} a^i_{-\nu} a^i_{-\mu} \right) |0_i^+\rangle, \end{aligned} \tag{6}$$

and quasiparticle creation and annihilation operators are $a^\dagger_\mu$ and a_μ, respectively. This quasiparticle basis is obtained by the HFB calculation determining $|0^+_{\mathrm{HFB},i}\rangle$. The index "$-\mu$" indicates that the K quantum number of this quasiparticle state is opposite to that of the state μ. $O_b^{i\dagger}$ is the creation operator of the QRPA state.

The overlap of the two QRPA states based on the initial and final states can be calculated by the expansion and truncation with respect to $v_i^{(K\pi)}$ and $v_f^{(K\pi)\dagger}$,

$$\begin{aligned} \langle b_f|b_i\rangle &\simeq \frac{1}{\mathcal{N}_f\mathcal{N}_i} \prod_{K\pi} \langle 0^+_{\mathrm{HFB},f}| \exp\left[v_f^{(K\pi)\dagger}\right] O_b^f O_b^{i\dagger} \exp\left[v_i^{(K\pi)}\right] |0^+_{\mathrm{HFB},i}\rangle \\ &\simeq \frac{1}{\mathcal{N}_f\mathcal{N}_i} \Bigg\{ \langle 0^+_{\mathrm{HFB},f}|O_b^f O_b^{i\dagger}|0^+_{\mathrm{HFB},i}\rangle \\ &\quad + \sum_{K\pi} \left(\langle 0^+_{\mathrm{HFB},f}|v_f^{(K\pi)\dagger} O_b^f O_b^{i\dagger}|0^+_{\mathrm{HFB},i}\rangle + \langle 0^+_{\mathrm{HFB},f}|O_b^f O_b^{i\dagger} v_i^{(K\pi)}|0^+_{\mathrm{HFB},i}\rangle \right) \Bigg\}. \end{aligned} \tag{7}$$

It has been checked that the next-order terms are negligible in test calculations using ^{26}Mg and ^{25}Si [15]. This truncation can be applied because many high-energy excitations over the Fermi surface region do not contribute to the overlap in which two ground states are states of different nuclei. Thus we can assume that this truncation is also applicable to those heavier nuclei which are interesting for the $0\nu\beta\beta$ decay studies. Note that the normalization factors need higher-order truncations; we calculate up to the fourth order in the expansion of $\mathcal{N}_i^2$ and $\mathcal{N}_f^2$ with the quasiboson approximation.

4 Calculation of QRPA ground state

We performed the QRPA and overlap calculations for $^{150}\mathrm{Nd} \to {}^{150}\mathrm{Sm}$. The input is the Skyrme energy-density functional with the parameter set SkM* [16] and the volume pairing energy density functional [17]. The strength of the latter was determined

so as to reproduce the pairing gaps of these nuclei obtained from the experimental mass differences. The HFB calculations were performed using a cylindrical box of the height ($z > 0$) and radius of 20 fm assuming the axial symmetry of nuclear states [18–20]. The cutoff energy of 60 MeV was introduced for the quasiparticle energy. The quasiparticle states of lower energies are used for calculating the density and pairing tensor. The calculated axial quadrupole deformation β is 0.279 for ^{150}Nd and 0.209 for ^{150}Sm.

We use $K = 0{-}8$ for getting the convergence of NME. The QRPA equation is solved by the so-called matrix formulation [21]. The size of the QRPA Hamiltonian matrix is near $58,000$ for $K = 0, 1$ and $\simeq 10,000{-}25,000$ for other K values. The size for $K = 0, 1$ is much larger than the others because it is necessary to separate the spurious states associated with symmetries of the Hamiltonian broken in the HFB states. We do not use the proton-neutron pairing energy density functional (see, e. g., Ref. [12]) because these nuclei are far from the $N = Z$ line.

There is a problem that we have to solve before proceeding to the calculation of NME. The QRPA correlation energy diverges because of the contact-interaction nature of the Skyrme and volume-pairing energy-density functionals. Since the normalization factors of the QRPA ground states are strongly correlated with the QRPA correlation energies through the backward amplitudes, the normalization factors also diverge or are too large. In order to avoid this problem, we first define the backward norm of the QRPA solution a,

$$\mathcal{N}^a_{\rm back} = \sum_{\mu\nu} \left| Y^a_{-\mu-\nu} \right|^2 . \tag{8}$$

Then we pick up the QRPA solutions with the largest backward norms so as to reproduce the semi-experimental correlation energy

$$E^{\rm exp}_{\rm cor} = E_{\rm exp} - E_{\rm HFB}, \tag{9}$$

where $E_{\rm exp}$ and $E_{\rm HFB}$ are the experimental energy (mass) and the HFB energy of the ground state, respectively. The QRPA correlation energy is calculated using the formula [22]

$$E^{\rm QRPA}_{\rm cor} \simeq \frac{1}{2} \sum_a (E_a - E^{\rm TDA}_a), \tag{10}$$

where E_a and $E^{\rm TDA}_a$ are the eigenenergies of the QPRA and Tamm–Dancoff approximation [21], respectively. We picked up 10 (18) QRPA solutions for ^{150}Nd (^{150}Sm) and obtained the QRPA correlation energies of -1.721 MeV for ^{150}Nd and -3.688 MeV for ^{150}Sm. The corresponding $E^{\rm exp}_{\rm cor}$ values are -1.696 MeV for ^{150}Nd and -3.661 MeV for ^{150}Sm (for the experimental masses, see Ref. [23]). Using this prescription, we obtained the product of the normalization factors of the initial and final QRPA ground states $\mathcal{N}_I\mathcal{N}_F = 1.860$; this implies that the NME is reduced significantly compared to the value obtained without the QRPA correlations in the ground states included in the overlaps. The calculation of the NME is now in progress.

5 Summary and future works

A new QRPA approach for calculating the NME has been presented; the QRPA ground state as the vacuum of the QRPA quasiboson is used in the overlaps of the intermediate QRPA states. The significant outcome of this approach is that the normalization factors are much larger than unity, and these normalization factors have an effect of reducing the NME. This calculation is a step toward obtaining the reliable NME.

We have many calculations to perform. First of all, the NME is necessary to calculate. One of the important tasks after the NME is to show that the two approaches

using the proton-neutron and like-particle QRPAs provide us with the same NME, as indicated by Eqs. (2) and (3). The extension of the QRPA ground state to the product wave function of the proton-neutron and like-particle QRPA ground states will be necessary for showing this equivalence. It is also an important task to investigate whether the NMEs of the two-neutrino double-beta decay are reproduced by our new approach. The explicit QRPA ground-state wave function is also entering this NME, therefore the reduction effect by the normalization factors also applies. It is also an important question whether the new NME values are close to the shell-model ones. For this comparison, we need to calculate the decay instances other than $^{150}\mathrm{Nd} \rightarrow {}^{150}\mathrm{Sm}$.

References

[1] Y. Fukuda *et al.*, Phys. Rev. Lett. **81**, 1562 (1998).

[2] Q. R. Ahmad *et al.*, Phys. Rev. Lett. **89**, 011301 (2002).

[3] K. Eguchi *et al.*, Phys. Rev. Lett. **90**, 021802 (2003).

[4] E. Aliu *et al.*, Phys. Rev. Lett. **94**, 081802 (2005).

[5] J. Lesgourgues and S. Pastor, Phys. Rep. **429**, 307 (2006).

[6] A. Mezzacappa and O. E. B. Messer, J. Comp. Appl. Math. **109**, 281 (1999).

[7] *Workshop on Calculation of Double-Beta-Decay Matrix Elements (MEDEX'13), Prague, Czech Republic, 11-14 June, 2013*, eds. O. Civitarese, I. Stekl and J. Suhonen. AIP Publishing, 2013.

[8] A. Faessler, J. Phys. Conf. Ser. **337**, 012065 (2012).

[9] M. Doi, T. Kotani and E. Takasugi, Progr. Theor. Phys. Suppl. **83**, 1 (1985).

[10] D.-L. Fang, A. Faessler, V. Rodin and F. Šimkovic, Phys. Rev. C **83**, 034320 (2011).

[11] L. Pacearescu, V. Rodin, F. Šimkovic and A. Faessler, Phys. Rev. C **68**, 064310 (2003).

[12] M. T. Mustonen and J. Engel, Phys. Rev. C **87**, 064302 (2013).

[13] M. Kortelainen and J. Suhonen, Phys. Rev. C **76**, 024315 (2007).

[14] R. Balian and E. Brezin, Nuovo Cim. **64**, 37 (1969).

[15] J. Terasaki, Phys. Rev. C **87**, 024316 (2013).

[16] J. Bartel, P. Quentin, M. Brack, C. Guet and H.-B. Håkansson, Nucl. Phys. A **386**, 79 (1982).

[17] J. Dobaczewski, W. Nazarewicz, T. R. Werner, J. F. Berger, C. R. Chinn and J. Dechargé, Phys. Rev. C **53**, 2809 (1996).

[18] V. E. Oberacker, A. Blazkiewicz and A. S. Umar, Rom. Rep. Phys. **59**, 559 (2007).

[19] A. Blazkiewicz, V. E. Oberacker, A. S. Umar and M. Stoitsov, Phys. Rev. C **71**, 054321 (2005).

[20] E. Terán, V. E. Oberacker and A. S. Umar, Phys. Rev. C **67**, 064314 (2003).

[21] P. Ring and P. Schuck, *The nuclear many-body problem.* Springer-Verlag, Berlin, 1980.

[22] F. Furche, J. Chem. Phys. **129**, 114105 (2008).

[23] http://www.nndc.bnl.gov/.

Large-Scale Shell-Model Studies for Exotic Nuclei: Probing Shell Evolution

Yutaka Utsuno[a,b], Takaharu Otsuka[b,c,d], Noritaka Shimizu[b], Yusuke Tsunoda[c], Michio Honma[e], Takashi Abe[c], Takahiro Mizusaki[f], Tomoaki Togashi[b] and B. A. Brown[d]

[a] *Advanced Science Research Center, Japan Atomic Energy Agency, Tokai, Ibaraki 319-1195, Japan*

[b] *Center for Nuclear Study, University of Tokyo, Hongo, Bunkyo-ku, Tokyo 113-0033, Japan*

[c] *Department of Physics, University of Tokyo, Hongo, Bunkyo-ku, Tokyo 113-0033, Japan*

[d] *National Superconducting Cyclotron Laboratory and Department of Physics and Astronomy, Michigan State University, East Lansing MI 48824, USA*

[e] *Center for Mathematical Sciences, University of Aizu, Ikki-machi, Aizu-Wakamatsu, Fukushima 965-8580, Japan*

[f] *Institute for Natural Sciences, Senshu University, Tokyo 101-8425, Japan*

Abstract

We report on recent advances in large-scale shell-model calculations for exotic nuclei, focusing on how shell evolution is probed from strongly correlated nuclei. We choose the $N \sim 28$ region as a typical case. The effective interaction is constructed on the basis of the monopole-based universal interaction which consists of a phenomenological central force and the bare tensor force. It is demonstrated that the proton spin-orbit splitting is significantly reduced in going from $N = 20$ to $N = 28$ due to the tensor force by comparing spectroscopic factors for the one-proton removal from ^{48}Ca. This narrowing spin-orbit splitting causes large deformation in ^{42}Si, as a consequence of the tensor-force-driven Jahn–Teller effect. It is predicted that the new $N = 34$ magic number found recently in ^{54}Ca enhances toward lower-Z isotopes and produces a new doubly-magic nucleus ^{48}Si.

Keywords: *Shell model; magic number; shell evolution; tensor force*

1 Introduction

Since a nucleus is a strongly correlated system, large-scale structure calculations are required to describe it accurately. The nuclear shell model is regarded as one of the most popular approaches for this purpose, including every possible correlation within the single-particle model space assumed. The usual shell model typically takes full one major shell for the single-particle space. Minor effects from the outside of the model space are taken into account by renormalizing the Hamiltonian and operators used in the calculation. The renormalized nuclear force and operators are called effective interaction and effective operators, respectively.

Constructing a good effective interaction is crucial for the descriptive power of the shell model. Microscopic effective interactions derived from the bare nucleon-nucleon forces are usually subject to empirical modification for better description. In particular, the monopole interaction is known to be critical [1, 2]. The monopole

Proceedings of the International Conference 'Nuclear Theory in the Supercomputing Era — 2014' (NTSE-2014), Khabarovsk, Russia, June 23–27, 2014. Eds. A. M. Shirokov and A. I. Mazur. Pacific National University, Khabarovsk, Russia, 2016, p. 29.

http://www.ntse-2014.khb.ru/Proc/Utsuno.pdf.

interaction $v_{ij}^{\rm m}$ works to change the single-particle energy of the orbit i with the orbit j occupied. Hence, the monopole interaction is responsible for the evolution of shell structure, often referred to as *shell evolution* [3]. Recently, shell evolution has received much attention in the study of exotic nuclei, because a number of phenomena that indicate the modification of shell structure have been observed. The breakdown of the conventional magic numbers is a good example. While the normal magic numbers $N = 8, 20, 28$ are known to disappear in very neutron-rich nuclei [4–6], new magic numbers $N = 16, 34$ have been discovered quite recently [7, 8].

An understanding of the source of the monopole interaction that causes the shell evolution is thus very important. Almost ignored over the years, the tensor force has been revisited for a decade as an essential ingredient of the effective interaction since Otsuka *et al.* pointed out that the tensor force produces significant changes of the spin-orbit splitting (Otsuka effect) [9]. Later, taking into account a phenomenological central force, the monopole-based universal interaction ($V_{\rm MU}$) has been proposed [10] to describe the shell evolution in a unified manner. Although the $V_{\rm MU}$ seems to give a rather reasonable evolution through a simple mean-field estimate, the experimental energy levels are not the pure single-particle states obtained from this approach.

The shell evolution thus should be probed with reliable many-body calculations such as the shell model. In this conference, we survey recent advances in the understanding of the shell evolution for exotic nuclei via large-scale shell-model calculations. We covered two major topics: the shell evolution in the $N \sim 28$ region based on the conventional shell-model calculation and the shape coexistence in Ni isotopes based on the advanced Monte Carlo shell-model calculation. Since the methodology of the advanced Monte Carlo shell model was also introduced in Abe's talk [11] in this conference and part of the results for Ni isotopes were reported in the proceedings of NTSE-2013 by Otsuka *et al.* [12], here we concentrate on the first subject.

2 Structure of exotic nuclei in the $N \sim 28$ region

Recently many intriguing phenomena concerning shell evolution has been observed in the neutron-rich $N \sim 28$ region. While $N = 28$ is known to be a good magic number for pf-shell nuclei, this magicity breaks down in ^{42}Si [6]. On the other hand, a new magic number $N = 34$ has been found very recently [8], more than a decade after its prediction [13]. Here we present our shell-model results for this region using an effective interaction based on $V_{\rm MU}$.

2.1 Shell evolution from $N = 20$ to $N = 28$

In this section, we perform shell-model calculations in the valence orbits consisting of the sd and pf shells. Since it is impossible to carry out shell-model calculations in the full $sd + pf$ model space, we introduce the truncation of the model space by not allowing nucleon excitation across the $N(Z) = 20$ shell gap. This truncation is valid except the "island of inversion" region [5] around ^{32}Mg, where the ground state is dominated by $2p$–$2h$ excitation across the $N = 20$ shell gap. Since the present study concentrates on neutron-rich nuclei having $Z \leq 20$ and $N \simeq 28$, the truncation should work well.

The cross-shell interaction, i. e. two-body matrix elements connecting the sd shell and the pf shell, plays a key role in the structure of neutron-rich nuclei evolving from the ^{40}Ca core. We use a refined $V_{\rm MU}$ interaction for this part. The refinement aims (1) to include the two-body spin-orbit force and (2) to better fit the semi-empirical GXPF1 interaction [14] than the original $V_{\rm MU}$ interaction. More details about the refinement can be found in Ref. [15].

We discuss the shell evolution in going from $N = 20$ to $N = 28$. Since the neutron $0f_{7/2}$ orbit is occupied, the monopole interaction concerning the $0f_{7/2}$ orbit

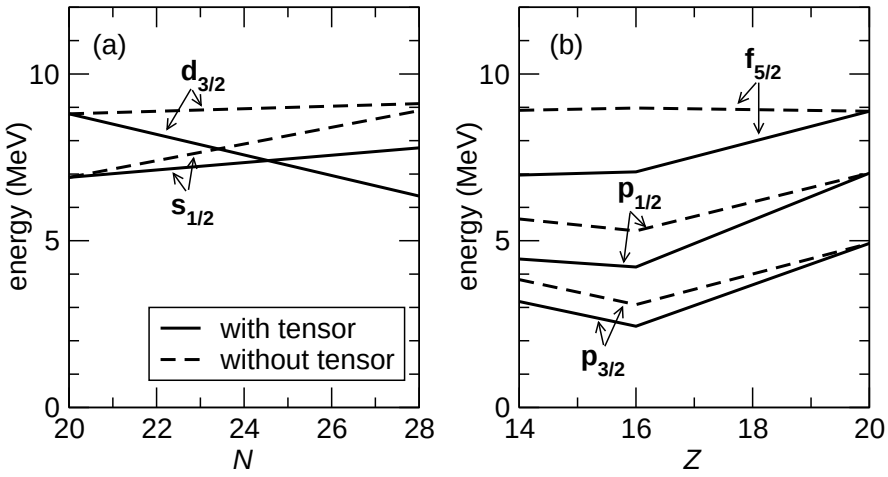

Figure 1: (a) Proton effective single-particle energies of the $1s_{1/2}$ and $0d_{3/2}$ orbits relative to the $0d_{5/2}$ in Si isotopes calculated with the present shell-model interaction. (b) Neutron effective single-particle energies of the $1p_{3/2}$, $1p_{1/2}$ and $0f_{5/2}$ relative to the $0f_{7/2}$ orbit in $N = 28$ isotones calculated with the present shell-model interaction. For both figures, the solid and dashed lines correspond to the Hamiltonian with and without the tensor force, respectively.

is relevant. Since the $0f_{7/2}$ orbit is a $j_>$ ($j = l + 1/2$) orbit, the tensor force works to pull down the $0d_{3/2}$ orbit and to push up the $0d_{5/2}$ orbit according to the Otsuka effect [9]. As a result, the spin-orbit splitting for protons decreases as shown in Fig. 1(a). The change of the spin-orbit splitting can be probed from the distribution of proton spectroscopic factors. As presented in Ref. [16], the proton-hole strengths measured from the $(e, e'p)$ reaction clearly support the reduction of the spin-orbit splitting obtained in the shell-model calculation including the tensor force. Thus, the present shell-model interaction describes the shell evolution quite well.

2.2 Disappearance of the $N = 28$ magic number and tensor-force-driven Jahn–Teller effect

It is very interesting to investigate how the shell evolution affects the nuclear collectivity such as deformation. The $N = 28$ nucleus ^{42}Si provides a good example in this context. In Fig. 2, the 2^+_1 and 4^+_1 energies in neutron-rich Si isotopes are compared with experiment. The shell-model calculation incorporating the tensor force successfully reproduces these energies including those measured after our calculation [17]. Two shell-model calculations, with and without the tensor force, give quite different results for ^{42}Si. The calculation with the tensor force reproduces the measured 2^+_1 level which is located very low, whereas the calculation without it leads to much higher energy. This means that the disappearance of the $N = 28$ magic number in ^{42}Si is caused by the tensor force. The calculated $B(E2)$ value and potential energy surface indicate that the very low 2^+_1 energy in ^{42}Si is due to a large deformation.

The reason why the tensor force induces the large deformation in ^{42}Si, is discussed in Ref. [16] in detail. As presented in Fig. 1, the tensor force reduces the spin-orbit splitting in $j-j$ closed nuclei such as ^{42}Si. The neighboring orbits belonging to the same major shell, such as $0d_{5/2}$ and $1s_{1/2}$, are then located closer. These neighboring orbits are easily mixed, and the resulting mixed orbit has a freedom of deformation. Since the residual interaction is dominated by the $Q \cdot Q$ term, a deformed state is favored in order to minimize the Hamiltonian. This mechanism is the Jahn–Teller effect [18, 19] which is triggered by the shell evolution due to the tensor force, which

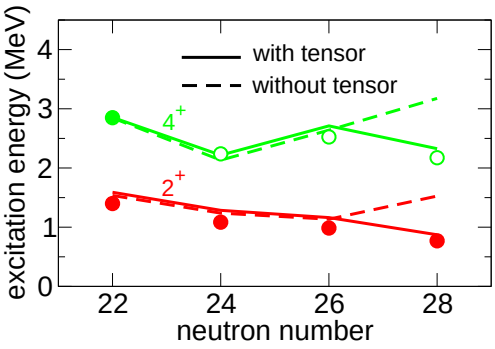

Figure 2: Comparison of theoretical predictions for the 2_1^+ and 4_1^+ energy levels in neutron-rich Si isotopes with experiment. The solid and dashed lines depict the shell-model calculations with and without the tensor force, respectively. The closed and open circles are the experimental data measured before and after our calculations.

we refer to as tensor-force-drive Jahn–Teller effect [16]. Since this is a general effect, it is very interesting to search for other cases in forthcoming experiments.

2.3 Evolution of the new $N = 34$ magic number

In 2001, the $N = 34$ magic number has been predicted to emerge around ^{54}Ca [13] in analogy with the appearance of the $N = 16$ magic number. According to the up-to-date shell-evolution mechanism, the $N = 34$ magic number appears due to a large attraction between the proton $0f_{7/2}$ and neutron $0f_{5/2}$ orbits that is favored by both central and tensor forces. Hence, the $0f_{5/2}$ orbit rises sharply with decreasing protons from the $0f_{7/2}$ orbit, positioning much higher than the $1p_{1/2}$ orbit in Ca isotopes. The $N = 34$ magic number is thus predicted to appear as a large sub-shell gap between $1p_{1/2}$ and $0f_{5/2}$. Much experimental effort has been devoted to detecting the predicted $N = 34$ magic number. Since it was extremely difficult to sufficiently produce the ^{54}Ca nucleus, the prediction has not been confirmed until the measurement of the 2_1^+ energy in ^{54}Ca was carried out in RIKEN in 2013 [8]. The measured 2_1^+ energy is much higher than those in singly-closed-shell nuclei such as $^{42-46,50}$Ca, demonstrating the occurrence of a new neutron magic number 34 in ^{54}Ca. What is amazing in this finding is that there is no a fingerprint of the $N = 34$ magic number in Ti ($Z = 22$) and Cr ($Z = 24$) isotopes, in a sharp contrast to the evolution of the $N = 32$ sub-shell closure [20–22]. This abrupt appearance of the $N = 34$ magic number is caused by a sharp evolution of the $0f_{5/2}$ orbit as a function of the proton number. Thus, the occurrence of the $N = 34$ magic number strongly validates the concept of shell evolution. The strength of the $N = 34$ shell gap is estimated to be $\sim$2.5 MeV from the shell-model calculations based on the GXPF1B semi-empirical interaction [23].

It is a very interesting issue how the $N = 34$ magic number behaves in more proton-deficient isotopes, Ar ($Z = 18$), S ($Z = 16$), and Si ($Z = 14$). Since the present interaction successfully describes the shell evolution without any direct adjustment to experimental data, it is considered to have a predictive power. Introducing a minor modification to the interaction aimed to almost exactly reproduce the proton single-hole-like spectra in K isotopes, we calculate the evolution of the $N = 34$ shell gap in Ar, S and Si isotopes. The resulting $N = 34$ gap is predicted to enhance at smaller proton numbers. For ^{48}Si, it becomes 3.9 MeV. This enlargement is mainly attributed to a large attraction of the central force between $\pi 0d_{3/2}$ and $\nu 0f_{5/2}$ compared to a repulsion of the tensor force. The effect of the enhanced $N = 34$ gap can be detected from experiment. Figure 3 shows the 2_1^+ energy levels in Ti, Ca, Ar, S, and Si isotopes

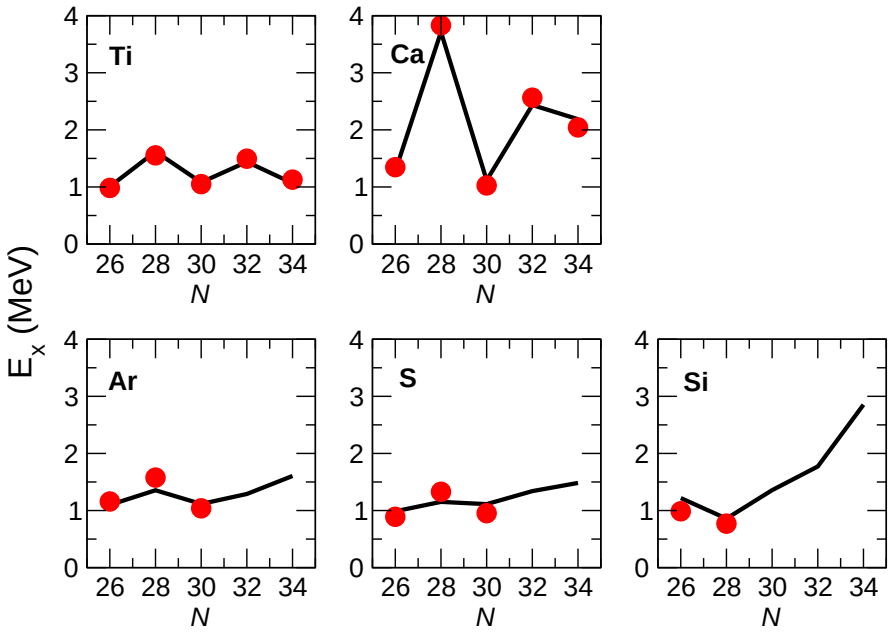

Figure 3: Comparison of theoretical predictions (lines) with experiment (circles) for the 2_1^+ levels in neutron-rich Ti, Ca, Ar, S and Si isotopes with $N = 26-34$.

with $N = 26-34$. The calculation predicts that the 2_1^+ level in the $N = 34$ nucleus ^{48}Si is located very high. As shown in Fig. 1 (a), the $Z = 14$ gap is also large in neutron-rich Si isotopes. As a result, ^{48}Si can be a new doubly-magic nucleus. Verifying this prediction in future RI-beam facilities will be a very attractive program.

3 Summary

We have investigated the shell evolution in the $N \sim 28$ exotic nuclei with large-scale shell-model calculations. The reduction of spin-orbit splitting due to the Otsuka effect [12] is probed by the distribution of spectroscopic strengths. This effect gives rise to a large deformation in the $j-j$ closed nucleus ^{42}Si. It is also predicted that the newly found $N = 34$ magic number enhances in ^{48}Si. The $N \sim 28$ region constitutes a typical case in which many-body properties are strongly affected by shell evolution. Thus, a high-performance computing in nuclear-structure calculations will be an indispensable tool for investigating unusual properties in exotic nuclei towards heavier-mass regions.

References

[1] J. B. McGrory, B. H. Wildenthal and E. C. Halbert, Phys. Rev. C **2**, 186 (1970).

[2] A. Poves and A. Zuker, Phys. Rep. **70**, 235 (1981).

[3] T. Otsuka, Phys. Scr. **T152**, 014007 (2013).

[4] A. Navin *et al.*, Phys. Rev. Lett. **85**, 266 (2000).

[5] E. K. Warburton, J. A. Becker and B. A. Brown, Phys. Rev. C **41**, 1147 (1990).

[6] B. Bastin *et al.*, Phys. Rev. Lett. **99**, 022503 (2007).

[7] R. V. F. Janssens, Nature **459**, 1069 (2009).

[8] D. Steppenbeck *et al.*, Nature **502**, 207 (2013).

[9] T. Otsuka, T. Suzuki, R. Fujimoto, H. Grawe and Y. Akaishi, Phys. Rev. Lett. **95**, 232502 (2005).

[10] T. Otsuka, T. Suzuki, M. Honma, Y. Utsuno, N. Tsunoda, K. Tsukiyama and M. Hjorth-Jensen, Phys. Rev. Lett. **104**, 012501 (2010).

[11] T. Abe, P. Maris, T. Otsuka, N. Shimizu, Y. Utsuno and J. P. Vary, *see these Proceedings*, p. 166, http://www.ntse-2014.khb.ru/Proc/Abe.pdf.

[12] T. Otsuka, Y. Tsunoda, N. Shimizu, M. Honma and Y. Utsuno, in *Proc. Int. Conf. Nucl. Theor. Supercomputing Era (NTSE-2013), Ames, IA, USA, May 13–17, 2013*, eds. A. M. Shirokov and A. I. Mazur. Pacific National University, Khabarovsk, Russia, 2014, p. 286, http://ntse-2013.khb.ru/Proc/Otsuka.pdf.

[13] T. Otsuka, R. Fujitmoto, Y. Utsuno, B. A. Brown, M. Honma and T. Mizusaki, Phys. Rev. Lett. **87**, 082502 (2001).

[14] M. Honma, T. Otsuka, B. A. Brown and T. Mizusaki, Phys. Rev. C **65**, 061301(R) (2002); *ibid.*, **69**, 034225 (2004).

[15] Y. Utsuno, T. Otsuka, N. Shimizu, M. Honma, T. Mizusaki, Y. Tsunoda and T. Abe, EPJ Web of Conf. **66**, 02106 (2014).

[16] Y. Utsuno, T. Otsuka, B. A. Brown, M. Honma, T. Mizusaki, and N. Shimizu, Phys. Rev. C **86**, 051301(R) (2012).

[17] S. Takeuchi *et al.*, Phys. Rev. Lett. **109**, 182501 (2012).

[18] H. A. Jahn and E. Teller, Proc. R. Soc. London, Ser. A **161**, 220 (1937).

[19] P.-G. Reinhard and E. W. Otten, Nucl. Phys. A **420**, 173 (1984).

[20] J. I. Prisciandaro *et al.*, Phys. Lett. B **510**, 17 (2001).

[21] R. V. F. Janssens *et al.*, Phys. Lett. B **546**, 55 (2002).

[22] S. N. Liddick *et al.*, Phys. Rev. Lett. **92**, 072502 (2004).

[23] M. Honma, T. Otsuka and T. Mizusaki, RIKEN Accelerator Progress Report **41**, 32 (2008).

Computational Approaches to Many-Body Dynamics of Unstable Nuclear Systems

Alexander Volya

Department of Physics, Florida State University, Tallahassee, FL 32306-4350, USA

Abstract

The goal of this presentation is to highlight various computational techniques used to study dynamics of quantum many-body systems. We examine the projection and variable phase methods being applied to multi-channel problems of scattering and tunneling; here the virtual, energy-forbidden channels and their treatment are of particular importance. The direct time-dependent solutions using Trotter–Suzuki propagator expansion provide yet another approach to exploring the complex dynamics of unstable systems. While presenting computational tools, we briefly revisit the general theory of the quantum decay of unstable states. The list of questions here includes those of the internal dynamics in decaying systems, formation and evolution of the radiating state, and low-energy background that dominates at remote times. Mathematical formulations and numerical approaches to time-dependent problems are discussed using the quasi-stationary methods involving effective non-Hermitian Hamiltonian formulation.

Keywords: *Quantum many-body dynamics, Time-Dependent Continuum Shell Model; Variable Phase Method; Trotter–Suzuki propagator expansion*

1 Introduction

There is no physical system that is truly isolated from the rest of the world, the closed system idealization may be convenient but becomes poor or completely invalid for many questions of modern-day science. In nuclear physics, as interests shift towards weakly bound, unbound or even dynamically evolving reaction states, the theoretical approaches for dealing with unstable dynamics of open quantum systems with multiple degrees of freedom should be revisited. The availability of advanced computational technologies calls forth innovative thinking and new philosophies in addressing these types of quantum many-body problems. In this presentation, using different models and realistic examples from the world of nuclear physics, we discuss computational strategies and techniques for dealing with dynamically unstable many-body systems. The *Nuclear Theory in the Supercomputing Era* venue is especially timely and allows us to put emphasis on some of the techniques, that due to their computational nature, remained behind the curtains in a number of recent investigations [1–3].

2 Intrinsic degrees of freedom in reactions

2.1 Projection method

Let us start by illustrating the difficulties that one faces while trying to reformulate reaction problems using the basis projection methods typical for structure physics;

Proceedings of the International Conference 'Nuclear Theory in the Supercomputing Era — 2014' (NTSE-2014), Khabarovsk, Russia, June 23–27, 2014. Eds. A. M. Shirokov and A. I. Mazur. Pacific National University, Khabarovsk, Russia, 2016, p. 35.

http://www.ntse-2014.khb.ru/Proc/Volya.pdf.

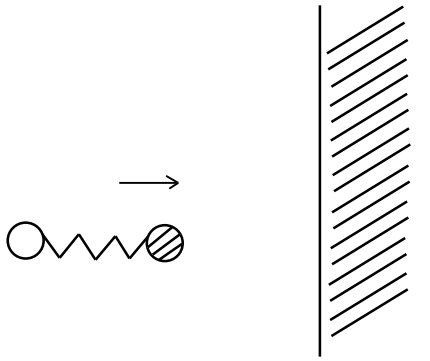

Figure 1: Schematic picture of scattering. A composite system of two particles bound by a harmonic oscillator potential scatters off an infinite wall. One of the particles does not interact with the wall, at the same time the wall is impenetrable for the second particle.

see also Refs. [2, 4]. Consider a model of scattering illustrated in Fig. 1. In this one-dimensional problem two particles with masses μ_1 and μ_2 comprise a composite system of unit mass $\mu_1+\mu_2 = 1$. The system can be described with the center-of-mass and relative coordinates, $X = \mu_1 x_1 + \mu_2 x_2$ and $x = x_1 - x_2$, respectively. The two particles are confined by a potential $v(x)$. The intrinsic Hamiltonian

$$h = -\frac{1}{\mu}\frac{\partial^2}{\partial x^2} + v(x) \tag{1}$$

is assumed to have a complete set of discrete eigenstates $\psi_n(x)$ with corresponding intrinsic energies ϵ_n:

$$h\psi_n(x) = \epsilon_n \psi_n(x), \qquad n = 0, 1, 2, ...$$

Here the reduced mass is $\mu = \mu_1\mu_2$ and we select our units so that $\hbar^2/2 = 1$. We assume that this system scatters off an infinite wall and the wall interacts only with the second particle. Therefore the full Hamiltonian is

$$H = -\frac{\partial^2}{\partial X^2} + U(x_2) + h, \text{ where } \quad U(x_2) = \begin{cases} \infty & \text{if} \quad x_2 \geq 0 \\ 0 & \text{if} \quad x_2 < 0 \end{cases} . \tag{2}$$

As illustrated in Fig. 1, we assume that the incident beam is traveling from the left and contains the projectiles in an intrinsic state (channel) n. A complete set of reflected waves is characterized by the amplitudes R_{nm} defined here so that $|R_{mn}|^2$ represents the probability for the initial beam in channel n to reflect in channel m; $R_{nm} = R_{mn}$ due to time-reversal invariance. The scattering wave function is

$$\Phi(X, x) = \frac{e^{iK_n X}}{\sqrt{|K_n|}}\psi_n(x) + \sum_{m=0}^{\infty} \frac{R_{mn}}{\sqrt{|K_m|}} e^{-iK_m X}\psi_m(x), \tag{3}$$

where

$$K_n(E) = \sqrt{(E - \epsilon_n)} \tag{4}$$

is the center-of-mass momentum of the two-particle system while in the n^{th} intrinsic state, and E is the total energy.

A channel n is considered to be open if $E \geq \epsilon_n$ and the corresponding momentum K_n is real. The conservation of particle-number in all open channels necessitates $\sum_{m\in\text{open}} |R_{mn}|^2 = 1$. The channel is closed if $E < \epsilon_n$, in which case K_n is purely imaginary. We stress that the principal value of the square root is implied in Eq. (4).

The boundary condition set by an impenetrable wall,

$$\Phi(X, x) = 0 \ \text{ at } \ x_2 = 0, \tag{5}$$

is to be used for determining the set of coefficients R_{mn}. Since the center-of-mass coordinate $X = \mu_1 x$ at $x_2 = 0$, the boundary condition can be expressed in the intrinsic coordinate x only, $\Phi(\mu_1 x,\, x) = 0$. Therefore we can project the reaction problem onto a complete set of intrinsic basis states, which leads to the following linear equation

$$\sum_m \frac{D_{n'm}\left[-i\mu_1(K_n + K_m)\right]}{\sqrt{|K_m|}}\, R_{mn} = -\frac{\delta_{n'n}}{\sqrt{|K_n|}}\,, \tag{6}$$

where the matrix D is defined as

$$D_{mn}(\varkappa) = \langle \psi_m | \exp(\varkappa x) | \psi_n \rangle\,. \tag{7}$$

Equation (6) represents a typical mathematical challenge associated with the formulation of reaction problems where reaction states are projected onto the intrinsic states; see also Section 3. It is a linear algebra problem where the construction of the scattering matrix amounts to matrix inversion in the projected space. The scattering energy E is a running parameter here, and studies of scattering at different energies is therefore time consuming. And, finally, the underlying matrix is highly singular and there are convergence issues. The latter difficulty is the one that we would like to illustrate using this example.

If the two particles forming a composite system are bound by a harmonic oscillator confinement, $v(x) = \mu\omega^2 x^2/2$ in Eq. (1), the D-matrix is known analytically [2]. Then to solve the problem we truncate the channel space at some large number N of oscillator quanta, and solve Eq. (6) using standard numerical techniques. This turns out to be a difficult task; the matrix element $D_{mn}(\varkappa)$ for virtual channels, where $\varkappa$ is real, are exponentially large, making the process of matrix inversion difficult and numerically unstable [2, 5, 6]. As shown in Fig. 2, left panel, the absolute values of the reflection amplitudes, $R_n \equiv R_{0n}$, exponentially diverge for increasingly remote virtual channels.

While it is possible to overcome the numerical issues, further examination shows that the approach has fundamental flaws. In Fig. 2, right panel, the phase shift, defined as $e^{2i\delta} = -R_{00}$, is shown as a function of N. While satisfactory and seemingly convergent results can be easily found for the cases where the mass of the non-interacting particle is small, in general the results start oscillating as N increases; situations where the non-interacting particle is heavy and therefore deeply penetrates the wall, are particularly difficult to handle. It was emphasized in Refs. [2, 4] that there is no numerical convergence with increasing N.

2.2 Variable Phase Method

The above example shows that reaction problems call for new techniques. One approach, based on the Variable Phase Method (VPM), see Ref. [7], is proposed in Ref. [2]. The VPM is an effective technique for solving the coupled-channel problem of the form

$$\left[\frac{\partial^2}{\partial X^2} + K_n^2\right]\Psi_n(X) - \sum_{n'} V_{nn'}(X)\Psi_{n'}(X) = 0, \tag{8}$$

where scattering observables are to be expressed relative to free-space solutions normalized to unit current

$$\Xi^{\pm}_{nn'}(X) = \frac{e^{\pm iK_n X}}{\sqrt{-2iK_n}}\,\delta_{nn'}; \tag{9}$$

the $\pm$ sign corresponds to a wave moving in the right/left direction. In the VPM approach, the coupled-channel Schrödinger equation (8) is reformulated as a set of first order differential equations for dynamic reflection and transmission amplitude

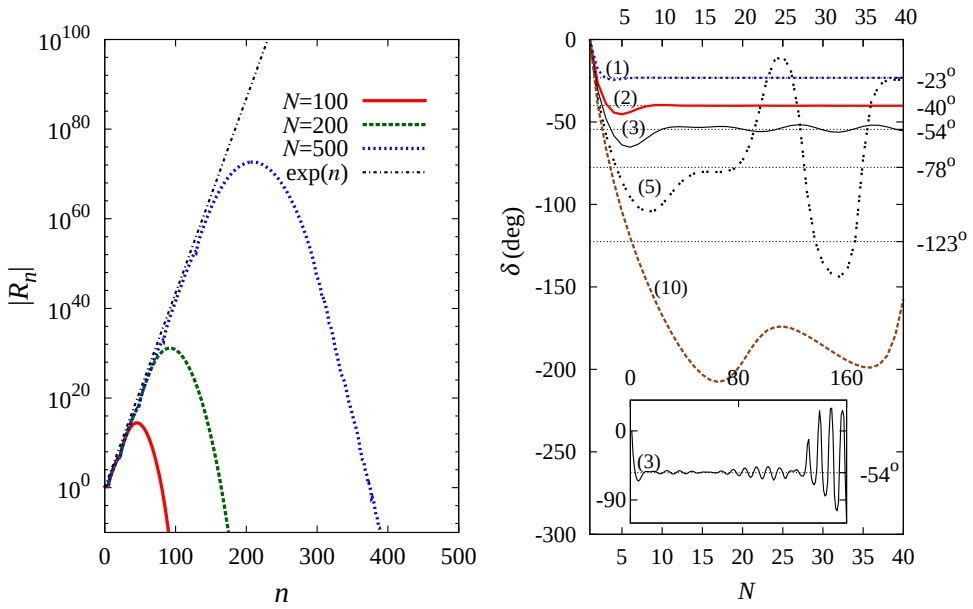

Figure 2: This figure refers to a system of two particles bound by a harmonic oscillator confinement, which collides with an infinite wall. The incident kinetic energy is exactly half of the oscillator quantum so that only the ground state channel is open. Left panel: For a system where $\mu_1 = \mu_2$ the absolute values of amplitudes $|R_n| \equiv |R_{0n}|$ in virtual channels are shown as functions of n assuming different truncations N. The asymptotic dependence is illustrated with the straight line "exp(n)". Right panel: The phase shift defined for a single open channel as $e^{2i\delta} = -R_{00}$, is plotted as a function of truncation N. The problems with the approach are highlighted by an unstable and oscillatory behavior of the phase shifts. The problem is particularly severe when the non-interacting particle of mass μ_1 is heavy. Different curves show phase-shifts for different mass ratios $\mu_1/\mu_2 = 1, 2, 3, 5, 10$, as labeled; the exact values obtained with Variable Phase Method (see Section 2.2) are shown by the horizontal grid lines with the tic-marks on the right. Inset shows the case when $\mu_1/\mu_2 = 3$ extending the study to considerably large values of N and emphasizing that for any choice of parameters the approach fails at some point.

matrices $R_{nn'}(X')$ and $T_{nn'}(X')$. These amplitudes correspond to a potential that is cut at X', namely, to $V_{nn'}(X)\,\theta(X - X')$:

$$\frac{dR(X)}{dX} = \left[\left(\Xi^+ + R(X)\,\Xi^-\right)\right] V \left[\Xi^+ + \Xi^-\,R(X)\right], \quad R_{nn'}(\infty) = 0, \tag{10}$$

$$\frac{dT(X)}{dX} = T(X)\,\Xi^-\,V\,\left[\Xi^+ + \Xi^-\,R(X)\right], \quad T_{nn'}(\infty) = \delta_{nn'}. \tag{11}$$

These equations being solved from $X = +\infty$ towards $X \to -\infty$, recover the reflection and transmission amplitudes $R_{nn'}(-\infty) = R_{nn'}$ and $T_{nn'}(-\infty) = T_{nn'}$.

Using factorization of the form

$$\Phi(X, x) = \sum_n \Psi_n(X)\,\psi_n(x),$$

the Schrödinger equation for the scattering problem described in Fig. 1 can be transformed into a coupled-channel equation (8) for the center-of-mass wave functions $\Psi_n(X)$, where the folded potentials are

$$V_{nn'}(X) = \int_{-\infty}^{\infty} \psi_n^*(x)\,U(X, x)\,\psi_{n'}(x)\,dx. \tag{12}$$

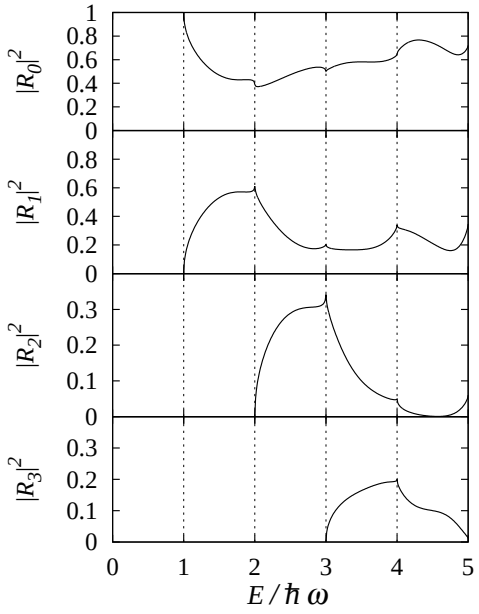

Figure 3: Reflection probabilities in different channels as functions of incident kinetic energy. The incident beam contains a composite projectile in the ground state. Equal masses $\mu_1 = \mu_2$ are assumed for both interacting and non-interacting particles.

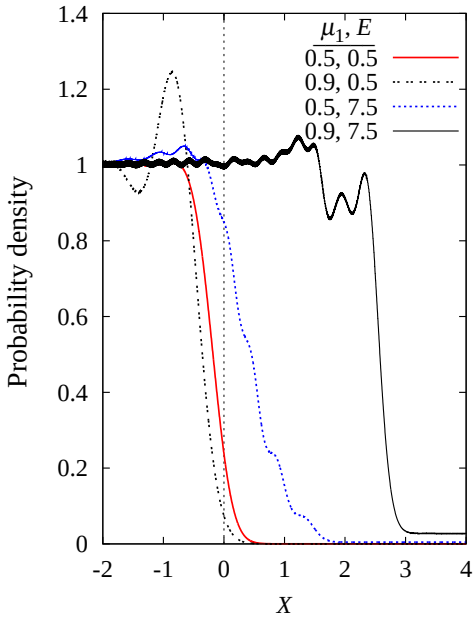

Figure 4: The density of probability for the center of mass of the projectile to be at a location X when it is reflected from an infinite wall at $X = 0$.

Some representative results for the scattering problem where an oscillator-bound system interacts with an infinite wall, are shown in Figs. 3 and 4. The reflection probabilities for different channels are shown in Fig. 3 as functions of incident kinetic energy. The kinetic energy is expressed in units of oscillator $\hbar\omega$, and therefore for each integer value thereof a new channel opens. One can notice typical cusps at thresholds associated with the loss of flux into newly opened channels. In Fig. 4, the probability distribution for the center of mass is shown. The four curves show four of the most representative situations: low and high incident kinetic energies $E = 0.5\hbar\omega$ and $E = 7.5\hbar\omega$, respectively, and two different mass-ratios $\mu_1 = 0.5$ and 0.9.

2.3 Time-dependent approach

Turning to a time-dependent approach is a natural strategy for dealing with non-stationary systems. There are various computational techniques; see Ref. [8] for some recent tests and comparisons of methods being applied to one-dimensional Schrödinger equation. In time-dependent techniques, a preservation of unitarity is often at the core of computational difficulties: the lack of unitarity could lead to an exponential amplification of numerical noise even for a single channel, while in multi-channel problems, discontinuities near thresholds are particularly challenging. Here we propose and demonstrate another approach that is computationally efficient, even in multi-variable cases, and preserves the unitarity exactly.

The time propagation,

$$\Phi(\mathbf{x}, t) = \exp\left(-\frac{i}{\hbar} H t\right) \Phi(\mathbf{x}, 0), \tag{13}$$

can be performed by considering separately the potential and kinetic parts

of the Hamiltonian $H = K + V$. In the discretized space of generalized coordinates $\mathbf{x} = \{x_1, x_2, ...\}$, the potential $V(\mathbf{x})$ is diagonal, so the exponential operator $\exp(-iVt/\hbar)$ can be readily applied. Similarly, in the conjugate momentum space $\mathbf{p} = \{p_1, p_2, ...\}$, the propagation with kinetic energy operator which is diagonal, is also easy to perform. While the operators K and V do not commute, the time evolution (13) with the combined Hamiltonian can be done efficiently with the Trotter–Suzuki approach [9, 10]. In this approach, the propagation is done in small time steps ΔT; for each of these steps the evolution operator is approximated as

$$\exp\left(-\frac{i}{\hbar}H\Delta t\right) = \exp\left(-\frac{i}{2\hbar}V\Delta t\right)\exp\left(-\frac{i}{\hbar}K\Delta t\right)\exp\left(-\frac{i}{2\hbar}V\Delta t\right) + O(\Delta t^3). \quad (14)$$

The Fast Fourier Transform allows for an efficient transition between the coordinate and momentum representations so that the exponentials of operators are always applied in the diagonal form. Even with the finite time steps, the unitarity is fully retained; the method is applicable to time-dependent Hamiltonians. The computational cost of two back and forth Fourier transforms involved in each step, is $N\log(N)$ assuming that the coordinate space is discretized into N points. While this appears at first to be higher than the typical $O(N)$ scaling of traditional methods, in practice the cost cN of any high quality method involves a constant factor c that exceeds often $\log(N)$. Moreover, the modern computer hardware often comes with signal processing tools which are optimized at the hardware and software levels to perform the Fast Fourier Transform with an incredible efficiency.

Let us return to the problem of scattering illustrated in Fig. 1. The time dependent picture of the scattering process is shown in Fig. 5 with a series of four plots showing the two-dimensional wave function using a density plot at four different times. The plot of the density projection onto the center-of-mass coordinate X, which is the time-dependent analog of Fig. 4, is shown below each of the four snapshots. The initial wave function at $t = 0$ shown on the first panel, is selected as the ground state wave function for the intrinsic potential, and as a moving Gaussian wave packet for the center of mass coordinate,

$$\Phi(X, x) = \frac{1}{\sqrt{\sigma_0\sqrt{\pi}}}\exp\left[\frac{1}{2\sigma_0^2}(X - X_0)^2 + iK_0X\right]\psi_0(x). \quad (15)$$

In this example, $\sigma_0 = 2$, $X_0 = -5$, and the initial momentum $K_0 = 1$, all quantities are being expressed here in dimensionless units of distance as defined earlier. While this time dependent consideration is different from the stationary state formulation studied above, the series of snapshots for different times shown in Fig. 5 highlights some similar features.

At high energies, the dynamics of virtual excitations is complex; this is illustrated in Fig. 6 where the initial wave packet is selected to have $K_0 = 5$. A semiclassical interpretation can be given to the stages of the process. An initial compression at $t = 1$ is followed by two particles bouncing apart at $t = 2$. Having equal masses, their center of mass remains at the origin but the relative separation x becomes large so that the particles are positioned roughly symmetrically on the opposite sides of the wall. Next, at $t = 3$, the center of mass moves into the $X < 0$ region pressing the interacting particle against the wall. Finally, the system is reflected at $t = 4$ with the initial wave packet being considerably distorted.

In comparison to the projection and VPM techniques discussed earlier, the time-dependent approach is substantially faster numerically; moreover, any potential $U(x_1, x_2)$ can be considered with ease in this approach. One has to keep in mind, however, that it is not always easy to provide quantitative answers to stationary state questions such as the determination of scattering phase shifts in this example, using the time-dependent techniques. The exact choice of the initial state as well as

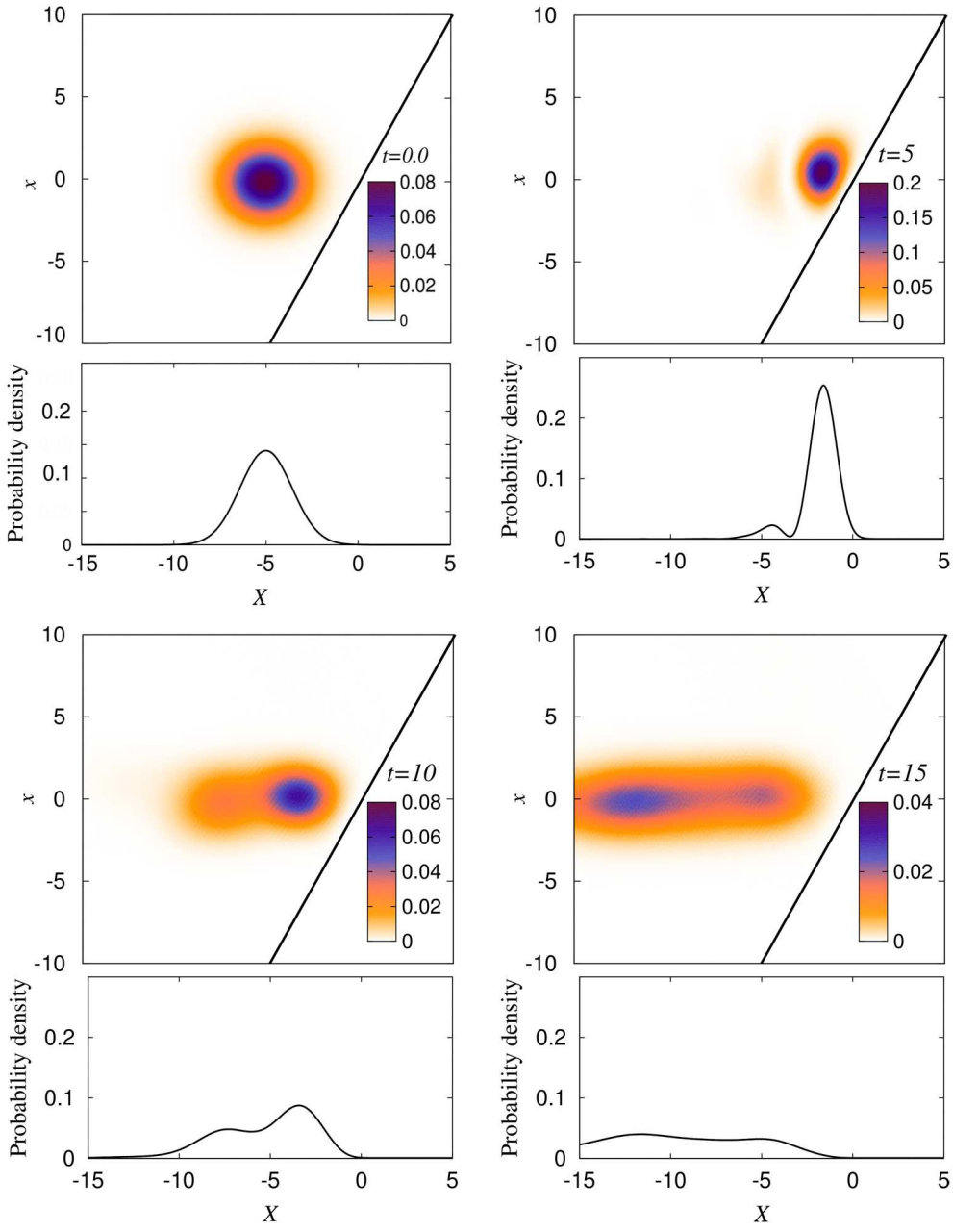

Figure 5: The four panels show the wave function $|\Phi(X,x)|^2$ as a density plot for different times $t = 0$, 5, 10 and 15, as labeled. For each of the time snapshots, the lower plot shows the density distribution over the center-of-mass coordinate computed as $\int |\Phi(X,x)|^2 dx$. The initial wave function at $t = 0$ is given by the Gaussian wave packet, Eq. (15). For this system $\mu_1 = \mu_2$, the border of inaccessible area $x_2 > 0$ is shown with a solid line.

the energy uncertainty of the initial state can be important for some stages of time evolution.

The physics of decay of unstable states represents a particularly important class of time-dependent processes. The familiar exponential decay law is only an incomplete picture requiring some subtle approximations, and being valid only within certain time limits. The complex intrinsic dynamics that can occur in the decaying many-body system, further complicates the time evolution. Non-exponential decay laws in

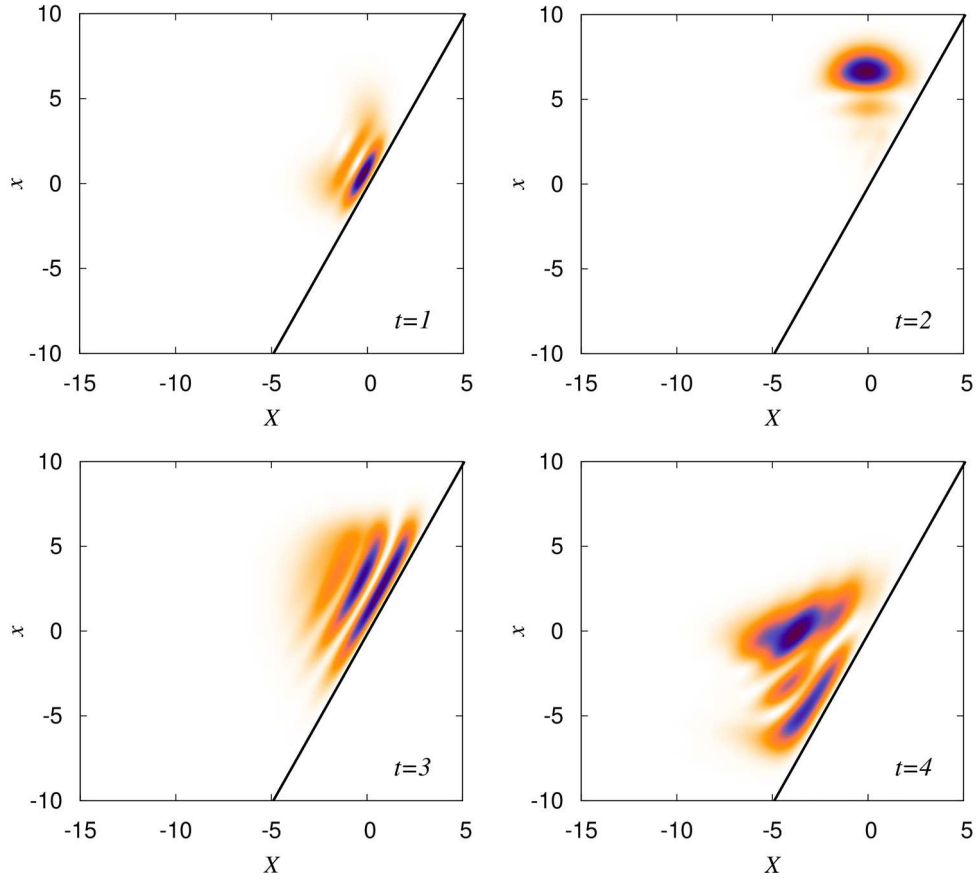

Figure 6: The four panes similar to those in Fig. 5, show the wave function $|\Phi(X,x)|^2$ at the most representative moments of time $t = 1$, 2, 3 and 4, during the high energy collision with the impenetrable wall. Here $K_0 = 5$, the remaining parameters being the same as in Fig. 5.

quantum mechanics have been studied and revisited by many authors (see Ref. [3] and references therein). The presence of three regimes, namely, the initial, the exponential, and the long-time power law, appears to be a universal feature of decay processes. The transitions from one regime to another are accompanied by the interference of corresponding quantum amplitudes that is seen as oscillations on the decay curve.

As another demonstration of the time-dependent technique based on the Trotter–Suzuki expansion and as an introduction to the section that follows, we demonstrate in Fig. 7 the decay process in Winter's model [11] which has been a very popular tool for exploring non-exponential features in decays. In this model, a particle is confined to the region $x \geq 0$ by the impenetrable wall at $x = 0$ and is held by a delta barrier at $x = 1$. The initial state at $t = 0$ is taken as $\Psi(x,0) = \sqrt{2}\sin(\pi x)$. The survival probability shown by a solid red line in the left panel of Fig. 7, illustrates three general regimes: the pre-exponential, the exponential, and the post-exponential. Oscillations can be seen in transitional regions. The snapshots of the wave function at different times are shown on the right.

The pre-exponential behavior at very early times is influenced by the memory of how the state was created and, in particular, by the high energy components of the state. Later in time, the internal structure and transitions between the intrinsic states become relevant. Short times correspond to remote energy components where the presence of other resonant states is to be considered. The high energy components have much shorter lifetimes and decay quickly leading to the exponential decay phase.

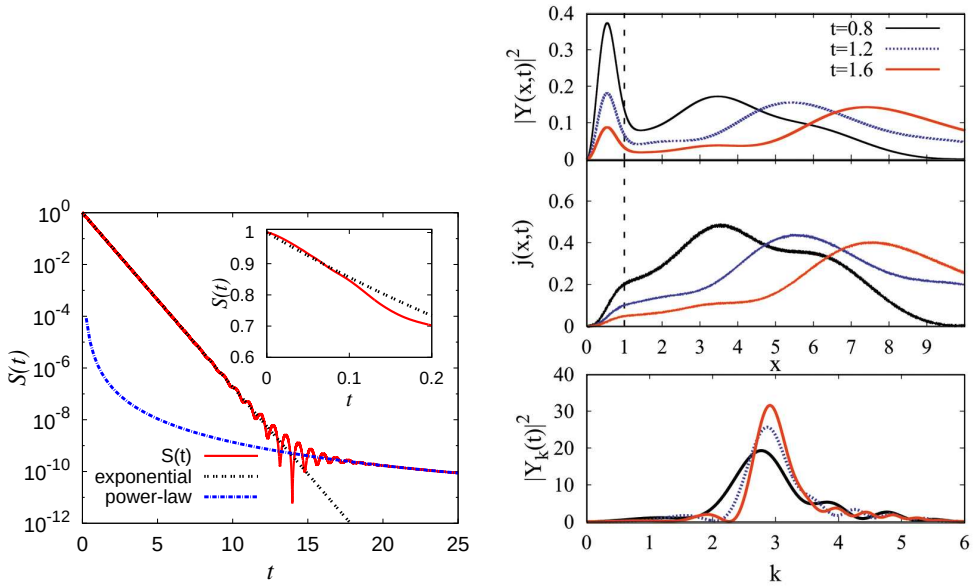

Figure 7: Left: the survival probability $S(t) = |\langle\Psi(0)|\Psi(t)\rangle|^2$ is shown as a function of time (solid red line). The exponential decay law where the mean lifetime $\tau = 0.65$ is known from the poles of the scattering matrix, is shown with a double-dotted black line, the background component that decays following a power law is shown with a dot-dash blue line. The survival probability at very early times is shown in the inset. Right: the wave function of a decaying state is shown at times $t = 0.8$, 1.2, and 1.6: the upper panel shows the probability distribution $|\Psi(x)|^2$, the middle panel displays the current $j(x,t)$, and the wave function in momentum space is shown in the lower panel. Here the strength of the delta function $G = 6$ in units where $\hbar = 2m = 1$.

This phase is dominated by a single resonant component, the radiating state, so that the wave function retains its shape while decreasing in amplitude. This can be seen in the right panel of Fig. 7. In the same figure, one can also trace a moving away background component. The background contains very low energy particles; being far off-resonance, they essentially do not interact but move slowly away from the interaction region. Near the decay threshold, the number of such particles with a certain energy is determined by the available phase space, which for neutral particles scales with energy following a power-law $E^{l+1/2}$ where l is the angular momentum quantum number. This type of scaling leads to non-resonant components that follow a power-law decay $S(t) \sim 1/t^{2\ell+3}$. While the non-resonant component can be very small in the initial state, eventually it becomes dominant due to its slower-than-exponential decay. Further discussion of decay processes in quantum mechanics and other examples can be found in Ref. [3]. The near-threshold phase space scaling with energy which leads to power-law decay at remote times, is an important consideration in the Time-Dependent Continuum Shell Model approach that is discussed in the following section, see also Refs. [1, 12, 13], as well as in more complicated sequential decay processes [14].

3 Time-Dependent Continuum Shell Model

3.1 Continuum Shell Model

A seamless transition between structure physics and reactions is one of the central present-day theoretical problems. The computational aspect associated with transitions from discrete levels to a continuum of reaction states is especially challeng-

ing. The Continuum Shell Model approach [12, 13] and its time-dependent version in particular, is one among several theoretical tools confronting these issues. In the Continuum Shell Model, the Feshbach projection formalism [15,16] is used to express the exact dynamics in the full Hilbert space using an effective Hamiltonian in the projected intrinsic subspace of interest, $\mathcal{Q}$:

$$\mathcal{H}(E) = H_{\mathcal{QQ}} + \tilde{H}(E), \tag{16a}$$

where

$$\tilde{H}(E) = H_{\mathcal{QP}} \frac{1}{E - H_{\mathcal{PP}}} H_{\mathcal{PQ}}. \tag{16b}$$

Here the effective Hamiltonian contains $H_{\mathcal{QQ}}$ which is the part of the original Hamiltonian that acts in the space $\mathcal{Q}$, and the energy-dependent non-Hermitian term $\tilde{H}(E)$ that emerges from the coupling of the space $\mathcal{Q}$ to the external space containing the continuum of reaction states, $\mathcal{P}$.

In practical applications the intrinsic space $\mathcal{Q}$ is assumed to represent the configuration space of the traditional shell model built from states $|1\rangle$ that are Slater determinants constructed from bound-state single-particle wave functions. The space $\mathcal{P}$ contains continua of reaction states $|c, E\rangle$ characterized by the channel index, c, and the continuous energy parameter, E. There is a certain threshold energy $E^{(c)}_{\rm thr}$ for each channel c. The energy-dependent non-Hermitian effective Hamiltonian (16) is represented by a matrix $\mathcal{H}_{12}(E) \equiv \langle 1|\mathcal{H}(E)|2\rangle$,

$$\mathcal{H}_{12}(E) = H_{12} + \Delta_{12}(E) - \frac{i}{2} W_{12}(E)\,, \tag{17a}$$

where

$$\Delta_{12}(E) = \sum_c \mathrm{PV} \int_{E^{(c)}_{\rm thr.}}^{\infty} dE' \frac{A^c_1(E') A^{c\,*}_2(E')}{E - E'}, \tag{17b}$$

$$W_{12}(E) = 2\pi \sum_{c(\rm open)} A^c_1(E) A^{c\,*}_2(E), \tag{17c}$$

and the channel amplitudes are the matrix elements $A^c_1(E) = \langle 1|H|c, E\rangle$. The traditional shell model Hamiltonian is recovered when the internal space $\mathcal{Q}$ is isolated and thus decoupled, $A^c_1(E) = 0$.

Computational challenges of the traditional shell model approach are well known, they are mainly associated with the need to find some selected eigenvalues and eigenvectors of the Hamiltonian matrix H_{12}. The matrix is generally sparse, thanks to few-body nature of the underlying nucleon-nucleon interactions which inhibit mixing of very remote configurations, thus iterative techniques such as Lanczos approach are commonly used.

The physics of weakly-bound and unstable nuclear systems is much more rich as questions of interest span from properties of bound states to features in scattering cross sections. Narrow resonances are well characterized by usual properties of bound states with the decay width being an additional characteristic. This requires the non-Hermitian eigenvalue problem $\mathcal{H}(E)|\mathcal{I}\rangle = \mathcal{E}|\mathcal{I}\rangle$ to be solved. The resulting complex energies $\mathcal{E}$ represent positions of resonances, $E = \mathrm{Re}(\mathcal{E})$, and their widths, $\Gamma = -2\,\mathrm{Im}(\mathcal{E})$. The most practical technique here is to start with a perturbative treatment and evaluate the term $\tilde{H}(E)$ associated with continuum using wave functions of the traditional shell model Hamiltonian $H_{\mathcal{QQ}}$. As coupling to the continuum increases the states become broad and one is forced to treat the non-Hermitian energy-dependent eigenvalue problem as an iterative non-Hermitian diagonalization process. In this limit, a major problem is associated with the physical interpretation of the resonances and their widths.

Formally, the energy-dependent non-Hermitian Hamiltonian provides an exact propagator for the intrinsic space, and therefore the scattering matrix is

$$\mathbf{S}_{cc'}(E) = \exp(i\xi_c + i\xi_{c'})\,[\delta_{cc'} - 2\pi i \mathbf{T}_{cc'}(E)], \tag{18a}$$

where

$$\mathbf{T}_{cc'}(E) = \sum_{12} A_1^c(E) \left\{ \frac{1}{E - \mathcal{H}} \right\}_{12} A_2^{c'}(E). \tag{18b}$$

Here ξ_c is a potential (direct-reaction) phase. The matrix is unitary (see Ref. [1]) and the unitarity is related to the factorized form of the imaginary $W_{12}(E)$ in Eq. (17). The eigenvalues of the non-Hermitian Hamiltonian are therefore the poles of the scattering matrix. In the limit of broad resonances, one has to address the reaction problem where obtaining a reaction cross section is the main goal. There are several numerical challenges associated with Eq. (18), many of these challenges being similar to the ones discussed in Section 2.1. First, the size of the Hamiltonian matrix and the complex arithmetic involved are not making this problem simpler as compared to matrix diagonalization. Second, the scattering energy E represents a running parameter so that the procedure should be repeated for all energies of interest. Finally, the problem is numerically unstable: bound states as well as resonances with widths ranging by many orders of magnitude, may be encountered and should be treated consistently. All of these technical issues are resolved by the Time-Dependent Continuum Shell Model approach which we discuss next.

3.2 Time-dependent many-body evolution operator

The many-body wave function follows the time evolution which is a Fourier image of the retarded propagator involved in the scattering matrix (18):

$$G(E) = \frac{1}{E - H} = -i \int_0^\infty dt\, \exp(iEt) \exp(-iHt). \tag{19}$$

Here H is an arbitrary Hamiltonian but, as discussed below, it is advantageous to include a factorized imaginary part W using a different procedure described in Section 3.3. Thus we view H as being a Hermitian Hamiltonian of the traditional shell model in which case it is set to have an infinitesimal negative-definite imaginary part. The time-dependent evolution operator can be factorized using a Chebyshev polynomial expansion method, see Ref. [1, 17, 18]:

$$\exp(-iHt) = \sum_{n=0}^{\infty} (-i)^n (2 - \delta_{n0})\, J_n(t)\, T_n(H), \tag{20}$$

where J_n is the Bessel function of the first kind and T_n represents Chebyshev polynomials. The Chebyshev polynomials defined as $T_n[\cos(\theta)] = \cos(n\theta)$ or, in explicit form,

$$T_n(x) = \frac{n}{2} \sum_{k=0,1,\ldots}^{k \le n/2} \frac{(-1)^k}{n-k} \left(\begin{array}{c} n-k \\ k \end{array} \right) (2x)^{n-2k}, \tag{21}$$

provide a complete set of orthogonal functions covering uniformly the interval [-1, 1]. In contrast, Taylor expansion relies on power functions which favor the edges of the interval and thus are more sensitive to extreme eigenvalues. The "angular addition" identity

$$2\, T_n(x)\, T_m(x) = T_{n+m}(x) + T_{n-m}(x)\,, \quad n \ge m, \tag{22}$$

which follows from the definition, allows one to obtain these polynomials using the recurrence relation

$$T_0(x) = 1, \tag{23a}$$
$$T_1(x) = x, \tag{23b}$$
$$T_{n+1}(x) = 2xT_n(x) - T_{n-1}(x). \tag{23c}$$

Therefore the process of evaluation of Chebyshev polynomials of the Hamiltonian operator is an iterative procedure similar to that in Lanczos approach. For a given initial state $|\lambda\rangle \equiv |\lambda_0\rangle$, a sequence $|\lambda_n\rangle = T_n(H)|\lambda\rangle$ can be constructed as

$$|\lambda_0\rangle = |\lambda\rangle, \tag{24a}$$
$$|\lambda_1\rangle = H|\lambda\rangle, \tag{24b}$$

and

$$|\lambda_{n+1}\rangle = 2H|\lambda_n\rangle - |\lambda_{n-1}\rangle. \tag{24c}$$

For overlap functions, assuming Hermitian H, one can also use the following identity:

$$\langle\lambda'|T_{n+m}(H)|\lambda\rangle = 2\langle\lambda'_m|\lambda_n\rangle - \langle\lambda'|\lambda_{n-m}\rangle, \quad n \geq m. \tag{25}$$

A well-controlled energy resolution is an advantage of the method. In applications of the method, the energy interval $[E_{min}, E_{max}]$ which should contain all eigenvalues of H, is mapped onto $[-1, 1]$ by rescaling the Hamiltonian as $H \to (H - \overline{E})/\Delta E$, where $\overline{E} = (E_{max} + E_{min})/2$ and $\Delta E = (E_{max} - E_{min})/2$. For a desired energy resolution $\Delta E/N$ where N is some even integer number, the discrete Fourier transform allows one to evaluate Green's function in the corresponding energy points of the rescaled interval $E_p = p/N$ with $p = -N/2, \ldots, N/2$,

$$\langle\lambda'|G(E_p)|\lambda\rangle = -i\pi \left\{ \sum_{\tau=0}^{N-1} e^{2\pi i p\tau/N} \sum_{n=0}^{n_{\max}(\tau)} (-i)^n (2-\delta_{n0}) J_n(\pi\tau) \langle\lambda'|T_n(H)|\lambda\rangle \right\}. \tag{26}$$

This requires the evaluation of the evolution operator at times $t = \pi\tau$, where $\tau = 0, \ldots, N-1$. For each desired time point τ the number of terms in expansion (20) needed for the convergence, is denoted as $n_{\max}(\tau)$. The Bessel function asymptotics $J_n(x) \approx \sqrt{1/(2\pi n)}[ex/(2n)]^n$ suggests $n_{\max}(\tau) \approx e\pi\tau/2 \approx 4\tau$. At fixed values of n but for large times the convergence remains stable due to $J_n(t) \approx \sqrt{2/(\pi t)}\cos(t - \pi n/2 - \pi/4)$ in this limit. For the desired energy resolution $\Delta E/N$, the propagation in time has to be extended up to $\approx \tau N$ which requires $n_{\max} \approx 4N$; therefore $2N$ matrix-vector multiplications are required if one also uses Eq. (25).

The time-dependent approach provides the Green's function for all energies at once; it is also exceptionally stable numerically when dealing with very narrow resonances or with stable states. Indeed, the time-dependent behavior of stationary states is regular and the corresponding delta function in energy is well handled by Fourier transform which at the desired energy resolution properly conservers the integrated strength.

In order to illustrate the approach, let us consider strength and integrated strength functions defined for a given state $|\lambda\rangle$ as

$$F_\lambda(E) = \langle\lambda|\delta(E-H)|\lambda\rangle = -\frac{1}{\pi}\,\mathrm{Im}\,\langle\lambda|G(E)|\lambda\rangle, \tag{27a}$$
$$I_\lambda(E) = \int_{-\infty}^{E} F_\lambda(E')\,dE'. \tag{27b}$$

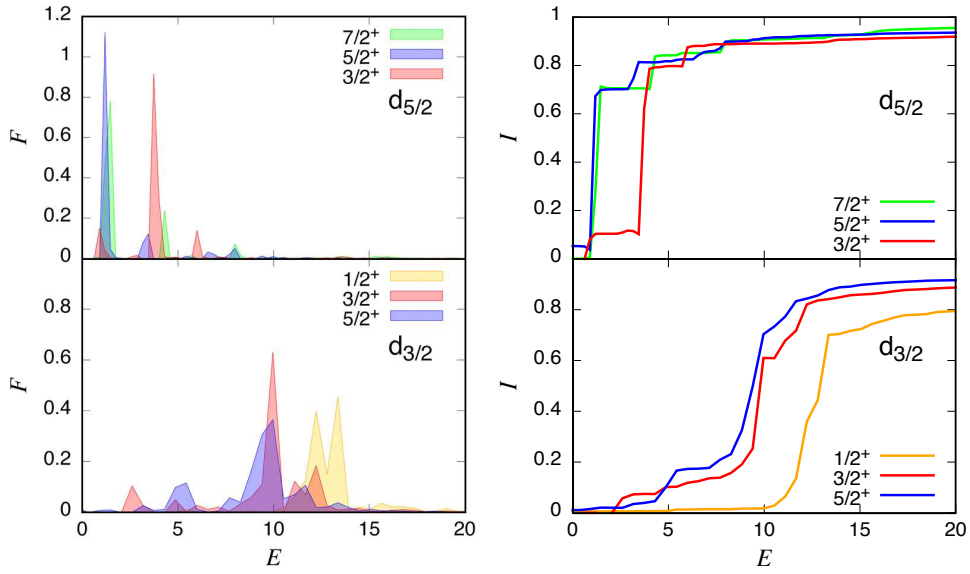

Figure 8: Single-particle strength function (left) and cumulative or integrated strength function (right) are shown as functions of excitation energy (in units of MeV) for ^{15}N.

In Fig. 8 both the strength (left) and the integrated strength (right) functions are shown for ^{15}N for neutron channels where $|\lambda\rangle$ corresponds to different angular momentum channels constructed from the 1^+ ground state in ^{14}N coupled to a single nucleon on either $d_{5/2}$ (top panels) or $d_{3/2}$ (bottom panels) single-particle states. This theoretical study follows recent experimental work in Ref. [19]. The full *p*-*sd* valence space is used with the Hamiltonian from Ref. [20]. With about 10^7 *m*-scheme basis states, obtaining and computing strength functions in energy regions around 20 MeV of excitation is impractical; the time-dependent method provides an excellent alternative.

3.3 Sherman–Morrison–Woodbury relations

It is certainly possible to implement the Chebyshev polynomial expansion procedure for the full non-Hermitian Hamiltonian using Eq. (20); however the factorized structure of $\tilde{H}$ offers a different alternative which is much more computationally advantageous. The two propagators corresponding to Eqs. (16),

$$G(E) = \frac{1}{E - H_{\mathcal{Q}\mathcal{Q}}} \tag{28a}$$

and

$$\mathcal{G}(E) = \frac{1}{E - \mathcal{H}(E)}, \tag{28b}$$

can be related through the Dyson equation $\mathcal{G}(E) = G(E) + G(E)\,\tilde{H}(E)\,\mathcal{G}(E)$. Since the contribution from the continuum emerges in the factorized form

$$\tilde{H}(E) = \sum_{cc'} |c\rangle \tilde{\mathbf{H}}_{cc'}(E) \langle c'|, \tag{29}$$

the expression for the full propagator can be found in a closed form in the space spanned by the channel states:

$$\mathbb{G} = \mathbf{G}\Big[\mathbf{1} - \tilde{\mathbf{H}}\mathbf{G}\Big]^{-1} = \Big[\mathbf{1} - \mathbf{G}\tilde{\mathbf{H}}\Big]^{-1}\mathbf{G}. \tag{30}$$

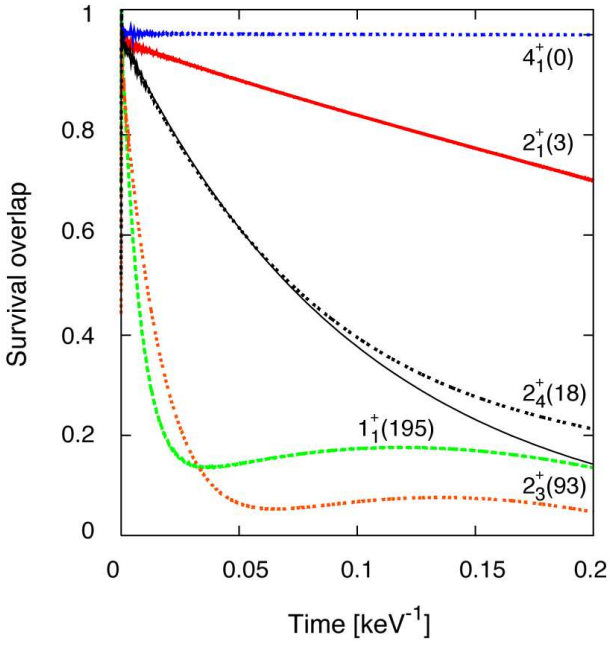

Figure 9: Time evolution of several low-lying states in ^{24}O. The absolute value of the survival overlap $|\langle\alpha|\exp(-i\mathcal{H}t)|\alpha\rangle|$ is shown as a function of time. Different lines, as marked, correspond to states $\alpha(E_\alpha,\Gamma_\alpha)$: 2_1^+ (4.180, 2.7), 1_1^+ (5291, 195.1), 4_1^+ (6947, 0.0), 2_3^+ (8107, 92.5) and 2_4^+ (9673, 17.5). They are eigenstates of the traditional USD shell model but are non-stationary resonances in the Time-Dependent Continuum Shell Model, except for the 4_1^+ state which due to its high spin does not decay within the *sd* valence space. To emphasize the non-exponentiality in the decay law, the unmarked solid line shows the $\exp(-\Gamma_\alpha t/2)$ function with parameters for the 2_4^+ state.

The operators here are represented by matrices in the channel subspace $\mathbb{G}_{ab} = \langle a|\mathcal{G}(E)|b\rangle$ and $\mathbf{G}_{ab} = \langle a|G(E)|b\rangle$. In computer science these relations are known as Sherman–Morrison–Woodbury matrix inversion equations [21]. The unitarity of the scattering matrix immediately follows from these relations, see [1].

We illustrate the Time-Dependent Continuum Shell Model approach in its complete form in Figs. 9 and 10 where the resonances in ^{24}O are considered. The system is treated in the *sd* valence space using the USD shell model Hamiltonian [22]. In Fig. 9 the norm of the survival amplitude is shown as a function of time for the following set of most representative states: 2_1^+ (4180, 2.7), 1_1^+ (5291, 195.1), 4_1^+ (6947, 0.0), 2_3^+ (8107, 92.5), and 2_4^+ (9673, 17.5). The states are listed here with their excitation energies followed by the decay widths, both in keV. The initial wave functions at $t = 0$ are taken as eigenstates of the traditional shell model. For the states such as 4_1^+ which cannot decay in this model due to high angular momentum, the norm of the survival amplitude remains constant. Narrow states exhibit a nearly exponential decay, for the state 2_4^+ the survival amplitude expected in exponential decay is shown. The decay is non-exponential for broad states such as 1_1^+ and 2_3^+. In Fig. 10 the scattering cross section is shown for elastic neutron scattering on the ground state of ^{23}O where the same resonant states can be observed.

The time-dependent approach provides an effective computational strategy for treating many-body systems that feature both bound and unbound states. In contrast to the stationary state formalism, the time dependent approach addresses the evolution of states in a natural way, thus providing a computationally robust and stable strategy where experimental observables are easily recovered and fundamental

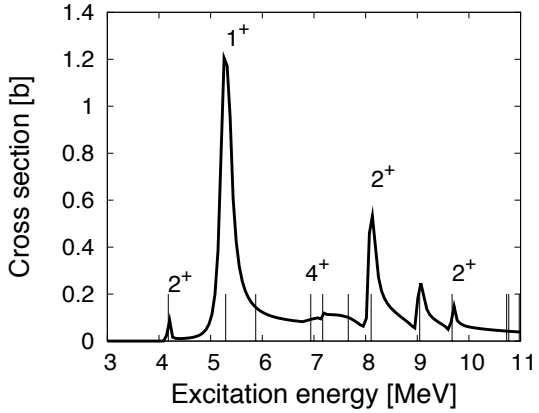

Figure 10: Scattering cross section for $^{23}\mathrm{O}(n,n)^{23}\mathrm{O}$ reaction showing resonances in $^{24}\mathrm{O}$.

principles of quantum mechanics, such as linearity and unitarity, are followed. From the computational perspective, the most efficient operation available for the matrix-vector multiplication is utilized in building the time evolution operator with full control of the desired energy and time resolution. The specifics of the terms that emerge due to coupling to continuum in Feshbach projection formalism can be used to build the full evolution operator using Sherman–Morrison–Woodbury relations. The Time-Dependent Continuum Shell Model found broad practical applications, see Refs. [23–25] for examples.

4 Conclusions

As our interests shift towards open, reacting, decaying, and otherwise evolving quantum many-body systems, new theoretical and computational techniques must be developed to address multiple new challenges that emerge. The goal of this presentation is to highlight some of the methods used in the recent scientific projects. We use a simple model to demonstrate three distinctly different techniques. The most straightforward method involves projecting the dynamics onto a set of basis states, allowing subsequently for the well-developed methods of linear algebra to be used; in certain reaction problems this method appears to have significant drawbacks associated with numerical instabilities and poor convergence. We demonstrate the Variable Phase Method that can treat reaction problems efficiently in a discretized coordinate space. Finally, we consider explicitly time-dependent techniques that are perhaps most adequate for the time-dependent dynamics associated with decay. We put forward the Time-Dependent Continuum Shell Model approach as a practical tool and demonstrate its application to realistic problems in nuclear physics.

This material is based upon work supported by the U.S. Department of Energy Office of Science, Office of Nuclear Physics under Award Number DE-SC0009883. The author is grateful to N. Ahsan, M. Peshkin, and V. Zelevinsky for collaboration.

References

[1] A. Volya, Phys. Rev. C **79**, 044308 (2009).

[2] N. Ahsan and A. Volya, Phys. Rev. C **82**, 064607 (2010).

[3] M. Peshkin, A. Volya and V. Zelevinsky, EPL **107**, 40001 (2014).

[4] N. Ahsan and A. Volya, J. Phys. Conf. Ser. **312**, 092011 (2011).

[5] A. Sakharuk and V. Zelevinsky, A toy model for the scattering of composite objects, in *APS Ohio Section Fall Meeting*, 1999APS..OSF..CD09S (1999).

[6] A. M. Moro, J. A. Caballero and Gómez-Camacho, arXiv:1010.4933 [nucl-th] (2010).

[7] V. V. Babikov, *Method of phase functions in quantum mechanics*. Nauka, Moscow, 1968 (*in Russian*).

[8] W. van Dijk, J. Brown and K. Spyksma, Phys. Rev. E **84**, 056703 (2011).

[9] H. F. Trotter, Proc. Am. Math. Soc. **10**, 545 (1959).

[10] M. Suzuki, Phys. Lett. A **146**, 319 (1990).

[11] R. G. Winter, Phys. Rev. **123**, 1503 (1961).

[12] A. Volya and V. Zelevinsky, Phys. Rev. Lett. **94**, 052501 (2005).

[13] A. Volya and V. Zelevinsky, Phys. Rev. C **74**, 064314 (2006).

[14] A. Volya, EPJ Web Conf. **38**, 03003 (2012).

[15] H. Feshbach, Ann. Phys. (NY) **5**, 357 (1958).

[16] C. Mahaux and H. A. Weidenmüller, *Shell-model approach to nuclear reactions.* North-Holland, Amsterdam, London, 1969.

[17] Y. L. Loh, S. N. Taraskin and S. R. Elliott, Phys. Rev. E **63**, 056706 (2001).

[18] T. Ikegami and S. Iwata, J. Comp. Chem. **23**, 310 (2002).

[19] C. E. Mertin *et al.*, Acta Phys. Pol. B **45**, 159 (2014).

[20] Y. Utsuno and S. Chiba, Phys. Rev. C **83**, 021301(R) (2011).

[21] W. H. Press, S. A. Teukolsky, W. T. Vetterling and B. P. Flannery, *Numerical recipes in C++: the art of scientific computing.* Cambridge University Press, Cambridge, New York, 2002.

[22] B. A. Brown, W. A. Richter, R. E. Julies and B. H. Wildenthal, Ann. Phys. (NY) **182**, 191 (1988).

[23] J. P. Mitchell *et al.*, Phys. Rev. C **87**, 054617 (2013).

[24] J. P. Mitchell *et al.*, Phys. Rev. C **82**, 011601(R) (2010).

[25] G. V. Rogachev *et al.*, Phys. Rev. C **75**, 014603 (2007).

Cluster Structure of Light Nuclei Superposing Multiple Slater Determinants

K. Yabana[a,b], Y. Fukuoka[b], Y. Funaki[c] and T. Nakatsukasa[a,b,c]

[a] *Center for Computational Sciences, University of Tsukuba, Tsukuba 305-8577, Japan*
[b] *Graduate School of Pure and Applied Sciences, University of Tsukuba, Tsukuba 305-8571, Japan*
[c] *RIKEN Nishina Center, Wako, 351-0198, Japan*

Abstract

We develop a computational approach superposing a number of Slater determinants to describe cluster-like as well as shell-model-like structures of light nuclei simultaneously. The Slater determinants are prepared using imaginary-time method starting with stochastically prepared initial configurations. A microscopic many-body Hamiltonian of Skyrme interaction is then diagonalized in the space spanned by Slater determinants with parity and angular momentum projections. The method is applied to ^{12}C. It is shown that low-lying excited states of both cluster-like and shell-model-like states are reasonably described.

Keywords: *Cluster structure; Skyrme interaction; multiple Slater determinants*

1 Introduction

It has been well-known that various cluster structures appear in excited states of light nuclei [1]. Although shell-model approaches have been successful for low-lying excited states in a wide mass region, it is difficult to describe cluster states since they require a number of many-particle and many-hole configurations across the major shell.

To describe both cluster-like and shell-model-like states simultaneously, we have been developing a new configuration mixing approach [2, 3]. In this approach, we start with a many-body Hamiltonian with an empirical nucleon-nucleon interaction. We attempt to calculate low-lying excited states as well as the ground state which are converged with respect to configurations included in the calculation. To prepare configurations which are sufficient to describe cluster-like states, we employ the imaginary-time method which is usually employed to obtain self-consistent solutions in the mean-field calculations. During the iterations before reaching the self-consistent solution, there often appear various cluster-like configurations in the imaginary-time calculations. We make use of this fact and employ them as basis functions.

In the following, we describe the outline of the method. Then we show an application to the ^{12}C nucleus [2].

2 Formalism

2.1 Preparation of Slater determinants

As a first step of our calculation, we prepare a set of Slater determinants, typically 50, which will be used for the configuration mixing calculation at the next step. The set of Slater determinants is constructed by the following procedure [2, 3].

Proceedings of the International Conference 'Nuclear Theory in the Supercomputing Era — 2014' (NTSE-2014), Khabarovsk, Russia, June 23–27, 2014. Eds. A. M. Shirokov and A. I. Mazur. Pacific National University, Khabarovsk, Russia, 2016, p. 51.

http://www.ntse-2014.khb.ru/Proc/Yabana.pdf.

As the Slater determinant which is labeled as no. 1, we choose the self-consistent solution from the mean field calculation. We obtain it as a final convergent solution in the imaginary-time method. Other Slater determinants are obtained in the following recursive procedure. Assuming that we have already N Slater determinants, the next $(N+1)$-th Slater determinant is obtained as follows. We prepare a Slater determinant in which each single-particle orbital is a Gaussian wave packet whose position is determined by random numbers. We then apply the imaginary-time method with the Slater determinant composed of Gaussian wave packets as the initial one. During the iteration before reaching the self-consistent solution, we examine whether the Slater determinant includes a new configuration which will be useful for configuration mixing calculations. In practice, if the expectation value of the Hamiltonian with respect to the Slater determinant is sufficiently close to the energy of the ground state (less than 30 MeV excitation), we calculate the overlap between the present Slater determinant and all Slater determinants which are already selected. If the maximum absolute value of the overlaps is sufficiently small, we adopt it as the $(N+1)$-th Slater determinant. During one imaginary-time iteration, a few Slater determinants are selected in this procedure. As the number of selected Slater determinants increases, it becomes more and more difficult to find a new one which satisfies the overlap criteria.

We note that cluster structures arise often during the imaginary-time iterations. Figure 1 shows energy expectation values obtained during imaginary-time iterations starting from different initial Slater determinants. Calculations are performed for the ^{12}C nucleus. At the initial stage of iterations, the energy expectation values decrease rapidly. In some cases, it is seen that the energy expectation values stay almost unchanged for a long period of iterations. In these flat regions, we find appearances of cluster structures. These configurations are not stable, however. Eventually the Slater determinants converge to the self-consistent ground state solution.

We show in Fig. 2 density distributions of several Slater determinants describing the ^{12}C nucleus obtained by the above procedure. In all calculations presented in this paper, we employ Skyrme SLy4 interaction. In the case of the 1st Slater determinant which is the self-consistent solution, a spherical shape is seen. A triangular shape is seen in the 3rd one and a linear-chain like structure is seen in the 14th one. In this way, various structures including both cluster-like and shell-model-like configurations may be efficiently obtained in this procedure.

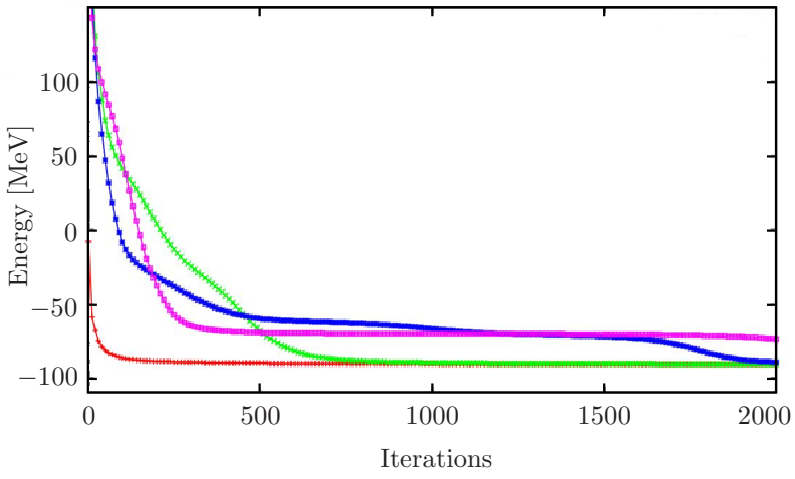

Figure 1: Energy expectation values of the Hamiltonian for ^{12}C nucleus during imaginary-time iterations are shown. Different curves show energy expectation values obtained starting from different initial configurations.

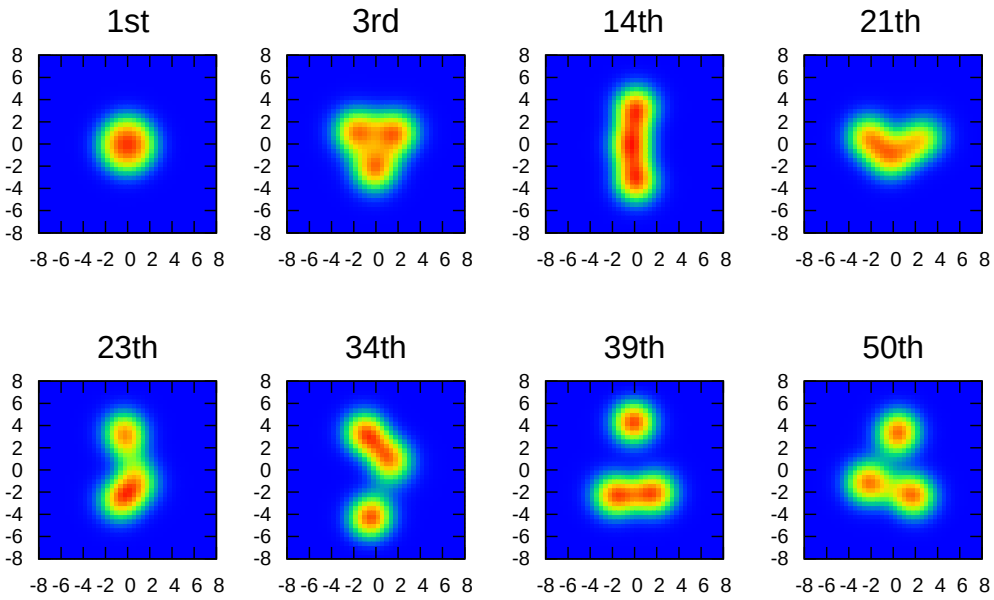

Figure 2: Density distribution in the ^{12}C nucleus corresponding to selected Slater determinants obtained in the imaginary-time calculations. The distance from the center of the nucleus is given in fm. Taken from Ref. [2].

2.2 Projection and configuration mixing calculations

We make a configuration mixing calculation in the space spanned by a set of Slater determinants. Since the microscopic Hamiltonian is invariant under parity and rotational operations, we carry out the projections with respect to the parity and angular momentum before the configuration mixing calculation.

In carrying out the configuration mixing calculations, it is essential to employ configurations which are linearly independent. As mentioned above, we only select those Slater determinants which have small overlaps with each other. However, after the projections, it usually happens that there appears a number of configurations which are not sufficiently independent.

The linear independence of the configurations may be examined using eigenvalues of the norm matrix. The norm matrix elements after parity and angular momentum projections are defined as

$$n^{J\pi}_{iK,jK'} \equiv \int d\Omega\, D^{J*}_{KK'}(\Omega) \langle \Phi_i | e^{-i\alpha \hat{J}_x} \hat{P}^\pi e^{-i\beta \hat{J}_y} e^{-i\gamma \hat{J}_x} | \Phi_j \rangle, \tag{1}$$

where J is the total angular momentum, π is the parity, i and j distinguish Slater determinants, K and K' are angular momentum components along the body-fixed z-axis, $\Omega = (\alpha\beta\gamma)$ is the set of Euler angles, $D^J_{KK'}(\Omega)$ is the Winger's D function.

In Fig. 3, we show the eigenvalues of the norm matrix for ^{12}C, $J^\pi = 2^+$. For 45 Slater determinants, there are 225 states in total. As seen from the figure, only a few eigenvalues have magnitude of order unity. Most of the eigenvalues are small and some of them are even negative (the eigenvalues starting from the number 212). From the definition, the eigenvalues of norm matrix are positive definite. The negative eigenvalues appear due to numerical errors. We need to remove the configurations associated with small and negative eigenvalues for stability of the configuration mixing calculations. In Refs. [2, 3], we describe in detail how we remove the configurations which cause small and even negative eigenvalues.

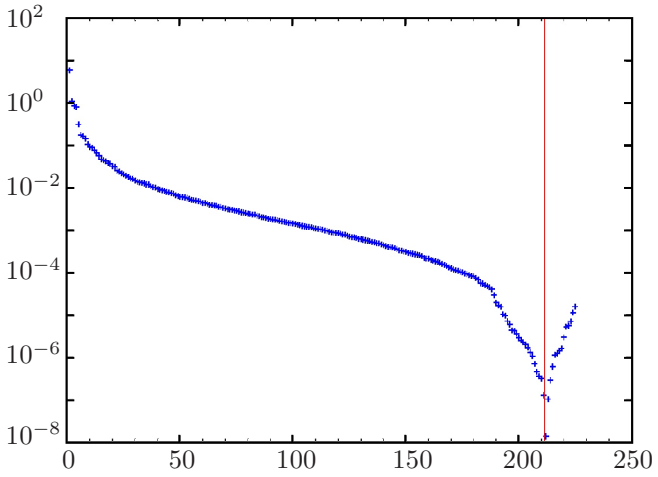

Figure 3: Absolute values of eigenvalues of the norm matrix for ^{12}C nucleus after parity and angular momentum projection.

3 Results for ^{12}C

^{12}C is a nucleus receiving substantial interests in different aspects. It is a key nucleus in nucleosynthesis producing heavy elements. The triple-alpha reaction is a key process to produce ^{12}C in which the 0_2^+ state, the so-called Hoyle state, plays a decisive role. Recently, we have reported a microscopic calculation of the triple-alpha reaction rates [4]. Regarding the structure of the 0_2^+ state, it has been recognized that this state can be understood as a Bose-condensed state composed of three alpha particles [5].

The structure of the ^{12}C nucleus has been extensively investigated within microscopic and semi-microscopic cluster models [1, 6–8]. In Figs. 4 and 5, we show our results for energy spectra of positive and negative parities, respectively.

In the figures, we show our results (Present), in comparison with measured spectra

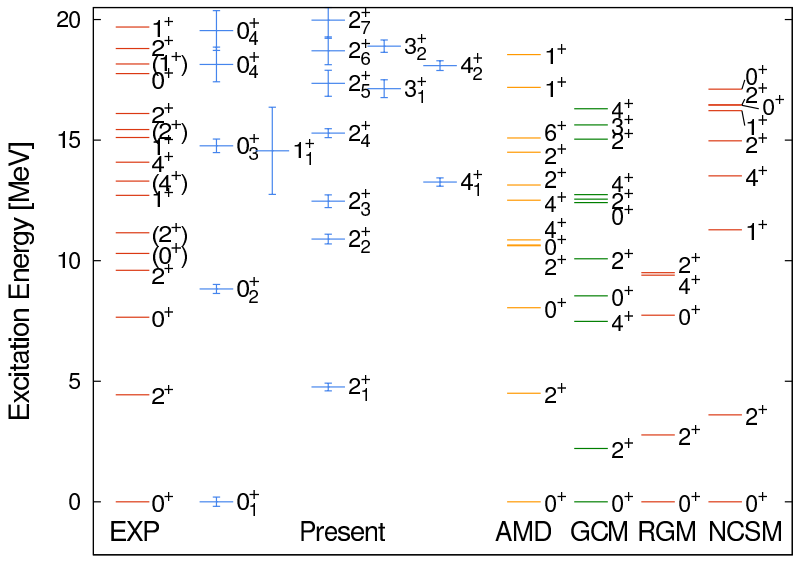

Figure 4: Excitation energies of positive parity levels of ^{12}C nucleus. The energies are obtained by averaging over ten sets of configurations. Taken from Ref. [2].

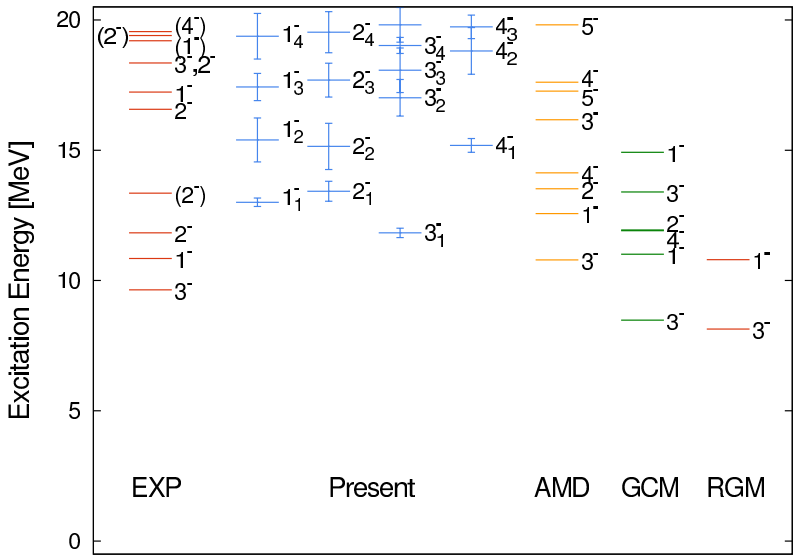

Figure 5: Excitation energies of negative parity levels of ^{12}C nucleus. Taken from Ref. [2].

(Exp) and other theoretical methods including antisymmetrized molecular dynamics method (AMD) [8], generator coordinate method (GCM) [6], resonating group method (RGM) [7], and ab-initio no-core shell model (NCSM) [9]. In the spectrum of our calculation, error bars are attached to the energy. The error bars indicate uncertainly in our calculated spectrum [2]. We carry out 10 different calculations employing different sets of Slater determinants. As mentioned in the section describing the formalism, we prepare 50 Slater determinants in which stochastically prepared initial Slater determinants of Gaussian wave packets are used. By changing the random numbers to generate the initial Slater determinants, we may obtain different sets of Slater determinants. A small error bar indicates that the deviation of energy eigenvalues among 10 different sets is small and that the results are reliable.

As seen from the figure, we may obtain a few low-lying states reliably for each parity and angular momentum. For example, for 0^+ states, three states, the 0^+_1 ground state, the 0^+_2 state which corresponds to the Hoyle state, and the 0^+_3 state are calculated with small uncertainties. The calculated energy levels with small error bars reproduce reasonably the measured spectra. They also coincide well with the results of the AMD calculation. It has been known that the no-core shell model calculations fail to describe the Hoyle state and higher 0^+ states. The GCM and RGM calculations underestimate the energies of 2^+_1 and 4^+_1 states, primarily due to insufficient treatments of spin-orbit interactions.

Regarding the negative parity levels, the lowest energy 3^-, 1^- and 2^- states are reasonably described, although the excitation energies are slightly too high as compared with measurements.

4 Conclusion

We developed a new method to calculate ground and low-lying excited states starting from a microscopic Hamiltonian with empirical two-body interactions. Applying the method to the ^{12}C nucleus, we demonstrate that it is possible to obtain low-lying spectra which are converged with respect to configurations. Both cluster-like and shell-model-like states are described simultaneously. There are two possible directions to extend the present approach. One is to apply the present approach to a wide mass

region and to neutron/proton-rich unstable nuclei, which are now under progress. The other is to employ a Hamiltonian with realistic nucleon-nucleon interactions.

References

[1] Y. Fujiwara, H. Horiuchi, K. Ikeda, M. Kamimura, K. Kato, Y. Suzuki and E. Uegaki, Progr. Theor. Phys. Suppl. **68**, 29 (1980).

[2] Y. Fukuoka, S. Shinohara, Y. Funaki, T. Nakatsukasa and K. Yabana, Phys. Rev. C **88**, 014321 (2013).

[3] S. Shinohara, H. Ohta, T. Nakatsukasa and K. Yabana, Phys. Rev. C **74**, 054315 (2006).

[4] T. Akahori, Y. Funaki and K. Yabana, arXiv:1401.4390 [nucl-th] (2014).

[5] Y. Funaki, A. Tohsaki, H. Horiuchi, P. Schuck and G. Röpke, Phys. Rev. C **67**, 051306 (2003).

[6] E. Uegaki, Y. Abe, S. Okabe and H. Tanaka, Progr. Theor. Phys. **62**, 1621 (1979).

[7] M. Kamimura, Nucl. Phys. A **351**, 456 (1981).

[8] Y. Kanada-En'yo, Progr. Theor. Phys. **117**, 655 (2007).

[9] P. Navrátil and W.E. Ormand, Phys. Rev. C **68**, 034305 (2003).

Study of Cluster Ceactions in Advanced Shell Model Approaches.

Yury M. Tchuvil'sky[a] **and Alexander Volya**[b]

[a] *Skobeltsyn Institute of Nuclear Physics, Lomonosov Moscow State University, 119991 Moscow, Russia*

[b] *Department of Physics, Florida State University, Tallahassee, FL 32306, USA*

Abstract

In the Cluster-Nucleon Configuration Interaction Model (CNCIM) presented in this work, the many-body cluster techniques are adopted for use in advanced shell model approaches including the modern *ab initio* schemes. The CNCIM is facilitated by the SU(3) symmetry which allows us to built orthogonal cluster channel wave functions with Pauli exclusion principle being taken into account. Multiple results concerning α spectroscopic factors for ground state to ground state transfers in *sd*-shell nuclei, and for transfers from low-lying and highly excited states in ^{16}O and ^{10}Be are presented. The results are in good agreement with experimental data. Clustering properties of the light nuclei are discussed and some predictions are made. We view our results as an important proof of the principle, showing that modern high performance computing permits studies of clustering within configuration interaction approaches.

Keywords: *α-clustering, shell model, resonance states*

1 Introduction

Clustering is an important feature of nuclei. The phenomenon has been investigated extensively over at least half-a-century and a large body of experimental data on this topic is available. Reaction techniques highlighting the clustering properties are being continuously improved. In particular, thick ^{4}He target inverse kinematics technique [1, 2] has recently provided a large amount of data concerning complicated α-particle resonance spectra [3–5].

Theoretical challenges on the subject of nuclear clustering include *ab initio* approach to nuclear structure, emergence of many-body correlations and many-body forces, nuclear reactions involving cluster knock-out, transfer and decay, as well as many questions in astrophysics. Multiple theoretical techniques have been put forward to study nuclear clustering; some selected ones can be found in Refs. [6–10] as well as in a broad review *Clusters in Nuclei* series [11]. However, many of these techniques, such as, a symmetry based approach found in Ref. [12], focus on the structure of highly clustered nuclear states where cluster degrees of freedom are introduced by construction. Moreover, connection to experimental results is often made using observables that are not directly related to clustering, such as nuclear moments of inertia, quadrupole moments, gamma-transitions, etc. This strategy may be inadequate for drawing conclusions about nuclear clustering based on experimental evidences. The current presentation focuses on the Cluster-Nucleon Configuration Interaction

Proceedings of the International Conference 'Nuclear Theory in the Supercomputing Era — 2014' (NTSE-2014), Khabarovsk, Russia, June 23–27, 2014. Eds. A. M. Shirokov and A. I. Mazur. Pacific National University, Khabarovsk, Russia, 2016, p. 57.

http://www.ntse-2014.khb.ru/Proc/Tchuvilsky.pdf.

Model (CNCIM) and its potential to bridge the gap between experimental results and clustering theory.

Nuclear shell model, which is also generally known as the configuration interaction (CI) method, is broadly used in studies of quantum many-body systems. It is a well established microscopic approach, where, within the same formalism, high quality description and good predictive power are obtained for numerous single-particle and collective nuclear properties [13–16]. In the nuclear shell model, cluster degrees of freedom are not introduced explicitly. This makes the shell model an ideal tool to study weakly clustered states and to address questions related to emergence of clustering and interplay of cluster and single nucleon degrees of freedom. Recent advances in computational techniques and exponential growth of computational power [13,17,18] facilitate work in this direction.

Shell-model microscopic approach to clustering has been extensively developed in the past [19–27]; it represents the path combining both microscopic single-nucleon and collective symmetry based properties of nuclear dynamics. In the CNCIM we advance the shell model approach by targeting the cluster spectroscopic characteristics, by implementing the orthogonality conditions model for description of exit and entrance cluster channels, by utilizing the SU(3) symmetry and some other algebraic properties inherent to the harmonic oscillator basis. This report provides a current summary of our recent results, see also Refs. [5, 28–30].

2 Formalism

Shell model configuration interaction approach and SU(3)-symmetric structures

In the shell model approach, the many-nucleon states

$$|\Psi\rangle \equiv \Psi^\dagger|0\rangle = \sum_{\{1,2,3,\ldots,A\}} \langle 1,2\ldots A|\Psi\rangle\, a_1^\dagger a_2^\dagger \ldots a_A^\dagger|0\rangle \tag{1}$$

are linear combinations of configurations, which are Slater determinants of single-particle states $1 \equiv \{n,l,j,m\}$. These single-particle states are built from the radial harmonic oscillator wave function (WF) $\varphi_{n_1,l_1}(r) \equiv \langle r|1\rangle \equiv \langle r|a_1^\dagger|0\rangle$ with angular momentum and spin variables coupled to total angular momentum j. The operator $a_1^\dagger$ is the nucleon creation operator in the second quantization. The numeric coefficient $\langle 1,2\ldots A|\Psi\rangle$ in Eq. (1) determines the weight of each Slater determinant in the linear superposition.

In our work clustering is approached using multi-nucleon structures related to a certain irreducible representation of the SU(3) group. In the present paper we discuss alpha clustering, therefore we construct four-nucleon states

$$|\Phi_{(n,0):L}\rangle \equiv \Phi^\dagger_{(n,0):L}|0\rangle \equiv |\{\mathfrak{n}_i^{\alpha_i}\}[f] = [4](n,0) : L, S=0,\, T=0\rangle. \tag{2}$$

Here $\{\mathfrak{n}_i^{\alpha_i}\}$ denotes a configuration where α_i is the number of particles in the major oscillator shell $\mathfrak{n}_i$; L, S, and T are orbital, spin, and isospin quantum numbers; (λ,μ) is the SU(3) Elliott's symbol; and the Young frame $[f]$ classifies the permutation symmetry. The states in Eq. (2) are constructed by diagonalization of linear combinations of the SU(3) Casimir operator of the second rank, L^2, T^2, S^2, and other operators as needed in the basis of four-nucleon shell-model states.

A direct correspondence between states $|\Psi\rangle$ and creation and annihilation operators $\Psi^\dagger$ and Ψ of the second quantization facilitates evaluation of the overlap integrals involved in fractional parentage coefficients (FPCs)

$$\mathcal{F}_{nl} \equiv \langle \Psi_P|\hat{\mathcal{A}}\left\{\Phi_{(n,0):l}\,\Psi_D\right\}\rangle \equiv \langle 0|\Psi_P\{\Phi_{(n,0):l}\Psi_D\}^\dagger|0\rangle. \tag{3}$$

Table 1: Selected FPCs and channel norms for SU(3) states. All WF and operators are for $L = 0$.

Ψ_P	Φ	$\left\|\langle\Psi_P\|\Phi^\dagger\|\Phi\rangle\right\|^2$	$\langle 0\|\Phi\Phi\Phi^\dagger\Phi^\dagger\|0\rangle$
$(p)^8\,(0,4)$	$(p)^4\,(4,0)$	1.42222*	1.42222
$(sd)^8\,(8,4)$	$(sd)^4\,(8,0)$	0.487903	1.20213
$(fp)^8\,(16,4)$	$(fp)^4\,(12,0)$	0.292411	1.41503
$(sdg)^8\,(24,4)$	$(sdg)^4\,(16,0)$	0.209525	1.5278

*For the p shell this result agrees with the value of $64/45 = 1.42222$ found in Ref. [31].

Here $\hat{\mathcal{A}}$ is the antisymmetrization operator and $|\Psi_P\rangle$ and $|\Psi_D\rangle$ are arbitrary states of type (1).

The FPCs for some selected states of SU(3) symmetry are shown in Table 1. The channel norms shown in the last column, provide a measure of bosonic enhancement. Indeed, if a four-nucleon $L = 0$ operator $\Phi^\dagger \equiv \Phi^\dagger_{(n,0):0}$ is thought of as a boson creation operator then $\Phi\Phi^\dagger = 1 + N_b$, where N_b is the boson number operator. Therefore for ideal bosons the norm of the one-boson channel state $\langle 0|\Phi\Phi\Phi^\dagger\Phi^\dagger|0\rangle$ should be 2. The numbers in the last column are less than 2, showing that the four-nucleon configurations are not true bosons. These objects are comprised of fermions, and residual Pauli blocking effects are noticeable. The blocking effects are naturally reduced for larger shells, which brings the norm closer to 2.

Cluster form factors and spectroscopic factors

The cluster form factor (CFF), also commonly known as the spectroscopic amplitude,

$$\phi_l(\rho) = \langle \Psi'_P | \hat{\mathcal{A}} \Big\{ \Psi'_D \, \frac{\delta(\rho - \rho')}{\rho^2} Y_{lm}(\Omega_{\rho'}) \Psi'_\alpha \Big\} \rangle \tag{4}$$

is one of the most basic measures of clustering. In Eq. (4), Ψ'_P, Ψ'_D, and Ψ'_α are WFs of the parent (P), the daughter (D) and the α-cluster, respectively, which are internal, translationally invariant, and free of the center of mass (c. m.) coordinate. Here and in what follows we use primed notation to distinguish these WFs from those of the shell model type (1) that implicitly depend on the c. m. motion. The coordinate ρ is the Jacobi radial coordinate of the relative cluster — daughter nucleus motion; a proper coupling to a relative angular momentum l is established.

In our shell model calculations the parent and daughter states are computed implementing a Glockner–Lawson procedure [32] leading the c. m. motion being in the lowest oscillator state $\varphi_{00}(R)$. The oscillator frequency in harmonic oscillator WF depends in the usual way on the mass number. In order to describe α channels we assume that the α-particle's translationally invariant WF is represented by the lowest four-nucleon oscillator function written through the Jacobi coordinates:

$$|\Psi'_\alpha\rangle \equiv |A = 4, n' = 0, [f] = [4](\lambda,\mu) = (0,0) : L = 0,\ S = 0,\ T = 0\rangle. \tag{5}$$

Therefore in the WF $|\Phi_{(n,0):l}\rangle$ we are interested in a component that includes the intrinsic 4-nucleon state (5) with the c. m. variable being in the oscillator state $\varphi_{nl}(R_\alpha)$. This component, referred to as cluster coefficient, is known analytically [21, 22, 33],

$$X_{nl} \equiv \langle \Phi_{(n,0):l} | \varphi_{nl}(R_\alpha)\, \Psi'_\alpha \rangle = \sqrt{\frac{1}{4^n}\, \frac{n!}{\prod_i (\mathfrak{n}_i!)^{\alpha_i}}\, \frac{4!}{\prod_i \alpha_i!}}\ . \tag{6}$$

The following steps (see also Refs. [20–22, 24]) include expansion of the parent state using FPC (3) and recoupling the c. m. variables R_α and R_D into their relative coordinate ρ and the parent c. m. coordinate R_P where the corresponding recoupling coefficient (known as recoil factor) is

$$\mathcal{R}_n = (-1)^n[(m_D + m_\alpha)/m_D]^{n/2}.$$

This leads to the expansion of the CFF (4) in oscillator states,

$$\phi_l(\rho) = \sum_n \mathcal{C}_{nl}\,\varphi_{nl}(\rho), \quad \mathcal{C}_{nl} = X_{nl}\,\mathcal{F}_{nl}\,\mathcal{R}_n. \tag{7}$$

In the past it was common to identify the CFF in Eq. (7) with the observable spectroscopic factors (SFs) $\mathcal{S}_l = \sum_n |\mathcal{C}_{nl}|^2$. However, it was argued in Refs. [34, 35] that the matching of $\phi_l(\rho)$ with the two-body cluster-nucleus solution is not appropriate. Instead, one should use the channel WF in the form of the Resonating Group Model or, for an easier reduction to the two-body problem, in the form of the Orthogonality Condition Model (OCM) [36]. Therefore the CFF should be redefined as

$$f_l(\rho) \equiv \hat{\mathcal{N}}_l^{-1/2}\phi_l(\rho), \tag{8}$$

where the norm operator

$$\hat{\mathcal{N}}_l\phi_l(\rho) \equiv \int \mathcal{N}_l(\rho',\rho)\phi_l(\rho')\rho'^2 d\rho'$$

contains the overlap norm kernel

$$\mathcal{N}_l(\rho',\rho'') = \left\langle \hat{A}\left\{\Psi'_D\Psi'_\alpha\tfrac{\delta(\rho-\rho')}{\rho^2}Y_{lm}\,(\Omega_\rho)\right\}\right|\,\hat{A}\left\{\Psi'_D\Psi'_\alpha\tfrac{\delta(\rho-\rho'')}{\rho^2}Y_{lm}\,(\Omega_\rho)\right\}\Big\rangle. \tag{9}$$

The validity and importance of this new definition are discussed in details in Refs. [10, 37]. We construct and diagonalize the norm kernel operator as a matrix in oscillator basis

$$\langle\varphi_{n'l}|\hat{\mathcal{N}}_l|\varphi_{nl}\rangle = \mathcal{R}_{n'}\mathcal{R}_n X_{n'l}X_{nl}\,\langle\hat{\mathcal{A}}\left\{\Phi_{(n',0):l}\,\Psi_D\right\}|\hat{\mathcal{A}}\left\{\Phi_{(n,0):l}\,\Psi_D\right\}\rangle. \tag{10}$$

This leads to a new definition of the SF:

$$S_l \equiv \int \rho^2 d\rho\,|f_l(\rho)|^2 = \sum_k \frac{1}{N_{kl}}\left|\sum_n \langle kl|\varphi_{nl}\rangle\,\mathcal{C}_{nl}\right|^2, \tag{11}$$

where $|kl\rangle$ is an eigenvector and N_{kl} is an eigenvalue of the norm kernel $\hat{\mathcal{N}}_l|kl\rangle = N_{kl}|kl\rangle$, both corresponding to angular momentum l. In this form the SFs are normalized; for any given parent nucleus the sum of all SFs for a given partial wave l and to a particular daughter state equals to the number of channels (characterized by different values of n in four-nucleon functions $\Phi_{(n,0):l}$) involved. In the one-channel case (such an example is considered in the next section), using completeness of the parent states $\sum_i |\Psi_{P_i}\rangle\langle\Psi_{P_i}| \equiv 1$, the single diagonal matrix element for the norm (10) can be expressed as

$$N_{nl} = \mathcal{R}_n^2 X_{nl}^2 \sum_i (\mathcal{F}_{nl}^i)^2 = \sum_i \mathcal{S}_l^i, \tag{12a}$$

thus

$$S_l^i = \mathcal{S}_l^i / \sum_{i'} \mathcal{S}_l^{i'} = (\mathcal{F}_{nl}^i)^2 / \sum_{i'} (\mathcal{F}_{nl}^{i'})^2. \tag{12b}$$

We refer to the technique outlined here as the Cluster-Nucleon Configuration Interaction Model (CNCIM), and in the following section we demonstrate some of its applications. Additional details can be found in Refs. [5, 29, 30].

3 Applications

Study of the ground state α-clustering in sd-shell nuclei

Transfer and knock-out reactions, such as the ones discussed in Refs. [38–41], provide a wealth of information on α strengths in low-lying states of sd-shell nuclei. Theoretical values of the corresponding SFs obtained in various papers are well-correlated [23,25]. The summary of these results as well as those from our calculations are presented in Table 2. In our calculations of α-particle SFs for ground state to ground state transitions the USDB Hamiltonian [42] was used. The basis is restricted by the sd shell. Within this model only one four-nucleon operator with SU(3) quantum numbers (8,0) contributes, and therefore the relationship (12) holds.

Prior to discussing the results in Table 2, let us clarify some problems associated with evaluation of the absolute values of experimental SFs. First, some problems emerge from poor knowledge of the imaginary part of nucleus-nucleus potential for the types of reactions involved. Second, transfer reactions usually determine only relative values of the SFs, while for knock-out reactions absolute values are commonly provided in the literature (see Table 2, columns 2, 3). Therefore in Table 2 all values evaluated in transfer reactions are normalized to the value of the SF in ^{20}Ne (column 4). Given that the experimental absolute value of SF in ^{20}Ne according to Ref. [43] is very close to 1.0, the remaining relative SFs in column 4 may be interpreted as the absolute ones. Both types of experiments are nevertheless consistent in the general pattern of variation of relative values of SFs with the increase in nuclear mass.

A comparison of theoretical values [23, 25] with the experimental data highlights some problems. First, the theoretical SFs are several times smaller than the measured ones; in certain cases the discrepancy is more than one order of magnitude. To demonstrate this in Table 2 we include the non-renormalized theoretical values of SFs from Ref. [23]. In analogy with the approach taken in experiments with transfer reactions, it is a common practice to renormalize theoretical data using the value of the α-particle SF in ^{20}Ne; and yet this practice needs some rigorous justification. Second, even after the renormalization, the tendency for the values of SFs to decrease rapidly while going from ^{20}Ne to ^{40}Ca, is not confirmed by the data.

Our results, shown in the last (7th) column in Table 2, appear to resolve the above mentioned long standing theoretical problems in a natural way. Indeed, the

Table 2: Ground state to ground state α-particle SFs, "new" S_0 and "old" $\mathcal{S}_0$ and the experimental SFs extracted from the cross sections of $(p, p\alpha)$ [43, 44] and (^{6}Li,d) [45] reactions, traditional S_0 obtained in Ref. [23] and in the current work, and "new" SFs S_0^{new}.

$A_P - A_D$	S^{exp} [43]	S^{exp} [44]	S^{exp} [45]	$\mathcal{S}_0$ [23]	$\mathcal{S}_0$	S_0
^{20}Ne-^{16}O	1.0	0.54	1	0.18	0.173	0.755
^{22}Ne-^{18}O			0.37	0.099	0.085	0.481
^{24}Mg-^{20}Ne	0.76	0.42	0.66	0.11	0.091	0.411
^{26}Mg-^{22}Ne			0.20	0.077	0.068	0.439
^{28}Si-^{24}Mg	0.37	0.20	0.33	0.076	0.080	0.526
^{30}Si-^{26}Mg			0.55	0.067	0.061	0.555
^{32}S-^{28}Si	1.05	0.55	0.45	0.090	0.082	0.911
^{34}S-^{30}Si				0.065	0.062	0.974
^{36}Ar-^{32}S				0.070	0.061	0.986
^{38}Ar-^{34}S			1.30	0.034	0.030	0.997
^{40}Ca-^{36}Ar	1.56	0.86	1.18	0.043	0.037	1

agreement between absolute SFs found in experiment (columns 2–4) and those from CNCIM (column 7) is good without any renormalization. This includes the trend of SFs to drop down towards the middle of the *sd* shell and to increase at the edges.

The values of the traditional spectroscopic factors obtained by us (column 6) and the ones presented in Ref. [23] (column 5) are close, thus showing that renormalization of the channel WFs proposed by Fliessbach is the main reason for this improvement.

Study of α-clustering in ^{16}O

A more advanced investigation using CNCIM is summarized in Table 3. Here we examine α-clustering of the ground and multiple excited states in ^{16}O relative to channels involving ^{12}C nucleus in the ground state. Both parent and daughter systems are treated in the unrestricted *p-sd* configuration space with effective interaction Hamiltonian from Ref. [17]. In Ref. [17] Utsuno and collaborators suggest that this effective Hamiltonian describes well the multi-particle correlations in ^{16}O, thus making it an ideal choice for exploring clustering. The *p-sd* valence space allows for the following SU(3)-classified four-nucleon configurations:

$$|\Phi_{(n,0):l}\rangle = |(0p)^q(2s-1d)^{4-q}\,[4](n,0) : l, S=0,\ T=0\rangle, \tag{13}$$

where $q = 0, 1...4$; $n = 8 - q$; $l = n, n-2, ..., 1$ or 0; and $\pi = (-1)^l$.

A broad part of the low-lying ^{16}O spectrum is examined in our study. For over 60 states the experimentally known characteristics that include spin, parity and α-decay reduced widths θ_α^2 turned out to be reasonably described by our model. Focusing on clustering properties in Table 3 we restrict our presentation to the states with SFs $S_\alpha > 0.1$. The table is organized based on the theoretically calculated spectrum of ^{16}O. We made an effort to identify each theoretically predicted state with an experimentally known counterpart. In this process an agreement within a factor of 3 to 4 in SF was the primary criterion, a theory-experiment agreement in excitation energy within about 1 MeV was considered as secondary.

Table 3: The α-particle SFs for states in ^{16}O.

J_i^π	E(sm)	S_l	E(exp)	θ_α^2
0_1^+	0.000	0.794	0.000	0.86[a]
3_1^-	5.912	0.663	6.13	0.41[a]
0_2^+	6.916	0.535	6.049	0.40[a]
1_1^-	7.632	0.150	7.117	0.14
2_1^+	8.194	0.500	6.917	0.47[a]
2_2^+	9.988	0.349	9.844[b]	0.0015
4_1^+	10.320	0.313	10.356	0.44
0_3^+	10.657	0.216	11.26	0.77
2_3^+	11.307	0.158	11.52[b]	0.033
4_2^+	11.334	0.203	11.097[b]	0.0014

continued

J_i^π	E (sm)	S_l	E(exp)	θ_α^2
2_4^+	12.530	0.123	—[c]	
6_1^+	13.286	0.465	14.815	0.17
4_3^+	13.308	0.160	14.62	0.19
3_3^-	13.733	0.144	14.1	0.21
2_6^+	14.646	0.102	14.926[b]	0.0098
1_4^-	15.298	0.174	16.2	0.085
4_5^+	15.474	0.152	16.844	0.13
5_1^-	15.945	0.289	14.66	0.55
6_2^+	16.304	0.415	16.275	0.43

[a] Recalculated value of the SF from [46] (see the text).

[b] Identified states are, probably, of different nature.

[c] No experimental analog has been found.

The most part of the experimental information was taken from the spectroscopic tables [47, 48]. Measured excitation energies and α spectroscopic strengths θ_α^2 are listed in Table 3 in the last two columns. The α-decay reduced widths were calculated using standard equations of resonance reaction theory. For evaluation of the SFs of sub-threshold states, the experimental data from (^{6}Li,d) reaction [46] were used, where SFs relative to 4_1^+ 10.356 MeV are presented. Taking into account some inconsistencies in determination of absolute values of the sub-threshold SFs, we rescale this data using an over-threshold reference state with known α-decay width.

The results displayed in Table 3 are encouraging. The model includes no additional parameters, nor fits, and yet for most levels observed in experiments theoretical partners may be found. Over 2/3 of states predicted to have strong clustering properties have been identified experimentally. Many states with lower α SF (not listed in Table 3) are also reproduced by the theory. Other properties of the ^{16}O states that include electric quadrupole transitions and possible identification of rotational bands are also well-described, see further details in Ref. [29].

The lack of configurations from the pf shell appears to be a reason for discrepancy related to α-decaying states 1^- E(exp)=9.585 MeV and 3^- E(exp)=11.6 MeV. Disagreements similar in nature were seen in ^{18}O, Ref. [5]. Some cases, such as those marked in Table 3 by ^{b}, point toward deficiencies of the Hamiltonian.

Study of α-clustering in ^{10}Be

^{10}Be is another popular system for studies of clustering because it is one of the lightest nuclei where the interplay between cluster and nucleon degrees of freedom is manifested. Apart from that, ^{10}Be provides a path for a better understanding of the exotic isobar-analogous system of ^{10}C [49]. The α-cluster properties of ^{10}Be are not easy to measure because ^{6}He beams lack intensity and there is no other convenient projectile for such studies. The lack of information has motivated active discussions and numerous loosely validated qualitative conclusions, that could benefit from additional theoretical work.

The study of ^{10}Be is similar to that of ^{16}O described in the previous section. We use the same unrestricted *p-sd* configuration space with the effective interaction Hamiltonian from Ref. [17], and consider the same set of four-nucleon operators in Eq. (13). A large number of the states with natural parity was obtained, and for each state the SF for the α+^{6}He channel was computed from Eq. (11). The results are summarized in Table 4 which includes all theoretically predicted states up to 10 MeV of excitation. In the region between 10 and 15 MeV only the states with $S_l > 0.01$ are listed, and this list includes all high-spin states ($J \geq 4$). For higher excitation energy low-spin levels are tabulated in the case where $\Gamma_\alpha > 300$ keV and high-spin levels where $\Gamma_\alpha > 100$ keV.

The three lowest states, 0_1^+, 2_1^+, and 4_2^+, in ^{10}Be are strongly clustered, which are the only states with $S_l > 0.3$. The clustering is explained by the large $|(1p)^6[42], (\lambda,\mu) = (2,2), L, S = 0,\ T = 1\rangle$ component, the weight of this component is 0.65, 0.53 and 0.35 for 0_1^+, 2_1^+, and 4_2^+, respectively. These states do not form a rotational band because the 0_1^+ ground state in the algebraic model has a value of projection $K = 0$, and this value of intrinsic angular momentum projection is not presented in the 4^+ state related to $(\lambda,\mu) = (2,2)$ SU(3) representation. Clustering effects are weak in high-spin states. For all 6^+ states $S_l < 0.04$; all 7^- and 8^+ states are found to have near zero SFs, to be specific, $S_l < 10^{-6}$.

The experimental information presented in Table 4 comes from Refs. [50–54]. As it is the case for the ^{16}O example presented in Table 3, agreement in spectroscopic factors is the primary criterion in establishing theory-experiment correspondence for ^{10}Be as presented in Table 4; the theory-experiment agreement in excitation energy is considered secondary. The traditional R-matrix relations, see for example Ref. [51],

Table 4: Results of the CNCIM calculations for ^{10}Be compared with the available experimental information. Energies are given in MeV; decay widths are in keV, or as indicated.

J^π_s	S_l	E^{th}_x	Γ^{th}_α	E^{exp}_x	Γ^{exp}_α	$\theta^2_\alpha(r_1)$	$\theta^2_\alpha(r_2)$
0^+_1	0.686	0.000		0			
2^+_1	0.563	3.330		3.368			
0^+_2	0.095	4.244		6.197			
2^+_2	0.049	5.741		5.958			
2^+_3	0.052	6.123					
1^-_1	0.027	6.290		5.96			
3^-_1	0.098	6.926		7.371		$0.42^{a,b}$	
2^+_4	0.116	7.650	0.3 eV	7.542	0.5 eV	$1.1^{a,b}$	0.19
0^+_3	0.023	8.068	17				
4^+_1	0.049	8.933	4.7				
1^-_2	0.045	9.755	180	10.57			
3^-_2	0.046	9.897	61				
2^+_5	0.027	10.819	50	9.56	141^d		0.074
2^+_6	0.023	11.295	43				
0^+_5	0.153	11.403	800				
4^+_2	0.370	11.426	180	10.15	185^b	1.5^b	0.38
5^-_1	0.148	11.440	150	11.93	200		0.20
1^-_5	0.013	12.650	76				
6^+_1	0.013	13.134	24	13.54^b	99	1.0^b	0.051
5^-_2	0.128	13.545	250				
2^+_{10}	0.040	13.789	240				
4^+_3	0.011	13.992	20	11.76	121		0.066
4^+_4	0.022	14.233	40				
0^+_6	0.018	14.252	120				
3^-_7	0.014	14.468	77				
5^-_3	0.059	14.992	180				
4^+_5	0.161	15.071	800	$15.3(6^-)^c$	800^d		0.16
2^+_{13}	0.046	15.534	330				
4^+_6	0.033	15.809	180				
4^+_7	0.03	16.426	150				
4^+_9	0.200	17.510	1300				
4^+_{11}	0.041	18.566	290				
5^-_8	0.017	19.448	110				
5^-_9	0.018	19.840	120				
5^-_{11}	0.017	21.395	130				
6^+_4	0.037	19.101	170				

[a] Widths deduced from the isobaric analog channel ^{10}B $\rightarrow ^6$Li$(0^+)+\alpha$ [50, 51].

[b] Results from Ref. [51].

[c] Results from Ref. [52].

[d] Total width Γ^{tot}.

are used to obtain theoretical predictions for the decay width Γ_α^{th}, and inversely, to obtain the reduced widths θ_α^2 from the experimentally observed α decay width Γ_α^{exp}. The R-matrix relations depend on the excitation energy and on the channel radius r. If the energy of the level is known experimentally, the observed value is used to compute Γ_α^{th}. Some significant dependence of the decay width on the channel radius is demonstrated by the last two columns in Table 4. For example, the reduced widths θ_α^2 presented in Ref. [51] (7th column) appear to be in disagreement, but those results were obtained using the channel radius r_1=4.77 fm, typical for stable nuclei. In the last column of Table 4 we demonstrate that another choice of the channel radius, $r_2 = 6.0$ fm, brings all values of θ_α^2 to a good agreement with calculated SFs. Moreover, the choice of a larger channel radius is more natural for a halo ^{6}He nucleus.

The calculated energy spectrum is consistent with the recent experimental findings. There are some discrepancies: somewhat noticeable deviations in excitation energy are observed for the 0_2^+ level and the doublet $4_{3,4}^+$. In addition to that, a number of theoretically predicted levels has not been observed in experiments; those, however, can often be explained by small decay widths, such as in the case of the 2_3^+ state.

Being encouraged by the success of the CNCIM, we are compelled to take part in discussions related to interpretation of recent experimental data. Our results summarized in Table 4 confirm that the branching ratio $\Gamma_\alpha/\Gamma_{tot}$ for the state at $E_x^{exp} = 7.543$ MeV is close to $1.3{\cdot}10^{-4}$ [51]. The conclusion of Refs. [51, 53] that the level 10.15 MeV is 4^+ and not 3^- [52] is also confirmed. Results in Table 4 suggest that the state at $E_x = 13.54$ MeV [51] is actually a 6^+ and 5^- doublet of resonances. The state at $E_x = 15.3$ MeV is characterized in Ref. [52] as J^π=6^- based on an expectation to see a $K = 1$ "band" member in this energy region; according to our results it is probably a 4^+ state. A number of theoretical results in Table 4 can potentially guide future experimental investigations.

4 Summary

In this work we develop formalism and methods for conducting studies of nuclear clustering using the advanced large-scale shell model technique. The effects of Pauli exclusion principle which, as found in previous works, result in the specific renormalization of wave functions of the cluster channels and require redefinition of traditional cluster characteristics are accurately taken into account. The developed formalism is applicable for all microscopic configuration interaction approaches, including *ab initio* no-core schemes. Cluster transitions between the states of all kinds (ground, excited, resonance; strongly and weakly clustered) can be treated in our approach. The end products of the approach are the cluster spectroscopic characteristics that can be directly compared with experimental observables.

We use a variety of examples to demonstrate the capability of our approach. Reviewing the α spectroscopic factors of ground state to ground state transitions in even-even nuclei of the *sd* shell we resolve a long-standing problem related to underestimation of absolute values of spectroscopic factors and obtain a good agreement with the experimental data.

We perform two large-scale studies of ^{16}O and ^{10}Be nuclei within the *p*-*sd* valence space. The ^{16}O system is chosen because α-decay widths and transfer strengths going to the ground state of ^{12}C nucleus have been measured for many states. The performed calculations provide a good description of both the spectrum and the alpha-decay widths. These results along with the ones related to the traditional single-particle excitations, electromagnetic transitions and cluster rotational bands, obtained both in our calculations and in preceding papers, validate the approach.

With the ^{10}Be study we join the recent debate about the nature of clustering in this exotic nucleus. The widths of known α-decaying resonances of the nucleus turn

out to be well-described in CNCIM. This allows us to discuss structure of these states and to make predictions.

We would like to conclude that the success of the CNCIM reported in this work indicate that in the era of supercomputers the study of clustering physics becomes feasible within the phenomenological or *ab initio* configuration interaction technique.

We thank V. Goldberg, T. Dytrych and G. Rogachev for motivating discussions. This material is based upon work supported by the U.S. Department of Energy Office of Science, Office of Nuclear Physics under Award Number DE-SC-0009883.

References

[1] K. Artemov *et al.*, Sov. J. Nucl. Phys. **52**, 406 (1990).

[2] V. Goldberg and A. Pakhomov, Phys. At. Nucl. **56**, 1167 (1993).

[3] T. Lonnroth *et al.*, Eur. Phys. J. A **46**, 5 (2010).

[4] M. Norrby *et al.*, Eur. Phys. J. A **47**, 73 (2011).

[5] M. Avila *et al.*, Phys. Rev. C **90**, 024327 (2014).

[6] K. Varga, R. G. Lovas and R. J. Liotta, Nucl. Phys. A **550** (1992).

[7] K. Varga and R. J. Liotta, Phys. Rev. C **50**, R1292 (1994).

[8] R. Id Betan and W. Nazarewicz, Phys. Rev. C **86**, 034338 (2012).

[9] A. Insolia, P. Curutchet, R. J. Liotta and D. S. Delion, Phys. Rev. C **44**, 545 (1991).

[10] S. G. Kadmensky, S. D. Kurgalin and Yu. M. Tchuvil'sky, Phys. Part. Nucl. **38**, 699 (2007).

[11] *Clusters in nuclei*, ed. C. Beck, Lecture Notes in Physics **818, 848, 875**. Springer, Berlin, New York, 2010, 2012, 2013.

[12] I. A. Gnilozub, S. D. Kurgalin and Yu. M. Tchuvl'sky, J. Phys. Conf. Ser. **436**, 012034 (2013).

[13] E. Caurier, G. Martinez-Pinedo, F. Nowacki, A. Poves and A. P. Zuker, Rev. Mod. Phys. **77**, 427 (2005).

[14] I. Talmi, *Fifty years of the nuclear shell model — the quest for the effective interaction*, Advances in Nuclear Physics **27**, 1. Kluwer, 2003.

[15] B. A. Brown, Progr. Part. Nucl. Phys. **47**, 517 (2001).

[16] A. Volya, Phys. Rev. C **79**, 044308 (2009).

[17] Y. Utsuno and S. Chiba, Phys. Rev. C **83**, 021301(R) (2011).

[18] *Proc. Int. Conf. Nucl. Theor. Supercomputing Era (NTSE-2013), Ames, IA, USA, May 13–17, 2013*, eds. A. M. Shirokov and A. I. Mazur. Pacific National University, Khabarovsk, 2014, http://ntse-2013.khb.ru/proceedings/.

[19] H. J. Mang, Z. Phys. **148**, 582 (1957).

[20] Yu. F. Smirnov and D. Chlebowska, Nucl. Phys. **26**, 306 (1961).

[21] M. Ichimura, A. Arima, E. C. Halbert and T. Terasawa, Nucl. Phys. A **204**, 225 (1973).

[22] Yu. F. Smirnov and Yu. M. Tchuvil'sky, Phys. Rev. C **15**, 84 (1977).

[23] W. Chung, J. van Hienen, B. H. Wildenthal and C. L. Bennett, Phys. Lett. B **79**, 381 (1978).

[24] O. F. Nemetz, V. G. Neudatchin, A. T. Rudchik, Yu. F. Smirnov and Yu. M. Tchuvil'sky, *Nucleon clusters in atomic nuclei and multi-nucleon transfer reactions*. Naukova Dumka, Kiev, 1988 (*in Russian*).

[25] M. Grigorescu, B. A. Brown and O. Dumitrescu, Phys. Rev. C **47**, 2666 (1993).

[26] Yu. M. Tchuvil'sky, W. W. Kurowsky, A. A. Sakharuk and V. G. Neudatchin, Phys. Rev. C **51**, 784 (1995).

[27] P. Navratil, Phys. Rev. C **70**, 054324 (2004).

[28] A. Volya and Yu. M. Tchuvil'sky, IOP Conf. Proc. (2014), *in press*.

[29] A. Volya and Yu. M. Tchuvil'sky, in *IASEN 2013 Proceedings*. World Scientific, (2014), *in press*.

[30] Yu. M. Tchuvil'sky and A. Volya, in *ARIS-2014 Proceeding*. 2014, *in press*.

[31] I. Rotter, Ann. der Phys. **16**, 242 (1965).

[32] R. D. Lawson, *Theory of the nuclear shell model*. Clarendon Press, Oxford, 1980.

[33] Yu. F. Smirnov and Yu. M. Tchuvil'sky, Czech. J. Phys. **33**, 1215 (1983).

[34] T. Fliessbach and H. Mang, Nucl. Phys. A **263**, 75 (1976).

[35] T. Fliessbach and P. Manakos, J. Phys. G **3**, 643 (1977).

[36] S. Saito, Progr. Theor. Phys. **41**, 705 (1969).

[37] R. G. Lovas, R. J. Liotta, A. Insolia, K. Varga and D. S. Delion, Phys. Rep. **294**, 265 (1998).

[38] W. Oelert, W. Chung, A. Djaloeis, C. Mayer-Böricke and P. Turek, Phys. Rev. C **22**, 408 (1980).

[39] W. Oelert *et al.*, Phys. Rev. C **20**, 459 (1979).

[40] H. W. Fulbright, Ann. Rev. Nucl. Part. Sci. **29**, 161 (1979).

[41] N. Anantaraman, H. W. Fulbright and P. M. Stwertka, Phys. Rev. C **22**, 501 (1980).

[42] B. A. Brown and W. A. Richter, Phys. Rev. C **74**, 034315 (2006).

[43] T. Carey *et al.*, Phys. Rev. C **23**, 576(R) (1981).

[44] T. Carey *et al.*, Phys. Rev. C **29**, 1273 (1984).

[45] N. Anantaraman *et al.*, Phys. Rev. Lett. **35**, 1131 (1975).

[46] F. D. Becchetti, D. Overway, J. J. Knecke and W. W. Jacobs, Nucl. Phys. A **344**, 336 (1980).

[47] D. R. Tilley, H. R. Weller and C. M. Cheves, Nucl. Phys. A **564**, 1 (1993).

[48] Evaluated nuclear structure data file, http://www.nndc.bnl.gov/ensdf/.

[49] V. Z. Goldberg and G. V. Rogachev, Phys. Rev. C **86**, 044314 (2012).

[50] A. N. Kuchera *et al.*, Phys. Rev. C **84**, 054615 (2011).

[51] A. N. Kuchera, *Clustering phenomena in the* $A = 10$ $T = 1$ *isobaric multiplet*, Florida State University, Electronic Theses, Treatises and Dissertations, 2013, Paper 8585, http://diginole.lib.fsu.edu/etd/8585/.

[52] D. R. Tilley *et al.*, Nucl. Phys. A **745**, 155 (2004).

[53] M. Freer *et al.*, Phys. Rev. Lett. **96**, 042501 (2006).

[54] D. Suzuki *et al.*, Phys. Rev. C **87**, 054301 (2013).

From Gogny Force to Shell-Model Calculations

Furong Xu[1], Baishan Hu, Weiguang Jiang, Wenjun Chen, Acan Dai and Junchen Pei

State Key Laboratory of Nuclear Physics and Technology, School of Physics, Peking University, Beijing 100871, China
State Key Laboratory of Theoretical Physics, Institute of Theoretical Physics, Chinese Academy of Sciences, Beijing 100190, China

Abstract

We use the Gogny force to calculate the two-body matrix elements of the nucleon-nucleon (NN) interaction for shell-model calculations. As the first step, we ignore the effective three-body force which is usually written in a density-dependent two-body form in the Gogny force, therefore the parameters of the Gogny force should be readjusted. In the present work, we investigate *sd*-shell nuclei. The comparison with experimental data shows that the shell-model calculations starting from the Gogny force can be successful. The present calculations are preliminary, and further work is going on. The aim is to obtain consistent descriptions in both shell-model and mean-field calculations using a unified Gogny force.

Keywords: *Gogny force; two-body matrix elements; shell model; sd-shell nuclei; spectra*

1 Introduction

In shell-model calculations, one of the most crucial tasks is how to calculate the two-body matrix elements (TBME's) of the nucleon-nucleon (NN) interaction. One can start from a realistic bare NN interaction and make necessary renormalization to soften it for shell-model calculations. For core shell-model calculations, a further renormalization is needed to include effects from excluded space (including core polarization). The renormalization approximations would bring restrictions on calculations. For example, the renormalization using the folded-diagram expansion restricts the shell-model calculations within a single shell. This means that the model space cannot include configurations from different shells due to perturbation approximation used [1]. On the other hand, such calculations are complicated mathematically and time-consuming computationally, and cannot be accurately quantitatively compared with experimental data.

As another way, one can use phenomenological interaction matrix elements obtained by fitting to experimental data, e.g., the USD interaction for the *sd* shell [2,3]. However such phenomenological method involves a big number of parameters to be determined by fitting data. This is a big task in fitting, particularly for heavy mass regions, and also requires enough experimental data available.

In the present work, we use the Gogny force [4,5] to calculate the effective TBME's. The Gogny force has been successfully used in mean-field calculations, involving

[1]e-mail: frxu@pku.edu.cn

Proceedings of the International Conference 'Nuclear Theory in the Supercomputing Era — 2014' (NTSE-2014), Khabarovsk, Russia, June 23–27, 2014. Eds. A. M. Shirokov and A. I. Mazur. Pacific National University, Khabarovsk, Russia, 2016, p. 69.

http://www.ntse-2014.khb.ru/Proc/Xu.pdf.

only 14 parameters. Similar works using the Skyrme force were done for the *sd*-shell nuclei ^{18}O and ^{36}Ar [6], and for *p*-shell nuclei [7]. These calculations indicate that the phenomenological Skyrme force which has been widely employed in mean-field calculations can be used for the calculations of effective TBME's in shell model. Such phenomenological calculations of TBME's involve much less parameters than in the case of the USD interaction.

2 The model and calculations

The Gogny force is written as [4, 5]

$$V(1,2) = \sum_{j=1,2} e^{-(\mathbf{r}_1-\mathbf{r}_2)^2/\mu_j^2}(W_j + B_j P_\sigma - H_j P_\tau - M_j P_\sigma P_\tau) + t_0\,(1+x_0 P_\sigma)\,\delta(\mathbf{r}_1-\mathbf{r}_2)\left[\rho\left(\frac{\mathbf{r}_1+\mathbf{r}_2}{2}\right)\right]^\alpha + iW_0 \overleftarrow{\nabla}_{12}\,\delta(\mathbf{r}_1-\mathbf{r}_2)\times\overrightarrow{\nabla}_{12}\cdot(\boldsymbol{\sigma}_1-\boldsymbol{\sigma}_2),$$

where P_σ (P_τ) is a two-body spin (isospin) exchange operator. Totally there are 14 parameters with μ_1 and μ_2 describing the short- and intermediate-range properties of the nuclear interaction, respectively.

As the first step of our work, we ignore the three-body-force density-dependent term, $t_0\,(1+x_0P_\sigma)\,\delta(\mathbf{r}_1-\mathbf{r}_2)\left[\rho\left(\frac{\mathbf{r}_1+\mathbf{r}_2}{2}\right)\right]^\alpha$. Such approximation should be reasonable in shell model calculations in which the two-body interaction provides the most important contributions. Now only 11 parameters are involved in calculations of TBME's. Because the existing Gogny parameters have been evaluated by mean-field model fitting to nuclear structure data mainly which included the three-body force, the Gogny parameters should be refitted for the shell-model calculations ignoring the three-body force.

In the present work, to test the validity of the Gogny shell model, we focus on the *sd*-shell nuclei which have been well investigated by shell-model calculations. Calculations are performed in the spherical harmonic oscillator basis with $\hbar\omega \approx 45A^{-1/3} - 25A^{-2/3}$ [3]. The *sd*-shell single-particle energies are the same as in the USDB shell model [3]: $e(d_{5/2}) = -3.9257$ MeV; $e(s_{1/2}) = -3.2079$ MeV; $e(d_{3/2}) = 2.1117$ MeV.

We choose five nuclei, ^{18}O, ^{18}F, ^{20}Ne, ^{22}Na, ^{24}Mg, for the fit of the 11 parameters. We fit the lowest level for each given spin in their spectra. The NuShellX code [8] is used for the shell-model calculations. We adopt the Monte Carlo simulated annealing algorithm in the process of parameter fittings. The fitted parameters are listed and compared with existing mean-field Gogny parameters in Table 1.

With the parameters determined, we calculate the TBME's for the *sd* shell and perform shell-model calculations using the NuShellX code [8] for this mass region. Figures 1–3 display some of spectroscopic calculations of *sd*-shell nuclei. We see that a good agreement has been obtained. The Gogny force involving only 11 parameters can describe well the effective shell-model interaction, providing a simple way to calculate the TBME's. This will be very useful.

3 Summary

We have used the Gogny force which is a non-zero-range effective interaction, to calculate the TBME's of the shell-model NN interaction. As the first step, we ignore the three-body force but readjust the Gogny parameters. In the present work, we focus on *sd*-shell nuclei. Five nuclei, ^{18}O, ^{18}F, ^{20}Ne, ^{22}Na and ^{24}Mg were chosen in

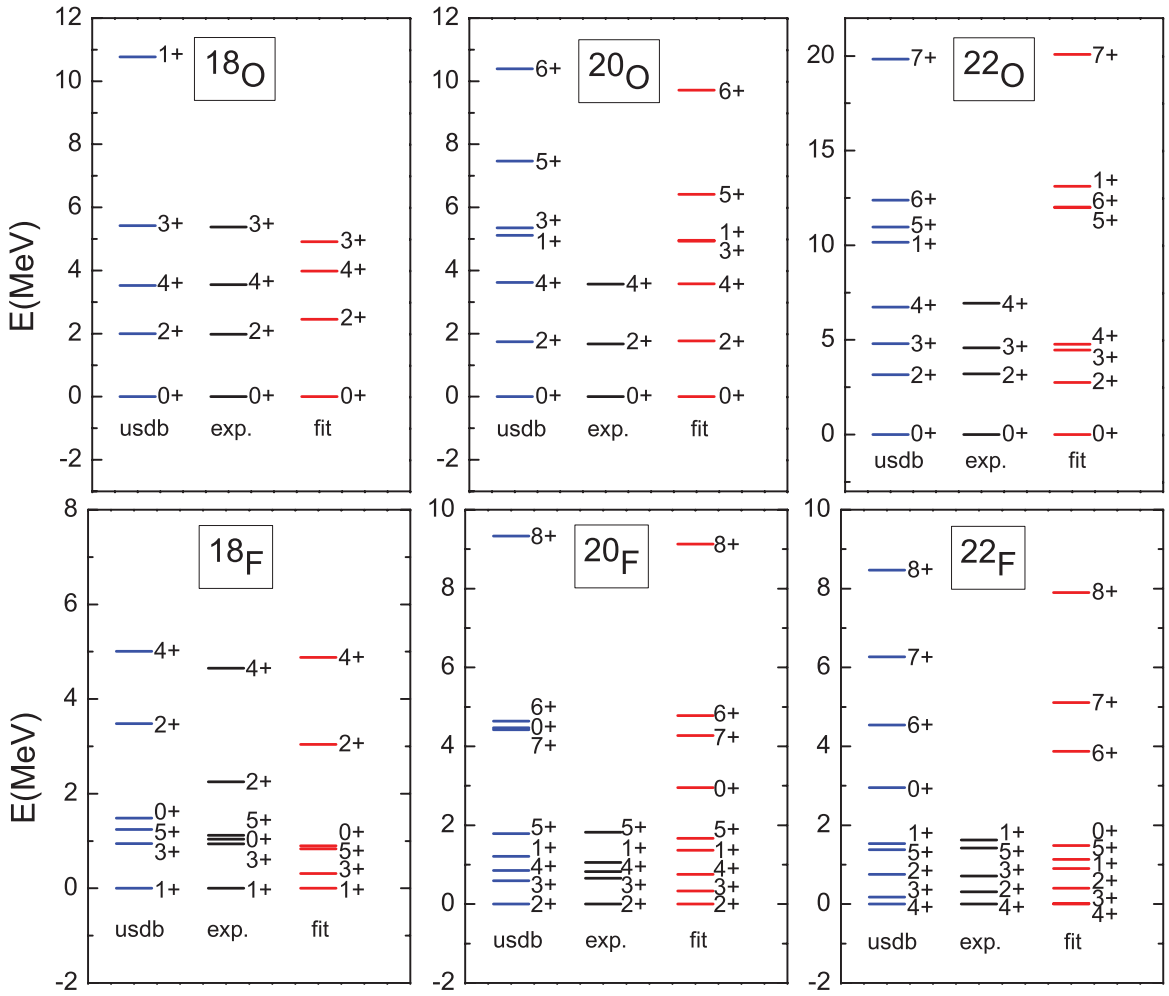

Figure 1: Shell-model calculations using TBME's calculated with the Gogny force with the refitted Gogny parameters given in Table 1, compared with the USDB calculations [3] and experimental data.

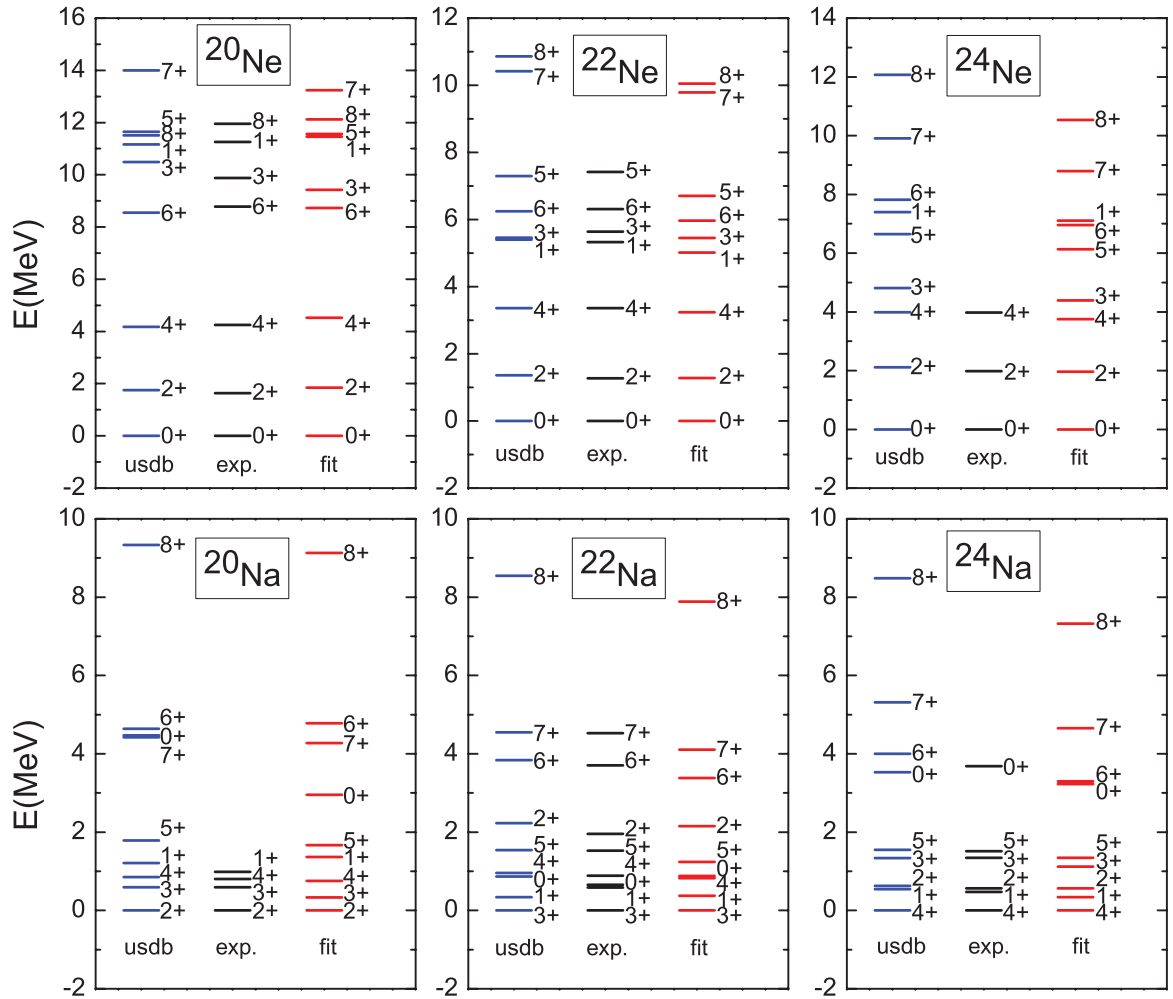

Figure 2: Same as Fig. 1 but for another set of nuclei.

Table 1: Readjusted Gogny parameters, compared with the existing mean-field values of the Gogny parameters.

	D1' [4]	D1 [4]	D1M [5]	D1N [9]	D1S [10]	FIT
μ_1 (fm)	0.7000	0.7000	0.5000	0.8000	0.7000	0.6537
μ_2 (fm)	1.2000	1.2000	1.0000	1.2000	1.2000	0.9837
W_1 (MeV)	−402.40	−402.40	−12797.57	−2047.61	−1720.30	−1951.8104
W_2 (MeV)	−21.30	−21.30	490.95	293.02	103.64	272.4556
B_1 (MeV)	−100.00	−100.00	14048.85	1700.00	1300.00	3280.8417
B_2 (MeV)	−11.77	−11.77	−752.27	−300.78	−163.48	−607.9833
H_1 (MeV)	−496.20	−496.20	−15144.43	−2414.93	−1813.53	−2433.3474
H_2 (MeV)	37.27	37.27	675.12	414.59	162.81	273.1813
M_1 (MeV)	−23.56	−23.56	11963.89	1519.35	1397.60	2562.6194
M_2 (MeV)	−68.81	−68.81	−693.57	−316.84	−223.93	−647.3149
W_0 (MeV · fm^5)	130.00	115.00	115.36	115.00	−130.00	460.8928

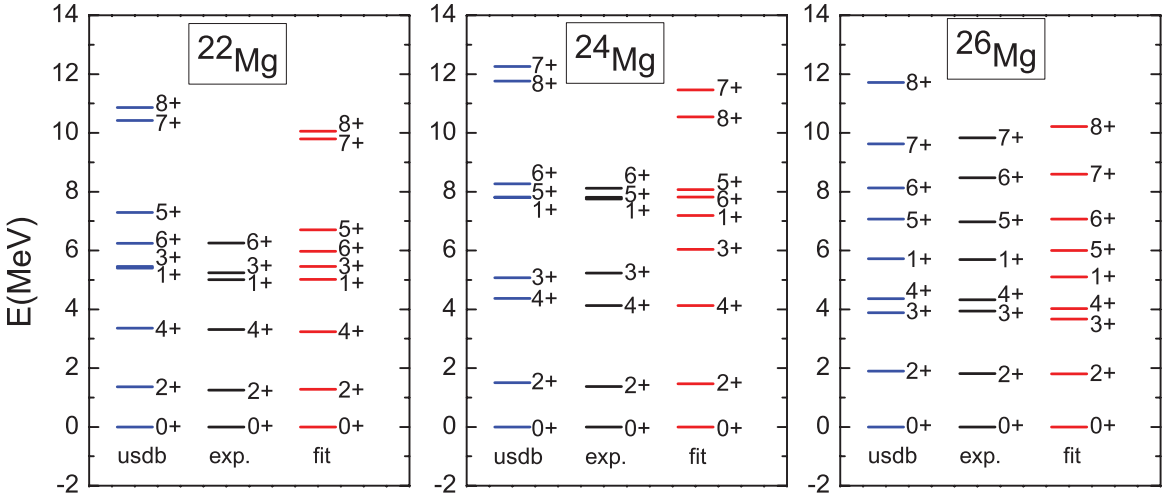

Figure 3: Same as Figs. 1 and 2 but for another set of nuclei.

the fitting of the parameters. With such determined parameters, we calculated the TBME's for the *sd* shell and performed shell-model calculations of nuclear spectra in this mass region. Good results have been obtained.

The further work should be to extend the method on other mass regions, for example, pf shell and $sd + pf$ shells. The Gogny force provides a powerful way to calculate the TBME's. We should also take the three-body force into account in the next work. By taking the existing Gogny parameters, we can test whether the Gogny force can give an unified description within both mean field and shell models.

Acknowledgements

This work has been supported by the National Key Basic Research Program of China under Grant No. 2013CB83440, the National Natural Science Foundation of China under Grants Nos. 11235001, 11320101004 and 11375016, and the Open Project Program of State Key Laboratory of Theoretical Physics, Institute of Theoretical Physics, Chinese Academy of Sciences, China (No. Y4KF041CJ1).

References

[1] T. T. S. Kuo and E. Osnes, Lecture Notes Phys. **364**, 1 (1990).

[2] B. H. Wildenthal, Progr. Part. Nucl. Phys. **11**, 5 (1984).

[3] B. A. Brown and W. A. Richter, Phys. Rev. C **74**, 034315 (2006).

[4] J. Dechargé and D. Gogny, Phys. Rev. C **21**, 1568 (1980).

[5] S. Goriely, S. Hilaire, M. Girod and S. Peru, Phys. Rev. Lett. **102**, 242501 (2009).

[6] H. Sagawa *et al.*, Phys. Lett. B **159**, 228 (1985).

[7] J. M. G. Gomez *et al.*, Nucl. Phys. A **551**, 451 (1993).

[8] B. A. Brown, W. D. M. Rae, E. McDonald and M. Horoi, NUSHELLX@MSU; B. A. Brown and W. D. M. Rae, Nucl. Data Sheets **120**, 115 (2014).

[9] F. Chappert, M. Girod and S. Hilaire, Phys. Lett. B **668**, 420 (2008).

[10] J. F. Berger, M. Girod and D. Gogny, Comp. Phys. Comm. **63**, 365 (1991).

Emergence of Simple Patterns in Complex Atomic Nuclei from First Principles

T. Dytrych[a], K. D. Launey[a], J. P. Draayer[a], P. Maris[b], J. P. Vary[b], D. Langr[c] and T. Oberhuber[d]

[a] *Department of Physics and Astronomy, Louisiana State University, Baton Rouge, LA 70803, USA*

[b] *Department of Physics and Astronomy, Iowa State University, Ames, IA 50011, USA*

[c] *Faculty of Information Technology, Czech Technical University, Prague 16000, Czech Republic*

[d] *Faculty of Nuclear Sciences and Physical Engineering, Czech Technical University, Prague 11519, Czech Republic*

Abstract

We study the structure of low-lying states in ^{6}Li, ^{6}He, ^{8}Be, ^{8}B, ^{12}C, and ^{16}O, using *ab initio* symmetry-adapted no-core shell model. The results of our study demonstrate that collective modes in light nuclei emerge from first principles. We investigate the impact of the symmetry-adapted model space on spectroscopic properties and, in the case of the ground state of ^{6}Li, on elastic electron scattering charge form factor. The results confirm that only a small symmetry-adapted subspace of the complete model space is needed to reproduce accurately complete-space observables and the form factor momentum dependence.

Keywords: *No-core shell model; SU(3) coupling scheme; p-shell nuclei; electron scattering*

1 Introduction

Ab initio approaches to nuclear structure and reactions have advanced our understanding and capability of achieving first-principle descriptions of p-shell nuclei [1–3]. These advances are driven by the major progress in the development of realistic nuclear potential models, such as J-matrix inverse scattering potentials [4] and two- and three-nucleon potentials derived from meson exchange theory [5] or by using chiral effective field theory [6], and, at the same time, by the utilization of massively parallel computing resources [7–9].

These new developments place serious demands on available computational resources for achieving converged properties of p-shell nuclei. This points to the need of further major advances in many-body methods to access a wider range of nuclei and experimental observables, while retaining the predictive power of *ab initio* methods which makes them suitable for, e. g., targeting short-lived nuclei that are inaccessible by experiment but essential to further modeling, for example, of the dynamics of X-ray bursts and the path of nucleosynthesis (see, e. g., Refs. [10, 11]).

The main limitation of *ab initio* approaches is inherently coupled with the combinatorial growth in the size of the many-particle model space with increasing number of nucleons and expansion in the number of single-particle levels in the model space.

Proceedings of the International Conference 'Nuclear Theory in the Supercomputing Era — 2014' (NTSE-2014), Khabarovsk, Russia, June 23–27, 2014. Eds. A. M. Shirokov and A. I. Mazur. Pacific National University, Khabarovsk, Russia, 2016, p. 75.

http://www.ntse-2014.khb.ru/Proc/Dytrych.pdf.

This rapid growth motivates us to develop and investigate a novel model, the *ab initio* symmetry-adapted no-core shell model (SA-NCSM) [12].

The SA-NCSM adopts the first-principle concept and joins a no-core shell model (NCSM) with a SU(3)-based coupling scheme [13]. The NCSM [2] calculations are carried out in many-particle basis constructed from harmonic oscillator (HO) single-particle states characterized by the HO frequency $\hbar\Omega$. The model space is spanned by nuclear configurations of fixed parity consistent with the Pauli principle, and truncated by a cutoff $N_{\max}$. The $N_{\max}$ cutoff is defined as the maximum number of HO quanta allowed in a many-particle state above the minimum for a given nucleus.

The many-nucleon basis states of the SA-NCSM for a given $N_{\max}$ are constructed in SU(3)-coupled proton-neutron formalism and are labeled as

$$|\vec{\gamma}; N(\lambda\,\mu)\kappa L; (S_p S_n S); JM\rangle, \tag{1}$$

where the quantum numbers S_p, S_n, and S denote proton, neutron, and total intrinsic spins, respectively. The label N signifies the number of HO quanta with respect to the minimal number for a given nucleus, and $(\lambda\,\mu)$ represent a set of quantum numbers associated with SU(3) irreducible representations, irreps. The label κ distinguishes multiple occurrences of the same orbital momentum L in the parent irrep $(\lambda\,\mu)$. The orbital momentum L is coupled with S to the total angular momentum J and its projection M. The symbol $\vec{\gamma}$ schematically denotes additional quantum numbers needed to unambiguously distinguish between irreps carrying the same $N(\lambda\,\mu)(S_p S_n S)$ quantum numbers.

In the current implementation of SA-NCSM, $\vec{\gamma}$ specifies a distribution of nucleon clusters over the major HO shells and their inter-shell coupling. Specifically, in each major HO shell η with degeneracy Ω_η, nucleon clusters are arranged into antisymmetric $\mathrm{U}(\Omega_\eta)\times\mathrm{SU}(2)_{S_\eta}$ irreps [14] with $\mathrm{U}(\Omega_\eta)$ further reduced with respect to SU(3). The quantum numbers, $\left[f_1,\dots,f_{\Omega_\eta}\right]\alpha_\eta(\lambda_\eta\,\mu_\eta)S_\eta$, along with $\mathrm{SU}(3)\times\mathrm{SU}(2)_S$ labels of inter-shell coupling unambiguously determine SA-NCSM basis states (1). Note that a spatial symmetry associated with a Young shape $\left[f_1,\dots,f_{\Omega_\eta}\right]$ is uniquely determined by the imposed antisymmetrization and the associated intrinsic spin S_η. A multiplicity index α_η is required to distinguish multiple occurrences of SU(3) irrep $(\lambda_\eta\,\mu_\eta)$ in a given $\mathrm{U}(\Omega_\eta)$ irrep. The SA-NCSM basis states (1) bring forward important information about nuclear shapes and deformation according to an established mapping [15]. For example, (00), $(\lambda\,0)$ and $(0\,\mu)$ describe spherical, prolate and oblate shapes, respectively.

2 Emergence of collective modes in light nuclei

The significance of the SU(3) group for a microscopic description of nuclear collective dynamics can be seen from the fact that it is a symmetry group of a successful Elliott model [13], and a subgroup of a physically relevant $\mathrm{Sp}(3,\mathbb{R})$ symplectic model [16] which provides a comprehensive theoretical foundation for understanding of the dominant symmetries of nuclear collective motion.

To explore the nature of the most important many-nucleon correlations, we analyze the four lowest-lying isospin-zero ($T=0$) states of ^{6}Li ($1^+_{\rm gs}$, 3^+_1, 2^+_1, and 1^+_2), the ground-state rotational bands of ^{8}Be, ^{6}He and ^{12}C, the lowest 1^+, 3^+, and 0^+ excited states of ^{8}B, and the ground state of ^{16}O. We study the probability distribution across Pauli-allowed $(S_p S_n S)$ and $(\lambda\,\mu)$ configurations.

Results for the ground state of ^{6}Li and ^{8}Be obtained with the JISP16 and chiral N^{3}LO interactions, respectively, are shown in Figs. 1 and 2. These figures illustrate a feature common to all low-energy solutions considered. In particular, a highly structured and regular mix of intrinsic spins and SU(3) spatial quantum numbers which, furthermore, does not seem to depend on a particular choice of realistic NN potential.

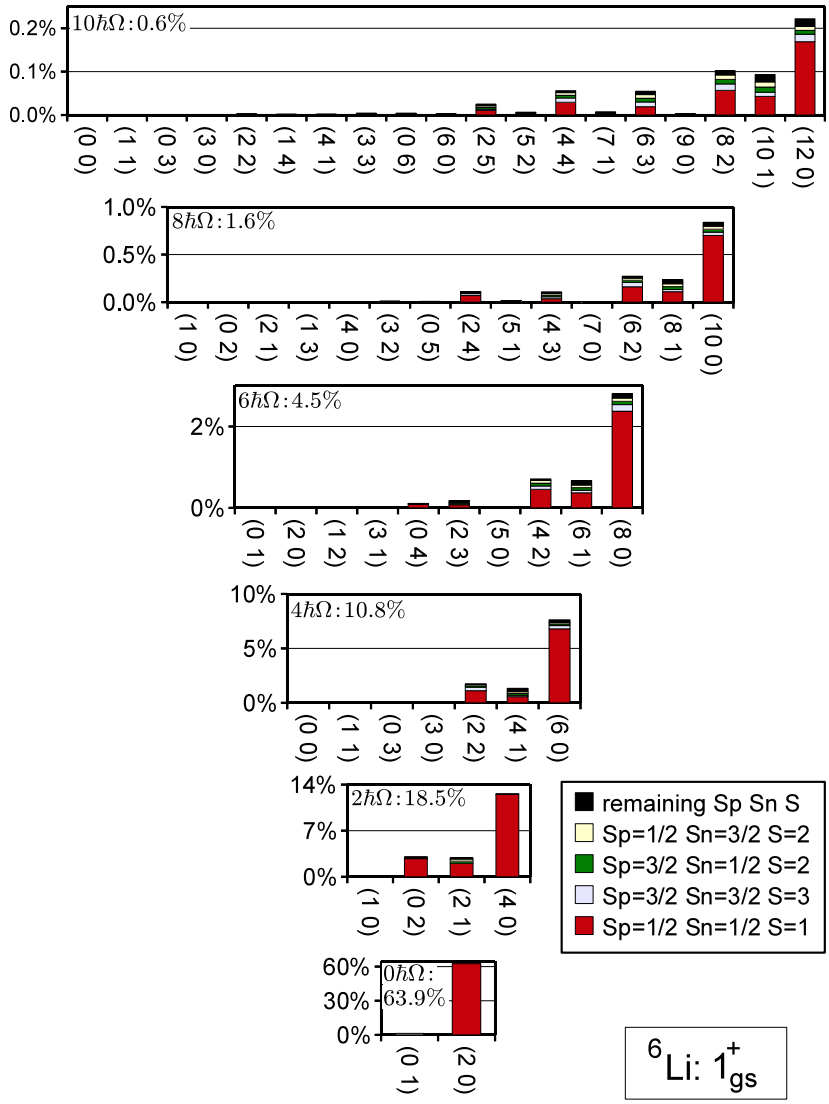

Figure 1: Probability distributions for proton, neutron, and total intrinsic spin components (S_pS_nS) across the Pauli-allowed ($\lambda\,\mu$) values (horizontal axis) for the 1^+ ground state of ^{6}Li obtained with $N_{\max} = 10$ and $\hbar\Omega = 20$ MeV with the JISP16 interaction. The total probability for each $N\hbar\Omega$ subspace is given in the upper left-hand corner of each histogram.

For a closer look at these results, first consider the spin content. We found that the calculated eigenstates project at a 99% level onto a comparatively small subset of intrinsic spin combinations. These combinations are characterized by the lowest allowed values of proton and neutron spins, S_p and S_n, and favor the total intrinsic spin S with maximal value, i. e., $S = S_p + S_n$. For instance, the ground state bands in even-even nuclei, e. g., ^{8}Be, ^{6}He, ^{12}C, and ^{16}O, are found to be dominated by many-particle configurations carrying total intrinsic spin of the protons and neutrons equal to zero and one, with the largest contributions due to (S_pS_nS)=(000) and (112) configurations. The lowest-lying eigenstates in ^{6}Li are almost entirely realized in terms of configurations characterized by the following intrinsic spin (S_pS_nS) combinations: $(\frac{1}{2}\frac{1}{2}1)$, $(\frac{3}{2}\frac{3}{2}3)$, $(\frac{1}{2}\frac{3}{2}2)$, and $(\frac{3}{2}\frac{1}{2}2)$, where the first combination is carrying over 90% of each eigenstate. Likewise, the same spin components as in the case of ^{6}Li are found

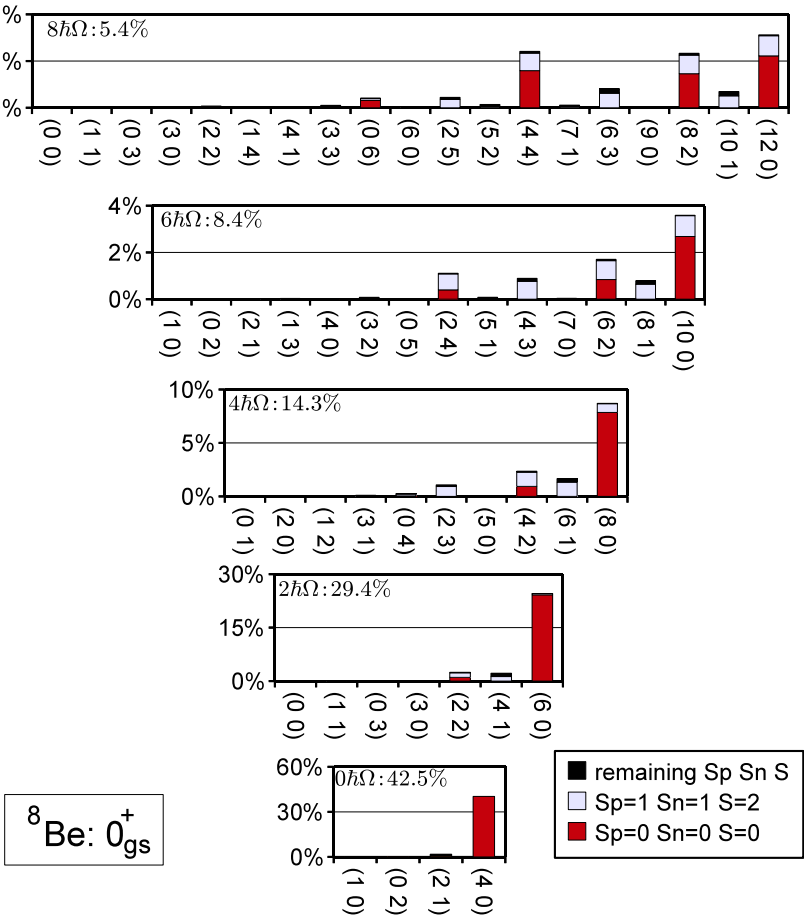

Figure 2: Probability distributions for proton, neutron, and total intrinsic spin components (S_pS_nS) across the Pauli-allowed $(\lambda\,\mu)$ values (horizontal axis) for the 0^+ ground state of ^{8}Be obtained with $N_{\max} = 8$ and $\hbar\Omega = 25$ MeV with the chiral N^{3}LO interaction. The total probability for each $N\hbar\Omega$ subspace is given in the upper left-hand corner of each histogram. The concentration of strengths to the far right within the histograms demonstrates the dominance of collectivity in the calculated eigenstates.

to dominate the ground state and the lowest 1^+, 3^+, and 0^+ excited states of ^{8}B (Table 1).

Second, consider the spatial degrees of freedom. Our results show that the mixing of $(\lambda\,\mu)$ quantum numbers, induced by the SU(3) symmetry breaking terms of realistic interactions, exhibits a remarkably simple pattern. One of its key features is the

Table 1: Total probabilities of the dominant $(S_p\,S_n\,S)$ spin configuration and the dominant nuclear shapes according to Eq. (2) for the ground states of p-shell nuclei.

Nucleus	$(S_p\,S_n\,S)$	Prob. [%]	$(\lambda_0\,\mu_0)$	Prob. [%]
^{6}Li	$(\frac{1}{2}\,\frac{1}{2}\,1)$	93.26	(2 0)	98.13
^{8}B	$(\frac{1}{2}\,\frac{1}{2}\,1)$	85.17	(2 1)	87.94
^{8}Be	(0 0 0)	85.25	(4 0)	90.03
^{12}C	(0 0 0)	55.19	(0 4)	48.44
^{16}O	(0 0 0)	83.60	(0 0)	89.51

preponderance of a single $0\hbar\Omega$ SU(3) irrep. This so-called leading irrep, according to the established geometrical interpretation of SU(3) labels $(\lambda\,\mu)$ [15], is characterized by the largest value of the intrinsic quadrupole deformation. For instance, the low-lying states of ^{6}Li project at a 40% – 70% level onto the prolate $0\hbar\Omega$ SU(3) irrep (2 0), as illustrated in Fig. 1 for the ground state. For the considered states of ^{8}B, ^{8}Be, ^{12}C, and ^{16}O, qualitatively similar dominance of the leading $0\hbar\Omega$ SU(3) irreps is observed — (2 1), (4 0), (0 4), and (0 0) irreps, associated with triaxial, prolate, oblate, and spherical shapes, respectively. The clear dominance of the most deformed $0\hbar\Omega$ configuration within low-lying states of light p-shell nuclei indicates that the quadrupole-quadrupole interaction of the Elliott SU(3) model of nuclear rotations [13] is realized naturally within an *ab initio* framework.

The analysis also reveals that the dominant SU(3) basis states at each $N\hbar\Omega$ subspace ($N = 0, 2, 4, ...$) are typically those with $(\lambda\,\mu)$ quantum numbers given by

$$\lambda + 2\mu = \lambda_0 + 2\mu_0 + N, \tag{2}$$

where λ_0 and μ_0 denote labels of the leading SU(3) irrep in the $0\hbar\Omega$ ($N = 0$) subspace. Furthermore, there is an apparent hierarchy among states that fulfill the condition (2). In particular, the $N\hbar\Omega$ configurations with (λ_0+N μ_0), the so-called stretched states, carry a noticeably higher probability than the others. For instance, the $(2+N\ 0)$ stretched states contribute at the 85% level to the ground state of ^{6}Li, as can be readily seen in Fig. 1. Moreover, the dominance of the stretched states is rapidly increasing with the increasing many-nucleon basis cutoff $N_{\max}$.

3 Efficacy of symmetry-adapted concept

The observed simple patterns of intrinsic spin and deformation mixing support a symmetry-adapted selection of configuration space that takes advantage of dominant symmetries and refines the definition of the NCSM model space based solely on the $N_{\max}$ cutoff.

To accommodate highly-deformed configurations (high-energy HO excitations) together with essential mixing of low-energy excitations, typical SA-NCSM calculations span the complete space up to a given $N^{\perp}_{\max}$, while beyond this, calculations include only selected many-nucleon basis states limited by the $N_{\max}$ cutoff. At each $N\hbar\Omega$ space, where $N^{\perp} < N \leq N_{\max}$, we select many-nucleon basis states carrying a fixed set of (S_pS_nS) and $(\lambda\,\mu)$ quantum numbers. It is important to note that such a defined model space keeps ability to factorize the center-of-mass motion exactly [17]. As a result, a SA-NCSM model space defined by a set of dominant U(3) irreps $N(\lambda\,\mu)$ and important intrinsic spins, (S_pS_nS), yields eigensolutions with the center-of-mass in the HO ground state. We adopt a notation where, for example, a SA-NCSM model space of "$\langle 4\rangle$12" includes all the configurations up through $N^{\perp}_{\max} = 4$ and a restricted subspace beyond $N^{\perp}_{\max} = 4$ up through $N_{\max} = 12$. When we quote only the $N_{\max}$ value, it is understood that the space is complete through that $N_{\max}$ (for example $N_{\max} = 8 = N^{\perp}_{\max}$).

The efficacy of the symmetry-adapted concept is illustrated for SA-NCSM results obtained in model spaces which are expanded beyond a complete $N^{\perp}_{\max}$ space with irreps that span a relatively few dominant intrinsic spin components and carry quadrupole deformation specified by Eq. (2). Specifically, we vary $N^{\perp}_{\max}$ from 2 to 10 with only the subspaces determined by Eq. (2) included beyond $N^{\perp}_{\max}$. This allows us to study a convergence of spectroscopic properties towards results obtained in the complete $N_{\max} = 12$ space and hence probes the efficacy of the symmetry-adapted model space selection concept. We use a Coulomb plus JISP16 NN interaction for $\hbar\Omega$ values ranging from 17.5 up to 25 MeV, along with the Gloeckner–Lawson prescription [18] for elimination of spurious center-of-mass excitations. The SA-NCSM eigenstates are

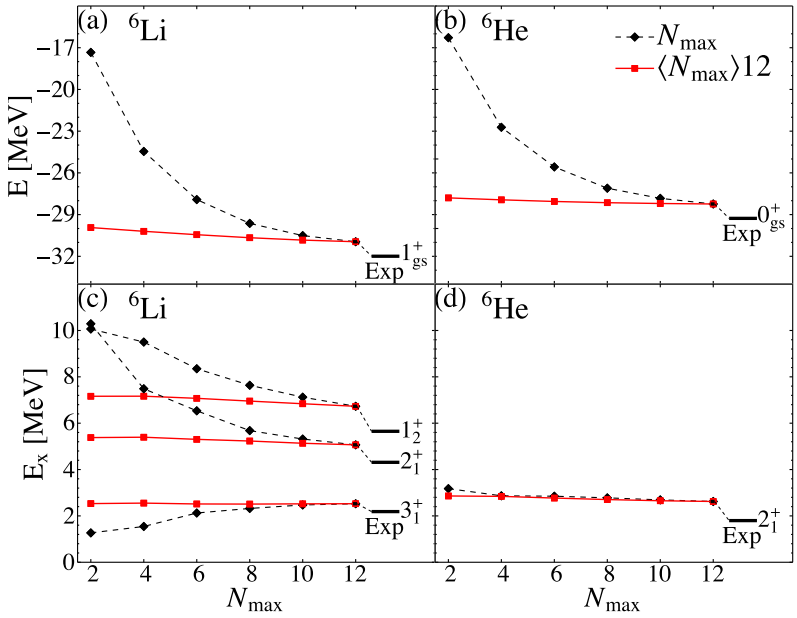

Figure 3: The ground-state energies of ^{6}Li (a) and ^{6}He (b), excitation energies of $T = 0$ states of ^{6}Li (c), 2^+_1 excited state of ^{6}He (d), shown for the complete $N_{\max}$ (dashed black curves) and truncated $\langle N^{\perp}_{\max} = N_{\max}\rangle 12$ (solid red lines) model spaces. Results shown are for JISP16 and $\hbar\Omega = 20$ MeV. Note relatively large changes when the complete space is increased from $N_{\max} = 2$ to $N_{\max} = 12$ as compared to nearly constant $\langle N_{\max}\rangle 12$ SA-NCSM outcomes.

used to determine spectroscopic properties of low-lying $T = 0$ states of ^{6}Li and the ground-state band of ^{6}He for $\langle N^{\perp}_{\max}\rangle 12$ model spaces.

The results indicate that the observables obtained in the $\langle N^{\perp}_{\max}\rangle 12$ symmetry-adapted truncated spaces are excellent approximations to the corresponding $N_{\max} = 12$ complete-space counterparts. Furthermore, the level of agreement achieved is only marginally dependent on $N^{\perp}_{\max}$. In particular, the ground-state binding energies obtained in a $\langle 2\rangle 12$ model space represent approximately 97% of the complete-space $N_{\max} = 12$ binding energy in the case of ^{6}Li and reach over 98% for ^{6}He [see Figs. 3 (a) and (b)]. The excitation energies differ only by 5 to a few hundred keV from the corresponding complete-space $N_{\max} = 12$ results [Figs. 3 (c) and (d)].

The electric quadrupole moments and reduced electromagnetic $B(E2)$ transition strengths are reproduced remarkably well by the SA-NCSM for ^{6}He in the restricted $\langle 8\rangle 12$ space. Notably, the $\langle 2\rangle 12$ eigensolutions for ^{6}Li yield results for $B(E2)$ strengths and quadrupole moments that track closely with their complete $N_{\max} = 12$ space counterparts (see Fig. 4). It is known that a further expansion of the model space beyond $N_{\max} = 12$ is needed to reach the convergence [20, 21]. However, the close correlation between the $N_{\max} = 12$ and $\langle 2\rangle 12$ results is strongly suggestive that this convergence can be obtained through the leading SU(3) irreps in the symmetry-adapted space.

3.1 Electron-scattering form factors

We also study the impact of the symmetry-adapted model space selection on the elastic electron scattering charge form factors for the ground state of ^{6}Li for momentum transfer up to $q \approx 4$ fm^{-1}. Namely, we examine the longitudinal form factor ($C0$) for a range of $\hbar\Omega = 15$, 20, and 25 MeV and for several SU(3)-selected spaces, $\langle 2\rangle 12$, $\langle 4\rangle 12$, $\langle 6\rangle 12$, $\langle 8\rangle 12$, $\langle 10\rangle 12$, together with the complete $N_{\max} = 12$ space. We use

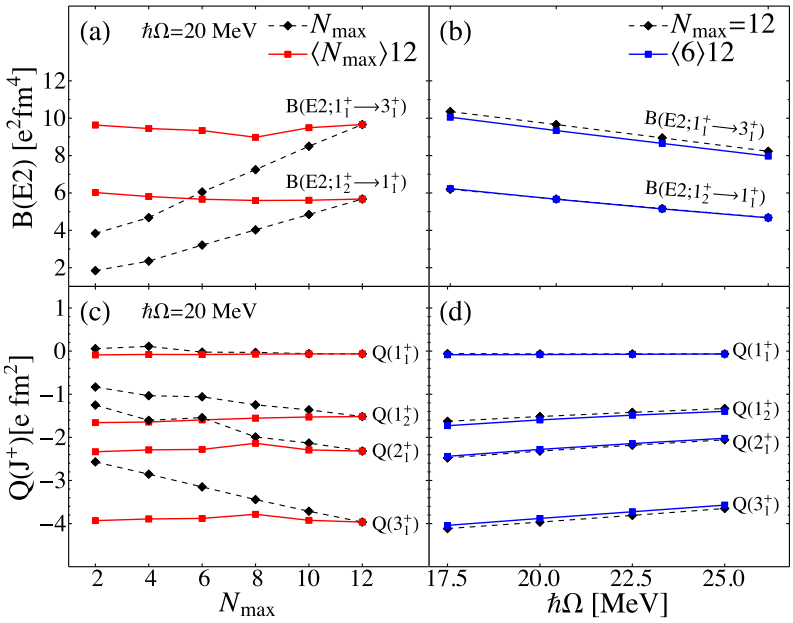

Figure 4: Electric quadrupole transition probabilities and quadrupole moments for $T = 0$ states of ^{6}Li calculated with JISP16 interaction without using effective charges, are shown for the complete $N_{\max}$ (dashed black lines) and $\langle N_{\max}^{\perp} = N_{\max}\rangle 12$ truncated (solid red lines) model spaces [(a) and (c)], and as functions of $\hbar\Omega$ for the complete $N_{\max} = 12$ and $\langle 6\rangle 12$ truncated (solid blue lines) model spaces [(b) and (d)]. Experimentally, $B(E2; 1_1^+ \to 3_1^+) = 25.6(20)\ e^2{\cdot}\mathrm{fm}^4$ [19].

the realistic nucleon-nucleon interactions N^{2}LOopt [22] and JISP16 [4]. The $C0$ form factor is a Fourier transform of the charge density, and hence it provides an indication on how well nuclear wave functions reproduce the low- and higher-momentum components of the nuclear charge density. This, in turn, can reveal important underlying physics responsible for achieving convergence of nuclear radii.

The charge form factors are calculated in the first-order plane-wave Born approximation. They have the center-of-mass contribution removed and are further adjusted to account for the finite proton size. They are derived using the formalism and an extension of the computer code developed by Lee [24] and described in detail in Ref. [25], as well as using an SU(3)-based apparatus [26, 27] for calculating charge and current density distributions in terms of the shell-model one-body density matrix elements (OBDMEs) and the single-particle matrix elements of the associated electromagnetic operators.

Longitudinal electron scattering form factors for the ground state of ^{6}Li are studied for the bare JISP16 and N^{2}LOopt NN interactions up to $N_{\max} = 12$ spaces. An important result is that in all cases, the $\langle 6\rangle 12$ selected-space results are found to be almost identical to the complete-space counterparts in low- and intermediate-momentum regions (see Fig. 5), and even above 3 fm^{-1} (not shown in the figure). This remains valid for various $\hbar\Omega$ values, as well as when different interactions are employed [Figs. 5 (a) and (b)]. This further confirms the validity of the symmetry-adapted concept of the SA-NCSM. Indeed, the present results indicate that using these selected spaces that constitute only a fraction of the complete model space (about 1% for $\langle 6\rangle 12$), it is possible to reproduce, in addition, the complete-space form factor momentum dependence. In short, symmetry-adapted model-space selection based on a straightforward prescription dictated by the approximate dynamical symmetries, eliminates many-nucleon basis states that are shown in this study to be also irrelevant

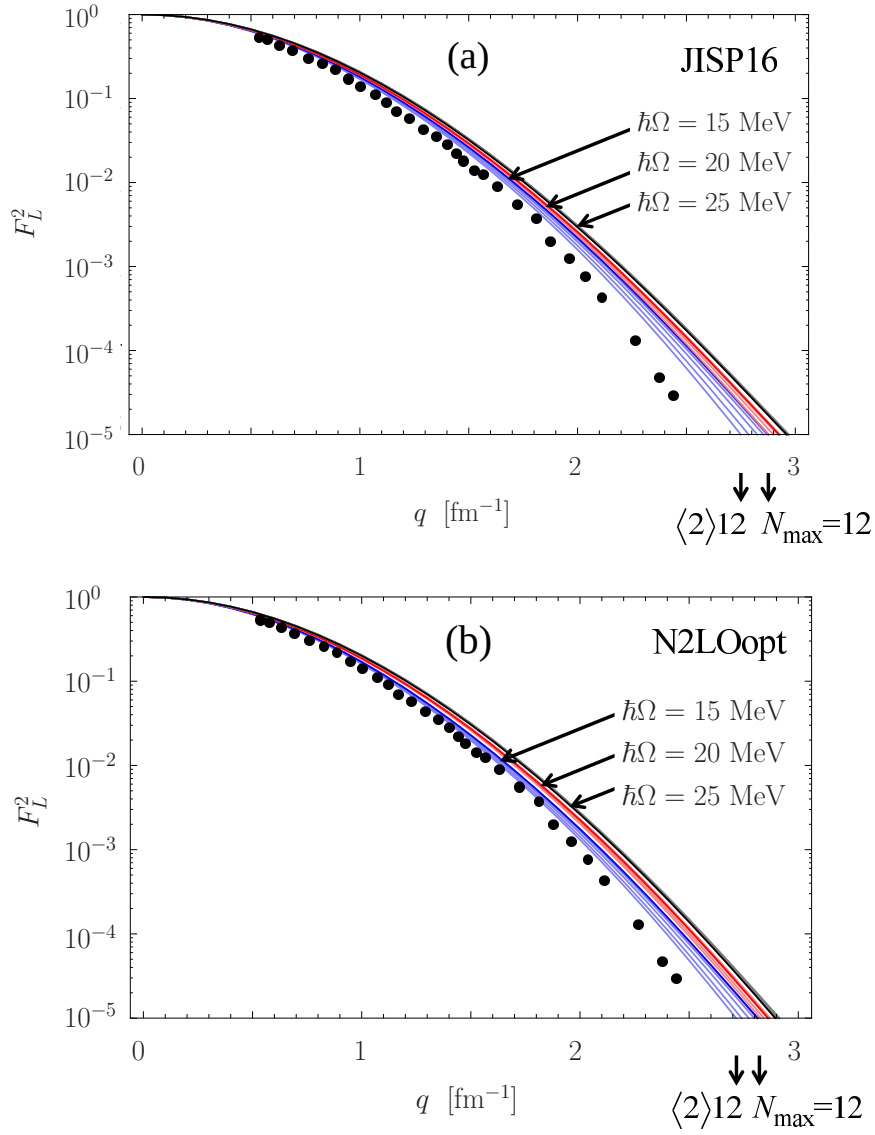

Figure 5: Longitudinal $C0$ electron scattering form factors F_L^2 (translationally invariant) for the SA-NCSM 1^+ ground state of ^{6}Li calculated in the complete $N_{\max} = 12$ space (darker colors) and the SU(3)-selected spaces, $\langle 2\rangle 12$, $\langle 4\rangle 12$, $\langle 6\rangle 12$, $\langle 8\rangle 12$, and $\langle 10\rangle 12$ (lighter colors), for $\hbar\Omega = 15$ MeV or $b = 1.66$ fm (blue), $\hbar\Omega = 20$ MeV or $b = 1.44$ fm (red), and $\hbar\Omega = 25$ MeV or $b = 1.29$ fm (black) with the bare JISP16 interaction (a) and with the bare N^{2}LOopt interaction (b). Experimental data are taken from Ref. [23].

for describing the single-proton momentum distribution in the ^{6}Li ground state as revealed by the $C0$ form factor at low/intermediate momentum transfers and above.

Deviations in the form factor as a result of the SU(3)-based selection of model spaces are found to decrease with $\hbar\Omega$ (see Fig. 5: the higher is the $\hbar\Omega$ value, the narrower is the curve). This effect is more prominent for momenta $q > 2$ fm^{-1}. The outcome suggests that for high enough $\hbar\Omega$ values, results are almost independent from the model-space truncation and, for $\hbar\Omega = 25$ MeV, the $\langle 2\rangle 12$ form factor already reproduces the complete-space result. For low $\hbar\Omega$ values, larger $N_{\max}^{\perp}$ spaces ($\langle 4\rangle 12$ or $\langle 6\rangle 12$) appear necessary pointing to a mixing of more deformation/spin configurations

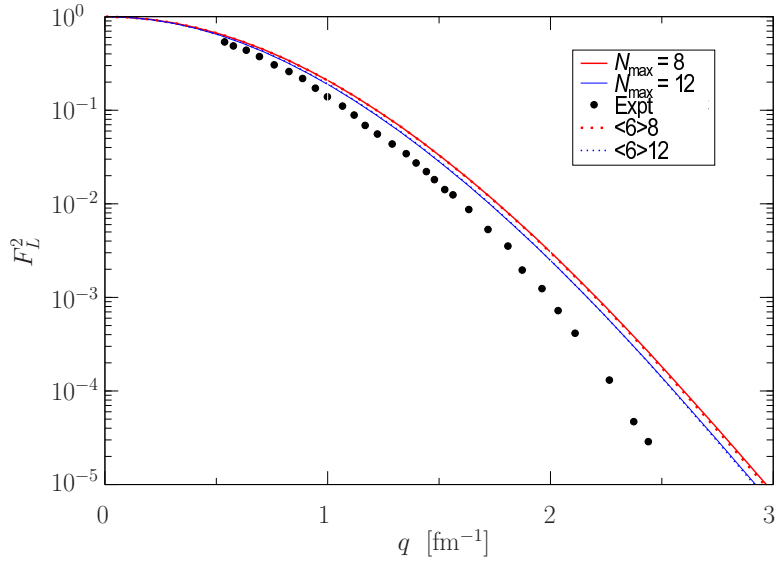

Figure 6: Longitudinal $C0$ electron scattering form factors F_L^2 (translationally invariant) for the SA-NCSM 1^+ ground state of ^{6}Li calculated for $\hbar\Omega = 20$ MeV or $b = 1.44$ fm and with the bare JISP16 interaction. The outcome for the SU(3)-selected spaces, $\langle 6\rangle 8$ (red dots) and $\langle 6\rangle 12$ (blue dots), accurately reproduces the corresponding results for the complete $N_{\max} = 8$ space (solid, red) and $N_{\max} = 12$ space (solid, blue), with larger-space $N_{\max} = 12$ results lying slightly closer to experiment [23].

within these low-$\hbar\Omega$ spaces. However, while low values, $\hbar\Omega \lesssim 15$ MeV, are known to require larger model spaces to obtain convergence of the ground state energy, such a mixing at the $4\hbar\Omega$ and $6\hbar\Omega$ subspaces is expected to decrease for $N_{\max} > 12$. In short, the SU(3)-based truncation of the model space yields reasonably small deviations in the form factor, especially for $q < 2$ fm^{-1} and for $\hbar\Omega > 15$ MeV.

While results using N^{2}LOopt lie slightly closer to experiment, both interactions show similar patterns with a small dependence on $\hbar\Omega$ (Fig. 5). Furthermore, as one increases $N_{\max}$ (e. g., from $N_{\max} = 8$ to $N_{\max} = 12$), SA-NCSM predictions are reasonably trending towards experiment, as illustrated for a $\langle 6\rangle N_{\max}$ selected space and for a reasonable $\hbar\Omega$ value of 20 MeV in Fig. 6. We note that the $N_{\max} = 12$ results continue to deviate from the experimental data for intermediate momenta, especially for $q \gtrsim 2$ fm^{-1}. Agreement with experiment could be improved by including contributions of three-body interactions in the SA-NCSM calculations and of two-body operators in the F_L^2 calculations.

4 Conclusions

We have developed a novel *ab initio* approach, SA-NCSM, that capitalizes on the SU(3) symmetry-adapted physically relevant many-particle basis. We analyzed the structure of low-lying states in p-shell nuclei obtained with JISP16, N^{2}LOopt, and chiral N^{3}LO realistic NN interactions using complete $N_{\max}$ model spaces. The resulting wave functions are dominated by many-nucleon basis states with large quadrupole deformations and low intrinsic spins. This simple orderly pattern does not seem to depend on the particular choice of realistic NN potential. The results demonstrate that observed collective phenomena in light nuclei emerge naturally from first-principles considerations.

We carried out the calculations of the binding energies, excitation energies, electromagnetic moments, $E2$ and $M1$ reduced transitions, for selected states in ^{6}Li and

^{6}He obtained with the symmetry-adapted model spaces. We have shown that the SA-NCSM reduces the configuration space to physically relevant subspaces without compromising the accuracy of *ab initio* NCSM approach. Furthermore, we demonstrated that the symmetry-adapted model space properly treats low- and higher-momentum components of the ^{6}Li ground state charge density. The outcome confirms the utility of the SA-NCSM concept for low-lying nuclear states.

Acknowledgments

We thank Anna Hayes for useful discussions. This work was supported in part by the US NSF [OCI-0904874 and OCI-0904782], the US Department of Energy [DE-SC0005248, DE-FG02-87ER40371, DESC0008485 (SciDAC-3/NUCLEI)], the National Energy Research Scientific Computing Center [supported by DOE's Office of Science under Contract No. DE-AC02-05CH1123], the Southeastern Universities Research Association, and the Czech Science Foundation under Grant No. P202/12/2011. This work also benefitted from computing resources provided by Blue Waters, as well as the Louisiana Optical Network Initiative and Louisiana State University's Center for Computation & Technology.

References

[1] S. C. Pieper, R. B. Wiringa and J. Carlson, Phys. Rev. C **70**, 054325 (2004); K. M. Nollett, S. C. Pieper, R. B. Wiringa, J. Carlson and G. M. Hale, Phys. Rev. Lett. **99**, 022502 (2007).

[2] P. Navrátil, J. P. Vary and B. R. Barrett, Phys. Rev. Lett. **84**, 5728 (2000); Phys. Rev. C **62**, 054311 (2000); S. Quaglioni and P. Navrátil, Phys. Rev. Lett. **101**, 092501 (2008); Phys. Rev. C **79**, 044606 (2009); B. R. Barrett, P. Navrátil and J. P. Vary, Progr. Part. Nucl. Phys. **69**, 131 (2013).

[3] G. Hagen, T. Papenbrock and M. Hjorth-Jensen, Phys. Rev. Lett. **104**, 182501(2010).

[4] A. M. Shirokov, A. I. Mazur, S. A. Zaytsev, J. P. Vary and T. A. Weber, Phys. Rev. C **70**, 044005 (2004); A. M. Shirokov, J. P. Vary, A. I. Mazur, S. A. Zaytsev and T. A. Weber, Phys. Lett. B **621**, 96 (2005); A. M. Shirokov, J. P. Vary, A. I. Mazur and T. A. Weber, *ibid.* **644**, 33 (2007).

[5] R. Machleidt, F. Sammarruca and Y. Song, Phys. Rev. C **53**, R1483 (1996); R. Machleidt, *ibid.* **63**, 024001 (2001).

[6] D. R. Entem and R. Machleidt, Phys. Rev. C **68**, 041001 (2003).

[7] P. Sternberg, E. G. Ng, C. Yang, P. Maris, J. P. Vary, M. Sosonkina and H. V. Le, in *Proc. 2008 ACM/IEEE Conf. on Supercomputing, Austin, November 15–21, 2008*. IEEE Press, Piscataway, NJ, 2008, p. 15:1.

[8] P. Maris, M. Sosonkina, J. P. Vary, E. G. Ng and C. Yang, Proc. Comp. Sci. **1**, 97 (2010).

[9] H. M. Aktulga, C. Yang, E. N. Ng, P. Maris and J. P. Vary, in *Euro-Par*, eds. C. Kaklamanis, T. S. Papatheodorou and P. G. Spirakis. Lecture Notes Comp. Sci. **7484**, 830 (2012).

[10] B. Davids, R. H. Cyburt, J. Jose and S. Mythili, Astrophys. J. **735**, 40 (2011).

[11] A. M. Laird *et al.*, Phys. Rev. Lett. **110**, 032502 (2013).

[12] T. Dytrych, K. D. Launey, J. P. Draayer, P. Maris, J. P. Vary, E. Saule, U. Catalyurek, M. Sosonkina, D. Langr and M. A. Caprio, Phys. Rev. Lett. **111**, 252501 (2013).

[13] J. P. Elliott, Proc. Roy. Soc. A **245**, 128 (1958); *ibid.* **245**, 562 (1958); J. P. Elliott and M. Harvey, *ibid.* **272**, 557 (1962).

[14] J. P. Draayer, Y. Leschber, S. C. Park and R. Lopez, Comp. Phys. Comm. **56**, 279 (1989).

[15] O. Castaños, J. P. Draayer and Y. Leschber, Z. Phys **329**, 33 (1988); G. Rosensteel and D. J. Rowe, Ann. Phys. (NY) **104**, 134 (1977); Y. Leschber and J. P. Draayer, Phys. Lett. B **190**, 1 (1987).

[16] G. Rosensteel and D. J. Rowe, Phys. Rev. Lett. **38**, 10 (1977).

[17] B. J. Verhaar, Nucl. Phys. A **21**, 508 (1960).

[18] D. H. Gloeckner and R. D. Lawson, Phys. Lett. B **53**, 313 (1974).

[19] D. R. Tilley *et al.*, Nucl. Phys. A **708**, 3 (2002).

[20] C. Cockrell, J. P. Vary and P. Maris, Phys. Rev. C **86**, 034325 (2012).

[21] P. Maris and J. P. Vary, Int. J. Mod. Phys. E **22**, 1330016 (2013).

[22] A. Ekström, G. Baardsen, C. Forssén, G. Hagen, M. Hjorth-Jensen, G. R. Jansen, R. Machleidt, W. Nazarewicz, T. Papenbrock, J. Sarich and S. M. Wild, Phys. Rev. Lett. **110**, 192502 (2013).

[23] G. C. Li, I. Sick, R. R. Whitney and M. R. Yearian, Nucl. Phys. A **162**, 583 (1971).

[24] H. C. Lee, Atomic Energy Canada Limited Report No. AECL-4839, 1974 (unpublished).

[25] A. C. Hayes and A. A. Kwiatkowski, Phys. Rev. C **81**, 054301 (2010).

[26] P. Rochford and J. P. Draayer, Ann. Phys. (NY) **214**, 341 (1992).

[27] J. Escher and J. P. Draayer, Phys. Rev. Lett. **82**, 5221 (1999).

Ordered Oxygen Arrangement in Titanium Nanoparticles: *Ab Initio* Study

A. N. Chibisov

Computational Center, Far Eastern Branch, Russian Academy of Sciences, 65 Kim Yu Chen Street, Khabarovsk, 680000, Russia

Abstract

We have used the density functional theory to investigate the interaction of titanium nanoparticles with oxygen. We observed the energy-favorable site for oxygen atoms and investigated the atomic structure of the oxidized cluster.

Keywords: *Nanoparticles; metals and alloys; oxidation; simulation and modeling*

1 Introduction

Titanium has a high corrosion resistance, a low thermal expansion, and a high mechanical strength [1, 2]. These properties make titanium and its alloys one of the most important structural materials for applications in aerospace vehicles, defense technology, and metal cutting.

The interaction of titanium with oxygen is an important scientific and technological problem [3] since its mechanical and electrical properties can be significantly modified [4–6]. The dissolution of oxygen in bulk titanium (up to 0.6 wt. %) has been shown recently [1] to improve its mechanical properties. Kyung-Ho Heo and coauthors [4] have shown the hardness and electrical resistivity of oxygen-doped bulk Ti to increase linearly with increasing oxygen concentration (500–7900 ppm O). The interaction of bulk and surface titanium with oxygen has been investigated for many years. It was shown by first-principles quantum-mechanical methods [3, 7–9] that the oxygen prefers to occupy an octahedral interstitial site in the bulk lattice. In addition, Henry *et al.* [9] have found three oxygen interstitial sites in titanium and quantified mechanisms for oxygen diffusion. Experimental results [10,11] have indicated different oxidation levels of metallic titanium at different temperatures. At low temperature, the oxygen is initially adsorbed on the surface layer of Ti (0001) [10] and then diffuses into lower layers when the temperature increases [11].

It is still unclear how the oxygen affects atomic and electronic structures as well as the agglomeration processes of Ti nanoparticles. Thus, we have investigated the oxygen adsorption on titanium nanoclusters and have calculated the binding energy as a function of oxygen concentration. Our results explain why the oxygen is adsorbed on faces of the icosahedral Ti_{13} cluster.

2 Methods and approaches

First-principles calculations were performed using the generalized gradient approximation and allowing for spin polarization within the density functional theory by

Proceedings of the International Conference 'Nuclear Theory in the Supercomputing Era — 2014' (NTSE-2014), Khabarovsk, Russia, June 23–27, 2014. Eds. A. M. Shirokov and A. I. Mazur. Pacific National University, Khabarovsk, Russia, 2016, p. 86.

http://www.ntse-2014.khb.ru/Proc/Chibisov.pdf.

means of the ABINIT software package [12]. Pseudopotentials for Ti and O atoms were constructed using the program fhi98PP [13]. A special $1 \times 1 \times 1$ G-point in the Monkhorst–Pack grid [14] with a cutoff energy of 816.34 eV was used to simulate the Ti clusters. The simulation clusters were placed in a very large cubic cell with the size of approximately 19 Å. The atomic structure was relaxed in the calculations while the interatomic forces were less than 0.005 eV/Å. In addition, the Ti_2 dimer structure was calculated to validate the titanium pseudopotentials. The calculated Ti-Ti distance was 1.9055 Å that is slightly less than the experimental value of 1.9422 ± 0.0008 Å [15].

3 Results and discussions

Experiments [16] have shown that the most stable titanium nanoparticle structures are the icosahedral clusters Ti_{13}, Ti_{19} and Ti_{55}. We investigated the Ti_{13} cluster here because larger clusters require considerable computing resources.

To study the interaction of the Ti_{13} cluster with the oxygen, we considered two oxygen coverages, 0.05 and 1 monolayer (ML). The 0.05 ML coverage corresponds to one O atom on the Ti_{13} surface whereas 1 ML corresponds to 20 oxygen atoms.

An average binding energy E_b of O atom on the Ti_{13} surface is given by

$$E_b = -\frac{1}{N_O}\left[E^{O/Ti} - \left(E^{Ti} + N_O E^O\right)\right], \tag{1}$$

where N_O is the number of O atoms on the surface, $E^{O/Ti}$ is the total energy of the adsorbate-substrate system, E^{Ti} is the energy of the Ti_{13} cluster, and E^O is the energy of the O atom.

From Eq. (1), we obtain $E_b = 12.01$ eV for the oxygen on the Ti_{13} surface (Fig. 1), which is slightly higher than the energy of dissolved oxygen (11.85 eV) in bulk titanium. Therefore the titanium nanoparticles are more reactive to oxygen than the bulk titanium [17]. To characterize the dissolved oxygen in bulk titanium, one oxygen atom has been incorporated in the favorable octahedral site of the bulk lattice [3,7–9]. Hence our calculations demonstrate that, despite the transition from bulk titanium to the nanoscale (including Ti_{13} clusters), the interacting O atoms are advantageously located in positions that correspond to "bulk" interstitial sites. These sites are certainly not octahedral (as in the bulk Ti). Due to the similarity of the local atomic structures of the bulk and isolated Ti_{13} clusters [18] and the coincidence of the Ti-O bonds, such a comparison is appropriate.

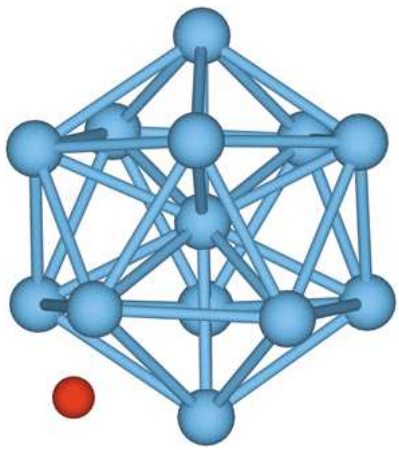

Figure 1: Position of one oxygen atom (red circle) adsorbed on the Ti_{13} cluster (blue circles).

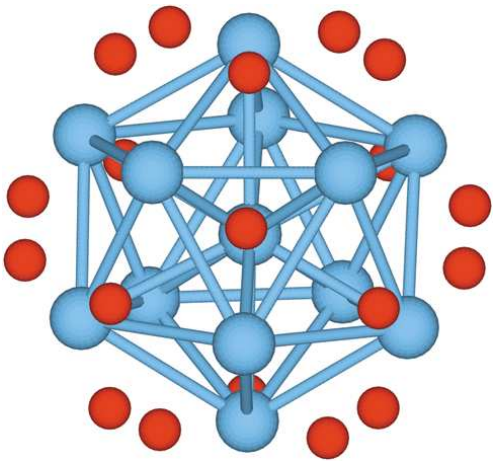

Figure 2: The Ti_{13} cluster structure (blue circles) with 20 adsorbed oxygen atoms (red circles).

When the oxygen coverage is increased to one monolayer, i. e., up to 20 atoms on the cluster surface (see Fig. 2), the oxygen binding energy reduces to 10.49 eV. The reduced binding energy manifests increased repulsive forces between the adsorbed oxygen atoms. It can be seen in Fig. 2 that the oxygen atoms are located on each face of the Ti_{13} icosahedron. Average Ti-O and O-O bond lengths are approximately 1.99 and 2.33 Å, respectively. However, when we allow all Ti atoms to relax in the cluster, it tends to form an oxide cluster where all Ti-Ti bonds are broken. Thus, in this case, we have fixed the titanium atoms during the relaxation.

Our results regarding the energetics and structural properties of oxygen adsorption on titanium nanoclusters, are very important for understanding an oxygen diffusion in nanostructured titanium materials. Specifically, the results will impact the design, production and application of these materials in aerospace and engineering.

4 Conclusions

In conclusion, we have used first-principles calculations to investigate the oxygen adsorption process on the stable Ti_{13} nanocluster. The atomic structure of the oxidized titanium clusters and the oxygen adsorption energy were studied in detail for low and high O coverages on the Ti_{13} surface. The results indicate that titanium during its interaction with oxygen, for both bulk and nanoscale states, has O atoms advantageously located in the positions corresponding to “bulk” interstitial sites.

References

[1] A. K. M. Nurul Amin, *Titanium alloys — towards achieving enhanced properties for diversified applications.* InTech, Rijeka, 2012.

[2] S.-Y. Wang, J.-Z. Yu, H. Mizuseki, J.-A. Yan, Y. Kawazoe and C.-Y. Wang, J. Chem. Phys. **120**, 8463 (2004).

[3] G. Boureau, N. Capron and R. Tétot, Scr. Mater. **59**, 1255 (2008).

[4] K.-H. Heo, N. R. Munirathnam, J.-W. Lim, M.-T. Le and G.-S. Choi, Mater. Chem. Phys. **112**, 923 (2008).

[5] S. Firstov, V. Kulikovsky, T. Rogul and R. Ctvrtlik, Surf. Coat. Technol. **206**, 3580 (2012).

[6] S. J. Li, M. T. Jia, F. Prima, Y. L. Hao and R. Yang, Scr. Mater. **64**, 1015 (2011).

[7] I. Lado-Tourino and F. Tsobnang, Comp. Mater. Sci. **32**, 13 (2005).

[8] A. V. Ruban, V. I. Baykov, B. Johansson, V. V. Dmitriev and M. S. Blanter, Phys. Rev. B **82**, 134110 (2010).

[9] H. H. Wu and D. R. Trinkle, Phys. Rev. Lett. **107**, 045504 (2011).

[10] Y. Takakuwa, S. Ishidzuka, A. Yoshigoe, Y. Teraoka, Y. Yamauchi, Y. Mizuno, H. Tonda and T. Homma, Appl. Surf. Sci. **216**, 395 (2003).

[11] Y. Takakuwa, S. Ishidzuka, A. Yoshigoe, Y. Teraoka, Y. Mizuno, H. Tonda and T. Homma, Nucl. Instr. Meth. Phys. Res. B **200**, 376 (2003).

[12] X. Gonze, B. Amadon, P.-M. Anglade, J.-M. Beuken, F. Bottin, P. Boulanger, F. Bruneval, D. Caliste, R. Caracas, M. Cote, T. Deutsch, L. Genovese, Ph. Ghosez, M. Giantomassi, S. Goedecker, D.R. Hamann, P. Hermet, F. Jollet, G. Jomard, S. Leroux, M. Mancini, S. Mazevet, M. J. T. Oliveira, G. Onida, Y. Pouillon, T. Rangel, G.-M. Rignanese, D. Sangalli, R. Shaltaf, M. Torrent, M. J. Verstraete, G. Zerah and J. W. Zwanziger, Comp. Phys. Comm. **180**, 2582 (2009).

[13] M. Fuchs and M. Scheffler, Comp. Phys. Comm. **119**, 67 (1999).

[14] H. J. Monkhorst and J. D. Pack, Phys. Rev. B **13**, 5188 (1976).

[15] M. Doverstal, B. Lindgren, U. Sassenberg, C. A. Arrington and M. D. Morse, J. Chem. Phys. **97**, 7087 (1992).

[16] L. Lian, C.-X. Su and P. B. Armentrout, J. Chem. Phys. **97**, 4048 (1992).

[17] J. S. Golightly and A. W. Castleman, J. Phys. Chem. B **110**, 19979 (2006).

[18] A. N. Chibisov, Mater. Lett. **104**, 91 (2013).

Vertex Functions and Asymptotics of Nuclear Bound-State Wave Functions

L. D. Blokhintsev

Skobeltsyn Institute of Nuclear Physics, Lomonosov Moscow State University, Moscow, 119991, Russia

Abstract

The paper deals with vertex functions representing matrix elements of two-fragment ($a \to 1+2$) or three-fragment ($a \to 1+2+3$) virtual decays of a bound nuclear system a. Much attention is given to the on-shell vertex functions corresponding to the case when all external particles (fragments) are on the mass shell. The relations are established between the on-shell vertex functions and the coefficients multiplying the asymptotic forms of wave functions and overlap integrals in two- or three-fragment channels. It is shown that the on-shell three-fragment vertex functions determine the contributions to the amplitudes of processes described by the Feynman diagrams containing loops. The anomalous asymptotics of the wave functions in the two-fragment channels is discussed.

Keywords: *Vertex function; bound state; asymptotics*

1 Introduction

The vertex function (VF) W for the virtual n-fragment decay of a bound state a is the matrix element of the process

$$a \to 1+2+\ldots+n. \tag{1}$$

If the system $1+2+\ldots+n$ possesses a bound state a, then the matrix element (the amplitude) of the scattering process

$$1+2+\ldots+n \to 1+2+\ldots+n \tag{2}$$

has a pole at the energy corresponding to that bound state, and the VF W is related to the residue of the matrix element at that pole (see Fig. 1).

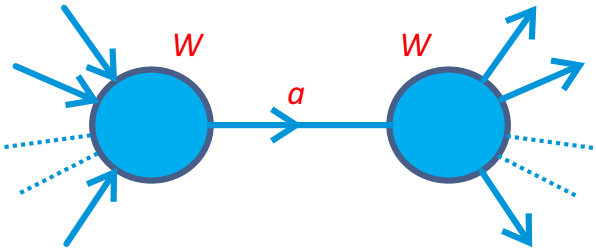

Figure 1:

Proceedings of the International Conference 'Nuclear Theory in the Supercomputing Era — 2014' (NTSE-2014), Khabarovsk, Russia, June 23–27, 2014. Eds. A. M. Shirokov and A. I. Mazur. Pacific National University, Khabarovsk, Russia, 2016, p. 90.

http://www.ntse-2014.khb.ru/Proc/Blokhintsev.pdf.

The matrix element of the process (2) can be written as

$$M = \left\langle \Phi_f | V | P \Psi_i^{(+)} \right\rangle = \langle \Phi_f | V | P(1 + GV) \Phi_i \rangle, \tag{3}$$

P is the (anti)symmetrization operator. Using the spectral decomposition of the Green's function G and the relation $V = H - H_0$ one easily gets

$$W\left(\vec{q}_1, \vec{q}_2, \ldots, \vec{q}_{n-1}\right) = -N^{1/2} \left(T + \epsilon\right) \langle \phi_1 \phi_2 \ldots \phi_n | \phi_a \rangle. \tag{4}$$

Here $\vec{q}_i$ are the Jacobi momenta, ϕ_i is the internal wave function of the fragment i, T is the relative kinetic energy, and $\epsilon > 0$ is the binding energy in the channel $a \to 1 + 2 + \ldots + n$.

The factor $N^{1/2}$ arises due to the identity of constituents. If all fragments consist of nucleons which are considered to be identical, then

$$N = \frac{A_a!}{A_1! A_2! \ldots A_n!}, \tag{5}$$

where A_i denotes the number of nucleons in the fragment i. If all fragments $1, 2, \ldots n$ are treated as structureless, then $\langle \phi_1 \phi_2 \ldots \phi_n | \phi_a \rangle$ turns into the wave function ϕ_a and N equals $n!$.

VFs W for $a \to 1 + 2 + \ldots + n$ are related to the coordinate asymptotics of ϕ_a in the channel $1 + 2 + \ldots + n$. In what follows we discuss this relation for the important cases $n = 2$ and $n = 3$.

The system of units $\hbar = c = 1$ is used throughout the paper.

2 Two-fragment case ($n = 2$)

2.1 General formalism

From general principles the expression for the vertex function (the matrix element) of the two-body decay (virtual or real) $a \to b + c$ can be written as [1]

$$W_{a \to b+c} = \sqrt{4\pi} \sum_{l s m_l m_s} G_{abc}(ls; \sigma_a, \sigma_b, \sigma_c) \times (J_b M_b J_c M_c | s m_s)(l m_l s m_s | J_a M_a) Y_{lm}(\vec{q}_{bc}/q_{bc}). \tag{6}$$

Here J_i and M_i are the spin of the particle i and its projection, $(a\alpha b\beta|c\gamma)$ are the Clebsh–Gordon coefficients, $\vec{q}_{bc}$ is the relative momentum of b and c, l and m_l are the relative angular momentum of b and c and its projection, s and m_s are the channel spin and its projection, Y_{lm} is the spherical function, $G_{abc}(ls; \sigma_a, \sigma_b, \sigma_c)$ are the invariant vertex form factors (VFF). Generally, when all three particles a, b, c are off-shell, VFFs G_{abc} may depend on three kinematic invariants and the quantities $\sigma_a, \sigma_b, \sigma_c$ are selected as such invariants in Eq. (6). σ_i is defined as $\sigma_i = E_i - \vec{p}_i^{\,2}/2m_i$ where E_i, $\vec{p}_i$ and m_i are the kinetic energy, the momentum, and the mass of the particle i. If the particle i is on-shell, then $\sigma_i = 0$.

However, if one relates the vertex function to the residue of a scattering amplitude and defines it according to Eq. (4), then the VFF $G_{abc}(ls; \sigma_a, \sigma_b, \sigma_c)$ depends on the relative momentum q_{bc} only which is related to σ_i:

$$q_{bc}^2 = -\varkappa^2 - 2\mu_{bc}(\sigma_b + \sigma_c - \sigma_a), \quad \varkappa^2 = 2\mu_{bc}\epsilon, \quad \epsilon = m_b + m_c - m_a, \tag{7}$$

μ_{ij} is the reduced mass of i and j. It follows from Eq. (7) that if all three particles are on shell ($\sigma_a = \sigma_b = \sigma_c = 0$), then $q_{bc} = i\varkappa$.

The on-shell values of VFFs are called vertex constants (VC): $G \equiv G(q)|_{q=i\varkappa}$. They are the analogues of the renormalized coupling constants in quantum field theory. The VCs thus defined are real.

Using Eq. (6) and the analogous expansion of the overlap function (4) in the coordinate representation one obtains

$$G_{abc}(ls;q) = -(\pi N_{bc})^{1/2}\,\frac{q^2+\varkappa^2}{\mu_{bc}}\int\limits_0^\infty j_l(qr)\,I_{abc}(ls;r)\,r^2dr, \tag{8}$$

where $I_{abc}(ls;r)$ is the radial overlap integral of the wave functions of a, b and c, and r is the distance between b and c.

The VC G is directly related to the asymptotic normalization coefficient (ANC) of $I_{abc}(ls;r)$ at $r\to\infty$. In the case of a short-range interaction,

$$I_{abc}(ls;r) \approx C_{abc}(ls)\,\frac{e^{-\varkappa r}}{r}, \quad r\to\infty. \tag{9}$$

Inserting Eq. (9) into Eq. (8) and setting $q=i\varkappa$, it is easy to obtain a relation between the VC $G_{abc}(ls)$ and the ANC $C_{abc}(ls)$ [1]:

$$G_{abc}(ls) = -\frac{(\pi N_{bc})^{1/2}}{\mu_{bc}}\,C_{abc}(ls). \tag{10}$$

Note that the factor $N_{bc}^{1/2}$ is often included into the definition of $C_{abc}(ls)$ and $I_{abc}(ls;r)$.

The long-range Coulomb interaction modifies the asymptotic behavior of the overlap integral $I_{abc}(ls;r)$, namely

$$I_{abc}(ls;r) \approx C_{abc}(ls)\,\frac{W_{-\eta,l+1/2}(\varkappa r)}{r} \approx C_{abc}(ls)\,\frac{e^{-\varkappa r-\eta\ln(2\varkappa r)}}{r}, \qquad r\to\infty. \tag{11}$$

Here $\eta = Z_bZ_ce^2\mu_{bc}/\varkappa$ is the Coulomb (Sommerfeld) parameter for a bound state a, Z_ie is the charge of the fragment i, and W is the Whittaker function.

In the presence of the Coulomb interaction Eq. (8) can not be used for determining the VC since at $q\to i\varkappa$ the right-hand-side of (8) tends to 0 for the repulsive Coulomb potential and to ∞ for the attractive potential.

There are different definitions of VCs in the presence of the Coulomb interaction. The most natural definition relates the VC to the Coulomb-modified scattering amplitude.

The total amplitude of elastic bc scattering in the presence of the Coulomb and short-range interactions is written as

$$f(\vec{k}) = f_C(\vec{k}) + f_{NC}(\vec{k}), \tag{12}$$

$$f_C(\vec{k}) = \sum_{l=0}^{\infty}(2l+1)\,\frac{\exp(2i\sigma_l)-1}{2ik}\,P_l(\cos\theta), \tag{13}$$

$$f_{NC}(\vec{k}) = \sum_{l=0}^{\infty}(2l+1)\,\exp(2i\sigma_l)\,\frac{\exp(2i\delta_l^{NC})-1}{2ik}\,P_l(\cos\theta). \tag{14}$$

Here $\sigma_l = \arg\Gamma(l+1+i\eta_s)$ and δ_l^{NC} are the pure Coulomb and Coulomb-nuclear phase shifts, $\Gamma(z)$ is the Gamma function and $\eta_s = Z_bZ_ce^2\mu/k$ is the Coulomb parameter for a scattering state.

The renormalized Coulomb-nuclear partial-wave amplitude $\tilde{f}_l^N$ in the case of the repulsive Coulomb potential is introduced as follows [2]:

$$\tilde{f}_l^N = \exp(2i\sigma_l)\,\frac{\exp(2i\delta_l^{NC})-1}{2ik}\left(\frac{l!}{\Gamma(l+1+i\eta_s)}\right)^2 e^{\pi\eta_s}. \tag{15}$$

The analytic properties of $\tilde{f}_l^N$ on the physical sheet are analogous to those for the scattering by a short-range potential. In particular, it is regular near zero energy.

If the $b+c$ system possesses a bound state a with the binding energy $\epsilon = \varkappa^2/2\mu$, then the amplitude $\tilde{f}_l^N(k)$ has a pole at $k = i\varkappa$. The residue at that pole is expressed in terms of the Coulomb-renormalized VC $\tilde{G}_l$ and ANC C_l:

$$\operatorname{res} \tilde{f}_l^N(k) = \lim_{k\to i\varkappa} [(k - i\varkappa)\tilde{f}_l^N(k] = i\frac{\mu^2}{2\pi\varkappa}\,\tilde{G}_l^2, \tag{16}$$

$$C_l = -\frac{\mu}{\sqrt{\pi}}\frac{\Gamma(l+1+\eta)}{l!}\,\tilde{G}_l. \tag{17}$$

The knowledge of ANCs is essential for an analysis of nuclear reactions between charged particles at low energies. In particular, the value of the ANC $C_{abc}(ls)$ determines essentially the cross section of the radiative capture $b(c,\gamma)a$ reaction at astrophysical energies [3].

2.2 Anomalous asymptotics

In fact, the asymptotic form (9) has been rigorously proved only for the simplest case when the composite system a consists of two elementary constituents. In that case the form (9) follows directly from the Schrödinger equation. It is shown below that the asymptotics of the overlap integral may differ from Eq. (9) if a consists of three or more constituents.

Consider the Fourier transform $J(q^2)$ of $I(r)$:

$$I(r) = (2\pi)^{-3}\int e^{i\vec{q}\vec{r}}\,J(q^2)\,d^3q. \tag{18}$$

According to Eqs.(2) and (6), $J(q^2)$ can be written in the form:

$$J(q^2) = -N_{bc}^{-1/2}\,\frac{2\mu_{bc}}{q^2+\varkappa^2}\,G(q^2), \tag{19}$$

Inserting Eq. (19) into Eq. (18) and integrating over angular variables, one obtains:

$$I(r) = \text{const}\cdot\frac{1}{ir}\int_{-\infty}^{\infty} e^{iqr}\,\frac{G(q^2)}{q^2+\varkappa^2}\,qdq. \tag{20}$$

In the upper half-plane of the complex variable q the integrand in Eq. (20) has a pole at $q = i\varkappa$ and a cut beginning from the nearest singular point $q = i\varkappa_1$ of the form factor $G(q^2)$. Making use of the Cauchy theorem one gets from Eq. (20)

$$I(r) = \text{const}\cdot\left\{\frac{\pi}{r}e^{-\varkappa r}G(-\varkappa^2) + \frac{1}{ir}\int\limits_{\varkappa_1}^{\infty}\frac{e^{-kr}\,\operatorname{disc} G(-k^2)}{k^2-\varkappa^2}\,kdk\right\} = I_0(r) + I_1(r). \tag{21}$$

An explicit asymptotic form of the second term on the r.h.s. of Eq. (21) depends on the behavior of $\operatorname{disc} G(q^2)$ at $q^2 \to -\varkappa_1^2$, that is, on the type of the singularity at $q = i\varkappa_1$. To investigate the singular behavior of $G(q^2)$, it is convenient to use the formalism of Feynman diagrams. In the vicinity of a proper singularity $z = z_0$, the singular part of the amplitude of a Feynman diagram having n inner lines and v vertices, behaves as [4,5]

$$\begin{aligned} &M_{nv}\,|_{z\to z_0} \sim (z-z_0)^s && \text{if } s \neq 0,1,2,..., \\ &M_{nv}\,|_{z\to z_0} \sim (z-z_0)^s\,\ln(z-z_0) && \text{if } s = 0,1,2,..., \end{aligned} \tag{22}$$

where $s = (3n-4v+3)/2$.

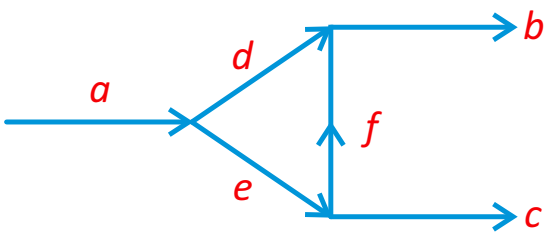

Figure 2: The simplest Feynman diagram for an $a \to b + c$ vertex.

The simplest Feynman diagram for an $a \to b + c$ vertex is a triangle diagram of Fig. 2.

For this diagram, $s = 0$ and it is easy to obtain from Eq. (21) that the contribution of that diagram results in

$$I(r)\,|_{r\to\infty} = c_0 \frac{e^{-\varkappa r}}{r} + c_1 \frac{e^{-\varkappa_1 r}}{r^2}, \tag{23}$$

$$\varkappa_1 = i\frac{m_b}{m_d}(\varkappa_{ade} + \varkappa_{bdf}), \quad \varkappa_{ijk}^2 = 2\mu_{jk}\epsilon_{ijk}, \quad \epsilon_{ijk} = m_j + m_k - m_i. \tag{24}$$

The first term on the r.h.s. of Eq. (23) corresponds to a 'normal' asymptotics. If $\varkappa < \varkappa_1$, then this term is a leading one and the overlap integral $I(r)$ possesses the normal asymptotics. However, in the opposite case, $\varkappa > \varkappa_1$, the asymptotics of $I(r)$ is governed by the second term in Eq. (23) (the 'anomalous' case).

Though there is no a general rules preventing the 'anomalous' condition $\varkappa > \varkappa_1$ from being satisfied, it appears that for real nuclear systems this condition is satisfied not very often. The nuclear vertices $^{16}\mathrm{O} \to {}^{13}\mathrm{N}(^{13}\mathrm{C}) + {}^{3}\mathrm{H}(^{3}\mathrm{He})$ and $^{20}\mathrm{Ne} \to {}^{17}\mathrm{F}(^{17}\mathrm{O}) + {}^{3}\mathrm{H}(^{3}\mathrm{He})$ can serve as examples of the anomalous asymptotics of the overlap integrals due to the triangle diagram of Fig. 2.

3 Three-fragment case ($n = 3$)

Consider a 3-body bound system $a = \{123\}$ with the wave function

$$\psi_a(\vec\rho, \vec r), \quad \vec\rho = \vec r_1 - \vec r_2, \quad \vec r = \vec r_3 - \frac{m_1\vec r_1 + m_2\vec r_2}{m_1 + m_2}. \tag{25}$$

The constituents 1, 2, and 3 might be composite, then ψ_a turns into an overlap integral.

Introduce the Fourier transform $\varphi_a(\vec k, \vec p)$ of $\psi_a(\vec\rho, \vec r)$ and the vertex function (VF) $W(\vec k, \vec p)$:

$$\vec k = (m_2\vec k_1 - m_1\vec k_2)/m_{12}, \quad \vec p = \left[m_{12}\vec k_3 - m_3(\vec k_1 + \vec k_2)\right]/M,$$

$$m_{ij} = m_i + m_j, \quad M = m_1 + m_2 + m_3. \tag{26}$$

$$\psi_a(\vec\rho, \vec r) = \int \exp\left[i(\vec k\vec\rho + \vec p\vec r)\right] \varphi_a(\vec k, \vec p)\, \frac{d\vec k}{(2\pi)^3}\frac{d\vec p}{(2\pi)^3}, \tag{27}$$

$$\varphi_a(\vec k, \vec p) = -W(\vec k, \vec p)/L(k, p), \quad L(k, p) = -(\epsilon + k^2/2\mu_1 + p^2/2\mu_2),$$

$$\epsilon = m_1 + m_2 + m_3 - m_a, \quad \mu_1 = m_1m_2/m_{12}, \quad \mu_2 = m_1m_{12}/M. \tag{28}$$

ψ_a and φ_a are normalized:

$$\int |\psi_a(\vec\rho, \vec r)|^2\, d\vec\rho\, d\vec r = 1, \quad \int |\varphi_a(\vec k, \vec p)|^2\, d\vec k\, d\vec p/(2\pi)^6 = 1. \tag{29}$$

Introduce modified Jacobi variables:

$$\vec{x}_1 = \sqrt{2\mu_1}\vec{\rho}, \quad \vec{x}_2 = \sqrt{2\mu_2}\vec{r}, \quad \vec{k}_1 = \vec{k}/\sqrt{2\mu_1}, \quad \vec{k}_2 = \vec{p}/\sqrt{2\mu_2},$$
$$x_1^2 + x_2^2 = R^2, \quad k_1^2 + k_2^2 = P^2. \tag{30}$$

$\psi_a(\vec{x}_1, \vec{x}_2)$ and $W(\vec{k}_1, \vec{k}_2)$ can be expanded through their partial-wave components $\psi_a^{(l,\lambda,L)}(x_1, x_2)$ and $W^{(l,\lambda,L)}(k_1, k_2)$ corresponding to Jacobi angular momenta l and λ ($\vec{l} + \vec{\lambda} = \vec{L}$). Spin variables could be taken into account as well. Strictly speaking, the following text applies to these partial-wave components. However, to simplify the presentation, we suppose that the $l = \lambda = 0$ components contribute only to ψ_a and W. Then after integrating over the angular variables Eq. (27) assumes the form

$$\psi_a(x_1, x_2) = \frac{(\mu_1\mu_2)^{3/2}}{2\pi^4} \frac{1}{x_1 x_2} \int_0^\infty dk_1 \int_0^\infty dk_2 k_1 k_2 \frac{W(k_1, k_2)}{\epsilon + P^2}$$
$$\times (e^{ik_1x_1} - e^{-ik_1x_1})(e^{ik_2x_2} - e^{-ik_2x_2}). \tag{31}$$

$W(k_1, k_2)$ should depend on k_1^2, k_2^2; that is $W(k_1, k_2)$ is an even function of k_1, k_2. Hence Eq. (31) can be written as

$$\psi_a(x_1, x_2) = \frac{(\mu_1\mu_2)^{3/2}}{2\pi^4} \frac{1}{x_1 x_2} \int_{-\infty}^\infty dk_1 \int_{-\infty}^\infty dk_2\, k_1 k_2 e^{i(k_1x_1 + k_2x_2)} \frac{W(k_1, k_2)}{\epsilon + P^2}. \tag{32}$$

We neglect the Coulomb interaction in what follows though the results could be easily generalized to the case when two of the particles 1, 2 and 3 are charged.

If a pair subsystem ij ($ij = 12, 23, 31$) can form a bound state with the binding energy ϵ_{ij}, then the VF $W(k_1, k_2)$ has a two-body pole at the relative kinetic energy $E_{ij} = -\epsilon_{ij}$. Such poles lead to the two-body asymptotics analogous to those considered in Section 2. In the present Section we will consider the true three-body asymptotics generated by the pole $P^2 = -\epsilon$ in Eq. (32). Denoting its contribution by ψ_3 and integrating over k_2 in the integral (32) by taking the residue at $k_2^2 = -\epsilon - k_1^2$, one obtains

$$\psi_3(x_1, x_2) = i\frac{(m_1m_2m_3/M)^{3/2}}{2\pi^3} \frac{1}{x_1 x_2} J(x_1, x_2),$$
$$J(x_1, x_2) = \int_{-\infty}^\infty dk_1\, k_1 \exp\Bigl(ik_1x_1 - \sqrt{\epsilon + k_1^2}\, x_2\Bigr)\, W\Bigl(k_1, i\sqrt{\epsilon + k_1^2}\Bigr). \tag{33}$$

Denoting $x_1 = R\cos\alpha$, $x_2 = R\sin\alpha$ one can evaluate $J(x_1, x_2)$ at $R \to \infty$ by the saddle-point method (the saddle-point is $k_1 = i\epsilon^{1/2}\cos\alpha$). As a result, one obtains the following expression for the leading contribution to the asymptotic form of $\psi_3(x_1, x_2)$:

$$\psi_{3as}^{(0)}(R, \alpha) = C_3 \frac{e^{-\sqrt{\epsilon}R}}{R^{5/2}},$$
$$C_3 = -\frac{(m_1m_2m_3/M)^{3/2}}{\sqrt{2}\pi^{5/2}} W(i\sqrt{\epsilon}\cos\alpha, i\sqrt{\epsilon}\sin\alpha). \tag{34}$$

The R dependence of the asymptotic form (34) agrees with that presented in [6].

C_3 is the three-body asymptotic normalization factor. It is expressed in terms of the on-shell three-body vertex function $W(\alpha) \equiv W(i\sqrt{\epsilon}\cos\alpha, i\sqrt{\epsilon}\sin\alpha)$ corresponding to $P^2 = -\epsilon$. Eq. (34) is the three-body analogue of the two-body relation (9).

The saddle-point method allows one to calculate corrections to the leading term (34). In the present work, the expressions for the correction terms of the order $(\sqrt{\epsilon}R)^{-1}$

and $(\sqrt{\epsilon}R)^{-2}$ are obtained. These corrections are expressed in terms of $W(\alpha)$ and its derivatives. The explicit expression for $\psi^{(2)}_{3as}$ including the corrections of the order $(\sqrt{\epsilon}R)^{-1}$ and $(\epsilon R^2)^{-1}$) is of the form:

$$\psi^{(2)}_{3as} = \psi^{(0)}_{3as}\left[1 + (\sqrt{\epsilon}R)^{-1}\chi_\alpha + (\epsilon R^2)^{-1}\xi_\alpha\right],$$
$$\chi_\alpha = \frac{15}{8} - 2\cot(2\alpha)\,\gamma_1(\alpha) - \frac{1}{2}\gamma_2(\alpha),$$
$$\xi_\alpha = \frac{105}{128} - \frac{11}{4}\cot(2\alpha)\,\gamma_1(\alpha) - \frac{43}{16}\gamma_2(\alpha) + \cot(2\alpha)\,\gamma_3(\alpha) + \frac{1}{8}\gamma_4(\alpha),$$
$$\gamma_n(\alpha) \equiv \frac{1}{W(\alpha)}\frac{d^n W(\alpha)}{d\alpha^n}. \qquad (35)$$

The asymptotics of the three-body wave function was considered in [7]. The results of that work include the corrections due to non-zero values of the angular momenta l and λ. However, these corrections do not include the terms of the same order due to using the saddle-point method. Making use of the results of the present work, one can calculate the reliable correction terms for $l + \lambda \leq 2$.

4 Discussion and Conclusions

The on-shell VFs $W(\alpha)$ are important three-body characteristics determining the asymptotics of three-body wave functions. Of a special interest are the quantities $W_0 = W(\alpha = \pi/2)$ corresponding to $k_1 = 0$ what means that the particles 1 and 2 move as a single body with the mass $m_{12} = m_1 + m_2$. W_0 is a constant which is an analog of the two-body vertex constant G_{abc}. It could be called the generalized vertex constant (GVC).

It follows from Landau equations [4] that the GVCs determine the contributions of proper singularities of Feynman diagrams containing the loops consisting of two particles (as in Fig. 3). Thus $W_0(a \to 1{+}2{+}3)$ and $W_0(1{+}2{+}4 \to c)$ in Fig. 3a determine a possible anomalous asymptotics of the overlap integral I_{abc}. In particular, the vertices $W_0(^9\mathrm{Be} \to n{+}\alpha{+}\alpha)$ and $W_0(n{+}\alpha{+}p \to {}^6\mathrm{Li})$ ($W_0(n{+}\alpha{+}n \to {}^6\mathrm{He})$) in the diagrams of the Fig. 3a type were used in Ref. [8] to analyze the anomalous asymptotics of the overlap integrals for the vertices $^9\mathrm{Be} \to {}^6\mathrm{Li} + {}^3\mathrm{H}$ ($^9\mathrm{Be} \to {}^6\mathrm{He} + {}^3\mathrm{He}$). $W_0(a \to 1 + 2 + 3)$ and $W_0(x + 1 + 2 \to y)$ in Fig. 3b determine the contribution of the t-channel normal threshold to the amplitude of the process $a + x \to 3 + y$.

The concept of the GVC could be directly extended to the loops containing more than two particles.

In conclusion it is worthwhile to note that the GVC W_0 for the vertex $a \to 1{+}2{+}3$ could in principle be determined by the analytic continuation of the differential cross section of the $a + x \to 1 + 2 + y$ reaction to the pole of the diagram of Fig. 4.

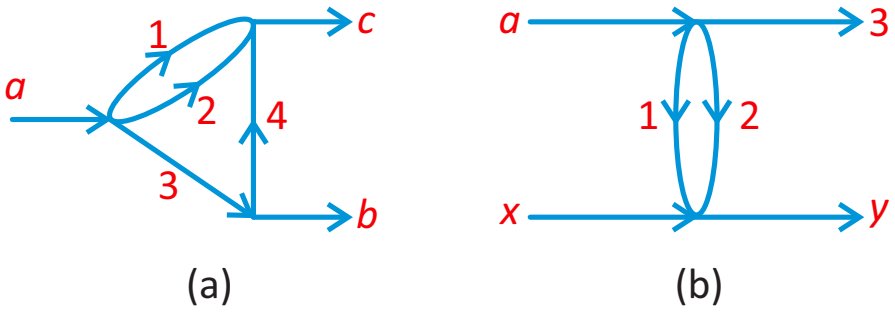

Figure 3:

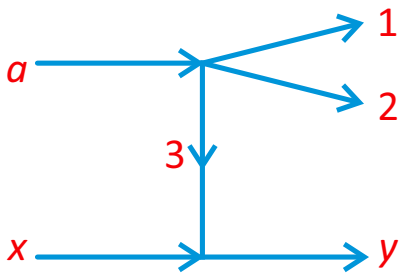

Figure 4:

The work is supported by the Russian Foundation for Basic Research under Grant No. 13-02-00399.

References

[1] L. D. Blokhintsev, I. Borbely and E. I. Dolinsky, Part. Nucl. **8**, 485 (1977).

[2] J. Hamilton, I. Øverbö and B. Tromborg, Nucl. Phys. B **60**, 443 (1973).

[3] A. M. Mukhamedzhanov and R. E. Tribble, Phys. Rev. C **59**, 3418 (1999).

[4] L. D. Landau, Nucl. Phys. **13**, 181 (1959).

[5] J. C. Polkinghorne and G. R. Screaton, Nuovo Cim. **15**, 289, 925 (1960).

[6] L. D. Faddeev and S. P. Merkuriev, *Quantum scattering theory for several particle systems*. Kluwer, Dordrecht, 1993.

[7] L. D. Blokhintsev, M. K. Ubaidullaeva and R. Yarmukhamedov, Phys. Atom. Nucl. **62**, 1289 (1999).

[8] L. D. Blokhintsev, A. M. Mukhamedzhanov and R. Yarmukhamedov, Eur. Phys. J. A **49**, 108 (2013).

Bounds on Variation of the Spectrum and Spectral Subspaces of a Few-Body Hamiltonian

Sergio Albeverio[a] **and Alexander K. Motovilov**[b]

[a] *Institut für Angewandte Mathematik and HCM, Universität Bonn, 60 Endenicher Allee, 53115 Bonn, Germany*

[b] *Bogoliubov Laboratory of Theoretical Physics, JINR, 6 Joliot-Curie, 141980 Dubna, Russia*

Abstract

We overview the recent results on the shift of the spectrum and norm bounds for variation of spectral subspaces of a Hermitian operator under an additive Hermitian perturbation. Along with the known results, we present a new subspace variation bound for the generic off-diagonal subspace perturbation problem. We also demonstrate how some of the abstract results may work for few-body Hamiltonians.

Keywords: *Few-body problem; subspace perturbation problem; variation of spectral subspace*

1 Introduction

In this short survey article, we consider the problem of variation of the spectral subspace of a Hermitian operator under an additive bounded Hermitian perturbation. It is assumed that the spectral subspace is associated with an isolated spectral subset and one is only concerned with the geometric approach originating in the papers by Davis [1, 2] and Davis and Kahan [3]. In this approach, a bound on the variation of a spectral subspace usually involves just two quantities: the distance between the relevant spectral subsets and a norm of the perturbation operator. We discuss only the *a priori* bounds, that is, the estimates that involve the distance between complementary disjoint spectral subsets of the unperturbed operator (and none of the perturbed spectral sets is involved). In the case where the perturbation is off-diagonal, we also recall the bounds on the shift of the spectrum.

The paper is organized as follows. In Section 2 we collect the results that hold for Hermitian operators of any origin. Along with the older results we present a new bound in the general off-diagonal subspace perturbation problem that was not published before. In Section 3 we reproduce several examples that illustrate the meaning of the abstract results in the context of few-body bound-state problems.

In this paper we only use the usual operator norm. For convenience of the reader, we recall that if V is a bounded linear operator on a Hilbert space $\mathfrak{H}$ then its norm may be computed by using the formula

$$\|V\| = \sup_{f\in\mathfrak{H},\,\|f\|=1} \big\|V|f\rangle\big\|,$$

where sup denotes the least upper bound. Thus, one has $\big\|V|f\rangle\big\| \le \|V\|\,\|f\|$ for any $|f\rangle \in \mathfrak{H}$. If V is a Hermitian operator with $\min\big(\mathrm{spec}(V)\big) = m_V$ and

Proceedings of the International Conference 'Nuclear Theory in the Supercomputing Era — 2014' (NTSE-2014), Khabarovsk, Russia, June 23–27, 2014. Eds. A. M. Shirokov and A. I. Mazur. Pacific National University, Khabarovsk, Russia, 2016, p. 98.

http://www.ntse-2014.khb.ru/Proc/Motovilov.pdf.

$\max\big(\mathrm{spec}(V)\big) = M_V$, where $\mathrm{spec}(V)$ denotes the spectrum of V, then $\|V\| = \max\{|m_V|, |M_V|\}$. In particular, if V is separable of rank one, i. e., if $V = \lambda|\phi\rangle\langle\phi|$ with $|\phi\rangle \in \mathfrak{H}$, $\|\phi\| = 1$, and $\lambda \in \mathbb{R}$, then $\|V\| = |\lambda|$. Another simple but important example is related to the case where $\mathfrak{H} = L_2(\mathbb{R}^n)$, $n \in \mathbb{N}$, and V is a bounded local potential, that is, $\langle x|V|f\rangle = V(x)f(x)$ for any $|f\rangle \in L_2(\mathbb{R}^n)$, with $V(\cdot)$ a bounded function from $\mathbb{R}^n$ to $\mathbb{C}$. In this case $\|V\| = \sup\limits_{x\in\mathbb{R}^n} |V(x)|$.

2 Abstract results

Let A be a Hermitian (or, equivalently, self-adjoint) operator on a separable Hilbert space $\mathfrak{H}$. It is well known that if V is a bounded Hermitian perturbation of A then the spectrum of the perturbed operator $H = A + V$ lies in the closed $\|V\|$-neighborhood $\mathcal{O}_{\|V\|}\big(\mathrm{spec}(A)\big)$ of the spectrum of A (see, e. g., Ref. [4]). Hence, if a subset σ of the spectrum of A is isolated from the remainder $\Sigma = \mathrm{spec}(A) \setminus \sigma$, then the spectrum of H also consists of two disjoint components,

$$\omega = \mathrm{spec}(H) \cap \mathcal{O}_{\|V\|}(\sigma) \ \text{ and } \ \Omega = \mathrm{spec}(H) \cap \mathcal{O}_{\|V\|}(\Sigma), \tag{1}$$

provided that

$$\|V\| < \frac{1}{2}\, d, \tag{2}$$

where

$$d := \mathrm{dist}(\sigma, \Sigma) > 0. \tag{3}$$

Under condition (2), the separated spectral components ω and Ω of the perturbed operator H may be viewed as the result of the perturbation of the respective disjoint spectral subsets σ and Σ of the initial operator A.

Let P and Q be the spectral projections of the operators A and H associated with the respective spectral sets σ and ω, that is, $P := \mathsf{E}_A(\sigma)$ and $Q := \mathsf{E}_H(\omega)$. The relative position of the perturbed spectral subspace $\mathfrak{Q} := \mathrm{Ran}(Q)$ with respect to the unperturbed one, $\mathfrak{P} := \mathrm{Ran}(P)$, may be studied in terms of the difference $P - Q$ and, in fact, the case where $\|P - Q\| < 1$ is of particular interest. In this case the spectral projections P and Q are unitarily equivalent and the transformation from the subspace $\mathfrak{P}$ to the subspace $\mathfrak{Q}$ may be viewed as the direct rotation (see, e. g., Sections 3 and 4 in Ref. [3]). Furthermore, one can use the quantity

$$\theta(\mathfrak{P}, \mathfrak{Q}) = \arcsin(\|P - Q\|),$$

as a measure of this rotation. This quantity is called the maximal angle between the subspaces $\mathfrak{P}$ and $\mathfrak{Q}$. For a short but concise discussion of the concept of maximal angle we refer to Section 2 in Ref. [5]; see also Refs. [3, 6–8]. If

$$\theta(\mathfrak{P}, \mathfrak{Q}) < \frac{\pi}{2} \tag{4}$$

and, thus, $\|P - Q\| < 1$, the subspaces $\mathfrak{P}$ and $\mathfrak{Q}$ are said to be in the acute-angle case.

Among the problems being solved in the subspace perturbation theory, the first and rather basic problem is to find an answer to the question on whether the requirement (2) is sufficient for the unperturbed and perturbed spectral subspaces $\mathfrak{P}$ and $\mathfrak{Q}$ to be in the acute-angle case, or, in order to ensure inequality (4), one has to impose a stronger condition $\|V\| < c\, d$ with some $c < \frac{1}{2}$. More precisely, the question is as follows.

(i) What is the largest possible constant c_* in the inequality

$$\|V\| < c_*\, d \tag{5}$$

securing the subspace variation bound (4)?

Another, practically important question is about the largest possible size of the subspace variation:

(ii) What function $M : [0, c_*) \mapsto \left[0, \frac{\pi}{2}\right)$ is best possible in the bound

$$\theta(\mathfrak{P}, \mathfrak{Q}) \leq M\left(\frac{\|V\|}{d}\right) \quad \text{for} \quad \|V\| < c_* \, d \, ? \tag{6}$$

Both the constant c_* and the function M are required to be universal in the sense that they should work simultaneously for all Hermitian operators A and V for which the conditions (2) and (3) hold.

Until now, the questions (i) and (ii) have been completely answered only for those particular mutual positions of the unperturbed spectral sets σ and Σ where one of these sets lies in a finite or infinite gap of the other one, say, σ lies in a gap of Σ. For such mutual positions,

$$c_* = \frac{1}{2} \quad \text{and} \quad M(x) = \frac{1}{2} \arcsin(2x). \tag{7}$$

This result is contained in the Davis–Kahan $\sin 2\theta$ theorem (see Ref. [3]).

In the general case where no assumptions are done on the mutual position of σ and Σ, except for condition (2), the best available answers to the questions (i) and (ii) are based on the bound

$$\theta(\mathfrak{P}, \mathfrak{Q}) \leq \frac{1}{2} \arcsin \frac{\pi \|V\|}{d} \quad \text{if} \quad \|V\| \leq \frac{1}{\pi} \, d \tag{8}$$

proven in Ref. [5] and called there the generic $\sin 2\theta$ estimate. The bound (8) remains the strongest known bound for $\theta(\mathfrak{P}, \mathfrak{Q})$ whenever $\|V\| \leq \frac{4}{\pi^2 + 4} \, d$ (see Remark 4.4 in Ref. [5]; cf. Corollary 2 in Ref. [8]).

In Ref. [5], it has been shown that the bound (8) can also be used to obtain estimates of the form (6) for $\|V\| > \frac{1}{\pi} d$. To this end, one introduces the operator path $H_t = A + tV$, $t \in [0, 1]$, and chooses a set of points

$$0 = t_0 < t_1 < t_2 < \ldots < t_n = 1 \tag{9}$$

in such a way that

$$\frac{(t_{j+1} - t_j)\|V\|}{\operatorname{dist}\big(\omega_{t_j}, \Omega_{t_j}\big)} \leq \frac{1}{\pi}, \tag{10}$$

where ω_t and Ω_t denote the disjoint spectral components of H_t originating from σ and Σ, respectively; $\omega_t = \operatorname{spec}(H_t) \cap \mathcal{O}_{d/2}(\sigma)$ and $\Omega_t = \operatorname{spec}(H_t) \cap \mathcal{O}_{d/2}(\Sigma)$. Applying the estimate (8) to the maximal angle between the spectral subspaces $\operatorname{Ran}(\mathsf{E}_{H_{t_j}}(\omega_{t_j}))$ and $\operatorname{Ran}(\mathsf{E}_{H_{t_{j+1}}}(\omega_{t_{j+1}}))$ of the corresponding consecutive operators H_{t_j} and $H_{t_{j+1}}$ and using, step by step, the triangle inequality for the maximal angles (see Ref. [9]; cf. Lemma 2.15 in Ref. [5]) one arrives at the optimization problem

$$\arcsin\big(\|P - Q\|\big) \leq \frac{1}{2} \inf_{n, \, \{t_i\}_{i=0}^n} \sum_{j=0}^{n-1} \arcsin \frac{\pi(t_{j+1} - t_j)\|V\|}{\operatorname{dist}\big(\omega_{t_j}, \Omega_{t_j}\big)} \tag{11}$$

over $n \in \mathbb{N}$ and $\{t_i\}_{i=0}^n$ chosen accordingly to Eqs. (9) and (10). Taking into account that

$$\operatorname{dist}\big(\omega_{t_j}, \Omega_{t_j}\big) \geq d - 2\|V\| t_j,$$

one then deduces from Eq. (11) the bound

$$\theta(\mathfrak{P}, \mathfrak{Q}) \leq M_{\mathrm{gen}}\left(\frac{\|V\|}{d}\right) \tag{12}$$

with the estimating function $M_{\rm gen}(x)$, $x \in [0, \frac{1}{2})$, given by

$$M_{\rm gen}(x) = \frac{1}{2} \inf_{n,\, \{\varkappa_i\}_{i=0}^{n}} \sum_{j=0}^{n-1} \arcsin \frac{\pi(\varkappa_{j+1} - \varkappa_j)}{1 - 2\varkappa_j}, \tag{13}$$

where the points

$$0 = \varkappa_0 < \varkappa_1 < \varkappa_2 < \ldots < \varkappa_n = x \tag{14}$$

should be such that

$$\frac{\varkappa_{j+1} - \varkappa_j}{1 - 2\varkappa_j} \le \frac{1}{\pi}.$$

An explicit expression for the function $M_{\rm gen}$ has been found by Seelmann in Theorem 1 of Ref. [10]. From this Theorem it also follows that the generic optimal constant c_* in Eq. (5) satisfies inequalities

$$c_{\rm S} \le c_* \le \frac{1}{2},$$

where

$$c_{\rm S} = \frac{1}{2} - \frac{1}{2}\left(1 - \frac{\sqrt{3}}{\pi}\right)^3 = 0.454839... \tag{15}$$

The earlier results from Refs. [5], [11] and [12] concerning the generic bound (6) might be of interest, too.

The questions like (i) and (ii) have been addressed as well in the case of off-diagonal perturbations. Recall that a bounded operator V is said to be off-diagonal with respect to the partition $\mathrm{spec}(A) = \sigma \cup \Sigma$ of the spectrum of A with $\sigma \cap \Sigma = \varnothing$ if V anticommutes with the difference $P - P^\perp$ of the spectral projections $P = \mathsf{E}_A(\sigma)$ and $P^\perp = \mathsf{E}_A(\Sigma)$, that is, if

$$V(P - P^\perp) = -(P - P^\perp)V.$$

When considering an off-diagonal Hermitian perturbation, one should take into account that conditions ensuring the disjointness of the respective perturbed spectral components ω and Ω originating from σ and Σ are much weaker than the condition (2). In particular, if the sets σ and Σ are subordinated, say $\max(\sigma) < \min(\Sigma)$, then for any (arbitrarily large) $\|V\|$ no spectrum of $H = A + V$ enters the open interval between $\max(\sigma)$ and $\min(\Sigma)$ (see, e. g., Remark 2.5.19 in Ref. [13]). In such a case the maximal angle $\theta(\mathfrak{P}, \mathfrak{Q})$ between the unperturbed and perturbed spectral subspaces $\mathfrak{P}$ and $\mathfrak{Q}$ admits a sharp bound of the form (6) with

$$M(x) = \frac{1}{2}\arctan(2x), \quad x \in [0, \infty). \tag{16}$$

This is the consequence of the celebrated Davis–Kahan $\tan 2\theta$ theorem [3] (also, cf. the extensions of the $\tan 2\theta$ theorem in Refs. [6, 7, 14]).

If it is known that the set σ lies in a finite gap of the set Σ then the disjointness of the perturbed spectral components ω and Ω is guaranteed by the (sharp) condition $\|V\| < \sqrt{2}\, d$. The same condition is optimal for the bound (4) to hold. Both these results have been established in Ref. [15]. An explicit expression for the best possible function M in the corresponding estimate (6),

$$M(x) = \arctan x, \quad x \in [0, \sqrt{2}),$$

was found in Refs. [7, 16].

As for the generic case — with no restrictions on the mutual position of the spectral components σ and Σ, the condition

$$\|V\| < \frac{\sqrt{3}}{2} d \tag{17}$$

is known to be optimal in order to ensure that the gaps between σ and Σ do not close under an off-diagonal V. Moreover, under this condition for the perturbed spectral sets ω and Ω we have the following enclosures:

$$\omega \subset \mathcal{O}_{\epsilon_V}(\sigma) \quad \text{and} \quad \Omega \subset \mathcal{O}_{\epsilon_V}(\Sigma)$$

with

$$\epsilon_V = \|V\| \tan\left(\frac{1}{2}\arctan\frac{2\|V\|}{d}\right) < \frac{d}{2} \tag{18}$$

and, hence,

$$\operatorname{dist}(\omega,\Omega) \geq d - 2\epsilon_V > 0. \tag{19}$$

The corresponding proofs were given initially in Theorem 1 of Ref. [17] for bounded A and then in Proposition 2.5.22 of Ref. [13] for unbounded A. From the condition (17) it follows that the optimal constant c_* in the condition (5) ensuring the strict inequality (4) in the generic off-diagonal case necessarily satisfies the upper bound

$$c_* \leq \frac{\sqrt{3}}{2} \quad \big(= 0.866025...\big). \tag{20}$$

Now we employ the approach suggested in Refs. [5] in order to get a lower bound for the above constant c_*. To this end, we simply apply the optimization estimate (11) to the off-diagonal perturbations. Due to Eq. (19), for the disjoint spectral components ω_{t_j} and Ω_{t_j} of the operator $H_{t_j} = A + t_j V$ we have

$$\operatorname{dist}\big(\omega_{t_j},\Omega_{t_j}\big) \geq d - 2t_j\|V\| \tan\left(\frac{1}{2}\arctan\frac{2t_j\|V\|}{d}\right) = 2d - \sqrt{d^2 + 4t_j^2\|V\|^2}.$$

The estimate (11) then yields

$$\theta(\mathfrak{P},\mathfrak{Q}) \leq M_{\text{off}}\left(\frac{\|V\|}{d}\right) \tag{21}$$

with the function $M_{\text{off}}(x)$, $x \in [0, \frac{\sqrt{3}}{2})$, given by

$$M_{\text{off}}(x) = \frac{1}{2} \inf_{n,\,\{\varkappa_i\}_{i=0}^n} \sum_{j=0}^{n-1} \arcsin\frac{\pi(\varkappa_{j+1} - \varkappa_j)}{2 - \sqrt{1 + 4\varkappa_j^2}}, \tag{22}$$

where $\varkappa_0 = 0$, $\varkappa_n = x$, and the remaining points $\varkappa_j$, $j = 1, 2, \ldots, n-1$, should satisfy inequalities

$$0 < \frac{\varkappa_{j+1} - \varkappa_j}{2 - \sqrt{1 + 4\varkappa_j^2}} \leq \frac{1}{\pi}.$$

We have only performed a partial numerical optimization of the r.h.s. term in Eq. (22) restricting ourselves to the case where the final function is smooth. As a result, our numerical approximation $\widetilde{M}_{\text{off}}$ for the estimating function M_{off} for sure satisfies the bound

$$\widetilde{M}_{\text{off}}(x) \geq M_{\text{off}}(x) \quad \text{for all} \quad x \in \big[0, \tfrac{\sqrt{3}}{2}\big). \tag{23}$$

The numerical function $\widetilde{M}_{\text{off}}(x)$ is plotted in Fig. 1 along with the two previously known estimating functions

$$M_{\text{KMM}}(x) = \arcsin\left(\min\left\{1,\ \frac{\pi\, x}{3 - \sqrt{1 + 4x^2}}\right\}\right), \quad x \in \big[0, \tfrac{\sqrt{3}}{2}\big),$$

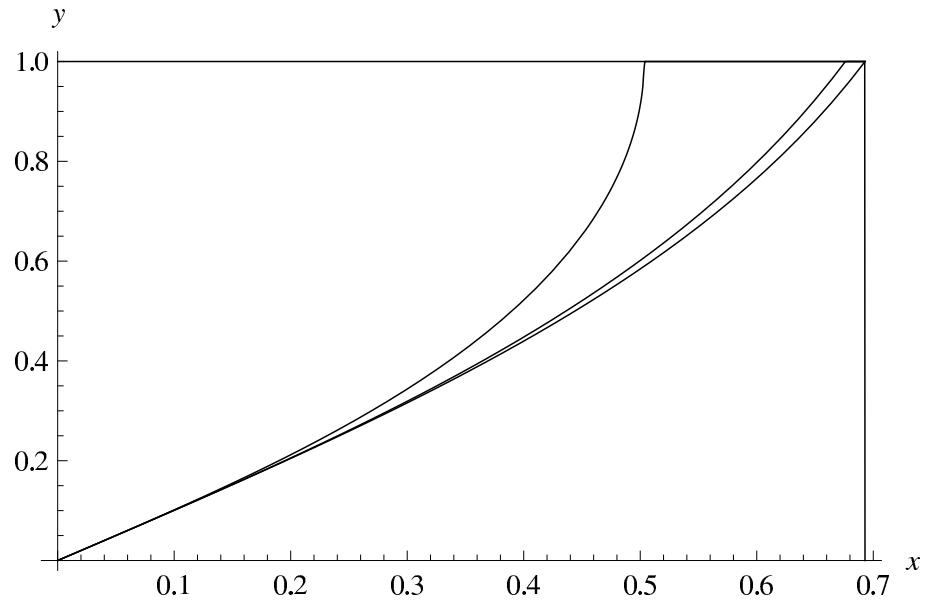

Figure 1: Graphs of the functions $\frac{2}{\pi}M_{\mathrm{KMM}}(x)$, $\frac{2}{\pi}M_{\mathrm{MS}}(x)$, and the numerical approximation $\frac{2}{\pi}\widetilde{M}_{\mathrm{off}}(x)$ for $\frac{2}{\pi}M_{\mathrm{off}}(x)$ while its value does not exceed 1. The upper curve depicts the graph of $\frac{2}{\pi}M_{\mathrm{KMM}}(x)$, the intermediate curve is the graph of $\frac{2}{\pi}M_{\mathrm{MS}}(x)$, and the lower curve represents the graph of $\frac{2}{\pi}\widetilde{M}_{\mathrm{off}}(x)$.

from Theorem 2 of Ref. [17] and

$$M_{\mathrm{MS}}(x) = \arcsin\left(\min\left\{1,\ \frac{\pi}{2}\int_0^x \frac{d\tau}{2-\sqrt{1+4\tau^2}}\right\}\right), \quad x \in \left[0, \tfrac{\sqrt{3}}{2}\right),$$

from Theorem 3.3 of Ref. [12] that both serve as M is in the bound (6) for the case of off-diagonal perturbations. For convenience of the reader, in the plot we divide all three functions M_{KMM}, M_{MS}, and $\widetilde{M}_{\mathrm{off}}$ by $\pi/2$.

For the (unique) numerical solution $x = \widetilde{c}_{\mathrm{off}}$ of the equation $\widetilde{M}_{\mathrm{off}}(x) = \pi/2$ within the interval $[0, \frac{\sqrt{3}}{2})$, we obtain

$$\widetilde{c}_{\mathrm{off}} = 0.692834... \tag{24}$$

Since the function $\widetilde{M}_{\mathrm{off}}$ is monotonous and the inequality (23) holds, the number $\widetilde{c}_{\mathrm{off}}$ is an approximation to the exact solution $x = c_{\mathrm{off}} > \widetilde{c}_{\mathrm{off}}$ of the equation $M_{\mathrm{off}}(x) = \pi/2$. Therefore we arrive at the new lower bound

$$c_* > 0.692834 \tag{25}$$

for the optimal constant c_* in the condition (5) ensuring the subspace variation estimate (4) in the generic off-diagonal subspace perturbation problem. The bound (25) is stronger than the corresponding best previously published bound $c_* > 0.67598$ from Ref. [12]. Furthermore, we have inequalities

$$M_{\mathrm{off}}(x) \le \widetilde{M}_{\mathrm{off}}(x) < M_{\mathrm{MS}}(x) \quad \text{for any} \quad x \in (0, \widetilde{c}_{\mathrm{off}}) \tag{26}$$

which show that already the approximate estimating function $\widetilde{M}_{\mathrm{off}}$ provides a bound of the form (6) that is stronger than the best known bound (with the function M_{MS}) from Ref. [12].

3 Applications to few-body bound-state problems

From now on, we assume that the "unperturbed" Hamiltonian A has the form $A = H_0 + V_0$ where H_0 is the kinetic energy operator of an N-particle system in the c. m. frame and the potential V_0 includes only a part of the interactions that are present in the system (say, only two-body forces). The perturbation V describes the remaining part of the interactions (say, three-body forces if $N = 3$; it may also describe the effect of external fields). We consider the case where V is a bounded operator. Of course, both A and V are assumed to be Hermitian. In order to apply the abstract results mentioned in the previous section, one only needs to know the norm of the perturbation V and a very basic stuff on the spectrum of the operator A.

Examples 3.1 and 3.2 below are borrowed from Ref. [18].

The first of the examples represents a simple illustration of the Davis–Kahan $\sin 2\theta$ and $\tan 2\theta$ theorems [3].

Example 3.1 Suppose that E_0 is the ground-state (g. s.) energy of the Hamiltonian A. Also assume that the eigenvalue E_0 is simple and let $|\psi_0\rangle$ be the g. s. wave function, i. e., $A|\psi_0\rangle = E_0|\psi_0\rangle$, $\|\psi_0\| = 1$. Set $\sigma = \{E_0\}$, $\Sigma = \mathrm{spec}(A) \setminus \{E_0\}$ and $d = \mathrm{dist}(\sigma, \Sigma) = \min(\Sigma) - E_0$ (we notice that the set Σ is not empty since it should contain at least the essential spectrum of A). If V is such that the condition (2) holds, then the g. s. energy E_0' of the total Hamiltonian $H = A + V$ is again a simple eigenvalue, with a g. s. wave function $|\psi_0'\rangle$, $\|\psi_0'\| = 1$. The eigenvalue E_0' lies in the closed $\|V\|$-neighborhood of the g. s. energy E_0, i. e., $|E_0 - E_0'| \leq \|V\|$. The corresponding spectral projections $P = \mathsf{E}_A(\sigma)$ and $Q = \mathsf{E}_H(\omega)$ of A and H associated with the one-point spectral sets $\sigma = \{E_0\}$ and $\omega = \{E_0'\}$ read as $P = |\psi_0\rangle\langle\psi_0|$ and $Q = |\psi_0'\rangle\langle\psi_0'|$. One verifies by inspection that

$$\arcsin\bigl(\|P - Q\|\bigr) = \arccos|\langle\psi_0|\psi_0'\rangle|.$$

Surely, this means that the maximal angle $\theta(\mathfrak{P}, \mathfrak{Q})$ between the one-dimensional spectral subspaces $\mathfrak{P} = \mathrm{Ran}(P) = \mathrm{span}(|\psi_0\rangle)$ and $\mathfrak{Q} = \mathrm{Ran}(Q) = \mathrm{span}(|\psi_0'\rangle)$ is nothing but the angle between the g. s. vectors $|\psi_0\rangle$ and $|\psi_0'\rangle$. Then the Davis–Kahan $\sin 2\theta$ theorem implies [see Eqs. (6) and (7)] that

$$\arccos|\langle\psi_0|\psi_0'\rangle| \leq \frac{1}{2}\arcsin\frac{2\|V\|}{d}.$$

This bound on the rotation of the ground state means, in particular, that, under the condition (2), the angle between $|\psi_0\rangle$ and $|\psi_0'\rangle$ can never exceed 45°.

If, in addition, the perturbation V is off-diagonal with respect to the partition $\mathrm{spec}(A) = \sigma \cup \Sigma$ then for any (arbitrarily large) $\|V\|$ no spectrum of H is present in the gap between the g. s. energy E_0 and the remaining spectrum Σ of A. Moreover, there are the following sharp universal bounds for the perturbed g. s. energy E_0':

$$E_0 - \epsilon_V \leq E_0' \leq E_0,$$

(see Lemma 1.1 of Ref. [17] and Proposition 2.5.21 of Ref. [13]). In this case, the Davis–Kahan $\tan 2\theta$ theorem [3] implies [see Eqs. (6) and (16)] that

$$\arccos|\langle\psi_0|\psi_0'\rangle| \leq \frac{1}{2}\arctan\frac{2\|V\|}{d} < \frac{\pi}{4}.$$

With a minimal change, the same consideration may be extended to the case where the initial spectral set σ consists of the $n+1$ lowest binding energies $E_0 < E_1 < \ldots < E_n$, $n \geq 1$, of A. We only underline that if V is off-diagonal than for any $\|V\|$ the perturbed spectral set ω of $H = A+V$ originating from σ will necessarily be confined in the interval $[E_0 - \epsilon_V, E_n]$ where the shift ϵ_V is given by Eq. (18); the interval $\bigl(E_n, \min(\Sigma)\bigr)$ will contain no spectrum of H. Furthermore, the $\tan 2\theta$-like

estimates for the maximal angle between the spectral subspaces $\mathfrak{P} = \mathrm{Ran}\big(\mathsf{E}_A(\sigma)\big)$ and $\mathfrak{Q} = \mathrm{Ran}\big(\mathsf{E}_H(\omega)\big)$ may be done even for some unbounded V (but, instead of d and $\|V\|$, those estimates involve quadratic forms of A and V), see Refs. [7,14].

Along with the $\sin 2\theta$ theorem, the next example illustrates the $\tan\theta$ bound from Refs. [7,16].

Example 3.2 Suppose that $\sigma = \{E_{n+1}, E_{n+2}, \ldots, E_{n+k}\}$, $n \geq 0$, $k \geq 1$, is a set formed by the consecutive binding energies of A and $\Sigma = \mathrm{spec}(A) \setminus \sigma = \Sigma_- \cup \Sigma_+$, where Σ_- is the increasing sequence of the energy levels $E_0, E_1, \ldots, E_n$ of A that lie below $\min(\sigma)$; Σ_+ denotes the remainder of the spectrum of A, that is, $\Sigma_+ = \mathrm{spec}(A) \setminus (\sigma \cup \Sigma_-)$. Under condition (3), this assumption means that the set σ lies in the finite gap $\big(\max(\Sigma_-), \min(\Sigma_+)\big)$ of the set Σ. If one only assumes for V the norm bound (2) and makes no assumptions on the structure of V, then not much can be said about the location of the perturbed spectral sets ω and Ω, except for Eq. (1). However the Davis–Kahan $\sin 2\theta$ theorem [3] still well applies and, thus, one has the bound

$$\theta(\mathfrak{P}, \mathfrak{Q}) \leq \frac{1}{2} \arcsin \frac{2\|V\|}{d} < \frac{\pi}{4}.$$

Much stronger conclusions are done if V is off-diagonal with respect to the partition $\mathrm{spec}(A) = \sigma \cup \Sigma$. In the Section 2 it was already mentioned that for off-diagonal V the gap-non-closing condition is of the form $\|V\| < \sqrt{2}d$ (and even a weaker but somewhat more detailed condition $\|V\| < \sqrt{dD}$ with $D = \min(\Sigma_+) - \max(\Sigma_-)$ is admitted, see Refs. [7, 15]). In this case the lower bound for the spectrum of $H = A + V$ reads as $E_0 - \epsilon_V$ where the maximal possible energy shift ϵ_V, $\epsilon_V < d$, is given again by Eq. (18). Furthermore, the perturbed spectral set ω is confined in the interval $[E_{n+1} - \epsilon_V, E_{n+k} + \epsilon_V]$, while the open intervals $(E_n, E_{n+1} - \epsilon_V)$ and $\big(E_{n+k} + \epsilon_V, \min(\Sigma_+)\big)$ contain no spectrum of H. For tighter enclosures for the perturbed spectral sets ω and Ω involving the the gap length D, we refer to Refs. [13,15,17]. In the case under consideration, the sharp bound for the size of rotation of the spectral subspace $\mathfrak{P} = \mathrm{Ran}\big(\mathsf{E}_A(\sigma)\big)$ to the spectral subspaces $\mathfrak{Q} = \mathrm{Ran}\big(\mathsf{E}_H(\omega)\big)$ is given by the *a priori* $\tan\theta$ theorem (see Theorem 1 of Ref. [16]; cf. Theorem 2 of Ref. [7]):

$$\theta(\mathfrak{P}, \mathfrak{Q}) \leq \arctan \frac{\|V\|}{d} < \arctan \sqrt{2}.$$

If the gap length D is known and $\|V\| < \sqrt{dD}$, then a stronger but more detailed estimate for $\theta(\mathfrak{P}, \mathfrak{Q})$ is available (see Theorem 4.1 of Ref. [16]).

Example 3.3 models the generic spectral disposition. Assume that the binding energies of A are numbered in the increasing order, $E_0 < E_1 < \ldots < E_n < \ldots$, and $\sigma = \{E_0, E_2, \ldots, E_{2k}\}$ is formed of the first $k+1$, $k \geq 1$, binding energies with even numbers. Let $\Sigma = \mathrm{spec}(A) \setminus \sigma$ and, thus, Σ contains the first k binding energies $E_1, E_3, \ldots, E_{2k-1}$ with the odd numbers, as well as the remaining point spectrum and the essential spectrum of A. If $d = \mathrm{dist}(\sigma, \Sigma) > 0$ and $\|V\| < c_{\mathrm{s}} d$ with c_{s} given by Eq. (15), then for the maximal angle $\theta(\mathfrak{P}, \mathfrak{Q})$ between the corresponding unperturbed and perturbed spectral subspaces $\mathfrak{P} = \mathrm{Ran}\big(\mathsf{E}_A(\sigma)\big)$ and $\mathfrak{Q} = \mathrm{Ran}\big(\mathsf{E}_H(\omega)\big)$ we have the bound (12).

If, in addition, the perturbation V is off-diagonal with respect to the partition $\mathrm{spec}(A) = \sigma \cup \Sigma$ then the disjointness of the perturbed spectral components ω and Ω is guaranteed by the weaker requirement $\|V\| < \frac{\sqrt{3}}{2} d$. In this case $\omega \subset \mathcal{O}_{\epsilon_V}(\sigma)$ and $\Omega \subset \mathcal{O}_{\epsilon_V}(\Sigma)$ where ϵ_V is given by Eq. (18). Furthermore, if $\|V\| < \widetilde{c}_{\mathrm{off}}\, d$ where $\widetilde{c}_{\mathrm{off}}$ is the solution (24) of the equation $\widetilde{M}_{\mathrm{off}}(x) = \pi/2$, then one can apply the bound (22).

Examples 3.1–3.3 show how one may obtain a bound on variation of the spectral subspace prior to any real calculations for the total Hamiltonian H. In order to get such a bound, only the knowledge of the values of d and $\|V\|$ is needed. Furthermore,

if V is off-diagonal, by using just these two quantities one can also provide the stronger estimates (via ϵ_V) for the binding energy shifts.

Acknowledgments. This work was supported by the Deutsche Forschungsgemeinschaft, by the Heisenberg-Landau Program, and by the Russian Foundation for Basic Research.

References

[1] C. Davis, J. Math. Anal Appl. **6**, 159 (1963).

[2] C. Davis, J. Math. Anal Appl. **11**, 20 (1965).

[3] C. Davis and W. M. Kahan, SIAM J. Numer. Anal. **7**, 1 (1970).

[4] T. Kato, *Perturbation theory for linear operators*. Springer–Verlag, Berlin, 1966.

[5] S. Albeverio and A. K. Motovilov, Compl. Anal. Oper. Theory **7**, 1389 (2013); arXiv:1112.0149 [math.SP] (2011).

[6] V. Kostrykin, K. A. Makarov and A. K. Motovilov, Oper. Theory Adv. Appl. **149**, 349 (2004); math/0302020 [math.SP] (2003).

[7] A. K. Motovilov and A. V. Selin, Integr. Equ. Oper. Theory **56**, 511 (2006); math/0409558 [math.SP] (2004).

[8] A. Seelmann, Integr. Equ. Oper. Theory **79**, 579 (2014); arXiv:1310.2036 [math.SP] (2013).

[9] L. G. Brown, Trans. Amer. Math. Soc. **227**, 279 (1993).

[10] A. Seelmann, arXiv:1310.4360 [math.SP] (2013).

[11] V. Kostrykin, K. A. Makarov and A. K. Motovilov, Proc. Amer. Math. Soc. **131**, 3469 (2003); math/0203240 [math.SP] (2002).

[12] K. A. Makarov and A. Seelmann, J. Reine Angew. Math. **2015**, 1 (2013), DOI:10.1515/crelle-2013-0099.

[13] C. Tretter, *Spectral theory of block operator matrices and applications*. Imperial College Press, London, 2008.

[14] L. Grubišić, V. Kostrykin, K. A. Makarov and K. Veselić, J. Spectr. Theory **3**, 83 (2013); arXiv:1006.3190 [math.SP] (2010).

[15] V. Kostrykin, K. A. Makarov and A. K. Motovilov, Integr. Equ. Oper. Theory **51**, 121 (2005); arXiv:math/0210032 [math.SP] (2002).

[16] S. Albeverio and A. K. Motovilov, Integr. Equ. Oper. Theory **73**, 413 (2012); arXiv:1012.1569 [math.SP] (2010).

[17] V. Kostrykin, K. A. Makarov and A. K. Motovilov, Trans. Amer. Math. Soc. **359**, 77 (2007); math/0306025 [math.SP] (2003).

[18] A. K. Motovilov, Few-Body Syst. **55**, 813 (2014); arXiv:1311.6604 [quant-ph] (2013).

Separable Optical Potentials for (d, p) Reactions

Ch. Elster[a], L. Hlophe[a], V. Eremenko[a,b], F. M. Nunes[c], G. Arbanas[d], J. E. Escher[e], I. J. Thompson[e]

(The TORUS Collaboration)

[a] *Institute of Nuclear and Particle Physics, and Department of Physics and Astronomy, Ohio University, Athens, OH 45701, USA*

[b] *D. V. Skobeltsyn Institute of Nuclear Physics, M. V. Lomonosov Moscow State University, Moscow, 119991, Russia*

[c] *National Superconducting Cyclotron Laboratory and Department of Physics and Astronomy, Michigan State University, East Lansing, MI 48824, USA*

[d] *Reactor and Nuclear Systems Division, Oak Ridge National Laboratory, Oak Ridge, TN 37831, USA*

[e] *Lawrence Livermore National Laboratory L-414, Livermore, CA 94551, USA*

Abstract

An important ingredient for applications of nuclear physics to, e. g., astrophysics or nuclear energy are the cross sections for reactions of neutrons with rare isotopes. Since direct measurements are often not possible, indirect methods like (d, p) reactions must be used instead. Those (d, p) reactions may be viewed as effective three-body reactions and described with Faddeev techniques. An additional challenge posed by (d, p) reactions involving heavier nuclei is the treatment of the Coulomb force. To avoid numerical complications in dealing with the screening of the Coulomb force, recently a new approach using the Coulomb distorted basis in momentum space was suggested. In order to implement this suggestion, one needs not only to derive a separable representation of neutron- and proton-nucleus optical potentials, but also compute the Coulomb distorted form factors in this basis.

Keywords: *Separable representation of optical potentials; momentum space Coulomb distorted form factors; Coulomb without screening*

1 Introduction

Nuclear reactions are an important probe to learn about the structure of unstable nuclei. Due to the short lifetimes involved, direct measurements are usually not possible. Therefore indirect measurements using (d, p) reactions have been proposed (see, e. g., Refs. [1–3]). Deuteron induced reactions are particularly attractive from an experimental perspective, since deuterated targets are readily available. From a theoretical perspective they are equally attractive because the scattering problem can be reduced to an effective three-body problem [4]. Traditionally deuteron-induced single-neutron transfer (d, p) reactions have been used to study the shell structure in stable nuclei, nowadays experimental techniques are available to apply the same approaches to exotic beams (see, e. g., [5]). Deuteron induced (d, p) or (d, n) reactions in inverse kinematics are also useful to extract neutron or proton capture rates on

Proceedings of the International Conference 'Nuclear Theory in the Supercomputing Era — 2014' (NTSE-2014), Khabarovsk, Russia, June 23–27, 2014. Eds. A. M. Shirokov and A. I. Mazur. Pacific National University, Khabarovsk, Russia, 2016, p. 107.

http://www.ntse-2014.khb.ru/Proc/Elster.pdf.

unstable nuclei of astrophysical relevance. Given the many ongoing experimental programs worldwide using these reactions, a reliable reaction theory for (d,p) reactions is critical.

One of the most challenging aspects of solving the three-body problem for nuclear reactions is the repulsive Coulomb interaction. While the Coulomb interaction for light nuclei is often a small correction to the problem, this is certainly not the case for intermediate mass and heavy systems. Over the last decade, many theoretical efforts have focused on advancing the theory for (d,p) reactions (e. g., [6, 7]) and testing existing methods (e. g., [4,8,9]). Currently, the most complete implementation of the theory is provided by the Lisbon group [10], which solves the Faddeev equations in the Alt, Grassberger and Sandhas [11] formulation. The method introduced in [10] treats the Coulomb interaction with a screening and renormalization procedure as detailed in [12,13]. While the current implementation of the Faddeev–AGS equations with screening is computationally effective for light systems, as the charge of the nucleus increases technical difficulties arise in the screening procedure [14]. Indeed, for most of the new exotic nuclei to be produced at the Facility of Rare Isotope Beams, the current method is not adequate. Thus one has to explore solutions to the nuclear reaction three-body problem where the Coulomb problem is treated without screening.

In Ref. [6], a three-body theory for (d,p) reactions is derived with explicit inclusion of target excitations, where no screening of the Coulomb force is introduced. Therein, the Faddeev–AGS equations are cast in a Coulomb-distorted partial-wave representation, instead of a plane-wave basis. This approach assumes the interactions in the two-body subsystems to be separable. While in Ref. [6] the lowest angular momentum in this basis ($l = 0$) is derived for a Yamaguchi-type nuclear interaction is derived as analytic expression, it is desirable to implement more general form factors, which are modeled after the nuclei under consideration.

In order to bring the three-body theory laid out in Ref. [6] to fruition, well defined preparatory work needs to be successfully carried out. Any momentum space Faddeev–AGS type calculation needs as input transition matrix elements in the different two-body subsystems. In the case of (d,p) reactions with nuclei these are the t-matrix elements obtained from the neutron-proton, the neutron-nucleus and proton-nucleus interactions. Since the formulation in Ref. [6] is designed for separable interactions, those need to be developed not only in the traditionally employed plane wave basis, but also the basis of Coulomb scattering states.

This contribution summarizes the three major developments required to provide reliable input to the three-body formulation for (d,p) reactions without screening the Coulomb force, namely:

- the derivation of momentum-space separable representations of neutron-nucleus optical potentials [15],
- the derivation of momentum-space separable representations of proton-nucleus optical potentials in the Coulomb basis [16],
- the calculation of neutron-nucleus form-factors in the basis of momentum-space Coulomb scattering states [17].

Sections 2, 3, and 4 summarize the necessary steps to achieve reliable calculations of those input quantities needed for three-body calculations that treat the Coulomb force without screening. Finally, we summarize in Section 5.

2 Separable representation of nucleon-nucleus optical potentials

Separable representations of the forces between constituents forming the subsystems in a Faddeev approach have a long tradition in few-body physics. There is a large body of work on separable representations of nucleon-nucleon (NN) interactions (see, e. g., Refs. [18–22]) or meson-nucleon interactions [23,24]. In the context of describing light nuclei like ^{6}He [25] and ^{6}Li [26] in a three-body approach, separable interactions have been successfully used. A separable nucleon-^{12}C optical potential was proposed in Ref. [27], consisting of a rank-1 Yamaguchi-type form factor fitted to the positive energies and a similar term describing the bound states in the nucleon-^{12}C configuration. However, systematic work along this line for heavy nuclei, for which excellent phenomenological descriptions exist in terms of Woods–Saxon functions [28–31] has not been carried out until recently [15].

The separable representation of two-body interactions suggested by Ernst–Shakin–Thaler [32] (EST) is well suited for achieving this goal. We note that this EST approach has been successfully employed to represent NN potentials [18, 19]. However, the EST scheme derived in Ref. [32], though allowing energy dependence of the potentials [33, 34], assumes that they are Hermitian. Therefore, we generalized the EST approach in Ref. [15] in order to be applicable for optical potentials which are complex. For the ease of the reader, we briefly summarize the main points of that work.

For applications to the theory of nuclear reactions all potential operators U need to satisfy

$$\mathcal{K}U\mathcal{K}^{-1} = U^\dagger, \tag{1}$$

where $\mathcal{K}$ is the time reversal operator appropriate to the system. This condition guarantees that the S-matrix corresponding to U is symmetric and that reaction amplitudes constructed from these potentials satisfy reciprocity relations. When U is a central potential in the space of a spinless particle, $\mathcal{K}$ can be chosen to be the anti-linear complex conjugation operator $\mathcal{K}_0$, which in the coordinate space basis $|\mathbf{r}\rangle$ is defined by

$$\mathcal{K}_0\ \alpha\,|\mathbf{r}\rangle = \alpha^*(\mathcal{K}_0|\mathbf{r}\rangle) = \alpha^*|\mathbf{r}\rangle, \tag{2}$$

and from which we deduce $\mathcal{K}_0|\mathbf{p}\rangle = |-\mathbf{p}\rangle$. Note that for this particular $\mathcal{K}$ we have $(\mathcal{K}_0)^{-1} = \mathcal{K}_0$.

Considering first a rank-1 separable potential, the EST scheme presented in Ref. [32] requires that a separable potential $\mathbf{U}$ leads to the same scattering wave functions at a specific energy E_{k_E} (support point) as the potential u it is supposed to represent. For u being a non-Hermitian potential, we define

$$\mathbf{U}(E_{k_E}) \equiv \frac{u|f_{l,k_E}\rangle\langle f^*_{l,k_E}|u}{\langle f^*_{l,k_E}|u|f_{l,k_E}\rangle} \equiv u|f_{l,k_E}\rangle\hat{\lambda}\langle f^*_{l,k_E}|u, \tag{3}$$

where the strength parameter is defined by $(\hat{\lambda})^{-1} = \langle f^*_{l,k_E}|u|f_{l,k_E}\rangle$. Here $f_{l,k_E}(r)$ is the unique regular radial wave function corresponding to u and $f^*_{l,k_E}(r)$ is the unique regular radial wavefunction corresponding to u^*. By a suitable choice of arbitrary normalization constants we can arrange that $f^*_{l,k_E}(r)$ is simply the complex conjugate of f_{l,k_E} and hence $\mathcal{K}_0|f_{l,k_E}\rangle = |f^*_{l,k_E}\rangle$.

If u satisfies $\mathcal{K}_0 u\mathcal{K}_0 = u^\dagger$ the definition of Eq. (3) gives a symmetric complex potential matrix that satisfies

$$\mathcal{K}_0\mathbf{U}(E_{k_E})\mathcal{K}_0 = \left[\mathcal{K}_0 u|f_{l,k_E}\rangle\right](\hat{\lambda})^*\left[\langle f^*_{l,k_E}|u\mathcal{K}_0\right] = u^\dagger|f^*_{l,k_E}\rangle(\hat{\lambda})^*\langle f_{l,k_E}|u^\dagger = U^\dagger, \tag{4}$$

where the square brackets mean that $\mathcal{K}_0$ here acts only on the quantities within the brackets.

In analogy to the procedure followed in Ref. [32] we define a complex separable potential of arbitrary rank in a given partial wave as

$$\mathbf{U} = \sum_{i,j} u|f_{l,k_{E_i}}\rangle\langle f_{l,k_{E_i}}|M|f^*{}_l, k_{E_j}\rangle\langle f^*_{l,k_{E_j}}|u. \tag{5}$$

Here $f_{l,k_{E_i}}$ and $f^*_{l,k_{E_i}}$ are the same unique regular radial wave function as used in Eq. (3). Note that u may also be energy dependent. The matrix M is defined and constrained by

$$\begin{aligned}\delta_{ik} &= \sum_j \langle f_{l,k_{E_i}}|M|f^*_{l,k_{E_j}}\rangle\langle f^*_{l,k_{E_j}}|u|f_{l,k_{E_k}}\rangle \\ &= \sum_j \langle f^*_{l,k_{E_i}}|u|f_{l,k_{E_j}}\rangle\langle f_{l,k_{E_j}}|M|f^*_{l,k_{E_k}}\rangle.\end{aligned} \tag{6}$$

The corresponding separable partial wave t-matrix must be of the form

$$t(E) = \sum_{i,j} u|f_{l,k_{E_i}}\rangle\tau_{ij}(E)\langle f^*_{l,k_{E_j}}|u, \tag{7}$$

with the following restrictions

$$\delta_{nj} = \sum_i \langle f^*_{l,k_{E_n}}|u - ug_0(E)u|f_{l,k_{E_i}}\rangle\ \tau_{ij}(E), \tag{8}$$

$$\delta_{ik} = \sum_j \tau_{ij}(E)\ \langle f^*_{l,k_{E_j}}|u - ug_0(E)u|f_{l,k_{E_k}}\rangle. \tag{9}$$

For the explicit calculation of the matrix $\tau_{ij}(E)$, we define a matrix

$$R_{ij}(E) \equiv \langle f^*{}_l, k_{E_i}|u - ug_0(E)u|f_{l,k_{E_j}}\rangle, \tag{10}$$

so that the condition of Eq. (9) reads

$$\sum_j \tau_{ij}(E)R_{jk}(E) = \delta_{ik}, \tag{11}$$

from which follows

$$\tau_{ij}(E) = (R(E))^{-1}_{ij}. \tag{12}$$

Using that $t(p', k_{E_i}, E_i) = \langle f^*_{l,k_{E_i}}|u|p'\rangle$, and $t(p, k_{E_i}, E_i) = \langle p|u|f_{l,k_{E_i}}\rangle$, the matrix elements R_{ij} are calculated in momentum space as given explicitly in Ref. [15].

In order to demonstrate the construction of a separable representation of a complex potential we apply the generalized EST scheme to neutron scattering from ^{48}Ca and ^{208}Pb and use as starting point the Chapel Hill phenomenological global optical potential CH89 [28], which has been widely used in the literature over the last decades. Like most phenomenological global optical potentials, CH89 is based on Woods–Saxon functions, which are more naturally given in coordinate space, and have an explicit energy dependence in the strength functions. In order to derive a separable momentum-space representation of CH89, we first must construct a momentum-space representation of the potential itself. The Fourier transform of Woods–Saxon functions leads to a series expansion in momentum space, of which only the first two terms are necessary to obtain a converged result [15]. The momentum-space potential then enters a Lippmann–Schwinger (LS) integral equation to obtain the half-shell t-matrices at fixed energies (support points) E_i, from which the separable representation given in Eq. (7) is then constructed after having obtained the coupling matrix $\tau_{ij}(E)$ from the solution of Eq. (12).

Table 1: The EST support points at c. m. energies E_{k_i} used for constructing the separable representation of the partial wave S-matrix of the $n + {}^{48}$Ca and $n + {}^{208}$Pb systems. The support points in the last row for the $n + {}^{208}$Pb system given in bold face indicate the universal set of support points, which can be used to construct a representation for all nuclei given by the CH89 [28] phenomenological optical potential.

system	partial wave(s)	rank	EST support point(s) [MeV]
$n + {}^{48}$Ca	$l \geq 10$	1	40
	$l \geq 8$	2	29, 47
	$l \geq 6$	3	16, 36, 47
	$l \geq 0$	4	6, 15, 36, 47
$n + {}^{208}$Pb	$l \geq 16$	1	40
	$l \geq 13$	2	35, 48
	$l \geq 11$	3	24, 39, 48
	$l \geq 6$	4	11, 21, 36, 45
	$\mathbf{l \geq 0}$	**5**	$\mathbf{5, 11, 21, 36, 47}$

A major finding of Ref. [15] is a systematic classification of support points for partial wave groups, so that the partial wave S-matrix elements are reproduced to at least four significant figures compared to the original momentum-space solution of the LS equation. It turns out that the low partial waves of the $n + {}^{208}$Pb system require a rank-5 separable potential to be well represented in the energy regime between 0 and 50 MeV center-of-mass energy. The rank required for achieving a good representation decreases with increasing angular momentum of the partial wave considered. The recommendation of Ref. [15] for both the rank and the locations of the support points to be used when describing medium-mass and heavy systems generated from the CH89 potential are repeated in Table 1 for the convenience of the reader.

In order to demonstrate the quality of the separable representations obtained with the generalized EST scheme, Fig. 1 depicts the unpolarized differential cross section for elastic scattering of neutrons from ^{48}Ca at 38 MeV laboratory kinetic energy and from ^{206}Pb at 45 MeV as function of the center-of-mass (c. m.) angle $\theta_{c.m.}$. The solid lines (i) represent the calculations with the separable representations, while the dotted lines (ii) stand for the corresponding coordinate space calculations. The agreement is excellent over the entire angular range, indicating that all partial wave S-matrix elements that enter the cross section are well described by the separable representation.

3 Separable representation of proton-nucleus optical potentials in the Coulomb basis

In order to implement the formulation of the Faddeev–AGS equations proposed in Ref. [6] we need the proton-nucleus form factors in the Coulomb distorted basis, and thus need to have a separable representation of proton-nucleus optical potentials. In Refs. [35, 36] rank-1 separable interactions of Yamaguchi form were introduced to represent the nuclear force up to a few MeV, and the Coulomb distorted basis was introduced to compute proton elastic scattering from light nuclei. This is not sufficient for considering the proton-nucleus interaction in a separable representation for scattering of heavy nuclei up to tens of MeV. Thus we need to extend the generalization of the EST scheme presented in the previous section such that it can be applied

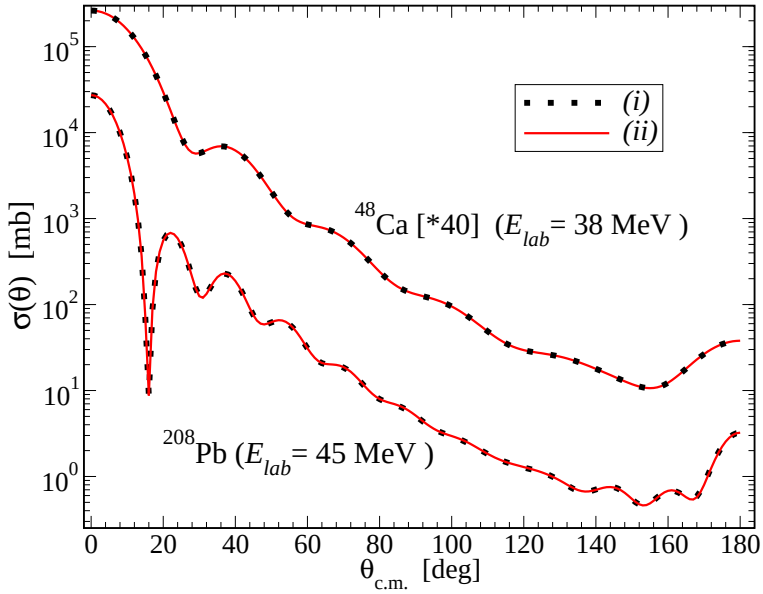

Figure 1: The unpolarized differential cross section for elastic scattering of neutrons from ^{48}Ca (upper) and ^{208}Pb (lower) as function of the c. m. angle. For ^{48}Ca the cross section is calculated at a laboratory kinetic energy of 38 MeV and is scaled by a factor 40. The calculation for ^{208}Pb is carried out at $E_{lab} = 45$ MeV. The solid lines (ii) depict the cross section calculated in momentum space based on the rank-5 separable representation of the CH89 [28] phenomenological optical potential, while the dotted lines (i) represent the corresponding coordinate space calculations.

in the Coulomb distorted basis [16].

In general the scattering between a proton and a nucleus is governed by a potential

$$w = v^c + u^s, \tag{13}$$

where v^c is the repulsive Coulomb potential and u^s an arbitrary short range potential. In general u^s consists of an optical potential, which describes the nuclear interactions and a short-ranged Coulomb potential traditionally parameterized as the potential of a charged sphere with radius R_0 from which the point Coulomb force is subtracted [28]. In practice,

$$u^s = u^N + (v^{cd} - v^c), \tag{14}$$

where u^N represents the nuclear (optical) potential, v^{cd} is the Coulomb potential inside the nucleus, and is usually taken as the Coulomb potential for a uniformly charged sphere of radius R_0, from which the point Coulomb potential is subtracted. The expressions for the short-ranged charge distribution is given in Ref. [28] as

$$(v^{cd} - v^c)(r) = \alpha Z_1 Z_2 \left[\frac{1}{2R_0}\left(3 - \frac{r^2}{R_0^2}\right) - \frac{1}{r}\right], \tag{15}$$

with Z_1 and Z_2 being the atomic numbers of the particles, and α the Coulomb coupling constant. Since the scattering problem governed by the point Coulomb force has an analytic solution, the scattering amplitude for elastic scattering between a proton and a spin-zero nucleus is obtained as the sum of the Rutherford amplitude $f^C(E_{p_0}, \theta)$ and the Coulomb distorted nuclear amplitude given by

$$M^{CN}(E_{p_0}, \theta) = f^{CN}(E_{p_0}, \theta) + \hat{\sigma} \cdot \hat{\mathbf{n}}\, g^{CN}(E_{p_0}, \theta), \tag{16}$$

with

$$f^{CN}(E_{p_0},\theta) = \\ -\pi\mu\sum_{l=0}^{\infty} e^{2i\sigma_l(E_{p_0})}P_l(\cos\theta)\times\Big[(l+1)\langle p_0|\tau_{l+}^{CN}(E_{p_0})|p_0\rangle + l\langle p_0|\tau_{l-}^{CN}(E_{p_0})|p_0\rangle\Big], \quad (17)$$

and

$$g^{CN}(E_{p_0},\theta) = \\ -\pi\mu\sum_{l=0}^{\infty} e^{2i\sigma_l(E_{p_0})}P_l^1(\cos\theta)\times\Big[\langle p_0|\tau_{l+}^{CN}(E_{p_0})|p_0\rangle - \langle p_0|\tau_{l-}^{CN}(E_{p_0})|p_0\rangle\Big]. \quad (18)$$

Here $E_{p_0} = p_0^2/2\mu$ is the c. m. scattering energy which defines the on-shell momentum p_0, and $\sigma_l = \arg\Gamma(1+l+i\eta)$ is the Coulomb phase shift. The Sommerfeld parameter is given by $\eta = \alpha Z_1 Z_2\mu/p_0$. The unit vector $\hat{\mathbf{n}}$ is normal to the scattering plane, and $\hat{\sigma}/2$ is the spin operator. The subscripts $'+'$ and $'-'$ correspond to a total angular momentum $j = l + 1/2$ and $j = l - 1/2$.

Suppressing the total angular momentum indices for simplicity, the Coulomb distorted nuclear t-matrix element is given by $\langle p_0|\tau_l^{CN}(E_{p_0})|p_0\rangle$, which is the solution of a LS type equation,

$$\langle p|\tau_l^{CN}(E_{p_0})|p_0\rangle = \langle p|u_l^s|p_0\rangle \\ + \int p'^2 dp'\langle p|u_l^s|p'\rangle\langle p'|g_c(E_{p_0}+i\varepsilon)|p'\rangle\langle p'|\tau_l^{CN}(E_{p_0})|p_0\rangle. \quad (19)$$

Here

$$g_c^{-1}(E_{p_0}+i\varepsilon) = E_{p_0} + i\varepsilon - H_0 - v^c \quad (20)$$

is the Coulomb Green's function and H_0 the free Hamiltonian. The Coulomb distorted nuclear t-matrix element $\langle p|\tau_l^{CN}(E_{p_0})|p_0\rangle$ is related to the proton-nucleus t-matrix $\langle p|t_l(E_{p_0})|p_0\rangle$ by the familiar two-potential formula

$$\langle p|t_l(E_{p_0})|p_0\rangle = \langle p|t_l^C(E_{p_0})|p_0\rangle + e^{2i\sigma_l(E_{p_0})}\langle p|\tau_l^{CN}(E_{p_0})|p_0\rangle, \quad (21)$$

where $\langle p|t_l^C(E_{p_0})|p_0\rangle$ is the point Coulomb t-matrix. When the integral equation, Eq. (19), is solved in the basis of Coulomb eigenfunctions, g_c acquires the form of a free Green's function and the difficulty of solving it is shifted to evaluating the potential matrix elements in this basis. For deriving a separable representation of the Coulomb distorted proton-nucleus t-matrix element, we generalize the approach suggested by Ernst, Shakin, and Thaler (EST) [32], to the charged particle case. The basic idea behind the EST construction of a separable representation of a given potential is that the wave functions calculated with this potential and the corresponding separable potential agree at given fixed scattering energies E_i, the EST support points. The formal derivations of [32] use the plane wave basis, which is standard for scattering involving short-range potentials. However, the EST scheme does not depend on the basis and can equally well be carried out in the basis of Coulomb scattering wave functions.

In order to generalize the EST approach to charged-particle scattering, one needs to be able to obtain the scattering wave functions or half-shell t-matrices from a given potential in the Coulomb basis, and then construct the corresponding separable representation thereof.

In order to calculate the half-shell t-matrix of Eq. (18), we evaluate the integral equation in the Coulomb basis as suggested in [37] and successfully applied in [38], and note that in this case the Coulomb Green's function behaves like a free Green's

function. Taking $|\Phi^c_{l,p}\rangle$ to represent the partial wave Coulomb eigenstate, the LS equation becomes

$$\langle\Phi^c_{l,p}|\tau^{CN}_l(E_{p_0})|\Phi^c_{l,p_0}\rangle = \langle\Phi^c_{l,p}|u^s|\Phi^c_{l,p_0}\rangle + \int_0^\infty \langle\Phi^c_{l,p}|u^s|\Phi^c_{l,p'}\rangle \frac{p'^2dp'}{E_{p_0}-E_{p'}+i\varepsilon}\langle\Phi^c_{l,p'}|\tau^{CN}_l(E_{p_0})|\Phi^c_{l,p_0}\rangle \equiv \langle p|\tau^{CN}_l(E_{p_0})|p_0\rangle, \quad (22)$$

which defines the Coulomb distorted nuclear t-matrix of Eq. (19).

To determine the short-range potential matrix element, we follow Ref. [37] and insert a complete set of position space eigenfunctions

$$\langle\Phi^c_{l,p'}|u^s_l|\Phi^c_{l,p}\rangle = \frac{2}{\pi}\int_0^\infty \langle\Phi^c_{l,p'}|r'\rangle\, r'^2dr'\, \langle r'|u^s_l|r\rangle\, r^2dr\, \langle r|\Phi^c_{l,p}\rangle = \frac{2}{\pi p'p}\int_0^\infty rr'drdr'\, F_l(\eta',p'r')\, \langle r'|u^s_l|r\rangle\, F_l(\eta,pr). \quad (23)$$

The partial wave Coulomb functions are given in coordinate space as

$$\langle r|\Phi^c_{l,p}\rangle \equiv \frac{F_l(\eta,pr)}{pr}, \quad (24)$$

where $F_l(\eta,pr)$ are the standard Coulomb functions [39], and $\eta(\eta')$ is the Sommerfeld parameter determined with momentum $p(p')$.

For our application we consider phenomenological optical potentials of Woods–Saxon form which are local in coordinate space. Thus the momentum space potential matrix elements simplify to

$$\langle\Phi^c_{l,p'}|u^s_l|\Phi^c_{l,p}\rangle = \frac{2}{\pi p'p}\int_0^\infty dr\, F_l(\eta',p'r)u^s_l(r)F_l(\eta,pr). \quad (25)$$

We compute these matrix elements for the short-range piece of the CH89 phenomenological global optical potential [28], which consists of the nuclear part parameterized in terms of Woods–Saxon functions and the short-range Coulomb force of Eq. (15). The integral of Eq. (25) can be carried out with standard methods, since $u^s(r)$ is short ranged and the coordinate space Coulomb wavefunctions are well defined. The accuracy of this integral can be tested by replacing the Coulomb functions with spherical Bessel functions and comparing the resulting matrix elements to the partial-wave decomposition of the semi-analytic Fourier transform used for the calculations in the previous Section. For the cases we studied a maximum radius of 14 fm, 300 grid points are sufficient to obtain matrix elements with a precision of six significant digits.

Extending the EST separable representation to the Coulomb basis involves replacing the neutron-nucleus half-shell t-matrix in Eqs. (6)-(8) by the Coulomb distorted nuclear half-shell t-matrix. This leads to the separable Coulomb distorted nuclear t-matrix

$$\tau^{CN}_l(E_{p_0}) = \sum_{i,j} u^s|f^c_{l,k_{E_i}}\rangle\, \tau^c_{ij}(E_{p_0})\, \langle f^{c*}_{l,k_{E_j}}|u^s, \quad (26)$$

with $\tau^c_{ij}(E_{p_0})$ being constrained by

$$\sum_i \langle f^{c*}_{l,k_{E_n}}|u^s - u^s g_c(E_{p_0})u^s|f^c_{l,k_{E_i}}\rangle\tau^c_{ij}(E) = \delta_{nj} \quad (27)$$

$$\sum_j \tau^{CN}_{ij}(E_{p_0})\, \langle f^{c*}_{l,k_{E_j}}|u^s - u^s g_c(E_{p_0})u^s|f^c_{l,k_{E_k}}\rangle = \delta_{ik}\ .$$

Here $|f^c_{l,k_{E_i}}\rangle$ and $|f^{c*}_{l,k_{E_i}}\rangle$ are the regular radial scattering wave functions corresponding to the short range potentials u^s and $(u^s)^*$ at energy E_i. The separable Coulomb distorted nuclear t-matrix elements are given by

$$\langle p'|\tau^{CN}_l(E_{p_0})|p\rangle \equiv \sum_{i,j} h^c_{l,i}(p')\tau^c_{ij}(E_{p_0})h^c_{l,j}(p)$$
$$= \sum_{i,j}\langle\Phi^c_{l,p'}|u^s|f^c_{l,k_{E_i}}\rangle\tau^c_{ij}(E_{p_0})\langle f^{c*}_{l,k_{E_j}}|u^s|\Phi^c_{l,p}\rangle, \quad (28)$$

where the form factor

$$h^c_{l,i}(p) \equiv \langle\Phi^c_{l,p}|u^s|f^c_{l,k_{E_i}}\rangle = \langle f^{c*}_{l,k_{E_i}}|u^s|\Phi^c_{l,p}\rangle = \langle p|\tau^{CN}_l(E_i)|k_{E_i}\rangle \quad (29)$$

is the Coulomb distorted short-range half-shell t-matrix satisfying Eq. (22). We want to point out that the generalization of the EST scheme to complex potentials is not affected by changing the basis from plane waves to Coulomb scattering states.

For studying the quality of the representation of proton-nucleus optical potentials we consider $p+{}^{48}$Ca and $p+{}^{208}$Pb elastic scattering and show the unpolarized differential cross sections divided by the Rutherford cross section as function of the c. m. angle $\theta_{c.m.}$ in Fig. 2. First, we observe very good agreement in both cases of the momentum space calculations using the separable representation with the corresponding coordinate space calculations. Second, we want to point out that we used for the separable representation of the proton-nucleus partial-wave t-matrices the same support points (Table 1) as in the neutron-nucleus case. This makes the determination of suitable support points E_i for a given optical potential and nucleus quite efficient. In Fig. 2 we also show a calculation in which the short-range Coulomb potential of

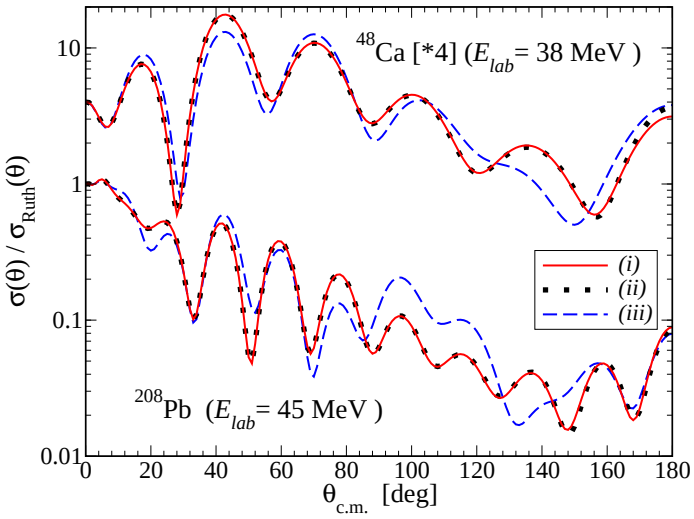

Figure 2: The unpolarized differential cross section for elastic scattering of protons from ^{48}Ca (upper) and ^{208}Pb (lower) divided by the Rutherford cross section as function of the c. m. angle $\theta_{c.m.}$. For ^{48}Ca the cross section is calculated at a laboratory kinetic energy of 38 MeV and is scaled by a factor 4. The calculation for ^{208}Pb is carried out at $E_{lab} = 45$ MeV. The solid lines (i) depict the cross section calculated in momentum space based on the rank-5 separable representation of the CH89 [28] phenomenological optical potential, while the dotted lines (ii) represent the corresponding coordinate space calculations. The dash-dotted lines (iii) show calculations in which the short-ranged Coulomb potential is omitted.

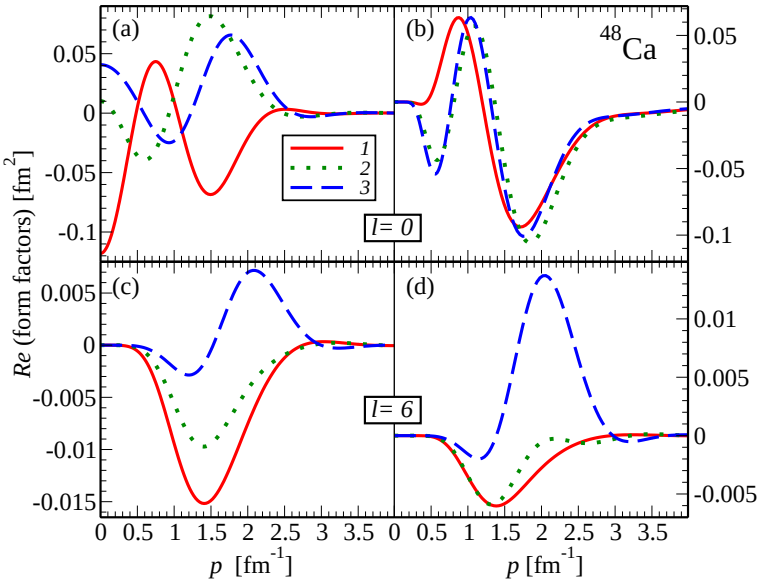

Figure 3: The real parts of the partial wave neutron form factors for ^{48}Ca as function of the momentum p for $l = 0$ (a) and $l = 6$ (c). The form factors are calculated at the energies indicated in Table 1 for the given angular momentum, $1 \equiv 6$ MeV, $2 \equiv 15$ MeV, and $3 \equiv 36$ MeV. The real parts of the proton form factors for ^{48}Ca as function of the momentum p are given for $l = 0$ in (b) and $l = 6$ in (d) for the energies indicated in Table 1.

Eq. (18) is omitted. The differences in the cross sections clearly demonstrate the importance of including this term. A detailed comparison of the partial-wave S-matrix elements as function of the angular momentum is given in Ref. [16].

In order to illustrate some details of the separable representation of the t-matrix of Eq. (7) that leads to the cross section given in Fig. 1, we display in the left panels of Fig. 3 the real parts of the form factors of the $n+^{48}$Ca t-matrix for $l = 0$ (a) and $l = 6$ (c) at support points given in Table 1 for the respective angular momentum. Only for $l = 0$ the form factors have a finite value at $p = 0$, while for the higher angular momentum all form factors go to zero for $p \to 0$ due to the angular momentum barrier. For comparison, the right panels in Fig. 3 display the form factors of the Coulomb distorted nuclear t-matrix from Eq. (19) for $p + ^{48}$Ca for the same angular momenta and support points. Those t-matrix elements enter the calculation of the cross section in Fig. 2. First we note that for $l = 0$ the $p + ^{48}$Ca form factors are quite different from the $n + ^{48}$Ca form factors. In addition, they fall off much slower as function of p, a property mainly caused by the short range Coulomb potential.

In Fig. 4 we carry out an analogous comparison between the form factors for the $n + ^{208}$Pb and $p + ^{208}$Pb form factors. Here the energies are chosen slightly higher, since in the $p + ^{208}$Pb the form factors at the lowest energies given in Table 1 are very small. The slow decrease of the $p + ^{208}$Pb form factor for the small angular momentum is even more pronounced in this case.

At this point it is crucial to note that in Figs. 3 and 4 we compare two quite different form factors. For $n + ^{48}$Ca and $n + ^{208}$Pb scattering the t-matrix elements leading to the form factors are calculated as described in Section 2 using as basis states in- and out-going plane-wave scattering states. For $p+^{48}$Ca and $p+^{208}$Pb, the Coulomb distorted nuclear t-matrix elements enter the cross section and lead to the form factors. Those Coulomb distorted t-matrix elements are evaluated in the basis of Coulomb scattering states. Thus, one should not be surprised that the form factors

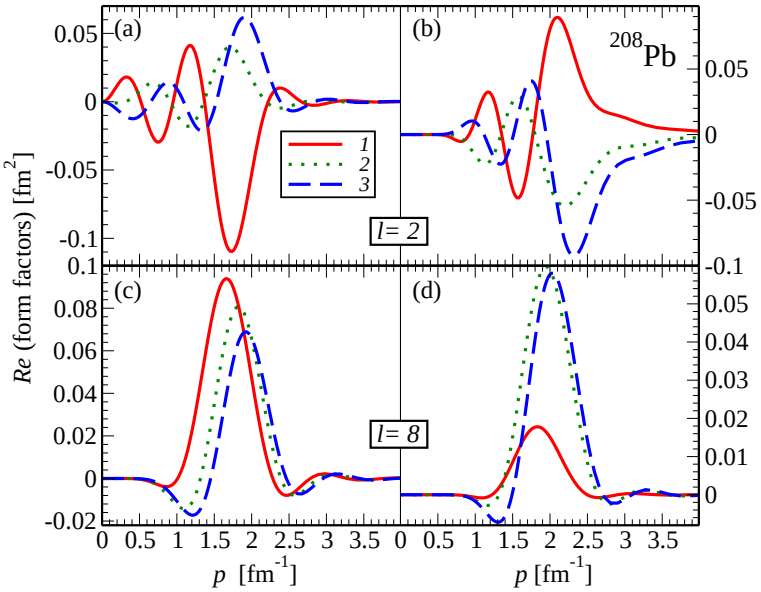

Figure 4: The real parts of the partial wave neutron form factors for ^{208}Pb as function of the momentum p for $l = 0$ (a) and $l = 8$ (c). The form factors are calculated at the first three energies indicated in Table 1 for the given angular momentum, $1 \equiv 21$ MeV, $2 \equiv 36$ MeV, and $3 \equiv 47$ MeV ($l = 2$) and 45 MeV ($l = 8$). The real parts of the proton form factors for ^{208}Pb as function of the momentum p are given for $l = 0$ in (b) and $l = 8$ in (d) for the same energies.

given in the left and right panels of Figs. 3 and 4 differ from each other.

4 Coulomb distorted neutron-nucleus form factors

In order to treat charged-particle scattering in momentum space without employing a screening procedure for the Coulomb force, it is necessary to formulate the scattering problem in a momentum space Coulomb basis. For proton-nucleus scattering, a two-body problem with a repulsive Coulomb force, the Coulomb distorted nuclear matrix elements are already derived in this bases, as described in the previous Section and Refs. [16, 37, 38]. When moving forward to (d, p) reactions, an effective three-body problem with two charged particles, one needs to solve generalized Faddeev–AGS equations in Coulomb basis, as was proposed in Ref. [6]. In order for this approach to be numerically practical, reliable techniques to calculate expectation values in this basis must exist. Here we evaluate the neutron-nucleus form factors from Section 2 in the Coulomb basis to illustrate the feasibility of the approach.

The starting point is the analytic expression for the Coulomb wave function in momentum space which, after a partial wave decomposition, can be written as (see [40] and Ref. [17])

$$\psi^C_{l,p}(q) \;=\; -\frac{2\pi\, e^{\eta\pi/2}}{pq}\,\lim_{\gamma\to+0}\,\frac{d}{d\gamma}\left\{\left[\frac{q^2-(p+i\gamma)^2}{2pq}\right]^{i\eta}\,(\zeta^2-1)^{-i\frac{\eta}{2}}\,Q_l^{i\eta}(\zeta)\right\}. \qquad (30)$$

Here, p is the magnitude of the fixed asymptotic momentum and $\zeta = (p^2+q^2+\gamma^2)/2pq$. The Sommerfeld parameter is given as $\eta = Z_1 Z_2 e^2 \mu/p$ where $Z_1 = 1$ and Z_2 corresponds to the number of protons in the nucleus, and μ is the reduced mass of the two-body system under consideration. The spherical function $Q_l^{i\eta}(\zeta)$ in Eq. (30) can be expressed in terms of hypergeometric functions ${}_2F_1$ [41].

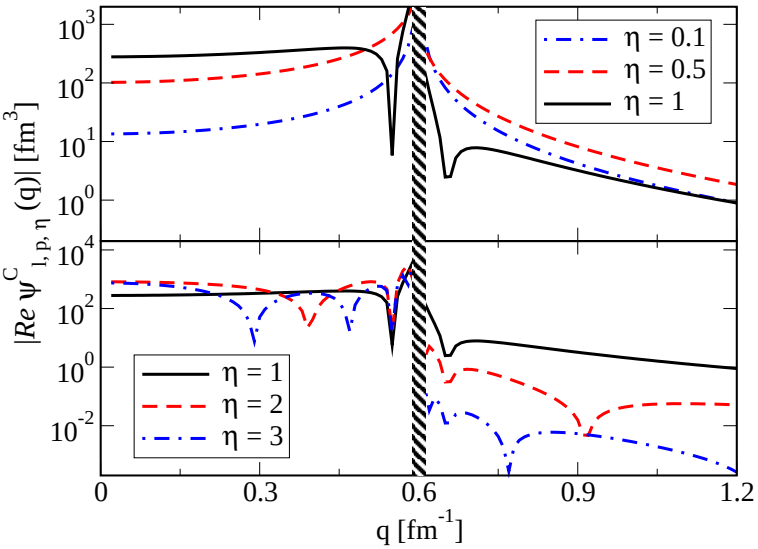

Figure 5: The absolute value of the real part of the $l = 0$ Coulomb wave function $\psi^C_{l,p,\eta}(p)$ for the external momentum $p = 0.6$ fm^{-1} and $\eta = 0.1, 0.5, 1$ (upper panel) and $\eta = 1, 3, 3$ (lower panel), as function of q. The shaded area masks the function around the singularity at $p \to q$, where it is highly oscillatory.

However, care must be taken in its evaluation, since there are specific limits of validity of the various expansions. Specific difficulties together with the expressions implemented in this work are discussed in detail in Refs. [17, 42].

In Fig. 5 we display $l = 0$ partial wave Coulomb functions for fixed external momentum $q = 0.6$ fm^{-1} as function of p for selected values of η. The functions exhibit oscillatory singular behavior for $p \to q$. This region is indicated in the figure by the shaded band. For values of $\eta \geq 1$ oscillatory behavior is already present way outside the singular region. It is also worthwhile to note that once the momentum p is larger than the external momentum q, the magnitude of the Coulomb function falls off by at least an order of magnitude.

For evaluating the neutron-nucleus form factors in the Coulomb basis, we start from the separable partial-wave t-matrix operator given in Eq. (7). Evaluating its momentum space matrix elements $\langle p|t_l(E)|p'\rangle$ in a plane-wave basis gives the nuclear form factors

$$\begin{aligned} \langle p|u|f_{l,k_E}\rangle &= t_l(p, k_E; E_{k_E}) \equiv u_l(p) \\ \langle f^*_{l,k_E}|u|p'\rangle &= t_l(p', k_E; E_{k_E}) \equiv u_l(p'), \end{aligned} \tag{31}$$

where the $t_l(p, k_E; E_{k_E})$ are the half-shell two-body t-matrices obtained as solution of a momentum space LS equation with the complex potential u.

The corresponding Coulomb-distorted form factors are obtained by replacing the plane-wave basis state by a Coulomb basis state $|\psi^C_{l,p}\rangle$ leading to

$$\langle \psi^C_{l,p}|u|f_{l,k_E}\rangle = \int_0^\infty \frac{dq\, q^2}{2\pi^2}\, u_l(q)\psi^C_{l,p}(q)^\star \equiv u^C_l(p) \tag{32}$$

$$\langle f^*_{l,k_E}|u|\psi^C_{l,p}\rangle = \int_0^\infty \frac{dq\, q^2}{2\pi^2}\, u_l(q)\ \psi^C_{l,p}(q) \equiv u^C_l(p)^\dagger \tag{33}$$

When $\eta \to 0$, Eqs. (32) and (33) tend to Eq. (31). This expression is a generalization of the form introduced in Ref. [6] to account for complex interactions.

The main challenge in computing the integrals of Eq. (32) and (33) is the oscilla-

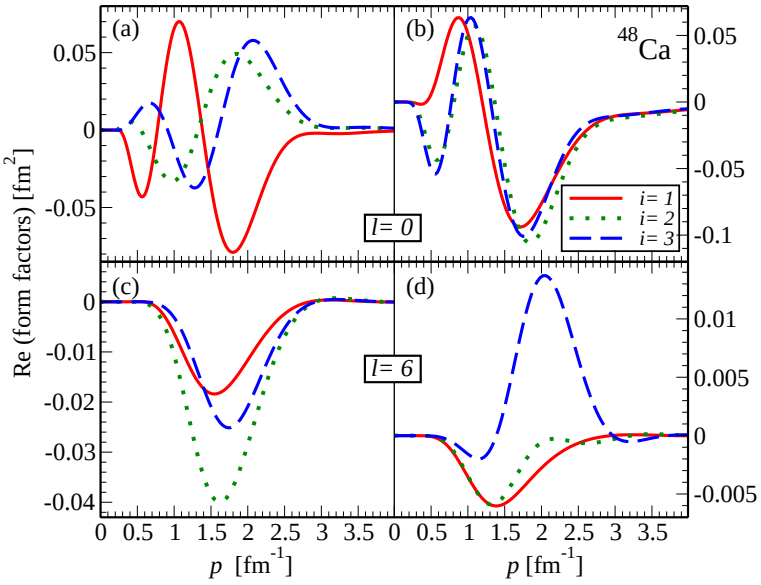

Figure 6: The real parts of the partial wave Coulomb distorted neutron form factors for ^{48}Ca as function of the momentum p for $l = 0$ (a) and $l = 6$ (c). The form factors are calculated at the energies indicated in Table 1 for the given angular momentum, $1 \equiv 6$ MeV, $2 \equiv 15$ MeV, and $3 \equiv 36$ MeV. The real parts of the proton form factors for ^{48}Ca as function of the momentum p are given for $l = 0$ in (b) and $l = 6$ in (d) for the energies given in Table 1.

tory singularity in the integrand for $q = p$, which is of the form

$$S(q-p) = \lim_{\gamma \to +0} \frac{1}{(q-p+i\gamma)^{1+i\eta}}. \tag{34}$$

This type of singularity cannot be numerically evaluated by the familiar principal value subtractions but rather needs to be treated using the scheme of Gel'fand and Shilov [43], as proposed by [6, 41]. The generalization to the complex form factors of our application is given in Ref. [17]. The essence of the Gel'fand and Shilov scheme is to subtract as many terms as needed of the Laurent expansion in a small region around the pole so that the oscillations around the pole become small, and the integral becomes regular. For further details of the calculations as well as numerical tests we refer to Ref. [17].

In order to illustrate the behavior of Coulomb distorted neutron form factors we show in Fig. 6 in the left panels the real parts of the Coulomb distorted neutron form factors of the $n + ^{48}$Ca t-matrix for $l = 0$ (a) and $l = 6$ (c) at the same support points as the plane-wave $n + ^{48}$Ca form factors shown in Fig. 3 and the Coulomb distorted $p + ^{48}$Ca form factors shown in the right panels. The effect of Coulomb distortions is clearly visible for $l = 0$, where the form factor goes to zero as $p \to 0$. The figure also shows that the Coulomb distorted neutron- and proton form factors are quite different.

In Fig. 7 a similar comparison is shown but for real parts of the Coulomb distorted $n + ^{208}$Pb and $p + ^{208}$Pb form factors. Drawing attention to the different scales for the left and right side panels, we note that the Coulomb distorted $p + ^{208}$Pb form factors do not only differ in shape, but also in magnitude from the Coulomb distorted $n + ^{208}$Pb form factors. This may not come as a surprise when having in mind that the Coulomb force is quite strong in heavy nuclei. The comparisons in Figs. 6 and 7 emphasize the need for a proper introduction of the Coulomb force in the EST scheme as presented in Section 3.

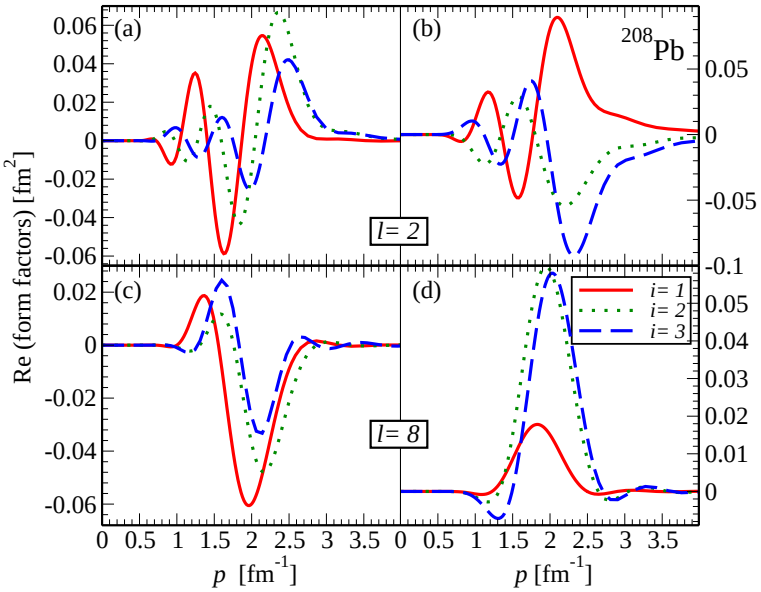

Figure 7: The real parts of the partial wave Coulomb distorted neutron form factors for ^{208}Pb as function of the momentum p for $l = 0$ (a) and $l = 8$ (c). The form factors are calculated at the first three energies indicated in Table 1 for the given angular momentum, $1 \equiv 21$ MeV, $2 \equiv 36$ MeV, and $3 \equiv 47$ MeV ($l = 2$) and 45 MeV ($l = 8$). The real parts of the proton form factors for ^{208}Pb as function of the momentum p are given for $l = 2$ in (b) and $l = 8$ in (d) for the same energies.

The realization that the Coulomb distorted neutron-nucleus form factors differ from the proton-nucleus ones has been already pointed out in Ref. [44] where separable t-matrices for proton-proton (pp) scattering were considered. There the authors used a separable representation in terms of Yukawa functions and re-adjusted the parameters in the two lowest partial wave to describe the experimentally extracted pp phase shifts. While such an approach may be viable in the pp system, it is not very practical when heavy nuclei are considered, since here many more partial waves are affected by the Coulomb force.

Finally, we want to inspect the Coulomb distorted form factor of Eq. (32) and consider an alternative way for its calculation in order to verify the quite involved integration procedure outlined in this Section and given in detail in Ref. [17]. The quantity $u|f_{l,k_E}\rangle$ satisfies an operator LS equation,

$$u|f_{l,k_E}\rangle = u|k_E\rangle + ug_0(E)u|f_{l,k_E}\rangle, \tag{35}$$

where $|k_E\rangle$ is the radial part of the solution of the free Hamiltonian at energy E with angular momentum l, and $g_0(E)$ is the free Green's function. Multiplying from the left with the Coulomb scattering wave function $\psi^c_{l,p}$ gives

$$\langle\psi^c_{l,p}|u|f_{l,k_E}\rangle = \langle\psi^c_{l,p}|u|k_E\rangle + \int dp' p'^2 \langle\psi^c_{l,p}|u|p'\rangle \frac{1}{E - E_{p'} + i\epsilon}\langle p'|u|f_{l,k_E}\rangle. \tag{36}$$

The term $\langle p'|u|f_{l,k_E}\rangle = t_l(p', k_E; E_{k_E})$ is the half-shell t-matrix at a support point E_{k_E} already calculated when obtaining the form factors for the separable representation

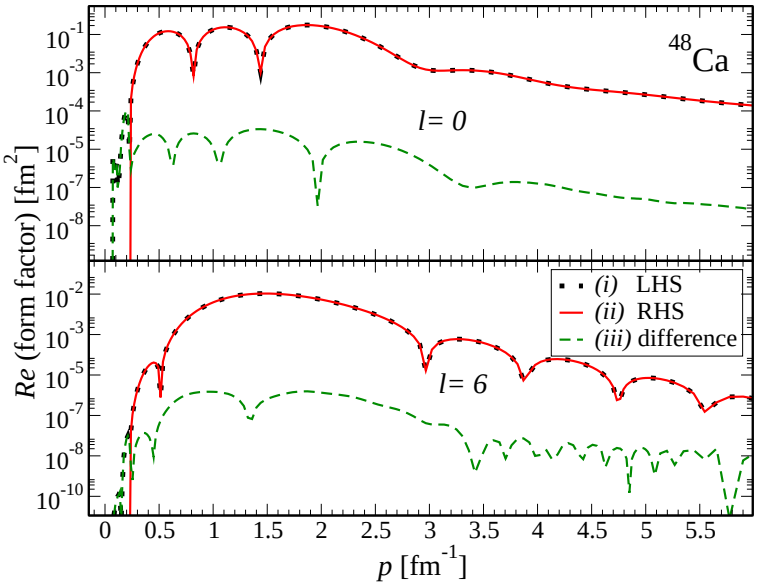

Figure 8: The absolute value of the real part of the partial-wave Coulomb distorted $n+^{48}$Ca for $l = 0$ (E=6 MeV) and $l = 6$ (E=16 MeV) as function of the momentum p. The dotted lines (i) represent the integration over the Coulomb wave functions, while the solid lines (ii) stands for the calculations according to right-hand side of Eq. (36). The absolute difference between the two calculation is shown as dashed line (iii).

(see Eq. (31)). It remains to calculate the driving term, which now is given as

$$\langle \Phi^c_{l,p'}|u|p\rangle\; r'^2 dr'\; \langle r'|u|r\rangle\; r^2 dr\; \langle r|p\rangle = \frac{2}{\pi p'} \int_0^\infty dr\, r^2\, dr'\, r'\, F_l(\eta', p'r')\; \langle r'|u|r\rangle\; j_l(pr), \quad (37)$$

which turns for the phenomenological Woods–Saxon potential into

$$\langle \Phi^c_{l,p'}|u|p\rangle = \frac{2}{\pi p'} \int_0^\infty dr\, r\, F_l(\eta', p'r)\; u^s(r)\; j_l(pr). \quad (38)$$

We now can evaluate the left-hand side (LHS) and the right-hand side (RHS) of Eq. (36) independently with two completely different algorithms. This comparison is shown in Fig. 8 for two different form factors for ^{48}Ca. For the $l = 0$ the form factor at $E = 6$ MeV is shown, for $l = 6$ the one at $E = 16$ MeV. The results of both independent calculations indistinguishable in the graph. Thus we show the absolute difference between the two calculations as dashed line. This shows that our numerical integration over the momentum-space Coulomb functions together with the Gel'fand-Shilov regularization is very accurate and can be used without any problem in Faddeev–AGS equations formulated in the Coulomb basis when matrix elements in this basis may only be obtained in this fashion.

5 Summary and Outlook

In a series of steps we developed the input that will serve as a basis for Faddeev–AGS three-body calculations of (d, p) reactions, which will not rely on the screening of the Coulomb force. To achieve this, Ref. [6] formulated the Faddeev–AGS equations in

the Coulomb basis using separable interactions in the two-body subsystems. For this ambitious program to have a chance of being successful, the interactions in the two-body subsystems, namely the NN and the neutron- and proton-nucleus systems, need to developed so that they separately describe the observables of the subsystems. While for the NN interaction separable representations are available, this is was not the case for the optical potentials describing the nucleon-nucleus interactions. Furthermore, those interactions in the subsystems need to be available in the Coulomb basis.

We developed separable representations of phenomenological optical potentials of Woods–Saxon type for neutrons and protons. First we concentrated on neutron-nucleus optical potentials and generalized the Ernst–Shakin–Thaler (EST) scheme [32] so that it can be applied to complex potentials [15]. In order to consider proton-nucleus optical potentials, we further extended the EST scheme so that it can be applied to the scattering of charged particles with a repulsive Coulomb force [16]. While the extension of the EST scheme to charged particles led to a separable proton-nucleus t-matrix in the Coulomb basis, we had to develop methods to reliably compute Coulomb distorted neutron-nucleus t-matrix elements [17]. Here we also show explicitly that those calculations can be carried out numerically very accurately by calculating them within two independent schemes.

Our results demonstrate, that our separable representations reproduce standard coordinate space calculations of neutron and proton scattering cross sections very well, and that we are able to accurately compute the integrals leading to the Coulomb distorted form factors. Now that these challenging form factors have been obtained, they can be introduced into the Faddeev–AGS equations to solve the three-body problem without resorting to screening. Our expectation is that solutions to the Faddeev–AGS equations written in the Coulomb-distorted basis can be obtained for a large variety of $n + p + A$ systems, without a limitation on the charge of the target. From those solutions, observables for (d, p) transfer reactions should be readily calculated. Work along these lines is in progress.

Acknowledgements

This material is based on work in part supported by the U.S. Department of Energy, Office of Science of Nuclear Physics under program No. DE-SC0004084 and DE-SC0004087 (TORUS Collaboration), under contracts DE-FG52-08NA28552 with Michigan State University, DE-FG02-93ER40756 with Ohio University; by Lawrence Livermore National Laboratory under Contract DE-AC52-07NA27344 and the U.T. Battelle LLC Contract DE-AC0500OR22725. F. M. Nunes acknowledges support from the National Science Foundation under grant PHY-0800026. This research used resources of the National Energy Research Scientific Computing Center, which is supported by the Office of Science of the U.S. Department of Energy under Contract No. DE-AC02-05CH11231.

References

[1] J. E. Escher *et al.*, Rev. Mod. Phys. **84**, 353 (2012).

[2] J. Cizewski *et al.*, J. Phys. Conf. Ser. **420**, 012058 (2013).

[3] R. Kozub *et al.*, Phys. Rev. Lett. **109**, 172501 (2012).

[4] F. Nunes and A. Deltuva, Phys. Rev. C **84**, 034607 (2011).

[5] K. Schmitt *et al.*, Phys. Rev. Lett. **108**, 192701 (2012).

[6] A. Mukhamedzhanov, V. Eremenko and A. Sattarov, Phys. Rev. C **86**, 034001 (2012).

[7] A. Deltuva, Phys. Rev. C **88**, 011601 (2013).

[8] A. Deltuva, A. Moro, E. Cravo, F. Nunes and A. Fonseca, Phys. Rev. C **76**, 064602 (2007); arXiv:0710.5933 [nucl-th] (2007).

[9] N. Upadhyay, A. Deltuva and F. Nunes, Phys. Rev. C **85**, 054621 (2012); arXiv:1112.5338 [nucl-th] (2011).

[10] A. Deltuva and A. Fonseca, Phys. Rev. C **79**, 014606 (2009).

[11] E. Alt, P. Grassberger and W. Sandhas, Nucl. Phys. B **2**, 167 (1967).

[12] A. Deltuva, A. Fonseca and P. Sauer, Phys. Rev. C **71**, 054005 (2005).

[13] A. Deltuva, A. Fonseca and P. Sauer, Phys. Rev. C **72**, 054004 (2005).

[14] F. M. Nunes and N. J. Upadhyay, J. Phys. Conf. Ser. **403**, 012029 (2012).

[15] L. Hlophe *et al.* (TORUS Collaboration), Phys. Rev. C **88**, 064608 (2013).

[16] L. Hlophe *et al.* (TORUS Collaboration), Phys. Rev. C **90**, 061602(R) (2014); arXiv:1409.4012 [nucl-th] (2014).

[17] N. Upadhyay *et al.* (TORUS Collaboration), Phys. Rev. C **90**, 014615 (2014).

[18] J. Haidenbauer and W. Plessas, Phys. Rev. C **27**, 63 (1983).

[19] J. Haidenbauer, Y. Koike and W. Plessas, Phys. Rev. C **33**, 439 (1986).

[20] G. Berthold, A. Stadler and H. Zankel, Phys. Rev. C **41**, 1365 (1990).

[21] W. Schnizer and W. Plessas, Phys. Rev. C **41**, 1095 (1990).

[22] D. Entem, F. Fernandez and A. Valcarce, J. Phys. G **27**, 1537 (2001).

[23] T. Ueda and Y. Ikegami, Prog. Theor. Phys. **91**, 85 (1994).

[24] A. Gal and H. Garcilazo, Nucl. Phys. A **864**, 153 (2011).

[25] A. Ghovanlou and D. R. Lehman, Phys. Rev. C **9**, 1730 (1974).

[26] A. Eskandarian and I. R. Afnan, Phys. Rev. C **46**, 2344 (1992).

[27] K. Miyagawa and Y. Koike, Prog. Theor. Phys. **82**, 329 (1989).

[28] R. Varner, W. Thompson, T. McAbee, E. Ludwig and T. Clegg, Phys. Rept. **201**, 57 (1991).

[29] S. Weppner, R. Penney, G. Diffendale and G. Vittorini, Phys. Rev. C **80**, 034608 (2009).

[30] A. Koning and J. Delaroche, Nucl. Phys. A **713**, 231 (2003).

[31] F. D. Becchetti, Jr. and G. Greenlees, Phys. Rev. **182**, 1190 (1969).

[32] D. J. Ernst, C. M. Shakin and R. M. Thaler, Phys. Rev. C **8**, 46 (1973).

[33] D. J. Ernst, J. T. Londergan, E. J. Moniz and R. M. Thaler, Phys. Rev. C **10**, 1708 (1974).

[34] B. Pearce, Phys. Rev. C **36**, 471 (1987).

[35] G. Cattapan, G. Pisent and V. Vanzani, Z. Phys. A **274**, 139 (1975).

[36] G. Cattapan, G. Pisent and V. Vanzani, Nucl. Phys. **A241**, 204 (1975).

[37] C. Elster, L. C. Liu and R. M. Thaler, J. Phys. G **19**, 2123 (1993).

[38] C. R. Chinn, C. Elster and R. M. Thaler, Phys. Rev. C **44**, 1569 (1991).

[39] M. Abramovitz and I. Stegun, *Handbook of mathematical functions. Dover books on mathematics*. Dover, New York, 1965).

[40] A. Mukhamedzhanov, *private communication* (2012).

[41] E. Dolinskii and A. Mukhamedzhanov, Sov. Jour. Nucl. Phys. **3**, 180 (1966).

[42] V. Eremenko *et al.* (TORUS Collaboration), *to appear in Comp. Phys. Comm.*

[43] I. Gel'fand and G. Shilov, *Generalized functions. Vol. 1. Properties and operations.* Academic Press, 1964.

[44] W. Schweiger, W. Plessas, L. Kok and H. van Haeringen, Phys. Rev. C **27**, 515 (1983).

Three-Nucleon Calculations within the Bethe–Salpeter Approach with Rank-One Separable Kernel

S. G. Bondarenko[a], V. V. Burov[a] and S. A. Yurev[a,b]

[a] *Joint Institute for Nuclear Research, Dubna, 141980, Russia*
[b] *Far Eastern Federal University, Vladivostok, 690950, Russia*

Abstract

Relativistic properties of a three-nucleon system are investigated using the Bethe–Salpeter approach. A system of integral Faddeev-type equations for the three-particle system amplitudes is obtained. The nucleon-nucleon interaction is chosen to be in a separable form. The Gauss quadrature method for solving the integral system of equations is considered. The binding energy and the partial-wave amplitudes ($^1S_0$ and $^3S_1$) of the triton are found by solving the system of the integral equations.

Keywords: *Bethe–Salpeter approach; three-nucleon system; Faddeev equation*

Introduction

Three-body calculations in nuclear physics are very interesting for describing three-nucleon bound states (^{3}He, T), processes of elastic, inelastic and deep inelastic scattering of leptons by light nuclei and also the hadron-deuteron reactions (for example, $pd \to pd$, $pd \to ppn$). The study of the ^{3}He and T nuclei is also interesting because it allows us to investigate a further (in addition to the deuteron) evolution of a bound nucleon thereby contributing to the explanation of the so-called EMC-effect.

Faddeev equations are used in quantum mechanics to describe three-particle systems. The main feature of Faddeev equations is that all three particles interact through a pair potential. We are interested in reactions at high momentum transfer where the relativistic methods should be used. One of such methods is the Bethe–Salpeter (BS) approach. The relativistic analog of the Faddeev equations can be considered in the BS formalism.

In this paper, all nucleons have equal masses. The scalar propagators instead of the spinor ones are used also for simplicity. The spin and isospin structure of the nucleons is taken into account by using the so-called recoupling-coefficient matrix. The work mainly follows the ideas of Ref. [1].

The paper is organized as follows. A two-particle problem is considered in Section 1 and Section 2 is devoted to three-particle equations. In Section 3 we present the calculations and results. The summary is given in Section 4.

1 Two-particle case

Since the formalism of the Faddeev equations is based on properties of the pair nucleon-nucleon interaction, here only some conclusions from the two-body problem

Proceedings of the International Conference 'Nuclear Theory in the Supercomputing Era — 2014' (NTSE-2014), Khabarovsk, Russia, June 23–27, 2014. Eds. A. M. Shirokov and A. I. Mazur. Pacific National University, Khabarovsk, Russia, 2016, p. 125.

http://www.ntse-2014.khb.ru/Proc/Yurev.pdf.

Table 1: Parameters λ and β for the ${}^1S_0$ and ${}^3S_1$ partial-wave states.

	${}^1S_0$	${}^3S_1$
λ (GeV^4)	-1.12087	-3.15480
β (GeV)	0.287614	0.279731

are given.

The Bethe–Salpeter equation for a relativistic two-particle system is written in the following form:

$$T(p,p';s) = V(p,p') + \frac{i}{4\pi^3}\int d^4k\, V(p,k)\, G(k;s)\, T(k,p';s), \tag{1}$$

where $T(p,p';s)$ is the two-particle T matrix and $V(p,p')$ is the kernel (potential) of the nucleon-nucleon interaction. The free two-particle Green's function $G(k;s)$ is expressed, for simplicity, thought the scalar propagator of the nucleons:

$$G^{-1}(k;s) = \big[(P/2+k)^2 - m_N^2 + i\epsilon\big]\big[(P/2-k)^2 - m_N^2 + i\epsilon\big]. \tag{2}$$

To solve Eq. (1), the separable *ansatz* for the nucleon-nucleon potential $V(p,p')$ is used (rank-one):

$$V(p_0,p,p_0',p') = \lambda\, g(p_0,p)\, g(p_0',p'). \tag{3}$$

In this case the two-particle T matrix has the following simple form:

$$T(p_0,p,p_0',p';s) = \tau(s)\, g(p_0,p)\, g(p_0',p'), \tag{4}$$

where

$$\tau(s) = \left[\lambda^{-1} - \frac{i}{4\pi^3}\int_{-\infty}^{\infty} dk^0 \int_0^{\infty} k^2 dk\, g^2(k^0,k)\, G(k^0,k;s)\right]^{-1}. \tag{5}$$

As the simplest assumption, the relativistic *Yamaguchi*-type form factor $g_Y(p_0,p)$ is used,

$$g_Y(p_0,p) = \frac{1}{-p_0^2 + p^2 + \beta^2}, \tag{6}$$

with parameters λ and β chosen to describe the experimental data. The values of the parameters are given in Table 1.

To calculate the scattering phase shifts of proton-neutron elastic collisions, the following parametrization of the on-mass-shell T matrix is used:

$$T_L(\bar{p}) = T_L(0,\bar{p},0,\bar{p};s) = \frac{-8\pi\sqrt{s}}{\bar{p}}\, e^{i\delta_L(\bar{p})} \sin\delta_L(\bar{p})$$

with $\delta_L(\bar{p})$ being the scattering phase shifts and $\bar{p} = \sqrt{s/4 - m_N^2} = \sqrt{\frac{1}{2} m_N T_{lab}}$. The calculated scattering phase shifts together with the experimental data are shown in Fig. 1. The results of calculations of the low-energy parameters and properties of the bound state (deuteron) are given in Table 2 together with the experimental data from Ref. [3].

As it seen from Table 2, the properties of low-energy proton-neutron scattering in the ${}^1S_0$ and ${}^3S_1$ partial waves and the deuteron binding are in a satisfactory agreement with the experimental data. However, as is seen in Fig. 1, the scattering phase shifts describe the experiment up to $T_{lab} = 100{-}120$ MeV only. This disadvantage is due to the simplest rank-one choice of the nucleon-nucleon kernel.

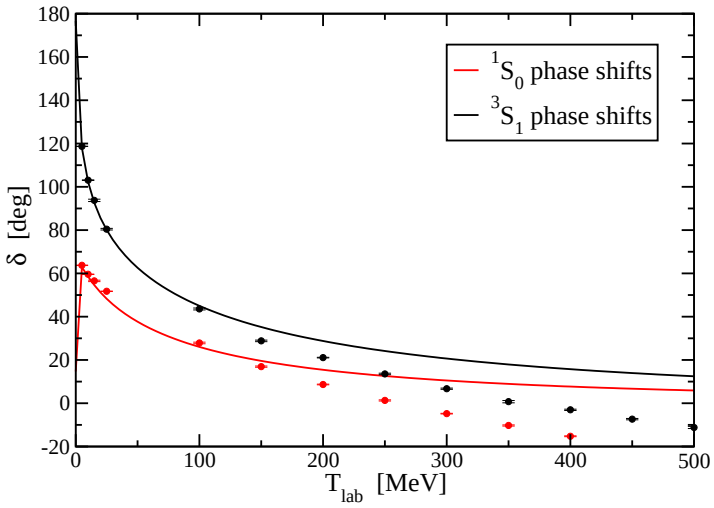

Figure 1: Scattering phase shifts for the relativistic Yamaguchi-type form factors. The experimental data are taken from Ref. [2]

Table 2: The scattering length a_0, the effective range r_0 and the deuteron binding energy E_d for the ${}^1S_0$ and ${}^3S_1$ partial waves.

	${}^3S_1$	experiment	${}^1S_0$	experiment
a_0 (fm)	5.424	5.424(4)	−23.748	−23.748(10)
r_0 (fm)	1.775	1.759(5)	2.75	2.75(5)
E_d (MeV)	2.2246	2.224644(46)		

2 Three-particle case

A three-particle system can be described by the Faddeev equations

$$\begin{bmatrix} T^{(1)} \\ T^{(2)} \\ T^{(3)} \end{bmatrix} = \begin{bmatrix} T_1 \\ T_2 \\ T_3 \end{bmatrix} - \begin{bmatrix} 0 & T_1G_1 & T_1G_1 \\ T_2G_2 & 0 & T_2G_2 \\ T_3G_3 & T_3G_3 & 0 \end{bmatrix} \begin{bmatrix} T^{(1)} \\ T^{(2)} \\ T^{(3)} \end{bmatrix}, \tag{7}$$

where the full matrix $T = \sum_{i=1}^{3} T^{(i)}$, G_i is the two-particle (j and n) Green's function [ijn is cyclic permutation of (1,2,3)],

$$G_i(k_j, k_n) = \frac{1}{(k_j^2 - m_N^2 + i\epsilon)(k_n^2 - m_N^2 + i\epsilon)}, \tag{8}$$

and T_i is the two-particle T matrix which can be written as

$$T_i(k_1, k_2, k_3; k_1', k_2', k_3') = (2\pi)^4\, \delta^{(4)}(K_i - K_i')\, T_i(k_j, k_n; k_j', k_n'). \tag{9}$$

For the system of equal-mass particles, the Jacobi momenta can be written as

$$p_i = \frac{1}{2}(k_j - k_n), \quad q_i = \frac{1}{3}K - k_i, \quad K = k_1 + k_2 + k_3. \tag{10}$$

Using expressions (10), Eq. (7) can be rewritten as

$$T^{(i)}(p_i, q_i; p_i', q_i'; s) = (2\pi)^4\, \delta^{(4)}(q_i - q_i')\, T_i(p_i; p_i'; s)$$
$$- i \int \frac{dp_i''}{(2\pi)^4}\, T_i(p_i; p_i''; s)\, G_i(k_j'', k_n'') \left[T^{(j)}(p_j'', q_i''; p_i', q_i'; s) + T^{(n)}(p_i'', q_i''; p_i', q_i'; s)\right]. \tag{11}$$

For the three-particle bound state it is suitable to introduce an amplitude

$$\Psi^{(i)}(p_i, q_i; s) = \langle p_i, q_i | T^{(i)} | M_B \rangle, \tag{12}$$

where $M_B = \sqrt{s} = 3m_N - E_B$ is the mass of the bound state (triton) and $s = K^2$ is the total momentum squared. Assuming the orbital angular momenta in the triton to be equal to zero ($l_p = l_q = 0$), only two partial-wave states ($^1S_0$ and $^3S_1$) should be taken into account. In the case of the two-particle T matrix in the separable form (4), the amplitude of the triton becomes

$$\Psi^{(i)}(p, q; s) = \sum_{j=1,2} g_j(p)\, \tau_j(s)\, \Phi_j(q; s), \tag{13}$$

where $j = 1(^1S_0), 2(^3S_1)$. The functions $\Phi_j(q)$ satisfy the following system of integral equations:

$$\Phi_j(q_0, q; s) = \sum_{j'} \frac{i}{4\pi^3} \int dq'_0 \int q'^2 dq' \times Z_{jj'}(q_0, q, q'_0, q'; s)\, \frac{\tau_{j'}\left[(\frac{2}{3}\sqrt{s} + q'_0)^2 - q'^2\right]}{\left(\frac{1}{3}\sqrt{s} - q_0\right)^2 - q'^2 - m_N^2 + i\epsilon}\, \Phi_{j'}(q'_0, q'; s). \tag{14}$$

The so-called effective energy-dependent potential Z is

$$Z_{jj'}(q_0, q, q'_0, q'; s) = C_{jj'} \int_{-1}^{1} d(cos\vartheta_{qq'}) \times \frac{g_j\left(-\frac{1}{2}q_0 - q'_0, |-\frac{1}{2}\mathbf{q} - \mathbf{q}'|\right) g_{jj'}\left(q_0 + \frac{1}{2}q'_0, |\mathbf{q} + \frac{1}{2}\mathbf{q}'|\right)}{\left(\frac{1}{3}\sqrt{s} + q_0 + q'_0\right)^2 - (\mathbf{q} + \mathbf{q}')^2 - m_N^2 + i\epsilon}, \tag{15}$$

where $C_{jj'}$ is the spin and isospin recoupling-coefficient matrix:

$$C_{jj'} = \begin{bmatrix} \frac{1}{4} & -\frac{3}{4} \\ -\frac{3}{4} & \frac{1}{4} \end{bmatrix}. \tag{16}$$

The system of integral equations (14)–(15) has a number of singularities, namely:

- poles from the one-particle propagator:

$$q'^0_{1,2} = \frac{1}{3}\sqrt{s} \mp [E_{|\mathbf{q}'|} - i\epsilon];$$

- poles from the propagator in the Z-function:

$$q'^0_{3,4} = -\frac{1}{3}\sqrt{s} - q^0 \pm [E_{|\mathbf{q}'+\mathbf{q}|} - i\epsilon];$$

- poles from the Yamaguchi-functions:

$$q'^0_{5,6} = -2q^0 \pm 2[E_{|\frac{1}{2}\mathbf{q}'+\mathbf{q}|,\beta} - i\epsilon]$$

and

$$q'^0_{7,8} = -\frac{1}{2}q^0 \pm \frac{1}{2}[E_{|\mathbf{q}'+\frac{1}{2}\mathbf{q}|,\beta} - i\epsilon];$$

- cuts from the two-particle propagator τ:

$$q'^0_{9,10} = \pm\sqrt{q'^2 + 4m_N^2} - \frac{2}{3}\sqrt{s} \quad \text{and} \quad \pm\infty;$$

- poles from the two-particle propagator τ:

$$q'^0_{11,12} = \pm\sqrt{q'^2 + 4M_d^2} - \frac{2}{3}\sqrt{s}.$$

However in the case of the bound three-particle system ($\sqrt{s} \leq 3m_N$), all above singularities do not cross the path of integration over q_0 and thus do not affect the Wick rotation procedure $q_0 \to iq_4$. Therefore Eqs. (14)–(15) become:

$$\Phi_j(q_4, q; s) = -\frac{1}{4\pi^3}\sum_{j'=1}^{2}\int_{-\infty}^{\infty} dq'_4 \int_0^{\infty} q^{'2} dq' \times Z_{jj'}(iq_4, q; iq'_4, q'; s)\, \frac{\tau_{j'}\left[(\frac{2}{3}\sqrt{s} + iq'_4)^2 - q^{'2}\right]}{\left(\frac{1}{3}\sqrt{s} - iq'_4\right)^2 - q^{'2} - m_N^2}\, \Phi_{j'}(q'_4, q'; s) \quad (17)$$

and

$$Z_{jj'}(q_4, q; q'_4, q'; s) = C_{jj'}\int_{-1}^{1} d(cos\vartheta_{qq'}) \times \frac{g_j\left(-\frac{1}{2}q^0 - q^{0'}, |\frac{1}{2}\mathbf{q} + \mathbf{q}'|\right) g_j\left(q^0 + \frac{1}{2}q^{0'}, |\mathbf{q} + \frac{1}{2}\mathbf{q}'|\right)}{\left(\frac{1}{3}\sqrt{s} + q^0 + q^{0'}\right)^2 - (|\mathbf{q} + \mathbf{q}'|)^2 - m_N^2}. \quad (18)$$

Various methods can be used to solve Eqs. (17)–(18). One of them is discussed in the next section.

3 Solution and results

In order to solve the system of integral equations, the Gaussian quadrature method is used. The integration variables q $[0, \infty)$ and q_4 $(-\infty, \infty)$ are mapped to the $[-1, 1]$ interval. The quadrature method replaces integrals by sums and transforms the system of homogeneous linear integral equations to a system of algebraic equations. These equations can be solved using FORTRAN codes.

The method can be presented schematically as

$$f(x) = \int A(x, y)\, f(y) \to f(x_i) = \sum_{j=1,n} A(x_i, y_j)\, w_j\, f(y_j),$$

where x_i, y_j and w_j are the Gauss points and weights and n is the number of points. The homogeneous system of linear equations takes the form

$$M\phi = 0$$

with $M_{ij} \equiv A_{ij} - \delta_{ij}$ and $\phi_i = f(x_i)$; $i, j = 1, 2, \ldots, n$. This system of equations has a solution if the determinant of the matrix is equal to zero. This condition is satisfied at the binding energy of the three-nucleon system:

$$\det M(s) = 0 \quad \text{at} \quad \sqrt{s} = 3m_N - E_B.$$

The result of calculations ($n = 15$) for the binding energy is $E_B = 11.09$ MeV which should be compared to the experimental value of 8.48 MeV. The difference can be explained by the simplicity of the rank-one separable kernel of the nucleon-nucleon interaction.

The obtained partial-wave amplitudes are shown in Figs. 2–4. The imaginary parts of the amplitudes arise as a pure relativistic effect which does not appears in nonrelativistic Faddeev equations.

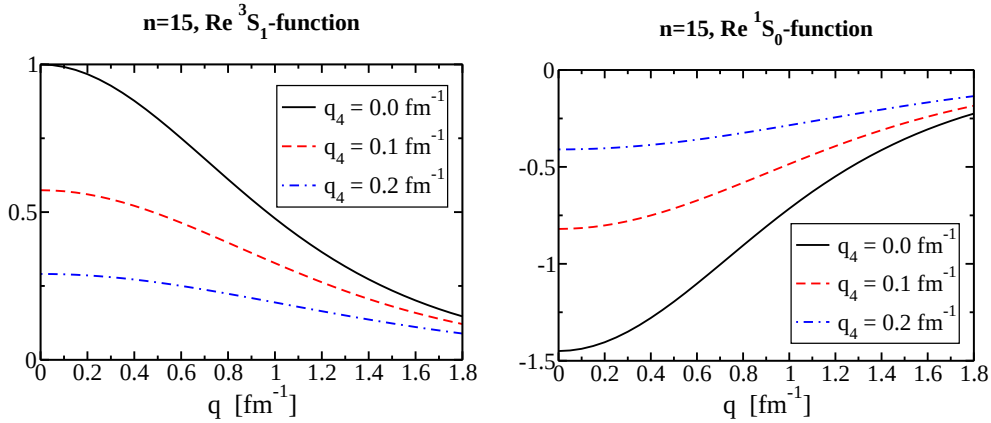

Figure 2: Real parts of the $^3S_1$ (left) and $^1S_0$ (right) amplitudes as functions of q at various q_4 values.

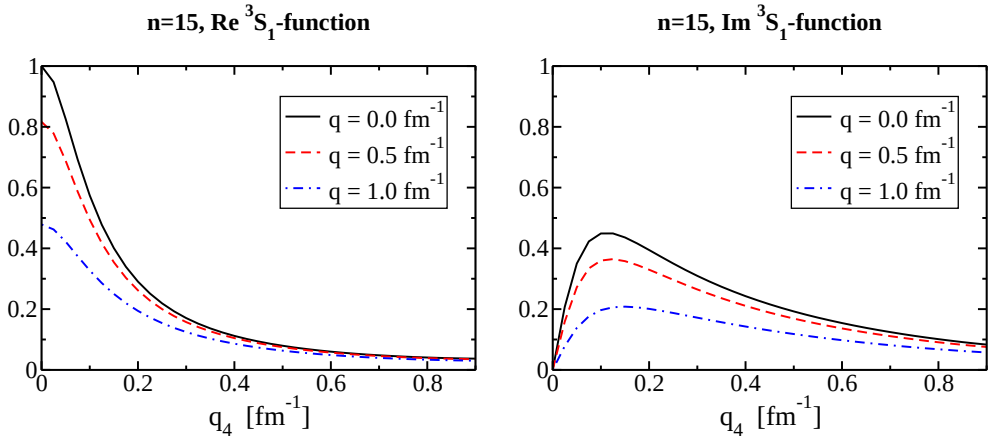

Figure 3: Real (left) and imaginary (right) parts of the $^3S_1$ amplitude as functions of q_4 at various q values.

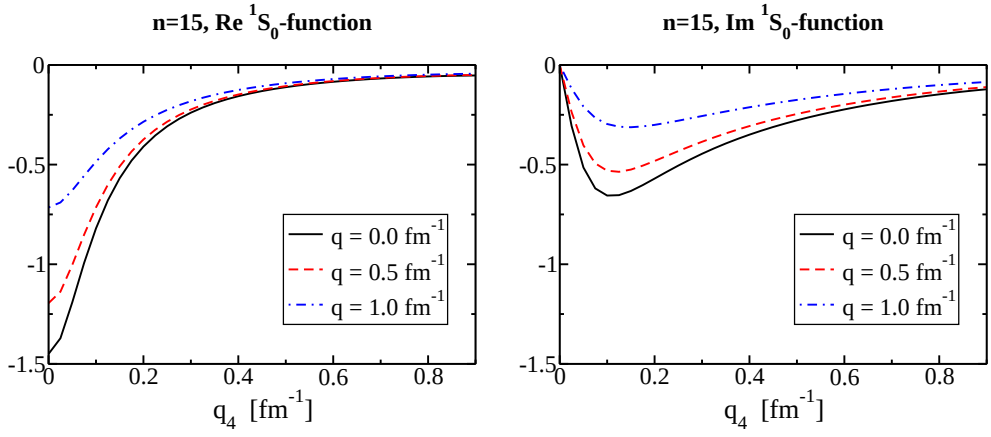

Figure 4: Real (left) and imaginary (right) parts of the $^1S_0$ amplitude as functions of q_4 at various q values.

4 Summary

In this paper a three-body system in the Bethe–Salpeter approach is investigated. A rank-one separable nucleon-nucleon interaction is utilized. The form factor is chosen in the form of a relativistic generalization of the Yamaguchi-type function. The parameters of the nucleon-nucleon potential in the ${}^1S_0$ and ${}^3S_1$ partial waves reproduce low-energy scattering parameters and deuteron properties as well as the phase shifts up to the laboratory energy of 100–120 MeV.

The Faddeev equations for the triton wave functions considered in the BS formalism are solved using the Gauss quadrature method. The triton binding energy and amplitudes of the ${}^1S_0$ and ${}^3S_1$ partial-wave states are calculated.

The triton binding energy is essentially overestimated. To improve the results, the rank of the separable kernel should be increased. Other partial waves, the P and D waves in particular, and the spinor propagators for nucleons should be also taken into account.

References

[1] G. Rupp and J. A. Tjon, Phys. Rev. C **37**, 1729 (1988).

[2] R. Arndt *et al.*, Rhys. Rev. D **28**, 97 (1983).

[3] O. Dumbrajs *et al.*, Nucl. Phys. B **216**, 277 (1983).

Problems of Theoretical Interpretation of COLTRIMS Results on Ionization of Helium by Fast Bare-Ion Impact

Konstantin A. Kouzakov

Department of Nuclear Physics and Quantum Theory of Collisions, Faculty of Physics, Lomonosov Moscow State University, Moscow 119991, Russia

Abstract

In a series of recent papers, the authors argued that the experimental resolution is responsible only for a part of the marked discrepancies between theory and experiment in the COLTRIMS studies on ion-impact ionization of helium. They also pointed out that the respective theoretical treatments based on time-independent scattering theory lack account for effects of the projectile coherence, which potentially can resolve the remaining disagreement. It is shown by means of time-dependent scattering theory that the projectile-coherence effects have no impact on the cross section, in contrast to those due to the target coherence. The results and conclusions of the usual time-independent formulation remain unaltered both in the case of the first-order approximation and in the case of higher-order approximations for the on-shell T-matrix.

Keywords: *Ion-impact ionization; COLTRIMS; projectile coherence*

1 Introduction

Ionization processes in collisions of charged projectiles with atomic systems are of fundamental importance for the physics of interaction of particles and radiations with matter. The basic theory of such processes in the case of fast ionic projectiles is well established (see, for instance, the textbooks [1–4]). In particular, it is expected that at[1] $|Z_p|/v_p \ll 1$, where Z_p and v_p are the projectile charge and velocity, respectively, the perturbation theory should be well applicable. The emergence of the cold-target-recoil-ion-momentum spectroscopy (COLTRIMS) [5, 6] made it possible to measure fully differential cross sections (FDCS) for the ionizing ion-atom collisions with high precision, thus providing a new, very stringent test of the theory. In this context, a theoretical explantation of the COLTRIMS results on singly ionizing 100 Mev/u C^{6+} + He ($Z_p/v_p \approx 0.10$) [7] and 1 Mev/u H^+ + He ($Z_p/v_p \approx 0.16$) [8] collisions at small momentum transfer presents a real challenge. Specifically, so far none of well-known approaches has been able to obtain a reasonable agreement with the measured electron angular distributions in a P-plane that contains the projectile momentum but is perpendicular to the scattering plane. At the same time, all approaches reasonably explain the experimental data for the scattering plane (see, for instance, Ref. [9] and references therein).

The discrepancies between theory and experiment in the 100 Mev/u C^{6+} + He case [7] were attributed in Ref. [10] to experimental uncertainties of the measurements

[1] Atomic units (a.u.) in which $\hbar = e = m_e = 1$ are used throughout unless otherwise stated.

Proceedings of the International Conference 'Nuclear Theory in the Supercomputing Era — 2014' (NTSE-2014), Khabarovsk, Russia, June 23–27, 2014. Eds. A. M. Shirokov and A. I. Mazur. Pacific National University, Khabarovsk, Russia, 2016, p. 132.

http://www.ntse-2014.khb.ru/Proc/Kouzakov.pdf.

which are due to a finite energy and angle resolution, as well as to a velocity spread of the He gas atoms in a supersonic jet caused by its nonzero temperature. However, this explanation was later refuted in Ref. [11] where the experimental data of Ref. [7] were analyzed with a Monte Carlo event generator based on quantum theory. Later, in a series of papers [12–14], it was argued that the experimental resolution can explain only part (less than 50% [14]) of the discrepancies between theory and experiment in the C^{6+} problem. It was further suggested that the remaining part of the discrepancies can be attributed to the so-called projectile coherence. The first statement is relevant to the FWHM values in the discussed measurements [7]. Since this issue concerns the particular experimental method and procedures, it is beyond the scope of the theoretical analysis. Therefore, the present contribution is focused on the second statement that attributes the discrepancies to the projectile-coherence effects.

As formulated in Ref. [13], in analogy to classical optics and in accordance with Huygens' principle, the projectile transverse coherence length is given by $\Delta r \approx \lambda L/2a$, where a and L are the width of the collimating slit and its distance to the target, respectively, and λ is the de Broglie wavelength of the projectile. If the projectile coherence length is larger than the spatial extent of the target (i. e., of the He atom), the projectile is coherent and incoherent otherwise. For example, the transverse coherence length of the projectile beam in the 100 Mev/u $C^{6+} + He$ experiment [7] was estimated as $\Delta r \approx 10^{-3}$ a.u. [13] thus suggesting that the C^{6+} projectiles were strongly incoherent in that experiment. This fact has a very important consequence, namely that the conventional time-independent formulation of quantum scattering theory is not applicable in the C^{6+} case. Indeed, this formulation follows from the nonstationary one, which treats time-dependent scattering of wave packets under an assumption that the colliding wave packets are sufficiently well delocalized (localized) in coordinate (momentum) space [3, 4].

In this contribution, it is analyzed and discussed, using an approach based on time-dependent quantum scattering theory, how the properties of the projectile wave packet can alter the conclusions of conventional time-independent treatments for the discussed COLTRIMS experiments. The paper is organized as follows. Section 2 delivers a general theoretical formulation in terms of projectile and target wave packets. Then, in Section 3, basic approximations for the on-shell T-matrix are presented. In Section 4, the wave-packet effects are analyzed and discussed. Finally, conclusions are drawn in Section 5.

2 General theory

Suppose the initial state of the ionic projectile in momentum space, as it is prepared in a COLTRIMS experiment, to be given by the wave packet $\Phi_p(\mathbf{q}_p)$, whereas that of the He atomic target to be given by $\Phi_T(\mathbf{q}_T)$. Then, according to the time-dependent scattering theory, the FDCS corresponding to the discussed experimental situation [7, 8] where only the momenta of ejected electron $\mathbf{k}_e$ and recoil He^+ ion $\mathbf{k}_I$ are measured while the final projectile momentum remains undetermined, is evaluated as [15]

$$d\sigma = \frac{d\mathbf{k}_e}{(2\pi)^3}\,\frac{d\mathbf{k}_I}{(2\pi)^3}\int\frac{d\mathbf{q}_p}{(2\pi)^3}\int\frac{d\mathbf{q}_T}{(2\pi)^3}\,\frac{2\pi}{v_z(\mathbf{q}_p)}\,\delta\big(E_e + I_1 - \mathbf{v}(\mathbf{q}_p)\cdot\mathbf{Q}(\mathbf{q}_T)\big) \times |\mathcal{T}_{fi}|^2|\Phi_p(\mathbf{q}_p)|^2|\Phi_T(\mathbf{q}_T)|^2, \quad (1)$$

where

$$\mathbf{Q}(\mathbf{q}_T) = \mathbf{k}_e + \mathbf{k}_I - \mathbf{q}_T$$

is the momentum-transfer function,

$$\mathbf{v}(\mathbf{q}_p) = c\,\mathbf{q}_p \Big/ \sqrt{q_p^2 + M_p^2c^2}$$

is the projectile velocity function, and $v_z(\mathbf{q})$ is its projection onto the direction of the mean projectile momentum,

$$\int \frac{d\mathbf{q}_p}{(2\pi)^3}\, \mathbf{q}_p |\Phi_p(\mathbf{q}_p)|^2 = \mathbf{k}_p. \tag{2}$$

The δ function in Eq. (1) reflects energy conservation. In its argument, kinetic energies of the target and recoil ion are neglected compared both to the electron kinetic energy E_e and to the ionization potential I_1, and the energy-transfer function $T(\mathbf{q}_p, \mathbf{q}_T)$ is approximated as follows:

$$T(\mathbf{q}_p, \mathbf{q}_T) = c\sqrt{\mathbf{q}_p^2 + M_p^2 c^2} - c\sqrt{\left[\mathbf{q}_p - \mathbf{Q}(\mathbf{q}_T)\right]^2 + M_p^2 c^2} \approx \mathbf{v}(\mathbf{q}_p) \cdot \mathbf{Q}(\mathbf{q}_T). \tag{3}$$

If the wave packets Φ_p and Φ_T are sufficiently well peaked about the respective mean momenta $\mathbf{k}_p$ and $\mathbf{k}_T$, the on-shell T-matrix $\mathcal{T}_{fi}$ and the functions $\mathbf{v}(\mathbf{q}_p)$ and $v_z(\mathbf{q}_p)$ in the integrand of (1) are accurately approximated by their values taken at these mean momenta. The remaining integrations over $\mathbf{q}_p$ and $\mathbf{q}_T$ then disappear as the normalization integrals for Φ_p and Φ_T [3]. As a result, the FDCS is given by [9]

$$\frac{d^3\sigma}{dE_e d\Omega_e d\Omega_p} = \frac{k_e E_p'^2}{(2\pi)^5 c^4} \frac{k_p'}{k_p} |\mathcal{T}_{fi}|^2, \tag{4}$$

where E_p' and k_p' are the final projectile energy and momentum. It should be noted that the condition of the well localized wave packets in momentum space is usually supposed to be met in scattering experiments. If for some reason it is not the case, one should take into account the wave-packet effects in the corresponding theoretical treatment.

3 Basic approximations for T-matrix

Collisions of fast charged particles with atomic systems are usually treated to the lowest order in projectile-target interaction. The nonrelativistic lowest-order perturbation amounts to the first Born approximation (FBA) and results for the on-shell T-matrix in [1]

$$\mathcal{T}_{fi}^{\mathrm{FBA}} = \frac{4\pi Z_p}{Q^2}\, \rho_{fi}(\mathbf{Q}), \tag{5}$$

with Z_p being the projectile charge and

$$\rho_{fi}(\mathbf{Q}) = \langle \Psi_f | \sum_{j=1}^{2} e^{i\mathbf{Q}\cdot\mathbf{r}_j} | \Psi_i \rangle,$$

where $\Psi_{i(f)}$ is the ground-state (final-state) wave function of He.

Effects beyond the FBA are typically estimated within the second Born approximation (SBA). For the present case, it takes the form

$$\mathcal{T}_{fi}^{\mathrm{SBA}} = \mathcal{T}_{fi}^{\mathrm{FBA}} + \delta\mathcal{T}_{fi}^{\mathrm{SBA}}, \tag{6}$$

where the SBA contribution evaluates as [9]

$$\delta\mathcal{T}_{fi}^{\mathrm{SBA}} = \sum_n \int \frac{d^3p}{(2\pi)^3} \frac{4\pi Z_p}{(\mathbf{Q}-\mathbf{p})^2} \frac{4\pi Z_p}{p^2} \frac{\left[\rho_{fn}(\mathbf{Q}-\mathbf{p}) - 2\delta_{fn}\right]\left[\rho_{ni}(\mathbf{p}) - 2\delta_{ni}\right]}{\mathbf{v}_p \cdot \mathbf{p} + \varepsilon_i - \varepsilon_n + i0}. \tag{7}$$

Here the sum over n runs over all helium states with energies ε_n, the terms $\sim v_p p^2/k_p$ are neglected in the denominator of the Green's function in the integrand.

The projectile–target nucleus interaction plays no role in FBA which assumes a single collision between the projectile and the ejected electron and treats the initial and final projectile's states as plane waves. It can be taken into account within the distorted-wave Born approximation (DWBA) [3]. To construct the distorted waves, one can involve the straight line or eikonal approximation that proved to be very useful in treatments of near-forward scattering of particles with short de Broglie wavelength. Neglecting the change in the projectile velocity, that is, $\mathbf{v}_p = \mathbf{v}'_p$, and assuming the z axis to be directed along the incident projectile momentum, one gets [9]

$$\mathcal{T}_{fi}^{\mathrm{DWBA}} = \int d^2b\, (v_p b)^{2i\eta} \int \frac{d^2q}{(2\pi)^2}\, e^{i\mathbf{q}\cdot\mathbf{b}}\, \mathcal{T}_{fi}^{\mathrm{FBA}}(\mathbf{Q}-\mathbf{q}), \tag{8}$$

where $\mathbf{b}$ can be viewed as an impact parameter vector, Z_T is the (effective) charge of the target nucleus, $\eta = Z_p Z_T / v_p$ is the Sommerfeld parameter, and $\mathbf{q}$ is perpendicular to the z axis. The $\mathbf{b}$ integration in Eq. (8) can be carried out analytically (see Ref. [9]).

4 Results and discussion

Let us examine, using general formula (1), the role of the projectile wave packet. First, consider the FBA on-shell T-matrix (5). In this case, it is a function of the momentum transfer only, that is $\mathcal{T}_{fi} = \mathcal{T}_{fi}^{\mathrm{FBA}}\big(\mathbf{Q}(\mathbf{q}_T)\big)$, and therefore it is not involved in the integral over $\mathbf{q}_p$. Thus the $\mathbf{q}_p$ integration is governed by the properties of the projectile initial wave function $\Phi_p(\mathbf{q}_p)$ in the case of discussed experiments. According to Refs. [13, 14], the transverse coherence length in the 100 Mev/u $\mathrm{C}^{6+} + \mathrm{He}$ experiment [7] was $\Delta r \approx 10^{-3}$ a.u. This value is related to the spatial extent of freely propagating projectile wave packet in real space $\Psi_p(\mathbf{r}_p, t)$ when it reaches the collision region (at the moment $t = 0$ [3]). Hence, we can estimate the transverse width of the wave packet in momentum space

$$\Phi_p(\mathbf{q}_p) = \int d\mathbf{r}\, e^{-i\mathbf{q}_p\cdot\mathbf{r}_p}\, \Psi_p(\mathbf{r}_p, t=0)$$

as[2] $\Delta p \sim 1/\Delta r \approx 10^3$ a.u. This number is very large in the atomic scale, but it appears to be insignificant as far as the projectile velocity is concerned. Indeed, the width in the velocity space is $\Delta v \simeq c\,\Delta p \Big/ \sqrt{k_p^2 + M_p^2 c^2} \sim 0.04$ a.u., thus in terms of velocity space, the wave packet $\Phi_p(\mathbf{q}_p)$ is very well peaked about the mean value of $\mathbf{v}_p = c\,\mathbf{k}_p \Big/ \sqrt{k_p^2 + M_p^2 c^2}$ ($v_p = 58.6$ a.u.). Hence the projectile velocity functions in the integrand of (1) are accurately approximated as $\mathbf{v}(\mathbf{q}_p) = \mathbf{v}_p$ and $v_z(\mathbf{q}_p) = v_p$, and the integration over $\mathbf{q}_p$ reduces to the normalization integral for Φ_p. As a result, we are left with the $\mathbf{q}_T$ integration where an absolute square of the FBA T-matrix on the energy shell is convoluted with an absolute square of the target wave packet $|\Phi_T(\mathbf{q}_T)|^2$.

In a recent theoretical analysis [9] of the 100 Mev/u $\mathrm{C}^{6+} + \mathrm{He}$ experiment [7], the target wave packet was effectively taken into account by convoluting the cross section (4) with a 2D Gaussian-like momentum distribution function that also mimicked the effect of experimental uncertainties of the measurements. The latter uncertainties are due to a finite energy and angle resolution as well as to a velocity spread of the He gas atoms in the supersonic jet caused by its nonzero temperature. The results of the convolution of the FBA calculations with the 2D Gaussian-like momentum distribution function are presented in Fig. 1 in comparison with experiment. Different values of momentum-transfer uncertainties, ΔQ_x and ΔQ_y (or FWHM), are

[2] Note that the shape of a freely propagating wave packet does not vary with time in momentum space, i. e., $|\Phi_p(\mathbf{q}_p, t)|^2 = |\Phi_p(\mathbf{q}_p)|^2$.

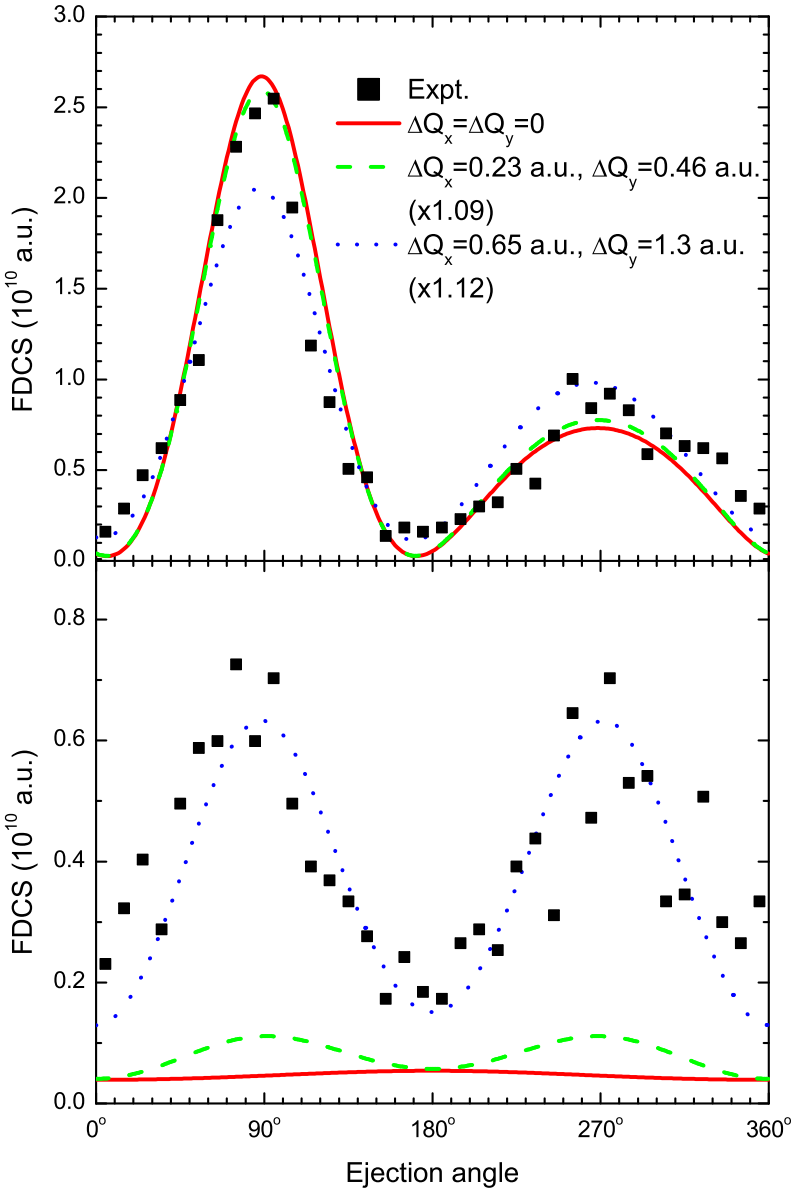

Figure 1: The FBA values for the angular distributions of the ejected electron in the scattering (top panel) and perpendicular (bottom panel) planes convoluted with experimental uncertainties. The kinetic energy of the ejected electron is $E_e = 6.5$ eV. The momentum transfer is $Q = 0.75$ a.u. All experimental and theoretical FDCS values are shown as normalized intensities relative to the FBA cross section for $Z_e = 1$. See Ref. [9] for details.

considered. The case of no uncertainties, $\Delta Q_x = \Delta Q_y = 0$, amounts to unconvoluted FBA calculations, while the FWHM values of $\Delta Q_x = 0.23$ a.u. and $\Delta Q_y = 0.46$ a.u. reported in Ref. [16] are supposed to correspond to the temperature of the He gas atoms of 1–2 K [11, 16]. It can be seen that the inclusion of uncertainties according to Ref. [16] insignificantly influences the FBA calculations in the scattering plane and only slightly reduces the large discrepancy in intensity between theory and experiment in the perpendicular plane. At the same time, it changes the theoretical angular distribution in the perpendicular plane resembling the experimental two-peak structure.

The latter observation hints at the importance of the experimental uncertainty effects in the perpendicular plane. This is illustrated in Fig. 1 by the results of convolution of the FBA calculations with the momentum uncertainties of $\Delta Q_x = 0.65$ a.u. and $\Delta Q_y = 1.3$ a.u. These values correspond to the temperature of the He gas atoms of 8–16 K which is eight times larger than that of Ref. [16]. Remarkably, the increase of temperature provides a reasonable agreement between the theory and experiment in the perpendicular plane, though it somewhat worsens the agreement in the scattering plane. This finding supports the results of Ref. [10] where continuum distorted wave calculations were convoluted with experimental uncertainties.

As remarked in Ref. [14], while it is not surprising that the convolution of FBA with the initial projectile wave packet does not change the FDCS, a proper theoretical test of a potential influence of the projectile coherence should be performed within a higher-order model. In particular, the authors of Ref. [14] suggested that a small value of Δr can lead to an incoherent contribution to the FDCS from the FBA and higher-order amplitudes (particularly, those containing projectile-nucleus interaction [16]). Higher order collision mechanisms, including those due to projectile-nucleus interaction, enter the SBA (6) and DWBA (8) models. Using them in the general formula (1), we find that in both cases the on-shell T-matrix depends not only on the momentum-transfer function $\mathbf{Q}(\mathbf{q}_T)$, as in the FBA case, but also on the projectile momentum variable $\mathbf{q}_p$. However, the latter dependence enters only through the projectile velocity function $\mathbf{v}(\mathbf{q}_p)$,

$$\mathcal{T}_{fi} = \mathcal{T}_{fi}^{\mathrm{SBA/DWBA}}\big(\mathbf{Q}(\mathbf{q}_T), \mathbf{v}(\mathbf{q}_p)\big). \tag{9}$$

As in the FBA case discussed above, we make use of the fact that the projectile wave packet Φ_p is very well peaked in velocity space, setting $\mathbf{v}(\mathbf{q}_p) = \mathbf{v}_p$ and $v_z(\mathbf{q}_p) = v_p$ in the integrand and performing the remaining integration over $\mathbf{q}_p$ as the normalization integral for Φ_p. Thus the effect of the projectile wave packet disappears, and we are left again with the convolution of FDCS with $|\Phi_T(\mathbf{q}_T)|^2$.

5 Summary and conclusions

In conclusion, using a rigorous approach based on time-dependent scattering theory, we find no evidence that the projectile wave packet (or the projectile coherence) can play any appreciable role. Moreover, both in the case of the first-order model (FBA) and in the case of higher-order models (SBA and DWBA), only the target wave packet appears to be important. This result is mainly due to the fact that, in the discussed experiments, only the momenta of final target fragments (the ejected electron and the recoil He^+ ion) were measured, whereas the final projectile momentum remained undetermined. One can readily see that determining the momentum transfer directly, that is, by measuring the final projectile momentum $\mathbf{k}'_p$ instead of the He^+ momentum $\mathbf{k}_I$, would bring about a huge effect of the initial projectile wave packet $\Phi_p(\mathbf{q}_p)$. Indeed, in such a case, the on-shell T-matrix $\mathcal{T}_{fi}$ varies strongly as a function of the momentum transfer $\mathbf{Q}(\mathbf{q}_p) = \mathbf{k}'_p - \mathbf{q}_p$ in the region of localization of $\Phi_p(\mathbf{q}_p)$, and hence the above cancelation of the projectile wave packet is not possible. This observation directly reflects the smallness of the coherence length of the projectile beam in comparison with the spatial extent of the target since the T-matrix is closely related to the Fourier transform of the target potential [3]. It thus shows that in the situation of the discussed experiments, one should compare the spatial extent of the target (the atomic size) with the coherence length of the target beam rather than the projectile beam.

Acknowledgments

This work was supported by the Russian Foundation for Basic Research (Grant No 14-01-00420-a).

References

[1] L. D. Landau and E. M. Lifshitz, *Quantum mechanics: nonrelativistic theory, 3rd ed.* Pergamon, Oxford, 1977.

[2] V. B. Berestetskii, E. M. Lifshitz and L. P. Pitaevskii, *Quantum electrodynamics, 2nd ed.* Butterworth-Heinemann, Oxford, 1982.

[3] J. R. Taylor, *Scattering theory: the quantum theory of nonrelativistic collisions*. Dover, New York, 2006.

[4] M. L. Goldberger and K. M. Watson, *Collision theory*. Dover, New York, 2004.

[5] J. Ullrich, R. Moshammer, R. Dörner, O. Jagutzki, V. Mergel, H. Schmidt-Böcking and L. Spielberger, J. Phys. B **30**, 2917 (1997).

[6] J. Ullrich, R. Moshammer, A. Dorn, R. Dörner, L. Ph. H. Schmidt and H. Schmidt-Böcking, Rep. Progr. Phys. **66**, 1463 (2003).

[7] M. Schulz, R. Moshammer, D. Fischer, H. Kollmus, D. H. Madison, S. Jones and J. Ullrich, Nature **422**, 48 (2003).

[8] M. Schöffler, private communication.

[9] K. A. Kouzakov, S. A. Zaytsev, Yu. V. Popov and M. Takahashi, Phys. Rev. A **86**, 032710 (2012).

[10] J. Fiol, S. Otranto and R. E. Olson, J. Phys. B **39**, L285 (2006).

[11] M. Durr, B. Najjari, M. Schulz, A. Dorn, R. Moshammer, A. B. Voitkiv and J. Ullrich, Phys. Rev. A **75**, 062708 (2007).

[12] K. N. Egodapitiya, S. Sharma, A. Hasan, A. C. Laforge, D. H. Madison, R. Moshammer and M. Schulz, Phys. Rev. Lett. **106**, 153202 (2011).

[13] X. Wang, K. Schneider, A. LaForge, A. Kelkar, M. Grieser, R. Moshammer, J. Ullrich, M. Schulz and D. Fischer, J. Phys. B **45**, 211001 (2012).

[14] M. Schulz, R. Moshammer, D. Fischer and J. Ullrich, Phys. Rev. A **87**, 046701 (2013).

[15] K. A. Kouzakov, S. A. Zaytsev, Yu. V. Popov and M. Takahashi, Phys. Rev. A **87** (2013), 046702.

[16] M. Schulz, M. Dürr, B. Najjari, R. Moshammer and J. Ullrich, Phys. Rev. A **76**, 032712 (2007).

Quasi-Sturmian Functions in Continuum Spectrum Problems

M. S. Aleshin[1], S. A. Zaytsev[1], G. Gasaneo[2] and L. U. Ancarani[3]

[1] *Pacific National University, Khabarovsk, 680035, Russia*
[2] *Departamento de Física, Universidad Nacional del Sur, 8000 Bahí Blanca, Argentina*
[3] *Equipe TMS, SRSMC, UMR CNRS 7565, Université de Lorraine, 57078 Metz, France*

Abstract

Quasi-Sturmian (QS) functions are proposed as an expansion basis to describe continuum states of a quantum system. A closed analytic representation of QS functions is derived. A two-body scattering example is given to demonstrate advantages of the method.

Keywords: *Inhomogeneous Schrödinger equation, Sturmian basis, Coulomb Green's function*

1 Introduction

The three-body Coulomb scattering is one of the fundamental unresolved problem. In atomic physics two-electrons systems are of great interest. In the one-electron continuum problem (e. g., when the electron is scattered by a bound pair) an expansion on the bispherical basis is applicable. In this case an expansion of the partial wave function on the basis of square integrable functions (of the electron coordinates r_1 and r_2) is recognized to be suitable. In the J-matrix method [1] as well as in the converge-close coupling (CCC) approach [2] the Laguerre basis functions are used for this purpose. Recently a new version of the Sturmian approach [3] has been developed, based upon an expansion on the so called generalized Sturmian functions (see, e. g., the papers [4, 5] and references therein) which are eigensolutions for integral or differential Sturm–Liouville equations with the outgoing- and incoming-wave boundary conditions. The Coulomb interaction within all these approaches is involved in the construction of the basis functions into the unperturbed part of the two-body Hamiltonian. In the framework of the J-matrix, the Coulomb Green's function have been obtained in a suitable analytic form [6, 7] in terms of hyper-geometric functions. In turn, the short-ranged operator of the potential energy is represented here in a finite subspace of L^2 basis functions. As a result, e. g., the phase shift corresponding to this truncated model potential, oscillates as the number of used basis functions increases [8]. Thus an application of the J-matrix method to the two-body scattering problem yet requires additional efforts in order to improve the convergence. The Sturmian function approach is free from such flaws. However these basis functions are calculated numerically, so the generation of the basis poses a problem as difficult as the original scattering problem.

In this paper, basis functions are proposed which we call Quasi Sturmians (QS). The QS functions formally are the solutions of the inhomogeneous Schrödinger equation

Proceedings of the International Conference 'Nuclear Theory in the Supercomputing Era — 2014' (NTSE-2014), Khabarovsk, Russia, June 23–27, 2014. Eds. A. M. Shirokov and A. I. Mazur. Pacific National University, Khabarovsk, Russia, 2016, p. 139.

http://www.ntse-2014.khb.ru/Proc/Aleshin.pdf.

whose right-hand-side contains the Laguerre L^2 functions. Hence, unlike the Sturmian functions, the QS functions with an appropriate asymptotic behavior can be obtained in a closed analytic form.

The atomic units are assumed throughout.

2 Quasi Sturmians

Let us consider the motion of a particle of mass μ in a potential $V(r) = V_C(r) + U(r)$ which is represented by the sum of the Coulomb potential $V_C(r) = \frac{Z_1 Z_2}{r}$ and a short-range one U. The scattering wave function $\Psi_\ell^{(+)}$ (we consider the outgoing-wave boundary condition) satisfies the Schrödinger equation

$$\left[-\frac{1}{2\mu}\left(\frac{d^2}{dr^2} - \frac{\ell(\ell+1)}{r^2}\right) + V(r) - E\right]\Psi_\ell^{(+)}(r) = 0. \tag{1}$$

To solve the scattering problem, we express the wave function as a sum of the Coulomb wave and of the so-called scattering wave $\Psi_{sc}^{(+)}$:

$$\Psi(k,r) = \Psi_\ell^C(k,r) + \Psi_{sc}^{(+)}(k,r), \tag{2}$$

where Ψ_ℓ^C is the regular Coulomb solution [9]:

$$\Psi_\ell^C(k,r) = \frac{1}{2}(2kr)^{\ell+1}\, e^{-\pi\alpha/2}\, e^{ikr}\, \frac{|\Gamma(\ell+1+i\alpha)|}{(2\ell+1)!}\, {}_1F_1(\ell+1+i\alpha; 2\ell+2; -2ikr). \tag{3}$$

Here $\alpha = \frac{\mu Z_1 Z_2}{k}$ is the Sommerfeld parameter, the energy is defined as $E = \frac{k^2}{2\mu}$.

Inserting (2) into (1) yields the following inhomogeneous equation for $\Psi_{sc}^{(+)}$:

$$\left[-\frac{1}{2\mu}\left(\frac{d^2}{dr^2} - \frac{\ell(\ell+1)}{r^2}\right) + \frac{Z_1 Z_2}{r} + U(r) - E\right]\Psi_{sc}^{(+)}(k,r) = -U(r)\Psi_\ell^C(k,r). \tag{4}$$

We suggest to find the solution $\Psi_{sc}^{(+)}$ of the Driven Equation (4) in form of the expansion

$$\Psi_{sc}^{(+)}(r) = \sum_{n=0}^{N-1} c_{n,\ell}\, Q_{n,\ell}^{(+)}(r). \tag{5}$$

The functions $Q_{n,\ell}^{(+)}$ satisfy the inhomogeneous equation

$$\left[-\frac{1}{2\mu}\left(\frac{d^2}{dr^2} - \frac{\ell(\ell+1)}{r^2}\right) + \frac{Z_1 Z_2}{r} - E\right]Q_{n,\ell}^{(+)}(r) = \frac{1}{r}\phi_{n,\ell}(r), \tag{6}$$

where the Laguerre basis functions

$$\phi_{n,\ell}(\lambda, r) = \sqrt{\frac{n!}{(n+2\ell+1)!}}\, e^{-\lambda r}\, (2\lambda r)^{\ell+1} L_n^{2\ell+1}(2\lambda r) \tag{7}$$

are used; λ is the scale parameter of the basis.

We call the functions $Q_{n,\ell}^{(+)}$ Quasi Sturmians due to their analogy with (using as a basis) Sturmian functions. QS with appropriate asymptotic properties can be obtained (unlike the Sturmian functions) in a closed form.

QS functions can be presented as an integral:

$$Q_{n,\ell}^{(+)}(r) = \int_0^\infty dr'\, G^{\ell(\pm)}(k; r, r')\, \frac{1}{r'}\, \phi_{n,\ell}(\lambda, r'). \tag{8}$$

The Green function operator $\hat{G}^{\ell(+)}$ kernel is expressed in terms of the Whittaker functions [10]:

$$G^{\ell(\pm)}(k;r,r') = \mp\frac{\mu}{ik}\frac{\Gamma(\ell+1\pm i\alpha)}{(2\ell+1)!}\,\mathcal{M}_{\mp i\alpha;\ell+1/2}(\mp ikr_<)\,\mathcal{W}_{\mp i\alpha;\ell+1/2}(\mp ikr_>). \tag{9}$$

Explicit expressions for the matrix elements

$$G^{\ell(\pm)}_{m,n}(k;\lambda) = \int_0^\infty\int_0^\infty dr dr'\,\frac{1}{r}\,\phi_{m,\ell}(\lambda,r)\,G^{\ell(\pm)}(k;r,r')\,\frac{1}{r'}\,\phi_{n,\ell}(\lambda,r') \tag{10}$$

have been obtained in Ref. [6] (see also Ref. [7]) using two linear independent J-matrix solutions [11]:

$$G^{\ell(\pm)}_{m,n}(k;\lambda) = \frac{2\mu}{k}\,\mathcal{S}_{n_<,\ell}(k)\,\mathcal{C}^{(\pm)}_{n_>,\ell}(k). \tag{11}$$

The coefficients of the QS function expansion in terms of the Laguerre basis functions (7) are calculated by multiplying Eq. (8) by $\frac{1}{r}\phi_{n,\ell}(\lambda,r)$ and integrating over r. As a result, in view of Eq. (10), we obtain

$$Q^{(\pm)}_{n,\ell}(r) = \sum_{m=0}^{\infty}\phi_{m,\ell}(\lambda,r)\,G^{\ell(\pm)}_{m,n}(k;\lambda). \tag{12}$$

3 Example

Let us consider an s-wave scattering of a particle of mass $\mu = 1$ and momentum $k = 1$ by the combination of the Coulomb potential with $Z_1Z_2 = 1$ and Yukawa potential

$$U(r) = b\,\frac{e^{-ar}}{r}, \quad a = 1.3,\ \ b = 1. \tag{13}$$

We study the expansion (5) convergence with increasing N. The functions $Q^{(+)}_{n,0}$ oscillate with different frequencies within the range of the potential U (see Fig. 1) while the Sturmians possess the same behavior up to the amplitude factor outside the range.

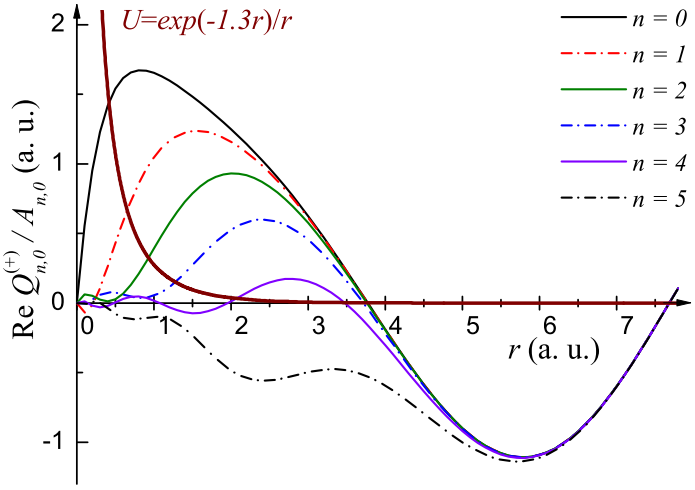

Figure 1: Real parts of the first six QS functions for a particle of mass $\mu = 1$ and momentum $k = 1$ in the Coulomb potential $V_C = \frac{1}{r}$. The scale parameter of the basis $\lambda = 2.6$.

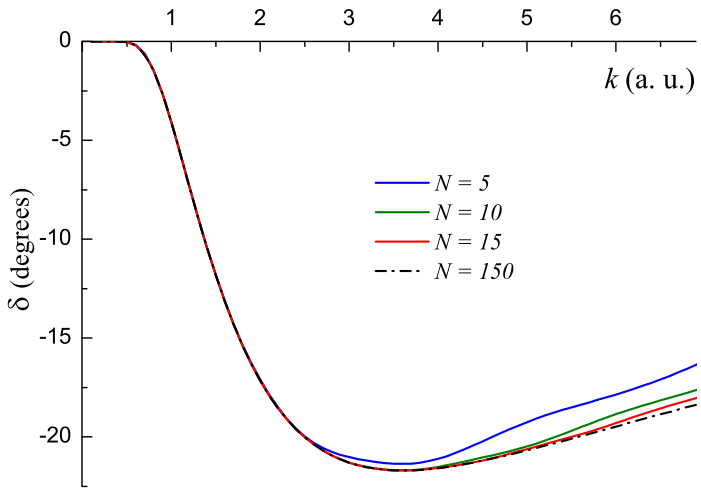

Figure 2: Convergence of the phase shift with N.

We insert the expansion (5) into Eq. (4), multiply the resulting expression by $\phi_{n,\ell}(\lambda, r)$ and integrate over r to obtain a discrete equation for the coefficients $c_{n,\ell}$:

$$[\mathbf{I} + \mathcal{U}]\, \mathbf{c} = \mathbf{d}. \tag{14}$$

The components d_m, $m = 0, \ldots, N-1$ of the vector $\mathbf{d}$ in the right-hand-side of Eq. (14) are defined as

$$d_m = -\int_0^\infty dr\, \phi_{m,0}(\lambda, r)\, U(r)\, \Psi_0^C(r), \tag{15}$$

the elements $\mathcal{U}_{m,n}$ of the $N \times N$ matrix $\mathcal{U}$ are defined as

$$\mathcal{U}_{m,n} = \int_0^\infty dr\, \phi_{m,0}(\lambda, r)\, U(r)\, Q_{n,0}^{(+)}(r) \tag{16}$$

The unit matrix I present in the left-hand-side of Eq. (14) appears due to the orthogonality relation for the Laguerre basis.

Convergence of the s-wave phase shift $\delta_0(k)$ with N is shown in Fig. 3.

4 Conclusion

A comparison of the phase shift obtained by our method with the phase shift from the J-matrix calculations shows advantages of the proposed approach over the J-matrix method.

In this work we suggested the Quasi-Sturmian functions and showed that their application to the two-body scattering problem is quite efficient. The convergence rate appeared to be comparable or even higher than that achieved in the J-matrix method and generalized Sturmian approach. Moreover, the QS functions have an obvious advantage that they can be expressed in a closed analytic form. An explicit representation of the basis QS function in terms of known special functions may be useful in applications to the Coulomb three-body problem.

References

[1] A. D. Alhaidari, E. J. Heller, H. A. Yamani and M. S. Abdelmonem (eds.), *The $J-$matrix method. Developments and applications*. Springer, New York, 2008.

[2] I. Bray and A. T. Stelbovics, Phys. Rev. Lett. **69**, 53 (1992).

[3] M. Rotenberg, Ann. Phys. (NY) **19**, 262 (1962).

[4] G. Rawitsher, Phys. Rev. C **25**, 2196 (1982).

[5] D. M. Mitnik, F. D. Colavecchia, G. Gasaneo and J. M. Randazzo, Comp. Phys. Comm. **182**, 1145 (2011).

[6] E. J. Heller, Phys. Rev. A **12**, 1222 (1975).

[7] F. Demir, Z. T. Hlousek and Z. Papp, Phys. Rev. A **74**, 014701 (2006).

[8] Z. Papp, Phys. Rev. A **46**, 4437 (1992).

[9] R. G. Newton, *Scattering theory of waves and particles*. McGraw-Hill, New York, 1966.

[10] L. Hostler, J. Math. Phys. **5**, 591 (1964).

[11] H. A. Yamani and L. Fishman, J. Math. Phys. **16**, 410 (1975).

Convoluted Quasi-Sturmian Basis in Three-Body Coulomb Problems

M. S. Aleshin[1], S. A. Zaytsev[1], G. Gasaneo[2] and L. U. Ancarani[3]

[1] *Pacific National University, Khabarovsk, 680035, Russia*
[2] *Departamento de Física, Universidad Nacional del Sur, 8000 Bahí Blanca, Argentina*
[3] *Equipe TMS, SRSMC, UMR CNRS 7565, Université de Lorraine, 57078 Metz, France*

Abstract

A new type of basis functions is proposed to describe an $(e, 3e)$ process on helium. This is done in the framework of the first Born approximation approach presented in Ref. [1]. The basis functions used to expand the three-body solutions are calculated in terms of the recently introduced quasi-Sturmian (QS) functions [2]. The QS functions satisfy a non-homogeneous Schrödinger equation with Coulomb interactions and possess outgoing-wave boundary condition. By construction, the basis functions look asymptotically like a six-dimensional spherical wave. The transition amplitude for the $(e, 3e)$ process is obtained directly from the asymptotic part of the wave function. A fast convergence is achieved for the calculated wave function. An agreement in the shape of differential cross sections is obtained with the available experimental data. While the disagreement in magnitude is found with the experimental data, a reasonable agreement with other *ab initio* theories is found.

Keywords: *Quasi-Sturmian functions; Coulomb Green's function; driven equation*

1 Introduction

The Coulomb three-body scattering problem is one of the most fundamental outstanding problems in theoretical nuclear, atomic and molecular physics. The primary difficulty in description of three charged particles in the continuum is imposing appropriate asymptotic behaviors of the wave function.

In order to describe the Coulomb three-body continuum we propose a set of two-particle functions which are calculated by using the recently introduced so-called quasi-Sturmian (QS) functions [2]. The QS functions satisfy a two-body non-homogeneous Schrödinger equation with the Coulomb potential and an outgoing-wave boundary condition. Specifically, the two-particle basis functions are obtained, by an analogy with the Green's function of two non-interacting hydrogenic atomic systems, as a convolution integral of two one-particle QS functions. The QS functions have the merit that they are expressed in a closed form, which allows us to find an appropriate integration path that is useful for numerical calculations of such an integral representation. We name these basis functions Convoluted Quasi Sturmian (CQS). Note that by construction, the CQS function (unlike a simple product of two one-particle ones) looks asymptotically (as the hyperradius $\rho \to \infty$) like a six-dimensional outgoing spherical wave.

The atomic units are assumed throughout.

Proceedings of the International Conference 'Nuclear Theory in the Supercomputing Era — 2014' (NTSE-2014), Khabarovsk, Russia, June 23–27, 2014. Eds. A. M. Shirokov and A. I. Mazur. Pacific National University, Khabarovsk, Russia, 2016, p. 144.

http://www.ntse-2014.khb.ru/Proc/Zaytsev.pdf.

2 Quasi-Sturmian basis functions

2.1 Driven equation

In the approach of Ref. [1] to the (e, 3e) process, the four-body Schrödinger equation is reduced to the following driven equation for the three-body system $(e^-, e^-, \mathrm{He}^{++}) = (1, 2, 3)$:

$$\left[E - \hat{H}\right] \Phi_{sc}^{(+)}(\mathbf{r}_1, \mathbf{r}_2) = \hat{W}_{fi}(\mathbf{r}_1, \mathbf{r}_2)\, \Phi^{(0)}(\mathbf{r}_1, \mathbf{r}_2). \tag{1}$$

$E = \frac{k_1^2}{2} + \frac{k_2^2}{2}$ is the energy of the two ejected electrons. The three-body helium Hamiltonian is given by

$$\hat{H} = -\frac{1}{2}\triangle_{r_1} - \frac{1}{2}\triangle_{r_2} - \frac{2}{r_1} - \frac{2}{r_2} + \frac{1}{r_{12}}, \tag{2}$$

$\Phi^{(0)}(\mathbf{r}_1, \mathbf{r}_2)$ represents the ground state of the helium atom. The perturbation operator $\hat{W}_{fi}$ is written as

$$\hat{W}_{fi}(\mathbf{r}_1, \mathbf{r}_2) = \frac{1}{(2\pi)^3} \frac{4\pi}{q^2} (-2 + e^{i\mathbf{q}\cdot\mathbf{r}_1} + e^{i\mathbf{q}\cdot\mathbf{r}_2}), \tag{3}$$

where $\mathbf{q} = \mathbf{k}_i - \mathbf{k}_f$ is the transferred momentum, $\mathbf{k}_i$ and $\mathbf{k}_f$ are the momenta of the incident and scattered electrons.

2.2 Two-particle quasi Sturmians

Our method of solving the driven equation (1) is to expand the solution in the series

$$\Phi_{sc}^{(+)}(\mathbf{r}_1, \mathbf{r}_2) = \sum_{L,\ell,\lambda} \sum_{n,\nu=0}^{N-1} C_{n\nu}^{L(\ell\lambda)}\, |n\ell\nu\lambda; LM\rangle_Q, \tag{4}$$

where the basis

$$|n\ell\nu\lambda; LM\rangle_Q \equiv \frac{Q_{n\nu}^{\ell\lambda(+)}(E; r_1, r_2)}{r_1 r_2}\, \mathcal{Y}_{\ell\lambda}^{LM}(\hat{\mathbf{r}}_1, \hat{\mathbf{r}}_2), \tag{5}$$

$$\mathcal{Y}_{\ell\lambda}^{LM}(\hat{\mathbf{r}}_1, \hat{\mathbf{r}}_2) = \sum_{m\mu} (\ell m \lambda\mu\, |LM\,)\, Y_{\ell m}(\hat{\mathbf{r}}_1)\, Y_{\lambda\mu}(\hat{\mathbf{r}}_2). \tag{6}$$

Each function $Q_{n\nu}^{\ell\lambda(+)}$ is assumed to satisfy the radial equation

$$\left[E - \hat{h}_1^\ell - \hat{h}_2^\lambda\right] Q_{n\nu}^{(\ell\lambda_2)(+)}(E; r_1, r_2) = \frac{\psi_n^\ell(r_1)\, \psi_\nu^\lambda(r_2)}{r_1 r_2}, \tag{7}$$

where

$$\hat{h}_i^\ell = -\frac{1}{2}\frac{\partial^2}{\partial r_i^2} + \frac{1}{2}\frac{\ell(\ell+1)}{r_i^2} - \frac{2}{r_i}, \tag{8}$$

ψ_n^ℓ are the Laguerre basis functions (b is a real scale parameter),

$$\psi_n^\ell(r) = [(n+1)_{2\ell+1}]^{-\frac{1}{2}}\, (2br)^{\ell+1} e^{-br} L_n^{2\ell+1}(2br), \tag{9}$$

which are orthogonal with the weight $\frac{1}{r}$:

$$\int_0^\infty dr\; \psi_n^\ell(r)\, \frac{1}{r}\, \psi_m^\ell(r) = \delta_{nm}. \tag{10}$$

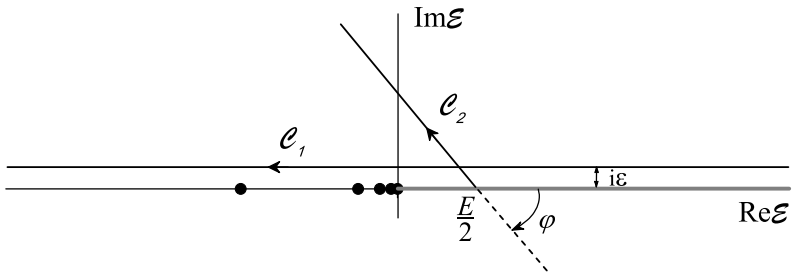

Figure 1: $\mathcal{C}_1$ is the straight-line path of integration of the convolution integral (11). The rotated contour $\mathcal{C}_2$ penetrates into the region of unphysical energies.

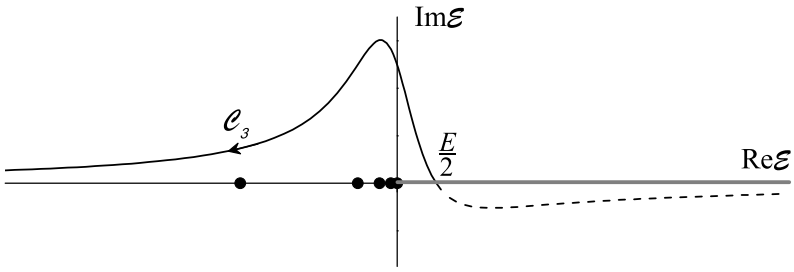

Figure 2: The deformed contour $\mathcal{C}_3$ asymptotically approaches the real energy axis.

In order to obtain the $Q_{n\nu}^{\ell\lambda(+)}$ with the outgoing-wave boundary condition, we use the Green's function $\hat{G}^{(\ell\lambda)(+)}(E)$ [which is the inverse of the operator in the left-hand-side of Eq. (7)] which can be expressed in the form of the convolution integral [3, 4],

$$\hat{G}^{(\ell\lambda)(+)}(E) = \frac{1}{2\pi i}\int\limits_{\mathcal{C}_1} d\mathcal{E}\, \hat{G}^{\ell(+)}(\sqrt{2\mathcal{E}})\, \hat{G}^{\lambda(+)}(\sqrt{2(E-\mathcal{E})}), \tag{11}$$

where the path of integration $\mathcal{C}_1$ in the complex energy plane $\mathcal{E}$ runs slightly above the branch cut and bound-state poles of $\hat{G}^{\ell(+)}$ (see Fig. 1). In order to avoid these singularities we, following the method of Ref. [3], rotate the contour about the point $\frac{E}{2}$ by an angle φ, $-\pi < \varphi < 0$. A part of the rotated straight-line contour $\mathcal{C}_2$ indicated by a dashed line in Fig. 1, lies on the unphysical energy sheet, $-2\pi < \arg(\mathcal{E}) < 0$. Note that $\hat{G}^{\ell(+)}$ grows exponentially for large $|\mathcal{E}|$ in the lower half-plane. In order to ensure a rapid convergence of the integral in Eq. (11), we deform the contour $\mathcal{C}_2$ in such a way that the resulting path $\mathcal{C}_3$ shown in Fig. 2 asymptotically approaches the real axis.

The one-particle Green's function operator $\hat{G}^{\ell(\pm)}$ kernel satisfies the equation

$$\left[\mathcal{E} - \hat{h}^{\ell}\right] G^{\ell(\pm)}(\sqrt{2\mathcal{E}}; r, r') = \delta(r - r') \tag{12}$$

and can be expressed, e. g., in terms of the Whittaker functions [5]:

$$G^{\ell(\pm)}(k; r, r') = \pm\frac{1}{ik}\frac{\Gamma(\ell \pm i\alpha)}{(2\ell+1)!}\, \mathcal{M}_{\mp i\alpha;\ell+1/2}(\mp 2ikr_<)\, \mathcal{W}_{\mp i\alpha;\ell+1/2}(\mp 2ikr_>), \tag{13}$$

where $\alpha = \frac{\mu Z}{k} = -\frac{2}{k}$. From the formulae above one deduces that $Q_{n\nu}^{\ell\lambda(+)}$ can be written as

$$Q_{n\nu}^{(\ell\lambda)(+)}(E; r_1, r_2) = \frac{1}{2\pi i}\int\limits_{\mathcal{C}_3} d\mathcal{E}\, Q_n^{\ell_1(+)}(\sqrt{2\mathcal{E}}; r_1)\, Q_\nu^{\lambda(+)}(\sqrt{2(E-\mathcal{E})}; r_2), \tag{14}$$

where the one-particle QS functions $Q_{n_j}^{\ell_j(+)}$ are defined by [2]

$$Q_n^{\ell(\pm)}(k;r) = \int_0^\infty dx'\, G^{\ell(\pm)}(k;r,r')\,\frac{1}{r'}\,\psi_n^\ell(r'). \tag{15}$$

2.3 Asymptotic behavior

It follows from the asymptotic behavior of the irregular Whittaker function $\mathcal{W}$ that

$$Q_n^{\ell(\pm)}(k;r) \underset{r\to\infty}{\sim} \mp 2\frac{i}{k}\,S_{n\ell}(k)\,(-2kr)^{\ell+1}e^{\pi\alpha/2}\,e^{\pm i(kr+\sigma_\ell(k))}\,U(\ell+1\pm i\alpha, 2\ell+2, \mp 2ikr)$$
$$\underset{r\to\infty}{\sim} -\frac{2}{k}\,S_{n\ell}(k)\,e^{\pm i\left(kr-\alpha\ln(2kr)-\frac{\pi\ell}{2}+\sigma_\ell(k)\right)}, \tag{16}$$

where $\sigma_\ell(k) = \arg\Gamma(\ell+1+i\alpha)$ is the Coulomb phase. Here $S_{n\ell}$ is the sine-like J-matrix solution [6],

$$S_{n\ell}(k) = \frac{1}{2}\left[(n+1)_{(2\ell+1)}\right]^{1/2}\,(2\sin\xi)^{\ell+1}\,e^{-\pi\alpha/2}\,\omega^{-i\alpha}\frac{|\Gamma(\ell+1+i\alpha)|}{(2\ell+1)!}$$
$$\times(-\omega)^n\,{}_2F_1\left(-n,\ell+1+i\alpha;2\ell+2;1-\omega^{-2}\right), \tag{17}$$

where

$$\omega \equiv e^{i\xi} = \frac{b+ik}{b-ik}, \quad \sin\xi = \frac{2bk}{b^2+k^2}, \tag{18}$$

$U(a,b,z)$ is the Kummer function. Recall that $S_{n\ell}$ are formally defined as the coefficients of the expansion

$$\Psi_\ell^C(k,r) = \sum_{n=0}^\infty S_{n\ell}(k)\psi_n^\ell(r) \tag{19}$$

of the regular Coulomb solution Ψ_ℓ^C [7]

$$\Psi_\ell^C(k,r) = \frac{1}{2}(2kr)^{\ell+1}\,e^{-\pi\alpha/2}\,e^{ikr}\frac{|\Gamma(\ell+1+i\alpha)|}{(2\ell+1)!}\,{}_1F_1(\ell+1+i\alpha;2\ell+2;-2ikr), \tag{20}$$

i. e.,

$$S_{n\ell}(k) = \int_0^\infty dr\,\frac{1}{r}\,\psi_n^\ell(r)\,\Psi_\ell^C(k,r). \tag{21}$$

The asymptotic behavior of the QS function (14) for $r_1\to\infty$ and $r_2\to\infty$ simultaneously (in the constant ratio $\tan(\phi) = r_2/r_1$, where ϕ is the hyperangle) is obtained by replacing $Q_n^{\ell(+)}$ and $Q_\nu^{\lambda(+)}$ by their asymptotic approximation (16) and making use of the stationary phase method to evaluate the resulting integral along the contour $\mathcal{C}_1$:

$$Q_{n\nu}^{(\ell\lambda)(+)}(E;r_1,r_2) \underset{\rho\to\infty}{\sim} \frac{1}{E}\sqrt{\frac{2}{\pi}}(2E)^{3/4}e^{\frac{i\pi}{4}}S_{n\ell}(p_1)\,S_{n\lambda}(p_2)\frac{1}{\sqrt{\rho}}$$
$$\times\exp\left\{i\left[\sqrt{2E}\rho-\alpha_1\ln(2p_1r_1)-\alpha_2\ln(2p_2r_2)+\sigma_\ell(p_1)+\sigma_\lambda(p_2)-\frac{\pi(\ell+\lambda)}{2}\right]\right\}, \tag{22}$$

where $\rho = \sqrt{r_1^2+r_2^2}$ is the hyperradius, $p_1 = \cos(\phi)\sqrt{2E}$, $p_2 = \sin(\phi)\sqrt{2E}$, $\alpha_1 = -\frac{2}{p_1}$, $\alpha_2 = -\frac{2}{p_2}$. Notice that on the left part of the contour $\mathcal{C}_3$ where $k\sim i|k|$ and $|k|\to\infty$, the function $Q_n^{\ell(+)}$ behaves like e^{-br} for large r (rather than e^{ikr}). Thus, for larger scale parameter b, the QS function (14) reaches its asymptotic form of Eq. (22) faster.

Finally, by inserting Eq. (22) into the Eq. (4), we find the following asymptotic expression:

$$\Phi_{sc}^{(+)}(\mathbf{r}_1,\mathbf{r}_2) \approx \frac{2}{E\sin(2\phi)}\sqrt{\frac{2}{\pi}}(2E)^{3/4}e^{\frac{i\pi}{4}}\frac{\exp\left\{i\left[\sqrt{2E}\rho-\alpha_1\ln(2p_1r_1)-\alpha_2\ln(2p_2r_2)\right]\right\}}{\rho^{5/2}} \times\sum_{\ell\lambda L}\mathcal{Y}_{LM}^{\ell\lambda}(\hat{\mathbf{r}}_1,\hat{\mathbf{r}}_2)\exp\left\{i\left[\sigma_\ell(p_1)+\sigma_\lambda(p_2)-\frac{\pi(\ell+\lambda)}{2}\right]\right\} \times\sum_{n,\nu=0}^{N-1}C_{n\nu}^{L(\ell\lambda)}S_{n\ell}(p_1)\,S_{\nu\lambda}(p_2). \quad (23)$$

2.4 Transition amplitude

On the other hand, the asymptotic limit of the Green's function of the three-body Coulomb system $(e^-,e^-,\mathrm{He}^{++})$ (for $\rho\to\infty$ while ρ' is finite) reads [1,8]

$$G^{(+)}(E;\mathbf{r}_1,\mathbf{r}_2;\mathbf{r}_1',\mathbf{r}_2') \approx \frac{(2E)^{3/4}e^{\frac{i\pi}{4}}}{(2\pi)^{5/2}}\,\frac{\exp\left\{i\left[\sqrt{2E}\rho+W_0(\mathbf{r}_1,\mathbf{r}_2)\right]\right\}}{\rho^{5/2}}\,\Psi_{\mathbf{k}_1',\mathbf{k}_2'}^{(-)*}(\mathbf{r}_1',\mathbf{r}_2'), \quad (24)$$

where the Coulomb phase W_0 is given by

$$W_0(\mathbf{r}_1,\mathbf{r}_2) = -\frac{\rho}{\sqrt{2E}}\left(-\frac{2}{r_1}-\frac{2}{r_2}+\frac{1}{r_{12}}\right)\ln 2\sqrt{2E}\rho, \quad (25)$$

$\mathbf{k}_1' = p_1\hat{\mathbf{r}}_1$, $\mathbf{k}_2' = p_2\hat{\mathbf{r}}_2$. Therefore, from Eq. (1) we obtain that in this region [1]

$$\Phi_{sc}^{(+)}(\mathbf{r}_1,\mathbf{r}_2) \approx \frac{(2E)^{3/4}e^{\frac{i\pi}{4}}}{(2\pi)^{5/2}}\,\frac{\exp\left\{i\left[\sqrt{2E}\rho+W_0(\mathbf{r}_1,\mathbf{r}_2)\right]\right\}}{\rho^{5/2}}\,T_{\mathbf{k}_1',\mathbf{k}_2'}, \quad (26)$$

where the transition amplitude

$$T_{\mathbf{k}_1',\mathbf{k}_2'} = \left\langle\Psi_{\mathbf{k}_1',\mathbf{k}_2'}^{(-)}\middle|\,\hat{W}_{fi}\,\middle|\Phi^{(0)}\right\rangle. \quad (27)$$

Then, comparing two asymptotic expressions (23) and (26), we find

$$T_{\mathbf{k}_1',\mathbf{k}_2'} = \frac{(4\pi)^2}{E\sin(2\phi)}\exp\left\{-i\left[W_0(\mathbf{r}_1,\mathbf{r}_2)+\alpha_1\ln(2p_1r_1)+\alpha_2\ln(2p_2r_2)\right]\right\} \times\sum_{\ell\lambda L}\left(\left[\sum_{n,\nu=0}^{N-1}C_{n\nu}^{L(\ell\lambda)}S_{n\ell}(p_1)S_{\nu\lambda}(p_2)\right] \times\exp\left\{i\left[\sigma_\ell(p_1)+\sigma_\lambda(p_2)-\frac{\pi(\ell+\lambda)}{2}\right]\right\}\mathcal{Y}_{\ell\lambda}^{LM}(\hat{\mathbf{r}}_1,\hat{\mathbf{r}}_2)\right). \quad (28)$$

Obviously, the differential cross section is expressed in terms of the 'reduced' transition amplitude:

$$\frac{d^5\sigma}{d\Omega_1 d\Omega_2 d\Omega_f dE_1 dE_2} = \frac{1}{(2\pi)^2}\frac{k_f k_1 k_2}{k_i}\left|T_{\mathbf{k}_1',\mathbf{k}_2'}\right|^2. \quad (29)$$

3 Solving driven equation

The QS approach is based on the assumption that the asymptotic behavior of the basis Sturmian functions is correct. Hence there remains a problem of finding the

wave function in the finite 'inner' spatial region. This calculation can be performed in the context of a set of square integrable basis functions. In this case, the left-hand-side of Eq. (1) decreases sufficiently fast to zero as $\rho \to \infty$ and therefore can be approximated by a finite linear combination of L^2 basis functions. In this work, we have tried to apply the method for obtaining the solution of the equation (1) by expanding it into a set of the pure CQS functions (14).

Inserting Eq. (4) into Eq. (1) and having in mind Eq. (7), yields

$$\sum_{L,\ell',\lambda'} \sum_{n',\nu'=0}^{N-1} C_{n'\nu'}^{L(\ell'\lambda')} \left[\mid n'\ell'\widetilde{\nu'\lambda'; LM} \rangle_L + \hat{V}_3^C \, |n'\ell'\nu'\lambda'; LM\rangle_Q \right] = \hat{W}_{fi} \left| \Phi^{(0)} \right\rangle, \quad (30)$$

where

$$\mid n\widetilde{\ell\nu\lambda; LM} \rangle_L \equiv \frac{\psi_n^\ell(r_1)\, \psi_\nu^\lambda(r_2)}{r_1^2 r_2^2} \, \mathcal{Y}_{LM}^{\ell\lambda}(\hat{\mathbf{r}}_1, \hat{\mathbf{r}}_2). \quad (31)$$

The method of obtaining the expansion coefficients $C_{n\nu}^{L(\ell\lambda)}$ is to multiply Eq. (30) by

$$|n\ell\nu\lambda; LM\rangle_L \equiv \frac{\psi_n^\ell(r_1)\, \psi_\nu^\lambda(r_2)}{r_1 r_2} \, \mathcal{Y}_{LM}^{\ell\lambda}(\hat{\mathbf{r}}_1, \hat{\mathbf{r}}_2), \quad (32)$$

(see, e. g., Refs. [9–11]), integrate over $\mathbf{r_1}$ and $\mathbf{r_2}$, and utilize the orthogonality condition

$${}_L\langle n\ell\nu\lambda; LM \mid n'\ell'\widetilde{\nu'\lambda'; LM} \rangle_L = \delta_{n,n'}\, \delta_{\nu,\nu'}\, \delta_{\ell,\ell'}\, \delta_{\lambda,\lambda'}. \quad (33)$$

As a result, we obtain the following matrix equation:

$$\sum_{L,\ell',\lambda'} \sum_{n',\nu'=0}^{N-1} \left[\delta_{n,n'}\, \delta_{\nu,\nu'}\, \delta_{\ell,\ell'}\, \delta_{\lambda,\lambda'} - U_{n\nu,n'\nu'}^{L(\ell\lambda)(\ell'\lambda')} \right] C_{n'\nu'}^{L(\ell'\lambda')} = R_{n\nu}^{L(\ell\lambda)}. \quad (34)$$

Here $R_{n\nu}^{L(\ell\lambda)}$ is the projection of the right-hand-side of Eq. (30):

$$R_{n\nu}^{L(\ell\lambda)} = {}_L\langle n\ell\nu\lambda; LM | \hat{W}_{fi} \left| \Phi^{(0)} \right\rangle. \quad (35)$$

Due to the definition

$$|n\ell\nu\lambda; LM\rangle_Q \equiv \hat{G}^{(\ell\lambda)(+)} \left| n\widetilde{\ell\nu\lambda; LM} \right\rangle_L, \quad (36)$$

the matrix element

$$U_{n\nu,n'\nu'}^{L(\ell\lambda)(\ell'\lambda')} = {}_L\langle n\ell\nu\lambda; LM | \frac{1}{r_{12}} \, |n'\ell'\nu'\lambda'; LM\rangle_Q \quad (37)$$

can be written as

$$U_{n\nu,n'\nu'}^{L(\ell\lambda)(\ell'\lambda')} = {}_L\langle n\ell\nu\lambda; LM | \frac{1}{r_{12}} \hat{G}^{(\ell'\lambda')(+)} \left| n'\ell'\widetilde{\nu'\lambda'; LM} \right\rangle_L. \quad (38)$$

Then using the Laguerre basis (32) completeness, we obtain

$$U_{n\nu,n'\nu'}^{L(\ell\lambda)(\ell'\lambda')} = \sum_{n'',\nu''=0} {}_L\langle n\ell\nu\lambda; LM | \frac{1}{r_{12}} | n''\ell'\nu''\lambda'; LM\rangle_L \times {}_L\left\langle n''\ell'\widetilde{\nu''\lambda'; LM} \right| \hat{G}^{(\ell'\lambda')(+)} \left| n'\ell'\widetilde{\nu'\lambda'; LM} \right\rangle_L. \quad (39)$$

In order to calculate the matrix elements of the Green's function in the basis of functions (31)

$$G_{n\nu,n'\nu'}^{(\ell\lambda)(+)} = {}_L\left\langle n\widetilde{\ell\nu\lambda; LM} \right| \hat{G}^{(\ell\lambda)(+)} \left| n'\ell\widetilde{\nu'\lambda; LM} \right\rangle_L, \quad (40)$$

we use the convolution integral [9–11]

$$G^{(\ell\lambda)(+)}_{n\nu,n'\nu'} = \frac{1}{2\pi i}\int\limits_{\mathcal{C}_3} d\mathcal{E}\, G^{\ell(+)}_{nn'}(\sqrt{2\mathcal{E}})\, G^{\lambda(+)}_{\nu\nu'}(\sqrt{2(E-\mathcal{E})}). \tag{41}$$

The matrix elements of the one-particle Green's function $G^{\ell(+)}$ (13)

$$G^{\ell(+)}_{nm}(k) = \int\limits_0^\infty\int\limits_0^\infty dr dr'\, \frac{1}{r}\,\psi^\ell_n(r)\, G^{\ell(+)}(k;r,r')\,\frac{1}{r'}\,\psi^\ell_m(r') \tag{42}$$

are expressed in terms of the two independent J-matrix solutions [12]:

$$G^{\ell(+)}_{nm}(k) = -\frac{2}{k}\, S_{n_<\ell}(k)\, C^{(+)}_{n_>\ell}(k), \tag{43}$$

$$C^{(+)}_{n\ell}(k) = -\sqrt{n!(n+2\ell+1)}\,\frac{e^{\pi\alpha/2}\,\omega^{i\alpha}}{(2\sin\xi)^\ell} \times \frac{\Gamma(\ell+1+i\alpha)}{|\Gamma(\ell+1+i\alpha)|}\,\frac{(-\omega)^{n+1}}{\Gamma(n+\ell+2+i\alpha)}\,{}_2F_1\big(-\ell+i\alpha, n+1; n+\ell+2+i\alpha;\omega^2\big). \tag{44}$$

Our numerical calculations showed that the values of the convolution integrals (41) along the contour $\mathcal{C}_3$ are equal to those on the straight-line path $\mathcal{C}_2$. Note that the integrand in Eq. (41) does not have exponentially divergent factors unlike that of Eq. (11).

We approximate $U^{L(\ell\lambda)(\ell'\lambda')}_{n\nu,n'\nu'}$ by a finite sum

$$U^{L(\ell\lambda)(\ell'\lambda')}_{n\nu,n'\nu'} = \sum_{n''\nu''=0}^{N-1} V^{L(\ell\lambda)(\ell'\lambda')}_{n\nu,n''\nu''} G^{(\ell'\lambda')(+)}_{n''\nu'',n'\nu'}. \tag{45}$$

Here $V^{L(\ell\lambda)(\ell'\lambda')}_{n\nu,n'\nu'}$ are the matrix elements of $\frac{1}{r_{12}}$ in the basis (32):

$$V^{L(\ell\lambda)(\ell'\lambda')}_{n\nu,n'\nu'} = {}_L\langle n\ell\nu\lambda; LM|\frac{1}{r_{12}}|n'\ell'\nu'\lambda'; LM\rangle_L. \tag{46}$$

In our calculations we take N in Eq. (45) to be equal to the number of QS functions (for each of the coordinates r_1 and r_2). In order to examine the applicability of the QS approach, in conjunction with the approximation (45), we study the convergence of the cross section with increasing N.

4 Results and discussion

We have applied the method outlined above to the problem of electron-impact double ionization of He. The corresponding fully resolved fivefold differential cross sections (FDCS) measurements have been performed by the Orsay group [13]. The geometry of the $(e,3e)$ process is coplanar with an incident energy $E_0 = 5599$ eV and a small momentum transfer $q = 0.24$ a. u. For a fixed value of one of the ejected electron angles, say, θ_1, the FDCS is measured as function of the other angle θ_2.

The energies of the two ejected electrons are $E_1 = E_2 = 10$ eV, so that $E = 0.737$ a. u. Hence for $\phi = \frac{\pi}{4}$ we have $p_1 = p_2 = k_1 = k_2 = 0.859$. As for the scale parameter b, note that the sine-like J-matrix solution (17) depends on the wave number k through its dependence on ω [see Eq. (18)]. Thus, it seems intuitively obvious that the parameter b must be chosen in such a way that the value of ω is far from its limits $\omega_0 = \pm 1$. In other words, b should be comparable to $k_{1,2}$. In our calculations we set $b = 0.78$.

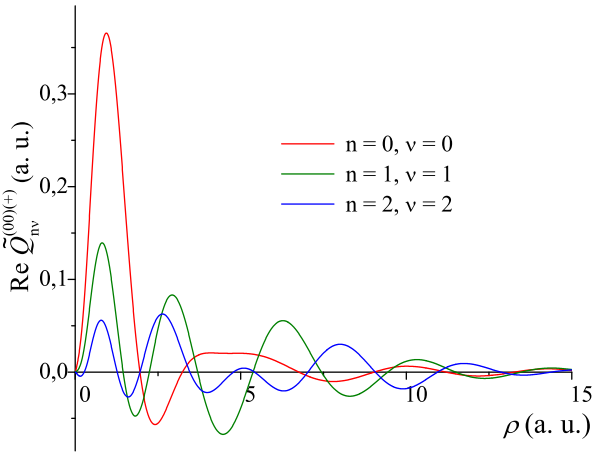

Figure 3: The real parts of the first three QS functions.

Note that the asymptotic behavior (22) of the two-particle QS functions (14) depends upon the indices n and ν. It follows from Eq. (17) that this dependence can be eliminated by dividing Eq. (14) by $A^{\ell}_{n}(p_1)\,A^{\lambda}_{\nu}(p_2)$, where

$$A^{\ell}_{n}(k) = [(n+1)_{2\ell+1}]^{1/2}(-\omega)^n\,{}_2F_1\big(-n, \ell+1+i\alpha; 2\ell+2; 1-\omega^{-2}\big). \tag{47}$$

The same result can be obtained using modified one-particle QS functions

$$\widetilde{Q}^{\ell(+)}_{n}(k;\ r) = \frac{Q^{\ell(+)}_{n}(k;\ r)}{A^{\ell}_{n}(k)} \tag{48}$$

in the integral in Eq. (14). To illustrate the use of the convolution integral representation (14), we present in Figs. 3 and 4 a few modified CQS functions

$$\widetilde{Q}^{(\ell\lambda)(+)}_{n\nu}(E; r_1, r_2) = \frac{1}{2\pi i}\int\limits_{\mathcal{C}_3} d\mathcal{E}\,\widetilde{Q}^{\ell(+)}_{n}(\sqrt{2\mathcal{E}}; r_1)\,\widetilde{Q}^{\lambda(+)}_{\nu}(\sqrt{2(E-\mathcal{E})}; r_2) \tag{49}$$

for $\ell = \lambda = 0$ on the diagonal $r_1 = r_2 = \rho/\sqrt{2}$. The energy $\mathcal{E}$ on the contour $\mathcal{C}_3$ is parametrized in the form

$$\mathcal{E} = t + i\frac{\frac{E}{2} - t}{1+t^2}, \tag{50}$$

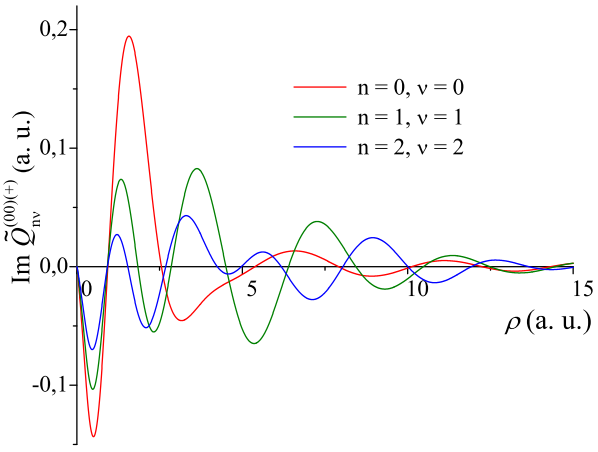

Figure 4: The same as Fig. 3 but for the imaginary parts.

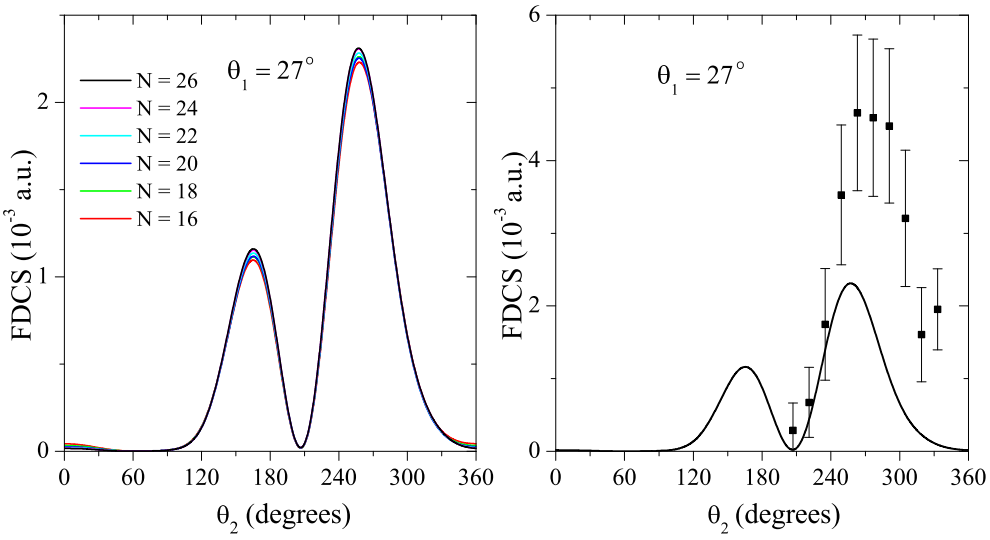

Figure 5: Convergence of FDCS for the $\mathrm{He}(e,3e)\mathrm{He}^{++}$ reaction with increasing N and comparison with experimental data [13].

where t runs from ∞ to $-\infty$.

To find the helium ground-state function $\Phi^{(0)}$, we diagonalize the matrix of the Hamiltonian (2) in the basis

$$|n\nu\ell\rangle \equiv \frac{\chi_n^\ell(r_1)\,\chi_\nu^\ell(r_2)}{r_1 r_2}\,\mathcal{Y}_{00}^{\ell\ell}(\hat{\mathbf{r}}_1,\hat{\mathbf{r}}_2), \tag{51}$$

where

$$\chi_n^\ell(r) = \sqrt{2b_0}\,[(n+1)_{2\ell+2}]^{-\frac{1}{2}}\,(2b_0 r)^{\ell+1} e^{-b_0 r} L_n^{2\ell+2}(2b_0 r). \tag{52}$$

In doing this, we limit ourselves to $\ell_{max} = 5$ and $n_{max} = \nu_{max} = 20$. Choosing the basis parameter $b_0 = 1.688$, we obtain $E_0 = -2.903542$ a. u. for the ground state energy.

We restrict ourselves to the maximal value of the total angular momentum $L_{\max} = 2$ and set the maximal angular momentum quantum numbers ℓ and λ to be 3 in the expansion (4). We examine the differential cross section convergence with increasing number N of the one-particle QS functions $Q_n^{\ell(+)}$ and $Q_\nu^{\lambda(+)}$, $n,\nu = 0,\ldots,N-1$ [see Eq. (15)] employed in the basis. A very good convergence of our numerical procedure is displayed in Fig. 5 where the FDCS (29) for $\theta_1 = 27°$ calculated with different N are plotted. This result is surprising keeping in mind the aforementioned shortcoming of the CQS basis functions (14) asymptotic behavior, which results in noncompactness of Eq. (1). In Fig. 5 we show results for FDCS (29) in comparison with the experimental data [13]. The results are in agreement in shape, but not in magnitude, with the experiment.

References

[1] G. Gasaneo, D. M. Mitnik, J. M. Randazzo, L. U. Ancarani and F. D. Colavecchia, Phys. Rev. A **87**, 042707 (2013).

[2] J. A. Del Punta, M. J. Ambrosio, G. Gasaneo, S. A. Zaytsev and L. U. Ancarani, J. Math. Phys. **55**, 052101 (2014).

[3] R. Shakehaft, Phys. Rev. A **70**, 042704 (2004).

[4] A. I. Baz', Ya. B. Zel'dovich and A. M. Perelomov, *Scattering, reactions and decay in non-relativistic quantum mechanics.* Israel Program for Scientific Translation, Jerusalem, 1969.

[5] L. Hostler, J. Math. Phys. **5**, 591 (1964).

[6] A. D. Alhaidari, E. J. Heller, H. A. Yamani and M. S. Abdelmonem (eds.), *The J-matrix method. Developments and applications.* Springer, New York, 2008.

[7] R. G. Newton, *Scattering theory of waves and particles.* McGraw-Hill, New York, 1966.

[8] L. D. Faddeev and S. P. Merkuriev, *Quantum scattering theory for several particle systems.* Kluwer, Dordrecht, 1993.

[9] Z. Papp, J. Darai, C.-Y. Hu, Z. T. Hlousek, B. Kónya and S. L. Yakovlev, Phys. Rev. A **65**, 032725 (2002).

[10] S. A. Zaytsev, V. A. Knyr, Yu. V. Popov and A. Lahmam-Bennani, Phys. Rev. A **75**, 022718 (2007).

[11] M. S. Mengoue, M. G. Kwato Njock, B. Piraux, Yu. V. Popov and S. A. Zaytsev, Phys. Rev. A **83**, 052708 (2011).

[12] E. J. Heller, Phys. Rev. A **12**, 1222 (1975).

[13] A. Kheifets, I. Bray, A. Lahmam-Bennani, A. Duguet and I. Taouil, J. Phys. B **32**, 5047 (1999).

Ab Initio No Core Shell Model — Recent Results and Further Prospects

James P. Vary[a], Pieter Maris[a], Hugh Potter[a], Mark A. Caprio[b], Robin Smith[c], Sven Binder[d,e], Angelo Calci[f], Sebastian Fischer[g], Joachim Langhammer[g], Robert Roth[g], Hasan Metin Aktulga[h,i] Esmond Ng[i], Chao Yang[i], Dossay Oryspayev[j], Masha Sosonkina[k], Erik Saule[l] and Ümit Çatalyürek[m,n].

[a] *Department of Physics and Astronomy, Iowa State University, Ames, IA 50011, USA*
[b] *Department of Physics, University of Notre Dame, Notre Dame, IN 46556, USA*
[c] *School of Physics and Astronomy, University of Birmingham, Birmingham B15 2TT, UK*
[d] *Department of Physics and Astronomy, University of Tennessee, Knoxville, TN 37996, USA*
[e] *Physics Division, Oak Ridge National Laboratory, Oak Ridge, TN 37831, USA*
[f] *TRIUMF, 4004 Wesbrook Mall, Vancouver, British Columbia, V6T 2A3, Canada*
[g] *Institut für Kernphysik, Technische Universität Darmstadt, 64289 Darmstadt, Germany*
[h] *Department of Computer Science, Michigan State University, East Lansing, MI 48844, USA*
[i] *Lawrence Berkeley National Laboratory, Berkeley, CA 94720, USA*
[j] *Department of Electrical and Computer Engineering, Iowa State University, Ames, IA 50011, USA*
[k] *Department of Modeling, Simulation and Visualization Engineering, Old Dominion University, Norfolk, VA 23529, USA*
[l] *Department of Computer Science, University of North Carolina Charlotte, Charlotte, NC 28223, USA*
[m] *Department of Biomedical Informatics, The Ohio State University, Columbus, OH 43210, USA*
[n] *Department of Electrical and Computer Engineering, The Ohio State University, Columbus, OH 43210, USA*

Abstract

There has been significant recent progress in solving the long-standing problems of how nuclear shell structure and collective motion emerge from underlying microscopic inter-nucleon interactions. We review a selection of recent significant results within the *ab initio* No Core Shell Model (NCSM) closely tied to three major factors enabling this progress: (1) improved nuclear interactions that accurately describe the experimental two-nucleon and three-nucleon interaction data; (2) advances in algorithms to simulate the quantum many-body problem with strong interactions; and (3) continued rapid development of high-performance computers now capable of performing 20×10^{15} floating point operations per second. We also comment on prospects for further developments.

Keywords: *No Core Shell Model; chiral Hamiltonians; JISP16; petascale computers; exascale computers*

Proceedings of the International Conference 'Nuclear Theory in the Supercomputing Era — 2014' (NTSE-2014), Khabarovsk, Russia, June 23–27, 2014. Eds. A. M. Shirokov and A. I. Mazur. Pacific National University, Khabarovsk, Russia, 2016, p. 154.

http://www.ntse-2014.khb.ru/Proc/Vary.pdf.

1 Introduction

The *ab initio* No Core Shell Model (NCSM), using realistic microscopic nucleon-nucleon (NN) and three-nucleon forces ($3N$Fs), has proven to be a powerful combination for describing and predicting properties of light nuclei [1–7]. The Hamiltonian framework results in a large sparse matrix eigenvalue problem for which we seek the low-lying eigenvalues and eigenvectors to form comparisons with experimental data and to make testable predictions. Given the rapid advances in hardware with frequent disruptions in architecture, it has become essential for physicists, computer scientists and applied mathematicians to work in close collaboration in order to achieve efficient solutions to forefront physics problems. Fortunately, US funding agencies have recognized these challenges at the interface of science and technology and have provided support leading to our recent successes [8–17].

We present here a selection of recent results for light nuclei and neutron drops in external traps and set out some of the challenges that lie ahead. The results include both those utilizing the JISP16 NN interaction and those using chiral effective field theory NN plus $3N$ interactions. We also present a selection of algorithms developed for high-performance computers that are helping to rapidly pave the way to efficient utilization of exascale machines (10^{18} floating point operations per second). We illustrate the scientific progress attained with multi-disciplinary teams of physicists, computer scientists and applied mathematicians.

This paper is aimed to complement presentations at this meeting that cover closely-related topics. In this connection, it is important to point especially to the papers by Dytrych *et al.* [18], by Abe *et al.* [19], by Shirokov *et al.* [20] and by Mazur *et al.* [21]. We therefore focus here on the following recent results: (1) demonstrating the emergence of collective rotations in light nuclei; (2) achieving an accurate description of the properties of ^{12}C with chiral Hamiltonians; (3) solving for properties of neutron drops with chiral Hamiltonians; (4) development of techniques for efficient use of computational accelerators; and (5) development of techniques for overlapping communication and computation.

2 Emergence of collective rotations

NCSM calculations of various types have been used to demonstrate the emergence of collective rotational correlations in p-shell nuclei, including ^{6}Li [18, 22], the Be isotopes [22–25], and ^{12}C [26]. Here we focus on the results for the Be isotopes solved in the No Core Full Configuration (NCFC) framework [4,6,7] using the realistic JISP16 NN interaction [27, 28] with the M-scheme harmonic oscillator (HO) basis. The NCFC framework uses many of the same techniques as the NCSM but additionally features extrapolations of observables to the infinite matrix limit [4].

With no prior selection of our basis to favor solutions with collective motion and using only the realistic bare NN interaction (i. e. we omit the Coulomb interaction to ensure exact conservation of isospin thereby simplifying the spectrum[1]) we face the task of analyzing our microscopic results and determining which particular states, among the large number of calculated levels, exhibit signatures of collective nuclear motion. We follow the path of calculating observables and post-analyzing their systematics to infer that they follow the patterns prescribed by collective rotation. This path is analogous to that taken when analyzing experimental data. When we discover patterns appropriate to a collective band in our calculated results, we assign the moniker of "collective motion" to our microscopic results. We further compare the so-detected band with experimental results and find good agreement which

[1]The primary effect of the Coulomb is to shift the binding energies which would not affect our analysis of rotational band observables. New analysis including Coulomb [29] confirms this.

further supports our discovery of emergent collective phenomena in light nuclei from the underlying microscopic many-body theory.

The details of this step-by-step analysis may be found in the Refs. [23–25]. We analyze the systematics of calculated excitation energies, quadrupole moments, dipole moments, electric quadrupole transition $B(E2)$'s and their reduced matrix elements to isolate states which have a clear rotation band assignment from those which do not. In this way, we have identified both ground state and excited state bands, both natural and unnatural parity bands, and bands in even-even as well as in even-odd nuclei.

Perhaps the most striking hallmark of collective rotation is the appearance of excited states with excitation energies that follow a simple pattern prescribed by the collective model. This pattern of collective rotational excitation energies is given in Eq. (1):

$$E(J) = E_0 + A\big[J(J+1) + a(-)^{J+1/2}(J+\tfrac{1}{2})\delta_{K,1/2}\big], \tag{1}$$

where E_0 is an offset to properly position excited band heads relative to the lowest band head, a is the Coriolis decoupling parameter for $K = \frac{1}{2}$ bands appearing in odd-A nuclei, J is the total angular momentum and $A \equiv \hbar^2/(2\mathcal{J})$ with $\mathcal{J}$ representing the moment of inertia of the deformed nucleus.

To be convinced that the states are indeed members of a rotational band one needs to find that these states also exhibit enhanced electromagnetic moments and transition rates that exhibit a dependence on angular momentum J that is also prescribed by the collective rotational model. We therefore adopt these additional criteria for assigning calculated states to rotational bands. It is worth noting here that, in light nuclei, gamma decay data are scarce due to the short-lived resonant nature of the states. Therefore, the calculations provide access to quantities that are typically inaccessible in experiment, yet crucial for confirming collectivity.

We extract parameters of the traditional rotational description through fits to our theoretical results after extrapolation to the the infinite matrix limit (for extrapolation details see Ref. [25]) and we compare these extracted parameters with rotational parameters determined from similar fits to the corresponding experimental data. The energy parameters for bands across the Be isotopic chain are summarized in Fig. 1: the band excitation energy E_x (defined relative to the yrast band as $E_x \equiv E_0 - E_{0,\mathrm{yrast}}$), the band rotational parameter or slope A, and the band Coriolis decoupling parameter or staggering a (for $K = 1/2$).

In total, we compare 23 theoretical and experimental collective rotation parameters for energies in the 6 Be isotopes depicted in Fig. 1. Overall the agreement between theory and experiment is remarkable. Additional analyses of the calculated electromagnetic observables in Refs. [23–25] and comparison with sparse data available confirm that we have observed the emergent phenomena of collective rotation in these *ab initio* calculations for the Be isotopes. At the same time, there are opportunities for additional theoretical and experimental research to explore, for example, where rotational bands terminate and whether additional bands may be found in these and other light nuclei. It appears that bands do not always terminate at the state corresponding to the maximum angular momentum supported by the nucleons occupying the standard valence shell model orbitals [23–25].

3 Chiral Hamiltonian description of ^{12}C

Recent significant theoretical advances for the underlying Hamiltonians, constructed within chiral effective field theory (EFT), provide a foundation for nuclear many-body calculations rooted in QCD [30,31]. These developments motivate us to adopt a chiral EFT Hamiltonian here and in the following section on neutron drops in an external trap. We also adopt the similarity renormalization group (SRG) approach [32–37]

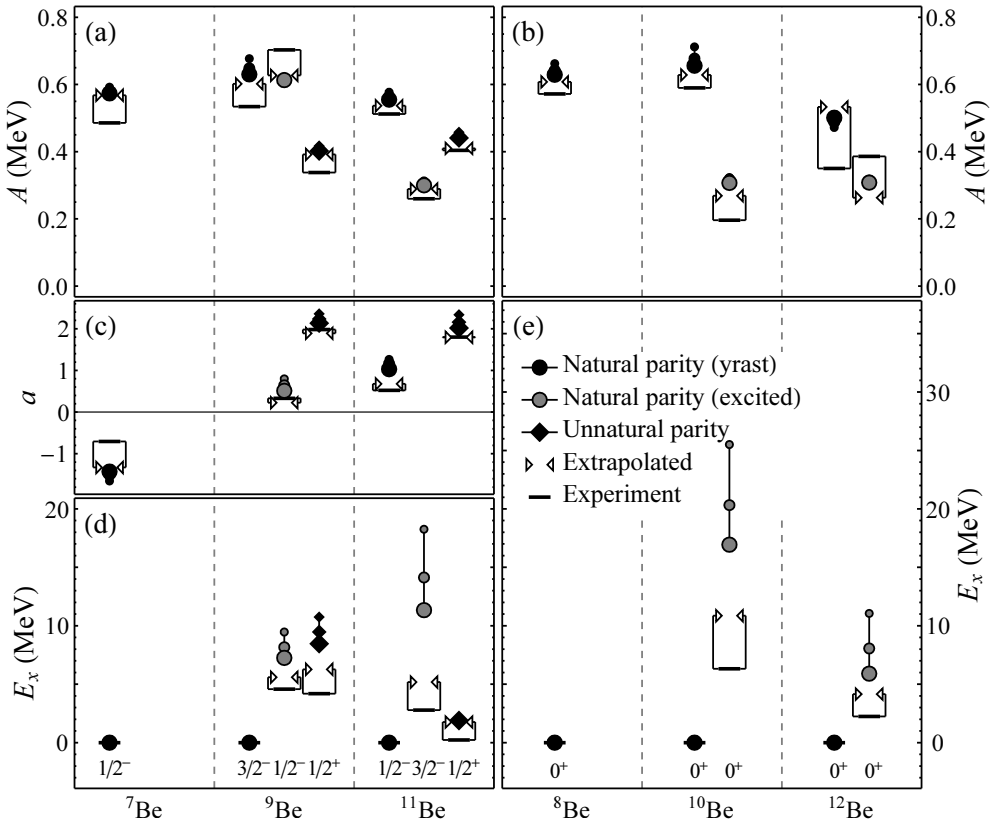

Figure 1: Rotational parameters A, a and E_x [defined relative to the yrast band as $E_x \equiv E_0 - E_{0,\mathrm{yrast}}$ — see Eq. (1)] for ground and excited bands of the Be isotopes (adapted from Ref [25]). Brackets highlight the difference between the parameters determined from experimental data (horizontal bars) and those extracted from NCFC calculations with extrapolation (parallel triangles) to the infinite matrix limit. Solid symbols connected by solid lines indicate the finite matrix results as a function of increasing $N_{\max}$ with larger symbols for larger $N_{\max}$ values. $N_{\max}$ is defined as the maximum number of oscillator quanta in the HO configurations above the minimum for the nucleus under investigation. The minimum $N_{\max}$ is 0 for natural parity and 1 for unnatural parity. The results indicated in the solid symbols correspond to $6 \leq N_{\max} \leq 10$ for natural parity and $7 \leq N_{\max} \leq 11$ for unnatural parity.

that allows us to consistently evolve (soften) the Hamiltonian and other operators, including $3N$ interactions [38–40].

We select the example of the spectroscopy of ^{12}C to illustrate the recent progress. In so doing, it is important to note that additional progress in achieving larger basis spaces is needed before we can realistically address cluster model states in light nuclei such as the celebrated "Hoyle state", a 0^+ state at 7.654 MeV of excitation energy in ^{12}C.

The theoretical excitation spectra are presented in Fig. 2 for the two highest $N_{\max}$ values currently achievable and are compared with experiment. For the negative parity states, we elect to show excitation energies relative to the lowest state of that parity whose experimental energy is 9.641 MeV above the ground state. The trends with increasing $N_{\max}$ (see the trends for additional observables in Ref. [41]) suggest convergence is sufficient to draw important conclusions regarding the underlying interaction. In particular, we note that the shifts from including the initial $3N$ interaction are substantial. In most cases, these shifts improve agreement between theory and

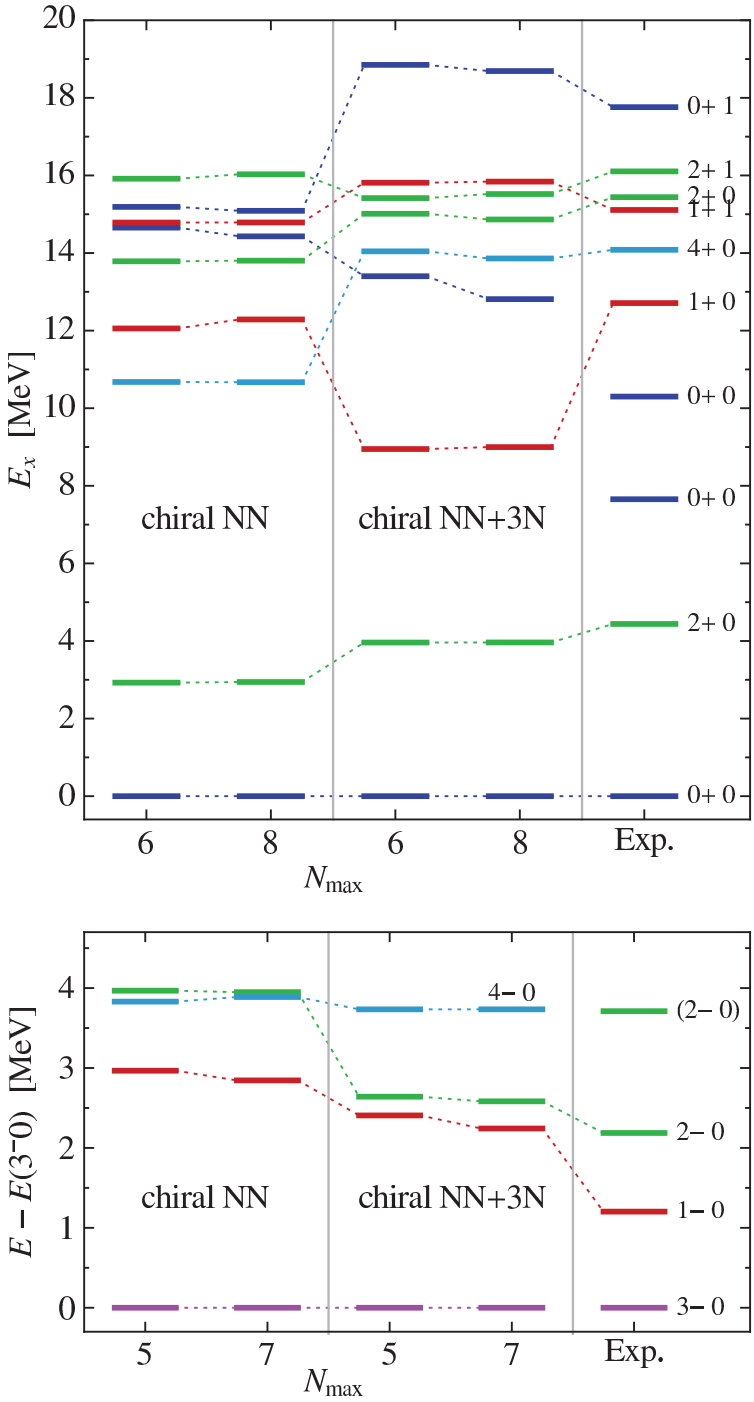

Figure 2: Theoretical and experimental excitation spectra of ^{12}C for both positive parity (top panel) and negative parity (bottom panel) states for two different values of $N_{\max}$ at $\hbar\Omega = 20$ MeV (adapted from Ref. [41]). The columns labelled "chiral NN" include the $3N$F induced by SRG while the sub panels labelled "chiral $NN + 3N$" include the initial $NN+3N$F evolved by SRG together with NN. The SRG evolution parameter is $\lambda = 2.0$ fm^{-1}. See Ref. [41] for additional details.

experiment. A notable exception is the $J^\pi = 1^+$, $T = 0$ positive parity state which shifts further from experiment when we include the initial $3N$ interaction.

From our results in ^{12}C, we conclude that we need further improvements in the chiral interactions. For example, we need to have NN and $3N$ interactions at the same chiral order to be consistent. We also need to extend the chiral order of the interactions to N4LO and, possibly, to include the derived four-nucleon ($4N$) interactions.

4 Confined neutron drops with chiral Hamiltonians

There are many motivations for considering artificial pure neutron systems confined by an external trap.

- Gain insights into the properties of systems dominated by multi-neutron degrees of freedom such as unstable neutron-rich nuclei and neutron stars.
- Isolate selected isospin components of the NN ($T = 1$) and $3N$ ($T = 3/2$) interactions for detailed study.
- Inform the development of nuclear energy density functionals that may be tuned to reproduce *ab initio* calculations, complementing their tuning to experimental data.

The external trap is required since realistic interactions do not bind pure neutron systems, though they do produce net attraction when the systems are confined. The

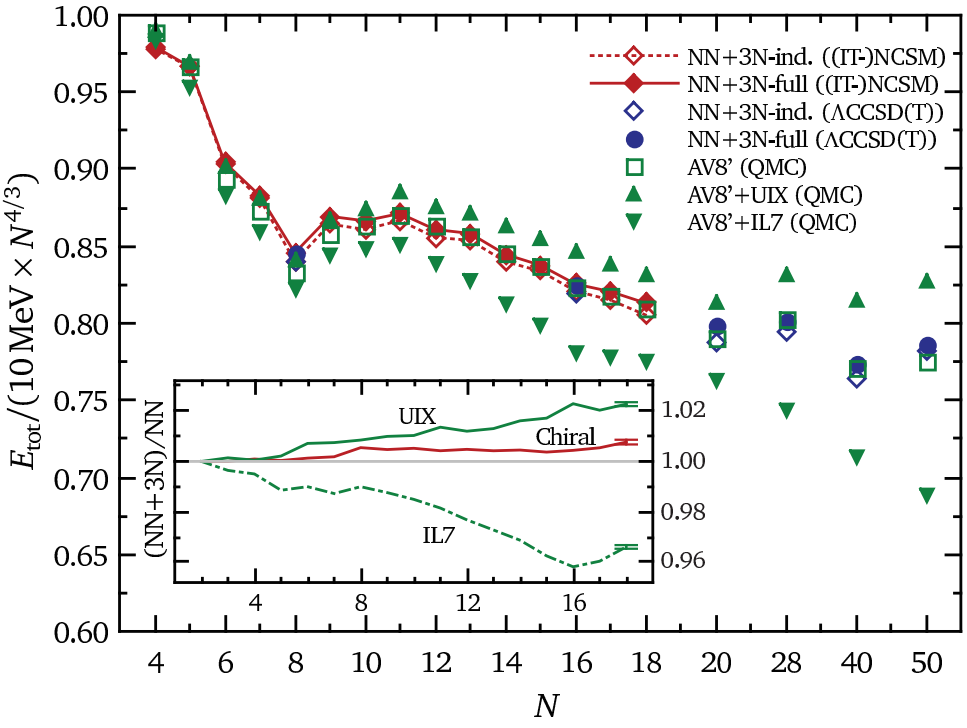

Figure 3: Comparison of ground state energies of systems with N neutrons trapped in a HO with strength 10 MeV. Solid red diamonds and blue dots signify results with $NN + 3N$ interactions derived from chiral effective field theory related to QCD. The inset displays the ratio of $NN + 3N$ to NN alone for the different interactions with the error indicated on the far right of each curve where it is maximum. The label indicates the many-body methods employed: (Importance-Truncated) No Core Shell Model ((IT-)NCSM); Coupled Cluster including Triples (ΛCCSD(T)); Quantum Monte Carlo (QMC). Figure adapted from Ref. [16].

main foci are to observe differences among realistic interactions and to see if subshell closures are predicted. For example, one may investigate spin-orbit splitting as a function of the chosen interaction and as a function of the external field parameters.

Using the same realistic chiral $NN + 3N$ interactions as used in the previous section, we investigated [15,16] neutron drop systems in a 10 MeV HO trap. In Ref. [16] we compared the results with those from Green's Function Monte Carlo (GFMC) and auxiliary field diffusion Monte Carlo (AFDMC) [42, 43] using the Argonne v_8' (AV8') NN interaction [44] and the Urbana IX (UIX) $3N$ interaction. We also compared with GFMC and AFDMC results using AV8' with the Illinois-7 (IL7) $3N$ interaction [44, 45].

For the investigations in Ref. [16] we employed both NCFC and coupled cluster (CC) methods. By implementing CC, we were able to obtain results for larger neutron drop systems.

We found important dependences on the selected interactions as shown in Fig. 3 which should have an impact on phenomenological energy-density functionals that may be derived from them. Note in Fig. 3 that, with increasing N, the chiral predictions lie between results from different high-precision phenomenological interactions, i. e. between AV8′+UIX and AV8′+IL7. It will be very important to see the influences the results of these different interactions have on energy density functionals.

One also notices in Fig. 3 there are surprisingly weak contributions from the inclusion of the chiral $3N$ interaction. Based on systematic trends shown in previous neutron-drop investigations [42,43,46], with non-chiral interactions we anticipate these conclusions will persist over a range of HO well strengths. Additional investigations are in progress to confirm this hypothesis and to extend the results to higher neutron numbers.

5 Computational accelerators and decoupling transformations

Fundamental physics investigations with chiral $NN + 3N$ interactions require forefront computational techniques in order to efficiently utilize leadership computational facilities. Many of our efforts are aimed to develop new algorithms that exploit the recent advances in hardware and software. Here we describe one of those projects that could only have been accomplished through our multidisciplinary team working in close collaboration.

This specific project focused on adapting our NCSM code, Many-Fermion Dynamics — nuclear (MFDn), for use with GPU accelerators on the supercomputer Titan at Oak Ridge National Lab. MFDn represents the input NN and $3N$ interactions in the "coupled-JT" basis with coupled angular momentum and isospin, exploiting rotational symmetry and isospin conservation to reduce memory requirements [26,38,40]. In one representative case, storing a $3N$ input interaction in the coupled-JT basis reduces the interaction file size from 33 GigaBytes (GB) to less than 0.5 GB. This method is crucial for pushing the boundaries of problem sizes that we can address, as the input interactions must be stored once per process; using the ideal process configuration on Titan, processes have access to 16 GB each. Such a reduction in memory usage, then, not only enables calculations with larger input interactions, which are required for larger model spaces, but also makes their memory footprints more manageable, leaving more room for the memory-limited NCSM calculation.

As a side-effect of this compression, as we construct the full many-nucleon Hamiltonian from the input NN and $3N$ interactions, we must perform basis transformations to extract input interaction matrix elements that our code can use directly. These basis transformations are both computationally intensive and amenable to parallelization; they are a natural fit for Titan's GPU accelerators. We have taken advantage of

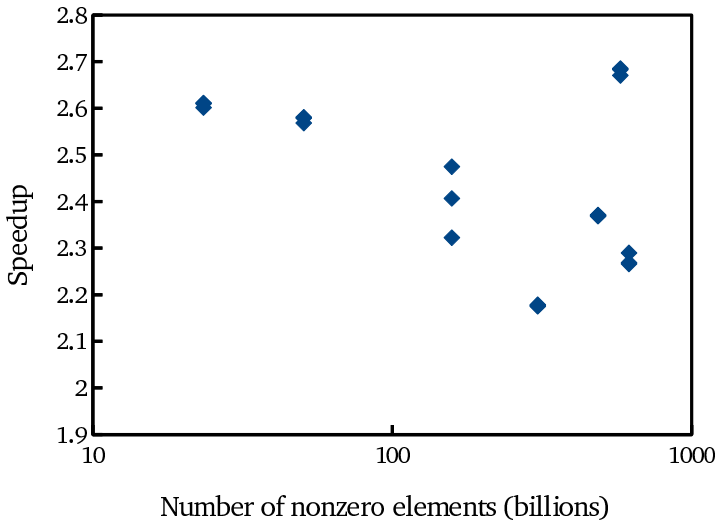

Figure 4: Speedup in the many-nucleon Hamiltonian construction stage due to implementation on GPU accelerators, graphed against the number of nonzero matrix elements in the Hamiltonian. There is no clear trend, but all speedups are in approximately the same region, indicating good weak scaling across this range of problem sizes. We graph matrix construction speedup here instead of overall speedup; overall speedup depends strongly on how long the matrix diagonalization takes, which is a function of the number of eigenstates required. Figure adapted from Ref. [15].

our multidisciplinary team of physicists, computer scientists, and applied mathematicians to port this section of our code to the GPU and optimize it [47]. Integrating the GPU-accelerated basis transformation into MFDn produces a speedup of 2.2x–2.7x in the many-nucleon Hamiltonian construction, as illustrated in Fig. 4, and a speedup of 1.2x–1.4x in the full calculation, with some variation depending on the particular problem chosen [15].

6 Overlapping communications and calculations

Our configuration interaction (CI) approach to the nuclear many-body problem results in a large sparse matrix eigenvalue problem with a symmetric real Hamiltonian matrix. This presents major technical challenges and is widely recognized as "computationally hard." One of the popular methods for obtaining the low-lying eigenvalues and eigenvectors is the Lanczos algorithm that we have implemented in MFDn. As the problem size increases with either increasing basis spaces or with the inclusion of $3N$ interactions, we face the challenge of communication costs rising with the increased numbers of nodes used in the calculations. The increase in nodes is driven by memory requirements as mentioned in the previous section.

In order to reduce communication costs, we developed an efficient mapping of the eigensolver onto the available hardware with a "topology-aware" mapping algorithm [13, 17]. We also developed an improved Lanczos algorithm that overlaps communications with calculations [14, 17].

For the challenge of efficiently overlapping communications with calculations, we worked with a hybrid MPI-OpenMP implementation and delegated one or a few threads to perform inter-process communication tasks, while the remaining threads carried out the multi-threaded computational tasks. In our algorithm, we also implemented a dynamical scheduling of the computations among the threads for the sparse matrix-vector multiplication (SpMV) so that, once a communication thread

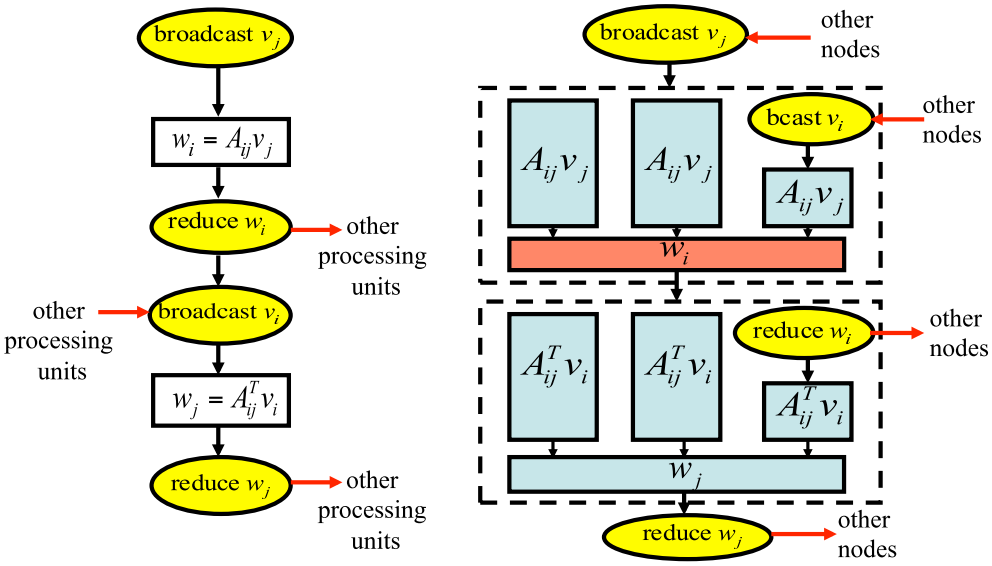

Figure 5: Comparison of SpMV and communication methods for an iteration of the Lanczos algorithm carried out by the majority of the processing units, the ones that store the off-diagonal blocks of the Hamiltonian matrix. The left subfigure displays a traditional sequential process that may be implemented with MPI. The right subfigure presents our algorithm suitable for hybrid MPI-OpenMP. Yellow ovals depict communication and rectangles depict computation. The red rectangle indicates where we require thread synchronization which incurs a small additional cost. The figure is adopted from Refs. [14, 17].

completes that task, it can participate in the multi-threaded computations.

In Fig. 5 we compare a straightforward SpMV implementation using sequential steps (left subfigure) with our algorithm (right subfigure). By mapping MPI processes in a balanced column-major order as well as developing and implementing our algorithm to overlap communications and calculations, we achieved over 80% parallel efficiency through reduction in communication overhead during the Lanczos iteration process. This includes both the SpMV and orthogonalization steps that occur in each iteration. We also found major improvements in the scalability of the eigensolver especially after adopting our topology-aware mapping algorithm. Since SpMV and vector-vector multiplication of these types are common to many other iterative methods, we believe our achievements have a wide range of applicability.

7 Future prospects

Most of our applications have focused on light nuclei with atomic number $A \leq 16$ where our theoretical many-body methods have achieved successes with leadership class facilities. However, the frontiers of our field include applications to heavier nuclei and utilizing new and improved interactions from chiral effective field theory. At the same time, we aim to evaluate observables with increasing sophistication using their operators also derived within chiral effective field theory. We mention the example of neutrinoless double beta decay as one exciting example of frontier research with *ab initio* computational nuclear theory.

We therefore face the dual challenge of advancing the underlying theory at the same time as advancing the algorithms to keep pace with the growth in the size and complexity of leadership class computers. Recent history in these efforts, with the

substantial support of the funding agencies, indicates we are experiencing a "Double Moore's Law" rate of improvement — i. e. Moore's Law for hardware improvements and a simultaneous Moore's Law improvement in the algorithms/software. We need continued support for multi-disciplinary collaborations and growth in leadership class facilities in order to achieve the full discovery potential of computational nuclear physics.

8 Acknowledgements

This work was supported in part by the US National Science Foundation under Grant No. PHY–0904782, the US Department of Energy (DOE) under Grant Nos. DE-FG02-87ER40371, DESC0008485 (SciDAC-3/NUCLEI) and DE-FG02-95ER-40934, by the Deutsche Forschungsgemeinschaft through contract SFB 634, by the Helmholtz International Center for FAIR (HIC for FAIR) within the LOEWE program of the State of Hesse, and the BMBF through contract 06DA7047I. This work was supported partially through GAUSTEQ (Germany and U.S. Nuclear Theory Exchange Program for QCD Studies of Hadrons and Nuclei) under contract number DE-SC0006758. A portion of the computational resources were provided by the National Energy Research Scientific Computing Center (NERSC), which is supported by the US DOE Office of Science, and by an INCITE award, "Nuclear Structure and Nuclear Reactions", from the US DOE Office of Advanced Scientific Computing. This research also used resources of the Oak Ridge Leadership Computing Facility at ORNL, which is supported by the US DOE Office of Science under Contract DE-AC05-00OR22725. This research also used resources of the Argonne Leadership Computing Facility, which is a DOE Office of Science User Facility supported under Contract DE-AC02-06CH11357. Further resources were provided by the computing center of the TU Darmstadt (Lichtenberg), the Jülich Supercomputing Centre (Juropa), and the LOEWE-CSC Frankfurt.

References

[1] P. Navrátil, J. P. Vary and B. R. Barrett, Phys. Rev. Lett. **84**, 5728 (2000).

[2] P. Navrátil, J. P. Vary and B. R. Barrett, Phys. Rev. C **62**, 054311 (2000).

[3] P. Navrátil, V. G. Gueorguiev, J. P. Vary, W. E. Ormand and A. Nogga, Phys. Rev. Lett. **99**, 042501 (2007).

[4] P. Maris, J. P. Vary, A. M. Shirokov, Phys. Rev. C **79**, 014308 (2009); P. Maris, A. M. Shirokov and J. P. Vary, Phys. Rev. C **81**, 021301(R) (2010).

[5] B. R. Barrett, P. Navrátil and J. P. Vary, Progr. Part. Nucl. Phys. **69**, 131 (2013) and references therein.

[6] P. Maris and J. P. Vary, Int. J. Mod. Phys. E **22**, 1330016 (2013).

[7] A. M. Shirokov, V. A. Kulikov, P. Maris and J. P. Vary, in *Nucleon-Nucleon and Three-Nucleon Interactions*, eds. L. D. Blokhintsev and I. I. Strakovsky. Nova Science, Hauppauge, NY, 2014, p. 231, http://www.novapublishers.com/catalog/product_info.php?products_id=49997.

[8] P. Sternberg, E. G. Ng, C. Yang, P. Maris, J. P. Vary, M. Sosonkina and H. V. Le, in *Proc. 2008 ACM/IEEE Conf. on Supercomputing, Austin, November 15–21, 2008*. IEEE Press, Piscataway, NJ, 2008, p. 15:1.

[9] J. P. Vary, P. Maris, E. Ng, C. Yang and M. Sosonkina, J. Phys. Conf. Ser. **180**, 012083 (2009), arXiv:0907.0209 [nucl-th] (2009).

[10] P. Maris, M. Sosonkina, J. P. Vary, E. G. Ng and C. Yang, Proc. Comp. Sci. **1**, 97 (2010).

[11] H. M. Aktulga, C. Yang, E. G. Ng, P. Maris and J. P. Vary, in *Proc. 2011 Int. Conf. on High Performance Computing and Simulation (HPCS 2011), July 4 — July 8, 2011, Istanbul, Turkey*. IEEE Press, 2011, p. 176.

[12] P. Maris, H. M. Aktulga, M. A. Caprio, Ü. Çatalyürek, E. G. Ng, D. Oryspayev, H. Potter, E. Saule, M. Sosonkina, J. P. Vary, C. Yang and Z. Zhou, J. Phys. Conf. Ser. **403**, 012019 (2012).

[13] H. M. Aktulga, C. Yang, E. N. Ng, P. Maris and J. P. Vary, in *Euro-Par*, eds. C. Kaklamanis, T. S. Papatheodorou and P. G. Spirakis. Lecture Notes Comp. Sci. **7484**, 830 (2012).

[14] H. M. Aktulga, C. Yang, E. N. Ng, P. Maris and J. P. Vary, Concurrency Computat.: Pract. Exper. **26**, 2631 (2013).

[15] H. Potter, D. Oryspayev, P. Maris, M. Sosonkina, J. Vary, S. Binder, A. Calci, J. Langhammer, R Roth, Ü. Çatalyürek and E. Saule, in *Proc. Int. Conf. Nucl. Theor. Supercomputing Era (NTSE-2013), Ames, IA, USA, May 13–17, 2013*, eds. A. M. Shirokov and A. I. Mazur. Pacific National University, Khabarovsk, Russia, 2014, p. 263, http://ntse-2013.khb.ru/Proc/Sosonkina.pdf.

[16] H. D. Potter, S. Fischer, P. Maris, J. P. Vary, S. Binder, A. Calci, J. Langhammer and R. Roth, Phys. Lett. B **739**, 445 (2014).

[17] C. Yang, H. M. Aktulga, P. Maris, E. Ng and J. Vary, in *Proc. Int. Conf. Nucl. Theor. Supercomputing Era (NTSE-2013), Ames, IA, USA, May 13–17, 2013*, eds. A. M. Shirokov and A. I. Mazur. Pacific National University, Khabarovsk, Russia, 2014, p. 272, http://ntse-2013.khb.ru/Proc/Yang.pdf.

[18] T. Dytrych, K. D. Launey, J. P. Draayer, P. Maris, J. P. Vary, D. Langr and T. Oberhuber, *see these Proceedings*, p. 75, http://www.ntse-2014.khb.ru/Proc/Dytrych.pdf.

[19] T. Abe, P. Maris, T. Otsuka, N. Shimizu, Y. Utsuno and J. P. Vary, *see these Proceedings*, p. 166, http://www.ntse-2014.khb.ru/Proc/Abe.pdf.

[20] A. M. Shirokov, G. Papadimitriou, A. I. Mazur, I. A. Mazur, R. Roth and J. P. Vary, *see these Proceedings*, p. 174, http://www.ntse-2014.khb.ru/Proc/Shirokov.pdf.

[21] A. I. Mazur, A. M. Shirokov, I. A. Mazur and J. P. Vary, *see these Proceedings*, p. 183, http://www.ntse-2014.khb.ru/Proc/A.Mazur.pdf.

[22] T. Dytrych, K. D. Launey, J. P. Draayer, P. Maris, J. P. Vary, E. Saule, U. Catalyurek and M. Sosonkina, D. Langr and M. A. Caprio, Phys. Rev. Lett. **111**, 252501 (2013).

[23] M. A. Caprio, P. Maris and J. P. Vary, Phys. Lett. B **719**, 179 (2013).

[24] P. Maris, M. A. Caprio and J. P. Vary, Phys. Rev. C **91**, 014310 (2015).

[25] M. A. Caprio, P. Maris, J. P. Vary and R. Smith, Rom. J. Phys. **60**, 738 (2015), arXiv:1502.01083 [nucl-th] (2015).

[26] P. Maris, H. M. Aktulga, S. Binder, A. Calci, Ü. V. Çatalyürek, J. Langhammer, E. Ng, E. Saule, R. Roth, J. P. Vary and C. Yang, J. Phys. Conf. Ser. **454**, 012063 (2013).

[27] A. M. Shirokov, J. P. Vary, A. I. Mazur, S. A. Zaytsev and T. A. Weber, Phys. Lett. B **621**, 96 (2005).

[28] A. M. Shirokov, J. P. Vary, A. I. Mazur and T. A. Weber, Phys. Lett. B **644**, 33 (2007); fortran subroutines to generate the JISP16 interaction in the HO basis are available at http://nuclear.physics.iastate.edu.

[29] M. A. Caprio, P. Maris, J. P. Vary and R. Smith, Int. J. Mod. Phys. E *invited review paper, submitted*.

[30] E. Epelbaum, H.-W. Hammer and U.-G. Meißner, Rev. Mod. Phys. **81**, 1773 (2009).

[31] R. Machleidt and D. R. Entem, Phys. Rep. **503**, 1 (2011).

[32] S. D. Glazek and K. G. Wilson, Phys. Rev. D **48**, 5863 (1993).

[33] F. Wegner, Ann. Phys. **506**, 77 (1994).

[34] S. K. Bogner, R. J. Furnstahl, P. Maris, R. J. Perry, A. Schwenk and J. P. Vary, Nucl. Phys. A **801**, 21 (2008).

[35] H. Hergert and R. Roth, Phys. Rev. C **75**, 051001 (2007).

[36] S. K. Bogner, R. J. Furnstahl and A. Schwenk, Progr. Part. Nucl. Phys. **65**, 94 (2010).

[37] R. Furnstahl, Nucl. Phys. Proc. Suppl. **228**, 139 (2012).

[38] R. Roth, J. Langhammer, A. Calci, S. Binder and P. Navrátil, Phys. Rev. Lett. **107**, 072501 (2011).

[39] E. D. Jurgenson, P. Navrátil and R. J. Furnstahl, Phys. Rev. Lett. **103**, 082501 (2009).

[40] R. Roth, A. Calci, J. Langhammer and S. Binder, Phys. Rev. C **90**, 024325 (2014).

[41] P. Maris, J. P. Vary, A. Calci, J. Langhammer, S. Binder and R. Roth, Phys. Rev. C **90**, 014314 (2014).

[42] S. Gandolfi, J. Carlson and S. C. Pieper, Phys. Rev. Lett. **106**, 012501 (2011).

[43] P. Maris, J. P. Vary, S. Gandolfi, J. Carlson and S. C. Pieper, Phys. Rev. C **87**, 054318 (2013).

[44] B. S. Pudliner, V. R. Pandharipande, J. Carlson, S. C. Pieper and R. B. Wiringa, Phys. Rev. C **56**, 1720 (1997).

[45] S. C. Pieper, AIP Conf. Proc. **1011**, 143 (2008).

[46] S. Bogner, R. Furnstahl, H. Hergert, M. Kortelainen, P. Maris, M. Stoitsov and J. P. Vary Phys. Rev. C **84**, 044306 (2011).

[47] D. Oryspayev, H. Potter, P. Maris, M. Sosonkina, J. P. Vary, S. Binder, A. Calci, J. Langhammer and R. Roth, in *Proc. IEEE 27th Int. Parallel and Distrib. Processing Symp. Workshops & PhD Forum, Boston, MA, USA, 20–24 May, 2013.* 2013, p. 1365.

Extrapolation to Infinite Basis Space in No-Core Monte Carlo Shell Model

T. Abe[a], P. Maris[b], T. Otsuka[a,c,d], N. Shimizu[c], Y. Utsuno[e] and J. P. Vary[b]

[a] *Department of Physics, the University of Tokyo, Hongo, Tokyo 113-0033, Japan*
[b] *Department of Physics and Astronomy, Iowa State University, Ames, Iowa 50011, USA*
[c] *Center for Nuclear Study, the University of Tokyo, Hongo, Tokyo 113-0033, Japan*
[d] *National Superconducting Cyclotron Laboratory, Michigan State University, East Lansing, Michigan 48824, USA*
[e] *Advanced Science Research Center, Japan Atomic Energy Agency, Tokai, Ibaraki 319-1195, Japan*

Abstract

We report a preliminary study of extrapolations to infinite basis space of ground-state energies in the no-core Monte Carlo shell model. Ground-state energies of ^{4}He, ^{8}Be, ^{12}C and ^{16}O are calculated in the basis spaces up to $N_{\rm shell} = 7$ with the JISP16 two-nucleon interaction. Then we extrapolate these energy eigenvalues obtained in the finite basis spaces to infinity. For the extrapolation to the infinite basis space, we employ two schemes: One of them is the traditional exponential extrapolation scheme. The other is the extrapolation scheme based on the infrared and ultraviolet regulators. From a preliminary investigation, both extrapolation schemes give consistent extrapolated energy eigenvalues in the $N_{\rm shell}$ truncation, however, estimations of the uncertainty are needed. We also compare the MCSM results to the NCFC results obtained from the different basis space truncation, $N_{\rm max}$. We find reasonable agreement between the MCSM and NCSM results.

Keywords: *No-core shell model; Monte Carlo shell model; infrared and ultraviolet regulators*

1 Introduction

The No-core Shell Model (NCSM) is one of powerful *ab initio* methods to investigate low-energy nuclear structure and reactions in light nuclei [1]. However, the computational cost is expensive and explodes factorially as the number of nucleons increases and/or the basis spaces are enlarged, because the NCSM retains all nucleon degrees of freedom explicitly. At present, the maximum size of the Hamiltonian matrix attainable for the direct diagonalization by the Lanczos technique is around 10^{10-11} in the M-scheme basis space. To avoid the large dimensionality of the Hamiltonian matrix to be diagonalized, several variants of the NCSM have emerged recently. One of these approaches is the Importance-Truncated NCSM [2] where the model spaces are extended by using an importance measure evaluated with perturbation theory. Another approach is the Symmetry-Adapted NCSM [3] where the model spaces are truncated according to selected symmetry groups. The No-core Shell Model with

Proceedings of the International Conference 'Nuclear Theory in the Supercomputing Era — 2014' (NTSE-2014), Khabarovsk, Russia, June 23–27, 2014. Eds. A. M. Shirokov and A. I. Mazur. Pacific National University, Khabarovsk, Russia, 2016, p. 166.

http://www.ntse-2014.khb.ru/Proc/Abe.pdf.

a Core [4] obtains microscopically the core, one- and two-body terms of the conventional shell-model framework, and the Hamiltonian matrix is diagonalized in the smaller basis space. Similar to these attempts, the No-core Monte Carlo Shell Model (MCSM) [5, 6] is one of the promising candidates to go beyond the Full Configuration Interaction (FCI) method which involves a different truncation of the basis space, $N_{\rm shell}$, than the one commonly used in the NCSM, $N_{\rm max}$. A proof of principle study of the MCSM without an assumed inert core has been demonstrated on the Be isotopes [5]. By exploiting the recent development in the MCSM algorithm [7], the no-core calculations with the MCSM algorithm can be performed efficiently on massively parallel supercomputers. From the benchmark calculations, the observables such as the energy, root-mean-square radius, electromagnetic dipole and quadrupole moments, give good agreement between the MCSM and FCI results in applications to p-shell nuclei [6].

Recently, extrapolation methods to the infinite basis space in the harmonic oscillator basis have been developed [8, 9]. In these proceedings, we extend the MCSM calculations in larger basis spaces and extrapolate the ground-state (g. s.) energies of ^{4}He, ^{8}Be, ^{12}C and ^{16}O to the infinite basis space. For the extrapolations, we apply a traditional extrapolation scheme and the recently proposed infrared and ultraviolet cutoff extrapolations in a harmonic oscillator basis.

2 Monte Carlo shell model

The MCSM has been developed mainly for conventional shell-model calculations with an assumed inert core [10]. The shell-model calculations with an assumed inert core by the MCSM have succeeded in obtaining approximate solutions where the direct diagonalization is difficult due to large dimensionalities. Recently, the algorithm and code itself have been significantly revised and rewritten so as to accommodate massively parallel computing environments [7]. We are able now to apply the MCSM method successfully to the no-core calculations [5, 6].

In the MCSM, a many-body basis state $|\Psi^{J^\pi M}\rangle$ is approximated as a linear combination of non-orthogonal angular-momentum, J, and parity, π, projected deformed Slater determinants with good total angular momentum projection, M,

$$|\Psi^{J^\pi M}\rangle = \sum_{n=1}^{N_b} f_n \sum_{K=-J}^{J} g_{nK}\, P^J_{MK}\, P^\pi |\phi_n\rangle, \tag{1}$$

where P^J_{MK} is the projection operator for the total angular momentum, J, with its z-projection in the laboratory (body-fixed) frame, M (K). P^π is the projection operator for the parity. N_b is the number of Slater determinants. A deformed Slater determinant is described by $|\phi\rangle = \prod_{i=1}^{A} a_i^\dagger |-\rangle$ with the vacuum $|-\rangle$ and the creation operator $a_i^\dagger = \sum_{\alpha=1}^{N_{\rm sp}} c_\alpha^\dagger\, D_{\alpha i}$. $N_{\rm sp}$ is specified by the cutoff of the single particle basis space, $N_{\rm shell}$.

One then stochastically samples the coefficient $D_{\alpha i}$ in all possible many-body basis states around the mean field solutions through auxiliary fields and/or automatically evaluates it by the conjugate gradient method. The coefficients, f_n and g_{nK}, are determined by the diagonalization of the Hamiltonian matrix. With increasing the number of basis states, N_b, the energy eigenvalue converges from above to the exact solution and gives the variational upper bound. In recent MCSM calculations, the energy eigenvalue obtained by the above way is extrapolated by using the energy variance so as to get better estimate of true eigenvalue in the chosen basis space. Recent development and the technical details of the MCSM algorithm can be found in Ref. [7]. The next step is to further extrapolate the MCSM results to those in the infinite basis space to get an *ab initio* solution and to compare them with another

solution by the NCFC method [11], which extrapolates from the different truncation of basis space, $N_{\max}$.

3 Extrapolations to infinite basis space

Extrapolation methods to the infinite basis space in the harmonic oscillator basis have been developed in recent years [8, 9]. In this section, we briefly summarize the extrapolation methods applied to the MCSM.

The extrapolation of the results in the harmonic oscillator basis has a long history. Until recently, the exponential fit of the energy with fixed $\hbar\omega$,

$$E(N) = E(N = \infty) + a \exp(-bN), \tag{2}$$

has been traditionally adopted. Here, N describes the size of basis space, and $E(N = \infty)$, a and b are the fit parameters. The NCFC method combines the NCSM with an elaborated scheme based on the traditional extrapolation scheme, which gives an *ab initio* solution by extrapolating the results in the $N = N_{\max}$ truncated basis space to infinity [11].

Recently proposed extrapolation scheme utilizes the infrared (IR) and ultraviolet (UV) cutoff scales [8, 9]. It is just a transformation from a two-parameter problem in $(N, \hbar\omega)$ to (λ, Λ), but the scaling properties can be different. In the harmonic oscillator basis, the IR cutoff scale is defined as $\lambda_{sc} = \sqrt{(m\hbar\omega)/(N + 3/2)}$, which corresponds to the inverse of the root-mean-square radius in the highest harmonic oscillator level in the basis space N, while the UV cutoff scale is defined as $\Lambda = \sqrt{m(N + 3/2)\hbar\omega}$, which is associated with the highest harmonic oscillator level in the basis space N. Note that there is another definition of the IR scale by $\lambda = \sqrt{m\hbar\omega}$, which is characterized by the minimum allowed energy difference between the harmonic oscillator levels. Here, we use λ_{sc}, not λ, as the IR cutoff due to its scaling property. Also note that there is another definition of the UV regulator ($\Lambda' = \sqrt{2}\Lambda$), but the extrapolated energy is not affected by the difference of the definitions. In this study, we use Λ as the UV regulator. The IR-cutoff extrapolation is performed by using UV-saturated results with

$$E(\lambda) = E(\lambda = 0) + a \exp(-b/\lambda), \tag{3}$$

where $E(\lambda = 0)$, a and b are the fit parameters. Note that the IR extrapolation formula, Eq. (3) was derived for a single-particle system and is widely applied to bound states of many-body systems [9]. Although the UV extrapolation formula has yet to be derived, the IR- and UV-cutoff combined extrapolation is applied, for example, in Ref. [12]. The IR- and UV-cutoff extrapolation is given by using the following formula,

$$E(\lambda, \Lambda) = E(\lambda = 0, \Lambda = \infty) + a \exp(-b/\lambda) + c \exp(-\Lambda^2/d^2), \tag{4}$$

where $E(\lambda = 0, \Lambda = \infty)$, a, b, c and d are the fit parameters.

By using the above formulae, Eqs. (2), (3) and (4), we attempt to extrapolate the MCSM results of the g. s. energies in the $N = N_{\text{shell}}$ truncation to the infinite basis space.

4 Results

We have calculated the ground-state energies of ^{4}He, ^{8}Be, ^{12}C and ^{16}O in the basis spaces up to $N_{\text{shell}} = 7$. In this study, we have taken $N_b = 100$ and extrapolated the energies obtained in each basis space by the energy variance. The energy-variance extrapolation is needed to obtain better estimate of true eigenvalue derived from

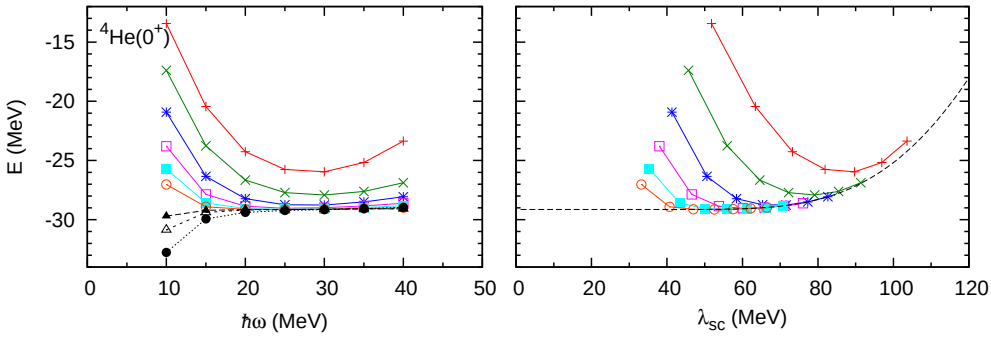

Figure 1: Extrapolations of ^{4}He g. s. energy. The JISP16 two-nucleon interaction is employed and Coulomb interaction is turned off. The color (symbol) difference corresponds to different size of basis space. The red (plus), green (cross), blue (asterisk), pink (open square), aqua (solid square), orange (open circle) symbols with solid lines are the MCSM results in $N_{\rm shell}$ = 2, 3, 4, 5, 6 and 7, respectively. The traditional exponential extrapolation by Eq. (2) is shown in the left panel. The black solid circles with dotted line, black open triangles with short-dashed line, and black solid triangles with long-dashed line denote the extrapolated results to infinite basis space from the MCSM results in $N_{\rm shell}$ = 2−7, 3−7, and 4−7, respectively. The IR-cutoff extrapolation by Eq. (3) is shown in the right panel as the black dotted curve.

the calculated eigenvalue and its variance in the N_b = 100 truncation of each finite MCSM basis space defined by $N_{\rm shell}$. In the MCSM calculations, the JISP16 two-nucleon interaction [13] is employed, and the Coulomb force is turned off. For simplicity, the effect of spurious center-of-motion is neglected. MCSM calculations have been performed on K computer, RIKEN AICS and FX10 at the University of Tokyo. The MCSM results of the energies have been extrapolated to the infinite basis space by using the extrapolation schemes discussed in the previous section. For the extrapolations to the infinite basis space, we take $N_{\rm shell}$ as N in Eqs. (2), (3) and (4).

Fig. 1 shows the extrapolations of the ^{4}He g. s. energy to the infinite basis space. In the figure, each color (symbol) corresponds to a different value of $N_{\rm shell}$. The red (plus), green (cross), blue (asterisk), pink (open square), aqua (solid square), orange (open circle) symbols with solid lines are the MCSM results in $N_{\rm shell}$ = 2, 3, 4, 5, 6 and 7, respectively. The traditional extrapolation is demonstrated in the left panel, while the IR-cutoff extrapolation in the right panel. In the left panel, the black symbols connected with dotted lines are the extrapolated results obtained by the traditional extrapolation scheme, Eq. (2). The black solid circles with dotted line, black open triangles with short-dashed line, and black solid triangles with long-dashed line denote the extrapolated results to infinite basis space from the MCSM results in $N_{\rm shell}$ = 2−7, 3−7, and 4−7, respectively. Traditional exponential fits to the MCSM results with $\hbar\omega$ = 15−35 MeV in $N_{\rm shell}$ = 3−7 give the ^{4}He g. s. energy ranging from −29.389 to −29.077 MeV. In the right panel, the dotted curve is the fit function of Eq. (3) determined by the MCSM results, which demonstrates the IR-cutoff extrapolation. The IR-cutoff extrapolation gives −29.142 MeV where $\lambda_{sc} = 0$. These extrapolated results give a good agreement with the NCFC result of −29.164(2) MeV, which is obtained by the traditional exponential extrapolation to infinite basis space from a different truncation of the basis space governed by $N_{\rm max}$.

Fig. 2 shows the extrapolations of the ^{8}Be g. s. energy to the infinite basis space. The notation conventions in Fig. 2 are the same as in Fig. 1. As shown in the left panel of Fig. 2, the traditional exponential fits to the MCSM results with $\hbar\omega$ = 25−35 MeV in $N_{\rm shell}$ = 3−7 give the ^{8}Be g. s. energy ranging from −59.289 to −57.396 MeV. From the right panel of Fig. 2, the IR-cutoff extrapolation gives −58.676 MeV. These

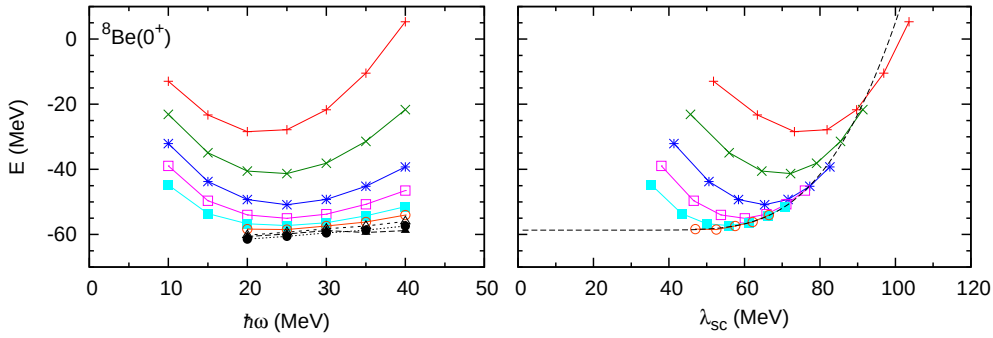

Figure 2: Extrapolations of ^{8}Be g. s. energy. Same caption as in Fig. 1, but for ^{8}Be.

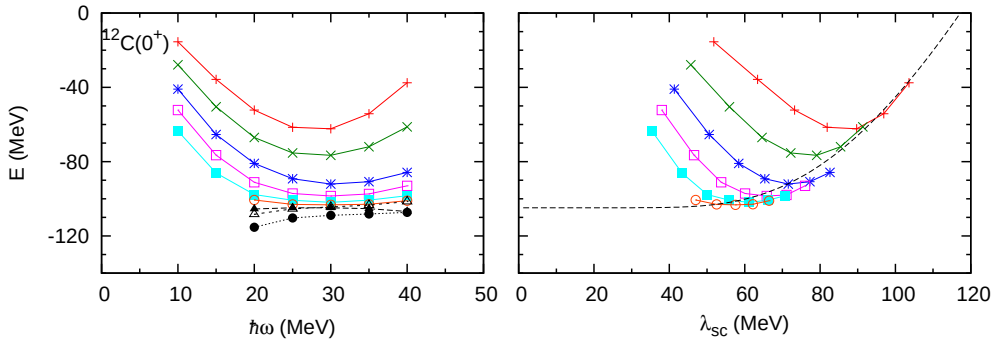

Figure 3: Extrapolations of ^{12}C g. s. energy. Same caption as in Fig. 1, but for ^{12}C.

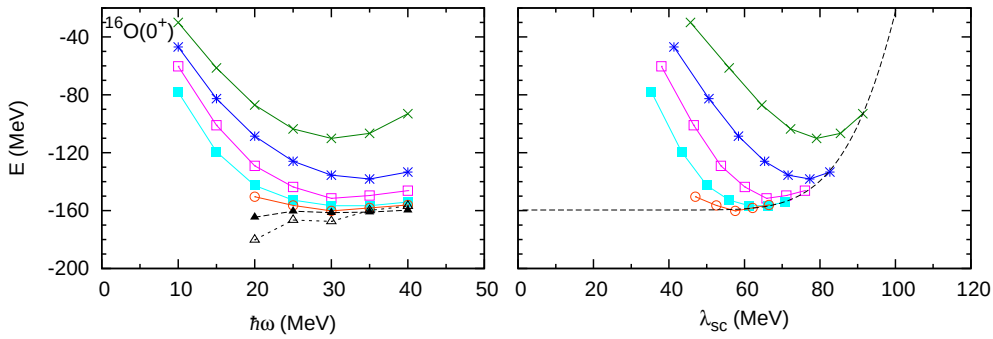

Figure 4: Extrapolations of ^{16}O g. s. energy. Same caption as in Fig. 1, but for ^{16}O, besides the absence of the $N_{\rm shell} = 2$ results and the traditional extrapolation to the infinite basis space from the MCSM results in $N_{\rm shell} = 2{-}7$.

extrapolated results are in a good agreement with the NCFC result of $-59.1(1)$ MeV.

Fig. 3 shows the extrapolations of the ^{12}C g. s. energy to the infinite basis space. The notation conventions in Fig. 3 are the same as in Fig. 1. From the left panel of Fig. 3, the traditional exponential fits to the MCSM results with $\hbar\omega = 25 - 35$ MeV in $N_{\rm shell} = 3 - 7$ give the ^{12}C g. s. energy ranging from -105.392 to -103.393 MeV. From the right panel of Fig. 3, the IR-cutoff extrapolation gives -104.812 MeV. Note that the NCFC result is not yet available.

Fig. 4 shows the extrapolations of the ^{16}O g. s. energy to the infinite basis space. The notation conventions in Fig. 4 are the same as in Fig. 1, except for the absence of the $N_{\rm shell} = 2$ results and for the traditional extrapolation to the infinite basis space

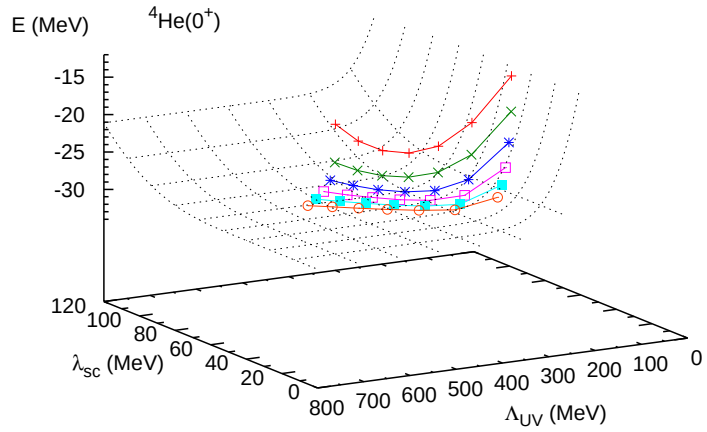

Figure 5: IR- and UV-cutoff extrapolations of ^{4}He g. s. energy. The color (symbol) difference corresponds to different size of basis spaces, see Fig. 1 for details. The black mesh shows the IR- and UV-cutoff extrapolations by Eq. (4).

from the MCSM results in $N_{\rm shell} = 2-7$. From the left panel of Fig. 4, the traditional exponential fits to the MCSM results with $\hbar\omega = 25-35$ MeV in $N_{\rm shell} = 4-7$ give the ^{16}O g. s. energy ranging from -161.435 to -160.378 MeV. From the right panel of Fig. 4, the IR-cutoff extrapolation gives -159.592 MeV. Note that the NCFC result, as in the case of ^{12}C, is not yet available.

Fig. 5 shows the IR- and UV-extrapolation of the ^{4}He g. s. energy to the infinite basis space. In the figure, each color (symbol) corresponds to a different value of N_{shell} as in Fig. 1. The dotted mesh is obtained by the fit with Eq. (4) to the MCSM results, which demonstrate the IR- and UV-cutoff extrapolation. The IR- and UV-cutoff extrapolation gives -29.139 MeV where $\lambda_{sc} = 0$ and $\Lambda = \infty$. Although the IR- and UV-cutoff extrapolated result is in a good agreement with those of the traditional and IR-cutoff extrapolations shown in Fig. 1 and also with the NCFC, further investigation on the extrapolation uncertainties is necessary to confirm these extrapolated results. The IR- and UV-cutoff extrapolations for ^{8}Be, ^{12}C and ^{16}O are under way.

Finally, we summarize the extrapolated results in Table 1. These MCSM results are preliminary. We have to obtain better MCSM results in each basis space by increasing N_b so as to quantify the uncertainties both of the energy-variance extrapolation in the finite basis space and of the extrapolations to the infinite basis space.

5 Summary

We have shown preliminary results of extrapolations to the infinite basis space for ground-state energies in no-core Monte Carlo shell model. The g. s. energies of ^{4}He,

Table 1: Comparison of the extrapolated g. s. energies of ^{4}He, ^{8}Be, ^{12}C and ^{16}O. The entries of Traditional, IR, IR and UV, and NCFC are the extrapolated MCSM results by Eqs. (2), (3), and (4), and the NCFC result, respectively. Energies are in MeV.

	Traditional	IR	IR and UV	NCFC
^{4}He 0^+ g. s. energy	$-29.389 \div -29.007$	-29.142	-29.139	$-29.164(2)$
^{8}Be 0^+ g. s. energy	$-59.289 \div -57.396$	-58.676		$-59.1(1)$
^{12}C 0^+ g. s. energy	$-105.392 \div -103.393$	-104.812		
^{16}O 0^+ g. s. energy	$-161.435 \div -160.378$	-159.592		

^{8}Be, ^{12}C and ^{16}O were calculated in the basis spaces up to $N_{\rm shell} = 7$ with the JISP16 two-nucleon interaction and without the Coulomb interaction. Then we extrapolate these energy eigenvalues obtained in the finite basis spaces to the infinite basis limit by the traditional exponential scheme and the schemes with the IR and UV cutoffs. From this preliminary investigation, both extrapolation schemes give consistent extrapolated energy eigenvalues in the $N_{\rm shell}$ truncation, however, estimations of the uncertainty are needed. We also compare the MCSM results for the ^{4}He and ^{8}Be g. s. energies to the NCFC results obtained from the different $N_{\rm max}$ basis space truncations. The agreement between them seems to be reasonable.

Acknowledgments

This work was supported in part by the SPIRE Field 5 from MEXT, Japan (hp130024 and hp140210). We also acknowledge Grants-in-Aid for Young Scientists (Nos. 20740127 and 21740204), for Scientific Research (Nos. 20244022 and 23244049), and for Scientific Research in Innovative Areas (No. 20105003) from JSPS, and the CNS-RIKEN joint project for large-scale nuclear structure calculations. This work was also supported in part by the US DOE Grants No. DESC0008485 (SciDAC-3/NUCLEI) and DE-FG02-87ER40371, by the US NSF Grant No. PHY-0904782, and through JUSTIPEN under grant No. DE-FG02-06ER41407. A part of the MCSM calculations was performed on K computer at RIKEN AICS and FX10 at the University of Tokyo. Computational resources for the FCI and NCFC calculations were provided by the National Energy Research Scientific Computing Center (NERSC) supported by the Office of Science of the U.S. Department of Energy under Contract No. DE-AC02-05CH11231, and by the Oak Ridge Leadership Computing Facility at the Oak Ridge National Laboratory supported by the Office of Science of the U.S. Department of Energy under Contract No. DE-AC05-00OR22725.

References

[1] P. Navrátil, J. P. Vary and B. R. Barrett, Phys. Rev. Lett. **84**, 5728 (2000); Phys. Rev. C **62**, 054311 (2000); S. Quaglioni and P. Navrátil, Phys. Rev. Lett. **101**, 092501 (2008); Phys. Rev. C **79**, 044606 (2009); for a recent review, see, e. g., B. R. Barrett, P. Navrátil and J. P. Vary, Progr. Part. Nucl. Phys. **69**, 131 (2013).

[2] R. Roth and P. Navrátil, Phys. Rev. Lett. **99**, 092501 (2007); R. Roth, Phys. Rev. C **79**, 064324 (2009); R. Roth, J. Langhammer, A. Calci, S. Binder and P. Navrátil, Phys. Rev. Lett. **107**, 072501 (2011); R. Roth, S. Binder, K. Vobig, A. Calci, J. Langhammer and P. Navrátil, *ibid.* **109**, 052501 (2012).

[3] T. Dytrych, K. D. Sviratcheva, C. Bahri, J. P. Draayer and J. P. Vary, Phys. Rev. Lett. **98**, 162503 (2007); Phys. Rev. C **76**, 014315 (2007); J. Phys. G **35**, 095101 (2008); T. Dytrych, K. D. Launey, J. P. Draayer, P. Maris, J. P. Vary, E. Saule, U. Catalyurek, M. Sosonkina, D. Langr and M. A. Caprio, Phys. Rev. Lett. **111**, 252501 (2013); for reviews, see T. Dytrych, K. D. Sviratcheva, J. P. Draayer, C. Bahri and J. P. Vary, J. Phys. G **35**, 123101 (2008); J. P. Draayer, T. Dytrych, K. D. Launey and D. Langr, Progr. Part. Nucl. Phys. **67**, 516 (2012).

[4] A. F. Lisetskiy, B. R. Barrett, M. K. G. Kruse, P. Navrátil, I. Stetcu and J. P. Vary, Phys. Rev. C **78**, 044302 (2008); A. F. Lisetskiy, M. K. G. Kruse, B. R. Barrett, P. Navrátil, I. Stetcu and J. P. Vary, *ibid.* **80**, 024315 (2009).

[5] L. Liu, T. Otsuka, N. Shimizu, Y. Utsuno and R. Roth, Phys. Rev. C **86**, 014304 (2012).

[6] T. Abe, P. Maris, T. Otsuka, N. Shimizu, Y. Utsuno and J. P. Vary, Phys. Rev. C **86**, 054301 (2012).

[7] N. Shimizu, Y. Utsuno, T. Mizusaki, T. Otsuka, T. Abe and M. Honma, Phys. Rev. C **82**, 061305(R) (2010); N. Shimizu, Y. Utsuno, T. Mizusaki, M. Honma, Y. Tsunoda and T. Otsuka, *ibid.* **85**, 054301 (2012); Y. Utsuno, N. Shimizu, T. Otsuka and T. Abe, Comp. Phys. Comm. **184**, 102 (2013); N. Shimizu, T. Abe, Y. Tsunoda, Y. Utsuno, T. Yoshida, T. Mizusaki, M. Honma and T. Otsuka, Progr. Theor. Exp. Phys. 01A205 (2012).

[8] S. A. Coon, M. I. Avetian, M. K. G. Kruse, U. van Kolck, P. Maris and J. P. Vary, Phys. Rev. C **86**, 054002 (2012); S. A. Coon, arXiv:1303.6358 [nucl-th] (2013); S. A. Coon and M. K. G. Kruse, arXiv:1408.0738 [nucl-th] (2014).

[9] R. J. Furnstahl, G. Hagen and T. Papenbrock, Phys. Rev. C **86**, 031301(R) (2012); S. N. More, A. Eksrom, R. J. Furnstahl, G. Hagen and T. Papenbrock, *ibid.* **87**, 044326 (2013); R. J. Furnstahl, S. N. More and T. Papenbrock, *ibid.* **89**, 044301 (2014); R. J. Furnstahl, G. Hagen, T. Papenbrock and K. A. Wendt, arXiv:1408.0252 [nucl-th] (2014); S. Konig, S. K. Bogner, R. J. Furnstahl, S. N. More and T. Papenbrock, arXiv:1409.5997 [nucl-th] (2014).

[10] M. Honma, T. Mizusaki and T. Otsuka, Phys. Rev. Lett. **75**, 1284 (1995); *ibid.* **77**, 3315 (1996); T. Otsuka, M. Honma and T. Mizusaki, *ibid.* **81**, 1588 (1998); for a review, see T. Otsuka, M. Honma, T. Mizusaki, N. Shimizu and Y. Utsuno, Progr. Part. Nucl. Phys. **47**, 319 (2001).

[11] P. Maris, J. P. Vary and A. M. Shirokov, Phys. Rev. C **79**, 14308 (2009); P. Maris, A. M. Shirokov and J. P. Vary, *ibid.* **81**, 021301 (2010); C. Cockrell, J. P. Vary and P. Maris, *ibid.* **86**, 034325 (2012); P. Maris and J. P. Vary, Int. J. Mod. Phys. E **22**, 1330016 (2013).

[12] E. D. Jurgenson, P. Maris, R. J. Furnstahl, W. E. Ormand and J. P. Vary, Phys. Rev. C **87**, 054312 (2013).

[13] A. M. Shirokov, J. P. Vary, A. I. Mazur and T. A. Weber, Phys. Lett. B **644**, 33 (2007); A. M. Shirokov, J. P. Vary, A. I. Mazur, S. A. Zaytsev and T. A. Weber, *ibid.* **621**, 96 (2005).

Tetraneutron Resonance from JISP16 NN Interaction

A. M. Shirokov[a,b,c], G. Papadimitriou[d], A. I. Mazur[c], I. A. Mazur[c], R. Roth[e] and J. P. Vary[b]

[a] *Skobeltsyn Institute of Nuclear Physics, Lomonosov Moscow State University, Moscow 119991, Russia*

[b] *Department of Physics and Astronomy, Iowa State University, Ames, IA 50011, USA*

[c] *Department of Physics, Pacific National University, Khabarovsk 680035, Russia*

[d] *Nuclear and Chemical Science Division, Lawrence Livermore National Laboratory, Livermore, CA 94551, USA*

[e] *Institut für Kernphysik, Technische Universität Darmstadt, 64289 Darmstadt, Germany*

Abstract

We utilize various *ab initio* approaches to search for a low-lying resonance in the four-neutron ($4n$) system using the JISP16 realistic NN interaction. Our most accurate prediction is obtained using a J-matrix extension of the No-Core Shell Model and suggests a $4n$ resonant state at an energy near $E_r = 0.8$ MeV with a width of approximately $\Gamma = 1.4$ MeV.

Keywords: *Four-neutron system, No-Core Shell Model; HORSE (J-matrix) formalism of quantum scattering theory; No-Core Gamow Shell Model; resonance energy and width; S-matrix poles*

With interest sparked by a recent experiment [1] on the possibility of a resonant four neutron ($4n$) structure (see also [2] for a recent communication) and while awaiting for forthcoming experiments on the same system [3–5], we search for $4n$ (tetraneutron) resonances using the high precision nucleon-nucleon interaction JISP16 [6]. The experiment has found a candidate $4n$ resonant state with an energy of $0.83 \pm 0.65(\text{stat}) \pm 1.25(\text{syst})$ MeV above the $4n$ disintegration threshold and with an upper limit of 2.6 MeV for the width. The $4n$ system was probed by studying the reaction between the bound ^{4}He nucleus and the weakly bound Helium isotope, ^{8}He. It has been shown [7] that the four neutrons in ^{8}He form a relatively compact geometry. Hence the experimental study of the $^4\text{He} + {}^8\text{He}$ collisions is a promising avenue for the isolation of the $4n$ subsystem.

The experimental quest for the very exotic $4n$ structure started almost fifteen years ago when the possibility of a bound $4n$ (or tetraneutron) was proposed [8] in ^{14}Be breakup reactions ($^{14}\text{Be} \to {}^{10}\text{Be} + 4n$). This experimental result however has not been confirmed. Early calculations of the $4n$ system in a small Harmonic Oscillator (HO) basis [9] found it unbound by about 18.5 MeV. More recent state-of-the-art theoretical calculations have concluded that without altering fundamental characteristics of the nuclear forces [10], the tetraneutron should not be bound. More theoretical calculations were performed [11, 12], all of them agreeing that a bound tetraneutron is not supported by theory. Calculations performed in the complex energy plane to search of multi-neutron resonances within the Complex Scaling Method [13–15] give

Proceedings of the International Conference 'Nuclear Theory in the Supercomputing Era — 2014' (NTSE-2014), Khabarovsk, Russia, June 23–27, 2014. Eds. A. M. Shirokov and A. I. Mazur. Pacific National University, Khabarovsk, Russia, 2016, p. 174.

http://www.ntse-2014.khb.ru/Proc/Shirokov.pdf.

quantitatively similar results and point to the fact that the $4n$ resonance, if it exists, would have a very large width ($\sim$15 MeV), likely prohibitive for experimental detection. The tetraneutron could however exist if confined in a strong external field. In Nature, this would be the case of ^{8}He, where the nuclear mean-field is strong enough to confine the tetraneutron around the tightly bound α-core. Once the field is suddenly removed by knocking out ^{4}He, it is expected that the tetraneutron will disintegrate very fast due to its anticipated large width.

There is also a work [16] where the continuum response of the tetraneutron was studied. The outcome was that there exists a resonant-like structure at around 4–5 MeV above threshold, however this structure depends on the tetraneutron production reaction mechanism represented by the source term in this study, and the conclusion was that the $4n$ probably cannot be interpreted as a well-defined resonance but most probably as a few-body continuum response in a reaction.

Nevertheless, our current knowledge of nuclear interactions and many-body methods provide new opportunities to probe exotic states above thresholds. We are further motivated by the conclusion in Ref. [10] that even though the existence of a bound tetraneutron is ruled out, extrapolations of (artificialy) bound state results to the unbound regime imply that there may be a $4n$ resonance at about 2 MeV above the four-neutron threshold.

A complete investigation of the tetraneutron as a resonant state, would consist of performing calculations of the actual experimental reaction ^{4}He(^{8}He,^{8}Be). However, such a realistic calculation is currently out of reach, though we are witnessing the first steps for such theoretical calculations to become a reality [17, 18].

We treat the $4n$ system with a realistic non-relativistic Hamiltonian which consists of the kinetic energy and the realistic inter-neutron potential defined by the JISP16 interaction [6]. We solve for the $4n$ energies by employing basis expansion techniques for the Hamiltonian. Specifically, we employ the No-Core Shell Model (NCSM) [19] and artificially bind the $4n$ system by scaling the interaction to track its lowest state as a function of that scaling. We also employ the No-Core Gamow Shell Model (NCGSM) [20, 21] which provides resonant parameters directly in the complex energy plane. Finally, we extend NCSM using the Single-State Harmonic Oscillator Representation of Scattering Equations (SS-HORSE) formalism [22–24] for calculations of the S-matrix resonant parameters. This paper elaborates on the work presented in Ref. [25].

First, to get an estimate of whether JISP16 can provide a $4n$ resonant state, we exploit the technique suggested in Ref. [10] and perform pure NCSM calculations by constructing an artificially bound $4n$ system by scaling up the NN interaction. Our extrapolations to the unbound regime are in quantitative agreement with Ref. [10] that predicts a resonance at around 2 MeV above threshold but without any indication of the width. We tried also a much more elaborate technique of Analytic Continuation in the Coupling Constant (ACCC) [26, 27]. The ACCC requires exact results for the $4n$ energy with scaled interactions while NCSM provides only variational energy upperbounds; extrapolations to the infinite basis space appear to lack the precision needed for a definite prediction of the resonance energy and width.

In order to shed further light on a possible $4n$ resonance, we solve the NCGSM with the JISP16 interaction. In the NCGSM one employs a basis set that is spanned by the Berggren states [28] which includes bound, resonant and non-resonant states; they correspond to solutions of the single particle (s. p.) Schrödinger equation obeying outgoing (bound-resonant states) and scattering (non-resonant states) boundary conditions. In this basis the Hamiltonian matrix becomes complex symmetric and its eigenvalues acquire both real and imaginary parts. The real part is identical to the position of the resonant state above the threshold and the imaginary part is related to its width, $\Gamma = -2\,\mathrm{Im}(E)$.

We adopt the basis provided by a Woods–Saxon (WS) potential for a neutron in relative motion with a $3n$ system. We modify the WS parameters in a way that it will

support a weakly bound $0s_{1/2}$ state and a resonant $0p_{3/2}$ state. For the $s_{1/2}$ and $p_{3/2}$ shells we include the $0s_{1/2}$ bound state, the $0p_{3/2}$ resonant state and the associated non-resonant states. We additionally include the $p_{1/2}$ real scattering continuum along the real momentum axis. We performed calculations for several WS parameterizations supporting both narrow and broad s. p. states. States with an angular momentum of $\ell > 2$ are taken as HO states. We retain states through the $3g_{9/2}$ shells. For our NCGSM calculations, the $\hbar\Omega$ parameter of the HO basis was varied from 4 MeV to 14 MeV. Due to the use of Berggren states for low angular momentum partial waves, we observe a weak dependence of the results on the $\hbar\Omega$ parameter.

For the $4n$ calculation we constructed Slater determinants allowing two neutrons to occupy continuum orbits, called the 2p-2h approximation. Taking the dependence on basis space parameters into account, the NCGSM results indicate a broad resonant state in the energy range $E_r \sim 2.5$ to 3 MeV above the $4n$ threshold and a width ranging from $\Gamma \sim 2.5$ to 6 MeV. These variations reflect the omission of additional p-h excitations. Nevertheless the real part of the resonance exhibits a robust character at the current level of p-h truncation, i. e., it is nearly independent of the WS parameterizations and independent of the frequency of the HO basis.

At the same time, we observe that the resonance energy decreases together with the width as the NCGSM basis increases. Getting the converged resonance pole position in this approach requires the NCGSM basis spaces beyond our current reach.

Finally, following the J-matrix formalism in scattering theory [29] as represented in the HORSE method [30], we extend the finite NCSM Hamiltonian matrix in the HO basis into the continuum by appending to it the infinite kinetic energy matrix.

For the kinetic energy extension of the NCSM Hamiltonian, we use the *democratic decay* approximation (also known as *true four-body scattering* or *4 → 4 scattering*) suggested [31, 32] and first applied to the tetraneutron problem [33–35] by Jibuti and collaborators. Later it was exploited in other tetraneutron studies (see, e. g., Refs. [13, 16, 36, 37]). Democratic decay implies a description of the continuum using a complete hyperspherical harmonics (HH) basis. In practical applications, a limited set of HH is selected which is adequate for the systems like the $4n$ which has no bound subsystems.

The general theory of the democratic decay within the HORSE formalism was proposed in Ref. [38]. We use here the minimal approximation for the four-neutron decay mode, i. e., only HH with hyperspherical momentum $K = K_{\min} = 2$ are retained in the kinetic energy extension to the NCSM. This approximation relies on the fact that the decay in the hyperspherical states with $K > K_{\min}$ is strongly suppressed by a large hyperspherical centrifugal barrier $\frac{\mathscr{L}(\mathscr{L}+1)}{\rho^2}$ where $\mathscr{L} = K + 3$ and the hyperradius $\rho^2 = \sum_{i=1}^{4}(\mathbf{r}_i - \mathbf{R})^2$, $\mathbf{R}$ is the tetraneutron center-of-mass coordinate and $\mathbf{r}_i$ are the coordinates of individual neutrons. Note, all possible HH are retained in the NCSM basis. The accuracy of this approximation was confirmed in studies of democratic decays in cluster models [39–42].

Realistic NN interactions require large NCSM basis spaces and extensive computational resources. For computational economy, we also adopt the SS-HORSE approach [22–24] where we calculate the $4 \to 4$ S-matrix $S(E)$ at one of the positive eigenenergies of the NCSM Hamiltonian, $E = E_\lambda$. In this case, the general HORSE formula for the S-matrix simplifies: expressing $S(E)$ through the $4 \to 4$ phase shifts $\delta(E)$,

$$S(E) = e^{2i\delta(E)}, \tag{1}$$

we obtain for the phase shifts [22–24]

$$\delta(E_\lambda) = -\tan^{-1}\frac{S_{N^{tot}_{\max}+2,\mathscr{L}}(E_\lambda)}{C_{N^{tot}_{\max}+2,\mathscr{L}}(E_\lambda)}. \tag{2}$$

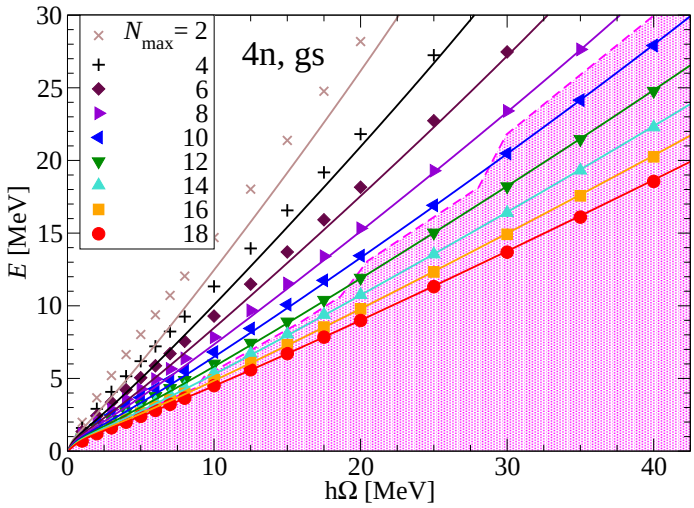

Figure 1: NCSM results for the tetraneutron ground state energy obtained with various $N_{\max}$ (symbols) plotted as functions of $\hbar\Omega$. The shaded area shows the NCSM result selection for the S-matrix parametrization; the solid curves are obtained from the phase shifts parametrized with a single resonance pole by solving Eq. (2) for the eigenenergies at given $N_{\max}$ and $\hbar\Omega$ values.

Here the maximal total quanta in the NCSM basis $N^{tot}_{\max} = N_{\min} + N_{\max}$, $N_{\min} = 2$ is the quanta of the lowest possible oscillator state of the $4n$ system, $N_{\max}$ is the maximal excitation quanta in the NCSM basis; analytical expressions for the regular $S_{N\mathscr{L}}(E)$ and irregular $C_{N\mathscr{L}}(E)$ solutions of the free many-body Hamiltonian in the oscillator representation can be found elsewhere [38]. Varying $N_{\max}$ and $\hbar\Omega$ in the NCSM calculations, we obtain the phase shifts and S-matrix over an energy interval. Parametrizing the S-matrix in this energy interval, we obtain information about its nearby poles and hence resonances in the system.

The NCSM calculations were performed with $N_{\max} = 2, 4, \ldots, 18$ using the code MFDn [43, 44] and with $\hbar\Omega$ values, 1 MeV $\leq \hbar\Omega \leq$ 40 MeV. The results for the 0^+ tetraneutron ground state are shown in Fig. 1.

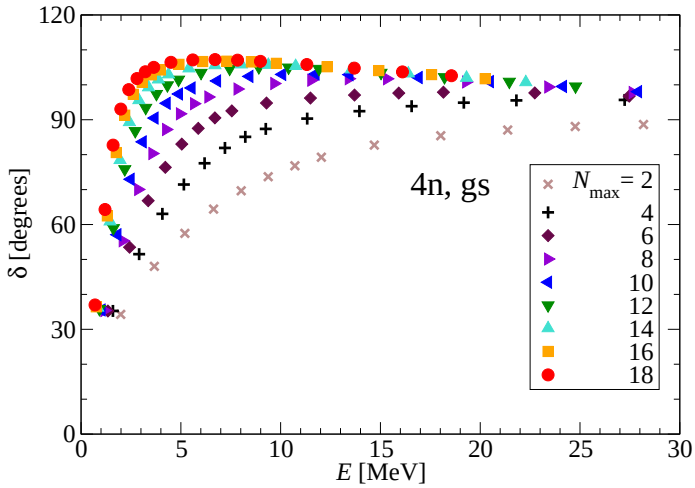

Figure 2: The $4 \to 4$ phase shifts obtained directly from the NCSM results using Eq. (2).

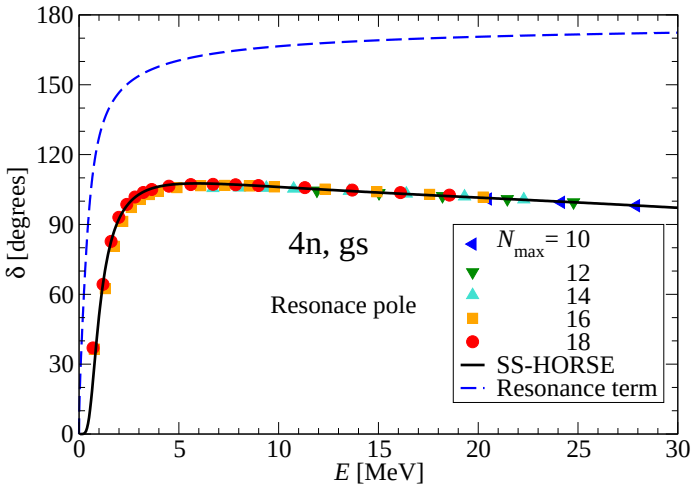

Figure 3: The $4 \to 4$ scattering phase shifts: parametrization with a single resonance pole (solid line) and obtained directly from the selected NCSM results using Eq. (2) (symbols). The dashed line shows the contribution of the resonance term.

The convergence patterns of the NCSM SS-HORSE approach to the $4 \to 4$ phase shifts using Eq. (2) are shown in Fig. 2. We observe that the phase shifts tend to the same curve when $N_{\max}$ is increased. The convergence is first achieved at the higher energies while larger $N_{\max}$ yield converged phase shifts at smaller energies. We obtain nearly completely converged phase shifts at all energies with $N_{\max} = 16$ and 18.

We need only phase shifts close to convergence for the phase shift parametrization. Our selected NCSM eigenenergies are enclosed by the shaded area in Fig. 1 since their resulting phase shifts form a single smooth curve (see Figs. 3 and 4).

We will describe now how we utilize the NCSM solutions within the SS-HORSE method in order to obtain resonance positions. Due to the S-matrix symmetry property,

$$S(k) = \frac{1}{S(-k)}, \tag{3}$$

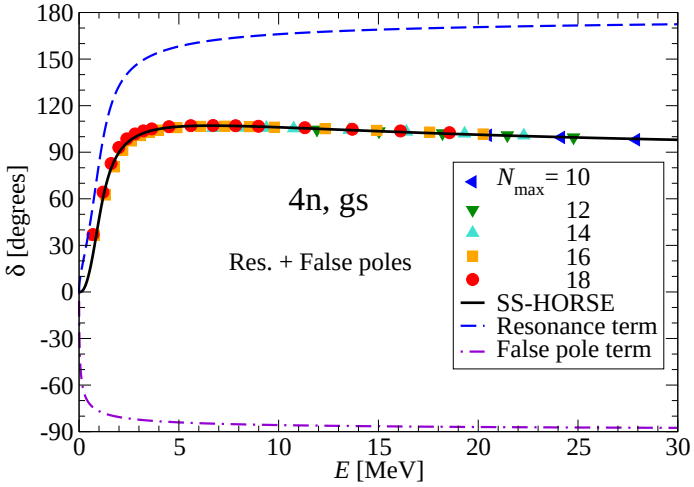

Figure 4: Same as Fig. 3 but for the parametrization with resonance and false state poles. The dashed-dotted line shows the contribution of the false state pole term.

and Eq. (1), the $4 \to 4$ phase shift $\delta(E)$ is an odd function of momentum k and its expansion in Taylor series of $\sqrt{E} \sim k$ includes only odd powers of $\sqrt{E}$:

$$\delta(E) = v_1\sqrt{E} + v_3\big(\sqrt{E}\big)^3 + ... + v_9\big(\sqrt{E}\big)^9 + v_{11}\big(\sqrt{E}\big)^{11} + ... \tag{4}$$

Furthermore, the $4 \to 4$ phase shifts at low energies, i. e., in the limit $k \to 0$, should behave as $\delta \sim k^{2\mathscr{L}+1}$. Note, in our case, $\mathscr{L} = K_{\min} + 3 = 5$, hence

$$v_1 = v_3 = ... = v_9 = 0, \tag{5}$$

and expansion (4) starts at the 11^{th} power.

Supposing the existence of a low-energy resonance in the $4n$ system, we express the S-matrix as

$$S(E) = \Theta(E)\, S_r(E), \tag{6}$$

where $\Theta(E)$ is a smooth function of energy E and $S_r(E)$ is a resonant pole term. The respective phase shift is

$$\delta(E) = \phi(E) + \delta_r(E), \tag{7}$$

where the pole contribution $\delta_r(E)$ takes the form

$$\delta_r(E) = -\tan^{-1}\left(\frac{a\sqrt{E}}{E - b^2}\right). \tag{8}$$

The resonance energy E_r and width Γ are expressed through parameters a and b entering Eq. (8) as

$$E_r = b^2 - \frac{1}{2}a^2, \tag{9}$$

$$\Gamma = a\sqrt{4b^2 - a^2}. \tag{10}$$

We use the following expression for the background phase:

$$\phi(E) = \frac{w_1\sqrt{E} + w_3\big(\sqrt{E}\big)^3 + c\big(\sqrt{E}\big)^5}{1 + w_2E + w_4E^2 + w_6E^3 + dE^4}. \tag{11}$$

The parameters w_i, $i = 1, 2, 3, 4, 6$ are uniquely defined through the parameters a and b and guarantee the fulfilment of the condition (5), i. e., the cancellation of the terms of powers up to 9 in the phase shift expansion (4).

Our phase shift parametrization is given by Eqs. (7), (8) and (11) with fitting parameters a, b, c and d. For each parameter set, we solve Eq. (2) to find the values of the energies $E_\lambda^{a,b,c,d}$, and search for the parameter set (a, b, c, d) minimizing the rms deviation of $E_\lambda^{a,b,c,d}$ from the selected set of NCSM eigenenergies E_λ. Following this route, we obtain an excellent description of the selected E_λ with an rms deviation of 5.8 keV with $a = 0.724$ MeV$^{-\frac{1}{2}}$, $b^2 = 0.448$ MeV, $c = 0.941$ MeV$^{-\frac{5}{2}}$, and $d = -9.1 \cdot 10^{-4}$ MeV^{-4}. The resulting predictions for the NCSM eigenenergies are shown by solid lines in Fig. 1; it is seen that we also describe well NCSM energies with large enough $N_{\max}$ and/or $\hbar\Omega$ not included in the minimization fit. We obtain an excellent description of NCSM-SS-HORSE predicted phase shifts as is shown by solid line in Fig. 3.

However the resonance parameters describing the location of the S-matrix pole obtained by this fit, are surprisingly small: the resonance energy $E_r = 0.186$ MeV and the width $\Gamma = 0.815$ MeV. Note, looking at the phase shift in Fig. 3, we would expect the resonance at the energy of approximately 0.8 MeV corresponding to the maximum of the phase shift derivative and with the width of about 1.5 MeV. The contribution of the pole term (8) to the phase shifts is shown by the dashed line in

Fig. 3. This contribution is seen to differ considerably from the resulting phase shift due to substantial contributions from the background phase (11) which is dominated by the terms needed to fulfill the low-energy theorem $\delta \sim k^{2\mathscr{L}+1}$ and to cancel low-power terms in the expansion of the resonant phase $\delta_r(E)$. Such a sizable contribution from the background in the low-energy region, impels us to search for additional poles or other singularities giving rise to a strong energy dependence which would be separate from the background phase.

After we failed to find a reasonable description of the NCSM-SS-HORSE phase shifts with a low-energy virtual state, we found the resolution of the strong background phase problem by assuming that the S-matrix has an additional low-energy false pole [45] at a positive imaginary momentum. We add the false term contribution

$$\delta_f(E) = -\tan^{-1}\sqrt{\frac{E}{|E_f|}} \tag{12}$$

to the phase shift to obtain the equation

$$\delta(E) = \phi(E) + \delta_r(E) + \delta_f(E) \tag{13}$$

replacing Eq. (7). This parametrization involves an additional fitting parameter E_f. We obtain nearly the same quality description of the selected $4n$ ground state energies with the rms deviation of 6.2 keV with the parameters $a = 0.701$ MeV$^{-\frac{1}{2}}$, $b^2 = 1.089$ MeV, $c = -27.0$ MeV$^{-\frac{5}{2}}$, $d = 0.281$ MeV^{-4}, and a low-lying false pole at energy $E_f = -54.9$ keV. The respective $4n$ resonance at $E_r = 0.844$ MeV and width $\Gamma = 1.378$ MeV appears consistent with what is expected from directly inspecting the $4n$ phase shifts. The parametrized phase shifts are shown by solid line in Fig. 4 together with separate contributions from the resonant and false pole terms. We note that corrections introduced by this new parametrization to the solid lines in Figs. 1 and 3 are nearly unseen in the scales of these figures.

Conclusions. Our results with the realistic JISP16 interaction and the SS-HORSE technique show a resonant structure near 0.8 MeV above threshold with a width Γ of about 1.4 MeV. This is the first theoretical calculation that predicts such a low energy $4n$ resonance without altering any of the properties of the realistic NN interaction. Our result is compatible with the recent experiment [1] which found a resonant structure at an energy of $0.86 \pm 0.65(\text{stat}) \pm 1.25(\text{syst})$ MeV and set an upper limit for the width at $\Gamma = 2.6$ MeV. Our complex energy calculations also suggest a broad low-lying $4n$ resonance that agrees marginally with experiment due to the large error bars for both the current application of the NCGSM and the experiment.

We acknowledge valuable discussions with Pieter Maris, Thomas Aumann, Stefanos Paschalis, Jaume Carbonell and Rimantas Lazauskas. This work was supported by the Russian Foundation for Basic Research under Grants No. 15-32-51239 and 15-02-06604, by the Ministry of Education and Science of Russian Federation, by the US Department of Energy under grants No. DESC0008485 (SciDAC/NUCLEI) and DE-FG02-87ER40371. This work was also supported by the US Department of Energy, Office of Science, Office of Nuclear Physics, under Work Proposal No. SCW0498 and Award Number DE-FG02-96ER40985. This work was supported partially through GAUSTEQ (Germany and U.S. Nuclear Theory Exchange Program for QCD Studies of Hadrons and Nuclei) under contract number DE-SC0006758. Computational resources were provided by NERSC, which is supported by the US Department of Energy under Contract No. DE-AC02-05CH11231 and by Lawrence Livermore National Laboratory (LLNL) institutional Computing Grand Challenge program under Contract No. DE-AC52-07NA27344.

References

[1] K. Kisamori *et al.*, Phys. Rev. Lett. **116**, 052501 (2016).

[2] C. A. Bertulani and V. Zelevinsky, Nature **532**, 448 (2016).

[3] S. Shimoura *et al., RIKEN-RIBF proposal on "Tetra-neutron resonance produced by exothermic double-charge exchange reaction,"* NP1512-SHARAQ10.

[4] K. Kisamori *et al., RIKEN-RIBF proposal on "Many-neutron systems: search for superheavy* ^7H *and its tetraneutron decay,"* NP-1512-SAMURAI34.

[5] S. Paschalis, S. Shimoura *et al., RIBF Experimental Proposal*, NP1406-SAMURAI19.

[6] A. M. Shirokov, J. P. Vary, A. I. Mazur and T. A. Weber, Phys. Lett. B **644**, 33 (2007).

[7] G. Papadimitriou, A. T. Kruppa, N. Michel, W. Nazarewicz, M. Płoszajczak and J. Rotureau, Phys. Rev. C **84**, 051304(R) (2011).

[8] F. M. Marqués *et al.*, Phys. Rev. C **65**, 044006 (2002).

[9] J. J. Bevelacqua, Nuc. Phys. A **341**, 414 (1980).

[10] S. C. Pieper, Phys. Rev. Lett. **90**, 252501 (2003).

[11] N. K. Timofeyuk, J. Phys. G **29**, L9 (2003).

[12] C. A. Bertulani and V. G. Zelevinsky, J. Phys. G **29**, 2431 (2003).

[13] S. A. Sofianos, S. A. Rakityansky and G. P. Vermaak, J. Phys. G **23**, 1619 (1997).

[14] R. Lazauskas and J. Carbonell, Phys. Rev. C **72**, 034003 (2005).

[15] E. Hiyama, R. Lazauskas, J. Carbonell and M. Kamimura, Phys. Rev. C **93**, 044004 (2016).

[16] L. V. Grigorenko, N. K. Timofeyuk, and M. V. Zhukov, Europ. Phys. J. A **19**, 187 (2004).

[17] S. Elhatisari *et al.*, Nature **528**, 111 (2015).

[18] S. Quaglioni, Nature **528**, 42 (2015).

[19] B. R. Barrett, P. Navrátil and J. P. Vary, Prog. Part. Nucl. Phys. **69**, 131 (2013).

[20] G. Papadimitriou, J. Rotureau, N. Michel, M. Płoszajczak and B. R. Barrett, Phys. Rev. C **88**, 044318 (2011).

[21] N. Michel, W. Nazarewicz, M. Płoszajczak and T. Vertse, J. Phys. G **36**, 013101 (2009).

[22] I. A. Mazur, A. M. Shirokov, A. I. Mazur and J. P. Vary, arXiv:1512.03983 [nucl-th] (2015).

[23] A. M. Shirokov, A. I. Mazur, I. A. Mazur and J. P. Vary, arXiv:1608.05885 [nucl-th] (2016).

[24] A. I. Mazur, A. M. Shirokov, I. A. Mazur and J. P. Vary, *see these Proceedings*, p. 183, http://www.ntse-2014.khb.ru/Proc/A.Mazur.pdf.

[25] A. M. Shirokov, G. Papadimitriou, A. I. Mazur, I. A. Mazur, R. Roth and J. P. Vary, arXiv:1607.05631 [nucl-th] (2016).

[26] V. M. Krasnopolsky and V. I. Kukulin, Phys. Lett. A **69**, 251 (1978).

[27] V. I. Kukulin, V. M. Krasnopolsky and J. Horácek, *Theory of Resonances. Principles and Applications.* Kluwer, Dordrecht, 1989.

[28] T. Berggren, Nucl. Phys. A **109**, 265 (1968).

[29] H. A. Yamani and L. Fishman, J. Math. Phys., **16**, 410 (1975).

[30] J. M. Bang, A. I. Mazur, A. M. Shirokov, Yu. F. Smirnov and S. A. Zaytsev, Ann. Phys. (NY), **280**, 299 (2000).

[31] R. I. Jibuti and N. B. Krupennikova, *The Method of hyperspherical functions in the quantum mechanics of few bodies.* Metsniereba, Tbilisi, 1984 (*in Russian*).

[32] R. I. Jibuti, Fiz. Elem. Chast. At. Yadra **14**, 741 (1983).

[33] R. I. Jibuti, R. Ya. Kezerashvili and K. I. Sigua, Yad. Fiz. **32**, 1536 (1980).

[34] R. I. Jibuti, R. Ya. Kezerashvili and K. I. Sigua, Phys. Lett. B **102**, 381 (1981).

[35] R. Ya. Kezerashvili, Yad. Fiz. **44**, 842 (1986) [Sov. J. Nucl. Phys. **44**, 542 (1986)].

[36] A. M. Badalyan, T. I. Belova, N. B. Konyuhova and V. D. Efros, Yad. Fiz. **41**, 1460 (1985) [Sov. J. Nucl. Phys. **41**, 926 (1985)].

[37] I. F. Gutich, A. V. Nesterov and I. P. Okhrimenko, Yad. Fiz. **50**, 19 (1989).

[38] A. M. Shirokov, Yu. F. Smirnov and S. A. Zaytsev, in *Modern problems in quantum theory*, eds. V. I. Savrin and O. A. Khrustalev. Moscow, 1998, p. 184; S. A. Zaytsev, Yu. F. Smirnov and A. M. Shirokov, Teoret. Mat. Fiz. **117**, 227 (1998) [Theor. Math. Phys. **117**, 1291 (1998)].

[39] Yu. A. Lurie, Yu. F. Smirnov and A. M. Shirokov, Izv. Ros. Akad. Nauk, Ser. Fiz. **57**, 193 (1993) [Bul. Rus. Acad. Sci., Phys. Ser. **57**, 943 (1993)].

[40] Yu. A. Lurie and A. M. Shirokov, Izv. Ros. Akad. Nauk, Ser. Fiz. **61**, 2121 (1997) [Bul. Rus. Acad. Sci., Phys. Ser. **61**, 1665 (1997)].

[41] Yu. A. Lurie and A. M. Shirokov, Ann. Phys. (NY) **312**, 284 (2004).

[42] Yu. A. Lurie and A. M. Shirokov, in *The J-matrix method. Developments and applications,* eds. A. D. Alhaidari, E. J. Heller, H. A. Yamani and M. S. Abdelmonem. Springer, 2008, p. 183.

[43] P. Maris, M. Sosonkina, J. P. Vary, E. G. Ng and C. Yang, Proc. Comput. Sci. **1**, 97 (2010).

[44] H. M. Aktulga, C. Yang, E. N. Ng, P. Maris and J. P. Vary, Concurrency Computat. Pract. Exper. **26**, 2631 (2013).

[45] A. I. Baz', Ya. B. Zel'dovich and A. M. Perelomov, *Scattering, reactions and decay in non-relativistic quantum mechanics.* Israel Program for Scientific Translation, Jerusalem, 1969.

Resonant States in the Shell Model

A. I. Mazur[a], A. M. Shirokov[a,b,c], I. A. Mazur[a] and J. P. Vary[c]

[a] *Department of Physics, Pacific National University, Khabarovsk 680035, Russia*
[b] *Skobeltsyn Institute of Nuclear Physics, Lomonosov Moscow State University, Moscow 119991, Russia*
[c] *Department of Physics and Astronomy, Iowa State University, Ames, Iowa 50011, USA*

Abstract

We suggest a method for calculating scattering phase shifts and energies and widths of resonances which utilizes only eigenenergies obtained in variational calculations with oscillator basis and their dependence on oscillator basis spacing $\hbar\Omega$. We make use of simple expressions for the S-matrix at eigenstates of a finite (truncated) Hamiltonian matrix in the oscillator basis obtained in the HORSE (J-matrix) formalism of quantum scattering theory. The validity of the suggested approach is verified in calculations with model Woods–Saxon potentials and applied to calculations of $n\alpha$ resonances and non-resonant scattering using the no-core shell model.

Keywords: *No-core shell model; HORSE (J-matrix) formalism of quantum scattering theory; resonance energy and width; S-matrix poles*

1 Introduction

To calculate energies of nuclear ground states and other bound states within various shell model approaches, one conventionally starts by calculating the $\hbar\Omega$-dependence of the energy $E_\nu(\hbar\Omega)$ of the bound state ν in some model space. The minimum of $E_\nu(\hbar\Omega)$ is correlated with the energy of the state ν. The convergence of calculations and accuracy of the energy prediction is estimated by comparing with the results obtained in neighboring model spaces. To improve the accuracy of theoretical predictions, various extrapolation techniques have been suggested recently [1–13] which make it possible to estimate the binding energies in the complete infinite shell-model basis space. The studies of extrapolations to the infinite model spaces reveal general trends of convergence patterns of shell model calculations.

Is it possible to study nuclear states in the continuum, low-energy scattering and resonant states in particular, in the shell model using bound state techniques? A conventional belief is that the energies of shell-model states in the continuum should be associated with the resonance energies. It was shown however in Ref. [14, 15] that the energies of shell-model states may appear well above the energies of resonant states, especially for broad resonances. Moreover, the analysis of Refs. [14, 15] clearly demonstrated that the shell model should also generate some states in a non-resonant nuclear continuum. The nuclear resonance properties can be studied in the Gamow shell model, including the *ab initio* no-core Gamow shell model (NCGSM) [16, 17]. Another option is to combine the shell model with resonating group method (RGM). An impressive progress in the description of various nuclear reactions was achieved by means of the combined no-core shell model/RGM (NCSM/RGM) approach [18–23].

Proceedings of the International Conference 'Nuclear Theory in the Supercomputing Era — 2014' (NTSE-2014), Khabarovsk, Russia, June 23–27, 2014. Eds. A. M. Shirokov and A. I. Mazur. Pacific National University, Khabarovsk, Russia, 2016, p. 183.

http://www.ntse-2014.khb.ru/Proc/A.Mazur.pdf.

Both NCGSM and NCSM/RGM complicate essentially the shell model calculations. Is it possible to get some information about unbound nuclear states directly from the results of calculations in NCSM or in other versions of the nuclear shell model without introducing additional Berggren basis states as in NCGSM or additional RGM calculations as in the NCSM/RGM approach?

The general behaviour of shell model eigenstates at positive energies (or just at the energies above various thresholds) is not well-studied and there is no well-established extrapolation technique to the infinite basis space for resonances. Generally, a complete study of the nuclear continuum can be performed by extending the nuclear shell model with the J-matrix formalism of scattering theory. The J-matrix formalism has been suggested in atomic physics [24, 25]. Later it was independently rediscovered in nuclear physics [26,27] and was successfully used in shell-model applications [28]. The J-matrix approach utilizes diagonalization of the Hamiltonian in one of two bases: the so-called Laguerre basis that is of a particular interest for atomic physics applications and the oscillator basis that is appropriate for nuclear physics. The version of the J-matrix formalism with the oscillator basis is also sometimes referred to as an Algebraic Version of RGM [26] or as a HORSE (Harmonic Oscillator Representation of Scattering Equations) method [29] — we shall use the latter nomenclature in what follows.

We note that a direct implementation of the HORSE formalism in modern large-scale shell-model calculations is very complicated and unpractical: the HORSE method requires calculation of a huge number of eigenstates while modern shell-model codes usually utilize the Lanczos algorithm which provides only the few lowest Hamiltonian eigenstates. Furthermore, the HORSE method needs also the weight of the highest component of the wave function of each eigenstate which is usually obtained with a low precision. On the other hand, the HORSE formalism can be used for a simple calculation of the scattering phase shift or S-matrix at a single energy $E_\nu(\hbar\Omega)$ which is an eigenstate of the shell-model Hamiltonian. In this case, the HORSE phase shift calculation requires only the value of the energy $E_\nu(\hbar\Omega)$ and the basis parameters (the $\hbar\Omega$ value and the basis truncation). We shall refer to such a simplified approach as a Single State HORSE (SS-HORSE) method. Varying the shell-model parameter $\hbar\Omega$ and using results from a set of basis spaces, we generate a variation of $E_\nu(\hbar\Omega)$ in some energy range and hence we can calculate the phase shifts in that energy range.

Calculations of scattering phase shifts at the eigenenergies of the Hamiltonian in the oscillator basis and obtaining the phase shift energy dependence by variation of basis parameters, was recently performed in Ref. [5] using another (not the HORSE) technique. A detailed study of scattering phase shifts at eigenenergies of the Hamiltonian in arbitrary finite $\mathcal{L}^2$ basis was performed in Ref. [30]. This study was based on the theory of spectral shift functions introduced by I. M. Lifshitz nearly 70 years ago [31] and later forgotten by physicists though used up to now by mathematicians (see Ref. [30] and references therein).

Another method to obtain scattering phase shifts from bound state calculations in a harmonic oscillator basis features the use of an additional harmonic oscillator potential [32]. The method was demonstrated with nucleon-nucleon scattering where it reveals a challenge of needing a large basis to access the low-energy scattering region.

It is worth noting here that approximate resonant widths can be extracted from bound state approaches to many-body nuclear systems using a relation between the partial width in a specified breakup channel and an integral over the "interaction region" where all of the nucleons are close to each other. This method was described in detail in Ref. [33] where it was used to evaluate widths of resonances in light nuclei based on the variational Monte Carlo calculations. It has been used before in combination with other many-body approaches (see Ref. [33] for the list of respective

references), in particular, it can be utilized within the nuclear shell model. However this approach is applicable to narrow enough resonances only and is unable to provide information about non-resonant scattering.

In this contribution, we suggest a simpler and more powerful approach. We formulate below a method for calculating low-energy phase shifts and for extracting resonant energies E_r and widths Γ from the shell model results, or, generally, from results of any variational calculation with a finite oscillator basis. We apply the SS-HORSE formalism to calculate the S-matrix in the energy interval of variation of one of the Hamiltonian eigenenergies $E_\nu(\hbar\Omega)$ due to variation of $\hbar\Omega$ and truncation boundary of the Hamiltonian matrix. We use either a low-energy expansion of the S-matrix or express the S-matrix as a pole term plus slowly varying with energy background terms and fit the expansion parameters to describe the S-matrix behaviour in the above energy interval. The low-energy phase shifts δ_ℓ, the resonant energy E_r and width Γ appear as a result of this fit. We obtain relations describing the general behaviour of shell-model states associated with a resonance or with a non-resonant continuum as functions of $\hbar\Omega$ and truncation boundary of the Hamiltonian matrix. This approach is tested in calculations of phase shifts and resonance parameters of two-body scattering with model potential. Next we apply the SS-HORSE method to the calculation of resonances and of non-resonant continuum in the neutron-α scattering based on No-core Shell Model (NCSM) results obtained with the JISP16 NN interaction [34, 35]. This paper elaborates on the work presented in Refs. [36, 37].

In our earlier study [38], we evaluated resonant energies E_r and widths Γ using the SS-HORSE and Breit–Wigner formula for the description of resonances. The Breit–Wigner formula describes the phase shifts and S-matrix only in the case of narrow resonances and only in a narrow energy interval in the vicinity of the resonance. As a result, the approach of Ref. [38] can be used only in rare cases when the eigenenergies of the truncated Hamiltonian are obtained very close to the resonant energy E_r and cannot provide an accurate description of resonant parameters even in these rare cases. This drawback is eliminated in the current study.

The paper is organized as follows. We present in Section 2 the basic relations of the HORSE formalism, derive the SS-HORSE method and present all equations needed to calculate phase shifts, S-matrix and resonant parameters E_r and Γ. The SS-HORSE approach to the calculation of resonant energy and width is verified in Section 3 using a two-body scattering with a model potential. Section 4 is devoted to calculations of resonances in $n\alpha$ scattering based on NCSM calculations of ^{5}He with JISP16 NN interaction. Conclusions are presented in Section 5.

2 SS-HORSE approach to calculation of low-energy scattering and resonant parameters

2.1 HORSE formalism

The J-matrix approach and HORSE in particular are widely used in various applications. Some of the recent applications together with pioneering papers where the J-matrix has been suggested, can be found in the book [39]. We sketch here the basic relations and ideas of the HORSE formalism for the two-body single-channel scattering following our papers [29, 40, 41].

The radial wave function $u_\ell(k, r)$ describing the relative motion in the partial wave with orbital momentum ℓ is expanded within the HORSE formalism in an infinite series of radial oscillator functions $R_{N\ell}(r)$,

$$u_\ell(k, r) = \sum_{N=N_0, N_0+2, \ldots, \infty} a_{N\ell}(k)\, R_{N\ell}(r), \tag{1}$$

where

$$R_{N\ell}(r) = (-1)^{(N-\ell)/2} \sqrt{\frac{2\Gamma(N/2-\ell/2+1)}{r_0\Gamma(N/2+\ell/2+3/2)}} \left(\frac{r}{r_0}\right)^{\ell+1} \exp\left(-\frac{r^2}{2r_0^2}\right) L^{\ell+\frac{1}{2}}_{(N-\ell)/2}\left(\frac{r^2}{r_0^2}\right). \tag{2}$$

Here k is the relative motion momentum, $L^\alpha_n(z)$ are associated Laguerre polynomials, the oscillator radius $r_0 = \sqrt{\frac{\hbar}{m\Omega}}$, m is the reduced mass of colliding particles, $\hbar\Omega$ is the oscillator level spacing, $N = 2n+\ell$ is the oscillator quanta while n is the oscillator principal quantum number, the minimal value of oscillator quanta $N_0 = \ell$. Using the expansion (1) we transform the radial Schrödinger equation

$$H^\ell\, u_\ell(k,r) = E\, u_\ell(k,r) \tag{3}$$

into an infinite set of linear algebraic equations,

$$\sum_{N'=N_0,N_0+2,\ldots,\infty} (H^\ell_{NN'} - \delta_{NN'}E)\, a_{N'\ell}(k) = 0, \qquad N = N_0, N_0+2, \ldots, \tag{4}$$

where $H^\ell_{NN'} = T^\ell_{NN'} + V^\ell_{NN'}$ are matrix elements of the Hamiltonian H^ℓ in the oscillator basis, and $T^\ell_{NN'}$ and $V^\ell_{NN'}$ are kinetic and potential energy matrix elements respectively.

The kinetic energy matrix elements $T^\ell_{NN'}$ are known to form a tridiagonal matrix, i. e., the only non-zero matrix elements are

$$\begin{aligned} T^\ell_{NN} &= \frac{1}{2}\hbar\Omega(N+3/2), \\ T^\ell_{N,N+2} &= T^\ell_{N+2,N} = -\frac{1}{4}\hbar\Omega\sqrt{(N-\ell+2)(N+\ell+3)}. \end{aligned} \tag{5}$$

These matrix elements are seen to increase linearly with N for large N. On the other hand, the potential energy matrix elements $V^\ell_{NN'}$ decrease as $N, N' \to \infty$. Hence the kinetic energy dominates in the Hamiltonian matrix at large enough N and/or N'. Therefore a reasonable approximation is to truncate the potential energy matrix at large N and/or N', i. e., to approximate the interaction V by a nonlocal separable potential $\tilde{V}$ of the rank $\mathcal{N} = (\mathbb{N} - N_0)/2 + 1$ with matrix elements

$$\tilde{V}^\ell_{NN'} = \begin{cases} V^\ell_{NN'} & \text{if} \quad N \le \mathbb{N} \text{ and } N' \le \mathbb{N}; \\ 0 & \text{if} \quad N > \mathbb{N} \text{ or } N' > \mathbb{N}. \end{cases} \tag{6}$$

The approximation (6) is the only approximation within the HORSE method; for the separable interaction of the type (6), the HORSE formalism suggests exact solutions. Note, the kinetic energy matrix is not truncated within the HORSE theory contrary to conventional variational approaches like the shell model. Hence the HORSE formalism suggests a natural generalization of the shell model.

The complete infinite harmonic oscillator basis space can be divided into two subspaces according to truncation (6): an internal subspace spanned by oscillator functions with $N \le \mathbb{N}$ where the interaction V is accounted for and an asymptotic subspace spanned by oscillator functions with $N > \mathbb{N}$ associated with the free motion.

Algebraic equations (4) in the asymptotic subspace take the form of a second order finite-difference equation:

$$T^\ell_{N,N-2}\, a^{ass}_{N-2,\ell}(E) + (T^\ell_{NN} - E)\, a^{ass}_{N\ell}(E) + T^\ell_{N,N+2}\, a^{ass}_{N+2,\ell}(E) = 0. \tag{7}$$

Any solution $a^{ass}_{N\ell}(E)$ of Eq. (7) can be expressed as a superposition of regular $S_{N\ell}(E)$ and irregular $C_{N\ell}(E)$ solutions,

$$a^{ass}_{N\ell}(E) = \cos\delta_\ell\, S_{N\ell}(E) + \sin\delta_\ell\, C_{N\ell}(E), \quad N \ge \mathbb{N}, \tag{8}$$

where δ_ℓ is the scattering phase shift. The solutions $S_{N\ell}(E)$ and $C_{N\ell}(E)$ have simple analytical expressions [25, 27, 29, 40]:

$$S_{N\ell}(E) = \sqrt{\frac{\pi\Gamma(N/2-\ell/2+1)}{\Gamma(N/2+\ell/2+3/2)}}\, q^{\ell+1} \exp\left(-\frac{q^2}{2}\right) L^{\ell+1/2}_{(N-\ell)/2}(q^2), \tag{9}$$

$$C_{N\ell}(E) = (-1)^\ell \sqrt{\frac{\pi\Gamma(N/2-\ell/2+1)}{\Gamma(N/2+\ell/2+3/2)}}\, \frac{q^{-\ell}}{\Gamma(-\ell+1/2)} \times \exp\left(-\frac{q^2}{2}\right) \Phi(-N/2-\ell/2-1/2, -\ell+1/2; q^2), \tag{10}$$

where $\Phi(a, b; z)$ is a confluent hypergeometric function and q is a dimensionless momentum,

$$q = \sqrt{\frac{2E}{\hbar\Omega}}. \tag{11}$$

The solutions $a_{N\ell}(E)$ of the algebraic set (4) in the internal subspace $N \le \mathbb{N}$ are expressed through the solutions $a^{ass}_{N\ell}(E)$ in the asymptotic subspace $N \ge \mathbb{N}$:

$$a_{N\ell}(E) = \mathcal{G}_{N\mathbb{N}}(E)\, T^\ell_{\mathbb{N},\mathbb{N}+2}\, a^{ass}_{\mathbb{N}+2,\,\ell}(E), \qquad N = N_0, N_0+2, \dots, \mathbb{N}. \tag{12}$$

Here the matrix elements

$$\mathcal{G}_{NN'}(E) = -\sum_{\nu=0}^{\mathcal{N}-1} \frac{\langle N\ell|\nu\rangle\langle\nu|N'\ell\rangle}{E_\nu - E} \tag{13}$$

are related to the Green's function of the Hamiltonian $H^{\mathbb{N}}$ which is the Hamiltonian H^ℓ truncated to the internal subspace, and are expressed through eigenenergies E_ν, $\nu = 0, 1, 2, \dots, \mathcal{N}-1$ ($\mathcal{N}$ is the dimensionality of the basis) and respective eigenvectors $\langle N\ell|\nu\rangle$ of the Hamiltonian $H^{\mathbb{N}}$:

$$\sum_{N'=N_0,N_0+2,\dots,\mathbb{N}} H^\ell_{NN'}\langle N'\ell|\nu\rangle = E_\nu\langle N\ell|\nu\rangle, \qquad N = N_0, N_0+2, \dots, \mathbb{N}. \tag{14}$$

A relation for calculation of the scattering phase shifts δ_ℓ can be obtained through the matching condition

$$a_{\mathbb{N}\ell}(E) = a^{ass}_{\mathbb{N}\ell}(E). \tag{15}$$

Using Eqs. (8), (12) and (15) it is easy to obtain [25, 27, 29, 40]

$$\tan\delta_\ell(E) = -\frac{S_{\mathbb{N}\ell}(E) - \mathcal{G}_{\mathbb{N}\mathbb{N}}(E)\, T^\ell_{\mathbb{N},\mathbb{N}+2}\, S_{\mathbb{N}+2,\ell}(E)}{C_{\mathbb{N}\ell}(E) - \mathcal{G}_{\mathbb{N}\mathbb{N}}(E)\, T^\ell_{\mathbb{N},\mathbb{N}+2}\, C_{\mathbb{N}+2,\ell}(E)}. \tag{16}$$

The respective expression for the S-matrix reads

$$S(E) = \frac{C^{(-)}_{\mathbb{N}\ell}(E) - \mathcal{G}_{\mathbb{N}\mathbb{N}}(E)\, T^\ell_{\mathbb{N},\mathbb{N}+2}\, C^{(-)}_{\mathbb{N}+2,\ell}(E)}{C^{(+)}_{\mathbb{N}\ell}(E) - \mathcal{G}_{\mathbb{N}\mathbb{N}}(E)\, T^\ell_{\mathbb{N},\mathbb{N}+2}\, C^{(+)}_{\mathbb{N}+2,\ell}(E)}, \tag{17}$$

where

$$C^{(\pm)}_{N\ell}(E) = C_{N\ell}(E) \pm S_{N\ell}(E). \tag{18}$$

We are using here the single-channel version of the HORSE formalism described above. The multi-channel HORSE formalism is discussed in detail in Refs. [25, 29, 40].

2.2 SS-HORSE method

A direct HORSE extension of modern large-scale shell-model calculations is unpractical. Note, Eq. (13) involves a sum over all shell-model eigenstates of a given spin-parity, i. e., over millions or even billions of states in modern NCSM applications. These states should be accurately separated from those having center-of-mass excitations. Unfortunately one cannot restrict the sum in Eq. (13) to some small enough set of eigenstates: even for the energies E close enough to one of the low-lying eigenstates E_ν, the contribution of some high-lying eigenstates to the sum in Eq. (13) can be essential: in model two-body problems describing, e. g., $n\alpha$ scattering, the growth of the denominator in the r.h.s. of Eq. (13) is compensated by the growth of the numerator; in NCSM calculations of ^{5}He, the many-body eigenstates concentrate around the eigenstates of the model two-body Hamiltonian and though the contribution of each particular NCSM eigenstate is small, the sum of their contributions is large and close to the contribution of the respective state of the model Hamiltonian. A calculation of a large number of many-body eigenstates is too computationally expensive. Note, in many-body applications, one also needs to calculate the components $\langle \mathbb{N}\ell|\nu\rangle$ of the wave function which should be projected on the scattering channel of interest; this projection requires numerous applications of Talmi–Moshinsky transformations which increase the computational cost and makes it very difficult to achieve a reasonable accuracy of the final sum in Eq. (13) due to computer noise.

To avoid these difficulties, we propose the SS-HORSE approach which requires calculations of the S-matrix or phase shifts only at $E = E_\nu$, i. e., at the energy equal to one of the lowest eigenstates lying above the reaction threshold. Equations (16) and (17) are essentially simplified in this case and reduce to

$$\tan\delta_\ell(E_\nu) = -\frac{S_{\mathbb{N}+2,\ell}(E_\nu)}{C_{\mathbb{N}+2,\ell}(E_\nu)} \tag{19}$$

and

$$S(E_\nu) = \frac{C^{(-)}_{\mathbb{N}+2,\ell}(E_\nu)}{C^{(+)}_{\mathbb{N}+2,\ell}(E_\nu)}. \tag{20}$$

Varying $\mathbb{N}$ and $\hbar\Omega$ we obtain eigenvalues E_ν and hence phase shifts and S-matrix in some energy interval. An accurate parametrization of $\delta_\ell(E)$ and S-matrix in this energy interval makes it possible to extrapolate them to a larger energy interval and to calculate the resonance energy and width.

The use of Eqs. (19) and (20) drastically reduces the computational burden in many-body calculations. Within this SS-HORSE approach we need only one or probably very few low-lying eigenstates which energies should be calculated relative to the respective threshold, e. g., in the case of $n\alpha$ scattering we need to subtract from the ^{5}He energies the ^{4}He ground state energy. Another interesting and important feature of the SS-HORSE technique is that the Eqs. (19) and (20) do not involve any information regarding the eigenvectors $\langle N\ell|\nu\rangle$. This essentially simplifies calculations, the information about a particular channel under consideration is present only in the threshold energy used to calculate the eigenenergies E_ν and in the channel orbital momentum ℓ. Equations (19) and (20) establish some correlations between scattering in different channels when the channel coupling can be neglected, a topic that deserves further investigation but is outside the scope of the present work.

We use here Eqs. (19) and (20) to obtain phase shifts and S-matrix from Hamiltonian diagonalization results. However these equations can be used in inverse manner: if the phase shifts are known from analysis of experimental scattering data, one can solve Eq. (19) to obtain eigenenergies E_ν which the shell model Hamiltonian should have to be consistent with scattering data. The direct use of Eq. (19) essentially simplifies the inverse approach to nucleon-nucleus scattering suggested in Refs. [14, 15].

We see that the scattering phase shifts are determined by the universal function

$$f_{\mathbb{N}\ell}(E) = -\arctan\left[\frac{S_{\mathbb{N}+2,\ell}(E)}{C_{\mathbb{N}+2,\ell}(E)}\right]. \tag{21}$$

This is a smooth monotonically decreasing function which drops down by $n\pi$ as energy E varies from 0 to ∞. At low energies when

$$E \ll \frac{1}{8}\hbar\Omega\,(\mathbb{N}+2-\ell)^2, \tag{22}$$

one can replace the functions $S_{\mathbb{N}+2,\ell}(E)$ and $C_{\mathbb{N}+2,\ell}(E)$ in Eq. (21) by their asymptotic expressions at large $\mathbb{N}$ (see Ref. [40]) to obtain

$$f_{\mathbb{N}\ell}(E) \approx f_\ell^{l.e.}(E) = \arctan\left[\frac{j_\ell\big(2\sqrt{E/s}\big)}{n_\ell\big(2\sqrt{E/s}\big)}\right], \tag{23}$$

where

$$s = \frac{\hbar\Omega}{\mathbb{N}+7/2}, \tag{24}$$

and $j_l(x)$ and $n_l(x)$ are spherical Bessel and spherical Neumann functions. If additionally

$$E \gg \frac{1}{4}s = \frac{\hbar\Omega}{4(\mathbb{N}+7/2)}, \tag{25}$$

one can use asymptotic expressions for spherical Bessel and Neumann functions in Eq. (23) to get a very simple expression for the function $f_{\mathbb{N}\ell}(E)$:

$$f_{\mathbb{N}\ell}(E) \approx -2\sqrt{\frac{E}{s}} + \frac{\pi\ell}{2}. \tag{26}$$

The universal function $f_{\mathbb{N}\ell}(E)$ and its low-energy approximations (23) and (26) are shown in Fig. 1. The basis space in shell model applications in conventionally labeled by the maximal oscillator excitation quanta $N_{\max}$, and we use $N_{\max}$ in Fig. 1 to distinguish functions $f_{\mathbb{N}\ell}(E)$ corresponding to different basis sizes. Obviously,

$$\mathbb{N} = N_{\max} + \ell \tag{27}$$

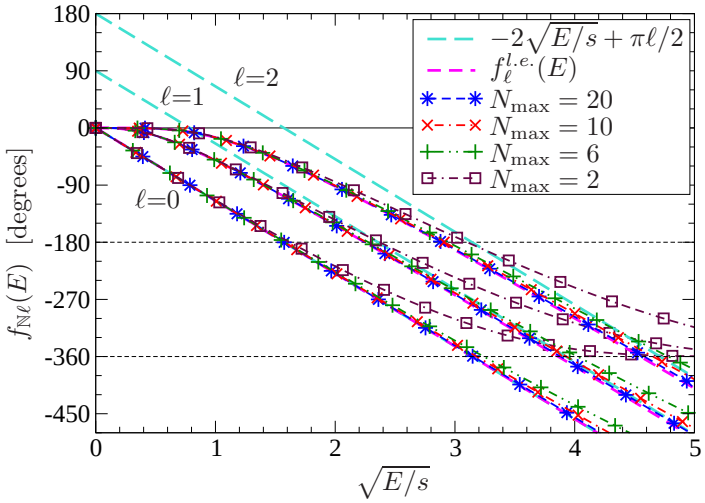

Figure 1: The function $f_{\mathbb{N}\ell}(E)$ (symbols) for different $\mathbb{N}$ and ℓ and its low-energy approximations $f_\ell^{l.e.}(E)$ [see Eq. (23)] and $-2\sqrt{E/s}+\pi\ell/2$ [see Eq. (26)].

in the two-body scattering problem. The approximation (23) is seen to be very accurate at low energies even for small $N_{\max}$. This low-energy approximation, as expected, deviates from the function $f_{\mathbb{N}\ell}(E)$ as the energy E increases; the energy interval where the approximation (23) accurately describes $f_{\mathbb{N}\ell}(E)$ increases with $\mathbb{N}$ or $N_{\max}$ in accordance with inequality (22). In the case $\ell = 0$, the simple expression (26) is equivalent to the Eq. (23) and therefore describes the function $f_{\mathbb{N}\ell}(E)$ with the same accuracy. For $\ell > 0$ the simplified approximation (26) deviates from the approximation (23) and the function $f_{\mathbb{N}\ell}(E)$ at low energies, it can only be used in a relatively small energy interval defined by inequalities (22) and (25).

Due to Eq. (23), equation (19) at low energies can be reduced to

$$\tan\delta_\ell(E_\nu) = \frac{j_\ell\big(2\sqrt{E_\nu/s}\big)}{n_\ell\big(2\sqrt{E_\nu/s}\big)}. \tag{28}$$

This equation reveals the scaling at low energies: the oscillator basis parameters $\mathbb{N}$ and $\hbar\Omega$ are not independent, they are entering equations relating the S-matrix and phase shifts with the eigenenergies of the Hamiltonian matrix in the oscillator basis not separately but only through the scaling variable s combining them in a particular manner. The scaling is useful within our approach for selecting eigenenergies E_ν obtained with different $\mathbb{N}$ and $\hbar\Omega$ for the further analysis of phase shifts and S-matrix poles: the convergence of the results obtained by diagonalization of the Hamiltonian in oscillator basis is achieved within some interval of $\hbar\Omega$ values starting from some $\mathbb{N}$; the converged results for E_ν should describe the same phase shifts with some accuracy, therefore, due to the scaling (28), these converged E_ν plotted as functions of the scaling parameter s should lie approximately on the same curve. By plotting E_ν vs s we can pick up for further analysis only those E_ν which form some curve as is illustrated later.

The scaling in variational oscillator-basis calculations of bound states was proposed in Refs. [2,3]. We extend here the scaling property of the oscillator-basis calculations to the continuum states. We prefer to use the scaling parameter s in energy units rather than the scaling parameter λ_{sc} of Refs. [2,3,6,13] in momentum units or the scaling parameter

$$L = \sqrt{2(\mathbb{N}+7/2)}\, r_0 \tag{29}$$

in the units of length suggested in Ref. [5]. The parameter L includes a small correction to the scaling proposed in Refs. [2,3] which was suggested in Ref. [5] based on numerical results. We obtain this correction automatically in our approach. Having this correction in mind, we get

$$s \sim \lambda_{sc}^2 \sim 1/L^2; \tag{30}$$

in other words, we propose generically the same scaling as discussed in Refs. [2–11,13] but using another scaling parameter and extending the scaling to continuum states.

We derive the scaling property in a very different approach than that utilized in Refs. [2–5]. Therefore it is interesting to compare these scalings in more detail. One can analytically continue the Eqs. (19) and (20) to the complex energy or complex momentum plane, in particular, one can use these expressions at negative energies corresponding to bound states. Using asymptotic expressions of the functions $C^{(+)}_{\mathbb{N}+2,\ell}(E)$ and $C^{(-)}_{\mathbb{N}+2,\ell}(E)$ at large $\mathbb{N}$ and negative energy E (see Ref. [40]), we obtain from Eq. (20):

$$S(E_\nu) = (-1)^\ell \exp\left(-4i\sqrt{\frac{E_\nu}{s}}\right), \qquad E_\nu < 0. \tag{31}$$

On the other hand, the S-matrix $S(E_\nu)$ at negative energies E_ν in the vicinity of the pole associated with the bound state at energy $E_b < 0$ can be expressed as [42]

$$S(E_\nu) = \frac{D_\ell}{i\varkappa_\nu - ik_b}, \tag{32}$$

where $E_\nu = -\frac{\hbar^2\varkappa_\nu^2}{2m}$, $E_b = -\frac{\hbar^2 k_b^2}{2m}$, momenta $\varkappa_\nu$ and k_b are supposed to be positive, and D_ℓ can be expressed through the asymptotic normalization constant A_ℓ [42]:

$$D_\ell = (-1)^{\ell+1}\, i\, |A_\ell|^2. \tag{33}$$

Combining Eqs. (31)–(33), we obtain:

$$\varkappa_\nu - k_b = -|A_\ell|^2 \exp\left(-\frac{4\varkappa_\nu\hbar}{\sqrt{2ms}}\right). \tag{34}$$

This expression can be used for extrapolating the eigenenergies E_ν (or respective momenta $\varkappa_\nu$) obtained in a finite oscillator basis to the infinite basis space supposing that $E_\nu \to E_b$ as $\mathbb{N} \to \infty$.

The respective expression for extrapolating the oscillator basis eigenenergies derived in Refs. [2–5] rewritten in our notations, takes the form:

$$E_\nu - E_b = C_\ell \exp\left(-\frac{4k_b\hbar}{\sqrt{2ms}}\right). \tag{35}$$

There is some similarity, however there is also an essential difference between Eqs. (34) and (35). Both equations have similar exponents in the right-hand-side, however the exponent in our Eq. (34) involves momentum $\varkappa_\nu$ associated with the eigenenergy E_ν while Eq. (35) involves momentum k_b associated with the converged energy E_b in the limit $\mathbb{N} \to \infty$. In the vicinity of the S-matrix pole [see Eq. (32)] $\varkappa_\nu$ should not differ much from k_b; we note however that k_b is conventionally treated as an additional fitting parameter (see Refs. [2–11]), i. e., it is supposed that $E_b \neq -\frac{\hbar^2 k_b^2}{2m}$, and hence there may be an essential difference between $\varkappa_\nu$ and k_b in applications. Even more important is that the exponent in the right-hand-side controls the difference between the energies E_ν and E_b in Eq. (35) while in our Eq. (34) the exponent controls the difference between the momenta $\varkappa_\nu \sim \sqrt{|E_\nu|}$ and $k_b \sim \sqrt{|E_b|}$. We plan to examine in detail in a separate publication which of the Eqs. (34) and (35) describes better the results of diagonalizations of realistic Hamiltonians in the oscillator basis for negative eigenenergies E_ν and which of them is more accurate in extrapolating the results for bound states obtained in finite oscillator bases to the infinite basis space.

Equations (19) and (20) can be used to obtain the phase shifts and S-matrix in some range of energies covered by eigenenergies E_ν obtained with various $\mathbb{N}$ and $\hbar\Omega$. To interpolate the energy dependences of the phase shifts and S-matrix within and to extrapolate them outside this interval, we need accurate formulas for the phase shifts and S-matrix as functions of energy which we discuss in the next subsection.

2.3 Phase shifts and *S*-matrix at low energies

The scattering S-matrix as a function of the complex momentum k is known [42, 43] to have the following symmetry properties:

$$S(-k) = \frac{1}{S(k)}, \qquad S(k^*) = \frac{1}{S^*(k)}, \qquad S(-k^*) = S^*(k), \tag{36}$$

where star is used to denote the complex conjugation. The S-matrix can have poles either in the lower part of the complex momentum plane or on the imaginary momentum axis [42, 43]. The poles in the lower part of the complex momentum plane

at $k = \kappa_r \equiv k_r - i\gamma_r$ ($k_r, \gamma_r > 0$) due to the symmetry relations (36) are accompanied by the poles at $k = -\kappa_r^* \equiv -k_r - i\gamma_r$ and are associated with resonances at the energy

$$E_r = \frac{\hbar^2}{2m}(k_r^2 - \gamma_r^2) \tag{37}$$

and with the width

$$\Gamma = \frac{2\hbar^2}{m} k_r \gamma_r. \tag{38}$$

Bound states at energy $E_b = -\hbar^2 k_b^2/2m$ are in correspondence with the poles on the positive imaginary momentum axis at $k = ik_b$ ($k_b > 0$), however some positive imaginary momentum poles can appear to be the so-called false or redundant poles [42] which do not represent any bound state. The poles at negative imaginary momentum at $k = -ik_v$ ($k_v < 0$) are associated with virtual states at energy $E_v = \hbar^2 k_v^2/2m$.

If the S-matrix has a pole close to the origin either in the lower part of the complex momentum plane or on the imaginary momentum axis, it can be expressed at low energies as

$$S(k) = \Theta(k)\, S_p(k), \tag{39}$$

where $\Theta(k)$ is a smooth function of k and the pole term $S_p(k)$ in the case of a bound state or false pole ($p = b$), virtual ($p = v$) or a resonant state ($p = r$) takes the form [43]:

$$S_b(k) = -\frac{k + ik_b}{k - ik_b}, \tag{40}$$

$$S_v(k) = -\frac{k - ik_v}{k + ik_v}, \tag{41}$$

$$S_r(k) = \frac{(k + \kappa_r)(k - \kappa_r^*)}{(k - \kappa_r)(k + \kappa_r^*)}. \tag{42}$$

The S-matrix is expressed through the phase shifts $\delta_\ell(k)$ as

$$S(k) = e^{2i\delta_\ell(k)}, \tag{43}$$

hence the respective phase shifts

$$\delta_\ell(k) = \phi(k) + \delta_p(k), \tag{44}$$

where the pole contribution $\delta_p(k)$ from the bound state takes the form

$$\delta_b(E) = \pi - \arctan\sqrt{\frac{E}{|E_b|}}, \tag{45}$$

where π appears due to the Levinson theorem [43]. The contributions from the false, virtual and resonant poles are

$$\delta_f(E) = -\arctan\sqrt{\frac{E}{|E_f|}}, \tag{46}$$

$$\delta_v(E) = \arctan\sqrt{\frac{E}{E_v}}, \tag{47}$$

$$\delta_r(E) = -\arctan\frac{a\sqrt{E}}{E - b^2}, \tag{48}$$

where the resonance energy E_r and width Γ can be expressed through the parameters a and b as

$$E_r = b^2 - a^2/2, \tag{49}$$

$$\Gamma = a\sqrt{4b^2 - a^2}. \tag{50}$$

Due to Eq. (43), the S-matrix symmetries (36) require the phase shift $\delta_\ell(E)$ to be an odd function of k and its expansion in Taylor series of $\sqrt{E} \sim k$ includes only odd powers of $\sqrt{E}$:

$$\delta_\ell(E) = c\sqrt{E} + d\big(\sqrt{E}\big)^3 + ... \tag{51}$$

More, since $\delta_\ell \sim k^{2\ell+1}$ in the limit $k \to 0$, $c = 0$ in the case of p-wave scattering, $c = d = 0$ in the case of d-wave scattering, etc.

In applications to the non-resonant $n\alpha$ scattering in the $\frac{1}{2}^+$ state ($\ell = 0$), we therefore are using the following parametrization of the phase shifts:

$$\delta_0(E) = \pi - \arctan\sqrt{\frac{E}{|E_b|}} + c\sqrt{E} + d\big(\sqrt{E}\big)^3 + f\big(\sqrt{E}\big)^5. \tag{52}$$

The bound state pole contribution here is associated with the so-called Pauli-forbidden state. There are resonances in the $n\alpha$ scattering in the $\frac{1}{2}^-$ and $\frac{3}{2}^-$ states ($\ell = 1$); hence we parametrize these phase shifts as

$$\delta_1(E) = -\arctan\frac{a\sqrt{E}}{E - b^2} - \frac{a}{b^2}\sqrt{E} + d\big(\sqrt{E}\big)^3. \tag{53}$$

This form guarantees that $\delta_1 \sim k^3$ in the limit of $E \to 0$.

3 Model problem

To test our SS-HORSE technique, we calculate the phase shifts and resonant parameters of $n\alpha$ scattering in a two-body approach treating neutron and α as structureless particles whose interaction is described by a Woods–Saxon type potential WSB

$$V_{n\alpha} = \frac{V_0}{1 + \exp\left[(r - R_0)/\alpha_0\right]} \; + \; (\boldsymbol{l}\cdot\boldsymbol{s})\;\frac{1}{r}\;\frac{d}{dr}\;\frac{V_{ls}}{1 + \exp\left[(r - R_1)/\alpha_1\right]}, \tag{54}$$

with parameters fitted in Ref. [44]: $V_0 = -43$ MeV, $V_{ls} = -40$ MeV$\cdot$fm^2, R_0=2.0 fm, α_0=0.70 fm, R_1=1.5 fm, α_1=0.35 fm. The matrix in the oscillator basis of the relative motion Hamiltonian with this interaction is diagonalized using $\hbar\Omega$ values ranging from 2.5 to 50 MeV in steps of 2.5 MeV and $N_{\max}$ up to 20 for natural parity states $\frac{3}{2}^-$ and $\frac{1}{2}^-$ and up to 19 for unnatural parity states $\frac{1}{2}^+$.

3.1 Partial wave $\frac{3}{2}^-$

The lowest eigenstates E_0 obtained by diagonalization of the model Hamiltonian with the WSB potential are presented in Fig. 2 as a function of the scaling parameter s. It is seen that the eigenstates obtained with large enough $N_{\max}$ values form a single curve in Fig. 2; however the eigenstates obtained with smaller $N_{\max}$ start deviating from this curve at smaller $\hbar\Omega$ which correspond to smaller s values reflecting the convergence patterns of calculations in the finite oscillator basis. This feature is even more pronounced in the plot of the phase shifts obtained directly from eigenstates E_0

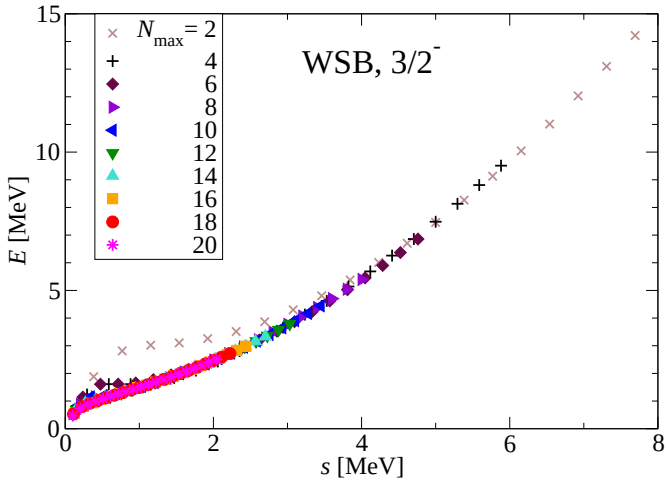

Figure 2: The lowest $\frac{3}{2}^-$ eigenstates E_0 of the model Hamiltonian with WSB potential obtained with various $N_{\max}$ and $\hbar\Omega$ plotted as a function of the scaling parameter s.

using Eq. (19) (see Fig. 3). We need to exclude from the further SS-HORSE analysis the eigenstates deviating from the common curves in Figs. 2 and 3.

As we already mentioned, the scaling property of our SS-HORSE formalism has much in common with those proposed in Refs. [2, 3]. Using the nomenclature of Refs. [2,3], we should use only eigenenergies E_0 which are not influenced by infra-red corrections. According to Refs. [2, 3], these eigenenergies are obtained with $N_{\max}$ and $\hbar\Omega$ fitting inequality

$$\Lambda \equiv \sqrt{m\hbar\Omega(N_{\max} + \ell + 3/2)} > \Lambda_0, \tag{55}$$

where Λ_0 depends on the interaction between the particles. The value of $\Lambda_0 = 385$ MeV/c seems to be adequate for the potential WSB resulting in a reasonable selection of eigenenergies E_0. The selection of eigenenergies according to this criterion is illustrated by the shaded area in Fig. 4 where we plot eigenenergies E_0 obtained with various $N_{\max}$ as functions of $\hbar\Omega$. These selected eigenstates plotted as a function of the scaling parameter s in Fig. 5 and the respective SS-HORSE phase shifts in Fig. 6 are seen to produce smooth single curves.

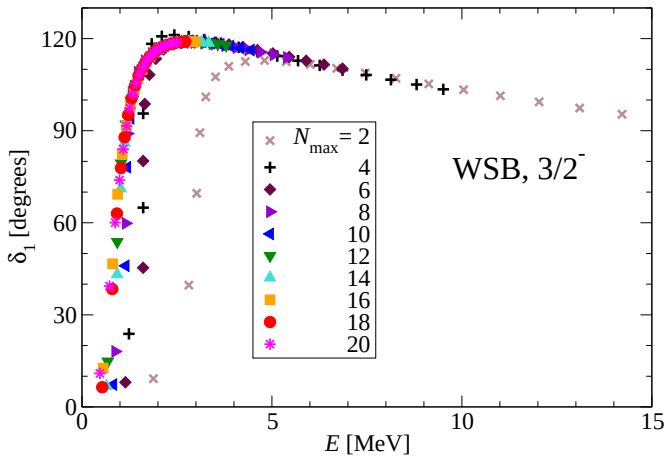

Figure 3: The $\frac{3}{2}^-$ phase shifts obtained directly from the WSB eigenstates E_0 using Eq. (19).

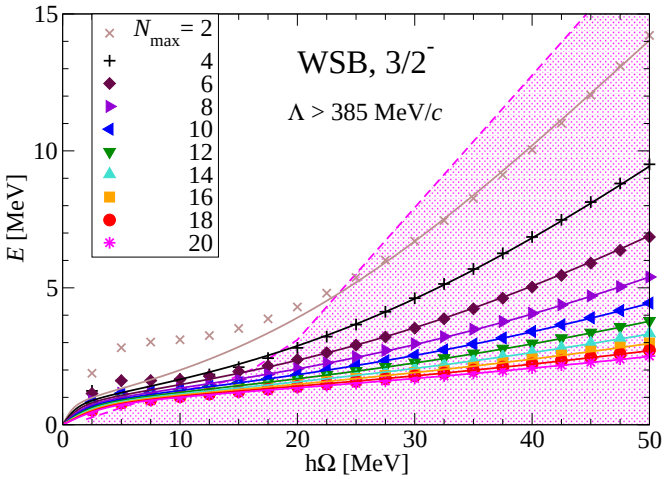

Figure 4: The lowest $\frac{3}{2}^-$ eigenenergies E_0 of the model WSB Hamiltonian obtained with various $N_{\max}$ as functions of $\hbar\Omega$ and selection of eigenstates for the SS-HORSE analysis according to inequality $\Lambda > 385$ MeV/c. The shaded area shows the selected E_0 values. Solid lines are solutions of Eq. (56) for energies E_0 with parameters a, b and d obtained by the fit.

The low-energy resonant $n\alpha$ scattering phase shifts in the $\frac{3}{2}^-$ state are described by Eq. (53). We need to fit the parameters a, b and d of this equation. Combining Eqs. (19), (27) and (53) we derive the following relation for resonant $n\alpha$ scattering in the $\frac{3}{2}^-$ state which can be also used for the $\frac{1}{2}^-$ state ($\ell = 1$ in both cases):

$$-\frac{S_{N_{\max}+3,\,1}(E_0)}{C_{N_{\max}+3,\,1}(E_0)} = \tan\left(-\arctan\frac{a\sqrt{E_0}}{E_0 - b^2} - \frac{a}{b^2}\sqrt{E_0} + d\left(\sqrt{E_0}\right)^3\right). \qquad (56)$$

We assign some values to the parameters a, b and d and solve this equation to find a set of E_0 values, $\mathcal{E}_0^{(i)} = E_0(N_{\max}^i, \hbar\Omega^i)$, $i = 1, 2, ..., D$, for each combination

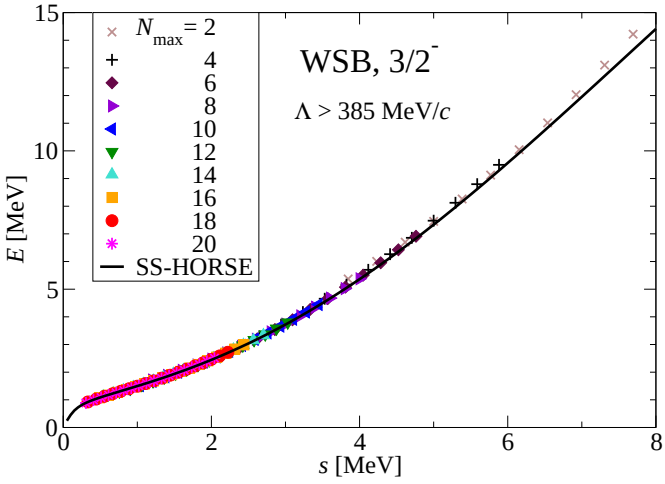

Figure 5: The $\frac{3}{2}^-$ WSB eigenstates E_0 selected according to $\Lambda > 385$ MeV/c plotted as a function of the scaling parameter s. The solid curve depicts solutions of Eq. (56) for energies E_0 with parameters a, b and d obtained by the fit with the respective selection of eigenstates.

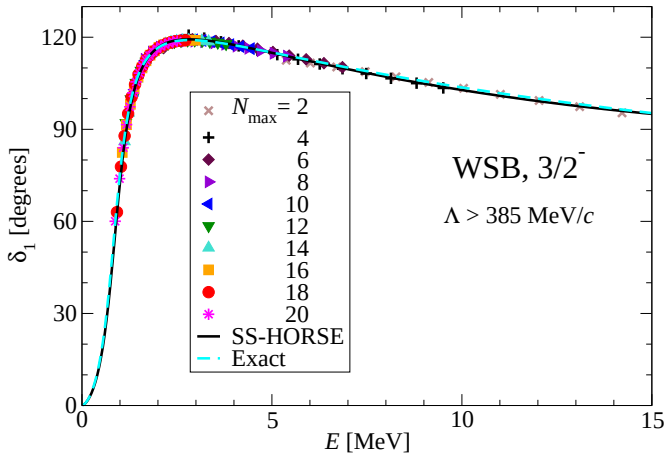

Figure 6: The $\frac{3}{2}^-$ WSB phase shifts obtained using Eq. (19) directly from eigenstates E_0 selected according to $\Lambda > 385$ MeV/c (symbols). The solid curve depicts the phase shifts of Eq. (53) with parameters a, b and d obtained by the fit with the respective selection of eigenstates; the dashed curve is obtained by a numerical integration of the Schrödinger equation.

of $N_{\max}$ and $\hbar\Omega$ [note, $\hbar\Omega$ enters definitions of functions $S_{N,\ell}(E)$ and $C_{N,\ell}(E)$, see Eqs. (9)–(11)]. The resulting set of $\mathcal{E}_0^{(i)}$ is compared with the set of selected eigenvalues $E_0^{(i)}$ obtained by the Hamiltonian diagonalization with respective $N_{\max}$ and $\hbar\Omega$ values, and we minimize the rms deviation,

$$\Xi = \sqrt{\frac{1}{D}\sum_{i=1}^{D}\left(E_0^{(i)} - \mathcal{E}_0^{(i)}\right)^2}, \tag{57}$$

to find the optimal values of the parameters a, b and d. The obtained parameters are listed in the first row of Table 1. The resonance energy E_r and width Γ obtained by Eqs. (49) and (50) are also presented in Table 1. Note the accuracy of the fit: the rms deviation of 156 fitted energy eigenvalues is only 37 keV.

The behavior of E_0 as functions of $\hbar\Omega$ dictated by Eq. (56) with the fitted optimal parameters for various $N_{\max}$ values is depicted by solid curves in Figs. 4 and 5. It is seen that these curves accurately describe the selected eigenvalues E_0 obtained by the Hamiltonian diagonalization. Note however a small deviation of the curve in Fig. 5 from the diagonalization results at large energies obtained with $N_{\max} = 2$ where the scaling become inaccurate, see Eq. (22). The phase shifts $\delta_1(E)$ obtained by Eq. (53) with fitted parameters are shown in the Fig. 6. It is seen that the SS-HORSE phase shifts are in excellent correspondence with the exact results obtained by numerical integration of the Schrödinger equation. The $\frac{3}{2}^-$ resonance energy and width are also well reproduced by our SS-HORSE technique (see Table 1).

In the above analysis we used oscillator bases with $N_{\max}$ values up to $N_{\max} = 20$. Such large $N_{\max}$ are accessible in two-body problems but are out of reach in modern many-body shell model applications. Therefore it is very important to check whether a reasonable accuracy of SS-HORSE phase shift and resonance parameter calculations can be achieved with significantly smaller $N_{\max}$.

We remove from the set of selected $\frac{3}{2}^-$ eigenstates $E_0^{(i)}$ those obtained with $N_{\max} > 6$ and use this new selection illustrated by Figs. 7 and 8 to calculate phase shifts and resonant parameters. All eigenenergies from this selection lie outside the resonance region as is seen in Fig. 9 where we plot the phase shifts as a function of energy. The SS-HORSE fit (see Table 1) nevertheless accurately reproduces the exact phase

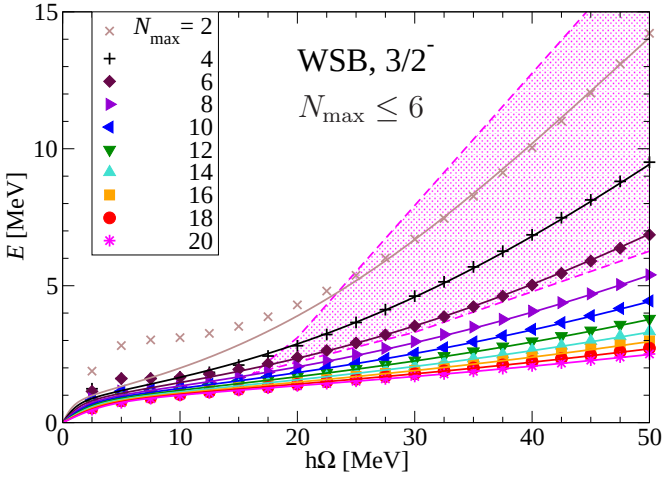

Figure 7: Selection of the lowest $\frac{3}{2}^-$ WSB eigenstates E_0 obtained with $N_{\max} \leq 6$. See Fig. 4 for details.

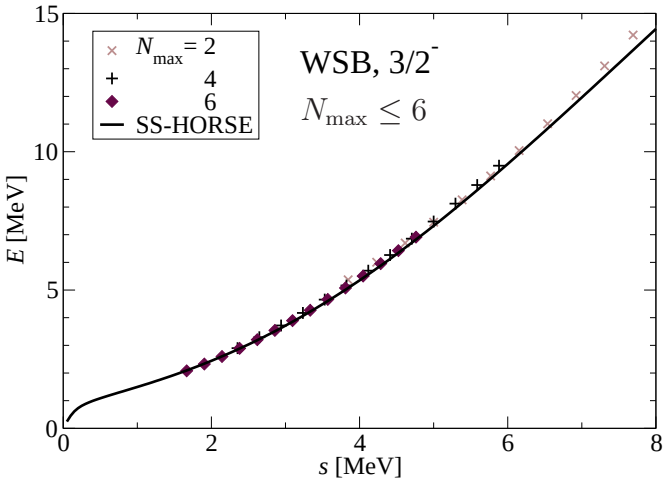

Figure 8: Selected lowest $\frac{3}{2}^-$ WSB eigenstates E_0 obtained with $N_{\max} \leq 6$ as a function of the scaling parameter s. See Fig. 5 for details.

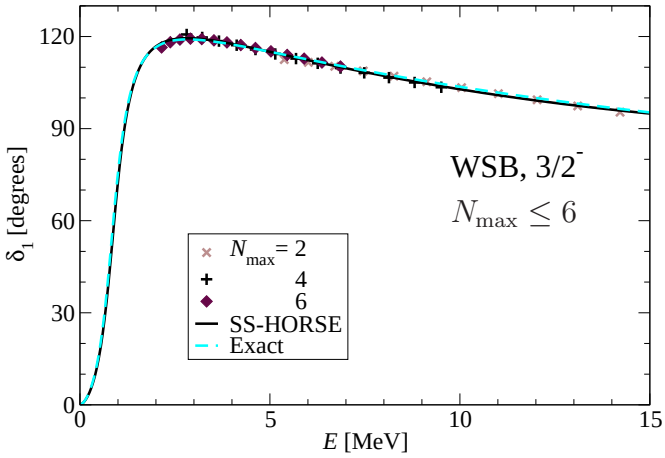

Figure 9: The $\frac{3}{2}^-$ WSB phase shifts generated by the selected eigenstates E_0 obtained with $N_{\max} \leq 6$. See Fig. 6 for details.

Table 1: $\frac{3}{2}^-$ resonance in $n\alpha$ scattering with model WSB potential: fitting parameters a, b, d of Eq. (56), resonance energy E_r and width Γ, rms deviation of fitted energies Ξ and the number of these fitted energies D for different selections of eigenvalues in comparison with exact results for E_r and Γ obtained by numerical location of the S-matrix pole. For the $N_{\max} \leq 6$ selection, Ξ and D for all energies from the previous selection are shown within brackets.

Selection	a (MeV$^{\frac{1}{2}}$)	b^2 (MeV)	$d \cdot 10^3$ (MeV$^{-\frac{3}{2}}$)	E_r (MeV)	Γ (MeV)	Ξ (keV)	D
$\Lambda > 385$ MeV/c	0.412	0.948	5.41	0.863	0.785	37	156
$N_{\max} \leq 6$	0.411	0.948	5.30	0.863	0.782	70(38)	38(156)
Exact				0.836	0.780		

shifts (see Fig. 9) even in the resonance region and the $\frac{3}{2}^-$ resonance energy E_r and width Γ (see Table 1). To get such accuracy, it is very important to use the adequate phase shift parametrization (53) which guarantees the low-energy phase shift behaviour $\delta_\ell \sim k^{2\ell+1}$ and an accurate description of the resonance region by the pole term (48): our previous study [38] has clearly demonstrated that it is impossible to reproduce the resonant parameters and phase shifts in a wide enough energy interval without paying special attention to the low-energy phase shift description and by using the less accurate Breit–Wigner resonant phase shifts instead of the pole term (48) even when large $N_{\max}$ eigenstates E_0 are utilized to say nothing about the selection of eigenstates obtained with small $N_{\max}$.

Solid lines in Figs. 4 and 7 present the eigenenergies E_0 for various $N_{\max}$ values as functions of $\hbar\Omega$ obtained from the respective phase shift parametrization. It is seen that we accurately describe not only the eigenenergies from the shaded area utilized in the fit but also those corresponding to a wider range of $\hbar\Omega$ values. It is even more interesting that in the case of Fig. 7 where fitted are only the states with $N_{\max} \leq 6$, we also reproduce the eigenenergies obtained with much larger $N_{\max}$ values with nearly the same rms deviation as in the case of the previous selection (see Table 1) when those larger $N_{\max}$ eigenenergies were included in the fit. In other words, our SS-HORSE fit to the diagonalization results in small basis spaces makes it possible to 'predict' the diagonalization results obtained with much larger oscillator bases. This is very important for many-body shell-model applications and suggests a very efficient method of extrapolating the shell-model results in continuum to larger basis spaces.

3.2 Partial wave $\frac{1}{2}^-$

The lowest $\frac{1}{2}^-$ eigenstates of the model Hamiltonian with the WSB potential are shown as functions of $\hbar\Omega$ for various $N_{\max}$ in Fig. 10 and as functions of the scaling parameter s in Fig. 11. All eigenenergies in this case seem to lie approximately on the same curve in Fig. 11; however the plot of the SS-HORSE phase shifts corresponding to these eigenstates (see Fig. 12) clearly indicates deviations from the common curve for eigenstates obtained with small $N_{\max}$ values. We have already mentioned that the phase shifts are more sensitive to the convergence patterns and are somewhat more instructive for the selection of the eigenenergies.

As in the case of the $\frac{3}{2}^-$ partial wave, we start with the $\Lambda > 385$ MeV/c selection of eigenenergies as is illustrated by Fig. 13 and by the shaded area in Fig. 10. The fitting method described in the previous subsection results in the parameters listed in the first row of Table 2. We obtain a reasonable fit with a small enough rms deviation of the 156 selected eigenenergies of 80 keV. The obtained phase shifts depicted in Fig. 14 are

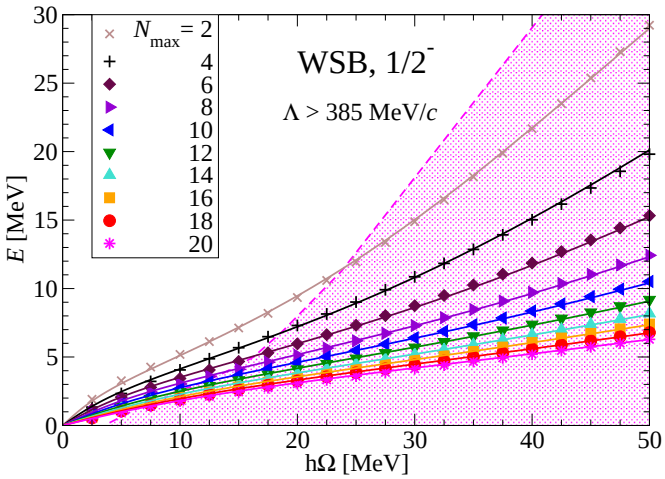

Figure 10: The lowest $\frac{1}{2}^-$ WSB eigenstates E_0 as functions of $\hbar\Omega$ and their $\Lambda > 385$ MeV/c selection. See Fig. 4 for details.

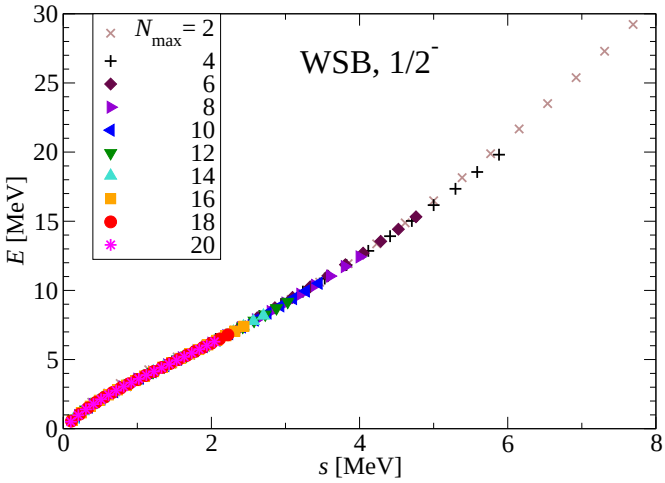

Figure 11: The lowest $\frac{1}{2}^-$ WSB eigenstates E_0 as a function of the scaling parameter s.

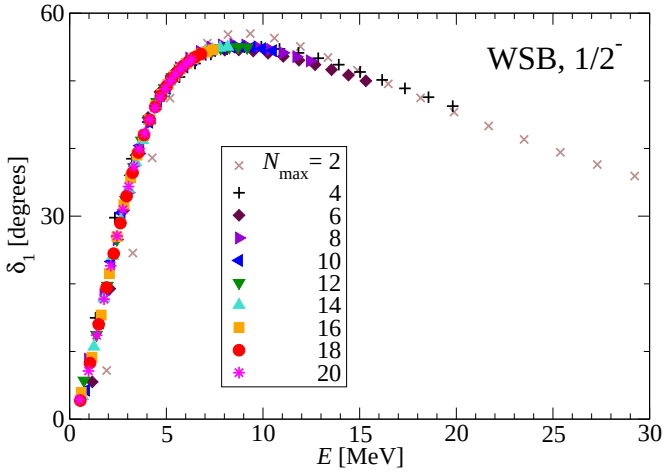

Figure 12: The $\frac{1}{2}^-$ phase shifts obtained directly from the WSB eigenstates E_0 using Eq. (19).

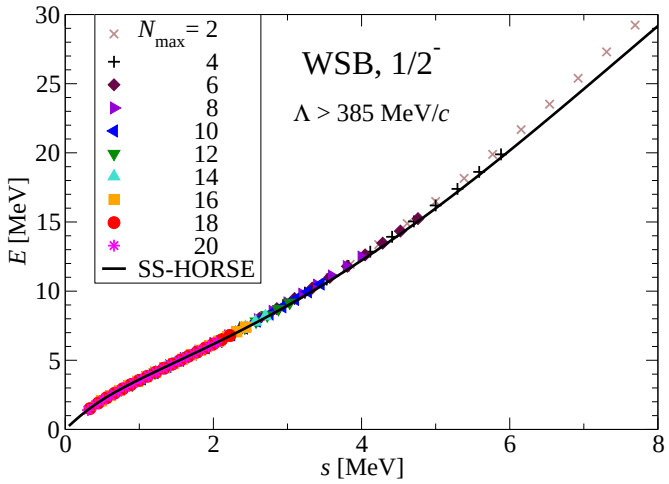

Figure 13: The $\Lambda > 385$ MeV/c selected $\frac{1}{2}^-$ WSB eigenstates E_0 as a function of the scaling parameter s. See Fig. 5 for details.

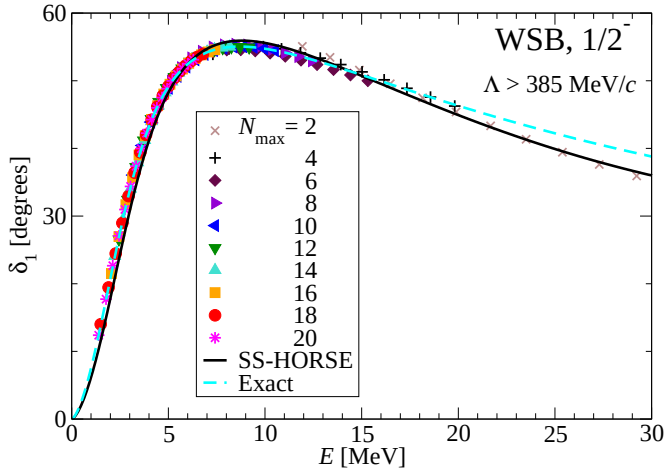

Figure 14: The $\frac{1}{2}^-$ WSB phase shifts generated by the $\Lambda > 385$ MeV/c selected eigenstates E_0. See Fig. 6 for details.

very close to the exact phases from numerical integration of the Schrödinger equation with the WSB potential up to the energy E of approximately 17 MeV. At higher energies we see some difference between the exact and SS-HORSE phases shifts which are completely governed in this energy region by the $N_{\max} = 2$ eigenenergies which are not expected to be close to convergence for the energy extrapolations and S-matrix description within the HORSE extension of the Hamiltonian. We note also

Table 2: Parameters of the $\frac{1}{2}^-$ WSB resonance. See Table 1 for details.

Selection	a (MeV$^{\frac{1}{2}}$)	b^2 (MeV)	$d \cdot 10^3$ (MeV$^{-\frac{3}{2}}$)	E_r (MeV)	Γ (MeV)	Ξ (keV)	D
$\Lambda > 385$ MeV/c	1.780	3.636	3.18	2.05	6.00	80	156
$N_{\max} \leq 6$	1.822	3.818	2.77	2.16	6.30	75(84)	38(156)
Exact				1.66	5.58		

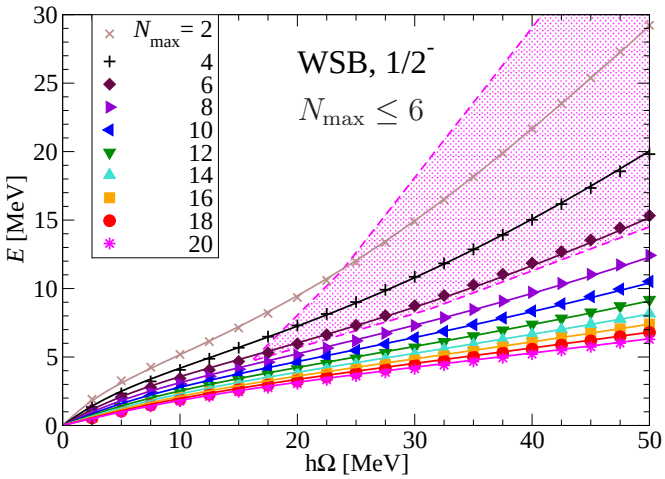

Figure 15: Selection of the lowest $\frac{1}{2}^-$ WSB eigenstates E_0 obtained with $N_{\max} \leq 6$. See Fig. 4 for details.

that contrary to the $\frac{3}{2}^-$ resonance we observe approximately 0.5 MeV differences between the resonance energy E_r and width Γ results obtained by the SS-HORSE technique and by numerical location of the respective S-matrix pole. We suppose that these differences originate from the fact that the $\frac{1}{2}^-$ resonance pole associated with this wide resonance is located far enough from the real energy axis; therefore the phase shifts even in the resonant region can be influenced by other S-matrix poles not accounted for by our phase shift parametrization (53).

We examine also a possibility of describing the $\frac{1}{2}^-$ phase shifts and resonance parameters by using only the eigenstates obtained with $N_{\max} \leq 6$ for our SS-HORSE analysis. We retain only these eigenstates from our previous selection as is shown by the shaded area in Fig. 15; this eigenstate selection is also illustrated by Fig. 16. The energies E_0 of all selected eigenstates are larger than the resonance region as is seen in Fig. 17. Nevertheless we reproduce the phase shifts and resonance parameters (see Fig. 17 and Table 2) nearly with the same accuracy as with the previous much more complete eigenstate selection. More, we accurately 'predict' eigenenergies in larger

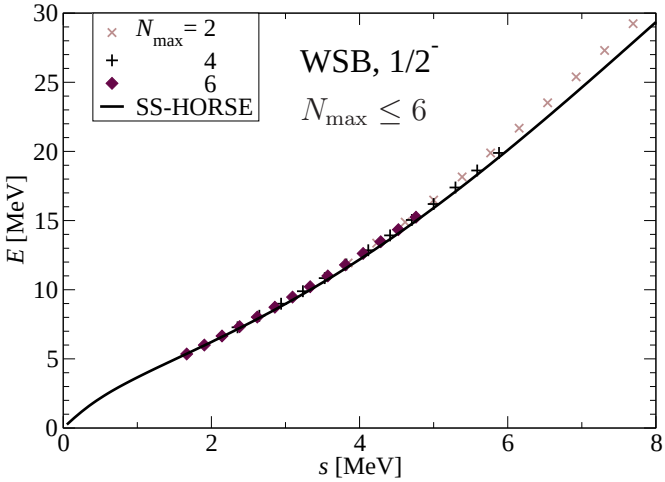

Figure 16: Selected lowest $\frac{1}{2}^-$ WSB eigenstates E_0 obtained with $N_{\max} \leq 6$ as a function of the scaling parameter s. See Fig. 5 for details.

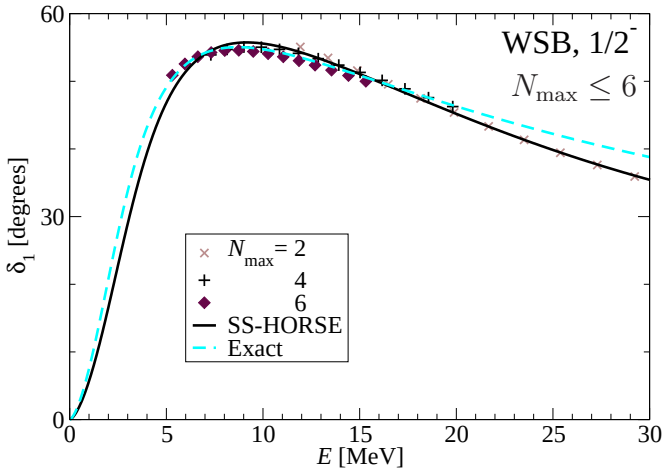

Figure 17: The $\frac{1}{2}^-$ WSB phase shifts generated by the selected eigenstates E_0 obtained with $N_{\max} \leq 6$. See Fig. 6 for details.

model spaces (see solid lines in Fig. 15) nearly with the same rms deviation as the fit involving those eigenstates as is indicated in Table 2.

3.3 Partial wave $\frac{1}{2}^+$

There are no resonances in the $n\alpha$ scattering in the $\frac{1}{2}^+$ partial wave. However, as it has been indicated in Ref. [14], the nuclear shell model should generate eigenstates in non-resonant energy intervals in continuum to be consistent with scattering observables. Therefore it is interesting to test with the WSB potential the ability of the SS-HORSE approach to describe the $\frac{1}{2}^+$ non-resonant $n\alpha$ scattering.

The low-energy $n\alpha$ scattering phase shifts in the $\frac{1}{2}^+$ state are described by Eq. (52). We shall see that to get the same quality fit as in the case of the odd-parity resonant scattering, we need in this case terms up to the 5^{th} power of $\sqrt{E}$ in the Taylor expansion of the background phase; therefore we preserve in Eq. (52) more terms than in Eq. (53). c, d and f are fitting parameters in Eq. (52). The WSB potential supports a bound state at energy E_b which mimics the Pauli-forbidden state in the $n\alpha$ scattering. We however treat E_b as an additional fitting parameter as a preparation to many-body NCSM calculations where it is impossible to obtain the energy of the Pauli-forbidden state. This bound state appears as the lowest state with negative energy obtained by the Hamiltonian diagonalization and is unneeded for our SS-HORSE analysis for which we use the first excited state $E_1 > 0$ which is the lowest state in the continuum.

The excitation quanta $N_{\max}$ is conventionally used to define the many-body NCSM basis space while the total oscillator quanta $\mathbb{N}$ is entering our SS-HORSE equations. The $\frac{1}{2}^+$ states in ^{5}He are unnatural parity states, hence $N_{\max}$ takes odd values within NCSM, the minimal oscillator quanta $N_0 = 1$ in the five-body $n\alpha$ system, and

$$\mathbb{N} = N_{\max} + N_0 \tag{58}$$

is even. To retain a correspondence with NCSM, we are using $N_{\max}$ to define the oscillator basis also in our model two-body problem. We note that in this case the $N_{\max}$ is formally related to $\mathbb{N}$ according to Eq. (27) where $\ell = 0$, and $N_{\max}$ should be even for even $\mathbb{N}$. To have a closer correspondence with NCSM, we use Eq. (58) with $N_0 = 1$ within our model two-body problem instead of Eq. (27) to relate $N_{\max}$ to $\mathbb{N}$, i. e., due to our NCSM-like definition, the $\frac{1}{2}^+$ eigenstates are labelled below by odd $N_{\max}$

values. Note, the definitions (27) and (58) result in the same $N_{\max}$ in the case of odd-parity $\frac{3}{2}^-$ and $\frac{1}{2}^-$ $n\alpha$ partial waves.

Combining Eqs. (19), (52) and (58), we derive for the $n\alpha$ scattering in the $\frac{1}{2}^+$ partial wave:

$$-\frac{S_{N_{\max}+3,\,0}(E_\nu)}{C_{N_{\max}+3,\,0}(E_\nu)} = \tan\left(\pi - \arctan\sqrt{\frac{E_\nu}{|E_b|}} + c\sqrt{E_\nu} + d\left(\sqrt{E_\nu}\right)^3 + f\left(\sqrt{E_\nu}\right)^5\right), \quad (59)$$

where $\nu = 1$. We assign some values to the fitting parameters E_b, c, d and f and solve Eq. (59) to find a set of E_1 values, $\mathcal{E}_1^{(i)} = E_1(N_{\max}^i, \hbar\Omega^i)$, $i = 1, 2, ..., D$, for each combination of $N_{\max}$ and $\hbar\Omega$ and minimize the rms deviation from the selected eigenvalues $E_1^{(i)}$ obtained by the Hamiltonian diagonalization, see Eq. (57) where the subindex 0 should be replaced by 1, to find the optimal values of the fitting parameters.

The lowest continuum $\frac{1}{2}^+$ eigenstates E_1 of the model WSB Hamiltonian are shown as functions of $\hbar\Omega$ for various $N_{\max}$ in Fig. 18 and as a function of the scaling parameter s in Fig. 19. All eigenenergies in this case seem to lie approximately on the same curve in Fig. 19; however, as in the case of odd parity partial waves, the deviations from the common curve are much more pronounced in the plot of the SS-HORSE phase shifts corresponding to these eigenstates (see Fig. 20) which clearly indicates the need to select eigenstates for the SS-HORSE fitting.

As in the case of the odd parity states, we use the $\Lambda > 385$ MeV/c selection of eigenenergies as is illustrated by Fig. 21 and by the shaded area in Fig. 18. The obtained fitting parameters of Eq. (59) are presented in Table 3. It is interesting that the fitted energy E_b differs essentially from the exact value which is the energy of the bound state in the WSB potential. The SS-HORSE $\frac{1}{2}^+$ phase shifts nevertheless are seen in Fig. 22 to be nearly indistinguishable from the exact ones up to the energies of about 70 MeV where the SS-HORSE phase shifts governed by $N_{\max} = 1$ eigenstates slightly differ from exact. We note that the WSB bound state has a large binding energy, the respective S-matrix pole is far enough from the real momentum axis and hence has a minor influence on the phase shifts. This result indicates that one should not take seriously the energies of bound states obtained by the fit to the scattering data only, at least for well-bound states.

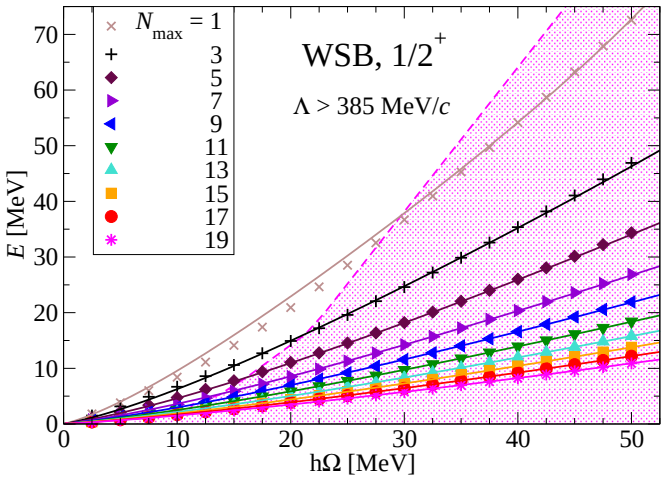

Figure 18: The lowest continuum $\frac{1}{2}^+$ WSB eigenstates E_1 as functions of $\hbar\Omega$ and their $\Lambda > 385$ MeV/c selection. Solid lines are solutions of Eq. (59) for energies E_1 with parameters E_b, c, d and f obtained by the fit with this selection of eigenstates.

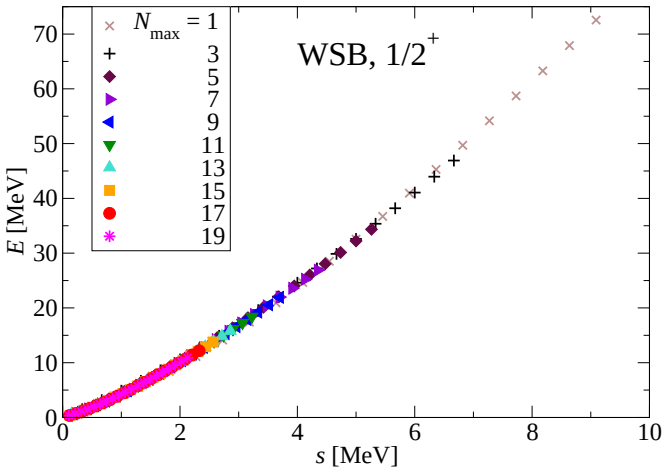

Figure 19: The lowest continuum $\frac{1}{2}^+$ WSB eigenstates E_1 as a function of the scaling parameter s.

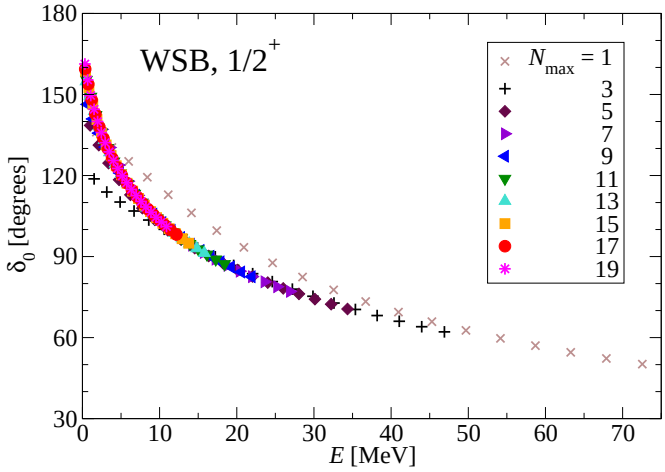

Figure 20: The $\frac{1}{2}^+$ phase shifts obtained directly from the WSB eigenstates E_1 using Eq. (19).

To examine a possibility of describing the low-energy $\frac{1}{2}^+$ phase shifts using only the diagonalization results in small basis spaces, we remove from the previous selection the eigenenergies E_1 obtained with $N_{\max} > 5$ as is illustrated by Figs. 23 and 24. We obtain nearly the same values of the fitting parameters as is seen from Table 3.

Table 3: $\frac{1}{2}^+$ $n\alpha$ scattering with model WSB potential: fitting parameters E_b, c, d and f of Eq. (59), rms deviation of fitted energies Ξ and the number of these fitted energies D for different selections of eigenvalues. For the $N_{\max} \leq 5$ selection, Ξ and D for all energies from the previous selection are shown within brackets.

Selection	E_b (MeV)	c (MeV$^{-\frac{1}{2}}$)	$d \cdot 10^3$ (MeV$^{-\frac{3}{2}}$)	$f \cdot 10^5$ (MeV$^{-\frac{5}{2}}$)	Ξ (keV)	D
$\Lambda > 385$ MeV/c	-6.841	-0.157	$+1.19$	-0.888	163	151
$N_{\max} \leq 5$	-6.853	-0.156	$+1.19$	-0.888	332(163)	35(151)
Exact	-9.85					

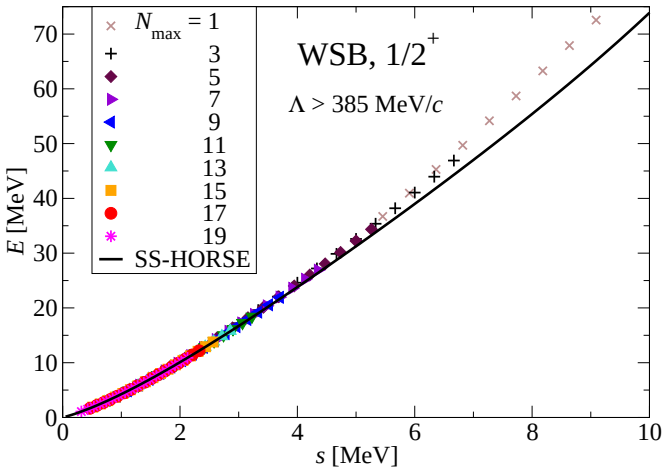

Figure 21: The $\Lambda > 385$ MeV/c selected $\frac{1}{2}^+$ WSB eigenstates E_1 as a function of the scaling parameter s. The solid curve depicts solutions of Eq. (59) for energies E_1 with parameters E_b, c, d and f obtained by the fit with this selection of eigenstates.

The largest though still small enough difference is obtained for the fitted E_b values which, as has been already noted, does not play an essential role in the phase shifts. Therefore it is not surprising that we get an excellent description of the exact phase shifts presented in Fig. 25. Figure 23 demonstrates that we describe accurately not only the eigenstates E_1 involved in the fitting procedure but also those obtained in much larger basis spaces which were not fitted. The rms deviation in the description of energies of all $\Lambda > 385$ MeV/c selected eigenstates is exactly the same as in the case when all these eigenstates were included in the fit.

As we already noted, the scaling of the eigenstates of finite Hamiltonian matrices in oscillator basis has been proposed by S. Coon and collaborators in Refs. [2, 3] who studied the convergence patterns of the bound states. They have demonstrated that the eigenenergies E_ν as functions of the scaling parameter $\lambda_{sc} \sim \sqrt{s}$ tend to a constant as λ_{sc} approaches 0; this constant is the convergence limit of the respective

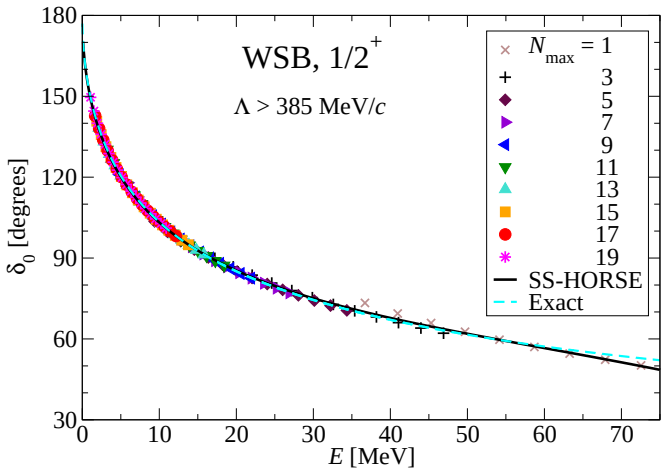

Figure 22: The $\frac{1}{2}^+$ WSB phase shifts generated by the $\Lambda > 385$ MeV/c selected eigenstates E_1 (symbols). The solid curve depicts the phase shifts of Eq. (52) with parameters E_b, c, d and f obtained by the fit with this selection of eigenstates; the dashed curve is obtained by a numerical integration of the Schrödinger equation.

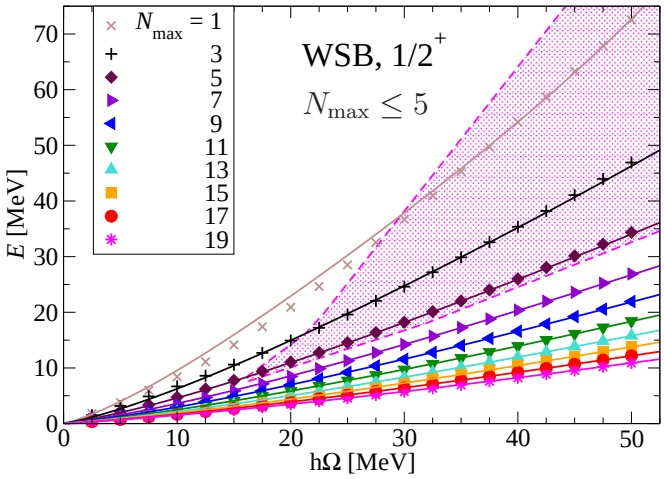

Figure 23: Selection of the lowest $\frac{1}{2}^+$ WSB eigenstates E_1 obtained with $N_{\max} \leq 5$. See Fig. 4 for details.

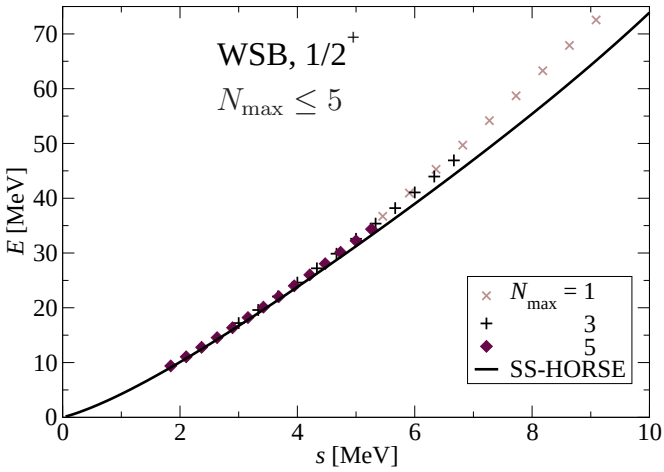

Figure 24: Selected lowest $\frac{1}{2}^+$ WSB eigenstates E_1 obtained with $N_{\max} \leq 5$ as a function of the scaling parameter s. See Fig. 21 for details.

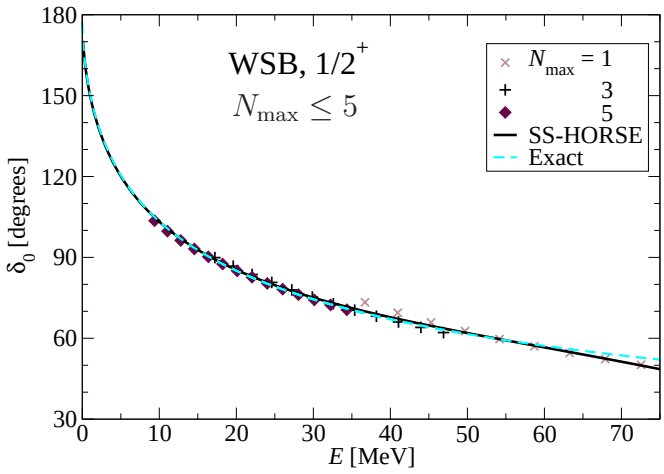

Figure 25: The $\frac{1}{2}^+$ WSB phase shifts generated by the selected eigenstates E_1 obtained with $N_{\max} \leq 6$. See Fig. 22 for details.

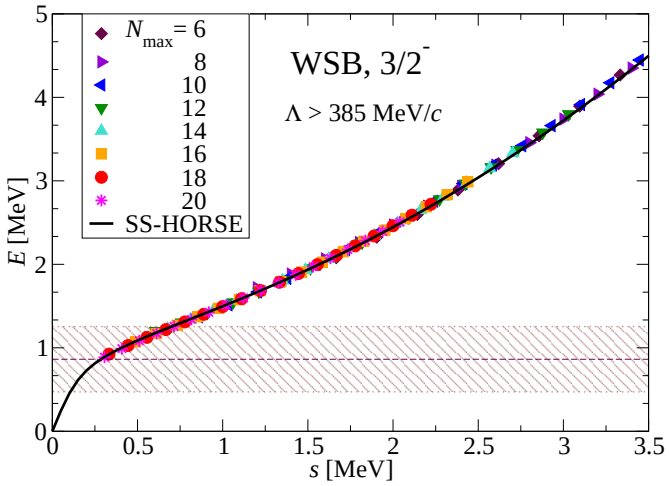

Figure 26: The same as Fig. 5 but in a larger scale. The dashed line corresponds to the resonance energy E_r, the shaded area shows the resonance width.

eigenenergy in the infinite basis. Our study extends the scaling patterns of the harmonic oscillator eigenstates to the case of states in the continuum. In this case the eigenenergies should approach 0 as the basis is expanded infinitely. The solid lines in Figs. 21 and 24 demonstrate the behaviour of eigenenergies in the continuum E_1 as a function of the scaling parameter s in the case of a system which has a bound state and does not have resonances in the low-energy region; the respective low-energy phase shifts are described by Eq. (52), a general formula for this case. The eigenstates are seen to be a smooth monotonic function of s (or λ_{sc}) which tends, as expected, to zero as $s \to 0$.

The solid lines in Figs. 5, 8, 13 and 16 demonstrate the behaviour of the eigenstates E_0 as a function of the scaling parameter s when the low-energy phase shifts are given by Eq. (53) which is a general formula describing a system which does not have a bound state but has a low-energy resonance. We see again a smooth monotonically increasing function of s with a large enough derivative at large s. At smaller s when the energy approaches the resonant region, the derivative of $E_0(s)$ decreases; this decrease of the derivative is more pronounced for narrow resonances as can be seen by comparing Figs. 5 and 13. Figure 26 where the function $E_0(s)$ from Fig. 5 is shown in a larger scale together with the resonant region, demonstrates that the further decrease of s strongly enhances the derivative of this function at the energies below the resonance energy E_r. When the function $E_0(s)$ leaves the resonant region at smaller s values, the next eigenstate $E_1(s)$ (not shown in the figure) approaches the resonant region from above.

These are the general convergence trends of the positive energy eigenstates obtained in the oscillator basis.

Concluding this section, we have demonstrated using the WSB potential as an example that the proposed SS-HORSE technique is adequate for the description of low-energy scattering phase shifts and resonance energies E_r and widths Γ. A very encouraging sign for many-body shell-model applications is that the resonance parameters and phase shifts can be obtained nearly without loosing the accuracy by using within the SS-HORSE approach only the Hamiltonian eigenstates obtained in small basis spaces; more, having the low-lying energies from small basis spaces we are able to 'predict' accurately the values of eigenenergies in much larger oscillator bases.

4 SS-HORSE NCSM calculation of resonances in $n\alpha$ scattering

We discuss here the application of our SS-HORSE technique to $n\alpha$ scattering phase shifts and resonance parameters based on *ab initio* many-body calculations of ^{5}He within the NCSM with the realistic JISP16 NN interaction. The NCSM calculations are performed using the code MFDn [45, 46] with $2 \leq N_{\max} \leq 18$ for both parities and with $\hbar\Omega$ values ranging from 10 to 40 MeV in steps of 2.5 MeV.

As it has been already noted above, for the SS-HORSE analysis we need the ^{5}He energies relative to the $n + \alpha$ threshold. Therefore from each of the ^{5}He NCSM odd (even) parity eigenenergies we subtract the ^{4}He ground state energy obtained by the NCSM with the same $\hbar\Omega$ and the same $N_{\max}$ (with $N_{\max} - 1$) excitation quanta, and in what follows these subtracted energies are called NCSM eigenenergies E_ν. Only these ^{5}He NCSM eigenenergies relatively to the $n + \alpha$ threshold are discussed below.

4.1 Partial wave $\frac{3}{2}^-$

We utilize the same Eq. (56) to fit the parameters describing the low-energy $\frac{3}{2}^-$ and $\frac{1}{2}^-$ phase shifts as in the model problem; the only difference is that the lowest energy eigenstates E_0 are obtained now from the many-body NCSM calculations. These lowest $\frac{3}{2}^-$ NCSM eigenstates are shown in Fig. 27 as functions of $\hbar\Omega$ for various $N_{\max}$ values. Figure 28 presents these eigenstates E_0 as a function of the scaling parameter s while Fig. 29 presents the $\frac{3}{2}^-$ phase shifts obtained directly from them using Eq. (19). Figures 28 and 29 clearly demonstrate the need of the eigenstate selection since many points in these figures deviate strongly from the common curves formed by other points. On the other hand, these figures demonstrate the convergence achieved in large $N_{\max}$ calculations: the deviation from the common curves occurs at smaller $\hbar\Omega$ values as $N_{\max}$ increases and all results from the largest available NCSM basis spaces seem to lie on the single common curves with the exception of only very few eigenenergies obtained with $\hbar\Omega < 15$ MeV.

Our first selection is the eigenstates fitting inequality $\Lambda > 600$ MeV/c, the value

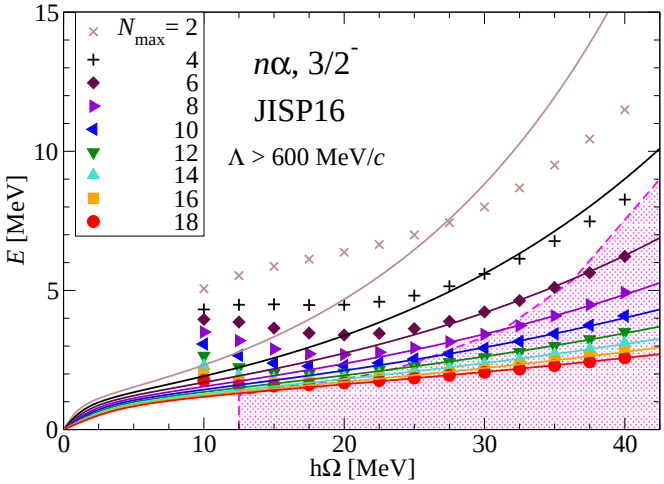

Figure 27: The lowest ^{5}He $\frac{3}{2}^-$ eigenstates E_0 obtained by the NCSM with various $N_{\max}$ as functions of $\hbar\Omega$. The shaded area shows the E_0 values selected for the SS-HORSE analysis according to inequality $\Lambda > 600$ MeV/c. Solid lines are solutions of Eq. (56) for energies E_0 with parameters a, b and d obtained by the fit.

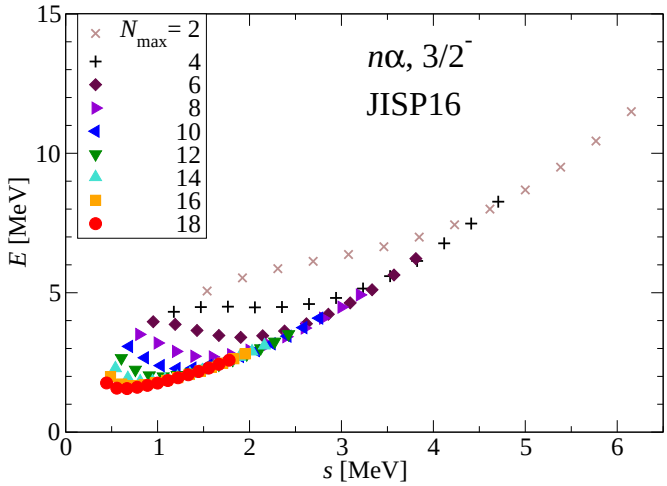

Figure 28: The lowest ^{5}He $\frac{3}{2}^-$ eigenstates E_0 as a function of the scaling parameter s.

recommended in Refs. [2, 3] for the JISP16 NN interaction. This selection is illustrated by the shaded area in Fig. 27; common curves are formed by the selected eigenenergies E_0 plotted as a function of the scaling parameter s in Fig. 30 and by the phase shifts obtained directly from these eigenenergies with the help of Eq. (53) in Fig. 31. We get an accurate fit of the selected NCSM eigenenergies with the rms deviation of 31 keV, the obtained values of the fitting parameters a, b, d of Eq. (56) and the $\frac{3}{2}^-$ resonance energy E_r and width Γ are presented in Table 4. The fit accuracy is also illustrated by solid lines in Figs. 27, 30 and 31 obtained using our fitting parameters: these curves are seen to reproduce the selected NCSM energies E_0 in Figs. 27 and 30 and the corresponding phase shifts in Fig. 31.

The JISP16 NN interaction generates the $\frac{3}{2}^-$ phase shifts reproducing qualitatively but not quantitively the results of phase shift analysis of Refs. [47] of $n\alpha$ scattering data as is seen in Fig. 31. We obtain the resonance energy E_r slightly above the experimental value, the difference is about 0.2 MeV (see Table 4). The resonance width Γ is also overestimated by JISP16, the difference between the JISP16 prediction and experiment is about 0.4 MeV. We present in Fig. 31 and in the last row of Table 4

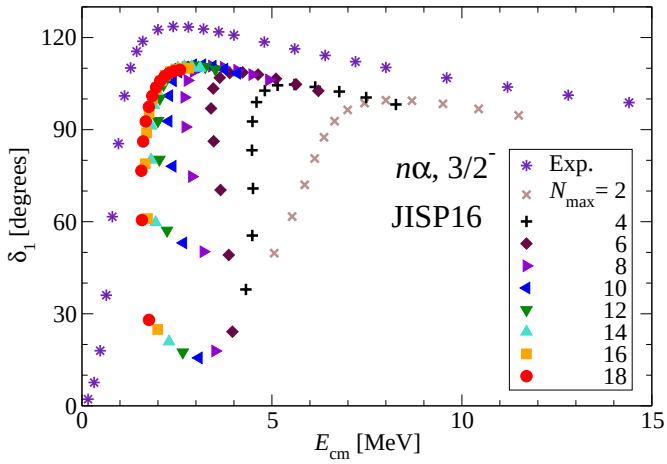

Figure 29: The $\frac{3}{2}^-$ $n\alpha$ phase shifts obtained directly from the ^{5}He eigenstates E_0 using Eq. (19) and the phase shift analysis of experimental data of Refs. [47] (stars).

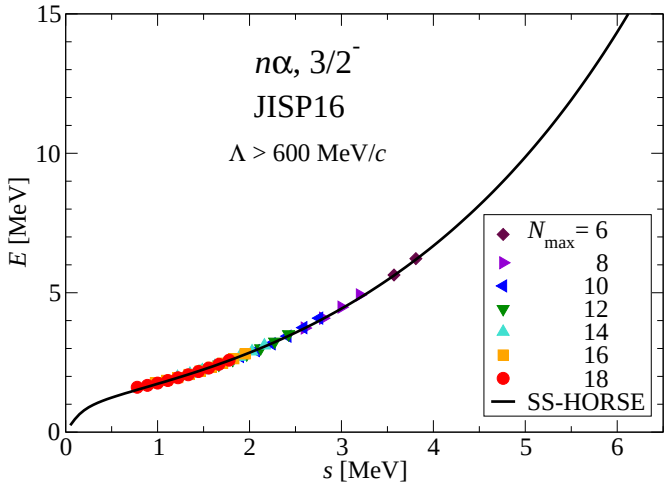

Figure 30: The ^{5}He $\frac{3}{2}^-$ eigenstates E_0 selected according to $\Lambda > 600$ MeV/c plotted as a function of the scaling parameter s (symbols). See Fig. 5 for other details.

also the fit by Eq. (53) of the phase shift analysis of experimental data of Refs. [47] obtained by minimizing the rms deviation of the phase shifts (column Ξ in the Table). The fit parameters derived from the experimental data are seen to be markedly different from those derived from JISP16 by the NCSM-SS-HORSE approach.

Returning to the $\frac{3}{2}^-$ ^{5}He eigenstates depicted in Fig. 27, we see that the solid curves presenting our fit in this figure describe not only the selected eigenstates from the shaded area but also many other eigenstates not involved in the fit. This signals that the $\Lambda > 600$ MeV/c selection is too restrictive and we can use for the SS-HORSE analysis and fits many more NCSM eigenstates. We can use within the SS-HORSE approach all eigenstates forming with the others a common curve in Fig. 28 and especially in Fig. 29 which is, as we have noted, more sensitive to convergence patterns. There is however a restriction: unacceptable for the SS-HORSE are eigenstates E_ν

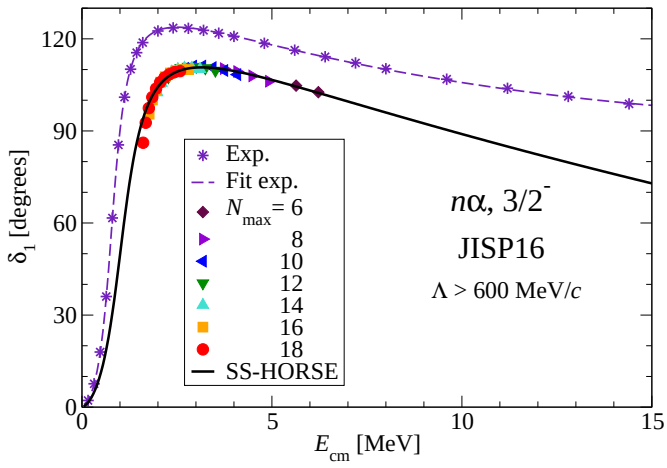

Figure 31: The $\frac{3}{2}^-$ $n\alpha$ phase shifts obtained using Eq. (19) directly from ^{5}He eigenstates E_0 selected according to $\Lambda > 600$ MeV/c (symbols). The solid curve depicts the phase shifts of Eq. (53) with parameters a, b and d obtained by the fit with the respective selection of eigenstates; stars and the dashed curve depict the phase shift analysis of experimental data of Refs. [47] and the fit by Eq. (53).

Table 4: $\frac{3}{2}^-$ resonance in $n\alpha$ scattering from the ^{5}He NCSM calculations with JISP16 NN interaction: fitting parameters a, b, d of Eq. (56), resonance energy E_r and width Γ, rms deviation of fitted energies Ξ and the number of these fitted energies D for different selections of eigenvalues in comparison with the analysis of experimental data in various approaches of Refs. [48] and [14] and with the fit by Eq. (53) of the phase shifts δ_1 extracted from experimental data in Ref. [47]. For the $N_{\max} \leq 4$ selection, Ξ and D for all energies from the manual selection are shown within brackets.

Selection	a (MeV$^{\frac{1}{2}}$)	b^2 (MeV)	$d \cdot 10^4$ (MeV$^{-\frac{3}{2}}$)	E_r (MeV)	Γ (MeV)	Ξ (keV)	D
$\Lambda > 600$ MeV/c	0.505	1.135	-0.9	1.008	1.046	31	46
Manual	0.506	1.019	$+93.2$	0.891	0.989	70	68
$N_{\max} \leq 4$	0.515	1.025	$+101$	0.892	1.008	106(81)	11(68)
Nature:							
R-matrix [48]				0.80	0.65		
J-matrix [14]				0.772	0.644		
Fit δ_1 of Ref. [47]	0.358	0.839	$+55.9$	0.774	0.643	0.21°	26

obtained with any given $N_{\max}$ from the range of $\hbar\Omega$ values where their energy decreases with $\hbar\Omega$, i. e., we can select only those eigenstates with a given fixed $N_{\max}$ which derivative $\frac{E_\nu}{\hbar\Omega} > 0$ — Eqs. (56) and (59) do not exclude mathematically the possibility of having $\frac{E_\nu}{\hbar\Omega} < 0$ but such solutions can arise only with unphysical parameters of these equations.

We would like to use within the SS-HORSE as many NCSM eigenstates as possible in order to enlarge the energy interval where the phase shifts are fitted and to improve the accuracy of the fit parameters. From this point of view, the selection according to inequality $\Lambda > \Lambda_0$ is not favorable. The $\Lambda > \Lambda_0$ rule excludes states with $\hbar\Omega < \hbar\Omega_0$ where $\hbar\Omega_0$ depends on $N_{\max}$ and decreases as $N_{\max}$ increases. As is seen from our study of the model problem, in particular, from Figs. 3, 4, 10, 12, 18, 20, we can utilize for the SS-HORSE the eigenstates obtained with sufficiently large $N_{\max}$ and with very small $\hbar\Omega$; the same conclusion follows from our *ab initio* many-body study of the system of four neutrons (tetraneutron) in the continuum [49,50]. According to the $\Lambda > \Lambda_0$ rule we either exclude these large $N_{\max}$ – small $\hbar\Omega$ eigenstates or include in the fit some small $N_{\max}$ states which strongly deviate from common curves on the plots of E_ν vs s or δ_ℓ vs E.

The ultraviolet cutoff Λ_0 was introduced in Refs. [2, 3] with an idea that the oscillator basis should be able to describe in the many-body system the short-range (high-momentum) behaviour of the two-nucleon interaction employed in the calculations; thus the $\hbar\Omega$ cannot be too small since oscillator functions with small $\hbar\Omega$ have a large radius (correspond to small momentum) and are not able to catch the short-range (high-momentum) peculiarities of a particular NN potential. We imagine this concept to be insufficient at least in some cases. In light nuclei where binding energies are not large, the structure of the wave function can be insensitive to the short-range NN potential behaviour associated with high relative momentum. Much more important is the radius of the state under consideration, e. g., we can expect an adequate description of the ground state only if the highest oscillator function in the basis has at least one node within the radius of this state, two nodes are required within the radius of the first excited state, etc. Therefore the minimal acceptable $\hbar\Omega$ value depends strongly on the state under consideration and may be insensitive to the inter-nucleon interaction. This is particularly important for loosely-bound nuclear states or for low-energy scattering states. In the case of scattering, the wave function at low energies can have a very distant first node and not only permits but just

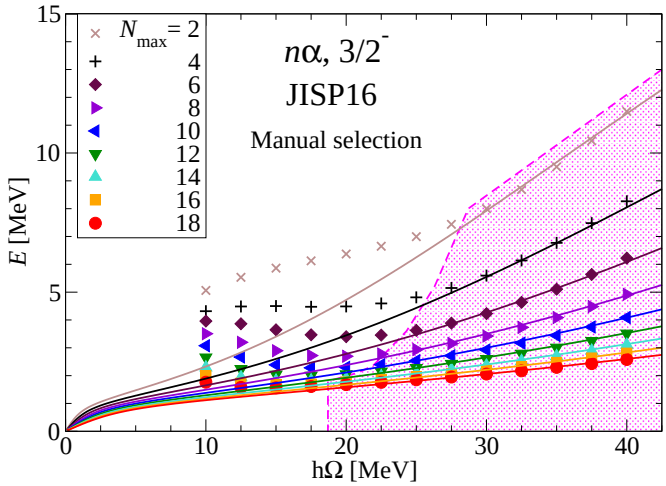

Figure 32: Manual selection the lowest ^{5}He $\frac{3}{2}^-$ eigenstates E_0. See Fig. 27 for details.

requires the use of oscillator functions with very small $\hbar\Omega$ values and large radius.

We cannot formulate a simple rule or formula for selecting eigenstates acceptable for the SS-HORSE analysis, instead we pick up manually individual states with eigenenergies E_0 lying to the right from the minimum of the $\hbar\Omega$ dependence for each $N_{\max}$ in Fig. 27 and lying on or close to the common curve in Figs. 28 and 29. These manually selected eigenstates and the respective phase shifts are presented in Figs. 32, 33 and 34. The results of the fit with this selection of eigenstates are presented in the second line of Table 4. We obtain an accurate fit with the rms deviation of eigenenergies of 70 keV; this number however depends on the selection criteria like the acceptable distance from the common curve formed by other points in Figs. 33 and 34. Comparing Figs. 27 and 32 we see that our manual selection makes it possible to describe eigenenergies with small $N_{\max}$ which were far from theoretical curves in Fig. 27. These small $N_{\max}$ states have large energies, and their inclusion in the SS-HORSE analysis extends the description of the phase shifts in the high-energy region in Fig. 34 pushing them closer to the phase shift analysis of the experimental

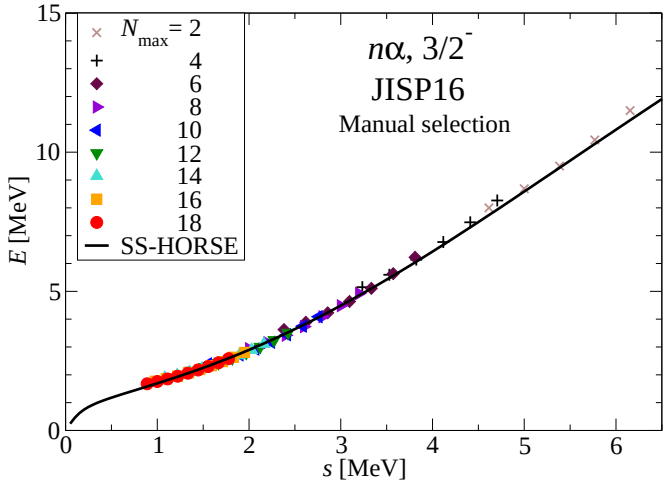

Figure 33: Manually selected ^{5}He $\frac{3}{2}^-$ eigenstates E_0 plotted as a function of the scaling parameter s (symbols). See Fig. 5 for other details.

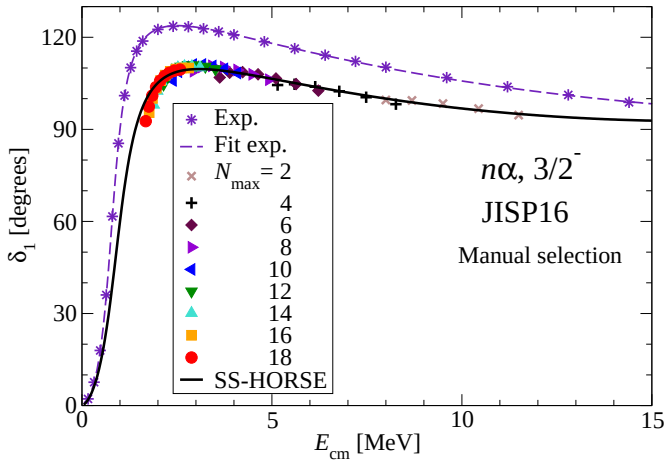

Figure 34: The $\frac{3}{2}^-$ $n\alpha$ phase shifts generated by the manually selected ^{5}He eigenstates E_0. See Fig. 31 for details.

$n\alpha$ scattering data in this region as compared with Fig. 31. These changes in the phase shift behavior at larger energies correspond to a drastic change of the fitting parameter d which is the coefficient of the highest power term in the expansion (53). At smaller energies including the resonance region, the phase shifts obtained from the fits with the manual and with the $\Lambda > 600$ MeV/c selections are nearly the same, and we get close values of the respective fitting parameters a and b and hence small changes of the resonance energy E_r and width Γ due to the switch from one selection to the other.

It is very interesting to investigate whether we can get reasonable phase shifts and resonance parameters using only the NCSM eigenstates from small basis spaces. From our manually selected eigenstates we select only those obtained with $N_{\max} = 2$ and 4. This selection and the results obtained by the fit are depicted in Figs. 35, 36 and 37. All eigenenergies E_0 involved in this fit are significantly above the resonant region (see Fig. 37). Nevertheless we obtain from these 11 small-$N_{\max}$ eigenstates nearly the same phase shifts as those from all 68 manually selected eigenstates and

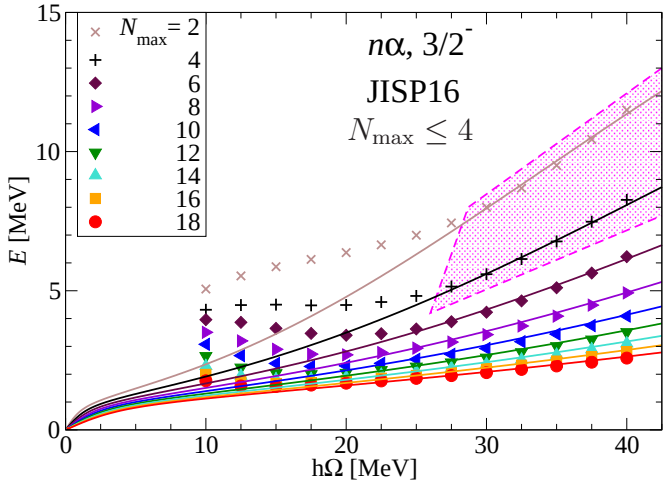

Figure 35: Selection of the lowest ^{5}He $\frac{3}{2}^-$ eigenstates E_0 obtained in NCSM with $N_{\max} \leq 4$. See Fig. 27 for details.

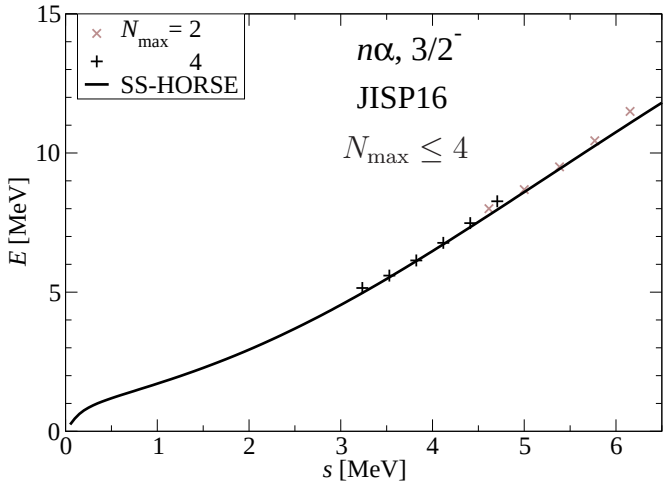

Figure 36: Selected lowest ^{5}He $\frac{3}{2}^-$ eigenstates E_0 obtained in NCSM with $N_{\max} \leq 4$ as a function of the scaling parameter s. See Fig. 5 for other details.

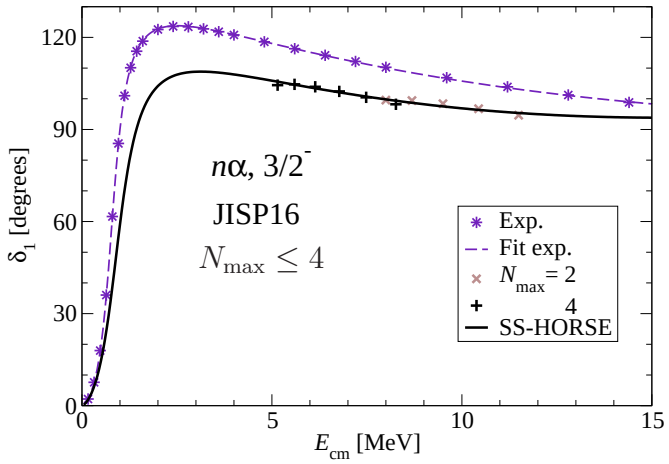

Figure 37: The $\frac{3}{2}^-$ $n\alpha$ phase shifts generated by the selected ^{5}He eigenstates E_0 obtained in NCSM with $N_{\max} \leq 4$. See Fig. 31 for details.

very close values of fit parameters and of the resonance energy and width presented in Table 4. Figure 35 demonstrates that, as in the case of the model problem, with these eigenstates E_0 from many-body NCSM calculations with $N_{\max} \leq 4$ we can accurately 'predict' the ^{5}He eigenstates obtained in much larger basis spaces and in a wider range of $\hbar\Omega$. The rms deviation Ξ of all manually selected eigenstates by this $N_{\max} \leq 4$ fit is only 81 keV as compared with 70 keV from the fit to all those eigenstates.

4.2 Partial wave $\frac{1}{2}^-$

The lowest $\frac{1}{2}^-$ eigenstates of ^{5}He from the NCSM calculations with JISP16 NN interaction are presented in Fig. 38 as functions of $\hbar\Omega$ and in Fig. 39 as a function of the scaling parameter s, Fig. 40 presents the respective $n\alpha$ phase shifts. The eigenenergies in Figs. 39 and 40 tend to form single common curves demonstrating the convergence of many-body NCSM calculations, however we see that many eigenstates diverge from the common curves and lie far from them thus demonstrating the need to select the states for the SS-HORSE analysis.

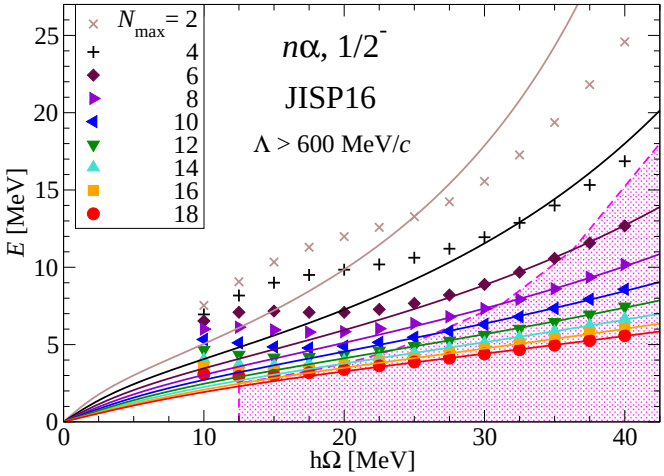

Figure 38: The lowest ^{5}He $\frac{1}{2}^-$ eigenstates E_0 as functions of $\hbar\Omega$ and their $\Lambda > 600$ MeV/c selection. See Fig. 27 for details.

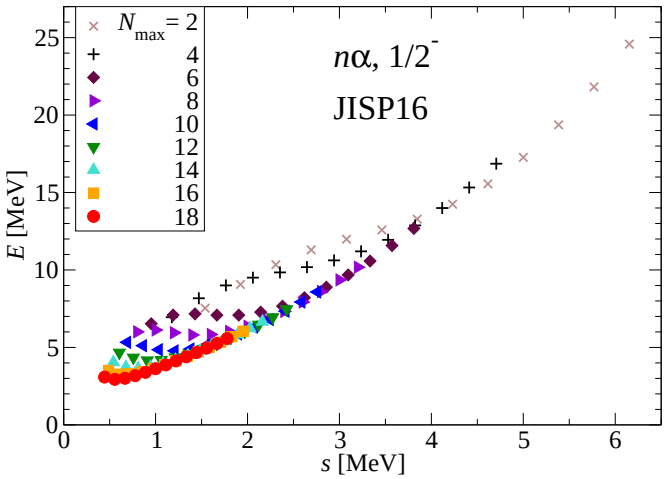

Figure 39: The lowest ^{5}He $\frac{1}{2}^-$ eigenstates E_0 as a function of the scaling parameter s.

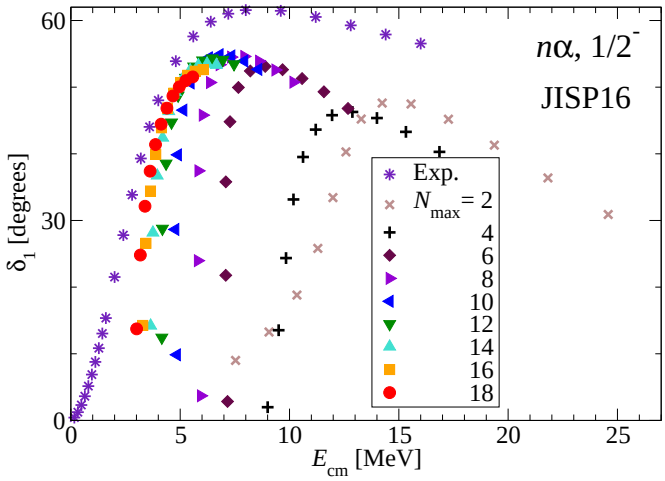

Figure 40: The $\frac{1}{2}^-$ $n\alpha$ phase shifts obtained directly from the ^{5}He eigenstates E_0 using Eq. (19). See Fig. 29 for other details.

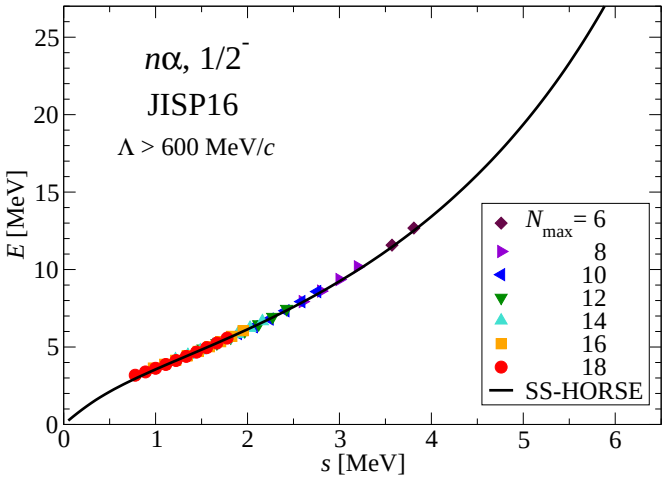

Figure 41: The ^{5}He $\frac{1}{2}^-$ eigenstates E_0 selected according to $\Lambda > 600$ MeV/c as a function of the scaling parameter s. See Fig. 5 for other details.

As in the case of the $\frac{3}{2}^-$ partial wave, we start from the $\Lambda > 600$ MeV/c eigenstate selection recommended for the JISP16 NN interaction in Refs. [2, 3] which is illustrated in Figs. 38 and 41, the respective phase shifts are shown in Fig. 42. The selected states form reasonably smooth common curves in Figs. 41 and 42 making possible an accurate fit of parameters in Eq. (53); the obtained fitted parameters can be found in Table 5. We get a good description of the $\frac{1}{2}^-$ resonance energy and width however the phase shift behaviour extracted from the experimental $n\alpha$ scattering data is reproduced qualitatively but not quantitatively (see Fig. 42). Note however that the fit parameters derived from the experimental data and JISP16 results (Table 5) are close with the exception of the parameter d which contribution is very small at energies below 20 MeV. Figure 38 shows that we reproduce not only the eigenstate energies from the shaded area that were fitted but also many other eigenstates not included in the fit, especially small-$N_{\max}$ eigenstates, thus suggesting to perform a manual eigenstate selection which will involve many more eigenenergies in the SS-HORSE analysis.

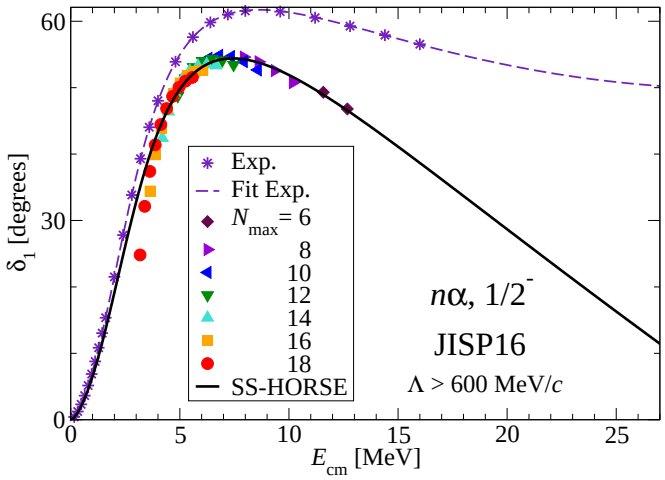

Figure 42: The $\frac{1}{2}^-$ $n\alpha$ phase shifts generated by the $\Lambda > 600$ MeV/c selected ^{5}He eigenstates E_0. See Fig. 31 for details.

Table 5: Parameters of the $\frac{1}{2}^-$ resonance in $n\alpha$ scattering from the ^{5}He NCSM calculations with JISP16 NN interaction. See Table 4 for details.

Selection	a (MeV$^{\frac{1}{2}}$)	b^2 (MeV)	$d \cdot 10^4$ (MeV$^{-\frac{3}{2}}$)	E_r (MeV)	Γ (MeV)	Ξ (keV)	D
$\Lambda > 600$ MeV/c	1.680	3.443	-3.6	2.031	5.559	61	46
Manual	1.699	3.299	21.3	1.856	5.456	11	60
$N_{\max} \leq 4$	2.460	6.734	-0.15	3.710	11.24	109(893)	9(60)
$4 \leq N_{\max} \leq 6$	1.718	3.310	25.0	1.834	5.511	25(92)	10(60)
Nature:							
R-matrix [48]				2.07	5.57		
J-matrix [14]				1.97	5.20		
Fit δ_1 of Ref. [47]	1.622	3.276	+46.3	1.960	5.249	0.038°	26

Our manual selection of the lowest $\frac{1}{2}^-$ eigenstates in ^{5}He is shown in Figs. 43 and 44 while the respective $n\alpha$ phase shifts are presented in Fig. 45, the results of the fit are given in Table 5. As in the case of the $\frac{3}{2}^-$ $n\alpha$ partial wave, the inclusion of the additional eigenstates in the fit does not affect the phase shifts at smaller energies including the resonance region. However, including the additional eigenstates pushes the phase shifts up in the direction of the phase shift analysis at larger energies. The $\frac{1}{2}^-$ resonance energy and width and the parameters of the phase shift fit by Eq. (53) are seen from Table 5 to change only slightly with the exception of the parameter d responsible for the phase shift behaviour at higher energies.

It is very interesting and important to examine whether it is possible to get a reasonable description of the resonance and phase shifts in the $\frac{1}{2}^-$ $n\alpha$ scattering using only eigenstates obtained in many-body NCSM calculations in small bases. In the case of the $\frac{3}{2}^-$ $n\alpha$ scattering we manage to derive very good phase shifts from the $N_{\max} \leq 4$ NCSM eigenstates. Therefore we try the $N_{\max} \leq 4$ eigenstate selection also in the $\frac{1}{2}^-$ partial wave, see Figs. 46, 47 and 48. This selection clearly fails to reproduce the phase shifts and resonance parameters which differ essentially from the converged results obtained with the manual selection of the $\frac{1}{2}^-$ ^{5}He eigenstates (see Fig. 31 and Table 5); we see also in Fig. 46 that the fit to the $N_{\max} \leq 4$ eigenstates

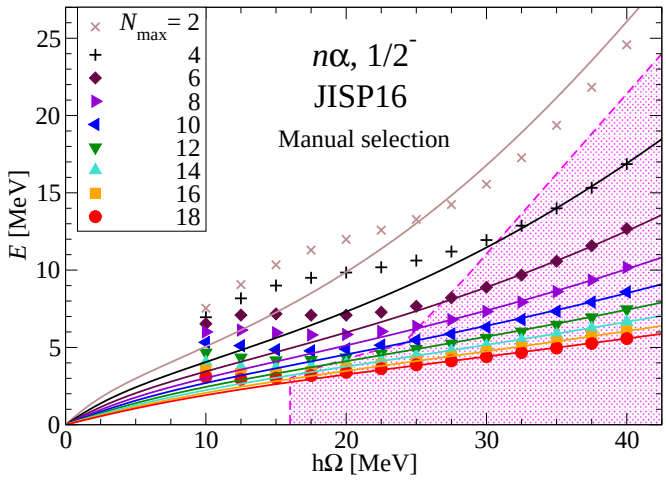

Figure 43: Manual selection the lowest ^{5}He $\frac{1}{2}^-$ eigenstates E_0. See Fig. 27 for details.

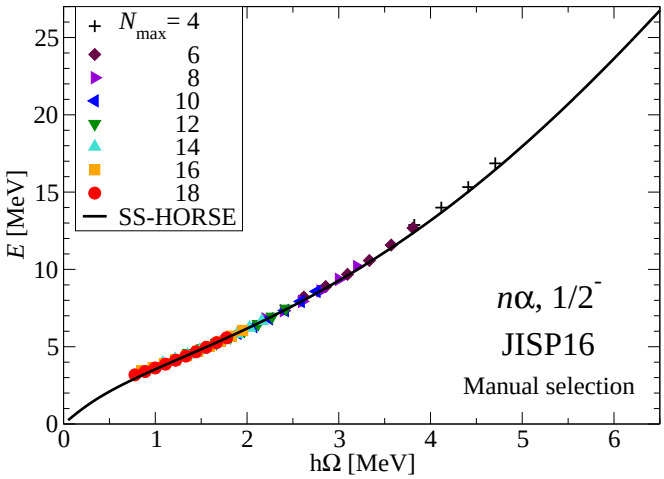

Figure 44: Manually selected ^{5}He $\frac{1}{2}^-$ eigenstates E_0 plotted as a function of the scaling parameter s (symbols). See Fig. 5 for other details.

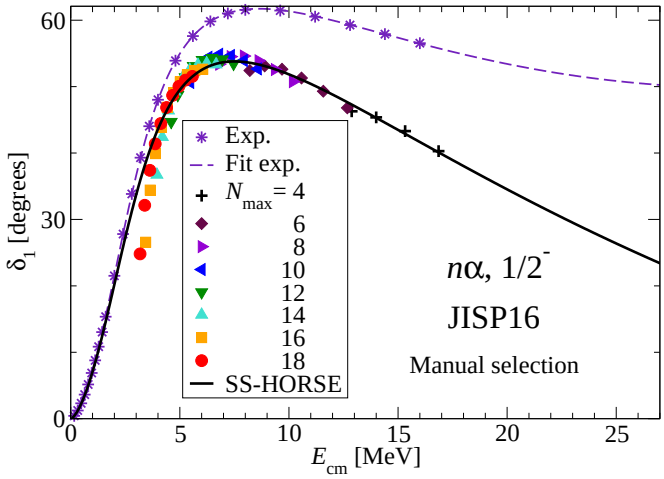

Figure 45: The $\frac{1}{2}^-$ $n\alpha$ phase shifts generated by the manually selected ^{5}He eigenstates E_0. See Fig. 31 for details.

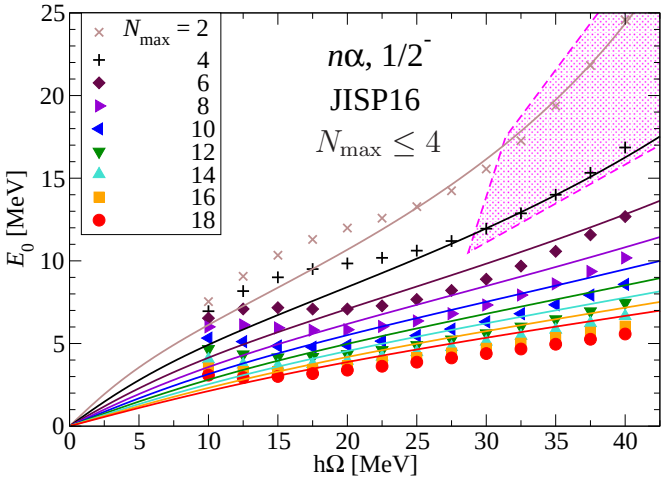

Figure 46: Selection of the lowest ^{5}He $\frac{1}{2}^-$ eigenstates E_0 obtained in NCSM with $N_{\max} \leq 4$. See Fig. 27 for details.

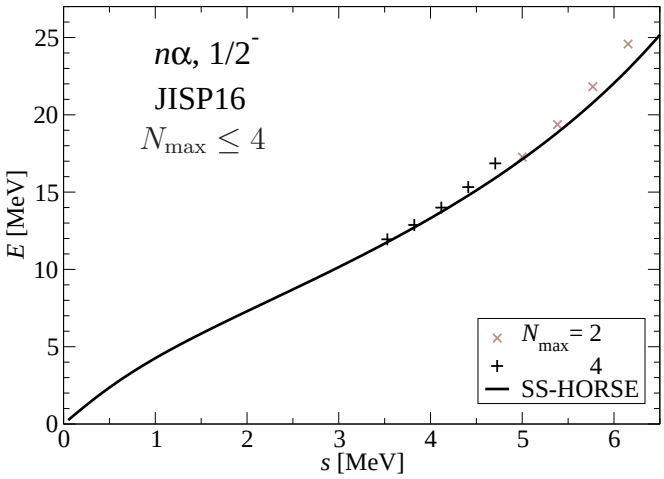

Figure 47: Selected lowest ^{5}He $\frac{1}{2}^-$ eigenstates E_0 obtained in NCSM with $N_{\max} \leq 4$ as a function of the scaling parameter s. See Fig. 5 for other details.

from the shaded area fails to 'predict' the eigenenergies E_0 obtained with larger $N_{\max}$ values. That is not surprising because the plots of the $N_{\max} \leq 4$ eigenenergies as a function of the scaling parameter s (Fig. 47) and of the respective phase shifts as a function of energy (Fig. 48) do not form smooth common curves.

However an entirely different result is obtained by selecting for the SS-HORSE analysis the ^{5}He $\frac{1}{2}^-$ NCSM results from basis spaces with $4 \leq N_{\max} \leq 6$. For the $4 \leq N_{\max} \leq 6$ selection we pick up 10 eigenstates with the smallest $N_{\max}$ values out of 60 manually selected before $\frac{1}{2}^-$ eigenstates. This eigenstate selection and the respective results are illustrated by Figs. 49, 50 and 51. The selected eigenenergies are seen to form sufficiently smooth curves in Figs. 50 and 51. The parameter fit results in nearly the same phase shifts (Fig. 51) as in the case of the manual eigenstate selection, we get also very close values of the resonance energy and width and fitting parameters listed in Table 5. Figure 49 demonstrates that by using only 10

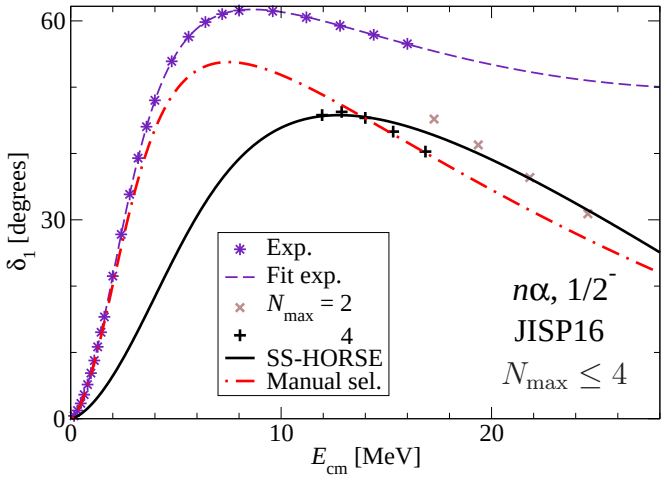

Figure 48: The $\frac{1}{2}^-$ $n\alpha$ phase shifts generated by the selected ^{5}He eigenstates E_0 obtained in NCSM with $N_{\max} \leq 4$. The dash-dotted curve depicts the phase shifts obtained by the fit to all manually selected eigenstates. See Fig. 31 for other details.

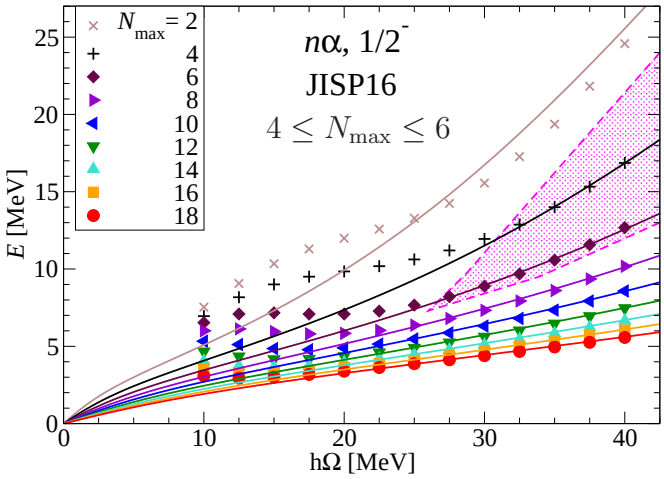

Figure 49: Selection of the lowest ^{5}He $\frac{1}{2}^-$ eigenstates E_0 obtained in NCSM with $4 \leq N_{\max} \leq 6$. See Fig. 27 for details.

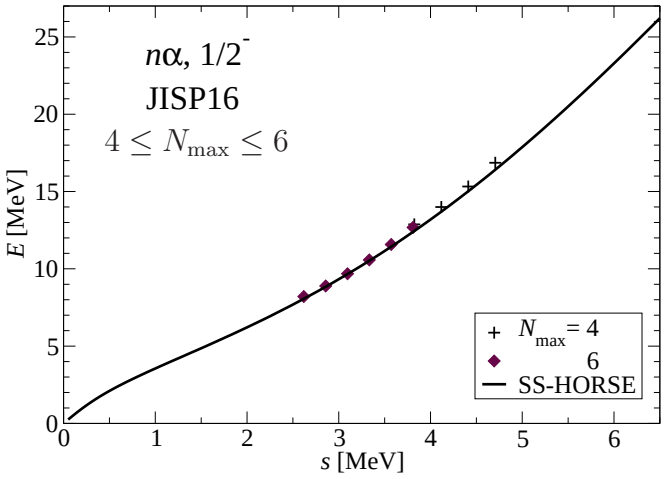

Figure 50: Selected lowest ^{5}He $\frac{1}{2}^-$ eigenstates E_0 obtained in NCSM with $4 \leq N_{\max} \leq 6$ as a function of the scaling parameter s. See Fig. 5 for other details.

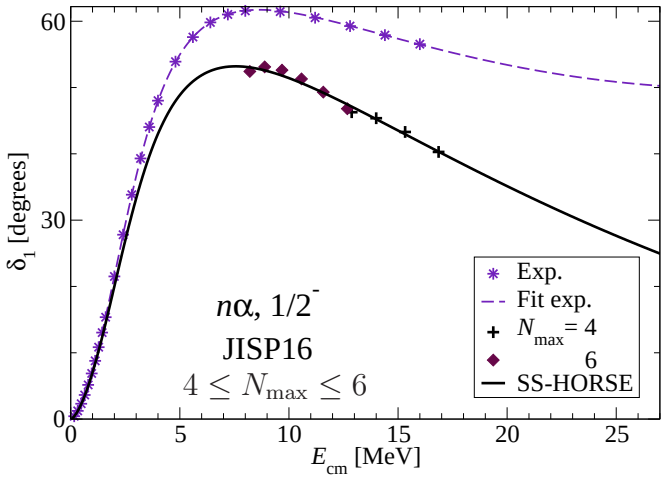

Figure 51: The $\frac{1}{2}^-$ $n\alpha$ phase shifts generated by the selected ^{5}He eigenstates E_0 obtained in NCSM with $4 \leq N_{\max} \leq 6$. See Fig. 31 for details.

small-$N_{\max}$ eigenstates from the shaded area we accurately 'predict' the energies of many higher-$N_{\max}$ eigenstates: the rms deviation Ξ of energies of all 60 manually selected eigenstates is 92 keV (see Table 5). Of course, 92 keV is much larger than the Ξ value of 11 keV obtained in the full fit to all these 60 eigenenergies, but it is still an indication of a good quality 'prediction' of many-body eigenenergies E_0 obtained with much larger bases in a wide range of $\hbar\Omega$ values.

4.3 Partial wave $\frac{1}{2}^+$

In this subsection we examine a possibility to describe neutron-nucleus non-resonant scattering using as input for the SS-HORSE analysis the results of many-body shell model calculations. The SS-HORSE fit is done in the same manner as in the case of resonant scattering. The difference is that the non-resonant low-energy $n\alpha$ scattering phase shifts in the $\frac{1}{2}^+$ state are described by Eq. (52) instead of Eq. (53) which parameters are fitted using Eq. (59) instead of Eq. (56). The parameter E_b of this equation mimics the Pauli-forbidden state in the $n\alpha$ scattering. As compared with the discussion of the $\frac{1}{2}^+$ scattering by the model WSB potential which supports the Pauli-forbidden state, this bound state does not appear as a result of the NCSM ^{5}He calculations. Therefore we should use for the SS-HORSE fit the lowest $\frac{1}{2}^+$ state obtained by the NCSM with the eigenenergy E_0 and set $\nu = 0$ in Eq. (59).

These lowest $\frac{1}{2}^+$ ^{5}He eigenstates E_0 are shown as functions of $\hbar\Omega$ for various $N_{\max}$ in Fig. 52 and as a function of the scaling parameter s in Fig. 53. We see a tendency of eigenstates to approach the common curve at smaller $\hbar\Omega$ values with increasing $N_{\max}$ which signals that the convergence is achieved at smaller energies in larger basis spaces. This tendency is much more pronounced in the plot of the SS-HORSE phase shifts corresponding to the NCSM eigenstates in Fig. 54. This figure however also clearly indicates the need to select eigenstates for the SS-HORSE fitting.

We start with selecting eigenstates according to the inequality $\Lambda > 600$ MeV/c as is illustrated by Figs. 52 and 55, the respective phase shifts are shown in Fig. 56, and the obtained fitting parameters are presented in Table 6. We obtain a reasonable accuracy of the fit with the rms deviation of the fitted energies of 85 keV. We reproduce reasonably the phase shift behaviour by the JISP16 NN interaction. We note that at energies $E_{\rm cm} > 25$ MeV the fit by Eq. (52) of the results of the phase shift analysis start going up with the energy. This seems unphysical, however the $\frac{1}{2}^+$

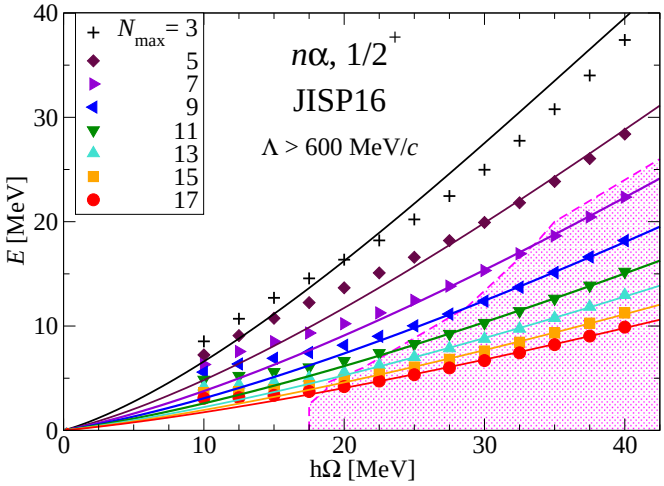

Figure 52: The lowest ^{5}He $\frac{1}{2}^+$ eigenstates E_0 as functions of $\hbar\Omega$ and their $\Lambda > 600$ MeV/c selection. See Fig. 18 for details.

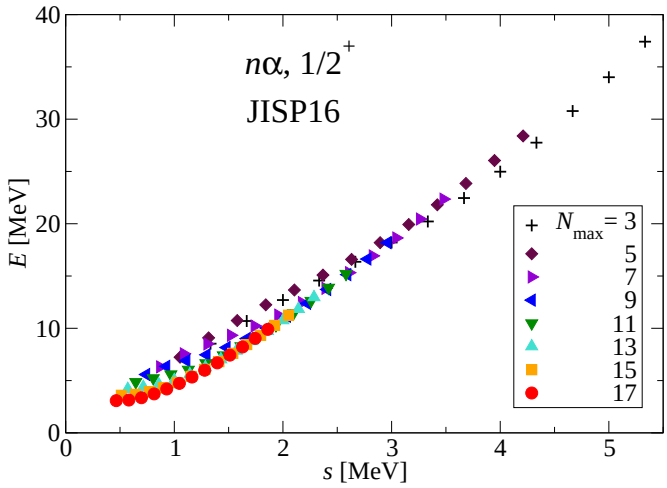

Figure 53: The lowest ^{5}He $\frac{1}{2}^+$ eigenstates E_0 as a function of the scaling parameter s.

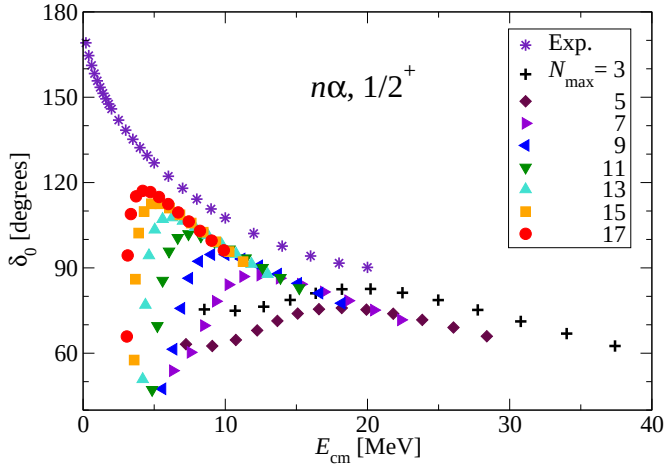

Figure 54: The $\frac{1}{2}^+$ $n\alpha$ phase shifts obtained directly from the ^{5}He eigenstates E_0 using Eq. (19). See Fig. 29 for other details.

Table 6: $\frac{1}{2}^+$ $n\alpha$ scattering from the ^{5}He NCSM calculations with JISP16 NN interaction: fitting parameters E_b, c, d and f of Eq. (59), rms deviation of fitted energies Ξ and the number of these fitted energies D for different selections of eigenvalues in comparison with the fit by Eq. (52) of the phase shifts δ_0 extracted from experimental data in Ref. [47]. For the $5 \le N_{\max} \le 7$ selection, Ξ and D for all energies from the manual selection are shown within brackets.

Selection	E_b (MeV)	c (MeV$^{-\frac{1}{2}}$)	$d \cdot 10^3$ (MeV$^{-\frac{3}{2}}$)	$f \cdot 10^5$ (MeV$^{-\frac{5}{2}}$)	Ξ (keV)	D
$\Lambda > 600$ MeV/c	−5.996	−0.171	−8.02	6.48	85	41
Manual	−6.733	−0.183	−13.0	30.8	120	53
$5 \le N_{\max} \le 7$	−3.347	−0.151	63.0	−86.7	168(259)	13(53)
Fit δ_0 of Ref. [47]	−13.75	−0.156	−429	220	0.018°	26

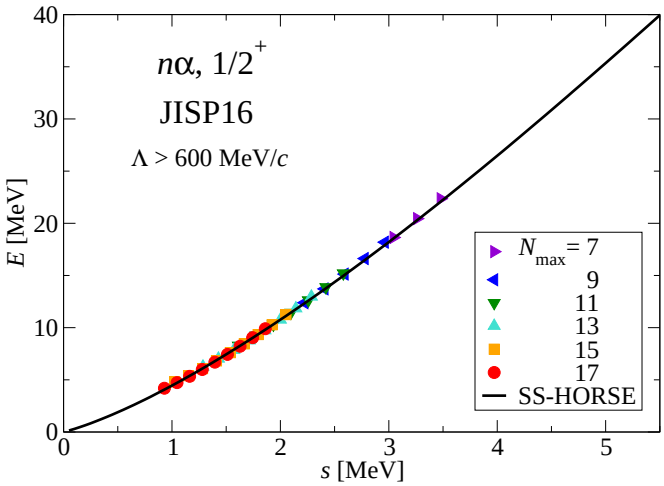

Figure 55: The ^{5}He $\frac{1}{2}^+$ eigenstates E_0 selected according to $\Lambda > 600$ MeV/c as a function of the scaling parameter s. See Fig. 21 for other details.

phases extracted from the $n\alpha$ scattering data are available only up to $E_{\rm cm} = 20$ MeV; the phase shift analysis at higher energies is needed to obtain a more realistic fit in this energy interval where the NCSM-SS-HORSE phase shifts look more realistic.

Figure 52 demonstrates that it would be reasonable to perform a manual selection and to include in the fit more eigenstates thus extending the energy interval of the fitted phase shifts. Our manual selection of the lowest $\frac{1}{2}^+$ ^{5}He eigenstates and the respective phase shifts are presented in Figs. 57, 58, 59 and Table 6. Some of the fitting parameters are profoundly altered due to the inclusion of additional eigenstates in the fit, however the resulting phase shifts are nearly the same with an exception of the energies $E_{\rm cm} > 30$ MeV where these additional eigenstates push the phase shifts slightly up. The phase shift analysis is unavailable at these energies, therefore it is impossible to judge whether this adjustment of the phase shifts improves the description of the experiment.

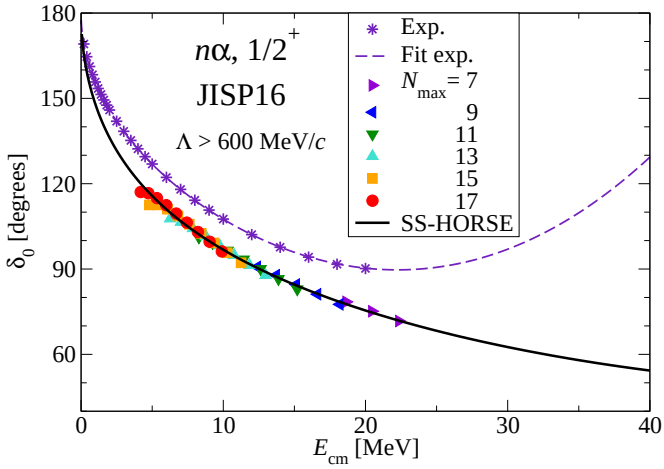

Figure 56: The $\frac{1}{2}^+$ $n\alpha$ phase shifts generated by the $\Lambda > 600$ MeV/c selected ^{5}He eigenstates E_0 (symbols). The solid curve depicts the phase shifts of Eq. (52) with parameters E_b, c, d and f obtained by the fit with this selection of eigenstates; stars and the dashed curve depict the phase shift analysis of experimental data of Refs. [47] and the fit by Eq. (52).

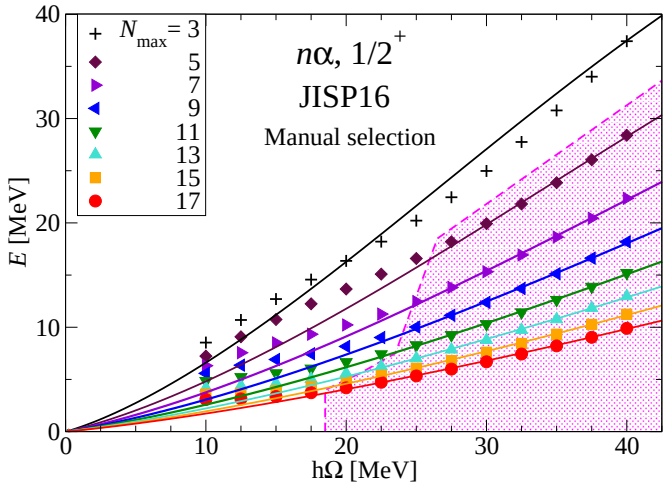

Figure 57: Manual selection the lowest ^{5}He $\frac{1}{2}^+$ eigenstates E_0. See Fig. 18 for details.

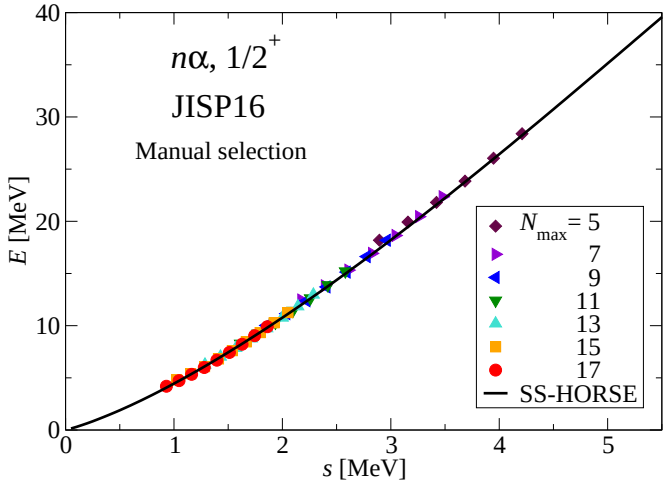

Figure 58: Manually selected ^{5}He $\frac{1}{2}^+$ eigenstates E_0 plotted as a function of the scaling parameter s (symbols). See Fig. 21 for details.

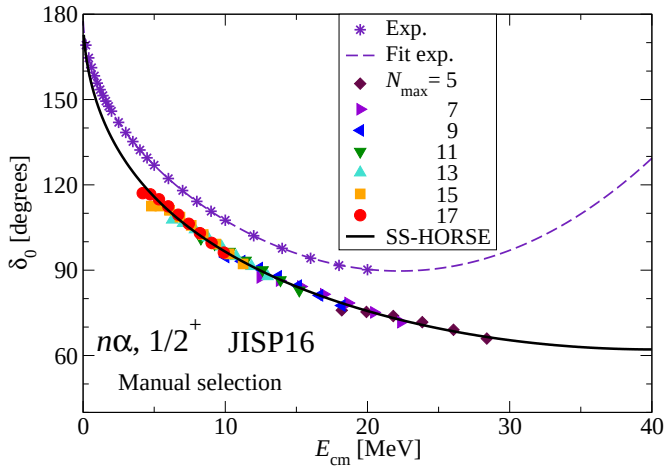

Figure 59: The $\frac{1}{2}^+$ $n\alpha$ phase shifts generated by the manually selected ^{5}He eigenstates E_0. See Fig. 56 for details.

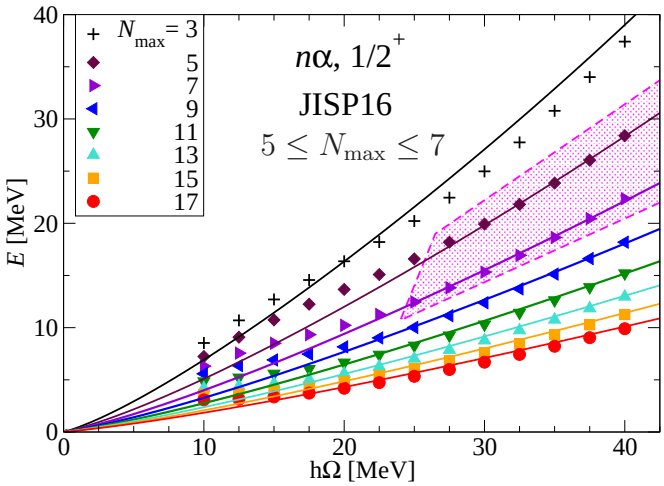

Figure 60: Selection of the lowest ^{5}He $\frac{1}{2}^+$ eigenstates E_0 obtained in NCSM with $5 \leq N_{\max} \leq 7$. See Fig. 18 for details.

It is interesting and important to examine the possibility of describing the eigenenergies and non-resonant phase shifts obtained in many-body calculations in large basis spaces by SS-HORSE fits based on results in much smaller basis spaces. As in the case of $\frac{1}{2}^-$ states, we do not succeed by choosing the eigenstates from the smallest available NCSM basis spaces with $N_{\max} = 3$ and 5: note, in both cases the results from the smallest basis space with $N_{\max} = 2$ for $\frac{1}{2}^-$ and $N_{\max} = 3$ for $\frac{1}{2}^+$ states are not included in our respective manual selections. However picking up eigenstates obtained with $5 \leq N_{\max} \leq 7$ from the manual selection of the ^{5}He $\frac{1}{2}^+$ eigenstates, we obtain reasonable phase shifts and 'predictions' for the eigenstates with larger $N_{\max}$, see Figs. 60, 61 and 62. It is interesting that we get similar phase shifts with three different selections of the $\frac{1}{2}^+$ eigenstates while the respective fitting parameters shown in Table 6 differ essentially. The rms deviation of all 53 manually selected $\frac{1}{2}^+$ eigenstates resulting from the fit to 13 eigenstates from the $5 \leq N_{\max} \leq 7$ selection is 259 keV

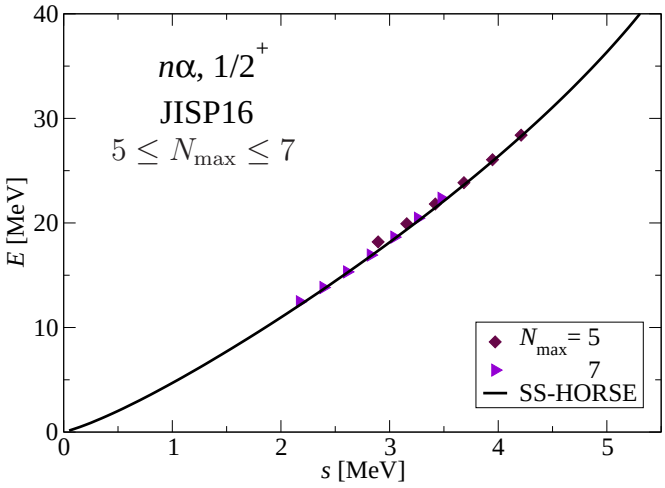

Figure 61: Selected lowest ^{5}He $\frac{1}{2}^+$ eigenstates E_0 obtained in NCSM with $5 \leq N_{\max} \leq 7$ as a function of the scaling parameter s. See Fig. 21 for details.
%vspace3ex

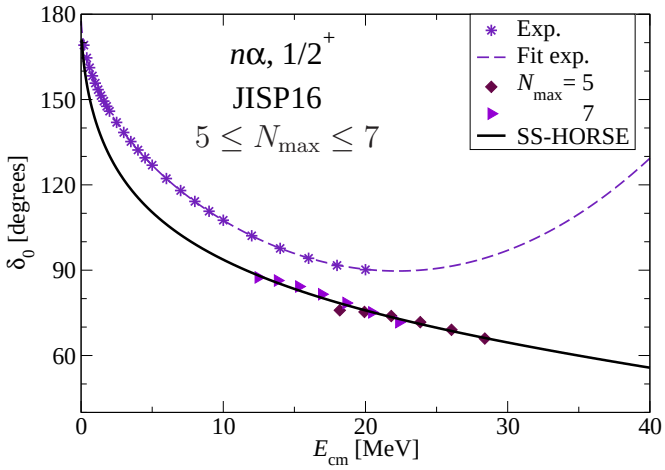

Figure 62: The $\frac{1}{2}^+$ $n\alpha$ phase shifts generated by the selected ^{5}He eigenstates E_0 obtained in NCSM with $5 \leq N_{\max} \leq 7$. See Fig. 56 for details.

that is much worse than the 'predictions' of the odd parity eigenstates. We suppose that this is related to the fact that the $\frac{1}{2}^+$ eigenstates lie higher in energy than the $\frac{3}{2}^-$ and $\frac{1}{2}^-$ eigenstates and the SS-HORSE fits, especially those to the small-$N_{\max}$ eigenstates, involve the phase shifts at higher energies where our low-energy phase shift expansions become less accurate and require higher order terms in Taylor series and more fitting parameters.

5 Conclusions

We develop a SS-HORSE approach allowing us to obtain low-energy scattering phase shifts and resonance energy and width in variational calculations with the oscillator basis, in the nuclear shell model in particular. The SS-HORSE technique is based on the general properties of the oscillator basis and on the HORSE (J-matrix) formalism in scattering theory, it utilizes general low-energy expansions of the S-matrix including the poles associated with the bound and resonant states.

The SS-HORSE approach is carefully verified using a model two-body problem with a Woods–Saxon type potential and is shown to be able to obtain accurate scattering phase shifts and resonance energy and width even with small oscillator bases. Next the SS-HORSE method is successfully applied to the study of the $n\alpha$ scattering phases and resonance based on the NCSM calculations of ^{5}He with the realistic JISP16 NN interaction.

Within the SS-HORSE approach we obtain and generalize to the states lying above nuclear disintegration thresholds the scaling property of variational calculations with oscillator basis suggested in Refs. [2, 3] which states that the eigenenergies do not depend separately on $\hbar\Omega$ and the maximal oscillator quanta $\mathbb{N}$ of the states included in the basis but only on their combination s (or the scaling parameter λ_{sc} as suggested in Refs. [2, 3], $s \sim \lambda_{sc}^2$). We demonstrate a typical behavior of eigenstates in the continuum as functions of s in cases when the system has or does not have a low-energy resonance. The scaling property is useful for extrapolating the results obtained in smaller basis spaces to larger bases, and we demonstrate using both the model problem and many-body NCSM calculations that we are able to 'predict' accurately the eigenenergies obtained in large bases using the results from much smaller calculations.

We anticipate that the suggested SS-HORSE method will be useful in numerous shell model studies of low-energy nuclear resonances.

We plan to extend the SS-HORSE approach to the case of scattering of charged particles in future publications. We intend also to examine an application of the SS-HORSE method to the study of S-matrix poles corresponding to bound states and to develop the SS-HORSE extrapolation of the variational bound state energies to the infinite basis space.

Acknowledgements

We are thankful to L. D. Blokhintsev and Pieter Maris for valuable discussions. This work was supported in part by the Russian Foundation for Basic Research under Grant No. 15-02-06604-a and by the U.S. Department of Energy under grants No. DESC0008485 (SciDAC/NUCLEI) and DE-FG02-87ER40371. Computational resources were provided by the National Energy Research Scientific Computing Center (NERSC) which is supported by the U.S. Department of Energy under Contract No. DE-AC02-05CH11231.

References

[1] P. Maris, J. P. Vary and A. M. Shirokov, Phys. Rev. C **79**, 014308 (2009).

[2] S. A. Coon, M. I. Avetian, M. K. G. Kruse, U. van Kolck, P. Maris and J. P. Vary, Phys. Rev. C **86**, 054002 (2012).

[3] S. A. Coon, in *Proc. Int. Workshop Nucl. Theor. Supercomputing Era (NTSE-2012), Khabarovsk, Russia, June 18–22, 2012*, eds. A. M. Shirokov and A. I. Mazur. Pacific National University, Khabarovsk, 2013, p. 171, http://www.ntse-2012.khb.ru/Proc/S_Coon.pdf.

[4] R. J. Furnstahl, G. Hagen and T. Papenbrock, Phys. Rev. C **86**, 031301 (2012).

[5] S. N. More, A. Ekström, R. J. Furnstahl, G. Hagen and T. Papenbrock, Phys. Rev. C **87**, 044326 (2013).

[6] S. A. Coon and M. K. G. Kruse, in *Proc. Int. Conf. Nucl. Theor. Supercomputing Era (NTSE-2013), Ames, IA, USA, May 13–17, 2013*, eds. A. M. Shirokov and A. I. Mazur. Pacific National University, Khabarovsk, 2014, p. 314, http://www.ntse-2013.khb.ru/Proc/Coon.pdf.

[7] M. K. G. Kruse, E. D. Jurgenson, P. Navrátil, B. R. Barrett and W. E. Ormand, Phys. Rev. C **87**, 044301 (2013).

[8] D. Sääf and C. Forssén, Phys. Rev. C **89**, 011303(R) (2014).

[9] R. J. Furnstahl, S. N. More and T. Papenbrock, Phys. Rev. C **89**, 044301 (2014).

[10] S. König, S. K. Bogner, R. J. Furnstahl, S. N. More and T. Papenbrock, Phys. Rev. C **90**, 064007 (2014).

[11] R. J. Furnstahl, G. Hagen, T. Papenbrock and K. A. Wendt, J. Phys. G **42**, 034032 (2015).

[12] K. A. Wendt, C. Forssén, T. Papenbrock and D. Sääf, Phys. Rev. C **91**, 061301(R) (2015).

[13] S. A. Coon and M. K. G. Kruse, Int. J. Mod. Phys. E **25**, 1641011 (2016).

[14] A. M. Shirokov, A. I. Mazur, J. P. Vary and E. A. Mazur, Phys. Rev. C **79**, 014610 (2009).

[15] A. M. Shirokov, A. I. Mazur, E. A. Mazur and J. P. Vary, Appl. Math. Inf. Sci. **3**, 245 (2009).

[16] J. Rotureau, in *Proc. Int. Conf. Nucl. Theor. Supercomputing Era (NTSE-2013), Ames, IA, USA, May 13–17, 2013.* eds. A. M. Shirokov and A. I. Mazur. Pacific National University, Khabarovsk, 2014, p. 236, http://www.ntse-2013.khb.ru/Proc/Rotureau.pdf.

[17] G. Papadimitriou, J. Rotureau, N. Michel, M. Płoszajczak and B. R. Barrett, Phys. Rev. C **88**, 044318 (2013).

[18] P. Navrátil, S. Quaglioni, I. Stetcu and B. R. Barrett, J. Phys. G **36**, 083101 (2009).

[19] P. Navrátil, in *Proc. Int. Conf. Nucl. Theor. Supercomputing Era (NTSE-2013), Ames, IA, USA, May 13–17, 2013*, eds. A. M. Shirokov and A. I. Mazur. Pacific National University, Khabarovsk, 2014, p. 211, http://www.ntse-2013.khb.ru/Proc/Navratil.pdf.

[20] G. Hupin, J. Langhammer, P. Navrátil, S. Quaglioni, A. Calci and R. Roth, Phys. Rev. C **88**, 054622 (2013).

[21] S. Quaglioni, P. Navrátil, G. Hupin, J. Langhammer, C. Romero-Redondo and R. Roth, Few-body Syst. **54**, 877 (2013).

[22] B. R. Barrett, P. Navrátil and J. P. Vary, Progr. Part. Nucl. Phys **69**, 131 (2013).

[23] G. Hupin, S. Quaglioni and P. Navrátil, Phys. Rev. C **90**, 061601(R) (2014).

[24] E. J. Heller and H. A. Yamany, Phys. Rev. A **9**, 1201 (1974); *ibid.* 1209 (1974).

[25] H. A. Yamany and L. Fishman. J. Math. Phys. **16**, 410 (1975).

[26] G. F. Filippov and I. P. Okhrimenko, Yad. Fiz. **32**, 932 (1980) [Sov. J. Nucl. Phys. **32**, 480 (1980)]; G. F. Filippov, Yad. Fiz. **33**, 928 (1981) [Sov. J. Nucl. Phys. **33**, 488 (1981)].

[27] Yu. F. Smirnov and Yu. I. Nechaev, Kinam **4**, 445 (1982); Yu. I. Nechaev and Yu. F. Smirnov, Yad. Fiz. **35**, 1385 (1982) [Sov. J. Nucl. Phys. **35**, 808 (1982)].

[28] V. A. Knyr, A. I. Mazur and Yu. F. Smirnov, Yad. Fiz. **52**, 754 (1990) [Sov. J. Nucl. Phys. **52**, 483 (1990)]; Yad. Fiz. **54**, 1518 (1991) [Sov. J. Nucl. Phys. **54**, 927 (1991)]; Yad. Fiz. **56**(10), 72 (1993) [Phys. At. Nucl. **56**, 1342 (1993)]; A. I. Mazur and S. A. Zaytsev, Yad. Fiz. **62**, 656 (1999) [Phys. At. Nucl. **62**, 608 (1999)].

[29] J. M. Bang, A. I. Mazur, A. M. Shirokov, Yu. F. Smirnov and S. A. Zaytsev, Ann. Phys. (NY) **280**, 299 (2000).

[30] V. I. Kukulin, V. N. Pomerantsev and O. A. Rubtsova, JETP Lett. **90**, 402 (2009); O. A. Rubtsova, V. I. Kukulin, V. N. Pomerantsev and A. Faessler, Phys. Rev. C **81**, 064003 (2010).

[31] I. M. Lifshitz, Zh. Eksp. Teor. Fiz. **17**, 1017 (1947) (*in Russian*); *ibid.* **17**, 1076 (1947) (*in Russian*); Usp. Mat. Nauk **7**, 171 (1952) (*in Russian*).

[32] T. Luu, M. J. Savage, A. Schwenk and J. P. Vary, Phys. Rev. C **82**, 034003 (2010).

[33] R. M. Nollett, Phys. Rev. C **86**, 044330 (2012).

[34] A. M. Shirokov, J. P. Vary, A. I. Mazur and T. A. Weber, Phys. Lett. B **644**, 33 (2007).

[35] A Fortran code generating the JISP16 matrix elements is available at http://nuclear.physics.iastate.edu.

[36] I. A. Mazur, A. M. Shirokov, A. I. Mazur and J. P. Vary, arXiv:1512.03983 [nucl-th] (2015).

[37] A. M. Shirokov, A. I. Mazur, I. A. Mazur and J. P. Vary, arXiv:1608.05885 [nucl-th] (2016).

[38] A. I. Mazur, A. M. Shirokov, J. P. Vary, P. Maris and I. A. Mazur, in *Proc. Int. Workshop Nucl. Theor. Supercomputing Era (NTSE-2012), Khabarovsk, Russia, June 18–22, 2012*, eds. A. M. Shirokov and A. I. Mazur. Pacific National University, Khabarovsk, 2013, p. 146, http://www.ntse-2012.khb.ru/Proc/A_Mazur.pdf.

[39] A. D. Alhaidari, E. J. Heller, H. A. Yamani and M. S. Abdelmonem (eds.), *The J-matrix method. Developments and applications.* Springer, 2008.

[40] A. M. Shirokov, Yu. F. Smirnov and S. A. Zaytsev, in *Modern problems in quantum theory*, eds. V. I. Savrin and O. A. Khrustalev. Moscow, 1998, p. 184; S. A. Zaytsev, Yu. F. Smirnov and A. M. Shirokov, Teoret. Mat. Fiz. **117**, 227 (1998) [Theor. Math. Phys. **117**, 1291 (1998)].

[41] A. M. Shirokov, A. I. Mazur, S. A. Zaytsev, J. P. Vary and T. A. Weber, Phys. Rev. C **70**, 044005 (2004); in *The J-matrix method. Developments and applications,* eds. A. D. Alhaidari, E. J. Heller, H. A. Yamani and M. S. Abdelmonem. Springer, 2008, p. 219.

[42] A. I. Baz', Ya. B. Zel'dovich and A. M. Perelomov, *Scattering, reactions and decay in non-relativistic quantum mechanics.* Israel Program for Scientific Translation, Jerusalem, 1969.

[43] R. G. Newton, *Scattering theory of waves and particles, 2nd. ed.* Springer-Verlag, New York, 1982.

[44] J. Bang and C. Gignoux, Nucl. Phys. A **313**, 119 (1979).

[45] P. Maris, M. Sosonkina, J. P. Vary, E. G. Ng and C. Yang, Proc. Comput. Sci. **1**, 97 (2010).

[46] H. M. Aktulga, C. Yang, E. G. Ng, P. Maris and J. P. Vary, Concurrency Computat. Pract. Exper. **26**, 2631 (2014).

[47] J. E. Bond and F. W. K. Firk, Nucl. Phys. A **287**, 317 (1977).

[48] A. Csótó and G. M. Hale, Phys. Rev. C **55**, 536 (1997).

[49] A. M. Shirokov, G. Papadimitriou, A. I. Mazur, I. A. Mazur, R. Roth and J. P. Vary, arXiv:1607.05631 [nucl-th] (2016).

[50] A. M. Shirokov, G. Papadimitriou, A. I. Mazur, I. A. Mazur, R. Roth and J. P. Vary, *see these Proceedings*, p. 174, http://www.ntse-2014.khb.ru/Proc/Shirokov.pdf.

Electromagnetic deuteron form factors in point form relativistic quantum mechanics

N. A. Khokhlov

Komsomolsk-na-Amure State Technical University

Abstract

A study of electromagnetic structure of the deuteron in the framework of relativistic quantum mechanics is presented. The deuteron form factors dependencies on the transferred 4-momentum Q up to 7.5 fm^{-1} are calculated. We compare results obtained with different realistic deuteron wave functions stemming from Nijmegen-I, Nijmegen-II, JISP16, CD-Bonn, Paris and Moscow (with forbidden states) potentials. A nucleon form factor parametrization consistent with modern experimental analysis was used as an input data.

Keywords: *Deuteron; nucleon; electromagnetic form factors*

1 Introduction

Elastic *ed* scattering observables are directly expressed within the Born approximation of one-photon exchange mechanism through electromagnetic (EM) deuteron form factors (FFs) [1–3]. Therefore this process allows to extract the EM FF dependencies on the transferred 4-momentum Q in the space-like region. Relativistic effects may be essential even at low Q [2, 3]. There are different relativistic models of deuteron EM FFs [4–8].

We apply the point-form (PF) relativistic quantum mechanics (RQM) to the elastic electron-deuteron scattering in a Poincaré-invariant way. The RQM concepts and an exhaustive bibliography are presented in the review by Keister and Polyzou [9]. The PF is one of the three forms of RQM proposed by Dirac [10]. The other two are the instant and front forms. These forms are associated with different subgroups of the Poincaré group which may be free of interactions. A general method of allowing for interactions in generators of the Poincaré group was derived in Ref. [11]. It was shown that all the forms are unitary equivalent [12]. Though each form has certain advantages, there are important simplifying features of the PF [13]. In the PF, all generators of the homogeneous Lorentz group (space-time rotations) are free of interactions. Therefore the spectator approximation (SA) preserves its spectator character in any reference frame (r. f.) only in the PF [14–16]. In the case of electromagnetic NN process, it means that the NN interaction does not affect the photon-nucleon interaction and therefore the sum of one-particle EM current operators is invariant under transformations from one r. f. to another. Two equivalent SAs for EM current operator of a composite system in PF RQM were derived in Refs. [13,15]. The PF SA was applied to calculation of deuteron, pion and nucleon EM FFs [7,17–21] providing reasonable results.

The present paper is an extension of our previous investigations where we have described the elastic NN scattering up to laboratory energy of 3 GeV [22], bremsstrahlung in pp scattering $pp \to pp\gamma$ [23], deuteron photodisintegration $\gamma D \to np$

Proceedings of the International Conference 'Nuclear Theory in the Supercomputing Era — 2014' (NTSE-2014), Khabarovsk, Russia, June 23–27, 2014. Eds. A. M. Shirokov and A. I. Mazur. Pacific National University, Khabarovsk, Russia, 2016, p. 230.

http://www.ntse-2014.khb.ru/Proc/Khokhlov.pdf.

[24–26] and exclusive deuteron electrodisintegration [27]. Here we demonstrate that the developed approach is applicable to the elastic eD scattering.

2 Potential model in PF of RQM

A system of two particles is described within PF RQM by the wave function which is an eigenfunction of the mass operator $\hat{M}$. We may represent this wave function as a product of external and internal parts. The internal wave function $|\chi\rangle$ is also an eigenfunction of the mass operator and for a system of two nucleons with masses $m_1 \approx m_2 \approx m = 2m_1m_2/(m_1+m_2)$ satisfies the equation

$$\hat{M}|\chi\rangle \equiv \left[2\sqrt{\mathbf{q}^2+m^2}+V_{int}\right]|\chi\rangle = M|\chi\rangle, \tag{1}$$

where V_{int} is an operator commuting with the full angular momentum operator and acting on internal variables (spins and relative momentum) only, $\mathbf{q}$ is a momentum operator of one of particles in the center of mass (c. m.) frame (relative momentum), $\hat{M}$ is a system mass operator and M is its eigenvalue. Here we adopt a natural system of units with $\hbar = c = 1$. A rearrangement of Eq. (1) gives

$$\left[\mathbf{q}^2 + mV\right]|\chi\rangle = q^2|\chi\rangle, \tag{2}$$

where the operator

$$mV = \frac{1}{4}\left(2\sqrt{\mathbf{q}^2+m^2}V_{int} + 2V_{int}\sqrt{\mathbf{q}^2+m^2} + V_{int}^2\right), \tag{3}$$

as well as V_{int}, acts on internal variables only, and the eigenvalue of the operator $\mathbf{q}^2 + mV$ is

$$q^2 = \frac{M^2}{4} - m^2. \tag{4}$$

Equation (2) is identical in form to a Schrödinger equation. Relativistic corrections affect the deuteron binding energy ε only and may be easily accounted for by replacing the experimental deuteron binding of 2.2246 MeV by an effective value of 2.2233 MeV. The origin of this relativistic correction is easy to understand [28–30]. Clearly,

$$M = 2m - \varepsilon, \tag{5}$$

and hence Eq. (4) can be rewritten as

$$q^2 = -m\varepsilon\left(1 - \frac{\varepsilon}{4m}\right). \tag{6}$$

Comparing Eq. (6) with the nonrelativistic relation

$$q^2 = -m\varepsilon, \tag{7}$$

one identifies the factor $\left(1 - \frac{\varepsilon}{4m}\right)$ as a relativistic correction to the deuteron binding energy. It is interesting and important to note that there is no similar correction in the scattering domain since $q^2 = mE_{lab}/2$ is a precise relativistic relationship (E_{lab} is the laboratory energy) used in the partial wave analysis [28].

The difference between the experimental and effective deuteron binding energies is negligible for our problem. Therefore, due to the formal identity between Eq. (2) and Schrödinger equation, we can use non-relativistic deuteron wave functions in our calculations.

3 *eD* elastic scattering

We sketch here some PF RQM results needed for our calculations. We use formalism and notations of Ref. [15].

We consider the *pn* system and neglect the difference between neutron and proton masses. Let p_i be the 4-momentum of nucleon i, $P \equiv (P^0, \mathbf{P}) = p_1 + p_2$ is the system 4-momentum, M is the system mass and $G = P/M$ is the system 4-velocity. The wave function of two particles with 4-momentum P is expressed through a tensor product of external and internal parts,

$$|P, \chi\rangle = U_{12}\,|P\rangle \otimes |\chi\rangle, \tag{8}$$

where the internal wave function $|\chi\rangle$ fits Eqs. (1)–(2). The unitary operator

$$U_{12} = U_{12}(G, \mathbf{q}) = \prod_{i=1}^{2} D[\mathbf{s}_i; \alpha(p_i/m)^{-1}\alpha(G)\alpha(q_i/m)] \tag{9}$$

relates the "internal" Hilbert space with the Hilbert space of two-particle states [15]. $D[\mathbf{s}; u]$ is a SU(2) operator corresponding to the element $u \in \mathrm{SU}(2)$, $\mathbf{s}$ are the SU(2) generators. In our case of spin $s = 1/2$ particles, we deal with the fundamental representation, i. e., $\mathbf{s}_i \equiv \frac{1}{2}\boldsymbol{\sigma}_i$ [$\boldsymbol{\sigma} = (\sigma_x, \sigma_y, \sigma_z)$ are the Pauli matrices] and $D[\mathbf{s}; u] \equiv u$. Matrix $\alpha(g) = (g^0 + 1 + \boldsymbol{\sigma} \cdot \mathbf{g})/\sqrt{2(g^0 + 1)}$ corresponds to a 4-velocity g. The momenta of particles in their c. m. frame are

$$q_i = L[\alpha(G)]^{-1} p_i, \tag{10}$$

where $L[\alpha(G)]$ is the Lorentz boost to the frame moving with 4-velocity G.

The "external" part of the wave function is defined as

$$\langle G|P'\rangle \equiv \frac{2}{M'}\, G'^0\, \delta^3(\mathbf{G} - \mathbf{G}'). \tag{11}$$

Its scalar product is

$$\langle P''|P'\rangle = \int \frac{d^3\mathbf{G}}{2G^0}\, \langle P''|G\rangle\langle G|P'\rangle = 2\sqrt{M'^2 + \mathbf{P}'^2}\, \delta^3(\mathbf{P}'' - \mathbf{P}'), \tag{12}$$

where $G^0(\mathbf{G}) \equiv \sqrt{1 + \mathbf{G}^2}$. The internal part $|\chi\rangle$ is characterized by momentum $\mathbf{q} = \mathbf{q}_1 = -\mathbf{q}_2$ of one of the particles in the c. m. frame.

According to the Bakamjian—Thomas procedure [11], the 4-momentum $\hat{P} = \hat{G}\hat{M}$ incorporates the interaction V_{int}, where $\hat{M}$ is the sum of the free mass operator M_{free} and interaction, $\hat{M} = M_{free} + V_{int}$ [see Eq. (1)]. The interaction operator acts only on internal variables. The operators V_{int} and V (and therefore $\hat{M}$ and M_{free}) commute with S, the spin (full angular momentum) operator, and $\hat{G}$, the 4-velocity operator. The generators of space-time rotations are interaction-free. Most of formal non-relativistic scattering theory results are valid in the case of two relativistic particles [9]. For example, the relative orbital angular momentum and spins are coupled in the c. m. frame in the same manner as in the non-relativistic case.

The deuteron wave function $|P_i, \chi_i\rangle$ is normalized,

$$\langle P_f, \chi_f|P_i, \chi_i\rangle = 2P_i^0\, \delta^3(\mathbf{P}_i - \mathbf{P}_f)\langle\chi_f|\chi_i\rangle. \tag{13}$$

There is a convenient r. f. for calculation of current operator matrix elements [15] (it coincides with the Breit r. f. in the case of elastic *ed* scattering). This r. f. is defined by the following condition for all EM reactions with two nucleons:

$$\mathbf{G}_f + \mathbf{G}_i = 0, \tag{14}$$

where $\mathbf{G}_f = \mathbf{P}_f/M_D$, $\mathbf{G}_i = \mathbf{P}_i/M_D$ are the final and initial 4-velocities of the deuteron and M_D is its mass. The matrix element of the current operator is [15]

$$\langle P_f, \chi_f|\hat{J}^\mu(x)|P_i, \chi_i\rangle = 2(M_f M_i)^{1/2} \exp(\imath(P_f - P_i)x)\langle\chi_f|\hat{j}^\mu(\mathbf{h})|\chi_i\rangle, \tag{15}$$

where $\hat{j}^\mu(\mathbf{h})$ defines action of current operator in the internal space of the NN system,

$$\mathbf{h} = \frac{2(M_i M_f)^{1/2}}{(M_i + M_f)^2}\,\mathbf{k} = \frac{\mathbf{k}}{2M_D} \tag{16}$$

is the vector-parameter [15] ($0 \le h \le 1$), $\mathbf{k}$ is the momentum of photon in the r. f. defined by Eq. (14), $M_i = M_f = M_D$ are the masses of the initial and final NN system (deuteron).

The internal deuteron wave function is

$$|\chi_i\rangle = \frac{1}{r}\sum_{l=0,2} u_l(r)|l, 1; J = 1M_J\rangle_{\mathbf{r}}; \tag{17}$$

it is normalized: $\langle\chi_i|\chi_i\rangle = 1$. We use the momentum space wave function

$$|\chi_i\rangle = \frac{1}{q}\sum_{l=0,2} u_l(q)\,|l, 1; 1M_J\rangle_{\mathbf{q}}, \tag{18}$$

where

$$u(q) \equiv u_0(q) = \sqrt{\frac{2}{\pi}}\int dr\,\sin(qr)u(r), \tag{19}$$

$$w(q) \equiv u_2(q) = \sqrt{\frac{2}{\pi}}\int dr\,\left[\left(\frac{3}{(qr)^2} - 1\right)\sin(qr) - \frac{3}{qr}\cos(qr)\right]w(r). \tag{20}$$

Transformations from the Breit r. f. (14) to the initial and final c. m. frame of the NN system are the boosts along vector $\mathbf{h}$ (axis z). Projection of the total deuteron angular momentum onto z axis are unaffected by these boosts. The initial deuteron moves in the Breit r. f. in the direction opposite to $\mathbf{h}$. Its internal wave function with the spirality Λ_i is

$$|\Lambda_i\rangle = \frac{1}{q}\sum_{l=0,2} u_l(q)\,|l, 1; 1, M_J = -\Lambda_i\rangle. \tag{21}$$

The wave function of the final deuteron with the spirality Λ_f is

$$|\Lambda_f\rangle = \frac{1}{q}\sum_{l=0,2} u_l(q)\,|l, 1; 1, M_J = \Lambda_f\rangle. \tag{22}$$

A conventional parametrization of the deuteron (spin-1 particle) EM current operator (CO) matrix element is [2, 3, 31]:

$$\begin{aligned}(4P_i^0 P_f^0)^{1/2}&\langle P_f, \chi_f|J^\mu|P_i, \chi_i\rangle \\ &= -\left\{G_1(Q^2)\,(\boldsymbol{\xi}_f^*\cdot\boldsymbol{\xi}_i) - G_3(Q^2)\,\frac{(\boldsymbol{\xi}_f^*\cdot\Delta P)(\boldsymbol{\xi}_i\cdot\Delta P)}{2M_D^2}\right\}(P_i^\mu + P_f^\mu) \\ &\quad - G_2(Q^2)\,[\xi_i^\mu\,(\boldsymbol{\xi}_f^*\cdot\Delta\ \mathbf{P}) - \xi_f^{*\mu}(\boldsymbol{\xi}_i\cdot\Delta\mathbf{P})],\end{aligned} \tag{23}$$

where $(a\cdot b) = a^0 b^0 - (\mathbf{a}\cdot\mathbf{b})$, form factors $G_i(Q^2)$, $i = 1, 2, 3$, are the functions of $Q^2 = -\Delta P^2$, $\Delta P = P_f - P_i$.

In the Breit r. f. $\mathbf{P}_f = -\mathbf{P}_i$, $P_i^0 = P_f^0 \equiv P^0 = M_D/\sqrt{1-h^2}$, $\Delta P = (0, 2\mathbf{P}_f)$, $P_i^\mu + P_f^\mu = (2P^0, \mathbf{0})$, $\mathbf{P}_f/P^0 = \mathbf{h}$, $\mathbf{P}_f = \mathbf{h}M_D/\sqrt{1-h^2}$, $\Delta P^2 = -4h^2M_D^2/(1-h^2)$, $Q^2 \equiv -\Delta P^2$, $h^2 = (\mathbf{h}\cdot\mathbf{h})$,

$$\langle\chi_f|j^0(\mathbf{h})|\chi_i\rangle = -G_1(Q^2)(\boldsymbol{\xi}'^*\cdot\boldsymbol{\xi}) + 2G_3(Q^2)\frac{(\boldsymbol{\xi}_f^*\cdot\ \mathbf{h})(\boldsymbol{\xi}_i\cdot\mathbf{h})}{1-h^2} + G_2(Q^2)[\xi_i^0(\boldsymbol{\xi}_f^*\cdot\mathbf{h}) - \xi_f^{0*}(\boldsymbol{\xi}_i\cdot\mathbf{h})], \quad (24)$$

$$\langle\chi_f|\mathbf{j}(\mathbf{h})|\chi_i\rangle = G_2(Q^2)[\xi_i(\boldsymbol{\xi}_f^*\cdot\mathbf{h}) - \xi_f^*(\boldsymbol{\xi}_i\cdot\mathbf{h})] = G_2(Q^2)[\mathbf{h}\times[\boldsymbol{\xi}_i\times\boldsymbol{\xi}_f^*]]. \quad (25)$$

It has been shown [15] that these expressions are equivalent to choosing j^ν as

$$j^0(\mathbf{h}) = G_C(Q^2) + \frac{2}{(1-h^2)}\,G_Q(Q^2)\left[\frac{2}{3}h^2 - (\mathbf{h}\cdot\mathbf{J})^2\right], \quad (26)$$

$$\mathbf{j}(\mathbf{h}) = -\frac{\imath}{\sqrt{1-h^2}}\,G_M(Q^2)\,(\mathbf{h}\times\mathbf{J}), \quad (27)$$

where $\mathbf{J}$ is the total angular momentum (spin) of the deuteron; G_C, G_Q and G_M are its charge monopole, charge quadruple and magnetic dipole FFs.

Spiral deuteron polarizations in the initial and final states are

$$\xi_i^\Lambda = \begin{cases} (0, \pm1, -\imath, 0)/\sqrt{2} & (\Lambda = \pm), \\ (-Q/2, 0, 0, P_0)/M_D = (-h, 0, 0, 1)/\sqrt{1-h^2} & (\Lambda = 0), \end{cases} \quad (28)$$

$$\xi_f^\Lambda = \begin{cases} (0, \mp1, -\imath, 0)/\sqrt{2} & (\Lambda = \pm), \\ (Q/2, 0, 0, P_0)/M_D = (h, 0, 0, 1)/\sqrt{1-h^2} & (\Lambda = 0). \end{cases} \quad (29)$$

A virtual photon polarization is

$$\epsilon^\lambda = \begin{cases} (0, \mp1, -\imath, 0)/\sqrt{2} & (\lambda = \pm), \\ (1, 0, 0, 0) & (\lambda = 0). \end{cases} \quad (30)$$

FFs G_i are expressed as

$$\begin{aligned} G_C &= G_1 + \frac{2}{3}\eta G_Q, \\ G_Q &= G_1 - G_M + (1+\eta)G_3, \\ G_1 &= G_C - \frac{2h^2}{3(1-h^2)}G_Q, \\ G_3 &= G_Q\left(1 - \frac{h^2}{3}\right) - G_C(1-h^2) + G_M(1-h^2), \end{aligned} \quad (31)$$

where $\eta = Q^2/4M_D^2 = h^2/(1-h^2)$. Supposing $Q^2 = 0$, we have $G_Q = G_1 - G_M + G_3$ and $G_C = G_1$. Form factors $G_C(0) = e$, $G_M(0) = \mu_D e/2M_D$ and $G_Q = Q_D e/M_D^2$ provide deuteron charge, magnetic and quadruple momenta respectively.

Denoting helicity amplitudes as $j^\lambda_{\Lambda_f\Lambda_i} \equiv \langle\Lambda_f|\left(\epsilon_\mu^\lambda\cdot j^\mu(\mathbf{h})\right)|\Lambda_i\rangle$, we arrive at

$$j^0_{00}(Q^2) = G_C + \frac{4}{3}\frac{h^2}{1-h^2}G_Q, \quad (32)$$

$$j^0_{+-}(Q^2) = j^0_{-+}(Q^2) = G_C - \frac{2}{3}\frac{h^2}{1-h^2}G_Q, \quad (33)$$

$$\frac{j^+_{+0}(Q^2) + j^+_{0-}(Q^2)}{2} = -\frac{h}{\sqrt{1-h^2}}G_M \quad (34)$$

and

$$j^+_{+0}(Q^2) = j^-_{-0}(Q^2) \approx j^+_{0-}(Q^2) = j^-_{0+}(Q^2). \quad (35)$$

The deuteron FFs are associated with unpolarized structure functions [32]:

$$A(Q^2) = G_C^2(Q^2) + \frac{2}{3}\,\eta\, G_M^2(Q^2), \tag{36}$$

$$B(Q^2) = \frac{4}{3}\,\eta\,(1+\eta)\, G_M^2(Q^2). \tag{37}$$

These quantities are extracted from the elastic eD scattering with unpolarized particles. A tensor polarization observable $t_{20}(Q^2,\theta)$ is conventionally used as an additional quantity needed for definition of all three FFs.

In the present paper, we use the EM CO obtained within SA in Ref. [15] without expanding it in powers of h and calculate its matrix elements in the momentum space. Therefore we use the following expansion of $\hat{j}^\mu(\mathbf{h}) \approx \hat{j}^\mu_{SA}(\mathbf{h})$ [27] for the matrix element calculations:

$$\hat{j}^\mu_{SA}(\mathbf{h}) = \big(1 + (\mathbf{A}_2\cdot\mathbf{s}_2)\big)\big(B_1^\mu + (\mathbf{C}_1^\mu\cdot\mathbf{s}_1)\big)\mathbf{I}_1(\mathbf{h}) + \big(1 + (\mathbf{A}_1\cdot\mathbf{s}_1)\big)\big(B_2^\mu + (\mathbf{C}_2^\mu\cdot\mathbf{s}_2)\big)\mathbf{I}_2(\mathbf{h}), \tag{38}$$

where $\mathbf{A}_i$, B_i^μ and $\mathbf{C}_i^\mu$ are some vector functions of $\mathbf{h}$ and $\mathbf{q}(q,\theta,\phi)$. In the spherical coordinate system (q,θ,ϕ), the dependence of these functions on ϕ appears as $e^{\pm im\phi}$ $(m = 0, 1, 2)$. The angle ϕ is analytically integrated out giving trivial equalities (35).

4 Results

In our calculations, we use as an input momentum space deuteron wave functions and nucleon EM FFs. The momentum space deuteron wave functions stemming from Nijmegen-I (NijmI), Nijmegen-I (NijmII) [33], JISP16 [34], CD-Bonn [29], Paris [35], Argonne18 [30] (the momentum space deuteron wave function is grabbed from Ref. [36]) and Moscow (with forbidden states) [22] potentials are shown in Figs. 1. We use two versions of Moscow type potential: Moscow06 [22] and Moscow14. The latter one was obtained by the author in the same manner outlined in Ref. [22] but with deuteron asymptotic constants fitted to describe static deuteron form factors. Parameters of both Moscow potentials may be obtained upon request from the author (e-mail: `nikolakhokhlov@yandex.ru`). The S wave functions of all potentials but JISP16 change sign at $q \approx 2$ fm^{-1}, and D wave functions change sign at $q \approx 6{-}8$ fm^{-1}. The S and D wave functions of Argonne18, Paris and NijmII are close at $q \lesssim 5$ fm^{-1}. The S wave functions of CD-Bonn and NijmI are close at $q \lesssim 5$ fm^{-1}. The JISP16 wave functions decrease rapidly at q larger than approximately 2 fm^{-1} without changing sign.

Our results for deuteron EM FFs are presented in Table 1 and in Figs. 2, 3, 4. The results for Argonne18, Paris and NijmII are close manifesting the closeness of their wave functions at $q \lesssim 5$ fm^{-1}. NijmI and CD-Bonn provide more distinct results. Our calculations demonstrate that G_M obtained with all potentials changes sign at rather low Q that is not seen experimentally. Nevertheless CD-Bonn and NijmI result in a reasonable description of G_M at $Q < 7$ fm. Moscow potentials provide the best description of charge form factor G_C.

An essential factor affecting our calculations is the nucleon FF dependency on the momentum transferred to the individual nucleon, $Q_p^2 \approx Q_n^2 \neq Q^2$. These FFs have been measured at discrete values of $Q^2_{i=p,n}$ while we need a continuous dependency on Q_i. In our calculations, we utilize phenomenological nucleon FF dependencies on Q_i^2 of Ref. [54]. It should be noted that the neutron EM FFs are extracted from experimental data on ${}^2\vec{\mathrm{H}}(\vec{e},e'n)p$ and other processes with deuteron and triton using various models of mechanism of these possesses and nuclei. Therefore these FFs are model dependent.

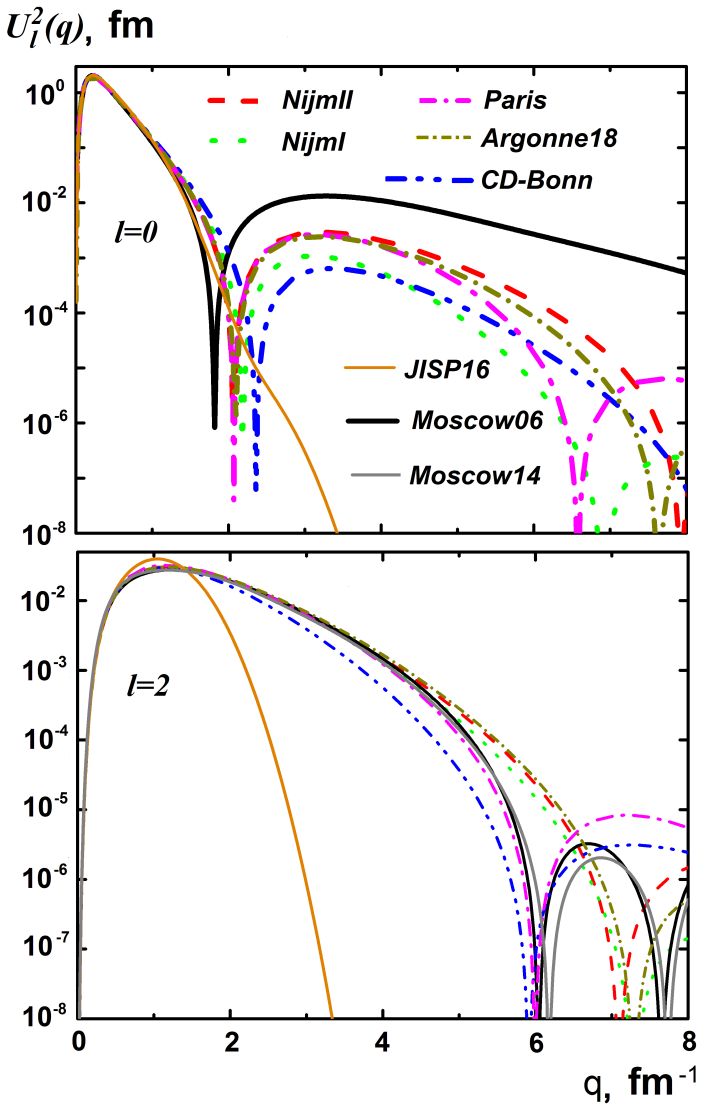

Figure 1: Momentum space deuteron wave functions used in calculations.

Table 1: Static deuteron form factors. The results of relativistic (nonrelativistic) calculations are given before (after) slash.

	$G_M(0) = \frac{M_d}{m_p}\mu_d$	$G_Q(0) = M_d^2 Q_d$
Exp	1.7148	25.83
NijmI	1.697/1.695	24.8/24.6
NijmII	1.700/1.695	24.7/24.5
Paris	1.696/1.694	25.6/25.2
CD-Bonn	1.708/1.704	24.8/24.4
Argonne18	1.696/1.694	24.7/24.4
JISP16	1.720/1.714	26.3/26.1
Moscow06	1.711/1.699	24.5/24.2
Moscow14	1.716/1.700	26.0/25.8

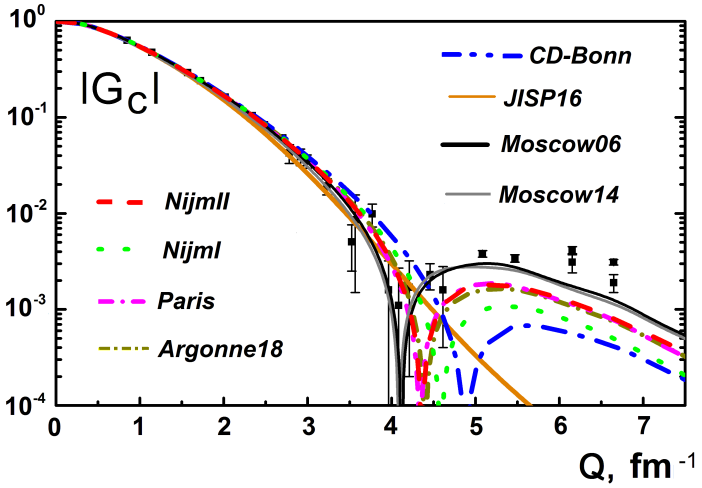

Figure 2: Deuteron form factor G_C as a function of Q. Experimental points are from compilation [3] where they were calculated using data for A, B and t_{20} obtained in Refs. [37–53].

We see a good overall agreement between the theory and experiment at $Q < 5$ fm^{-1}. Discrepancies at larger Q are comparable with differences of results for different potentials. Model calculations [55] show that meson exchange currents may provide a significant contribution to EM processes in the np-system. We do not take into account these currents. However it is not clear how these currents can be derived consistently with the short-range NN interaction of the QCD origin. In addition, the EM FFs of nucleons are not described by meson degrees of freedom at intermediate and high energies [56].

To complete this line of our investigation, we plan to calculate neutron EM FFs compatible with Moscow potential model which has not been used for the extraction of these FFs.

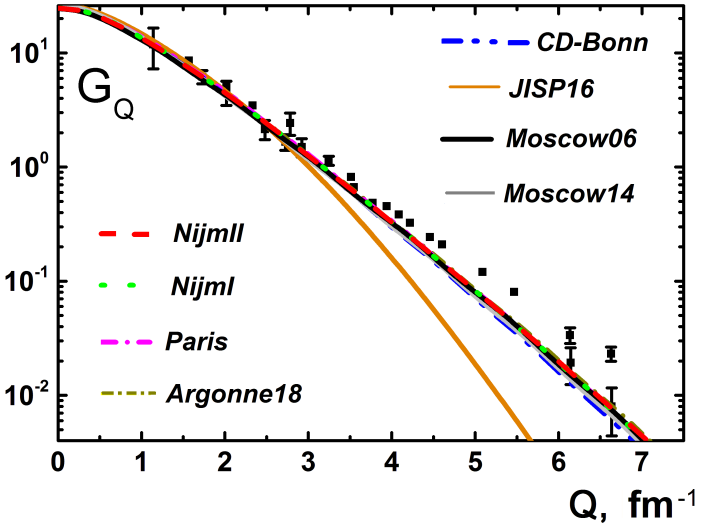

Figure 3: Deuteron form factor G_Q as a function of Q. See Fig. 2 for details.

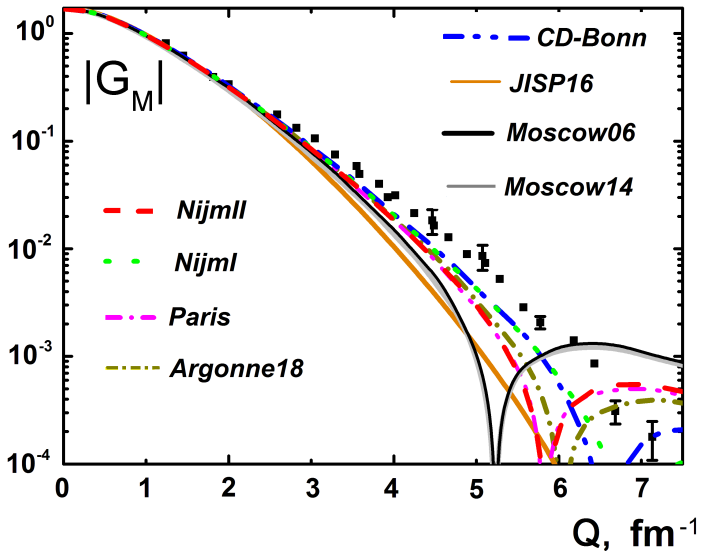

Figure 4: Deuteron form factor G_M as a function of Q. See Fig. 2 for details.

References

[1] A. I. Akhiezer, A. G. Sitenko and V. K. Tartakovskii, *Nuclear Electrodynamics.* Springer-Verlag, Berlin, 1994.

[2] R. Gilman and F. Gross, J. Phys. G **28**, R37 (2002).

[3] M. Garçon and J. W. Van Orden, Adv. Nucl. Phys. **26**, 293 (2001).

[4] H. Arenhövel, F. Ritz and T. Wilbois, Phys. Rev. C **61**, 034002 (2000).

[5] J. Adam, Jr. and H. Arenhövel, Nucl. Phys. A **614**, 289 (1997).

[6] K. Tamura, T. Niwa, T. Sato and H. Ohtsubo, Nucl. Phys. A **536**, 597 (1992).

[7] T. W. Allen, W. H. Klink and W. N. Polyzou, Phys. Rev. C **63**, 034002 (2001).

[8] F. M. Lev, E. Pace and G. Salmè, Phys. Rev. C **62** 064004 (2000); Nucl. Phys. A **663**, 365c (2000).

[9] B. D. Keister and W. Polyzou, Adv. Nucl. Phys. **20**, 325 (1991).

[10] P. A. M. Dirac, Rev. Mod. Phys. **21**, 392 (1949).

[11] B. Bakamjian and L. H. Thomas, Phys. Rev. **92**, 1300 (1953).

[12] S. N. Sokolov and A. M. Shatny, Theor. Math. Phys. **37**, 1029 (1978).

[13] W. H. Klink, Phys. Rev. C **58**, 3587 (1998).

[14] B. Desplanques and L. Theußl, Eur. Phys. J. A **13**, 461 (2002).

[15] F. M. Lev, Ann. Phys. (NY) **237**, 355 (1995); hep-ph/9403222.

[16] T. Melde, L. Canton, W. Plessas and R. F. Wagenbrunn, Eur. Phys. J. A **25**, 97 (2005).

[17] T. W. Allen and W. H. Klink, Phys. Rev. C **58**, 3670 (1998).

[18] F. Coester and D. O. Riska, Few-Body Syst. **25**, 29 (1998).

[19] R. F. Wagenbrunn, S. Boffi, W. Klink, W. Plessas and M. Radici, Phys. Lett. B **511**, 33 (2001).

[20] A. Amghar, B. Desplanques and L. Theußl, Phys. Lett. B **574**, 201 (2003).

[21] F. Coester and D. O. Riska, Nucl. Phys. A **728**, 439 (2003).

[22] N. A. Khokhlov and V. A. Knyr, Phys. Rev. C **73**, 024004 (2006).

[23] N. A. Khokhlov, V. A. Knyr and V. G. Neudatchin, Phys. Rev. C **68**, 054002 (2003).

[24] V. A. Knyr, V. G. Neudatchin and N. A. Khokhlov, Phys. Atom. Nucl. **70**, 879 (2007).

[25] N. A. Khokhlov, V. A. Knyr and V. G. Neudatchin, Phys. Rev. C **75**, 064001 (2007).

[26] V. A. Knyr, V. G. Neudatchin and N. A. Khokhlov, Phys. Atom. Nucl. **70**, 2152 (2007); V. A. Knyr and N. A. Khokhlov, Phys. Atom. Nucl. **66**, 1994 (2008).

[27] V. A. Knyr and N. A. Khokhlov, Phys. Atom. Nucl. **70**, 2066 (2007).

[28] F. Coester, S. C. Pieper, S. J. D. Serduke, Phys. Rev. C **11**, 1 (1974).

[29] R. Machleidt, Phys. Rev. C **63**, 024001 (2001).

[30] R. B. Wiringa, V. G. J. Stoks and R. Schiavilla, Phys. Rev. C **51**, 38 (1995).

[31] R. G. Arnold, C. E. Carlson and F. Gross, Phys. Rev. C **23**, 363 (1981).

[32] T. W. Donnelly and A. S. Raskin, Ann. Phys. (NY) **169**, 247 (1986).

[33] V. G. J. Stoks, R. A. M. Klomp, C. P. F. Terheggen and J. J. de Swart, Phys. Rev. C **49**, 2950 (1994).

[34] A. M. Shirokov, J. P. Vary, A. I. Mazur and T. A.Weber, Phys. Lett. B **644**, 33 (2007).

[35] M. Lacombe, B. Loiseau, R. Vinh Mau, J. Côté, P. Pirés and R. de Tourreil, Phys. Lett. B **101**, 139 (1981).

[36] S. Veerasamy and W. N. Polyzou, Phys. Rev. C **84**, 034003 (2011).

[37] J. E. Elias, J. I. Friedman, G. C. Hartmann, H. W. Kendall, P. N. Kirk, M. R. Sogard, L. P. Van Speybroeck and J. K. De Pagter, Phys. Rev. **177**, 2075 (1969).

[38] R. G. Arnold, B. T. Chertok, E. B. Dally, A. Grigorian, C. L. Jordan, W. P. Schütz, R. Zdarko, F. Martin and B. A. Mecking, Phys. Rev. Lett. **35**, 776 (1975).

[39] R. Cramer *et al.*, Z. Phys. C **29**, 513 (1985).

[40] S. Platchkov, A. Amroun, S. Auffret, J.M. Cavedon, P. Dreux, J. Duclos, B. Frois, D. Goutte, H. Hachemi, J. Martino and X. H. Phan, Nucl. Phys. A **510**, 740 (1990).

[41] L. C. Alexa *et al.*, Phys. Rev. Lett. **82**, 1374 (1999).

[42] D. Abbott *et al.*, Phys. Rev. Lett. **82**, 1379 (1999).

[43] S. Auffret *et al.*, Phys. Rev. Lett. **54**, 649 (1985).

[44] P. E. Bosted *et al.*, Phys. Rev. C **42**, 38 (1990).

[45] M. E. Schulze *et al.*, Phys. Rev. Lett. **52**, 597 (1984).

[46] M. Garçon *et al.*, Phys. Rev. C **49**, 2516 (1994); I. The *et al.*, Phys. Rev. Lett. **67**, 173 (1991).

[47] D. Abbott *et al.*, Phys. Rev. Lett. **84**, 5053 (2000).

[48] V. F. Dmitriev *et al.*, Phys. Lett. B **157**, 143 (1985).

[49] B. B. Voitsekhovskii, D. M. Nikolenko, K. T. Ospanov, S. G. Popov, I. A. Rachek, D. K. Toporkov, E. P. Tsentalovich and Yu. M. Shatunov, JETP Lett. **43**, 733 (1986).

[50] R. Gilman *et al.*, Phys. Rev. Lett. **65**, 1733 (1990).

[51] M. Ferro-Luzzi *et al.*, Phys. Rev. Lett. **77**, 2630 (1996).

[52] M. Bouwhuis *et al.*, Phys. Rev. Lett. **82**, 3755 (1999).

[53] D. Abbott *et al.*, Eur. Phys. J. A **7**, 421 (2000).

[54] R. Bradford, A. Bodek, H. Budd and J. Arrington, Nucl. Phys. Proc. Suppl. B **159**, 127 (2006).

[55] H. Arenhoevel, E. M. Darwish, A. Fix and M. Schwamb, Mod. Phys. Lett. A **18**, 190 (2003).

[56] C. F. Perdrisat, V. Punjabi and M. Vanderhaeghen, Progr. Part. Nucl. Phys. **59**, 694 (2007).

Approach to Three Nucleon Forces from Experiment

Kimiko Sekiguchi

Department of Physics, Tohoku University, Sendai, 980-8578, JAPAN

Abstract

Nucleon-deuteron (Nd) scattering for which a rigorous formulation in terms of Faddeev equations exists and exact solutions of these equations for any dynamical input can be obtained, offers a good opportunity to study the dynamical aspects of 3NFs such as momentum, spin dependences. Since the first indication of 3NF effects in Nd elastic scattering around 100 MeV/nucleon, precise measurements of proton-deuteron/neutron-deuteron scattering have been extensively performed at 60–250 MeV/nucleon. Direct comparison between the data and the Faddeev calculations based on realistic nucleon-nucleon forces plus 2π-exchange three nucleon forces draws the following conclusions, (1) the 3NF is definitely needed in Nd elastic scattering, (2) the spin dependent parts of the 3NF may be deficient, (3) the short-range components of the 3NF are probably required for high momentum transfer region, and (4) establishment of 3NFs in Nd breakup processes should be performed in the framework of relativistic Faddeev calculations.

Keywords: *Three-nucleon force; few-nucleon systems; nucleon-deuteron scattering*

1 Introduction

Experimentally, one must utilize systems with more than two nucleons ($A \geq 3$) to investigate properties of three nucleon forces (3NFs). The 3NFs arise naturally in the standard meson exchange picture in which the main ingredient is considered to be a 2π-exchange between three nucleons along with the Δ-isobar excitation initially proposed by Fujita and Miyazawa in 1957 [1]. Further augmentations have led to the Tucson–Melbourne (TM) [2], the Urbana [3] 3NFs, etc. A new impetus to study 3NFs has come from chiral effective field theory (χEFT) descriptions of nuclear interactions. In that framework consistent two-, three-, and many-nucleon forces are derived on the same footing [4, 5]. The first non-zero contribution to 3NFs appears in χEFT at the next-to-next-to-leading order ($\mathrm{N^2LO}$) of the chiral expansion. Generally, the 3NFs are relatively small compared to the nucleon-nucleon (NN) forces and their effects are easily masked. Therefore it is hard to find an evidence for them experimentally.

The first evidence for a 3NF was found in the three-nucleon bound states, ^{3}H and ^{3}He [6, 7]. The binding energies of these nuclei are not reproduced by exact solutions of three-nucleon Faddeev equations employing modern NN forces only, i. e., AV18 [8], CD Bonn [9], Nijmegen I, II [10]. The underbinding of ^{3}H and ^{3}He can be explained by adding a 3NF, mostly based on 2π-exchange, acting between three nucleons [6, 7, 11]. The importance of 3NFs has been further supported by the binding energies of light mass nuclei and by the empirical saturation point of symmetric nuclear matter. *Ab*

Proceedings of the International Conference 'Nuclear Theory in the Supercomputing Era — 2014' (NTSE-2014), Khabarovsk, Russia, June 23–27, 2014. Eds. A. M. Shirokov and A. I. Mazur. Pacific National University, Khabarovsk, Russia, 2016, p. 241.

http://www.ntse-2014.khb.ru/Proc/Sekiguchi.pdf.

initio microscopic calculations of light mass nuclei, such as Green's Function Monte Carlo [12] and no-core shell model calculations [13], highlight the necessity of including $3N$Fs to explain the binding energies and low-lying levels of these nuclei. As for the density of symmetric nuclear matter, it has been reported that all NN potentials provide saturation at a too high density, and a short-range repulsive $3N$F is one possibility to shift the theoretical results to the empirical point [14].

Three-nucleon ($3N$) scattering has been studied for a long time as one of the most promising tools to explore the properties of $3N$Fs because this process provides a rich set of energy dependent spin observables and differential cross sections. At lower energies ($E/A \leq 20$ MeV), very high precision measurements were carried out in proton-deuteron (pd) and neutron-deuteron (nd) scattering, including elastic and breakup reactions. However, theoretically predicted $3N$F effects are rather small and a generally good description for nucleon-deuteron (Nd) elastic scattering data is obtained by exact solutions of $3N$ Faddeev equations employing only NN forces [15, 16][1]. Study of the $3N$F has changed since the end of 1990's. The following advances have made it possible to explore the $3N$F effects contained in $3N$ scattering.

(i) Generation of the so-called realistic NN forces (e. g., AV18 [8], CD Bonn [9], Nijmegen I, II and 93 [10]) which reproduce a rich set of experimental NN data for laboratory energy up to 350 MeV with an accuracy of $\chi^2 \sim 1$.

(ii) Achievement of rigorous numerical Faddeev calculations based on the realistic NN potentials below the π-threshold energy (the incident nucleon energy $E/A \leq 215$ MeV) [15].

(iii) Development of experimental techniques to obtain precision data for $3N$ scattering at intermediate energies ($E/A \approx 100$ MeV).

In the last decade the experimental studies of intermediate-energy pd and nd elastic scattering have been extensively performed by groups at RIKEN, KVI, RCNP, and IUCF providing precision data for cross sections and a variety of spin observables [17–21]. This is partly due to the fact that the first indication of $3N$F was pointed out [22, 23] in the elastic channel. A compilation of recent experiments for pd and nd elastic scattering at intermediate energies is shown in Fig. 1. It should be noted that the experimental study of dp scattering have been recently extended at the new facility of RIKEN RI beam factory (RIBF) [24] where polarized deuteron beams are available up to ~ 400 MeV/nucleon.

Complete dp breakup ($d + p \rightarrow p + p + n$) reactions would be more interesting because they cover different kinematic conditions. By selecting a particular kinematic configuration, one hopes to enhance the effects which are sensitive to specific components of $3N$Fs. Thus the study of dp breakup reactions has been in progress as the second step in investigating $3N$F dynamics [25–28].

The experiments for dp scattering at RIKEN [17, 27] are described in Section 2. The recent achievements in the study of $3N$Fs in intermediate-energy Nd scattering are discussed in Section 3. Section 4 presents a summary.

2 Experiment

The experiments at RIKEN have been performed with unpolarized/polarized deuteron beams. The observables we have obtained for elastic dp scattering are: **(i)** differential cross section $\frac{d\sigma}{d\Omega}$ at 70–135 MeV/nucleon, the angles in the center of mass system $\theta_{\mathrm{c.m.}} = 10^\circ - 180^\circ$; **(ii)** all deuteron analyzing powers (A_y^d, A_{yy}, A_{xx}, and A_{xz}) at 70–294 MeV/nucleon, $\theta_{\mathrm{c.m.}} = 10^\circ - 180^\circ$; **(iii)** deuteron-to-proton polarization transfer coefficients ($K_y^{y'}$, $K_{xx}^{y'} - K_{yy}^{y'}$, and $K_{xz}^{y'}$) at 135 MeV/nucleon, $\theta_{\mathrm{c.m.}} = 90^\circ - 180^\circ$. We also extended the measurement to the dp breakup reaction at 135 MeV/nucleon. Spin observables for specific kinematical conditions have been measured.

[1] Exceptions are the vector analyzing powers A_y and iT_{11} for pd elastic scattering.

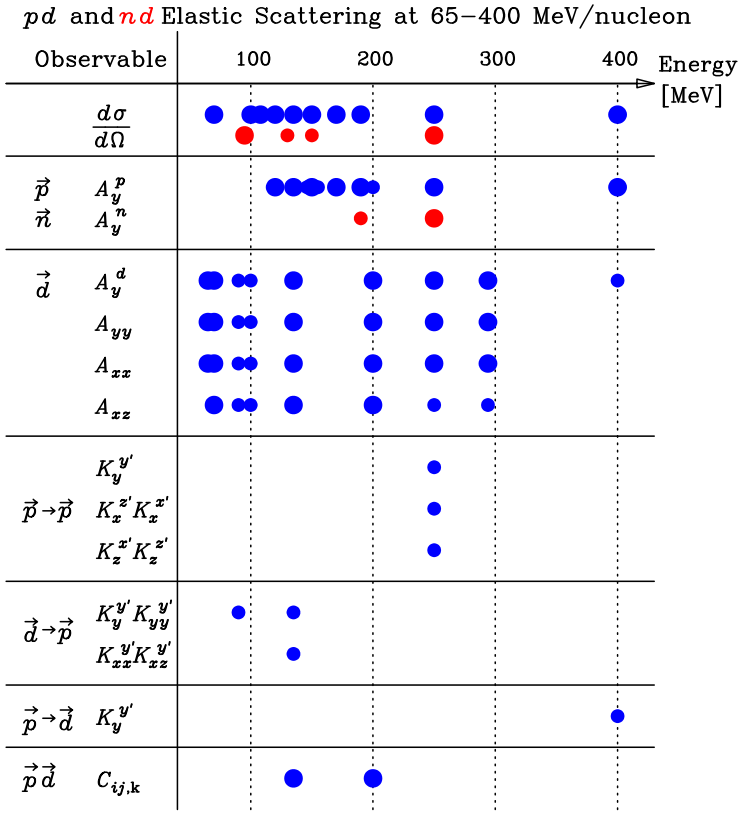

Figure 1: Compilation of recent experiments of *pd* and *nd* elastic scattering at 65–400 MeV/nucleon. Solid blue circles denote *pd* experiments and solid red circles denote *nd* experiments. The measurements with large circles cover a wide angular range while those with small circles cover a limited angular range.

A schematic view of the experimental setup is shown in Fig. 2. The vector and tensor polarized deuteron beams [29] accelerated by the cyclotrons bombarded a hydrogen target [liquid hydrogen or polyethylene (CH_2)]. Either the scattered deuteron or the recoil proton was momentum analyzed by the magnetic spectrograph SMART (Swinger and Magnetic Analyzer with Rotator and Twister) [30] depending on the scattering angle and detected at the focal plane. For the polarization transfer measurement, a double scattering experiment was performed to obtain the polarizations of elastically scattered protons from the hydrogen target [31]. One characteristic feature of the RIKEN polarized deuteron beams was that we could obtain beams which axis was controlled in an arbitrary direction on the target making it possible to obtain all the deuteron analyzing powers A_y^d, A_{yy}, A_{xx}, A_{xz}. The polarization axis of the deuteron beams was controlled by the spin rotator Wien Filter prior to acceleration [32]. Due to the single-turn extraction feature of the RIKEN cyclotrons the polarization amplitudes were maintained during acceleration. The beam polarizations were monitored with the beam line polarimeter by using the analyzing powers for *dp* elastic scattering. To obtain the absolute values of the deuteron beam polarizations, the analyzing powers for *dp* elastic scattering were calibrated by the $^{12}C(d,\alpha)^{10}B^*$ $[2^+]$ reaction which $A_{yy}\,(0^\circ)$ is exactly $-1/2$ because of parity conservation [33]. In all measurements the actual magnitudes of the polarizations were 60–80% of theoretical maximum values.

It was essential to obtain precise absolute values of the cross section to compare with the state-of-the-art Faddeev calculations. However, it is usually difficult to know experimentally the systematic uncertainty. We performed the cross section

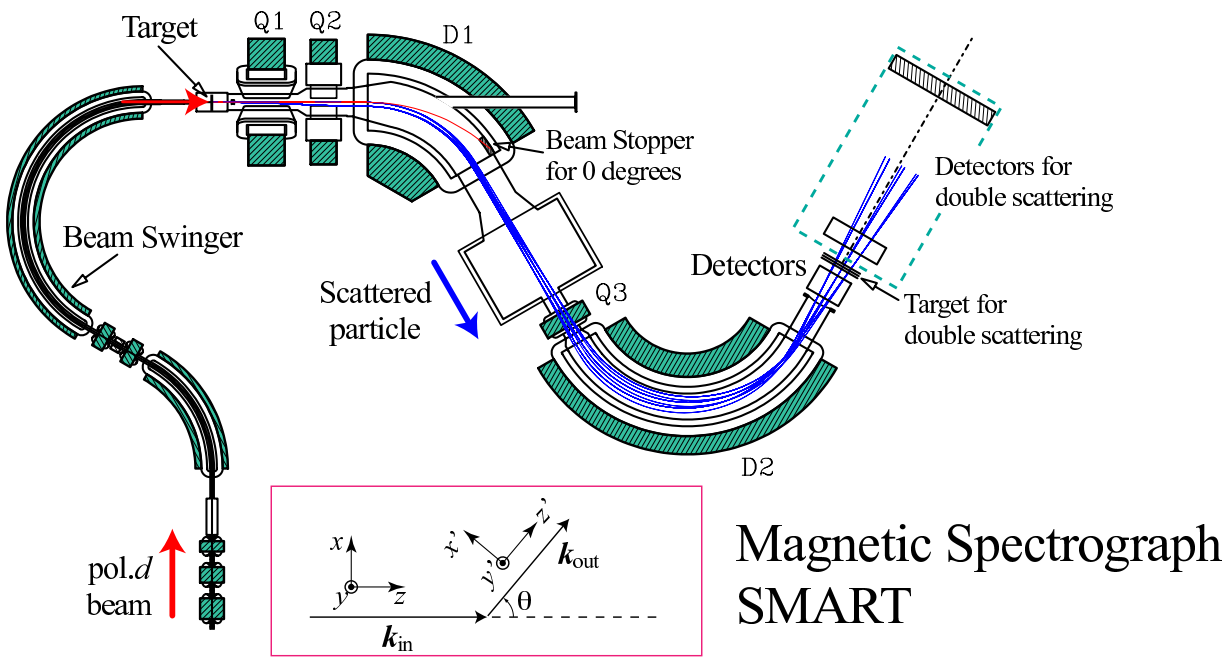

Figure 2: Schematic view of the experimental setup for the measurements of *dp* elastic and breakup reactions at RIKEN.

measurements with three different experimental techniques and tried to estimate the systematic uncertainties. First, we made a measurement at RIKEN with the proton beam at 135 MeV and a CD_2–CH_2 sandwiched solid target at the angles where the *pp* and *pd* elastic scattering were simultaneously measured with the magnetic spectrograph SMART. Using the well-known elastic *pp* cross sections we can estimate the overall systematic uncertainty for the *pd* cross section. Secondly, to confirm the angular distribution, we performed a measurement with 135 MeV/A deuterons, a CH_2 solid target, and the SMART system. In this measurement we tried to check the fluctuations of the target thickness during the experiment by measuring the *dp* scattering at the fixed angle $\theta_{\mathrm{c.m.}} = 69.7^\circ$ where the scattered deuterons and recoil protons were detected in coincidence in the scattering chamber. The cross section at $\theta_{\mathrm{c.m.}} = 165.1^\circ$ was measured for that same purpose with the SMART system several times during the experiment. We also measured the carbon background events. Finally, we performed a totally independent measurement at the Research Center for Nuclear Physics (RCNP) of Osaka University using a 135 MeV proton beam and deuterated polyethylene target. The absolute normalization of the cross sections has been performed by taking the data with a D_2 gas target and the double slit system for which the RCNP group has already established the procedure to obtain the absolute *pd* cross section [18]. A very good agreement between these independent measurements allows us to conclude that the systematic uncertainty due to the detection setup is small [17].

3 Results and discussion

Elastic Nd scattering

In Fig. 3 some representative experimental results for *pd* and *nd* elastic scattering are compared with the Faddeev calculations with and w/o 3*N*Fs. The red (blue) bands are the calculations with (without) TM′99 3*N*F [34] which is a version of the Tucson–Melbourne 3*N*F consistent with chiral symmetry [35, 36], based on modern NN potentials, i. e., CD Bonn, AV18, Nijmegen I and II. The solid lines are the calculations based on the AV18 potential with including the Urbana IX 3*N*F.

Note, so far the calculations with the next-to-next-to-leading order χEFT potential have been available for three-nucleon scattering [5] up to 100 MeV/nucleon. Since our discussion is on 3*N*F effects for higher energies ($\gtrsim$100 MeV/nucleon) we don't show the results on χEFT potentials here. The theoretical analysis for energies $\gtrsim$100 MeV/nucleon is now in progress [37].

For the cross section, specific features are seen depending on scattering angles in the center of mass system $\theta_{\mathrm{c.m.}}$. **(i)** At forward angles $\theta_{\mathrm{c.m.}} \lesssim 80^\circ$ where the direct processes by the NN interactions are dominant, the theoretical calculations based on various NN potentials are well converged and the predicted 3*N*F effects are very small. The experimental data are well described by the calculations except for the very forward angles. This discrepancy comes from that fact that the calculations shown in the figure do not take into account the Coulomb interaction between protons [38]. **(ii)** At middle angles $\theta_{\mathrm{c.m.}} \sim 80^\circ$–$140^\circ$ where the cross sections take minimum, the clear discrepancies between the data and the calculations based on the NN potentials are found. They become larger as the incident energy increases. The discrepancies are explained by taking into account the 2π exchange type 3*N*F models (TM′99 and Urbana IX). **(iii)** At backward angles $\theta_{\mathrm{c.m.}} \gtrsim 140^\circ$ where the exchange processes by the NN interactions are dominant, the differences begin to appear between the experimental data and the calculations even including the 3*N*F potentials with increasing the incident energy. Since this feature is clearly seen at higher energies, the relativistic effects have been estimated by using the Lorentz boosted NN potentials with the TM′99 [39]. However the relativistic effects have turned out to be small and only slightly alter the cross sections (see Fig. 4).

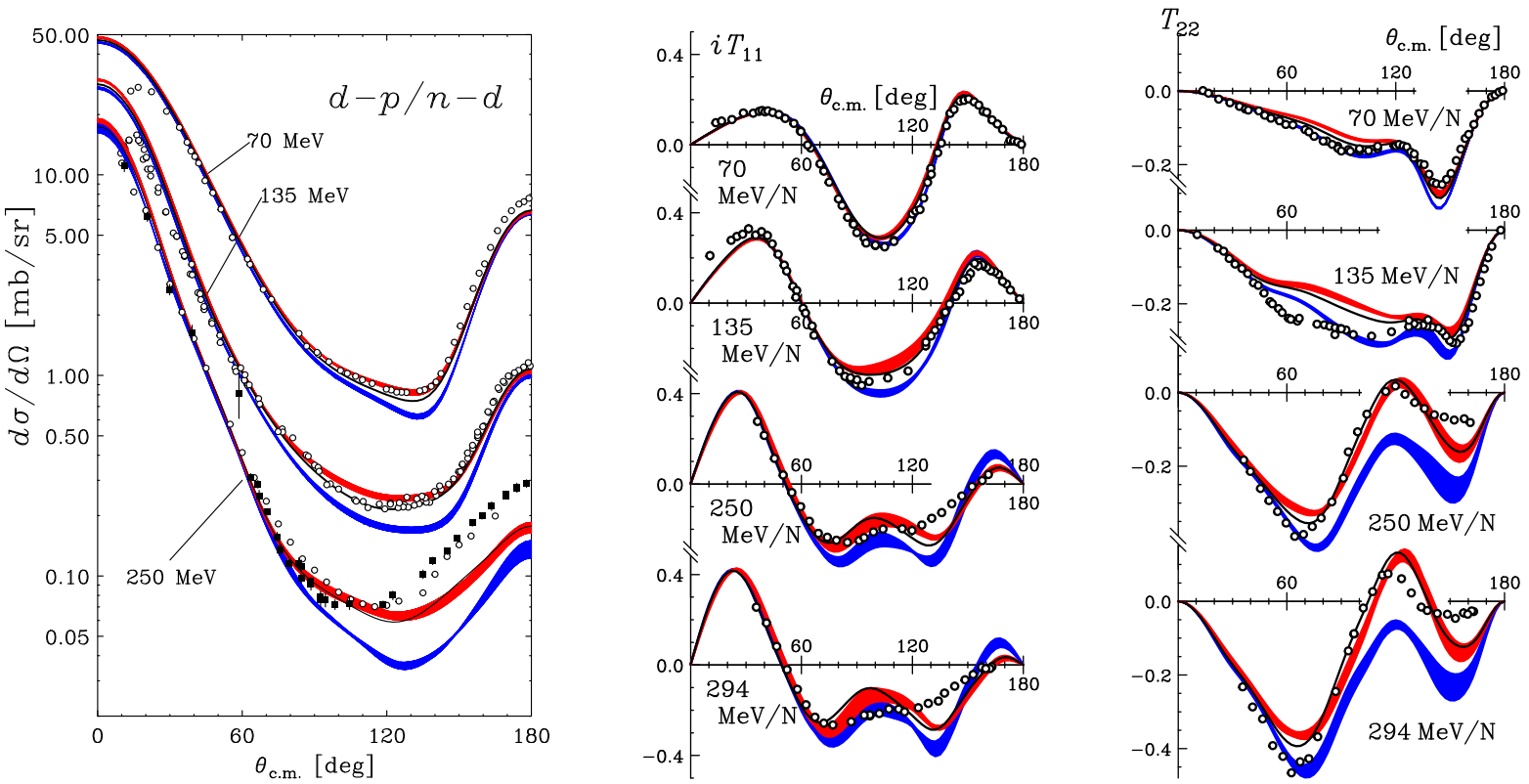

Figure 3: Differential cross sections and deuteron analyzing powers iT_{11}, T_{22} for elastic Nd scattering at 70–294 MeV/nucleon (MeV/N). The red (blue) bands are the calculations with (w/o) TM99 3NF based on the modern NN potentials, namely CD Bonn, AV18, Nijmegen I and II. The solid lines are the calculations with including Urbana IX 3NF based on AV18 potential. For the cross sections, the open circles are the data of Refs. [17]. The open squares and circles are the pd and nd data at 250 MeV/nucleon [18], respectively. For the deuteron analyzing powers, the data at 70 and 135 MeV/nucleon are from Refs. [17]. The data at 250 and 294 MeV/nucleon are taken at the RIBF [24].

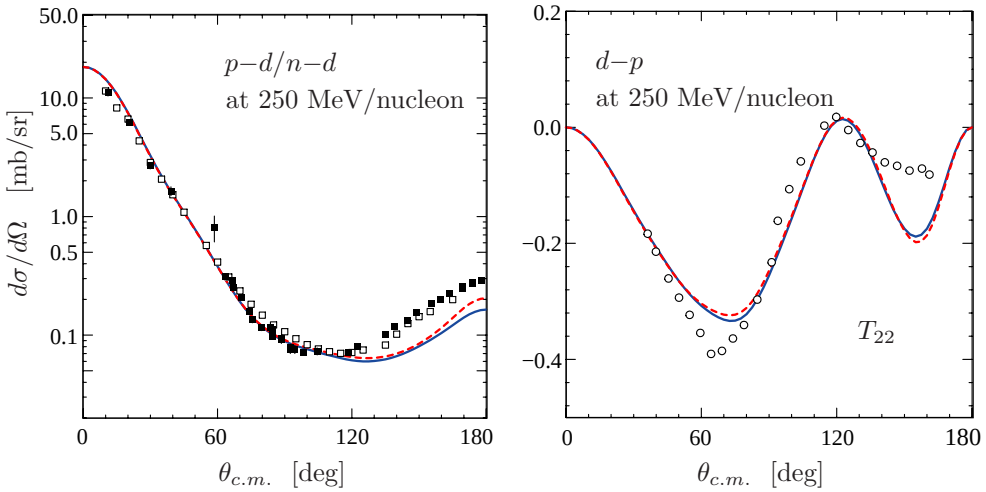

Figure 4: Differential cross section and the tensor analyzing power T_{22} for Nd elastic scattering at 250 MeV/nucleon. Faddeev calculations based on the CD Bonn potential with the TM′99 3NF are shown by blue solid lines. The calculations based on the Lorentz boosted NN potential with the 3NF are shown by red dashed lines.

As for the polarization observables, the energy dependence of the predicted 3NF effects and the difference between the theory and the data are not always similar to that of the cross section. The deuteron vector analyzing power iT_{11} has features similar to those of the cross section. Meanwhile the tensor analyzing power T_{22} reveals a different energy dependence from that of iT_{11}. Large 3NF effects are predicted starting from $\sim$100 MeV/nucleon. At 135 MeV/nucleon and below, adding 3NFs worsens the description of data in a large angular region. It is contrary to what happens at higher energies above 250 MeV/nucleon where large 3NF effects are supported by the T_{22} data. The relativistic effects are estimated to be small also for these polarization observables for Nd elastic scattering (see Fig. 4).

The results obtained for Nd elastic scattering draw the following conclusions: **(i)** the 3NF is definitely needed in Nd elastic scattering; **(ii)** the spin dependent parts of the 3NF may be deficient; **(iii)** the short-range components of the 3NF are probably required for backward scattering at higher energies.

Breakup Nd reactions

Studies in a large amount of kinematical configurations for the deuteron breakup reactions have been reported for the cross section as well as deuteron analyzing powers at the incident nucleon energy of 65 MeV/nucleon [25]. Generally the effects of 3NFs are predicted to be small at 65 MeV/nucleon, and the agreement to the data is good for all calculations both including and not including 3NFs. Focusing on particular kinematical configurations strong effects of the Coulomb interaction are found in the cross section.

The situation seems to change at higher energies $\gtrsim$100 MeV/nucleon. In recently reported relativistic Faddeev calculations with the TM′99 3NF, large relativistic effects are predicted in specific kinematical configurations [39]. For example, the agreement to the data for the polarization transfer coefficient $K_{yy}^{y'}$ at 135 MeV/nucleon is rather improved by taking into account the relativistic effects in the calculation with 3NF (see Fig. 5). The results of these new calculations suggest that the final explanation of the breakup reactions will be achieved when both two- and three-nucleon forces will be treated in the framework of relativistic Faddeev calculations.

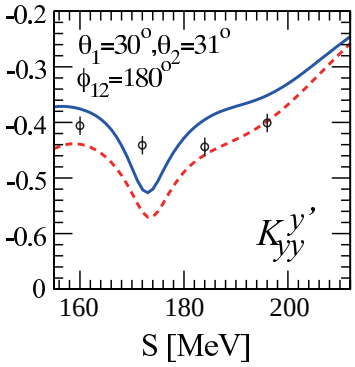

Figure 5: Polarization transfer coefficient $K_{yy}^{y'}$ for $^1\mathrm{H}(\vec{d},\vec{p}_1p_2)n$ at 135 MeV/nucleon shown as a function of S-curve arc-length. For descriptions of the calculations, see Fig. 4.

4 Summary

The 3NFs are now accepted as key elements in understanding various nuclear phenomena such as the binding of light mass nuclei and the equation of state for nuclear matter properties. The Nd scattering data provide rich sources to explore the properties of 3NFs such as momentum and spin dependences. In this talk the experiments performed with polarized deuteron beams at RIKEN are presented and recent achievements in the study of 3NFs in intermediate-energy Nd scattering are discussed.

In the last decade extensive experimental studies of pd and nd elastic scattering at intermediate energies ($E \gtrsim 100$ MeV) were performed at several facilities. The energy and angular dependent results for the cross section as well as the polarization observables show that **(i)** clear signatures of the 3NF effects are found in the cross section, **(ii)** the spin dependent parts of the 3NF may be deficient, and **(iii)** short-range components of the 3NF are probably required for description of backward scattering at higher energies.

Studies of pd breakup reactions ($p + d \to p + p + n$) followed as the second step in investigation of the 3NF dynamics. In the break up reactions at 65 MeV/nucleon in a wide range of kinematical configurations the 3NF effects are predicted to be small and the agreements to the data are generally good. At a higher energy of 135 MeV/nucleon, large 3NF effects as well as those of the relativity are predicted for some observables in relativistic Faddeev calculations recently reported. The calculations indicate that the establishment of 3NFs in the pd breakup reactions will be achieved when both two- and three-nucleon forces will be treated in the framework of relativistic Faddeev calculations.

As the next step of the 3NF study in few-nucleon scattering, it would be interesting to see how well the theoretical approaches, e. g., inclusion of 3NFs other than that of the 2π-exchange type and the potentials based on chiral effective field theory, describe these data. Experimentally, it is interesting to measure spin correlation coefficients as well as polarization transfer coefficients for elastic pd scattering at higher energies of 200–400 MeV/nucleon. Various kinematic configurations of the exclusive pd breakup reactions should also be measured in order to study the properties of 3NFs as well as relativistic effects. As a first step from few- to many-body systems, it is interesting to extend the measurements to 4N scattering systems, e. g., $p + ^3$He scattering, which would provide a valuable source of information on 3NFs including their isospin dependences.

Acknowledgments

The author would like to thank the collaborators for the experimental work performed with the polarized deuteron beams at RIKEN RI Beam Factory. She is also grateful to the strong supports from the theorists, H. Witała, W. Glöckle, H. Kamada, J. Golak, A. Nogga, R. Skibiński, P. U. Sauer, A. Deltuva, and A. C. Fonseca.

References

[1] J. Fujita and H. Miyazawa, Progr. Theor. Phys. **17**, 360 (1957).

[2] S. A. Coon and W. Glöckle, Phys. Rev. C **23**, 1790 (1981).

[3] B. S. Pudliner *et al.*, Phys. Rev. C **56**, 1720 (1997).

[4] U. van Kolck, Phys. Rev. C **49**, 2932 (1994).

[5] E. Epelbaum, H.-W. Hammer and U.-G. Meißner, Rev. Mod. Phys. **81**, 1773 (2009).

[6] C. R. Chen *et al.*, Phys. Rev. C **33**, 1740 (1986).

[7] T. Sasakawa and S. Ishikawa, Few-Body Syst. **1**, 3 (1986).

[8] R. B. Wiringa *et al.*, Phys. Rev. C **51**, 38 (1995).

[9] R. Machleidt, Phys. Rev. C **63**, 024001 (2001).

[10] V. G. J. Stoks *et al.*, Phys. Rev. C **49**, 2950 (1994).

[11] A. Nogga *et al.*, Phys. Rev. C **65**, 054003 (2002).

[12] S. C. Pieper *et al.*, Phys. Rev. C **66**, 044310 (2002).

[13] P. Navrátil and W. E. Ormand, Phys. Rev. C **68**, 034305 (2003).

[14] See, for example, A. Akmal *et al.*, Phys. Rev. C **58**, 1804 (1998).

[15] W. Glöckle, H. Witała, D. Hüber, H. Kamada and J. Golak, Phys. Rep. **274**, 107 (1996).

[16] A. Kievsky, M. Viviani and S. Rosati, Phys. Rev. C **64**, 024002 (2001).

[17] N. Sakamoto *et al.*, Phys. Lett. B **367**, 60 (1996); H. Sakai *et al.*, Phys. Rev. Lett. **84**, 5288 (2000); K. Sekiguchi *et al.*, Phys. Rev. C **65**, 034003 (2002); K. Sekiguchi *et al.*, *ibid.* **70**, 014001 (2004); K. Sekiguchi *et al.*, Phys. Rev. Lett **95**, 162301 (2005).

[18] K. Hatanaka *et al.*, Phys. Rev. C **66**, 044002 (2002); Y. Maeda *et al.*, *ibid.* **76**, 014004 (2007).

[19] R. Bieber *et al.*, Phys. Rev. Lett. **84**, 606 (2000); K. Ermisch *et al.*, *ibid.* **86**, 5862 (2001); K. Ermisch *et al.*, Phys. Rev. C **68**, 051001 (2003); K. Ermisch *et al.*, *ibid.* **71**, 064004 (2005); H. R. Amir-Ahmadi *et al.*, *ibid.* **75**, 041001 (2007); H. Mardanpour *et al.*, Eur. Phys. J. A **31**, 383 (2007).

[20] E. J. Stephenson *et al.*, Phys. Rev. C **60**, 061001 (1999); R. V. Cadman *et al.*, Phys. Rev. Lett. **86**, 967 (2001); B. v. Przewoski *et al.*, Phys. Rev. C **74**, 064003 (2006).

[21] P. Mermod *et al.*, Phys. Rev. C **72**, 061002 (2005).

[22] H. Witała *et al.*, Phys. Rev. Lett. **81**, 1183 (1998).

[23] S. Nemoto *et al.*, Phys. Rev. C **58**, 2599 (1998).

[24] K. Sekiguchi *et al.*, Phys. Rev. C **83**, 061001 (2011); K. Sekiguchi *et al.*, *ibid.* **89**, 064007 (2014).

[25] St. Kistryn *et al.*, Phys. Rev. C **68**, 054004 (2003); St. Kistryn *et al.*, *ibid.* **72**, 044006 (2005); St. Kistryn *et al.*, Phys. Lett. B **641**, 23 (2006); H. Mardanpour *et al.*, *ibid.* **687**, 149 (2010); E. Stephan *et al.*, Phys. Rev. C **82**, 014003 (2010).

[26] H. O. Meyer *et al.*, Phys. Rev. Lett. **93**, 112502 (2004).

[27] K. Sekiguchi *et al.*, Phys. Rev. C **79**, 054008 (2009).

[28] K. Sagara, Few-Body Syst. **48** 59 (2010).

[29] H. Okamura *et al.*, AIP Conf. Proc. **293**, 84 (1994).

[30] T. Ichihara *et al.*, Nucl. Phys. A **569**, 287c (1994).

[31] S. Ishida *et al.*, AIP Conf. Proc. **343**, 182 (1995).

[32] H. Okamura *et al.*, AIP Conf. Proc. **343**, 123 (1995).

[33] K. Suda *et al.*, Nucl. Instr. Meth. Phys. Res. A **572**, 745 (2007).

[34] S. A. Coon and H. K. Han, Few-Body Syst. **30**, 131 (2001).

[35] J. L. Friar *et al.*, Phys. Rev. C **59**, 53 (1999).

[36] D. Hüber *et al.*, Few-Body Syst. **30**, 95 (2001).

[37] E. Epelbaum, private communications.

[38] A. Deltuva *et al.*, Phys. Rev. C **71**, 054005 (2005).

[39] H. Witała *et al.*, Phys. Rev. C **83**, 044001 (2011); H. Witała *et al.*, *ibid.* **88**, 069904(E) (2013).

Chiral EFT and Nuclear Forces: Are We in Trouble?

R. Machleidt

Department of Physics, University of Idaho, Moscow, Idaho 83844, USA

Abstract

During the past two decades, chiral effective field theory has become a popular tool to derive nuclear forces from first principles. Two-, three-, and four-nucleon forces have been calculated up to next-to-next-to-next-to-leading order (N^3LO) and (partially) applied in nuclear few- and many-body systems — with, in general, a good deal of success. But in spite of these achievements, we are still faced with some great challenges. Among them is the issue of a proper renormalization of the two-nucleon potential, which is highly controversial in the community. Another issue are the subleading many-body forces, where we are faced with an "explosion" of the number of terms with increasing order that no practitioner can ever handle. I will comment on the current status and will provide hints for how to deal with it.

Keywords: *Low-energy QCD; chiral effective field theory; nucleon-nucleon scattering; few-nucleon forces*

1 Introduction

The problem of a proper derivation of nuclear forces is as old as nuclear physics itself, namely, almost 80 years [1]. The modern view is that, since the nuclear force is a manifestation of strong interactions, any serious derivation has to start from quantum chromodynamics (QCD). However, the well-known problem with QCD is that it is non-perturbative in the low-energy regime characteristic for nuclear physics. For many years this fact was perceived as the great obstacle for a derivation of nuclear forces from QCD — impossible to overcome except by lattice QCD.

The effective field theory (EFT) concept has shown the way out of this dilemma. For the development of an EFT, it is crucial to identify a separation of scales. In the hadron spectrum, a large gap between the masses of the pions and the masses of the vector mesons, like $\rho(770)$ and $\omega(782)$, can clearly be identified. Thus, it is natural to assume that the pion mass sets the soft scale, $Q \sim m_\pi$, and the rho mass the hard scale, $\Lambda_\chi \sim m_\rho \sim 1$ GeV, also known as the chiral-symmetry breaking scale. This is suggestive of considering a low-energy expansion arranged in terms of the soft scale over the hard scale, $(Q/\Lambda_\chi)^\nu$, where Q is generic for an external momentum (nucleon three-momentum or pion four-momentum) or a pion mass. The appropriate degrees of freedom are, obviously, pions and nucleons, and not quarks and gluons. To make sure that this EFT is not just another phenomenology, it must have a firm link with QCD. The link is established by having the EFT to observe all relevant symmetries of the underlying theory, in particular, the broken chiral symmetry of low-energy QCD [2].

The early applications of chiral perturbation theory (ChPT) focused on systems like $\pi\pi$ and πN, where the Goldstone-boson character of the pion guarantees that the

Proceedings of the International Conference 'Nuclear Theory in the Supercomputing Era — 2014' (NTSE-2014), Khabarovsk, Russia, June 23–27, 2014. Eds. A. M. Shirokov and A. I. Mazur. Pacific National University, Khabarovsk, Russia, 2016, p. 251.

http://www.ntse-2014.khb.ru/Proc/Machleidt.pdf.

expansion converges. But the past 20 years have also seen great progress in applying ChPT to nuclear forces (see Refs. [3,4] for recent reviews and find comprehensive lists of references therein). As a result, nucleon-nucleon (NN) potentials of high precision have been constructed, which are based upon ChPT carried to next-to-next-to-next-to-leading order ($\mathrm{N^3LO}$) [5,6], and applied in nuclear structure calculations with great success.

However, in spite of this progress, we are not done. Due to the complexity of the nuclear force issue, there are still many subtle and not so subtle open problems. We will not list and discuss all of them, but just mention two, which we perceive as the most important ones:

- The proper renormalization of chiral nuclear potentials and
- Subleading chiral few-nucleon forces.

I discussed the renormalization issue in my contribution to the NTSE-2013 [7], where the interested reader will also find a broad introduction into the topic of nuclear interactions. In this contribution, I will focus on nuclear many-body forces.

2 The chiral NN potential

In terms of naive dimensional analysis or "Weinberg counting", the various orders of the low-energy expansion which define the chiral NN potential, are given by:

$$V_{\rm LO} = V_{\rm ct}^{(0)} + V_{1\pi}^{(0)}, \tag{1}$$

$$V_{\rm NLO} = V_{\rm LO} + V_{\rm ct}^{(2)} + V_{1\pi}^{(2)} + V_{2\pi}^{(2)}, \tag{2}$$

$$V_{\rm NNLO} = V_{\rm NLO} + V_{1\pi}^{(3)} + V_{2\pi}^{(3)}, \tag{3}$$

$$V_{\rm N^3LO} = V_{\rm NNLO} + V_{\rm ct}^{(4)} + V_{1\pi}^{(4)} + V_{2\pi}^{(4)} + V_{3\pi}^{(4)}, \tag{4}$$

where the superscript denotes the order ν of the expansion. LO stands for leading order, NLO for next-to-leading order, etc. Contact potentials carry the subscript "ct" and pion-exchange potentials can be identified by an obvious subscript.

NN potentials have been constructed at all of the above orders, and it has been shown [5] that at $\mathrm{N^3LO}$ the precision is finally achieved, which is necessary and sufficient for reliable applications in *ab initio* nuclear structure calculations. Thus, the NN problem appears to be under control, at least for the time being.

3 Nuclear many-body forces

The chiral two-nucleon force (2NF) at $\mathrm{N^3LO}$ has been applied in microscopic calculations of nuclear structure with, in general, a great deal of success. However, from high-precision studies conducted in the 1990s, it is well-known that certain few-nucleon reactions and nuclear structure issues require three-nucleon forces (3NFs) for their microscopic explanation. Outstanding examples are the A_y puzzle of N-d scattering and the ground state of ^{10}B. *An important advantage of the EFT approach to nuclear forces is that it creates two- and many-nucleon forces on an equal footing.* In this section, I will now explain in some detail those chiral three- and four-nucleon forces.

3.1 Three-nucleon forces

The order of a 3NF is given by

$$\nu = 2 + 2L + \sum_i \Delta_i \,, \tag{5}$$

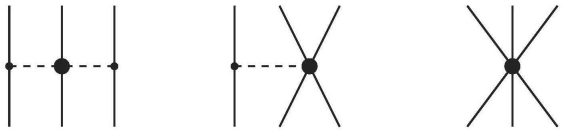

Figure 1: The three-nucleon force at NNLO. From left to right: 2PE, 1PE, and contact diagrams. Solid lines represent nucleons and dashed lines pions. Small solid dots denote vertices of index $\Delta_i = 0$ and large solid dots are $\Delta_i = 1$.

where L denotes the number of loops and Δ_i is the vertex index. We will use this formula to analyze 3NF contributions order by order.

3.1.1 Next-to-leading order.

The lowest possible power is obviously $\nu = 2$ (NLO), which is obtained for no loops ($L = 0$) and only leading vertices ($\sum_i \Delta_i = 0$). As it turns out, the contribution from these NLO diagrams vanishes. So, the bottom line is that there is no genuine 3NF at NLO. The first non-vanishing 3NF appears at NNLO.

3.1.2 Next-to-next-to-leading order.

The power $\nu = 3$ (NNLO) is obtained when there are no loops ($L = 0$) and $\sum_i \Delta_i = 1$; i.e., $\Delta_i = 1$ for one vertex while $\Delta_i = 0$ for all other vertices. There are three topologies which fulfill this condition, known as the two-pion exchange (2PE), one-pion exchange (1PE), and contact graphs (Fig. 1).

The 1PE and contact 3NF terms involve each a new parameter, which are commonly denoted by D and E and which do not appear in the 2N problem. There are many ways to pin these two parameters down. The triton binding energy and the nd doublet scattering length ${}^2a_{nd}$ have been used for this purpose. But one may also choose the binding energies of ^{3}H and ^{4}He, an optimal over-all fit of the properties of light nuclei, or electroweak processes like the tritium β decay. Once D and E are fixed, the results for other 3N, 4N, etc. observables are predictions.

The 3NF at NNLO has been applied in calculations of few-nucleon reactions, structure of light- and medium-mass nuclei [8,9], and nuclear and neutron matter [10–12] with a good deal of success. Yet, the famous 'A_y puzzle' of nucleon-deuteron scattering is not resolved. When only 2NFs are applied, the analyzing power in p-^{3}He scattering is even more underpredicted than in p-d. However, when the NNLO 3NF is added, the p-^{3}He A_y substantially improves (more than in p-d) [13] — but a discrepancy remains. Furthermore, the spectra of light nuclei leave room for improvement.

To summarize, the 3NF at NNLO is a remarkable contribution: It represents the leading many-body force within the scheme of ChPT; it includes terms that were advocated already some 50 years ago; and it produces noticeable improvements in few-nucleon reactions and the structure of light nuclei. But unresolved problems remain. Moreover, in the case of the 2NF, we have pointed out that one has to proceed to N^{3}LO to achieve sufficient accuracy. Therefore, the 3NF at subleading order is needed for at least two reasons: for consistency with the 2NF and to hopefully resolve outstanding problems in microscopic nuclear structure and reactions.

3.1.3 Next-to-next-to-next-to-leading order.

At N^{3}LO, there are loop and tree diagrams. For the loops (Fig. 2), we have $L = 1$ and, therefore, all Δ_i have to be zero to ensure $\nu = 4$. Thus, these one-loop 3NF diagrams can include only leading order vertices, the parameters of which are fixed from πN and NN analysis. The long-range part of the chiral N^{3}LO 3NF has been tested in the triton [14] and in three-nucleon scattering [15] yielding only moderate effects and

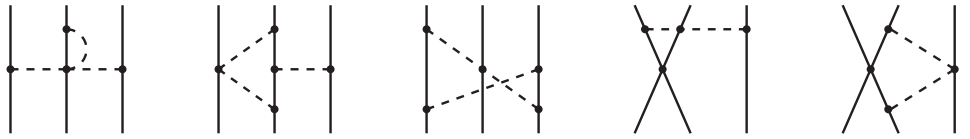

(a) (b) (c) (d) (e)

Figure 2: Leading one-loop 3NF diagrams at N^{3}LO. We show one representative example for each of five topologies, which are: (a) 2PE, (b) 1PE-2PE, (c) ring, (d) contact-1PE, (e) contact-2PE. Notation as in Fig. 1.

no improvement of the A_y puzzle. The long- and short-range parts of this force have been used in neutron matter calculations (together with the N^{3}LO 4NF) producing surprisingly large contributions from the 3NF [16]. Thus, the ultimate assessment of the N^{3}LO 3NF is still outstanding and will require more few- and many-body applications. But we expect that, overall, the 3NF at N^{3}LO is small and will most likely not solve the outstanding problems.

3.1.4 The 3NF at N^{4}LO.

Because the 3NF at N^{3}LO is presumably small, it is necessary to move on to the next order of 3NFs, which is N^{4}LO or $\nu = 5$ (of the Δ-less theory which we have silently assumed so far). The loop contributions that occur at this order are obtained by replacing in the N^{3}LO loops one vertex by a $\Delta_i = 1$ vertex (with LEC c_i), Fig. 3, which is why these loops may be more sizable than the N^{3}LO loops. The 2PE, 1PE-2PE, and ring topologies have been evaluated [17]. Note that each diagram in Fig. 3 stands symbolically for a group of diagrams. We demonstrate this for the 1PE-2PE topology, for which we display in Fig. 4 all diagrams for that topology. This applies to each topology and, thus, provides an idea of the "explosion" of 3NF contributions at subleading orders.

In addition to the loops, we have at N^{4}LO three 'tree' topologies (Fig. 5), which include a new set of 3N contact interactions, which have recently been derived by the Pisa group [18]. Contact terms are typically simple (as compared to loop diagrams) and their coefficients are essentially free. Therefore, it would be an attractive project to test some terms (in particular, the spin-orbit terms) of the N^{4}LO contact 3NF [18] in calculations of few-body reactions (specifically, the p-d and p-^{3}He A_y) and spectra of light nuclei.

3.2 Four-nucleon forces

For four-nucleon forces (4NFs), the power is given by

$$\nu = 4 + 2L + \sum_i \Delta_i \,. \tag{6}$$

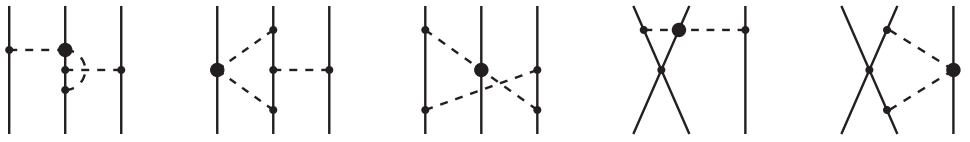

(a) (b) (c) (d) (e)

Figure 3: Sub-leading one-loop 3NF diagrams which appear at N^{4}LO. We show one representative example for each of five topologies, which are: (a) 2PE, (b) 1PE-2PE, (c) ring, (d) contact-1PE, (e) contact-2PE. Notation as in Fig. 1.

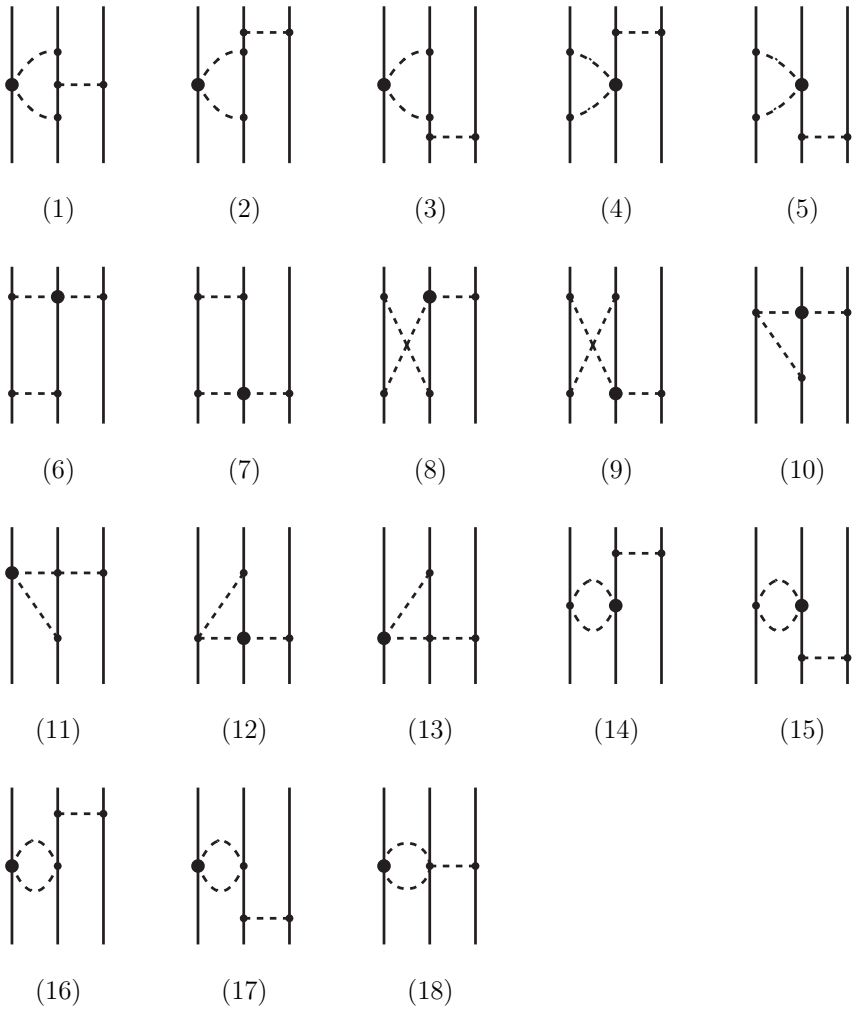

Figure 4: The topology (b) of Fig. 3 (1PE-2PE) in detail. Notation as in Fig. 1.

Therefore, a 4NF appears for the first time at $\nu = 4$ (N^3LO), with no loops and only leading vertices, Fig. 6. This 4NF includes no new parameters and does not vanish [19]. It has been applied in a calculation of the ^{4}He binding energy, where it was found to contribute a few 100 keV [20]. It should be noted that this preliminary calculation involves many approximations, but it provides an idea of the order of magnitude of the 4NF, which is indeed small as compared to the full ^{4}He binding energy of 28.3 MeV.

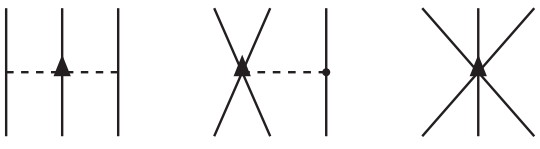

Figure 5: 3NF tree graphs at N^4LO ($\nu = 5$) denoted by: (a) 2PE, (b) 1PE-contact, and (c) contact. Solid triangles represent vertices of index $\Delta_i = 3$. Other notation as in Fig. 1.

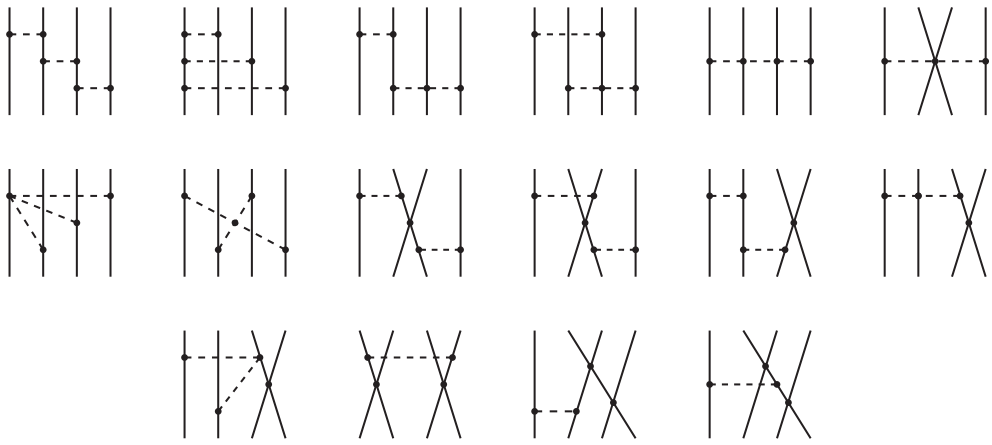

Figure 6: Leading four-nucleon force at N^{3}LO.

4 Conclusions

The past 20 years have seen great progress in our understanding of nuclear forces in terms of low-energy QCD. Key to this development was the realization that low-energy QCD is equivalent to an effective field theory (EFT) which allows for a perturbative expansion that has become known as chiral perturbation theory (ChPT). In this framework, two- and many-body forces emerge on an equal footing and the empirical fact that nuclear many-body forces are substantially weaker than the two-nucleon force is explained naturally.

In this contribution, I have focused mainly on nuclear many-body forces based upon chiral EFT. The 3NF at NNLO has been known for a while and applied in few-nucleon reactions, structure of light- and medium-mass nuclei, and nuclear and neutron matter with some success. However, the famous 'A_y puzzle' of nucleon-deuteron scattering is not resolved by the 3NF at NNLO. Thus, one important open issue are the few-nucleon forces beyond NNLO ("sub-leading few-nucleon forces") which, besides the A_y puzzle, may also resolve some important outstanding nuclear structure problems. As explained, this may require going even beyond N^{3}LO. However, as demonstrated, with each higher order, the number of diagrams increases enormously. Thus, practitioners are faced with the problem of how to deal with this explosion of 3NF contributions. My advice is that, for a while, one should not aim at complete calculations at given higher orders. Rather one will have to be selective and try to identify the more important 3NF terms in the "forrest" of diagrams. The N^{4}LO 3NF contact terms [Fig. 5(c)] [18] are a promising and manageable starting point.

Finally, let me note that, because of lack of space, I have discussed here only the so-called Δ-less version of ChPT. There is also the Δ-full version (see Ref. [3] for details), in which the number of diagrams is even larger.

This work was supported by the US Department of Energy under Grant No. DE-FG02-03ER41270.

References

[1] R. Machleidt, Adv. Nucl. Phys. **19**, 189 (1989).

[2] S. Weinberg, Physica A **96**, 327 (1979).

[3] R. Machleidt and D. R. Entem, Phys. Rep. **503**, 1 (2011).

[4] E. Epelbaum, H.-W. Hammer and U.-G. Meißner, Rev. Mod. Phys. **81**, 1773 (2009).

[5] D. R. Entem and R. Machleidt, Phys. Rev. C **68**, 041001 (2003).

[6] E. Epelbaum, W. Glöckle and U.-G. Meißner, Nucl. Phys. A **747**, 362 (2005).

[7] R. Machleidt, in *Proc. Int. Conf. Nucl. Theor. Supercomputing Era (NTSE-2013), Ames, IA, USA, May 13–17, 2013*, eds. A. M. Shirokov and A. I. Mazur. Pacific National University, Khabarovsk, Russia, 2014, p. 336, http://ntse-2013.khb.ru/Proc/Machleidt.pdf.

[8] G. Hagen, M. Hjorth-Jensen, G. R. Jansen, R. Machleidt and T. Papenbrock, Phys. Rev. Lett. **108**, 242501 (2012).

[9] G. Hagen, M. Hjorth-Jensen, G. R. Jansen, R. Machleidt and T. Papenbrock, Phys. Rev. Lett. **109**, 032502 (2012).

[10] F. Sammarruca, B. Chen, L. Coraggio, N. Itaco and R. Machleidt, Phys. Rev. C **86**, 054317 (2013).

[11] L. Coraggio, J. W. Holt, N. Itaco, R. Machleidt and F. Sammarruca, Phys. Rev. C **87**, 014322 (2013).

[12] L. Coraggio, J. W. Holt, N. Itaco, R. Machleidt, L. E. Marcucci and F. Sammarruca, Phys. Rev. C **89**, 044321 (2014).

[13] M. Viviani, L. Giarlanda, A. Kievsky and L. E. Marcucci, Phys. Rev. Lett. **111**, 172302 (2013).

[14] R. Skibiński *et al.*, Phys. Rev. C **84**, 054005 (2011).

[15] H. Witała *et al.*, Few-Body Syst. **54**, 897 (2013).

[16] I. Tews, T. Krüger, K. Hebeler and A. Schwenk, Phys. Rev. Lett. **110**, 032504 (2013).

[17] H. Krebs, A. Gasparyan and E. Epelbaum, Phys. Rev. C **85**, 054006 (2012); *ibid.* **87**, 054007 (2013).

[18] L. Girlanda, A. Kievsky and M. Viviani, Phys. Rev. C **84**, 014001 (2011).

[19] E. Epelbaum, Eur. Phys. J. A **34**, 197 (2007).

[20] D. Rozpedzik *et al.*, Acta Phys. Polon. B **37**, 2889 (2006).

List of participants

- **Takashi Abe**, University of Tokyo, Japan
- **Maxim Aleshin**, Pacific National University, Russia
- **Denis Avdeev**, Pacific National University, Russia
- **Leonid Blokhintsev**, Moscow State University, Russia
- **Sergey Burkov**, Pacific National University, Russia
- **Andrey Chibisov**, Computational Center, Russian Academy of Sciences, Khabarovsk, Russia
- **Kirill Drachev**, Pacific National University, Russia
- **Tomáš Dytrych**, Louisiana State University, USA
- **Charlotte Elster**, Ohio University, USA
- **Evgeny Epelbaum**, University of Bochum, Germany
- **Sergey Ivanchenko**, Pacific National University, Russia
- **Nikolay Khokhlov**, Komsomolsk-on-Amur State Technical University, Russia
- **Youngman Kim**, Institute for Basic Science, South Korea
- **Konstantin Kouzakov**, Moscow State University, Russia
- **Ruprecht Machleidt**, University of Idaho, USA
- **Andrey Maslov**, Pacific National University, Russia
- **Nikolay Mazanik**, Pacific National University, Russia
- **Alexander Mazur**, Pacific National University, Russia
- **Evgeny Mazur**, Pacific National University, Russia
- **Igor Mazur**, Pacific National University, Russia
- **Alexander Motovilov**, Joint Institute for Nuclear Research, Russia
- **Takashi Nakatsukasa**, University of Tsukuba, Japan
- **Junchen Pei**, Peking University, China
- **Egor Proskuryakov**, Pacific National University, Russia
- **Kimiko Sekiguchi**, Tohoku University, Japan

- **Ik Jae Shin**, Institute for Basic Science, South Korea
- **Andrey Shirokov**, Moscow State University, Russia
- **Yurii Tchuvil'sky**, Moscow State University, Russia
- **Jun Terasaki**, University of Tsukuba, Japan
- **Yutaka Utsuno**, Japan Atomic Energy Agency, Japan
- **James Vary**, Iowa State University, USA
- **Alexander Volya**, Florida State University, USA
- **Furong Xu**, Peking University, China
- **Kazuhiro Yabana**, University of Tsukuba, Japan
- **Sergey Yurev**, Far Eastern Federal University, Russia
- **Sergey Zaytsev**, Pacific National University, Russia

NUCLEAR THEORY IN THE SUPERCOMPUTING ERA – 2014 (NTSE-2014)

International Conference Proceedings

Khabarovsk, Russia
June 23–27, 2014

Printing date: 07.09.16. Format 70x108 1/16.
Writing paper. "Computer modern" font. Digital printing.
Quire 22,15. Number of copies 60. Order number 216.

Publisher: Pacific National University,
136 Tikhookeanskaya street, Khabarovsk 680035, Russia.